CRANFIELD UNIVERSITY

Hasani Azamar Aguirre

Analytical Transonic Flow Simulation in Streamline Curvature Methods for Axial-Flow Compressor Design

SCHOOL OF AEROSPACE, TRANSPORT AND MANUFACTURING
Centre for Propulsion

Full time PhD
PhD Thesis
Academic Year: 2018

Supervised by: Prof. Vassilios Pachidis
March 2018

CRANFIELD UNIVERSITY

SCHOOL OF AEROSPACE, TRANSPORT AND MANUFACTURING
Centre for Propulsion

Full Time PhD
PhD Thesis

Academic Year 2018

Hasani Azamar Aguirre

Analytical Transonic Flow Simulation in Streamline Curvature Methods for Axial-Flow Compressor Design

Supervisor: Prof. Vassilios Pachidis
March 2018

© Cranfield University 2018. All rights reserved. No part of this publication may be reproduced without the written permission of the copyright owner.

To invent an airplane is nothing. To build one is something. But to fly is everything.

Otto Lilienthal

To my father Bernardo and my mother Cristina

EXECUTIVE SUMMARY

Aircraft gas-turbine engine component design and analysis is still a pleasant art to be further explored to satisfy the optimum engineering limits. One of the challenges for aero-engines is to provide high efficiencies while being light and compact. As a responding solution for these requisites, modern axial-flow transonic fans and compressors provide high shock-induced single-stage pressure ratios, reducing weight and size. The problem becomes thus to attain this within acceptable isentropic efficiencies and working ranges, at least comparable to those from the subsonic axial-flow compressors.

The constant and crescent demand to obtain more accurate turbomachinery blading performance in the analysis and design process has led the designer to explore different levels of simulation fidelities and optimisation strategies. The extensive use of Computational Fluid Dynamics (CFD) methods in aerodynamics has made the three-dimensional (3-D) Reynolds-averaged Navier-Stokes (RANS) numerical simulations the preferred technique for turbomachinery analysis. Despite their high-order resolution and extensive flow field information that can be collected, it comes at intolerably high computational costs in terms of time and resources, especially if they are used as solvers within an optimisation framework. In contrast, two-dimensional (2-D) through-flow methods such as streamline curvature (SLC), keystone in the turbomachinery design, provide a rapid flow solution whilst offering accurate results.

In the context of transonic axial-flow fans and compressors, previous 2-D SLC tools have failed to replicate the real physics related to compressible flow. More specifically, the prediction of the highly-complex shock-system shape and location for an accurate estimation of shock-associated losses has always been assumed and oversimplified. The situation aggravates, when the assumed overall shock configuration applies only for design point at unstarted operations, requiring of empirical correlations to estimate the shock-loss coefficient for off-design operations. The overall performance prediction of the fan and compressor is thereby highly-dependant on the shock modelling quality.

For this reason, an analytical transonic-flow simulation package was developed and implemented into an existing in-house 2-D SLC compressor performance simulator

with the aim of enhancing the aerodynamic prediction for transonic axial-flow fans and compressors. The novel toolkit to handle transonic flow and fully coupled to the 2-D SLC software consists of the following contributions: (1) a 3-D blade-element-layout method; (2) an adaptation of the full radial-equilibrium equation (REE) to handle the effects of 3-D blade shaping; (3) a physics-based shock- structure and loss model for unstarted and started operations that uses an iterative-solution method to locate the choke-induced passage-shock; (4) a choking mass flow redistribution model.

In this way, shock losses were determined throughout the blade span and for various off-design operating conditions, including those at choking, where the mass flow was limited and redistributed spanwise according to the unique incidence. 2-D SLC simulations were conducted for the NASA Rotor 67 and the NASA Advanced Duct Propulsor (ADP) Fan to calibrate and validate the models accordingly against experimental rig-test data and 3-D CFD results. The analytical shock- loss and structure model improved the shock-loss prediction between 40-50% with respect of the state-of-the-art models, and showed satisfactory agreement against measured data within 0.6% at the blade tip and 0.3% at mid-span sections. A parametric study was conducted for the NASA Rotor 67 to demonstrate design trends when varying 2-D and 3-D blade-element parameters utilizing the transonic-flow toolkit in its entirety, evidencing the impact on the shock-loss radial distribution.

A new cutting-edge variable-pitch fan (VPF) was designed using the NASA ADP Fan 2-D SLC model, which was further optimised using an evolutionary genetic algorithm (EGA) to demonstrate the application of the novel transonic-flow package. The single-objective optimisation consisted in the variation of sweep and lean angles with the purpose of studying the pure influence of shock losses on the overall isentropic efficiency. The optimised geometry resulted in a backward-swept and mostly pressure-side leaned VPF that incremented the isentropic efficiency by 0.4% with respect of the baseline configuration.

Keywords:

Blade, Choking, Compressor, Fan, Streamline Curvature, Shock Losses, Shock Waves, Throughflow, Transonic

ACKNOWLEDGEMENTS

This is probably the hardest section to write, for which the whole page or even a thousand pages would not be enough to thank and express my most genuinely gratitude to those that supported the completion of this PhD work.

Undoubtedly, this research and thesis itself would have not been possible without the continuous supervision and technical support from my supervisor Prof. Vassilios Pachidis. I feel honoured and pleased to have had him as a tutor and want to thank him for the opportunity given to start these doctoral studies. His guidance, knowledge, and patience motivated me every time throughout the three-year journey of the PhD programme. I hereby express my most sincere acknowledgement and recognition to his immense expertise, where this thesis is just a small reflection of his clinical eye to address every engineering detail. Besides being an academic mentor, he became a colleague and a very true friend, from whom I learned a lot in each of his facets. Meeting him as a friend increased my admiration and respect for him, expecting that I gave in return at least a little in comparison to the immeasurable he gave me.

A backbone for the development and continuous enhancement of this research was Prof. Ioannis Templalexis. I was fortunate in meeting and collaborating with him, where his critical inputs made a significant difference for the contributions presented herein. I had the pleasure as well to meet him as a friend, to whom all my recognition goes.

The present PhD thesis is dedicated to my dad from the first to the last word, who gave all his effort and life for me being here writing this. I know that wherever my dad is, he is considering this little dedication in comparison to all the teachings and unconditional endeavour he put on me. It is challenging to express in words how much work my dad did for me to come and study a PhD abroad, supporting me anytime, in any way and I still truly believe that anywhere. Describing how my dad helped me to start and carry on with the doctorate studies would definitely be lengthier than this document. Even during this thesis writing-up my dad was still present every day. Had I known that I was going to lose my dad during my PhD, I would have never come so far from him; but of course, the future is still unpredictable. I just hope all the missed opportunities to tell how much I need, admire, and love him pay off.

Infinite apologies and endless words of love would not suffice to say sorry to my mom, for all the days that I could not to talk to her for being working. My boundless thankfulness to my mom for being there every time I needed her, for listening to me, and for giving me very wise life advices. She understood all my frustrations, whilst motivating me and encouraging me to continue throughout this tough journey. The life-changing events have shown me a very strong, dedicated and determined woman, from whom I am still learning and I think I would never finish learning from her. The reason for being here writing this PhD thesis is undoubtedly because of her, as she was the cornerstone of my education since I was a child. Thank you mom for tolerating me in every way, I expect to be one day at least a piece of what you are. Through this little text I want to express and demonstrate to my mom, the uncountable love and admiration I have for her.

I had the pleasure if not the blessing of meeting Nithya Subramanian at the early stage of my PhD. Through almost three years, she has become an integral part of my academic and personal life. Without her unconditional presence and love, I would definitely not being here. During all my PhD reviews and for every single day she was there to unconditionally help me regardless of the day and time. I would definitely not understand my PhD life without her since she became an essential component in every aspect. Thank you Nithya for your incalculable patience and for standing by me whenever I needed you. My most deep and sincere love goes to her.

I also want to thank to the Centre of Propulsion staff, Prof. Pilidis, Dr. Sethi and Dr. Nalianda for their academic support and friendly advices.

I would also like to acknowledge all the MSc and visiting students who directly or indirectly supported this work. Particularly Marina Gonzalez, whose work contributed substantially for the early initiation of this research.

Finally, I want to thank the government of Mexico for funding these research studies and punctual participation though the CONACYT and SEP organizations.

TABLE OF CONTENTS

EXECUTIVE SUMMARY i
ACKNOWLEDGEMENTS iii
LIST OF FIGURES viii
LIST OF TABLES xix
NOMENCLATURE xx
1 INTRODUCTION 1
1.1 Background 1
1.2 Transonic Axial-Flow Compressors 2
1.3 Turbomachinery Flow Simulation 5
1.4 Blading Shock-Wave Structures 7
1.5 Project Scope, Aims and Objectives 9
1.6 Knowledge Contribution 10
1.7 Thesis Structure 11
2 LITERATURE REVIEW 14
2.1 Introduction 14
2.2 Transonic Axial-Flow Compressors 15
2.2.1 Transonic Rotor Operation 15
2.2.2 Blading Flow Field Losses 20
2.2.3 Blade profile studies 24
2.2.4 Three-Dimensional Blading 27
2.3 Turbomachinery Flow Simulation 36
2.3.1 Background 36
2.3.2 Streamline Curvature Methods 40
2.4 High-Speed Compressible Flow Aerodynamics 59
2.4.1 Normal Shock Waves 59
2.4.2 Oblique Shock Waves 62
2.4.3 Detached Shock Waves 64
2.4.4 Prandtl-Meyer Expansion 70
2.5 Choking 72
2.5.1 One-Dimensional Isentropic Flow 72
2.5.2 Convergent-Divergent Nozzle 76
2.5.3 Area-Velocity Relationship 81
2.6 Shock Waves in Transonic Compressors 84
2.6.1 Overview 84
2.6.2 Flow Description 87
2.6.3 Shock Losses 91
2.6.4 Shock Loss Models 94
2.6.5 Empirical Shock-Loss Models 110
2.7 Transonic Axial-flow Compressor Blading Choking 115

2.7.1 Loss-Incidence Relation 115
2.7.2 Blade-Passage Choking Models 117
2.8 Summary 121
3 METHODOLOGY 124
3.1 Introduction 124
3.2 Compressor Blade Modelling 126
3.2.1 Overview 126
3.2.2 Blade-Element-Layout Method Definition 127
3.2.3 Streamline Curvature Modification 141
3.3 Shock- Structure and Loss Model 143
3.3.1 Overview 143
3.3.2 Subsonic Supercritical Conditions 146
3.3.3 Supersonic Flow Description 149
3.3.4 Detached Bow-Shock 154
3.3.5 Bow-Wave Losses 165
3.3.6 Passage-Shock Location 168
3.3.7 Flow Expansion 172
3.3.8 Passage-Shock Losses 186
3.3.9 Iterative Method for Started-Flow Shock Configurations 191
3.4 Choking Mass Flow Redistribution 200
3.4.1 Overview 200
3.4.2 Choking Incidence 202
3.4.3 Choking Margin 206
3.4.4 Mass Flow Redistribution 211
3.5 Summary 214
4 VALIDATION & VERIFICATION 217
4.1 Introduction 217
4.2 2-D SLC NASA Rotor 67 Validation 217
4.2.1 Model Generation 217
4.2.2 Model Validation 218
4.3 2-D SLC NASA ADP Fan Validation 223
4.3.1 Model Generation 223
4.3.2 Model Validation 224
4.3.3 Model Generation 228
4.4 Choking Model Verification 230
4.4.1 Choke Condition 230
4.4.2 Mass Flow Redistribution 236
4.5 Shock-Loss Model Validation and Verification 239
4.5.1 Design Shock-Losses 239
4.5.2 Off-design Shock-Loss Performance 250
4.5.3 Compressor Performance 255

4.6 Shock-Structure Verification 258
4.6.1 Detached Bow-Shock 258
4.6.2 Passage-Shock Configuration 262
5 RESULTS & DISCUSSION 266
5.1 3-D CFD NASA Rotor 67 Shock Physics 266
5.2 Shock-Loss Parametric Studies 271
5.2.1 Overview 271
5.2.2 Influence of 2-D Blade-Element Parameters 271
5.2.3 Influence of 3-D Blade-Element Parameters 274
5.2.4 Influence on Relative Total-Pressure Loss 277
5.2.5 Influence on Isentropic Efficiency 279
5.3 Choking Prediction and Mass flow limitation 280
5.4 Single-Objective Variable-Pitch Fan Optimisation 287
5.4.1 Variable-Pitch Fan Dynamics 287
5.4.2 Variable-Pitch Fan Design 288
5.4.3 Optimisation Strategy 291
5.4.4 Optimised Variable-Pitch Fan Geometry 295
6 CONCLUSIONS AND CONTRIBUTION TO KNOWLEDGE 302
6.1 General Conclusions 302
6.2 Main Conclusions 303
6.2.1 State-Of-the-Art 303
6.2.2 3-D Blade-Element-Definition & Full-REE Adaptation 305
6.2.3 Shock- Structure and Loss Model 306
6.2.4 Choking Mass Flow Redistribution Scheme 308
6.2.5 2-D and 3-D Parametric Studies 309
6.2.6 Single-Objective Variable-Pitch Fan Optimisation 311
7 FUTURE RECOMMENDATIONS 314
REFERENCES 316
BIBLIOGRAPHY 349
APPENDICES 350
Appendix A Approximation Methods for the Geometry Layout in Analysis and Optimisation 350
Appendix B NASA Rotor 67 3-D CFD Simulation 357
Appendix C SOCRATES GUI Development 365

LIST OF FIGURES

Figure 1.1 Transonic axial-flow compressors and fan types [7]. a) Single-stage fan. b) Multi-stage fan or low-pressure compressor. c) Multi-stage compressor..... 4

Figure 2.1 Flow chart to describe the literature-review structure conducted for the current research work..... 15

Figure 2.2 Shock structure at blade span locations with inlet relative supersonic flow for the NASA Rotor 67 [40] at 100% of design speed and near-peak efficiency. a) Tip location. b) 85% span from hub to tip. c) 50% from hub to tip. 17

Figure 2.3 Shock structure at blade span locations with inlet relative subsonic flow for the NASA Rotor 67 [40] at 100% of design speed and near-peak efficiency. a) 40% span from hub to tip. b) 35% span from hub to tip. c) 25% from hub to tip. 17

Figure 2.4 Flow interaction with a non-transonic axial-flow compressor rotor blade (modified from [43]). 21

Figure 2.5 Radial flow migration occurring downstream of the shock on the blade suction surface [32]. 22

Figure 2.6 Traditional sweep and lean angle definition in cylindrical coordinate system. a) Forward sweeping along z-axis. b) Backward sweeping along z-axis. c) Leaning towards pressure side in θ-direction. d) Leaning towards suction side in θ-direction 29

Figure 2.7 Sweep and lean angle definition with respect to the chord line (modified from [68]). a) Sweep along the chord line. b) Lean perpendicular to chord line.30

Figure 2.8 Full space for sweep and lean angle definition around a baseline blade [69]. 30

Figure 2.9 S-shaped blading at 33%, 67% and 100% of span [8]. a) Axial Sweep. b) Tangential Lean..... 32

Figure 2.10 S-shaped backward-curvature axial-sweep applied to a blade [8]. 33

Figure 2.11 Blade sweep definition using 2 length parameters (modified from [75]). a) Axisymmetric view. b) Top view. 34

Figure 2.12 Definition of the blade-to-blade S1 surface and the meridional hub-to-tip S2 surface [89]. 38

Figure 2.13 2-D SLC mesh definition on the meridional plane. 47

Figure 2.14 High-level flow-chart for the 2-D SLC axial-flow fan/compressor performance simulator (SOCRATES) [14,17,31]. 48

Figure 2.15 Control volume for a normal shock process. 60

Figure 2.16 Oblique shock waves. a) Flow past a wedge. b) Flow past an inclined wall. 62

Figure 2.17 Shock angle vs deflection angle chart for oblique shock waves [173]. 64

Figure 2.18 Detached shock wave ahead of a sharp-nosed body [173]. 65

Figure 2.19 Bow shock-wave system in a blunt-nose body. 66

Figure 2.20 Weak and strong shock solutions for a detached wave in an engine intake (modified from [178]). 68

Figure 2.21 Detached shock solution through shock polar diagrams [178]. 69

Figure 2.22 Supersonic flow past a gradually-inclined wall [173]. a) Compression due to concave curvature. b) Expansion due to convex curvature. 70

Figure 2.23 Supersonic flow expansion past a sudden convex corner causing a Prandtl-Meyer expansion [173]. 71

Figure 2.24 Flow Mach numbers for converging and diverging ducts. a) Subsonic inlet conditions. b) Supersonic inlet conditions. 73

Figure 2.25 Convergent-divergent nozzle to continuously accelerate the flow from subsonic to supersonic speeds. 76

Figure 2.26 Convergent-divergent nozzle operating at different inlet conditions when Mach number is not unity at the throat. a) Subsonic inlet flow. b) Supersonic inlet flow. 77

Figure 2.27 Flow patterns in a convergent-divergent nozzle. a) Subsonic flow. b) Flow just choked. c) Shock in nozzle. d) Shock at exit. e) Overexpanded flow. f) Design condition. g) Underexpanded flow. 79

Figure 2.28 Static-to-total pressure-ratio distribution in a convergent-divergent nozzle for different outlet static pressure levels. 80

Figure 2.29 Area-Mach Number relationship chart for a $\boldsymbol{\gamma = 1.4}$. 83

Figure 2.30 Variation of $\boldsymbol{f\gamma, M}$ with Mach number for a $\boldsymbol{\gamma = 1.4}$. 84

Figure 2.31 Expansion and shock system for an infinite flat plate cascade. a) Low supersonic inlet relative Mach number. b) High supersonic inlet relative Mach number. 85

Figure 2.32 Shock-wave structure in a transonic compressor blade-element. 88

Figure 2.33 Flow field and shock-wave configuration around a blade cascade operating under supersonic upstream relative flow. 90

Figure 2.34 Outlet total-pressure distribution in the circumferential direction due to blade-profile viscous losses for low-speed compressor rotors (modified from [4]). 91

Figure 2.35 Circumferential outlet relative total-pressure distribution for high-speed compressor rotors (modified from [4]). a) Shock-induced relative total-pressure drop. b) Profile-and-shock-induced relative total-pressure drop. 92

Figure 2.36 Circumferential total-loss coefficient distribution (replotted from [197]). 93

Figure 2.37 Assumed shock-configuration by Schwenk *et al*. [4] for shock-loss estimation (modified from [4]). 95

Figure 2.38 Shock-configuration established by Lewis *et al*. [197] from experimental tests for shock-loss estimation (modified from [197])..... 98

Figure 2.39 Relative total-pressure loss coefficient variation with incidence for measured total-losses and for an analytical shock model [3]. 99

Figure 2.40 Extension method for the remaining part of the detached shock (modified from [219]). 102

Figure 2.41 Shock model by Sayari and Bolcs [24] assuming a normal passage-shock to the stagnation streamline. a) Attached leading-edge oblique-shock. b) Detached bow-wave 104

Figure 2.42 Shock model by Bloch *et al*. [34] assuming a passage-shock with a hyperbolic and a straight portion, where the latter originates at the bow-shock sonic point. 107

Figure 2.43 Shock configurations assumed by Boyer and O'Brien [13,35,36] for near-stall, peak-efficiency, and near-choke operating conditions [36]. 108

Figure 2.44 Shock model by Balzer [222] assuming a single-shock configuration normal to the midchannel stramline and attached to the pressure blade leading-edge. 110

Figure 2.45 Empirical shock-loss parameter correlation [38]. 114

Figure 2.46 Loss coefficient vs incidence plot for different inlet relative Mach numbers [136]. 116

Figure 2.47 Loss coefficient variation with incidence (modified from [239]). 117

Figure 3.1 Structure of the incorporated modules into the 2-D SLC simulation strategy to improve the transonic-flow performance prediction..... 124

Figure 3.2 Blade-element-layout method to compose blade profiles on conical stream surfaces, implemented in the 2-D SLC axial-flow fan/compressor performance software. 126

Figure 3.3 Unwrapped view of the conical coordinate system used for the constant turning blade-element-layout method (obtained and modified from Crouse *et al*. [107])..... 128

Figure 3.4 Camberline blade elements on a conical coordinate system (obtained and modified from Crouse *et al*. [107]) 129

Figure 3.5 Surface blade-elements on a conical coordinate system (obtained and modified from Crouse *et al*., [107]). 133

Figure 3.6 Sweep and lean angle definition on a cartesian coordinate system. 136

Figure 3.7 Sweep and lean angle definition on a cylindrical coordinate system..... 136

Figure 3.8 Blade profile sections determined with the conical blade-element-layout method implemented into the 2-D SLC code for the NASA two-stage fan [246]. a) Meridional view. b) 3-D view..... 140

Figure 3.9 Blade-to-blade projection for mid-span blade-element sections obtained with the conical blade-element-layout method implemented into the 2-D SLC code for the NASA two-stage fan [246]. 141

Figure 3.10 Flow-chart diagram for the current shock- loss and structure model developed and implemented into the 2-D SLC axial-flow fan/compressor performance simulator. 145

Figure 3.11 Inlet relative subsonic supercritical condition for blade rows. 146

Figure 3.12 Single-shock structure for unchoked blade-elements or unstarted blade-passages consisting only in the detached bow-shock..... 150

Figure 3.13 3-D CFD RANS simulation for the NASA Rotor 67 [40] at 100% of design speed and w=34.45 kg/s. a) 60% hub-to-tip span. b) 70% hub-to-tip span. c) 80% hub-to-tip span. 151

Figure 3.14 Dual-shock structure for choked blade-elements or started blade-passages consisting in a detached bow-shock and a choke-induce shock. a) No intersection between the first and second passage-shocks b) Intersection between the first and second passage-shocks..... 153

Figure 3.15 Hyperbolic approximation for a detached bow-shock on a blade-row stream surface. 155

Figure 3.16 Hyperbolic approximation for a detached bow-shock ahead of a blade-profile leading-edge. 156

Figure 3.17 Hyperbolic approximation for a highly-oblique detached bow-shock of the NASA Rotor 67 [40] at 95% span at 100% of design speed and near-choke operating point. a) 2-D SLC simulation. b) 3-D CFD simulation. 157

Figure 3.18 Parameters for the calculation of the detachment distance in a hyperbolic approximation for a bow wave..... 158

Figure 3.19 Detached bow-shock and free-stream Mach wave projections on the meridional plane for a blade row using the 2-D SLC compressor simulator..... 164

Figure 3.20 Detached bow-shocks and free-stream Mach waves in the blade-to-blade plane for the set of transonic blade-elements using the 2-D SLC compressor simulator 164

Figure 3.21 Passage-shock impingement-point definition for a single-shock configuration in unstarted flows. 169

Figure 3.22 Second passage-shock impingement-point assumption for a dual-shock configuration in started flows. 170

Figure 3.23 Dual-shock configuration situation depending on the choke-induced passage-shock location. a) No intersection between both passage shocks. b) Coalescence of both passage shocks. 171

Figure 3.24 First-captured Mach or limiting wave for the flow expansion that interacts with the passage shock. 172

Figure 3.25 Normal cross-sectional area to the inlet relative flow. a) Far upstream or inlet. b) First-captured Mach wave. 173

Figure 3.26 Width definition for the flow areas at the inlet and at the first-captured Mach wave. 174

Figure 3.27 Field-point calculation to determine the characteristic slopes of the zone-V flow expansion. 179

Figure 3.28 Highly-loaded blading for which there is an expansion fan intruding in the zone-v expansion field. a) Gradual-expansion characteristics. b) Expansion-fan waves arising from the limiting wave impingement on the suction surface 183

Figure 3.29 Pre-compression shocks arising from the suction-surface ramp and coalescing at the leading edge of the next adjacent blade 186

Figure 3.30 Choke-induced passage-shock situation in a blade-element passage as a function of the current total-to-static pressure ratio. 197

Figure 3.31 Implementation of the full choke-prediction model in the 2-D SLC axial-flow fan/compressor performance simulator (SOCRATES) [14,17,31]. 202

Figure 3.32 Control volume definition for a blade-element passage to predict the onset of the choking incidence. 203

Figure 4.1 NASA Rotor 67 blade inlet and outlet comparison between 2-D SLC simulation and test data at 100% NRT and w=34.56 kg/s. a) Meridional velocity. b) Meridional Mach number. 219

Figure 4.2 NASA Rotor 67 blade inlet and outlet comparison between 2-D SLC simulation and test data at 100% NRT and w=34.56 kg/s. a) Meridional absolute velocity. b) Meridional relative velocity. 220

Figure 4.3 NASA Rotor 67 blade inlet and outlet comparison between 2-D SLC simulation and test data at 100% NRT and w=34.56 kg/s. a) Meridional absolute angle. b) Meridional relative angle. 220

Figure 4.4 NASA Rotor 67 blade incidence and deviation angle comparison between 2-D SLC simulation and test data at 100% NRT and w=34.56 kg/s. 221

Figure 4.5 NASA Rotor 67 SLC pressure ratio compressor map verification against experimental results. 222

Figure 4.6 NASA Rotor 67 SLC temperature ratio compressor map verification against experimental results. 222

Figure 4.7 NASA Rotor 67 SLC isentropic efficiency compressor map verification against experimental results and SLC NASA Two-stage fan first-stage rotor. 223

Figure 4.8 2-D SLC model for the NASA ADP Fan. a) Blade sections definition. b) Flowpath and fan blade definition. 223

Figure 4.9 Pressure-ratio comparison between the 2-D SLC NASA ADP Fan model and measured data [252] at design point and cruise speed of 8396.5 rpm. 224

Figure 4.10 Temperature-ratio comparison between the 2-D SLC NASA ADP Fan model and measured data [252] at design point and cruise speed of 8396.5 rpm. 225

Figure 4.11 Isentropic-efficiency comparison between the 2-D SLC NASA ADP Fan model and measured data [252] at design point and cruise speed of 8396.5 rpm 225

Figure 4.12 Pressure ratio map for different flight conditions: Approach, cutback, SLTO and cruise. 226

Figure 4.13 Pressure ratio map for a 0 deg stagger configuration. 227

Figure 4.14 Temperature ratio map for a 0 deg stagger configuration 227

Figure 4.15 Adiabatic efficiency map for a 0 deg stagger configuration. 228

Figure 4.16 Extended inlet and outlet duct domains for the 3-D CFD and 2-D SLC models. 228

Figure 4.17 Outlet static pressure vs mass flow comparison for the NASA Rotor 67 at 100% of design speed between and 2-D and 3-CFD simulation results. 231

Figure 4.18 Pressure ratio compressor map comparison for the NASA Rotor 67 at 100% of design speed between experimental data, and 2-D and 3-CFD simulation results. 231

Figure 4.19 Temperature ratio compressor map plot for the NASA Rotor 67 at 100% of design speed between experimental data, and 2-D and 3-CFD simulation results. 232

Figure 4.20 Isentropic efficiency compressor map plot for the NASA Rotor 67 at 100% of design speed between experimental data, and 2-D and 3-CFD simulation results. 232

Figure 4.21 Relative flow angle spanwise distribution for the NASA Rotor 67 at 100% of design speed for the leading edge, and 25, 50, 75 and 100% of chord upstream of the leading edge. 233

Figure 4.22 Relative flow angle spanwise distribution for the NASA Rotor 67 at 100% of design speed for the leading edge. 234

Figure 4.23 Relative flow angle spanwise distribution for the NASA Rotor 67 at 100% of design speed for the leading edge. 234

Figure 4.24 Meridional velocity spanwise distribution for the NASA Rotor 67 at 100% of design speed for the leading edge, and 25, 50, 75 and 100% of chord upstream of the leading edge. 235

Figure 4.25 Meridional velocity spanwise distribution for the NASA Rotor 67 at 100% of design speed for the leading edge. 236

Figure 4.26 Meridional velocity spanwise distribution for the NASA Rotor 67 at 100% of design speed for the leading edge. 236

Figure 4.27 Streamtube mass flow radial distribution for the uncorrected choke conditions in 2-D SLC. 237

Figure 4.28 Stream tube mass flow radial distribution with the mass flow redistribution model activated in 2-D SLC for choking conditions. 237

Figure 4.29 Spanwise mass flow distribution comparison between 2-D SLC and 3-D CFD simulations for the NASA Rotor 67 at 100% NRT..... 238

Figure 4.30 Spanwise comparison for the choking prediction between the 2-D SLC and 3-D CFD simulation. a) Mass flow distribution. b) Inlet relative flow angle... 239

Figure 4.31 Annular cascade rig-test correlation [38] for the profile-loss parameter as a function of the diffusion factor for experimental measurements. 240

Figure 4.32 Shock-loss coefficient radial distribution comparison for the NASA Rotor 67 [40] at 100% of design speed and w=34.03 kg/s (NPE) between test data, and historical and current models. 241

Figure 4.33 Shock-loss coefficient radial distribution comparison for the NASA Rotor 67 [40] at 100% of design speed and w=34.03 kg/s (NPE) between test data, current model, and variations of Schwenk *et al*. [4]. 246

Figure 4.34 Shock-loss coefficient radial distribution comparison for the NASA Rotor 67 [40] at 100% of design speed and w=34.03 kg/s (NPE) between test data, current model, and historical-model variations. a) Schwenk *et al*. [4]/BELM. b) Schwenk *et al*. [4]/ Bloch *et al*. [34]. c) Sayari and Bolcs [24]. 247

Figure 4.35 Shock-loss coefficient radial distribution comparison for the NASA Rotor 67 [40] at 100% of design speed and w=34.03 kg/s (NPE) between test data, current model, and historical models. a) Miller *et al*. [3]. b) Koning *et al*. [153,155]. c) Bloch *et al*. [34]..... 249

Figure 4.36 Shock-loss coefficient radial distribution comparison for the NASA Rotor 67 [35] at 100% of design speed and w=34.03 kg/s (NPE) between test data, current model, and empirical model of Cunnan *et al*. [38]. 250

Figure 4.37 Shock-loss coefficient radial distribution comparison for the NASA Rotor 67 [40] at 100% of design speed for different off-design points. a) Schwenk *et al*. [4]. b) Miller *et al*. [3]. c) Cunnan *et al*. [38]. 251

Figure 4.38 Off-design evolution of the shock-loss coefficient radial distribution for the NASA Rotor 67 [35] at 100% of design speed. 253

Figure 4.39 Off-design comparison of shock-loss coefficient radial distribution between experimental and current shock-loss model data for the NASA Rotor 67 [35] at 100% of design speed. a) $\boldsymbol{m = 34.03 kgs}$ (NPE) b) $\boldsymbol{m = 34.16 kgs}$ c) $\boldsymbol{m = 34.26 kgs}$ d) $\boldsymbol{m = 34.38 kgs}$ e) $\boldsymbol{m = 34.45 kgs}$ f) $\boldsymbol{m = 34.51 kgs}$ g) $\boldsymbol{m = 34.56 kgs}$ g) $\boldsymbol{m = 34.70 kgs}$ (NC). 254

Figure 4.40 NASA Rotor 67 [35] compressor total-pressure ratio map comparison between experiments, and the previous and updated 2D-SLC performance simulation codes. 255

Figure 4.41 NASA Rotor 67 [35] compressor isentropic-efficiency ratio map comparison between experiments, and the previous and updated 2D-SLC performance simulation codes. 256

Figure 4.42 2-D SLC-estimated bow shock angles for the NASA Rotor 67. 258

Figure 4.43 Bow-wave angles comparison as a function of the inlet relative Mach number against chart presented by Moeckel [180]. 259

Figure 4.44 2-D SLC bow-wave non-dimensional detachment distance and non-dimensional sonic point height for the NASA Rotor 67. 260

Figure 4.45 Bow-wave non-dimensional detachment distance and non-dimensional sonic point height comparison as a function of the inlet relative Mach number against chart presented by Moeckel [180]. 261

Figure 4.46 Comparison for the bow-wave non-dimensional distance from the wedge tangency point as a function of the inlet relative Mach number against chart presented by Miller and Hartmann [208]. 261

Figure 4.47 Overall shock configuration comparison between 2-D SLC with the current shock model and 3-D CFD RANS simulations for the NASA Rotor 67 [35] at 100% of design speed and near peak-efficiency ($\boldsymbol{m = 34.03 kgs}$). a) 45.5% Span. b) 58.6% Span. c) 68.5% Span. d) 78.4% Span. e) 88.6% Span. f) 100.0% Span. 263

Figure 4.48 Overall shock configuration comparison between 2-D SLC with the current shock model and 3-D CFD RANS simulations for the NASA Rotor 67 [35] at 100% of design speed and near peak-choking ($\boldsymbol{m = 34.45 kgs}$). a) 46.2% Span. b) 65.7% Span. c) 82.6% Span. d) 100.0% Span. 264

Figure 4.49 Shock-configuration radial evolution determined by the current shock-structure and loss model in the context of a 2-D SLC simulation for the NASA

Rotor 67. a) Meridional view. b) 3-D projection view for the entire compressor rotor. 265

Figure 5.1 3-D CFD NASA Rotor 67 simulation for 100% of design speed at 95% span from hub to tip. 267

Figure 5.2 CFD NASA Rotor 67 simulation for 100% of design speed at 80% span from hub to tip. 269

Figure 5.3 CFD NASA Rotor 67 simulation for 100% of design speed at 70% span from hub to tip 270

Figure 5.4 2-D blade-element parameter variation for the NASA Rotor 67 [40] baseline geometry. a) %Maximum-Thickness Location/Chord. b) %Maximum Thickness/Chord. c) Solidity. 272

Figure 5.5 Influence of 2-D blade-element parameters in the shock-loss coefficient radial distribution. 274

Figure 5.6 Sweep angle variation for the NASA Rotor 67 parametric study. a) Forward sweep. b) Backward sweep. 275

Figure 5.7 Lean angle variation for the NASA Rotor 67 parametric study. a) Suction side lean. b) Pressure side lean. 275

Figure 5.8 Influence of 3-D blade-element parameters in the shock-loss coefficient radial distribution. 276

Figure 5.9 Pitchwise distribution of relative total-pressure along the passage shock for the 2-D blade-element parameters variation. 278

Figure 5.10 Pitchwise distribution of relative total-pressure along the passage shock for the 3-D blade-element parameters variation. 279

Figure 5.11 Influence of sweep and lean variations on the overall isentropic efficiency. 280

Figure 5.12 Current-flow and choking incidence angles from choking to peak efficiency for the NASA Rotor 67 2-D SLC simulation. 281

Figure 5.13 Current-flow and choking incidence angles from peak efficiency to stall efficiency for the NASA Rotor 67 2-D SLC simulation. 281

Figure 5.14 Current-flow and choking inlet flow angles from choking to peak efficiency for the NASA Rotor 67 2-D SLC simulation. 282

Figure 5.15 Current-flow and choking inlet flow angles from peak efficiency to stall for the NASA Rotor 67 2-D SLC simulation. 283

Figure 5.16 2-D SLC-estimated incidence and choking incidence evolution for the NASA Rotor 67 speedline at 100% NRT. 283

Figure 5.17 2-D SLC-estimated inlet flow angle and inlet choking flow angle evolution for the NASA Rotor 67 speedline at 100% NRT. 284

Figure 5.18 2-D SLC-estimated incidence and choking incidence for the NASA Rotor 67. 285

Figure 5.19 2-D SLC-estimated inlet flow angle and inlet choking flow angle for the NASA Rotor 67. 285

Figure 5.20 Inlet flow angle correction for choke conditions through a mass flow redistribution. 286

Figure 5.21 Radial distribution of the inlet relative flow angle and choking margin compared to the limiting values of choking. 287

Figure 5.22 Scaling for the NASA ADP fan 2-D SLC geometry to a fan diameter of 2.735 m for the variable-pitch fan. 289

Figure 5.23 Hub-to-tip radius ratio decrease for the NASA ADP fan 2-D SLC model from 0.42 to 0.3 to build up the variable-pitch fan geometry. 289

Figure 5.24 Flowpath hub modification to match the required hub-to-tip radius ratio of 0.3 for the variable-pitch fan geometry. 290

Figure 5.25 2-D blade-element parameter modification for the NASA ADP Fan [252] to compose the variable-pitch fan. a) Maximum-thickness-location-to-chord ratio. b) Maximum-thickness-to-chord ratio. 290

Figure 5.26 Evolutionary genetic algorithm design -optimisation strategy using a 2-D SLC fan/compressor performance simulator as solver. 291

Figure 5.27 Flow chart for the 3-D variable-pitch fan design optimisation using an evolutionary genetic algorithm coupled to a 2-D SLC fan/compressor software as solver. 292

Figure 5.28 Decision-variable structure for the sweep and lean angle variation for the 3-D VPF EGA design-optimisation. 293

Figure 5.29 Percentage of stalled blade-span at 0 degrees pitch-setting for the NASA ADP fan [252] at 100% of design speed. 295

Figure 5.30 Modified design variables along the span for the 40th generation cycle of the 3-D VPF EGA design-optimisation. a) Sweep angle variation. b) Lean angle variation. 296

Figure 5.31 Full design-space exploration for the cummulative decision variables from the 45th generation cycle of the 3-D VPF EGA design-optimisation. a) Sweep angle variation. b) Lean angle variation. 296

Figure 5.32 Radial distribution of the optimised 3-D blade-element parameters for the variable-pitch fan. a) Sweep angle. b) Lean angle. 297

Figure 5.33 Variable-pitch fan comparison between the baseline and optimised geometry models. a) Meridional view. b) Forward-looking-aft view. 297

Figure 5.34 3-D variable-pitch-fan model comparison between the baseline and optimised geometries. 298

Figure 5.35 Isentropic efficiency map comparison for the baseline and optimised variable-pitch fan at cutback and cruise (design) speed. 299

Figure 5.36 Shock-loss coefficient radial distribution comparison between the baseline and optimised geometries for the variable-pitch fan..... 300

Figure 5.37 Overall shock-configuration for the variable-pitch fan blade tip. a) 2-D cascade view. b) 3-D projection view. 301

Figure 5.38 Relative total-pressure loss pitchwise distributon comparison between the baseline and optimised geometries for the variable-pitch fan..... 301

LIST OF TABLES

Table 2.1 Full/semi-empirical and simple analytical correlations for losses, deviation angle, and stall prediction employed in axial-flow compressor SLC methods..... 51

Table 2.2 Flow regimes for incompressible and compressible flow depending on the Mach number. 76

Table 3.1 Range of total-to-static pressure ratios at the blade-element exit to validate the situation of the assumed passage-shock pattern. 196

Table 4.1 NASA Rotor 67 [40] design specifications. 218

Table 4.2 NASA Rotor 67 [40] flow path dimensions. 218

Table 4.3 Blockage factors for 100% NRT applied to NASA Rotor 67 model. 219

Table 4.4 NASA ADP Fan [252] design parameters. 224

Table 4.5 Solution settings for the 3-D CFD RANS NASA Rotor 67 model. 229

Table 4.6 Inlet boundary conditions for the 3-D CFD RANS NASA Rotor 67 model. 229

Table 4.7 Outlet boundary conditions for the 3-D CFD RANS NASA Rotor 67 model. 229

Table 4.8 Matrix of the assessed historical shock-loss models and their modifications. 244

Table 5.1 Decision variable limits for the 3-D variable-pitch fan design-optimisation. 294

Table 5.2 Percentage of stalled blade-span for the NASA ADP fan [252] at 100% of design speed and near-stall and stall operating conditions. 295

NOMENCLATURE

Abbreviations

0-D	Zero–Dimensional
1-D	One-Dimensional
2-D	Two-Dimensional
3-D	Three-Dimensional
ADP	Advanced Duct Propeller
BLI	Boundary Layer Ingestion
CFD	Computational Fluid Dynamics
DCA	Double-Circular-Arc
DCC	Dynamic Convergence Scheme
DP	Design Point
FLA	Forward-Looking-Aft
IGV	Inlet Guide Vane
LHS	Left Hand Side
MCA	Multiple Circular Arc
NACA	National Advisory Committee for Aeronautics
NASA	National Aeronautics and Space Administration
NC	Near-Choking
NPE	Near-Peak Efficiency
NS	Near-Stall
OEM	Original Equipment Manufacturer
OGV	Outlet Guide Vane
PDE	Partial Differential Equation
R&R	Rolls-Royce
RANS	Reynolds-Averaged Navier-Stokes
REE	Radial Equilibrium Equation
RHS	Right Hand Side
RPM	Revolutions per Minute
SLC	Streamline Curvature
SOCRATES	Synthesis of Correlations for the Robust Assessment of

	Turbomachinery Engine Systems
SWBLI	Shock-wave and boundary-layer interaction
USA	United States of America
UTC	University Technology Centre
VPF	Variable-Pitch Fan

Symbols

Latin

A	Acceleration, Area, Contraction Ratio, Coefficient
a	Speed of sound
ar	Aspect ratio
B	Coefficient
b	Distance between the leading-edge sonic point and leading-edge centre
C	Absolute velocity, Parameter, Coefficient, Turning Rate
c	Chord
CA	Centre of area
Ch	Characteristic
C_p	Specific heat at constant pressure
C_v	Specific heat at constant volume
d	Detachment distance
D	Drag, Diffusion Factor
E	Error function
e	Strain or rate of deformation, length between leading-edge foremost point and leading-edge sonic point
F	Force, Newton-Cotes function
f	Factor, Force per unit volume
h	Stagnation streamline deflection, Enthalpy
H	Streamtube height
I	Rothalpy

i	Incidence
IC	Integration Constant
J	Moment of Area
k	Blade angle
L	Distance between sonic point of hyperbola index
l	length
M	Mach number
m	Mass, Meridional direction
N	Maximum number of integration or discretization points
NRT	Corrected speed
n	Integration or discretization points
o	Hyperbola centre
P	Total pressure, Momentum
p	Static pressure
PR	Total pressure ratio
pr	Static pressure ratio
q	Correction factor
R	Gas constant, Radius of curvature, Ray coordinate in conical system
r	Radial coordinate in cylindrical system, Radius
S	Entropy, Blade-Camberline path
s	Spanwise direction, Spacing or pitch
$\mathcal{S}$	Characteristic slope
$\mathscr{s}$	Blade-surface path
T	Temperature
t	Blade thickness, Time
U	Blade speed
u	Flow velocity
V	Relative velocity, Velocity, Volume
v	Specific volume
W	Working Range
w	Streamtube width

x	Flow direction, Radial coordinate in Cartesian system
y	Tangential coordinate in Cartesian system
z	Axial coordinate in Cartesian and cylindrical system

Greek

α	Absolute flow angle, Streamline cone angle or cone half-angle
β	Relative flow angle
γ	Specific heat ratio
Δy	Increment in y direction
Δz	Increment in z direction
δ	Kronecker delta, Tangential deflection, Deflection angle or wedge half-angle
ε	Angle between ray and reference ray in a cylindrical system
ϵ	Mach number increase
ζ	Constant
η	Lean angle
Θ	Momentum thickness
θ	Circumferential or whirl coordinate in cylindrical system, Camber angle
K	Riemman's invariant
Λ	Mass flow choking coefficient
λ	Second viscosity term, Sweep angle
μ	Normal dynamic viscosity, Mach angle
ν	Prandtl-Meyer angle
Ξ	Choking margin
ξ	Stagger or setting angle
Π	Loss parameter
ρ	Density
ς	Shock angle
σ	Solidity, Stress

τ	Surface traction
Υ	Hyperbola co-vertex
ϑ	Flow turning
Φ	Characteristic slope angle
ϕ	Staggered gap
φ	Streamline slope
X	Direction
χ	Hyperbola ratio
ψ	Second viscosity term
Ω	Laval number
ω	Rotational speed, loss

Subscripts

0	Absolute, Total or Stagnation
1	Inlet state
2	Outlet state
A	Point A on suction surface
a	Speed of sound, First-captured Mach wave suction-surface impingement
ap	Blade-surface axial-points
ax	Axial
B	Intersection between stagnation streamline and bow-wave vertex
b	First-captured Mach wave passage-shock impingement
bow	Bow wave
c	Camberline, Centroid of mass
C	Absolute velocity
ch	Choked
cr	Critical
detach	Detachment
dwn	Downstream

dwsl	λ-shock downstream limb
E	First-captured wave
eff	Effective
eq	Equivalent
ex	Blade-passage exit
f	Expansion fan
g	Stagnation streamline
g	Gradual expansion
hub	Blade hub
hy	Hyperbola
i	Tensorial direction i, counter
id	Ideal
in	Inlet
j	Tensorial direction j, Streamline number, Jet
k	Tensorial direction k
LE	Leading edge
m	Meridional
max	Maximum
mid	Blade mid-span
min	Minimum
mt	Maximum thickness point
n	Blade Surface point, Integration or Discretization point
norm	Transition between off-design and stall condition
ns	Normal shock
nst	Negative stall
o	Centre
On	Interpolation distribution
out	Outlet
PM	Prandtl-Meyer expansion
prof	Profile
ps	Pressure surface

psh	Passage shock
psh2	Second passage shock or choke-induced passage-shock
q	Quasi-orthogonal, Choked-induced passage-shock impingement point on suction surface
Re	Reynolds
rel	Relative
s	Stream surface normal, Sonic point
sb	Intersection between sonic line and blade-profile leading edge
sec	Secondary
sh	Overall shock system
Sl	Streamline
sp	Stacking point
ss	Suction surface
st	Stall
St	Stream tube
sub	Subsonic
sup	Supersonic
t	Passage-shock transition point
T	Blade-surface transition point
theory	Theoretical value
thr	Throat
tip	Blade tip
tot	Total
TR	Trailing edge
u	Choked-induced passage-shock impingement point on pressure surface
uch	unchoke
up	upstream
v	Detached bow-shock vertex
w	Wake
wf	Weight flow

μ	Mach wave

Superscripts

*	Critical, Design
.	Flow rate or first derivative
~	Obtained from assumed value
‘	Relative
⌣	Axis or Plane Projection
¯	Mass averaged
,,	Characteristic Field Point

1 INTRODUCTION

1.1 Background

The increasing demand from civil and military aviation to reduce costs in the design and operation of engines has led to continuous gas-turbine engine component performance improvement. Key components in the axial-flow engines are the fan and compressor, which can be further explored to meet the aviation needs of lightness and compactness. Transonic axial-flow fans and compressors are well-known for giving high single-stage pressure ratios, requiring fewer compression stages to attain the desired overall total-pressure ratio. The interest in advanced-design (low aspect ratio ar and high solidity σ) transonic axial-flow fans and compressors from the aviation industry is continuously expanding. Inasmuch as modern aero gas-turbine engines, especially turbofans, are required to reduce weight and size, transonic compressing systems fit the purpose due their high shock-induced single-stage pressure ratio.

One of the challenges for transonic fans and compressors is to still provide high efficiencies comparable to those from a subsonic system, whilst being light and compact and robust. Research in transonic fans and compressors has reached acceptable efficiencies between 83-90% for design conditions. Nevertheless, the efficiency can significantly decrease due to a rise in aerodynamic losses at off-design points, limiting the working range. Aircraft, particularly the military, do not operate at constant engine throttles, which depend on the flight mission. Henceforth, it is of high importance to assure high efficiencies and acceptable working ranges even at part-speeds. Even a small efficiency increment would result in significant less fuel consumption, yielding in fuel savings and fewer polluting emissions.

The current cost of product development and research is rising enormously. The use of high-resolution computational tools for component performance simulation and mainly for design optimisation adds to the problem due to the intolerably high solution times and utilization of resources. In the aim of improving the performance prediction for transonic axial-flow fans and compressors in the analysis and design process, the present research develops a comprehensive transonic-flow modelling package to be

implemented in a through-flow performance simulation software. In this way, the cost of research and product development can be potentially reduced.

1.2 Transonic Axial-Flow Compressors

Gas-turbine engine performance is mainly determined by the fan and the compressor. Transonic axial-flow fans and compressors have continuously gained attention during the last 60 years due to their high pressure-ratios per single-stage capability. As a consequence, engine weight and size are reduced, resulting in reduction of design, manufacture, operation, and maintainability costs. Hereafter, the present document refers only to compressors due to practicality, since both turbomachinery components carry a pressure increase into effect. Nonetheless, the reader can apply the same compressor frame to fans, with exception of where it is explicitly indicated to make a particular emphasis.

If the rotor blade or peripheral speed is large enough, the inlet relative velocity can be higher than the speed of sound, generating supersonic inlet relative Mach number $M_1{}'$. The application of rotors with inlet relative supersonic flow, often known as transonic rotors, has become widespread in almost every modern gas-turbine engines for both axial-flow components, fans and first compressor stages [1]. Nonetheless, the prefix *transonic* in axial-flow compressors can be misleading throughout the literature and practice, as it can refer to the mixed supersonic and subsonic flow behaviour in the chordwise, pitchwise or spanwise direction.

As the main purpose of a compressor rotor is to convert kinetic energy into static pressure, there is flow deceleration or diffusion. In a transonic compressor rotor, the flow is usually discharged at subsonic velocities, hence, having mixed relative supersonic flow at the inlet and subsonic flow at the outlet in the streamwise direction. For this to happen, the flow becomes subsonic somewhere along the chord requiring of a strong shock-wave within the blade passage to produce this step change. However, the compressible flow field in a blade row is far more complex than having a unique passage shock. Instead, there is a complete high-speed aerodynamic system that in short, consists in a detached shock wave ahead of the blade-leading edge and a flow expansion at the blade entrance region.

Because the pressure surface and suction surface have opposite effects and the fact that the shock-system has some degree of obliquity with respect to the axial axis, the flow is not circumferentially constant. This three-dimensional (3-D) effect yields a mixed supersonic and subsonic flow field along the pitch on a stream surface of revolution.

In the radial direction, the inlet relative velocity increases with the blade height. At low blade radii, the blade speed is low enough that results in subsonic entry relative velocities. As the blade radii increases so the blade speed, leading to supersonic inlet relative flow. The disposition of inlet relative supersonic flow at high-span blade locations and inlet relative subsonic flow at low-span sections is the most recognized transonic behaviour to be used within axial-flow compressors or fans.

In the early 1940s, it was believed that axial-flow compressor blading having an inlet relative subsonic Mach number will provide a better performance than that with a supersonic inlet relative flow [2]. For this reason, axial-flow compressors were limited to an inlet relative Mach number below 0.75 to avoid any shock pattern that would increase even more the losses [3]. Experimental investigations conducted by the NACA between 1955 and 1957 identified that subsonic compressor blading design needed to be adapted to efficiently handle transonic flow [4]. This motivated the flow study through the blade passages and loss-models modification to consider shock-associated effects. Experimental compressor performance data [5,6] with inlet relative flow around $M_1' = 1$ revealed the potential success of having supersonic relative flow at the rotor inlet.

In general, transonic compressors can be mainly classified in three groups [7]: single-stage commercial fans, multi-stage fans or low-pressure compressors for military applications, and multi-stage compressors for commercial aircrafts or industrial gas turbines engines, illustrated in Figure 1.1. With the latest improvements in transonic axial-flow compressor aerodynamics, isentropic efficiencies have reached acceptable values around 83-90 % and pressure ratios between 1.7–1.8 per single stage at design condition for typical commercial-aircraft inlet tip relative flow Mach numbers around 1.3 [8]. Multi-stage military fans have even reached higher inlet tip Mach numbers up to 1.7 [7]. Research efforts have focused in increasing pressure ratio and efficiency,

particularly at off-design conditions, while keeping a stable operating range, as the surge margin is compromised in transonic compressors. Even a small efficiency increment can bring significant fuel savings. For this reason, the use of transonic speeds in compression has found application in commercial and military aircraft engines.

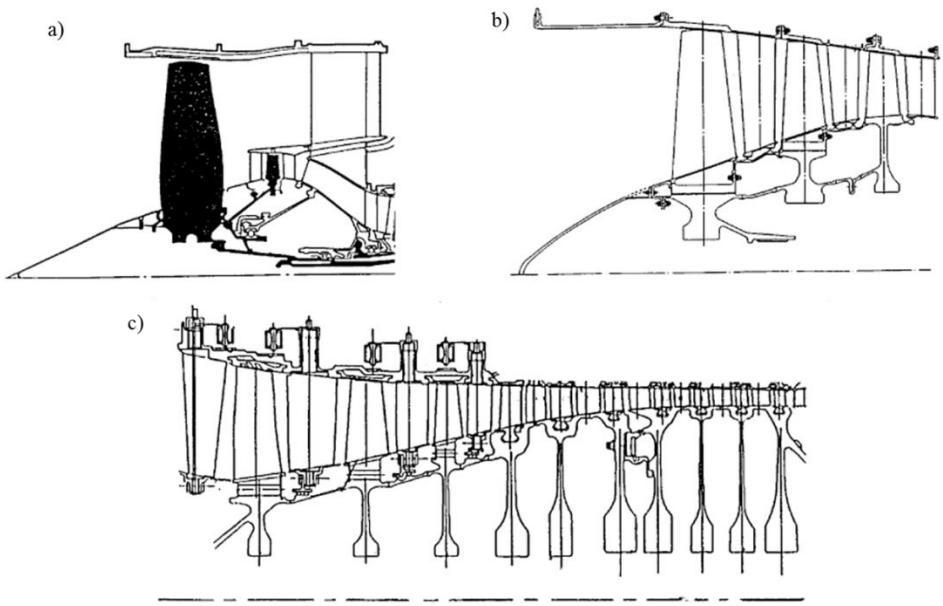

Figure 1.1 Transonic axial-flow compressors and fan types [7]**. a) Single-stage fan. b) Multi-stage fan or low-pressure compressor. c) Multi-stage compressor.**

In transonic compressor rotors, the inlet supersonic relative velocities are only confined in the blade high-span locations in the radial direction. In the axial direction, the supersonic region extends from the leading to a finite point on the blade surface, where a strong-shock mechanism decelerates the flow to subsonic relative velocities. Despite inlet flow speed is significantly reduced for a second-stage rotor due to a large temperature increase in the first-stage rotor and flow path diameter reduction, a small supersonic region at the second-stage rotor-blade tip can still be found in some cases [9]. These features have made the transonic axial-flow compressor widely used in every modern aero-engine. Nevertheless, transonic compressors have also found an application in industrial gas-turbine plants with transonic flow at the tip section of the front stages [10,11]. Because these stationary gas-turbine engines operate at low constant rotational speeds to satisfy the alternate current frequency, the mass-flow rate

requirements are high, increasing the axial Mach number, and thus, leading to supersonic relative speeds at high blade radii.

Increasing the single-stage pressure ratio is useful to achieve lightweight and compact aero-engines; nevertheless it inevitably implicates a loading increment per stage, increasing the flow diffusion, and reducing the isentropic efficiency [12]. Thence, the challenge for the transonic axial-flow compressor designer has become twofold: Maximize the pressure ratio to reduce the stage number whilst keeping an acceptable performance, and control the losses due to any shock-wave system.

The constant design requirements of high-efficiency axial-flow compressors have led to investigate and develop models that can estimate more realistically the losses. In this respect, transonic axial-flow compressors demand higher-fidelity loss-analysis models due to the associated shock-wave configurations. The prediction of blading shock-wave losses has remained a topic of discussion due to the complex three-dimensional flow physics occurring both, ahead and within the blade passages.

1.3 Turbomachinery Flow Simulation

Accurate and robust fan and compressor flow field prediction remains elusive [13]. Off-design performance estimation is still a challenge for conventional simulation tools, which show significant deviation against real behaviour [14]. Even though computational fluid dynamics (CFD) plays an essential role in the turbomachinery design than it does in any other fluid-related field [15], there are still limitations in turbulence and transition, particularly for off-design cases [13]. Turbomachinery CFD analysis is three dimensional (3-D) and numerically solve the viscosity effects at a reasonably small scale, however, it is not an exact science [16]. Additionally, CFD simulations come at high computational costs in terms of solution time and memory, complexity to obtain the required initial and boundary conditions, and lack of flexibility to incorporate or even modify any loss or deviation model [14,17–19].

Alternatively, through-flow methods provide fast and fairly reasonable solution at low cost in terms of computational run-time and resources [14,18–20]. Since the development of turbomachinery through-flow codes in the late forties and fifties,

streamline curvature [21] and stream function or matrix methods [22] have evolved. Among the different through-flow techniques, streamline curvature (SLC) is the most preponderant numerical method for turbomachinery design and analysis [13,15] as it represents the backbone for the design process [23] due to economical and practical reasons [24]. Flow in SLC is assumed to be two dimensional (2-D), compressible, inviscid, and steady. In fact, a fully detailed analysis for an isolated gas-turbine engine component can be obtained through SLC methods. In contrast to CFD, SLC is flexible to incorporate empiricism in the form of loss and deviation models. Besides, SLC numerical simulations require less time to set up the model and the initial and boundary conditions than in CFD analyses. If design optimisation is intended, SLC techniques are the most suitable to avoid the intolerably high computational times of CFD simulations [24]. Furthermore, 2-D SLC component analyses can be coupled with a low-fidelity zero-dimensional (0-D) solver for the entire engine, known as component zooming [25–29]. Through this amalgamation, influence of high-fidelity analysed components is incorporated into the low-fidelity engine-cycle performance.

In the subsonic-flow analysis, SLC and matrix methods are similar in the results. On the contrary, for transonic or supersonic applications, matrix techniques are not suitable as there are two possible velocity fields for any stream function and moreover, the relative Mach number is restricted to unity [23]. On the contrary, SLC methods are able to handle subsonic and supersonic inlet relative Mach numbers, while giving a single solution that satisfies the governing equations.

Transonic flow analysis in compressors and fans is complex due to the resulting highly three-dimensional flow field. Shock waves presence, their interaction with the endwall and blade boundary layer (SWBLI), spanwise mixing and tip clearance secondary flows are key phenomena observed in transonic compressors [13]. Apart from the profile and secondary losses, transonic blade rows have additional losses due to the shock wave formation and SWBLI. In general, SLC computer programs lack of robustness to handle transonic and supersonic flows [23] and their use in transonic compressors has been limited [13]. In recent years, emphasis has been placed to develop flow-physics-based models instead of fully and semi- empirical aerodynamic correlations in the SLC simulations [30]. For these reasons, a comprehensive transonic flow model was

devised, implemented, and tested in an in-house 2-D SLC axial-flow single-stage and multi-stage fan/compressor simulation software, SOCRATES (Synthesis of correlations for the robust assessment of turbomachinery engine systems) [14,17,31], to improve solver capability, reliability, and robustness in the flow field performance prediction. The high-fidelity transonic flow model mainly consists of two parts: (1) a physics-based shock-wave model to predict its structure and associated losses; (2) a choked-flow treatment model to estimate choking evolution and choke-induced radial mass flow redistribution.

1.4 Blading Shock-Wave Structures

Shock waves, and in consequence shock losses, are only present in transonic or supersonic compressors. Shock structures involve complex 3-D flow field physics triggering negative effects as shock waves, shock wave and boundary layer interaction, radial flow migration, shock wave interaction and tip clearance secondary flow interaction, blockage, corner stall and upstream wake destabilization, resulting in shock losses that induce an energy loss and hence, efficiency reduction [32].

Shock structure depends on the blade geometry and operating conditions. Shock waves, in set with alternating expansion waves and weak shock waves, move along the blade passage and emanate from the blade suction side to the leading edge of the other adjacent blade. In general, shock waves are oblique, tending to become more normal as the operating point moves towards surge condition when the back static pressure is increased or the mass flow is reduced. Nevertheless, the shock configuration can complicate even more as the back static pressure is reduced and decreasing the incidence. Further outlet static pressure reduction reaches the maximum mass flow, choking the passage, fixing the incidence, and leading to another oblique shock past the throat to match the back conditions as the inlet properties cannot longer be changed. When this phenomenon occurs, the cascade is known to be operating in the “started mode”. Prior to this occurrence, the cascade operation is in the “unstarted mode” [33].

The flow field behaviour and therefore, the compressor performance, are significantly determined by the blade geometry. Different solutions to diminish the flow negative impact can be found in the literature as blade profile geometry design, 3-D blade-

shaping, casing treatments, and air injection or bleeding. The scope of this research is not focused on flow-control solutions that involve further manufacturing modifications to the casing; however a brief summary on these methods is given in the next paragraph, whereas in the following sections, blade profile design and 3-D blading are further reviewed in Sec. 2.5 and Sec. 2.6 as this research explores the optimisation of the blade-element parameters.

Casing treatments consists of introducing hollow structures in there, to reduce tip endwall losses, improving rotor stability by increasing the operating range and efficiency [32]. Hollow structures can be divided in slot, groove or pattern –type, featured by the slot length and depth. Slots can be axial, skewed or angled; grooves are usually circumferential; and patterns consist in a hole or honeycomb distribution. Groove-type treatment is beneficial when there is tip clearance vortex, by aligning the vortex with the blade suction side, preventing the rotating stall inception. Slot-type treatment provides an avoidance of the tip leakage vortex negative effects by weakening or even destroying the vortex. Air injection and bleeding are particularly favourable at low mass flow rates due to the air recirculation induced as the rotor tip is unloaded, increasing the stall limit, and widening the working range.

Inasmuch as the shock-wave situation in compressor blading is complicated, simplification in the analysis is required to describe the flow physics. Although shock waves introduce three-dimensional effects, traditionally, two-dimensional analyses are used in the blade-to-blade plane to treat the shock phenomenon [1]. Apart from simplifying the shock problem, a two-dimensional analysis allows the interface with streamline curvature and cascade data.

Even though shock waves contribute to the conversion of the passing-flow dynamic pressure into static pressure and leading to higher polytropic efficiencies, they generate a stagnation pressure loss that shortens the operation range. For this reason, it is not feasible to have supersonic flow all along the blade as the operation range can be considerably compromised. Conversely, when there is subsonic flow in a rotor, efficiencies increase and a wider operation range is obtained. Whereupon, the combination of a wide operation range with high efficiencies from subsonic flow and

the high pressure ratio that can be obtained due the shock wave compression in supersonic flow, represents an ideal trade-off to enhance the engine performance.

1.5 Project Scope, Aims and Objectives

The aim of this research is to develop a framework that analytically simulates the transonic flow physics in axial-flow compressors to improve the accuracy of the aerodynamic performance prediction in the context of 2-D SLC compressor performance simulator (SOCRATES), and its application in the design optimisation of a variable-pitch-fan.

To this end, the fidelity of an in-house 2-D SLC compressor performance simulation software was improved, requiring to develop and implement various transonic-flow-associated models and libraries to deal with the flow field encountered in modern fans and compressors. The objectives of this research work are described as follows:

1. Implementation of a blade-element-layout method into SOCRATES to account for 3-D blade-element-layout design in terms of sweep and lean.
2. Development and implementation of a physics-based shock- structure and loss model into SOCRATES to analytically represent the shock-system and the shock-associated losses for unstarted and started operations.
3. Generation of a choking prediction model in set with a mass flow redistribution module to fix the mass flow and incidence limits when choke conditions are reached.
4. Coupling of the choking mass flow redistribution model to the shock model,
5. Application of the transonic-flow handling package within SOCRATES for the NASA Rotor 67, the NASA Advanced Duct Propulsor (ADP) Fan, and a new variable-pitch fan (VPF) design.
6. Conduct a parametric study to assess the influence of the 2-D and 3-D blade-element parameters in the shock-loss behaviour.
7. Full integration of SOCRATES with an evolutionary genetic algorithm (EGA) to perform a single-objective optimisation for the currently designed VPF to develop a swept and leaned modern transonic fan design.

1.6 Knowledge Contribution

Previously published shock- structure and loss- models have assumed and oversimplified the location and shape of the overall shock configuration in the context of the 2-D SLC method, critical for the overall shock-loss computation. The different model assumptions based essentially on the pioneer elementary model of Schwenk *et al*. [4] and on experimental observations are limited only to design conditions and unstarted operations. Henceforth, the estimated shock losses remain insensitive to the off-design conditions since the shock-configuration is imposed. Especially at started conditions, where the shock-loss magnitudes are considerably higher, the models fail to resolve the flow due to the inability of handling choked-flow in the 2-D SLC methods.

Even the widely used shock-loss model from Miller *et al*. [3] across 2-D SLC codes, assumes a passage-shock configuration based on the simplified model of Schwenk *et al*. [4], over predicting the shock-loss in 43%. Despite of an acceptable analytical approach, one of the most recent state-of-the-art shock-loss models by Bloch *et al*. [34] completely disregard the started operations. The other recent state-of-the-art shock-loss model by Boyer and O'Brien [13,35,36], provides a solution for choking conditions but using empirical correlations which are not universal. This has led to over and under – estimations of the shock losses along the blade span and across the working range, resulting in an inaccurate prediction of the overall isentropic efficiency of the fan and compressor for both design and off-design conditions.

The knowledge contribution is thus the development and implementation of a novel analytical physics-based shock- loss and structure model for both unstarted and started operations, utilizing an additional novel mass flow redistribution model that resolves the choking within the context of a 2-D SLC method. Therewithal, the knowledge contribution extends to the full integration of the improved 2-D SLC compressor performance solver with an EGA optimiser to demonstrate the current shock-loss model practical application in the design optimisation of a modern transonic variable-pitch fan.

The shock-loss prediction was improved by 42% with respect of the model of Miller *et al*. [3] and between 40-50% with respect of other state-of-the art shock-loss models. The application of the shock-loss and choking mass flow redistribution models in the

design optimisation scheme coupled to the 2-D SLC solver proved an improvement of 0.4% in isentropic efficiency due to a shock-loss reduction.

1.7 Thesis Structure

The present manuscript is divided in seven chapters, each one containing a number of sections and subsections. Chapters are numbered with Arabic numerals (i.e. Chapter 1 - Introduction), while sections and subsections are referenced by two and three numbers, respectively (i.e. 2.2 Turbomachinery Flow Simulation and Subsection 3.2.3 Supersonic Flow Description). Few subsections are even further divided, establishing an additional section level (i.e. 3.2.7.3 Expansion Fan).

Chapter 2 - Literature Review, discusses four key areas central to this research: Transonic compressors, turbomachinery flow simulation, theoretical aspects of shock waves and choking, and the relevant contributions in shock and choke modelling in SLC. An introduction of the literature review is provided in Sec. 2.1 The operation, associated losses, and 2-D and 3-D blading studies of transonic axial-flow compressors are referred in Sec. 2.2. An introduction of the different turbomachinery simulation methodologies and the fundamentals of the SLC methods are discussed in Sec. 2.3. Sec. 2.4 and Sec. 2.5 explain the fundamental physics of shock waves and choking, respectively, to allow the reader understand the implementation of this theory in the blading. The most important part of this chapter are Sec. 2.6 and Sec. 2.7 where the state-of-the-art and previously published models are reviewed and commented for shock-loss and choke modelling in SLC methods, respectively. Sec. 2.8 provides a summary of the relevant information reviewed across the literature explored.

Chapter 3 – Methodology, reviews the four main improvements done to the SLC axial-flow compressor performance simulator (SOCRATES). An introduction is provided in Sec. 3.1 to sketch the different sections and subsections covered. The blade-element-layout method implemented to represent sweep and lean and the modification to the full-REE second-order differential equation to account for lean effects in 2-D SLC are examined in Sec. 3.2 The main contribution to knowledge is discussed in Sec. 3.3 for the novel analytical and physics-based shock – structure and loss model. This exhaustive subsection offers a thorough description of the strategies and equations used

to calculate the loss coefficient due to the shock-wave strength. This subsection includes then the subsonic supercritical region, bow-shock structure and associated bow-wave losses, flow expansion ahead of the passage shock, an iterative method to locate the passage shock, and the passage-shock losses. Sec. 3.4 describes the choke-prediction model required to operate the current shock-loss model in choked operations, explaining the choking incidence and choking margin calculations, which are used in the mass flow redistribution algorithm for started cases. A summary of the methodology highlights is given in Sec. 3.5.

Chapter 4 – Validation, shows the legitimacy of the results presented herein for the compressor geometries used as test cases in 2-D SLC, and for the transonic-flow models developed for shock loss and choking mass flow redistribution. A short introduction to present the different validation cases is provided in Sec. 4.1. A comparison of the 2-D SLC simulations for the NASA Rotor 67 and NASA ADP Fan against experimental data is presented in Sec. 4.2 and Sec. 4.3, respectively. The validated NASA Rotor 67 2-D SLC model serves as reference to verify the choking condition and mass flow redistribution models in Sec. 4.4. Similarly, the validated NASA Rotor 67 2-D SLC model is used a study case to verify current shock-loss model in Sec. 4.4. As a matter of fact, a thorough verification of the current shock-loss model is presented in Sec. 4.5 against the most notable previously published shock-loss methodologies. The shock-structure prediction is verified in Sec. 4.6 in terms of the detached bow-shock against NACA charts, and the passage-shock against 3-D CFD RANS simulations.

Chapter 5 – Results & Discussion, presents the main findings of the transonic behaviour observed across different simulation strategies. Sec. 5.1 discusses the shock physics identified in a 3D CFD RANS simulation for different off-design points. To demonstrate the operation of the current shock-loss model and the impact of geometry on shock-strength losses, the results of 2-D and 3-D parametric studies are shown in Sec. 5.2. These parametric studies consisted in the variation of the maximum-thickness location, maximum thickness and solidity in terms of 2-D parameters, and in the variation of sweep and lean angles for 3-D parameters. The parameter influence on the shock structure is assessed by examining the relative total-pressure loss in the pitchwise direction and its final impact on the isentropic efficiency. The streamtube mass flow

and incidence correction for those choked streamlines is evidenced in Sec. 5.3 due to the mass flow redistribution model developed and implemented within the 2-D SLC code. Finally, Sec. 5.4 exhibits the applicability of the improved 2-D SLC code with the novel shock-loss and mass flow redistribution models. The 2-D SLC solver is coupled with an evolutionary genetic algorithm to optimise a modern variable-pitch fan in terms of sweep and lean angles, demonstrating a rise in isentropic efficiency due to a reduction in shock-strength losses.

Chapter 6 – Conclusions and Contribution to Knowledge, summarizes the general conclusions of this investigation in Sec. 6.1. Furthermore, Sec. 6.2 discusses the main highlights and main conclusions of the key sections of this thesis: Previously published shock-loss and choking models for 2-D SLC methods, the improvements and contributions to the 2-D SLC framework, and the parametric and optimisation studies

Chapter 7 – Future Recommendations, acknowledges the limitations of the current research and provides a list of future work to be conducted to increment the potential of the tools developed herein towards a more accurate prediction of the transonic flow physics in axial-flow compressors.

2 LITERATURE REVIEW

2.1 Introduction

The literature review of this work was focused on the following three key areas of interest, identified as necessary to understand the contribution to knowledge and its relevance:

- A broad review on design aspects of transonic axial-flow compressors and turbomachinery simulation.
- A fundamental review on 2-D SLC theory, high-speed compressible flow theory and choking in convergent-divergent ducts.
- A specific literature review upon shock waves and choking occurring in the transonic axial-flow compressor blading.

The broader literature review about transonic axial-flow compressors describes their operation and associated flow losses. Given the introduction to transonic axial-flow compressors, the recent advances in 2-D and 3-D blade designs are reviewed. Inasmuch as this research focuses in the prediction improvement of a 2-D SLC simulation tool, a generic review is provided on turbomachinery flow simulation.

A detailed and fundamental review is given about the formulation of the 2-D SLC methods to provide the reader the structure of the internal mathematics and algorithms involved. Since this investigation develops a shock- structure and loss model for unchoked and choked cascades, a subsection is dedicated to compressible flow, where the concepts and formulations for shock compression and wave expansion are explained. One of the major assets of the developed model is its operation for unchoked and choked cascades. To understand the choking basics, a subsection explains the process inside of convergent-divergent ducts, which approximate the blade passages.

More important is the specific and relevant literature review performed for the compressible-flow phenomenon present in transonic blading. The shock configuration and associated losses are described in an attempt to understand the features of the previously published and state-of-the-art shock-loss models, which are reviewed thoroughly. Similarly, the choking process in transonic blade passages and its relation

with incidence is addressed to introduce the problem of the previous choke-prediction models within 2-D SLC.

To provide the reader a layout of the literature review, Figure 2.1 pictorially describes the key items reviewed in this chapter.

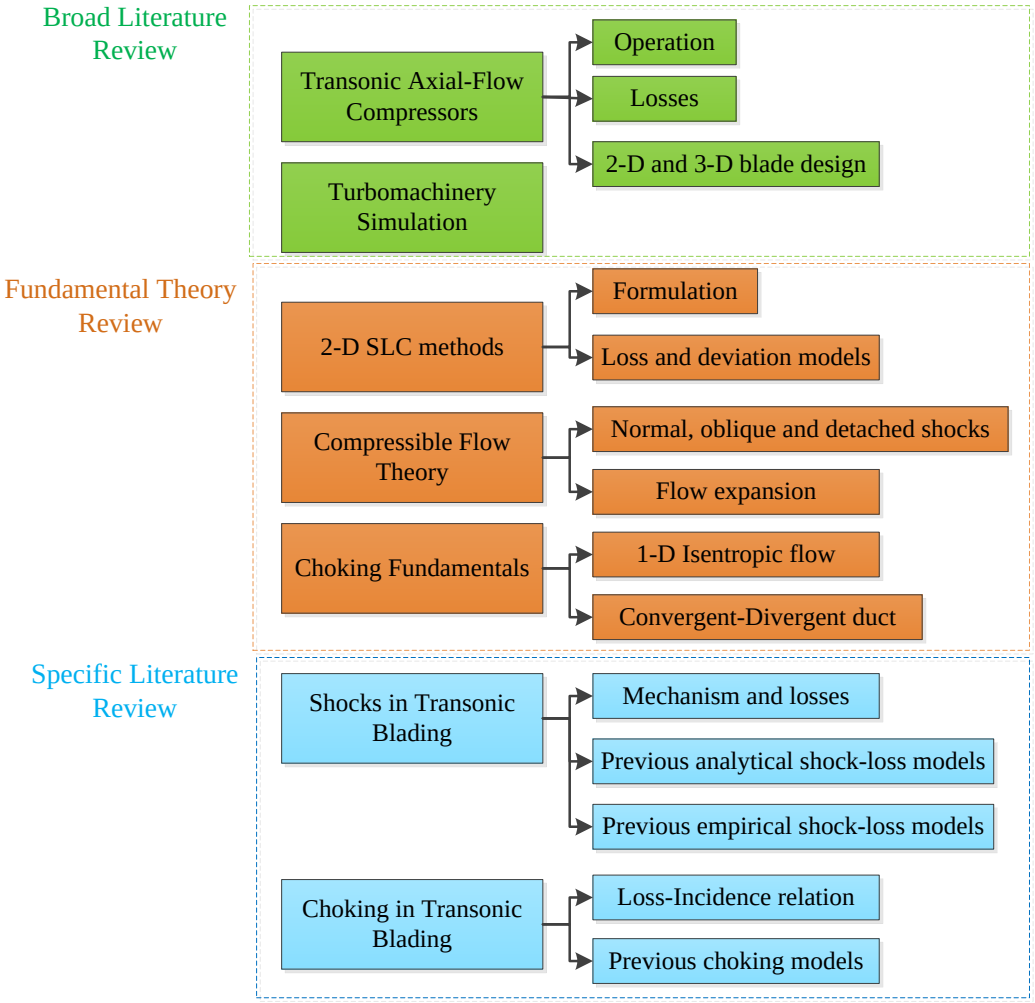

Figure 2.1 Flow chart to describe the literature-review structure conducted for the current research work.

2.2 Transonic Axial-Flow Compressors

2.2.1 Transonic Rotor Operation

Modern high-speed compressor rotor blades spin at high angular velocities ω, generating blade tip speeds U between 450 [37,38] and 550 m/s [39]. The blade or peripheral speed at any radius r is calculated from the rotational speed as follows

$$U = \omega r \tag{2.2.1}$$

Regardless of the incidence level, having high blade speeds means large inlet relative velocities V. In the absence of swirl, or in other words, a zero absolute flow angle α, the relative inlet velocity increment with the blade speed is demonstrated from the turbomachinery velocity triangles as follows

$$V_1 = \frac{U}{\sin \beta_1} \tag{2.2.2}$$

In general, the presence of transonic flow within an axial-flow compressor requires the inlet relative flow entering a blade row to be supersonic. This in turn generates a complex shock-wave configuration ahead of the blade leading edge and within the blade passage, central to this research. Transonic axial-flow compressors can be understood as those compressing systems with a distribution of subsonic and supersonic inlet relative flow either in the span or chord –wise direction.

Because the blade speed, relative velocity, flow area, and mass flow are larger at blade high-span locations, there is a major influence on the pressure rise, loss generation and surge margin at this region. As inferred from Sec. 1.2, in the presence of incoming relative supersonic flow triggers the appearance of shock waves. At the outer part of the blades, the inlet relative flow is supersonic generating complex shock wave structures ahead and within the blade passages as seen in Figure 2.2 for three different high and mid -span locations, where at high-span locations a dual-shock structure can be formed. Figure 2.2 shows Mach number contour plots in the blade-to-blade plane, where the shock waves are evidenced when there is an abrupt change of velocity.

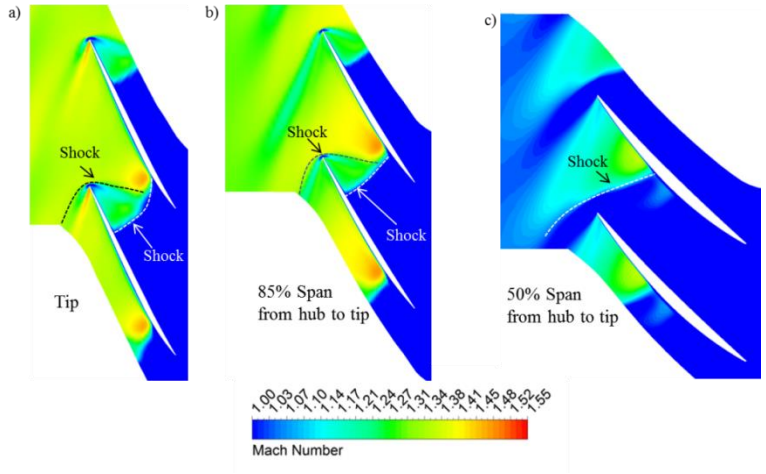

Figure 2.2 Shock structure at blade span locations with inlet relative supersonic flow for the NASA Rotor 67 [40] **at 100% of design speed and near-peak efficiency. a) Tip location. b) 85% span from hub to tip. c) 50% from hub to tip.**

Not only inlet relative Mach numbers M'_1 above or equal to unity can lead to shock-wave patterns, but also inlet relative subsonic flows below one in the supercritical regime can raise the flow to supersonic speeds within the passage. This is an effect due to the acceleration induced by the suction-surface turning, reaching a peak relative Mach number, and terminating in a shock wave as seen in Figure 2.3 for three different low-span locations.

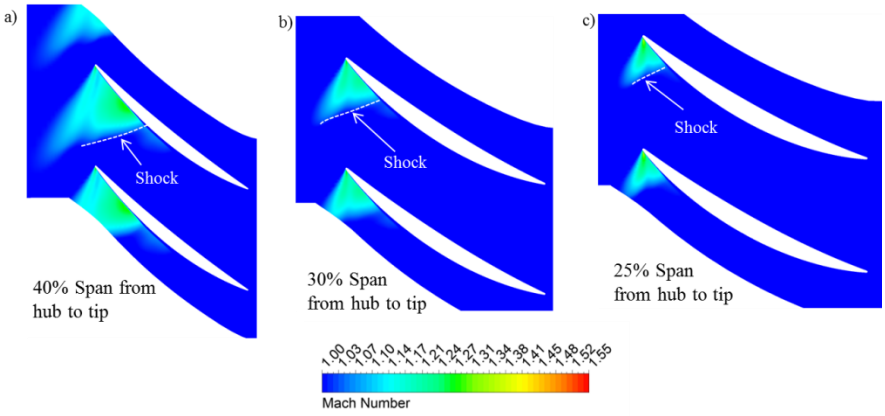

Figure 2.3 Shock structure at blade span locations with inlet relative subsonic flow for the NASA Rotor 67 [40] **at 100% of design speed and near-peak efficiency. a) 40% span from hub to tip. b) 35% span from hub to tip. c) 25% from hub to tip.**

In choking condition, where the back static-pressure is low and mass flow is high, the shock structure becomes highly complex, similar to that in Figure 2.2 a) and Figure 2.2

b). The shock system ahead of the leading edge is a detached bow-shock composed of an upstream and downstream –running shocks [7]. The upstream-running shock drives the inlet flow angle to satisfy the unique-incidence condition, which restricts the inlet relative flow angle to a minimum. The downstream-running shock penetrates into the passage, interacting with the suction-surface boundary layer, inducing boundary layer separation and limiting diffusion. Although the downstream-running shock within the passage joins the passage shock, the shock wave and boundary layer interaction (SWBLI) generated is minimal at that axial location since the boundary layer is reattached downstream. Near the maximum suction-surface relative Mach number, the passage-shock impingement shows a lambda-foot structure that reduces the shock losses, as the shock strength is split between the upstream and downstream limb. Despite the shock-loss reduction at the impingement, the profile losses increase, reducing the loading and incrementing the boundary-layer blockage While inside of the choking region the back static-pressure can be further increased, the unique incidence angle and the inlet mass flow rate remain constant, reflected in the compressor maps as an asymptotic curve.

As the back static-pressure is increased and crosses the choking threshold, mass flow starts to reduce until peak-efficiency condition is reached. At maximum efficiency, the detached bow-shock is still close to the leading edge with a dual-shock structure at the passage at least for the tip profiles, analogous to that in Figure 2.2 b). At this design point, shock losses slightly increase and profile losses decrease with respect of choking, so that total losses remain essentially unchanged [7].

With further back static-pressure increase, mass flow drops and the shock-wave pattern moves upstream becoming more normal near stall condition comparable to that shock configuration in Figure 2.2 c). At stall condition the bow-shock is completely detached from the leading edge, and thence, increasing the incidence angle. Near surge condition, any shock loss rise is due to a pre-shock Mach number increase caused by the supersonic turning ahead of the shock in set with the loss from the upstream-running wave, similar to the contour distributions displayed in Figure 2.3.

The compressor efficiency is driven by the total-pressure loss magnitude, which depends on the through-flow losses arising from an entropy increase induced by the loss mechanisms. Total flow-loss can be generally approached by considering the blade profile, secondary and shock losses [14,20,41]. As it is later discussed in Sec. 2.2.2, to obtain a high-fidelity gas turbine or component performance analysis, it is not enough to consider the conventional performance theory, but also the complex 3-D internal flow behaviour that induces the flow losses must be addressed. For instance, as mentioned further in Sec. 2.3.2, 2-D through-flow performance simulators assume a non-viscous flow assumption, requiring empirical correlation models to assign a loss factor for the aforementioned flow-loss types.

In the design process of gas-turbine engine components, the pressure ratio, mass flow and rotational speed demanded by the turbine determine the axial-flow compressor parameters such as: inlet, outlet and inter-stage diameters, number of blade row stages, number of blades per stage, chord lengths, and tip clearances [42]. In the early years of axial-flow compressors around 1930s, blade profiles were based on typical NACA (National Advisory Committee for Aeronautics) design-series. Further development of transonic compressors led to test British-standard profiles and eventually double-circular-arc (DCA) and multiple-circular-arc (MCA) profiles, to match the stage loading criteria and efficiency requirements. The necessity of having a wider compressor operating range, specially extending surge margin, has resulted in the design of controlled-diffusion profiles, which are none other than customized aerofoil shapes.

Further development in 2-D compressor blade-profile shaping at tip locations, consisting in maximum-thickness-location increase, maximum-thickness reduction, and solidity increment, made the blade elements less susceptible to shock losses while reducing the loading at high-span regions [3]. At mid and low -span locations, conventional cambered blade profiles are used to still provide flow turning to increase the pressure ratio at subsonic inlet relative speeds. To this end, the transonic compressor justifies its design and operation if the associated performance, and mainly efficiency, is at least comparable to that of a subsonic compressor unit.

2.2.2 Blading Flow Field Losses

The flow field across any turbomachinery component is complex to analyse and despite the physics-based approaches and numerical methods, its nature is yet to be fully understood. The flow character through an axial-flow compressor is viscous, 3-D and unsteady. The flow viscosity retards the flow within the boundary layer through friction-induced shear stress mechanisms, increasing entropy and hence, loss production. It is well-known that any boundary layer subjected to an adverse pressure gradient grows faster and tends to separate. In a compressor axial-flow, the problem is aggravated because the chordwise flow-diffusion slows down the velocity distribution normal to the blade surfaces, increasing the boundary layer thickness δ, and thus, raising the friction-force-induced losses. Unsteadiness arises from blade rotation, causing an intermittent air flow that leads to cyclic wake appearance, and non-constant but periodic back pressure. Added to these effects, there is a 3-D interaction between the flow mechanisms that complicates the problem.

In spite of the highly-complex flow circulating around axial-flow compressor blades and the difficulty of separating the losses, the different loss mechanisms have been identified and described [43] as shown in Figure 2.4. Without the presence of shock waves, the only interactions are profile, and secondary losses. Profile losses emerge from the blade boundary-layer frictional effects and wakes.

Secondary losses involve the effects from passage secondary flows, spanwise mixing, leakage at the leading and trailing edge, and the end-wall interactions between the annulus wall boundary layer (AWBL) and the blade rows. These end-wall interactions lead to tip clearance flow and corner separation, where the latter develops corner vortices at the shroud and at the hub. The situation can aggravate more, as these secondary flows can be further disturbed by unsteady inlet conditions or inlet end-wall boundary layer status, such as initial deviation or skew.

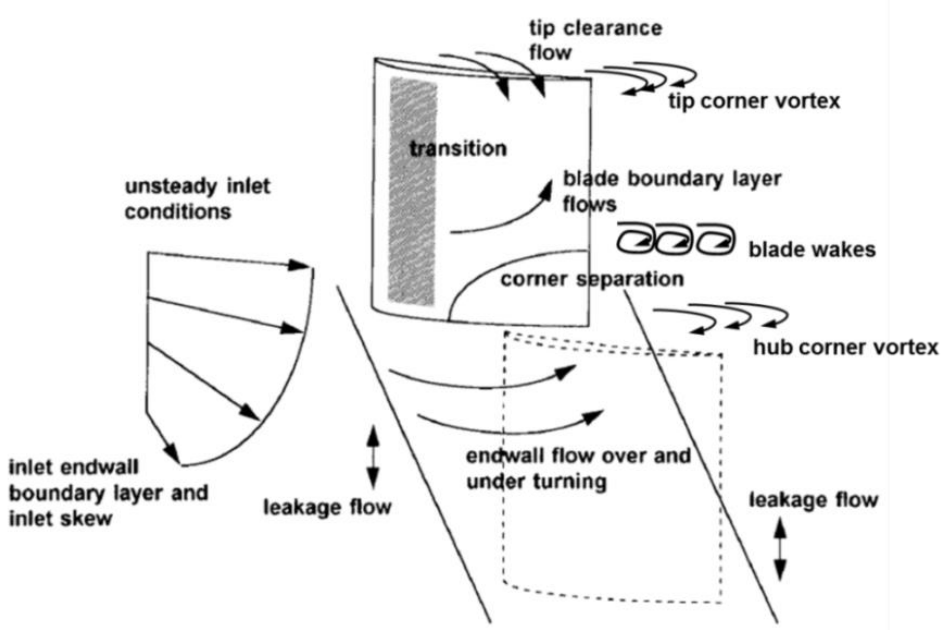

Figure 2.4 Flow interaction with a non-transonic axial-flow compressor rotor blade (modified from [43]**).**

For the case of transonic axial-flow compressors, additional losses due to shock waves and their interactions with the flow itself and boundary layer dominate at the blade tip. As it is known, every real fluid passing over a surface develops a boundary layer and a corresponding boundary layer thickness that increases when is subjected to an adverse pressure gradient. In compressors, besides of the adverse pressure gradient that the flow experiences due to the compression in the flow direction, this gradient is magnified due to the shock, having a shock wave and boundary layer interaction (SWBLI), resulting in a higher boundary layer thickness increase that can eventually result in reverse flow, generating a separation bubble and contributing to aerodynamic losses. Boundary layer can reattach to the surface or not before the trailing edge; in the case of no reattachment, wakes are formed downstream of the trailing edge and energy losses are raised.

In addition, a spanwise flow migration occurs at the blade suction side, downstream of the passage shock, illustrated in Figure 2.5. Radial flow motion forms a low-momentum region at the blade trailing edge, contributing to a boundary layer thickening and hence, building up for wake development, leading to an unfavourable stability by shortening the engine working range.

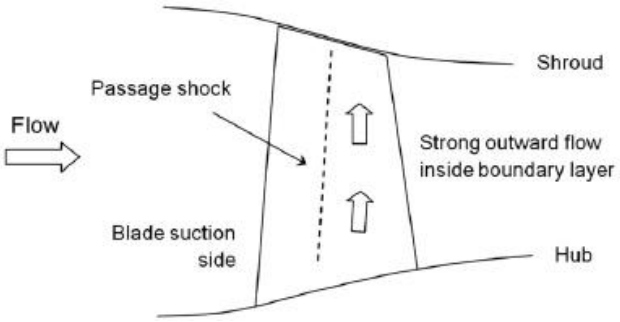

Figure 2.5 Radial flow migration occurring downstream of the shock on the blade suction surface [32]**.**

Besides of the clearance secondary flows, there is a strong interaction between the shock wave and them which has been studied more than the other shock-related negative effects due to its high influence on entropy production. The pressure gradient between the suction and pressure side pulls up the flow to the tip surface, generating a jet throughout the main flow, resulting in an interaction between them and forming a vortex known as tip-clearance or tip-leakage vortex [32]. This tip-clearance vortex initiates at the leading edge and develops within the passage, interacting all its way with the shock wave and the casing boundary layer, decrementing the rotor performance. As the operating point moves towards surge condition, flow becomes stronger and unsteady, increasing the blade loading and inducing a tip-clearance vortex breakdown. This in turn causes a blockage near the blade tip and flow oscillation, leading to shock-induced flow separation that varies in time, and thus, rotor instability. This vortex breakdown is considered to be a sudden change in the vortex core structure [44].

To quantify the total loss due to entropy generation, the total-pressure drop or loss is measured by the difference between the ideal outlet total-pressure $P_{02_{id}}$ and the actual circumferentially mass-averaged outlet total-pressure $\overline{P_{02}}$ with respect of the inlet pressure conditions. Thus, the mass-averaged total-pressure loss coefficient or total-loss coefficient $\bar{\omega}$ is

$$\bar{\omega} = \frac{P_{02_{id}} - \overline{P_{02}}}{P_{01} - p_1} \qquad \textbf{(2.2.3)}$$

The actual outlet total-pressure is a mass-averaged value as there is a circumferential variation if the total loss coefficient is measured per blade element. In very simplified

analyses where ω accounts for the full blade, the mass-averaged outlet total-pressure must consider as well the radial variation. The ideal outlet total-pressure is equal to the inlet uniform total-pressure as there is no total-pressure loss, then $\bar{\omega}$ becomes

$$\bar{\omega} = \frac{P_{01} - \overline{P_{02}}}{P_{01} - p_1} = \frac{1 - \frac{\overline{P_{02}}}{P_{01}}}{1 - \frac{p_1}{P_{01}}} \quad \textbf{(2.2.4)}$$

Substituting the isentropic relationship between total and static conditions and expressing the total pressures in the relative frame of reference for the rotor case, the total-loss coefficient or factor transforms in

$$\overline{\omega'} = \frac{{P_{01}}' - \overline{{P_{02}}'}}{{P_{01}}' - p_1} = \frac{1 - \overline{PR'}}{1 - (1 + \frac{\gamma - 1}{2}{M_1}'^2)^{\frac{\gamma}{1-\gamma}}} \quad \textbf{(2.2.5)}$$

where γ is the specific heat ratio, M_1 is the inlet relative Mach number, and $\overline{PR'}$ is the relative total-pressure ratio between inlet and outlet.

The mass-averaged total-loss factor can be divided in profile, shock and secondary losses, corresponding to an individual loss coefficient, ω_{prof}, ω_{sh}, ω_{sec}, respectively. Hence, the total-loss factor is typically defined as the summation of the different source-loss coefficients, where the profile loss coefficient might be corrected by a Reynolds-effect factor f_{Re} [3,20,41,45–48]. This is,

$$\overline{\omega'} = f_{Re}\overline{\omega_{prof}'} + \overline{\omega_{sh}'} + \overline{\omega_{sec}'} \quad \textbf{(2.2.6)}$$

Although the total-loss coefficient in Eq. 2.2.6 is a standard definition, it is not universal. The total-loss factor can be redefined depending on the models used to calculate the profile, shock and secondary losses. For instance, Boyer and O'Brien [36] suggested the calculation of $\overline{\omega'}$ as in Eq. 2.2.7, where the secondary losses are split in tip and hub losses, whereas the shock loss is corrected. Because the shock-loss coefficient is calculated using a simplified model for unstarted conditions only, a correction factor based on the difference between the actual incidence i and the minimum-loss incidence i_{min} with respect of the working range width W is applied to account for the unique-incidence effect at started operations.

$$\overline{\omega'} = \overline{\omega_{prof}{}'} + \overline{\omega_{tip}{}'} + \overline{\omega_{hub}{}'} + \overline{\omega_{sh}{}'}\left[1 + \left(\frac{i - i_{min}}{W}\right)^2\right] \quad \textbf{(2.2.7)}$$

Note that a fully comprehensive and physics-based shock-loss coefficient estimation eliminates the need of correction factors. The prediction of a physics-based shock-loss coefficient as a function of the operation is cardinal of the present work. A thorough discussion on physics-based and empirical shock-loss models is given in Sec. 2.6.4 and Sec. 2.6.5, respectively.

2.2.3 Blade profile studies

Blade geometry significantly influences the flow field in a compressor and particularly in transonic axial-flow compressor, where the performance is greatly affected by small 2-D or 3-D geometric modifications due to the shock-wave presence and its interaction with the flow field. Chung *et al*. [49] demonstrated that a transonic rotor blade is more sensitive to geometric changes at the hub, which is the region that yields the highest adiabatic efficiency and total pressure ratio. As a matter of fact, 2-D geometry modification focuses on blade-profile shaping, whereas 3-D blading includes not only the later but also blade sweeping and leaning.

In terms of blade profile design, Wadia and Copenhaver [50] demonstrated that the flow field across a transonic blade row is highly sensitive to camberline angle variations, modifying the blade profile and passage area, due to the shock-wave existence. A zero or near-zero curvature at the suction-surface forward part that can even result in pre-compression shocks would be ideal to decrease the pre-shock Mach numbers to reduce the shock-induced pressure losses originated from its strength and the SWBLI [32]. Additionally, flow Mach numbers can be further reduced upstream of the passage shock at the blade tip profile sections by keeping low thicknesses along the blade length around 2% of the chord. Biollo and Benini [32] reported that one of the most important factors for the flow field behaviour around blades is the chordwise location of the maximum thickness. Wadia and Law [12] demonstrated that the more rearwards the maximum thickness is located, the better high-speed performance that can be obtained, so that the length for the shock-induced separation extent is reduced. A similar paper

by Chen *et al*. [51] proved that an increase of the maximum thickness location from the leading edge reduces the thermal-loss coefficient regardless of the spanwise location of the profile section. Besides the maximum-thickness chordwise location, the value itself impacts on the flow field behaviour. A study by Suder *et al*. [52] where the leading edge thickness was increased by 10% at the hub and 20% at the tip due to a coating addition, showed a total pressure loss of 4% across the rotor blade.

2-D flow analysis techniques and CFD simulations have assessed the performance impact due to aerofoil changes. In fact, comprehensive blade profile optimisation studies have been carried out by coupling flow analysis simulators with optimisation algorithms, exploring the design space in a more efficient, faster and less expensive framework to deliver optimal blade profiles for design and off-design points. In fact, the study of Chen *et al*. [51] was performed by blade parametrization, where ten parameters were searched to find an increase in maximum adiabatic efficiency of 1.73%. Burguburu *et al*. [53] carried out a quasi-3-D numerical optimisation of the blade profile sections to reduce the flow Mach number upstream of the passage shock, obtaining a negative curvature at the blade profile frontal part. Consequently, the peak relative Mach number decreased from 1.4 to 1.2, creating two weak shocks instead of a strong normal shock wave.

Not only one objective function can be maximized, but also several objective functions can be maximized by means of multi-objective optimisation algorithms. A multi-objective optimisation for the well-known transonic compressor NASA Rotor 67 [40] blade profiles to maximize pressure ratio and minimize blade weight at design point was performed by Lian and Liou [54]. In this optimisation a new rotor blade was obtained by modifying the camberline while keeping the leading and trailing edges constant, and varying the thickness distributions for the tip, hub and two part-spanwise distributions. This geometry variation led to an increase of 1.8% in total pressure ratio. The optimized rotor blade gave thinner blade profiles that account for a lower weight and a reduced separation region downstream of the shock yielding in a higher total-pressure ratio. In fact, when structural stability is used as a constraint apart from the aerodynamic performance, multi-disciplinary optimisations come into play using neural networks. Lee *et al*. optimized a transonic axial-flow compressor rotor blade to

maximize the isentropic efficiency and rotor safety factor, increasing the former by 3.69%, using genetic algorithms (GA) coupled with CFD and Finite Element Analysis (FEA).

In addition, a blade profiles have been optimized for several operating points. Luo *et al*. [55] performed a multi-point blade optimisation for the NASA rotor 67 [40] using entropy production, mass flow rate and total pressure ratio as objective functions at three different points: near-stall, peak-efficiency, and near-choking. As stated in Sec. 2.2.2, there is an interaction between the shock wave and the tip-clearance vortex that produces entropy, which was investigated and reduced in the blade optimisation process of Luo *et al*. [55]. In this study, a CFD-analysis tool and an adjoint method were coupled to obtain the blade optimisation where, the optimisation methodology took twice the computational time of the flow solution for each analysed operating point.

CFD tools are the preferred method for optimisation; however, they involve high computational cost and intolerably large solution times, since for every parameter modification, a new model is built and analysed using CFD. For this reason, Chung *et al*. [49] developed an affordable design method based on a quasi-3-D blade profile flow analysis at strategic spanwise stations, which were numerically optimised to enhance adiabatic efficiency. For validation purposes, such optimised blade-profile sections were used to interpolate at intermediate locations, which were stacked to build up the 3-D geometry, and later analysed using a 3-D CFD tool. It was found that CFD performance characteristics were different from those in the quasi-3-D analysis, due to the 3-D effects that were not considered in the latter. Therefore, geometry modifications computed by the optimisation had a low impact on the final blade as three-dimensionality was not considered in the quasi-3-D analysis. In this way, optimisation through quasi-3-D analyses offers low computational costs at the expense of fidelity. Through-flow techniques, such as streamline curvature method (SLC), represent an alternative for optimisation due to their low analysis-times of minutes without compromising accuracy since loss and deviation process models can be implemented. Particularly for multistage axial-flow compressors, a sort of empiricism is required to account for accuracy [42]. In this context, the 2-D SLC compressor performance simulation software (SOCRATES) [18,19,29,41] developed by Pachidis

[14] and central to the research presented herein, matches the capabilities of a rapid solution, acceptable results, and freedom to incorporate loss and deviation models.

Additional efforts to optimize the NASA Rotor 67 [40] at different operating conditions have been conducted. For instance, Wang *et al*. [56] performed an optimisation near choking point at 100% speed by changing the blade profile camberline type from MCA to a reverse-camberline type while increasing the camber blade-profile at the hub. As a result, isentropic efficiency was increased by 1.7% with a low penalty in total pressure ratio.

Advanced evolutionary algorithms have led to non-traditional aerofoil geometries as in the optimisation carried out by Oyama *et al*. [57]. The optimized blade resulted in double-humps at the pressure surface for different spanwise positions. Therefore, a flow deceleration reduction at pressure side was obtained, particularly at near-tip spanwise locations, where the shock on the suction surface moved aft, and, thereby, reducing the flow separation extent. This in turn, resulted in an isentropic efficiency rise of 2.0% for all the operating range at 100% speed.

2.2.4 Three-Dimensional Blading

As mentioned in Sec. 2.2.2, 3-D effects should be considered to obtain an accurate flow analysis or design optimisation. Research has shown that 3-D shape blading, namely modifying blade sweep and lean, has a significant impact in 3-D behaviour, particularly due to shock waves and flow interaction. In the case of swept transonic compressor blades, the flow is highly 3-D and interacts with the radially swept shock wave [58].

Wennerstrom was the first to propose and test shock structure control by blade sweep [59]. Yamaguchi *et al*. [60] demonstrated that blade sweep significantly contributes to the radial loading redistribution and to shock-wave control in transonic rotors. Gallimore *et al*. [61,62] mentioned that sweep contributes to the reduction of shock losses, leading to an enhanced efficiency and a wider operating range. Passrucker *et al*. [63] acknowledged that blade sweep is considered to be a technique that reduces shock wave strength, yielding an improvement for both efficiency and surge margin . A

significant 3-D behaviour to be contemplated is the shock wave and tip-leakage vortex interaction [32], which can be controlled as well by blade sweep and lean.

Conventionally, the blade profile sections are stacked along the stacking line, which is an axis that passes through all the centres of area of all the blade aerofoil sections. When the blade is swept or leaned, the centre of areas are moved forwards and backwards in the axial direction for the case of sweep, and positive or negative in the tangential direction for the case of lean, with respect to the stacking axis.

Other blade sweep and lean influences on the flow field and its mechanisms have been investigated. Wadia *et al*. [64] carried out an experimental investigation to study forward and backward swept blades, whose results were assisted with a 3-D viscous flow analysis to understand the behaviour. Overall, it was observed that both, forward and backward -swept rotors increase efficiency. In the case of forward-swept blades, stall margin is amplified in contrast to the backward-swept blade, where it was significantly diminished. It was concluded that improved efficiency was due to a less intense SWBLI as there was less axial-flow diffusion and a blade tip surface boundary layer thinning. Similar results were reported by Hah *et al*. [65], where forward and backward -swept rotors increased in the same rate the peak efficiency, nevertheless, the stall margin is smaller in the latter case. Conversely to Wadia *et al*. [64], Hah *et al*. [65] explained the efficiency increase due to 2 mechanisms. The first mechanism consisting in a radial shape change of the shock near the tip due to the endwall effect, while the second consists in the radial flow migration towards the blade tip [32]. Similarly, Passrucker *et al*. [63] investigated the forward sweep influence in transonic compressor rotors through a CFD code, finding a higher efficiency and stall margin for the forward-swept rotor in comparison to the baseline radially-stacked blade. Near stall, it was observed that the swept blade pushes the flow to the tip, creating stability at this point although flow separation is developed at the hub without triggering rotating stall. Templalexis *et al*. [66] evaluated the effect of blade sweep through SLC methods, finding that a backward sweep increases pressure ratio.

Design studies have shown the high influence of blade sweeping apart from the 2-D blade-profile-element parameters on transonic axial-flow compressor performance

characteristics. Denton and Xu [67], and Denton [68], performed CFD analyses for five different transonic fan blade designs to assess the sweep and lean angle effects, finding a little impact of sweeping and leaning near the tip. Whereas at mid-span and near-hub locations shock was swept, reducing the losses. Nevertheless, surge margin was contracted, increasing losses along the spanwise for off-design near-surge points. An important observation from this study was the radial flow migration downstream of the shock on the suction surface. This phenomenon affects the flow behaviour near the tip producing a larger blockage even if there is no annulus wall boundary layer (AWBL) or tip gap, agreeing with Hah *et al*. [65] remarks. This flow-migration-induced blockage moves the shock upstream, reducing the stall margin.

Sweep and lean angle have been defined in different manners in the literature. Traditionally, the blade profile sweep angle is defined on the axial axis (z-axis) while lean angle moves along the circumferential direction (θ-axis) as shown in Figure 2.6.

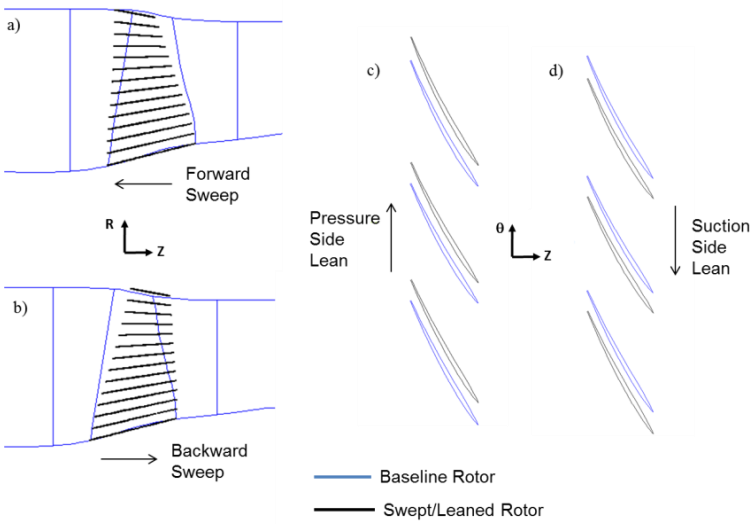

Figure 2.6 Traditional sweep and lean angle definition in cylindrical coordinate system. a) Forward sweeping along z-axis. b) Backward sweeping along z-axis. c) Leaning towards pressure side in θ-direction. d) Leaning towards suction side in θ-direction .

Nevertheless, a different definition of sweep and lean was used , in the study of Denton and Xu [67], and Denton [68]. Sweep was considered to be along the blade chord line and lean to move perpendicular to the chord line as shown in Figure 2.7. According to the authors, sweep in this direction does not introduce spanwise blade forces so that tilting loads are distributed in the lean direction.

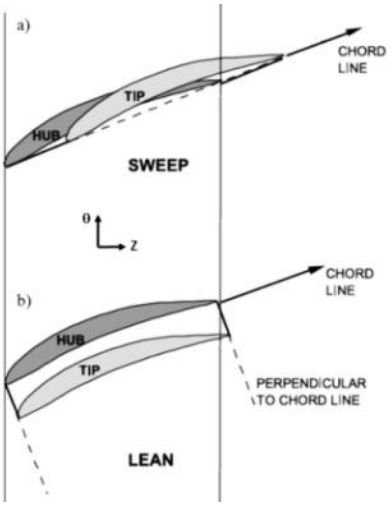

Figure 2.7 Sweep and lean angle definition with respect to the chord line (modified from [68]**). a) Sweep along the chord line. b) Lean perpendicular to chord line.**

Ramakrishna and Govardhan [69] performed a sweeping study, where a conical design-space as observed in Figure 2.8 was defined for different angles. This comprehensive space is a combination of the typical sweep/lean angle definition and the approach used by Denton [68]. To avoid confusion, Ramakrishna and Govardhan [69] defined the sweep angle in axial direction as axial sweep and perpendicular to it, as tangential lean. In the case the blade moves along the chord line, the sweep is considered to be chordwise; while perpendicular to the chord, the motion is in the dihedral direction. In any of the aforementioned cases, the sweep or lean angle is always considered with respect to the hub stacking point, which is no other than the intersection between the blade stacking axis and the corresponding blade profile section centre of area.

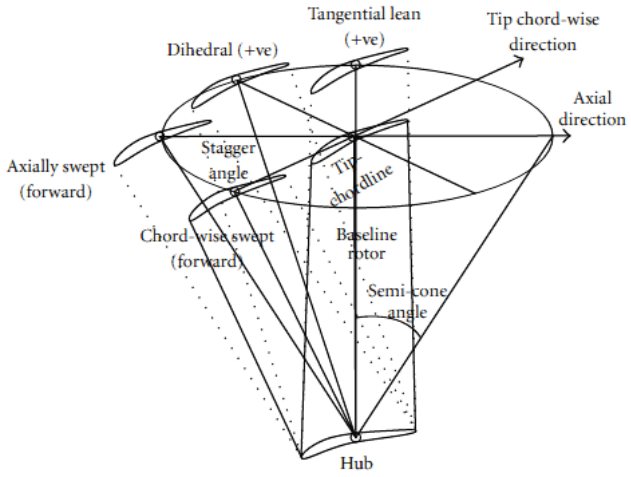

Figure 2.8 Full space for sweep and lean angle definition around a baseline blade [69]**.**

Similar to Denton and Xu [67] and Denton [68], Ramakrishna and Govardhan [69] studied particular sweep configurations for axially swept and chordwise swept blades through CFD but for subsonic axial-flow compressors. It was observed that forward sweeping reduces the incidence angle and flow turning. Forward axial-sweep was found to be more efficient in energy transfer between the stages, while forward chordwise-sweep introduced flow deflection. In a blade sweep influence study by Vad [70] for low-speed axial-flow rotors, the tangential lean of Ramakrishna and Govardhan [71] was defined as circumferential skew. These sample of studies proves the different terminology used in the literature to define the blade inclination. The present author considers that the definition used by Ramakrishna and Govardhan [69] is the most convenient since it does not leave space for ambiguity and covers a comprehensive design space for blade tilting options.

Chen *et al*. [72] performed a similar sweeping study through CFD to evaluate the impact of a forward-swept and backward-swept rotor blade in transonic compressors for a value of -4^{o} and 4^{o}, respectively. In contrast to other studies, the blade leading edge was tilted with respect to the hub leading edge point. Likewise Denton [68], sweeping effect had different influence along the span height and little effect at near-tip locations. Adiabatic efficiency at low-span positions was higher for the backward-swept rotor, whereas at mid-span, efficiency increased for the forward-back swept blade. This led to a further simple gradient-based optimisation of two spanwise locations at mid- and tip-span heights, by axially moving them. The optimised blade had a forward displacement at mid-span height and a backward displacement at tip-span, obtaining an adiabatic efficiency increase of 0.31% and loss coefficient decrease of 2.74% at design condition.

A recent study from Razavi and Boroomand [73] evaluated the axial sweep and tangential lean impact in the NASA Rotor 67 [40] using a CFD method to solve the flow field. A huge number of models were built, varying both angles, sweep and lean from -20^{o} to 20^{o}. Results showed that axial sweep increased the efficiency by 2%, the operating range by 30% and the pressure ratio by 1%. In terms of tangential lean, no significant improvement was observed for efficiency or pressure ratio, whereas working range was increased by 14%. Despite the comprehensive study, no further attempts were made to assess the impact of combined sweep and lean.

Studies from Denton [68], Ramakrishna and Govardhan [69], Chen *et al*. [72], and Razavi and Boroomand [73] were limited to study the effect of constant sweep or lean angle along the whole blade length for specific angle values. In these studies, the constant blade inclination as a whole, did not allow to independently move different profile sections, which is required as the flow behaviour varies in the radial direction. Moreover, a comprehensive design-space exploration was not performed, leaving aside the possibility to optimize for blade sweep and lean angle. Under these circumstances, spanwise distribution of sweep has been investigated in optimisation methods to cover a wider range of design-variable parameters.

Inasmuch as the blade sweep brings positive effects for some heights and negative for others, curved S-shaped blades provide a solution. Biollo and Benini [8] evaluated the effect of S-shaped axial-sweep and S-shaped tangential-lean for the NASA Rotor 37 [74] transonic compressor by means of a CFD package. Instead of conducting an optimisation, 26 models were built to evaluate the S-shaped sweep and other 26 models to assess the S-shaped lean effects. Conversely to define a sweep angle for specific radial positions, control points were defined to be moved with respect to the stacking axis. Control points defined at 33%, 67%, and 100% of the blade span were displaced along the merdional plane to account for axial sweep and along the circumferential plane to account for tangential lean, as depicted in Figure 2.9.

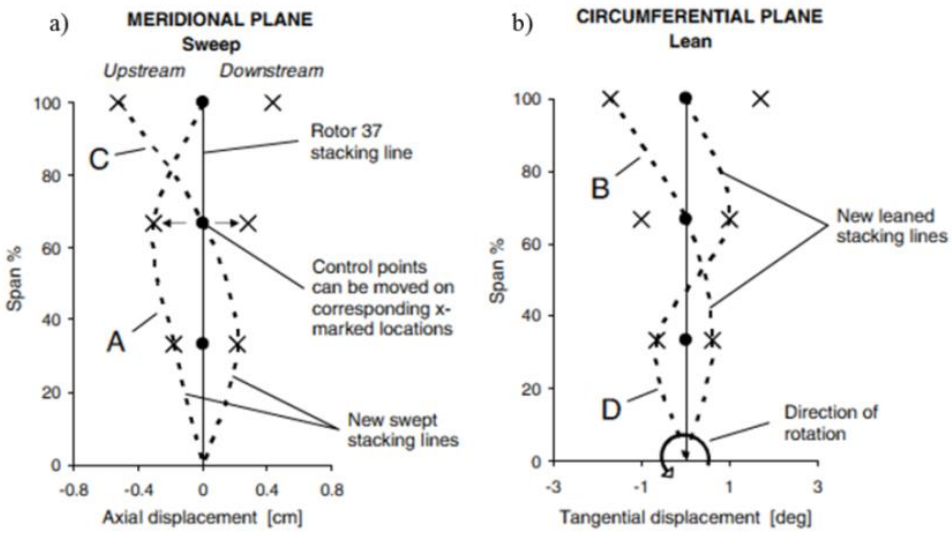

Figure 2.9 S-shaped blading at 33%, 67% and 100% of span [8]. **a) Axial Sweep. b) Tangential Lean.**

The control points were shifted according to a curvature pattern, so that they could be identified as forward or backward -swept, and positive or negative –leaned, as shown in Figure 2.10. It was demonstrated that S-shaped blades with forward-curvature sweep trent could give 1.3% higher efficiency than the baseline due to a shock weakening. On the other hand, S-shaped blades with backward-curvature sweep trent could only provide 0.5-0.6% but handle a higher choking mass flow than the original blade. Although tested, lean proved not to significantly modify the performance. Nonetheless, simulatenous sweep and lean angles were not tested, where the influence of lean can take more presence.

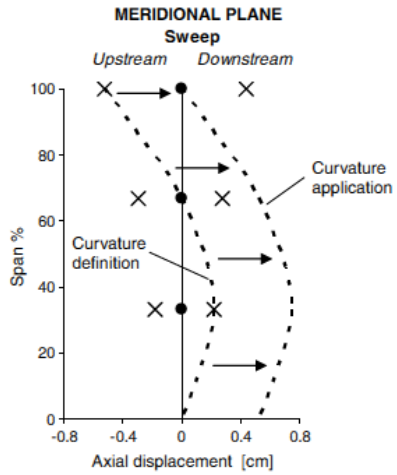

Figure 2.10 S-shaped backward-curvature axial-sweep applied to a blade [8]**.**

A single-objective optimisation of blade sweep for the NASA Rotor 37 [74] transonic compressor was performed by Jang *et al.* [75]. The optimisation was performed by means of a response surface method, while the actual flow was analysed through a 3-D Navier-Stokes code. Adiabatic efficiency was set as the objective function, having as design variables 2 lengths, Δ_1 and Δ_2 (shown in Figure 2.10) to define the sweep. In fact, this is another manner of defining the blade sweep, as optimisation can allow for the leading edge tilting to start at any radius and not necessarily at the hub. Design variable space was constrained for the blade to be moved only backwards; there is no further detail that explains this limitation and not exploring forward sweep as well. Overall with the optimized blade, an increase of 1.25% in adiabatic efficiency was achieved, as it was observed that the sweep retarded the flow separation, and hence reducing separation extent. From results, it was observed that in the spanwise direction,

adiabatic efficiency remained the same near tip between baseline and optimized rotor blade, at mid-span locations, efficiency increased for the optimized blade, and near hub, efficiency was higher for the baseline case. Hence, efficiency improvement came only from mid-span locations and it could have been improved if a forward sweep would have been introduced at low-span heights. These results match with those from Denton [67,68] and Chen *et al*. [72], where there was no influence of sweep at near-tip locations, backward-sweep provided higher efficiency at mid-span heights and forward-sweep increased efficiency near-hub radii.

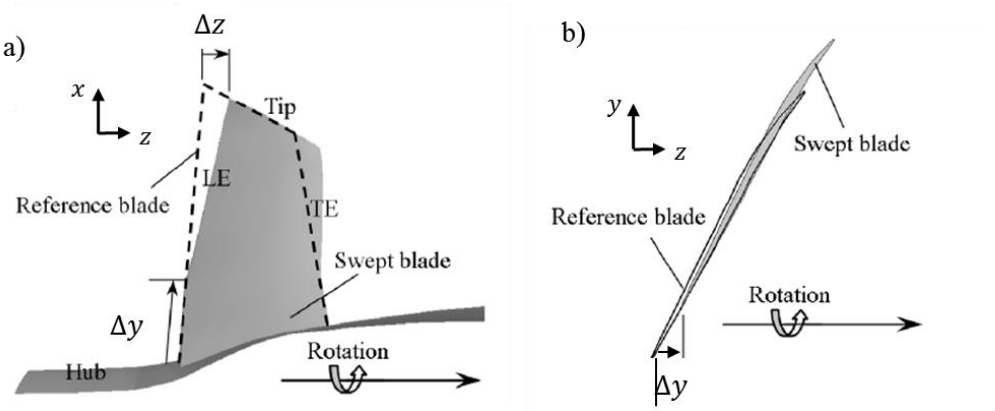

Figure 2.11 Blade sweep definition using 2 length parameters (modified from [75]**). a) Axisymmetric view. b) Top view.**

Further, Jang *et al*. [76] optimised the same transonic axial-flow compressor rotor blade for three parameters, sweep, lean, and skew at design point using the same strategy to maximize adiabatic efficiency. Whereafter, the adiabatic efficiency was increased due to a reduction in hub corner loss, tip loss, and SWBLI-induced separation extension, being the skew the design variable that influenced more the performance.

A more recent three-dimeensional blading multi-objective optimisation for transonic axial-flow compressors was done in an study by Okui *et al*. [77]. In this study, the camberline, chord length and sweep angle spanwise distribution were searched to maximize efficiency, while keeping the surge margin by shock wave control and off-design performance. The resulting S-shaped camberline and backward-swept rotor, enhanced the efficiency by 0.6% at the same baseline stall margin. A slight efficiency increase of 0.7% was obtained when the sweep was compound, reducing losses at mid-span and weakening the leading edge shock. The authors remarked that same effects

from backward sweep can be obtained with an S-shaped camberline since the tip shock can be made oblique, shifting the load downstream, reducing the shock and tip-leakage losses, and thence, increasing the operating range.

Besides blade optimisation, further sweeping and leaning studies have been produced to investigate its influence in transonic axial-flow compressors [78,79]. For instance, Hah *et al*. [65] stated that performance improvement in transonic rotors is observed with sweep in both cases, forward and backward, however the mechanisms are different. Forward-sweep reduces both, secondary flow effects and entropy generation, whereas backward-sweep lessens the shock loss intensity. Gümmer *et al*. [80] studied the blade sweep and dihedral angle effects on endwall loss mechanisms, and consquently the impact on transonic compressor performance using a 3-D Navier-Stokes solver. Hah and Shin [44,81] examined the near-stall flow conditions through CFD for a transonic fan blade with compound (or composite) sweep. It was concluded that flow and shock structure near the blade tip are more stable in compound-swept blades as the passage shock remains relatively close to the leading edge even at near-surge condition, following an earlier detachment at radii where sweep was in opposite direction. However, flow fields and behaviours at different radial positions along the same blade are not comparable. In this respect, Chen *et al*. [72] demonstrated that same sweep magnitude for opposite directions has different effects depending on the radius. In addition, the studies of Hah and Shin [44,81] do not specify sweep directions, sweep spanwise distribution, and sweep values. Despite the unfair sweep comparison between different radii for the same blade, the magnitude increase of the passage-shock and tip-clearance-vortex interaction was recognized as the fan throttles near surge. This in turn, generates a vortex breakdown that leads to transient operation. Using quasi-3-D methods, Gui *et al*. [82] showed that sweep in axial-flow compressors introduce flow circumferential fluctuation, which rather than affecting the passage shock structure, it modifies the radial equilibrium. Therefore, a new radial equilibrium is established, leading to a circulation modification along the meridional streamline direction, inducing a rearrangement of the inlet flow.

Furthermore, blade sweep and lean aerodynamic effects have been investigated on transonic axial-flow compressors, as well as in low-speed axial-flow compressors.

Although subsonic axial-flow compressors are not covered in this research, a look into blade sweeping techniques performed to them is of interest, as the same efficiency and stall margin effect produced in transonic behaviour is generated in subsonic speeds. Corsini and Rispoli [83] assessed the sweep effect through CFD analysis for a low-speed axial-flow fan, where forward sweeping increased the stall margin due to attenuation in both, non-free vortex secondary and leakage flows. Vad [70] presented a literature survey about the sweep and tangential lean effect on axial-flow fans and compressors to increase efficiency and stall-free working range. Gallimore *et al*. [61,62] described the sweep and dihedral effects in low-speed multi-stage axial-flow compressors using CFD. Studies from Breugelmans *et al*. [84], and Sasaki and Breugelmans [85] have shown that end-wall losses can be significantly reduced as well by dihedral introduction at the blade tip in low-speed compressors.

2.3 Turbomachinery Flow Simulation

2.3.1 Background

For rapid assessment, zero-dimensional (0-D) gas-turbine cycle simulation tools have been used to predict engine performance using non-dimensional experimental data maps to represent the individual components [14,28,29,86]. These analyses are 0-D as there is no flow resolution in the axial, radial, nor circumferential direction within a given engine component [87]. Because the rig experiments are performed at design point, 0-D analyses provide acceptable results at design conditions; however, results can significantly vary against experiment data at off-design conditions [14,17–19,25,29,86]. Even though adjustments of variable geometry, Reynolds effects, and clearances are applied for off-design conditions, there is still a matching deviation against test data [87]. Low-fidelity map-based performance simulators cannot resolve an independent gas-turbine engine-component analysis since the complex physics are not captured inside of compressors, turbines or ducts [14,28,29,86].

The simulation of turbomachinery flow began in the late forties and fifties with the development of mathematical models and numerical algorithms to solve the flow equations. In the last decades, the following numerical methods have been in application for the compressor analysis and design process [7]: mean-line, stage

stacking, through-flow methods, blade-to-blade calculations, quasi-3-D and fully 3-D CFD analyses. In the next paragraphs, a brief description of these methodologies is given.

One of the preliminary design methods is the one-dimensional (1-D) mean-line or pitch-line analysis. A mean flow is defined at the inlet and outlet of every blade row, where flow properties are estimated using 1-D calculations to obtain the mean blade loadings. Given this and supported by empirical correlations of test data, an overall performance is established. More sophisticated mean-line analysis versions suggest annulus and blade geometry choices to achieve the design requirements.

Stage stacking analyses provide an axial matching between stages. Given the rotational speed and inlet mass flow as initial conditions, the pressure ratio and efficiency are obtained at the first stage. These in turn can be used as inlet conditions for the second stage to be solved and so on for the subsequent stages. As a result, it is possible to assemble all stage characteristics to build up the overall component performance map. In addition, empirical correlations can be implemented to obtain better performance estimation.

The development of computational technology in the seventies, permitted through-flow methods to find a wider and a more confident application in the turbomachinery flow simulation [88]. Through-flow methods solve the flow field in 2-D on the meridional or hub-to-tip plane. This plane is frequently thought as the S2 surface [89] (see Figure 2.12) and contains the axisymmetric projections of the streamsurfaces known as streamlines. The method then obtains the flow solution for each streamline at the inlet and outlet of every blade row [90]. The different available through-flow techniques are [14]: simple radial equilibrium, streamfunction or matrix, streamline curvature (SLC), finite difference, finite element, finite volume, and time-dependent Euler method.

The typical through-flow method in the analysis and design process for economic and practical reasons is the SLC. The SLC method solves the radial equilibrium equation (REE) to determine the gradient of the meridional velocity in the spanwise direction at the intersections between the streamlines and the blade rows. Additionally, inter- or intra-blade row calculating stations can be added to solve the flow in between and

within blade rows. Since the flow is assumed inviscid, losses and deviation angles are accounted through empirical models which are based and limited to standard blade profiles. A more detailed discussion in SLC methods is provided in Sec. 2.3.2, as this is the central simulation method used for this research.

In blade-to-blade techniques, the analysis is based on isolated aerofoil theory, projecting the blade profile on a conical surface or surface of revolution that approximates a streamsurface. The flow field is resolved then in the blade-to-blade steamsurface or S1 surface [89] (see Figure 2.12). Empirical correlations can be employed for a rapid calculation of loss constituents, deviation angles, and to limit the blade-section operating range. However, due to the impact of the blade-surface boundary layer on the profile loss, it is important to consider viscosity, either by a boundary layer calculation, wall functions, near-wall interactions or any other numerical algorithm [91]. Fully viscous methods [91,92] are ideal but computationally expensive. Yet, inviscid-viscous analyses [93,94] reduce computational running times while maintaining high accuracy levels.

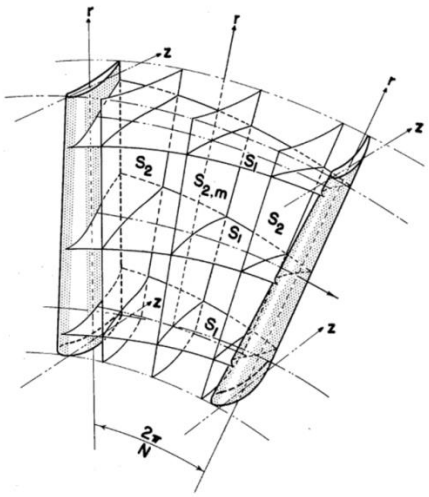

Figure 2.12 Definition of the blade-to-blade S1 surface and the meridional hub-to-tip S2 surface [89].

Through-flow methods and blade-to-blade calculations can be combined to build up a quasi-3-D procedure. This is an iterative procedure in which the meridional analysis provides a spanwise flow solution in the S2 surface, whilst the blade-to-blade method calculates the pitchwise flow field in the S1 plane. Intersections are then computed

between the through-flow-calculated axisymmetric streamsurfaces and the 3-D blade geometry to produce data that is compared against the blade-to-blade calculations. However, this procedure is not free of empiricism in particular cases. Empirical inputs might be required for a more accurate end-wall loss estimation and swept-blade influence [7].

Fully 3-D viscous analyses, such as CFD, play an essential role in the turbomachinery design than it does in any other fluid-related field, becoming a common practice at the last stage of the design process [15]. CFD simulations introduce viscosity and turbulence models to obtain an accurate engine component flow field solution, resolving complex internal flow interactions at small scale through numerical solution of the Reynolds-Averaged Navier-Stokes (RANS) equations. Besides the improved accuracy, full 3-D CFD methods avoid the iterative process between the meridional and blade-to-blade plane from the quasi-3-D simulations. One of the major purposes of CFD is to predict the 3-D secondary flows, particularly at the endwall boundary layers. 3-D effects from blade sweep, lean and twist are reasonably well-captured. In addition, unsteady flow solutions can be obtained depending on the numerical scheme used.

Nonetheless there are still limitations in turbulence and transition modelling, particularly at off-design cases [13]. In spite of the solution algorithms improvements, 3-D CFD it is still not an exact science [16]. CFD discrepancies can be due to a) numerical errors related to mesh size and finite difference approximation, b) physics modelling assumptions as in turbulence and transition, c) unknown boundary conditions, d) geometry simplification as in the blade leading edge and tip clearance, and e) steady flow assumption [16]. Additionally, CFD simulations come at high computational costs in terms of solution time and resources, complexity to obtain the required initial and boundary conditions, and lack of flexibility to incorporate or even modify any loss or deviation model [14,17–19]. In terms of multi-stage simulations, the interaction between two consecutive stages is unsteady, increasing both, the CFD problem from steady to transient and the computational effort. It is clear that 3-D CFD simulations continue limited to single blade-row models, although multi-stage analyses [95–97] are increasing in number with the rise in computational processing speed and memory [23]. Most notably is the fact that in the recent years, CFD tools are more

widely employed by professionals and young engineers, who despite of their expertise, might not realise the CFD drawbacks, representing a potential risk for reliable results procurement.

2.3.2 Streamline Curvature Methods

As it has been mentioned, the turbomachinery flow is complex, 3-D, highly viscous, and turbulent. For this reason, the problem is limited to be analysed in the hub-to-tip plane considering axisymmetric conditions so that the flow field solution is obtained on a meridional surface. The very first approach to establish a solution in between adjacent blade rows to obtain the overall component performance was the mean-line method defined by Howell [98]. However, Wu and Wolfenstein [99] and Hamrick *et al*. [100] defined the first representations of the streamline slope and streamline curvature in the REE [14]. Later, Wright and Kovach [101] considered the streamline curvature radius in the radial-axial plane to compute flow calculations. With the further expansion of flow simulation through REE, Wright and Novak [102] programmed its solution using a computational code. Swan [103] developed a computer program where viscous and shock loss models based on statistics-based empirical models were introduced in the REE. Smith [21] properly defined the REE equation for turbomachinery components and similar works in the United Kingdom were presented by Silvester and Hetherington [104]. Nevertheless, authors [14,105] agree that a well-defined SLC method for turbomachinery components was firstly introduced by Novak [106]. Following this progress, SLC codes were developed by Crouse *et al*. [107] and Hearsey [108] to solve the through-flow equations. Eventually, more sophisticated SLC-based computer programs [13,14,113,114,45,46,105,108–112] have been introduced, improving the solution algorithms, and the empirical loss and deviation correlations towards a more accurate component performance prediction.

SLC methods follow an iterative-computation approach to calculate the position, slope and curvature of the streamlines, where the flow is assumed to be compressible, axisymmetric, steady and inviscid. SLC flow field solution is mainly based on the solution of the governing equation of conservation of linear momentum or Newton's second law. This fundamental equation establishes that in an inertial frame of

reference, the rate of change of linear momentum P of an infinitesimal continuum is proportional to the resultant applied forces. At an instant of time t, the linear momentum of all the particles contained in a domain V is

$$P_i = \int_V \rho u_i dV \tag{2.3.1}$$

Where ρ is the density and u_i is the tensorial velocity in the direction i.

If the body is subjected to surface traction τ_i and a body force per unit volume f, the resultant force F is

$$F_i = \int_S \tau_i dS + \int_V f_i dV \tag{2.3.2}$$

According to Cauchy's theorem, the surface traction is a stress vector τ_i acting on a boundary surface S with outer unit normal vector ν_j that may be expressed in terms of the stress field tensor σ_{ij} as

$$\tau_i = \sigma_{ji}\nu_j \tag{2.3.3}$$

Transforming the surface traction from a surface integral into a volume integral by Gauss's Theorem, the resultant force on the continuum becomes

$$\begin{aligned} F_i = \int_S \sigma_{ji}\nu_j dS + \int_V f_i dV = \int_S \frac{\partial \sigma_{ji}}{\partial \mathrm{X}_i} dV + \int_V f_i dV \\ = \int_V \left(\frac{\partial \sigma_{ji}}{\partial \mathrm{X}_i} + f_i\right) dV \end{aligned} \tag{2.3.4}$$

Where X_i is the direction in the tensorial direction i.

Conservation of linear momentum states that

$$\frac{DP_i}{Dt} = F_i \tag{2.3.5}$$

Substituting the linear momentum contained in a volume and the applied resultant force in the Newtons's second law,

$$\frac{D}{Dt}(\int_V \rho u_i dV) = \int_V \left(\frac{\partial \sigma_{ji}}{\partial \mathrm{X}_i} + f_i\right) dV \quad \textbf{(2.3.6)}$$

Conceding ρu_i as a continuously differentiable function defined over a spatial domain V occupied by a given set of material particles, the volume-integral material derivative of Eq. 2.3.6 LHS, gives

$$\int_V \left(\frac{\partial(\rho u_i)}{\partial t} + \frac{\partial(\rho u_i u_j)}{\partial \mathrm{X}_j}\right) dV = \int_V \left(\frac{\partial \sigma_{ji}}{\partial \mathrm{X}_i} + f_i\right) dV \quad \textbf{(2.3.7)}$$

Since the conservation of linear momentum must hold for an arbitrary domain V, the volume integrands must be equal in Eq. 2.3.7, thus.

$$\frac{\partial(\rho u_i)}{\partial t} + \frac{\partial(\rho u_i u_j)}{\partial \mathrm{X}_j} = \frac{\partial \sigma_{ji}}{\partial \mathrm{X}_i} + f_i \quad \textbf{(2.3.8)}$$

Expanding the linear-momentum conservation equation,

$$u_i(\frac{\partial \rho}{\partial t} + \frac{\partial(\rho u_j)}{\partial \mathrm{X}_j}) + \rho(\frac{\partial u_i}{\partial t} + u_j \frac{\partial u_i}{\partial \mathrm{X}_j}) = \frac{\partial \sigma_{ji}}{\partial \mathrm{X}_i} + f_i \quad \textbf{(2.3.9)}$$

However, the mass contained in a domain V at a time t is

$$m = \int_V \rho dV \quad \textbf{(2.3.10)}$$

The governing conservation of mass requires that $Dm/Dt = 0$. Then, the continuity equation or mass flow conservation is formulated as

$$\frac{Dm}{Dt} = \frac{D}{Dt}\left(\int_V \rho dV\right) = 0 \quad \textbf{(2.3.11)}$$

Inasmuch as ρ is the density of a continuum at the location X at time t, the mass flow conservation can be expressed in terms of the material derivative of the density volume integral as

$$\frac{Dm}{Dt} = \int_V \frac{\partial \rho}{\partial \mathrm{t}} dV + \int_V \frac{\partial(\rho u_j)}{\partial \mathrm{X}_j} dV = \frac{\partial \rho}{\partial \mathrm{t}} + \frac{\partial(\rho u_j)}{\partial \mathrm{X}_j} = 0 \quad \textbf{(2.3.12)}$$

Thus, the mass flow continuity defined in Eq. 2.3.9, turns into

$$0 + \rho(\frac{\partial u_i}{\partial t} + u_j \frac{\partial u_i}{\partial \mathrm{X}_j}) = \frac{\partial \sigma_{ji}}{\partial \mathrm{X}_i} + f_i \qquad \textbf{(2.3.13)}$$

The LHS of Eq. 2.3.13 is the material derivative of the velocity vector u_i. Therefore, the linear-momentum conservation becomes the Euler equation of motion of a continuum, expressed as

$$\rho \frac{Du_i}{Dt} = \frac{\partial \sigma_{ji}}{\partial \mathrm{X}_i} + f_i \qquad \textbf{(2.3.14)}$$

Given a Newtonian viscous fluid, as air, for which shear stress is linearly proportional to the rate of deformation, the stress-strain relationship is defined by the Stokes formulation as

$$\sigma_{ij} = -p\delta_{ij} + 2\mu e_{ij} - \psi e_{kk}\delta_{ij} \qquad \textbf{(2.3.15)}$$

Assuming inviscid flow, the normal dynamic viscosity μ and the second viscosity term ψ are neglected. Consequently, the rate of deformation or strain e gets cancelled, and hence, there is no shear stress, resulting in an isotropic normal stress tensor, whose partial derivative with respect of X_i may be written as

$$\frac{\partial(\sigma_{ij})}{\partial \mathrm{X}_i} = \frac{\partial(-p\delta_{ij})}{\partial \mathrm{X}_i} = \frac{\partial}{\partial \mathrm{X}_i}\begin{pmatrix} -p & 0 & 0 \\ 0 & -p & 0 \\ 0 & 0 & -p \end{pmatrix} = -\frac{\partial p}{\partial \mathrm{X}_i} = -\nabla p \qquad \textbf{(2.3.16)}$$

Thence, the Euler equation of motion of a continuum becomes the simplified version of the Navier-Stokes equation for an inviscid fluid in the form

$$-\frac{1}{\rho}\nabla p = \frac{Du_i}{Dt} - \frac{F_i}{m} \qquad \textbf{(2.3.17)}$$

In the case of rotating flow within a duct, the centripetal and Coriolis acceleration must be added to Eq. 2.3.17, then

$$-\frac{1}{\rho}\nabla p = \frac{Du_i}{Dt} - (\omega_i \times \omega_i \times r_i) + (2\omega_i \times u_i) - \frac{F_i}{m} \qquad \textbf{(2.3.18)}$$

For convenience in the solution of turbomachinery flow, in this case an axial-flow compressor, the terms of Eq. 2.3.18 can be expanded into cylindrical coordinates. The LHS of Eq. 2.3.18 is

$$-\frac{1}{\rho}\nabla p = -\frac{1}{\rho}\frac{\partial p}{\partial \mathrm{X}_1}\widehat{e_1} + -\frac{1}{\rho}\frac{\partial p}{\partial \mathrm{X}_2}\widehat{e_2} + -\frac{1}{\rho}\frac{\partial p}{\partial \mathrm{X}_3}\widehat{e_3}$$
$$= -\frac{1}{\rho}\frac{\partial p}{\partial r}\widehat{e_r} + -\frac{1}{\rho}\frac{\partial p}{\partial \theta}\widehat{e_\theta} + -\frac{1}{\rho}\frac{\partial p}{\partial z}\widehat{e_z} \qquad \textbf{(2.3.19)}$$

The term $\frac{\partial u_i}{\partial t} = 0$ in the material derivative of u_i since the flow is assumed to be steady. Then the term $\frac{Du_i}{Dt}$ expressed in cylindrical coordinates is

$$\frac{Du_i}{Dt} = u_j\frac{\partial u_i}{\partial \mathrm{X}_j} = u_1\frac{\partial u_i}{\partial \mathrm{X}_1} + u_2\frac{\partial u_i}{\partial \mathrm{X}_2} + u_3\frac{\partial u_i}{\partial \mathrm{X}_3}$$
$$= u_r\frac{\partial u_i}{\partial \mathrm{r}} + u_\theta\frac{\partial u_i}{\partial \theta} + u_z\frac{\partial u_i}{\partial \mathrm{z}} \qquad \textbf{(2.3.20)}$$

which can be further expanded to

$$\frac{Du_r}{Dt} = u_r\frac{\partial u_r}{\partial \mathrm{r}} + u_\theta\frac{\partial u_r}{\partial \theta} + u_z\frac{\partial u_r}{\partial \mathrm{z}}$$
$$\frac{Du_\theta}{Dt} = u_r\frac{\partial u_\theta}{\partial \mathrm{r}} + u_\theta\frac{\partial u_\theta}{\partial \theta} + u_z\frac{\partial u_\theta}{\partial \mathrm{z}} \qquad \textbf{(2.3.21)}$$
$$\frac{Du_z}{Dt} = u_r\frac{\partial u_z}{\partial \mathrm{r}} + u_\theta\frac{\partial u_z}{\partial \theta} + u_z\frac{\partial u_z}{\partial \mathrm{z}}$$

The centripetal acceleration is

$$\omega_i \times \omega_i \times r_i = (\omega_i \cdot r_i)\cdot\omega_i - (\omega_i\cdot\omega_i)\cdot r_i = -(\omega^2 r)\widehat{e_r} + \widehat{e_\theta} + \widehat{e_z} \qquad \textbf{(2.3.22)}$$

where the terms in the unit directions $\widehat{e_\theta}$ and $\widehat{e_z}$ are considered as negligible.

And the Coriolis acceleration is

$$2\omega_i \times u_i = (-2\omega u_r)\widehat{e_r} + (2\omega u_r)\widehat{e_\theta} + \widehat{e_z} \qquad \textbf{(2.3.23)}$$

where the unit direction $\widehat{e_z}$ can be neglected.

If the blade forces are neglected [18,19,41,48], then $F_i = 0$. Therefore, the simplified steady-flow solution of Eq. 2.3.18 in a cylindrical coordinate system is

$$\begin{aligned} &-\frac{1}{\rho}\frac{\partial p}{\partial r}\widehat{e_r} - \frac{1}{\rho}\frac{\partial p}{\partial \theta}\widehat{e_\theta} - \frac{1}{\rho}\frac{\partial p}{\partial z}\widehat{e_z} \\ &= u_r\frac{\partial u_i}{\partial \mathrm{r}} + u_\theta\frac{\partial u_i}{\partial \theta} + u_z\frac{\partial u_i}{\partial \mathrm{z}} - \omega^2 r\widehat{e_r} - 2\omega u_r\widehat{e_r} + 2\omega u_r\widehat{e_\theta} \end{aligned} \quad \textbf{(2.3.24)}$$

The pressure gradient $\frac{\partial p}{\partial r}$ at any point within the blade rows must balance the flow acceleration component in the radial direction [115]. The radial acceleration is affected by the radius of curvature of a streamline R_{Sl}, the velocity tangent to the streamline V_m or the velocity in the meridional direction m, and the acceleration tangent to that streamline or meridional acceleration $\dot{V}_m$. Then, the balance solution of the pressure gradient with the acceleration in the radial direction from the above system of equations can be expressed in a form in which the derivatives occurring in the axial direction z are related to the geometrical shape of the streamlines, resulting in

$$\begin{aligned} \frac{\partial {V_m}^2}{\partial s} = 2{V_m}^2\cos^2\alpha &\left\{\frac{\cos(\varphi+\lambda)}{R_{Sl}} - \frac{\tan\alpha\,(\frac{\partial \alpha}{\partial s})}{\cos^2\alpha}\right. \\ &\left. + \sin(\varphi+\lambda)\left[\frac{\tan(\varphi+\lambda)}{R_{Sl}} - \frac{1}{\cos(\varphi+\lambda)}\frac{\partial \varphi}{\partial s} - \frac{\partial(\ln(r\rho))}{\partial m}\right]\right\} \\ &+ 2\cos^2\alpha\left[\frac{\partial I}{\partial s} - 2cos\gamma\omega(C_\theta - U) - T\frac{\partial S}{\partial s}\right] \end{aligned} \quad \textbf{(2.3.25)}$$

The variables φ and λ are the streamline slope and the sweep angle, respectively, representing the streamline shape. In terms of the absolute velocity vector, C and α correspond to the flow magnitudes and angle, respectively. Whereas T is the static temperature, S is the entropy, and I is the rothalpy.

Eq. 2.3.25 is a non-linear partial differential equation (PDE) that represents the full REE, central to the SLC method. The full REE resolves the gradient of the meridional

velocity in the spanwise direction s. Alternatively to solve the full REE, its most general and convenient form [66,116–118] is given by

$$\begin{aligned} V_m \frac{dV_m}{ds} = {V_m}^2 \Bigg[& \sin(\varphi-\lambda)\tan(\varphi+\lambda)\frac{\partial\varphi}{\partial m} - \frac{\partial\varphi}{\partial s}\frac{\sin(\varphi-\lambda)}{\cos(\varphi+\lambda)} \\ & - \frac{\sin\varphi\sin(\varphi-\lambda)}{r} - \frac{1}{\rho}\frac{d\rho}{dm}\sin(\varphi-\lambda) + \frac{\cos(\varphi-\lambda)}{R_{Sl}} \Bigg] \\ & + V_m \left[\tan\lambda \frac{d(rV_\theta)}{dm}\frac{1}{r} + 2\omega\sin\varphi\tan\lambda \right] \\ & + \Bigg[-\frac{V_\theta}{r}\frac{d(rV_\theta)}{ds} - 2\omega V_\theta\cos\lambda + \frac{dI}{ds} - T\frac{dS}{ds} \\ & + T\frac{dS}{dm}(\sin(\varphi-\lambda)\cos^2\beta - \tan\lambda\sin\beta\cos\beta) \Bigg] \end{aligned} \quad \textbf{(2.3.26)}$$

Eq. 2.3.26 is a second-order differential equation with respect of the meridional velocity [66,116,117] which can be reduced to

$$V_m \frac{dV_m}{ds} = A{V_m}^2 + BV_m + C \quad \textbf{(2.3.27)}$$

where the coefficients A, B and C correspond to those terms in Eq. 2.3.26. Hence, the solution for a second-order differential equation form is

$$\frac{\ln(A{V_m}^2 + BV_m + C)}{2A} - \frac{B}{A\sqrt{4AC-B^2}}\operatorname{atan}\left(\frac{2AV_m+B}{\sqrt{4AC-B^2}}\right) = s + IC \quad \textbf{(2.3.28)}$$

The integration constant IC may be calculated using the full REE second-order differential equation from Eq. 2.3.28 in a finite-difference approximation for two consecutive streamlines j as

$$\begin{aligned} \frac{1}{2A}\left[\ln\left(\frac{A{V_{m_{j+1}}}^2 + BV_{m_{j+1}} + C}{A{V_{m_j}}^2 + BV_{m_j} + C}\right)\right] - \frac{B}{A\sqrt{4AC-B^2}}\left[\operatorname{atan}\left(\frac{2AV_{m_{j+1}}+B}{\sqrt{4AC-B^2}}\right)\right] \\ - \left[\operatorname{atan}\left(\frac{2AV_{m_j}+B}{\sqrt{4AC-B^2}}\right)\right] = s_{j+1} - s_j \end{aligned} \quad \textbf{(2.3.29)}$$

Nevertheless, the full REE just solves the gradient of the meridional velocity in the *s* direction from hub to tip but not its magnitude, requiring of an additional equation. Mass flow continuity formulation provides the integration of the meridional velocity at each streamline across the blade rows to obtain V_m. In between streamlines, the confined stream tube mass flow [18,19,41,48] is defined as

$$\dot{m}_J = \int_A \bar{\rho}_J \, \overline{V_{m_J}} dA \tag{2.3.30}$$

which might be numerically solved, giving

$$\dot{m}_J = \frac{\pi}{2}\left[\rho_{j+1} V_{m\,j+1} \cos\left(\varphi_{j+1} + \lambda_{j+1}\right) + \rho_j V_{m_j} \cos\left(\varphi_j + \lambda_j\right)\right]\left[\frac{{r_{j+1}}^2 - {r_j}^2}{cos\left(\frac{\lambda_{j+1} + \lambda_j}{2}\right)}\right] \tag{2.3.31}$$

The full REE in set with the mass-flow continuity are iteratively solved based on a computational mesh on the meridional plane (S2 surface). The mesh is constructed between the intersection of the streamlines and quasi-orthogonal or quasi-normal calculation station lines to the stream surface as sketched in Figure 2.13.

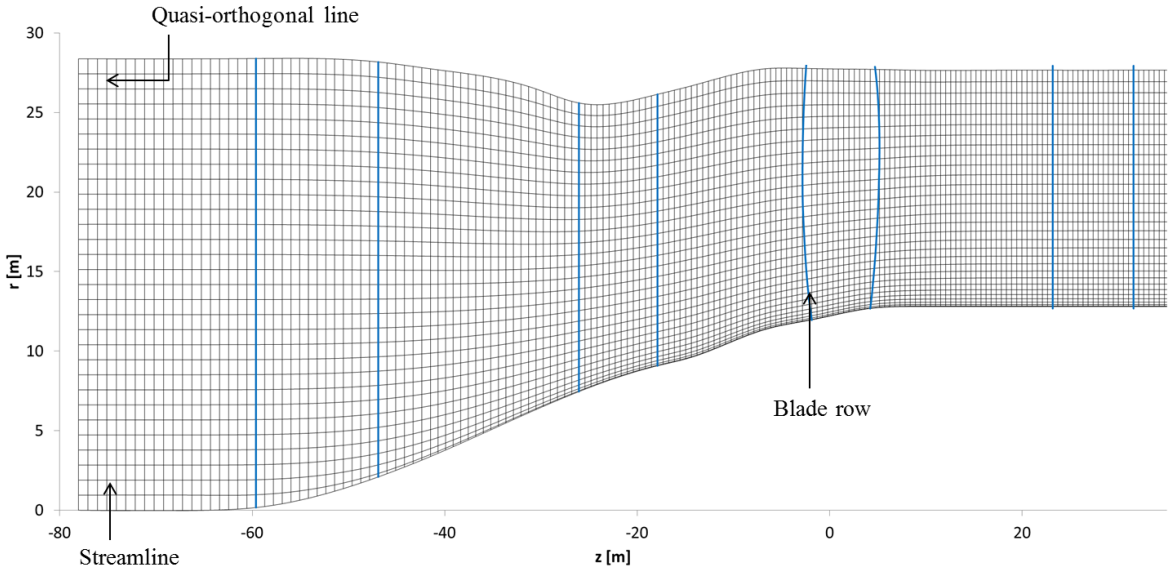

Figure 2.13 2-D SLC mesh definition on the meridional plane.

To start the computation, as displayed in the flow chart of Figure 2.14, a meanline meridional velocity and streamline distribution are assumed. Given V_m, velocity properties and flow thermodynamic properties are calculated along the given streamline position. The full REE in the form of Eq. 2.3.29 resolves the meridional velocity gradient in the spanwise direction. The meridional velocity profile is then integrated through Eq. 2.3.31, giving the stream tube mass-flows and setting the compressor total mass-flow to be compared against the required overall mass-flow. The mass flow difference establishes the adjustment in meridional velocity for the next iteration. The new streamlines positions for the successive iterations are determined based on the computed stream tube mass-flows. The iterative scheme converges when both, full REE and mass flow conservation, are satisfied within the error tolerances specified.

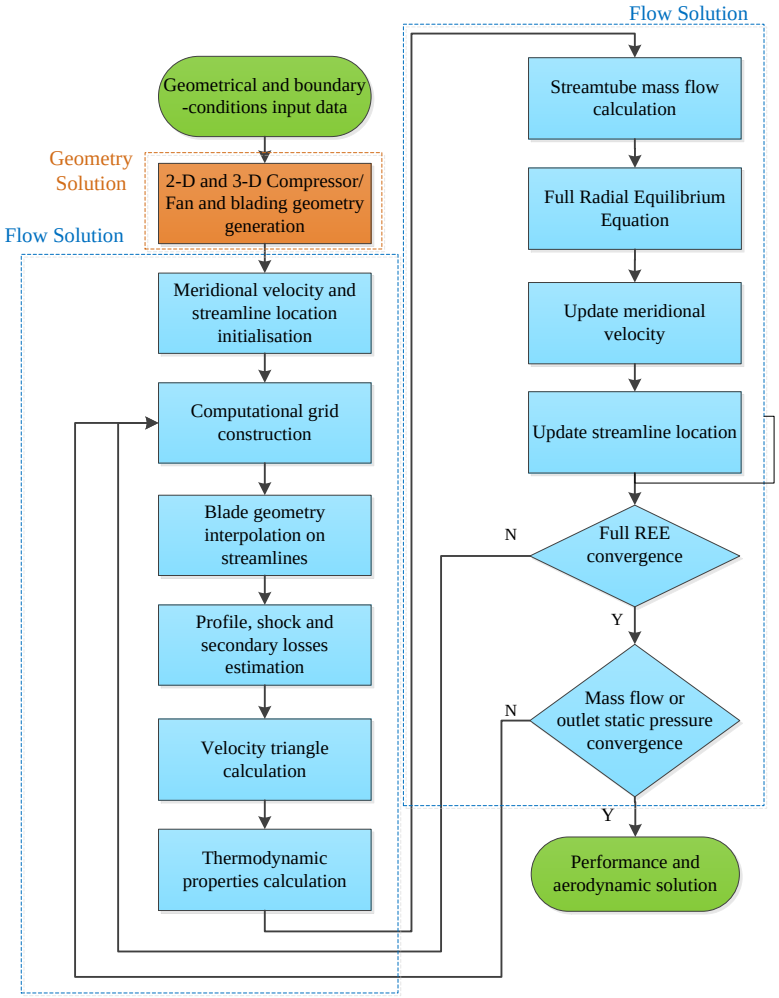

Figure 2.14 High-level flow-chart for the 2-D SLC axial-flow fan/compressor performance simulator (SOCRATES) [14,17,31]**.**

Due to the inviscid and 2-D flow treatment in SLC methods, the compressor blading losses and deviations should be considered separately. The very complicated flow situation have made almost impossible to resolve the loss and deviation angle theoretically. For this reason, empirical correlations determined from statistics-based two-dimensional (or in some cases annular) cascade rig-test data for standard blade section types are used to compensate for the total-pressure loss. A vast number of empirical correlations define directly a 2-D low-speed operation. In high-speed compressors, correction factors are used for Mach number, Reynolds number, blade-surface roughness, and 3-D effects. In transonic compressor SLC analyses, shock-induced losses must be considered as well. For this matter, empirical or very simple shock-loss models have been implemented. A thorough discussion upon the various shock-loss models developed is provided in Sec. 2.6.4 and Sec. 2.6.5, for simple analytical and full/semi-empirical models, respectively.

To ensure performance prediction fidelity, an axial-flow compressor SLC algorithm should include a set of empirical correlations for: design incidence, design total-loss, off-design total loss, design deviation angle and off-design deviation angle. In parallel, these correlations might require of supplementary cascade-data-based models to work, such as: equivalent diffusion factor, design angle of attack, and stall angles (positive and negative stall angle of attacks, and stall incidence). The diffusion factor, which can be understood as a measure of the blade loading, might be applied in its fullest form definition derived by Lieblein [119] and presented in other distinguished reviews [120–123], expressed as

$$D = \left(1 - \frac{V_2}{V_1}\right) + \frac{V_{\theta_2} - V_{\theta_1}}{2\sigma V_1} \qquad \textbf{(2.3.32)}$$

where the subindex θ represents the whirl or circumferential component of the relative velocity. Alternatively, the diffusion factor can be empirically computed as a function of the wake-momentum-thickness to chord ratio Θ_w/c.

In the case of transonic axial-flow compressor SLC simulations, the total losses are split into the three main contributions: profile, shock, and secondary losses. To attain an accurate performance estimation, additional empirical or semi-empirical correlations are

required for: minimum-loss incidence, minimum-loss profile loss, profile loss, shock loss, and secondary loss (passage secondary flows, tip clearance flows, shroud/seal leakage and hub vortices).

In respect of the profile losses, because the viscosity terms are involved, it is not feasible to resolve the boundary-layer PDE's at a small length-scale. Even if numerical methods are applied to solve the PDE system, it would result prohibitive as the algorithm would head towards a 2-D RANS solver, losing the real SLC spirit of accuracy at low computational cost. Simple flat-plate boundary-layer equations would not represent the actual flow retardation physics on a blade surface. Whereupon, blade boundary-layers models [124–126] are used, which due to their complexity are not applied in their fullest form, ending up in being over-simplified. Experimental investigations on compressor blade boundary-layers [93,126–133] have demonstrated this simplification is excessive since there is significant performance disparity against the proposed models. Up to this dates, there is still a great debate between the known approaches, with different concepts each, on how to solve the turbulence and wake mixing, which in fact affects the radial transport or spanwise mixing [134]. In this scenario, empirical profile-loss models are still in widespread use as physical effects are captured within a quick, non-complex and inexpensive approach.

Conversely, shock losses might be treated with full/semi-empirical or simple shock models, however attention must be taken as to know what losses are being considered. Through conventional shock theory, the relative total-pressure loss due to the non-isentropic shock process can be computed. Nevertheless, the mentioned complexity of an explicit boundary-layer resolution makes almost impossible to resolve the SWBLI with the current known analytical methods. On the other hand, empirical shock-loss models confine the shock-only and SWBLI losses in a single coefficient, without the possibility of isolating these two effects from blade-cascade measured data.

At present-day situation, a large number of empirical correlations can be found in the literature, which are still used by engine design groups and industrial turbomachinery companies. An early collection of empirical cascade-test data charts and correlations was given by Johnsen and Bullock [121]. Cahill [135] provided a more dedicated

identification of empirical loss and deviation models for transonic axial-flow compressors. A distinguished compilation of empirical models by Aungier [136], curve-fits and extrapolates the empirical blade-cascade data to provide continuous approximating functions for the various correlations even if they fall outside of the testing range. Table 2.1 lists the most relevant and widely used empirical correlations across the SLC performance simulation programs for subsonic and transonic axial-flow compressors.

Table 2.1 Full/semi-empirical and simple analytical correlations for losses, deviation angle, and stall prediction employed in axial-flow compressor SLC methods.

Axial-Flow Compressor Type		Loss/Deviation Mechanism	Loss/Deviation Sub-Mechanism	Correlation Reference
Subsonic		Design-total loss		Lieblein [137], Swan [103], Jansen and Moffat [138], Dettmering [139], Koch and Smith Jr. [140]
		Off-design total-loss		Howell [98], Lieblein [119], Swan [103], Jansen and Moffatt [138], Creveling and Carmody [45], Cetin *et al*. [141]
	Transonic	Design incidence		Johnsen and Bullock/Lieblein [121,122], Lieblein [142], Herrig *et al*. [143], Aungier [136]
		Design deviation angle		Constant [144], Carter's rule [145,146], Modified Carter's rule by Cetin *et al*. [141], Aungier [136]
		Off-design deviation angle		Howell [98], Swan [103], Johnsen and Bullock/Lieblein [121,122],

			Jansen and Moffatt [138], Pollard and Gostelow [147], Creveling and Carmody [45], Aungier [136]
		Diffusion Factor	Johnsen and Bullock/Lieblein [121,122]
		Equivalent Diffusion Factor	Lieblein [137,148], Aungier [136]
		Design angle of attack	Lieblein [142], Aungier [136]
		Stall prediction: Negative and Positive Stall Angle of Attack	Herrig *et al*. [143], Aungier [136]
		Stall prediction: Stall Angle of Attack	Aungier [136]
		Stall prediction: Stall Incidence	Aungier [136]
		Minimum-loss incidence	Chauvin and Weyer [149], Cetin *et al*., [141], Aungier [136]
		Minimum-loss profile loss	Aungier [136]
		Profile loss	Koning *et al*. [150,151] for subsonic flow, Koning *et al*. for supersonic flow [152,153], Aungier [136]
		Shock loss: Shock-only	†Schwenk *et al*., †Miller *et al*. [3], Koch and Smith Jr. [140], †Bloch [34], †Boyer [13,35,36]

			SWBLI	Swan [103], *Fottner [154], Cunnan *et al*. [38], ‡Hirsch and Denton [90], Koning *et al*. [155]
		Secondary loss	Tip clearance flow and hub vortices	Howell [98]
			Tip clearance flow	Aungier [136]
			Shroud/Seal leakage loss	*Aungier [136]
			Passage secondary flows, tip clearance flow, hub vortices, spanwise mixing	Hearsey [156]

* Semi-empirical, †Simple Analytical, ‡Empirical model from two or more reported

Note that all the correlations in Table 2.1 are empirical, except for those where an indication is given. In particular, shock-loss models show both, analytical for shock-only losses and full/semi-empirical for merged shock-wave and SWBLI mechanisms.

Improvements in loss modelling, off-design calculations and stall prediction have been implemented in recent years in SLC methods. For instance, Howard and Gallimore [157] improved the SLC program from Jennions and Stow [112], which already included a spanwise mixing model consisting in a turbulent diffusion model, by including end-wall shear force calculations. This improvement came as a substitution of empirical blockage factors or AWBL calculations, to guarantee a more realistic prediction of velocity and flow angle distribution near the end-wall. Dunham developed end-wall loss models for a more realistic performance in SLC methods for axial-flow

compressors, reported by Dunham [158–161]. Additionally, Dunham [159,160] studied the spanwise mixing in axial flow due to turbulent diffusion for SLC compressor analysis, which was further improved in Dunham [161] as turbulent convection due to secondary flow, spanwise surface boundary layer migration and spanwise convection between flow and blade wake, were considered.

Boyer and O'Brien [13,35,36] enhanced the SLC computer code for transonic axial-flow compressors developed by Boyer [13], to obtain a more accurate pressure loss modelling at off-design conditions. This was achieved through the implementation of a physics-based shock loss model that considers shock-structure changes depending on the inlet relative Mach number, flow turning and blade profile section geometry.

As mentioned, deviation and loss models rely on statistics-based experimental curve approximations; however, they show large differences against actual performance. To compensate it, Pachidis *et al*. [41] developed a strategy of adapting a blade profile loss model against performance experimental data through an iterative process.

Hu *et al*. [162] improved the minimum-loss incidence and total-pressure-loss model for SLC methods at design and off-design points. The minimum-loss incidence was set up to be dependent on the inlet Mach number and blade profile geometry parameters, such as solidity, camber, and thickness distribution. Total-pressure losses were divided in a minimum loss as a function of Mach number and Reynolds number, and in an additional loss that accounts for the off-design condition as a function of the minimum-loss incidence and the actual incidence difference. Later, Hu *et al.* [163] implemented more elegant models for incidence and total losses in an existing SLC method to analyse transonic axial-flow compressors analysis.

Templalexis *et al*. [20] reported the deviation and loss models included in the SLC code (SOCRATES) developed by and Pachidis [14] and Pachidis *et al*. [17]. Minimum loss incidence angle was calculated with model from Lieblein [122], while models from Carter [145], Lieblein [142] and Cetin *et al*. [141] were used to calculate deviation angle. Deviation angle at off-design was coded from Creveling and Carmody [45]. Blade row stall prediction was considered from Aungier [136], whereas blade passage choking was a critical Mach number-based approach. In terms of loss models, the

following correlations were programmed and implemented in SOCRATES: profile loss were obtained from Swan [103], and Jansen and Moffatt [138], shock loss from Schwenk *et al*. [4], and secondary losses from Howell [98] and Griepentrog [164].

A recent study by Tiwari *et al*. [23] showed the improvement of a SLC solver to deal with subsonic and supersonic flow solution. The procedure was developed to identify supersonic flow, calculate the SLC gradient term to avoid singularities at supersonic meridional Mach numbers, and a method to handle choked flow. The SLC gradient term calculation is based on Denton [111] and Came [165]. This SLC enhancement led to substantially increase the solution accuracy, providing robustness for transonic flow analyses.

SLC methods have suffered variations along their existence, particularly in the body force inclusion to the REE. Horlock [166] introduced in the REE, the effect of entropy production along the streamline as a body force that acts as drag D opposite to the flow given by

$$D = T\frac{\partial S}{\partial m} \tag{2.3.33}$$

Horlock and March [167] discussed the nature of the blade forces by comparing meridional-flow models against blade pitch-averaged equations. The pressure force was then related to the circumferential flow turning rate along a streamline. Similarly, Jennions and Stow [112] considered the blade-to-blade plane body force terms to account for circumferential flow variation in the meridional surface.

The effect of the body-force terms in the full REE for SLC methods was demonstrated by Templalexis [118]. A better agreement between SLC and experimental data was found when the force terms were addressed. Despite the increase in the REE complexity, more solutions were converged and fewer iterations were required to achieve convergence when the force terms were included. The body forces F may be resolved in pressure forces F_p acting normal to the blade surface and drag forces D acting tangentially to the blade surface, as follows

$$F_i = F_{p_i} + D_i \tag{2.3.34}$$

The body force F_i is a vector with components F_m, F_q and F_θ, corresponding to the three orthogonal directions in a meridional plane, streamline m, stream surface normal or quasi-orthogonal line q and whirl θ, respectively. Considering the blade forces in Eq. 2.3.18, and expanding it in the meridional system, the Euler system of equations of motion of a continuum with the inertial terms becomes

$$V_m \frac{dV_m}{ds} - \frac{{V_\theta}^2}{r} \sin\varphi = -\frac{1}{\rho}\frac{dp}{dm} + F_m$$

$$\frac{{V_m}^2}{R_{Sl}} - \frac{{V_\theta}^2}{r} \cos\varphi = -\frac{1}{\rho}\frac{dp}{ds} + F_q \qquad \textbf{(2.3.35)}$$

$$\frac{V_m}{r}\frac{d(rV_\theta)}{dm} = F_\theta$$

However, it is only the whirl component of the pressure force F_{p_θ} that affects the REE, as it acts perpendicular to the meridional plane. Then, for instance, the body-force whirl component F_θ is composed of the pressure force F_{p_θ} acting in the same direction and the projected drag acting opposite to the blade-row rotation, written as

$$F_\theta = F_{p_\theta} - D \sin\alpha \qquad \textbf{(2.3.36)}$$

Likewise to the solution of the Euler equations of motion with no body forces, the full REE might be expressed in a form that the derivatives along m are related to the streamline shape. Thus, the full REE with body forces is conveniently arranged for its solution in the form of a second-order differential equation as in Eq. 2.3.27. The term *A* remains unaffected, whilst *B* and *C* terms become

$$B = V_m[2\omega \sin\varphi \tan\eta \cos\lambda]$$

$$C = \left[-\frac{V_\theta}{r}\frac{d(rV_\theta)}{ds} - 2\omega V_\theta \cos\lambda + \frac{dI}{ds} - T\frac{dS}{ds} + T\frac{dS}{dm}(\sin(\varphi-\lambda)\cos^2\beta - \tan\lambda \sin\beta\cos\beta) - F_\theta \tan\eta\cos\lambda\right] \quad \textbf{(2.3.37)}$$

where the last term of the coefficient C is the body force acting on the quasi-orthogonal direction, so that

$$F_q = F_\theta \tan\eta \cos\lambda \quad \textbf{(2.3.38)}$$

Substituting the circumferential body-force of Eq. 2.3.36, the coefficient C equation is defined as

$$C = \left[-\frac{V_\theta}{r}\frac{d(rV_\theta)}{ds} - 2\omega V_\theta \cos\lambda + \frac{dI}{ds} - T\frac{dS}{ds} + T\frac{dS}{dm}(\sin(\varphi-\lambda)\cos^2\beta - \tan\lambda \sin\beta\cos\beta) - F_{p_\theta} \tan\eta\cos\lambda + D\sin\alpha\tan\eta\cos\lambda\right] \quad \textbf{(2.3.39)}$$

Not only empirical or analytical flow models have been improved in SLC methods but also the stability and convergence algorithms. Katsanis [168] replaced the normal lines to the flow in the computational mesh for quasi-orthogonal lines to enhance solution stability and speed, avoiding the tedious shape and length calculation of the streamlines and normal lines at every iteration. Wilkinson [169] implemented a damping factor to control the quasi-orthogonal lines displacement during the calculation to improve stability, while guarantying convergence and accuracy. The numerical scheme consisted in determining an optimum damping factor as a function of the mesh aspect ratio, Mach number distribution and differentiation approach. Pachidis *et al*. [116,117] developed, implemented and tested a dynamic convergence control (DCC) algorithm for

the solution of the REE in a 2-D SLC solver (SOCRATES). The new DCC algorithm was introduced with the purpose of avoiding user intervention during the REE solution execution while keeping a reasonable, speed, accuracy and robustness. Although the DCC scheme had more convergence difficulties at off-design conditions; convergence was achieved with good agreement against experimental results.

Particularly, SLC simulation codes have been adapted to satisfy the needs of the compression system structures, such as fans, where the flow is split to the bypass and core channels. Shan [170] devised an approach for mass flow addition in SLC methods to treat inverse design in fans.

Furthermore, SLC methods have found application in analysing complex flow processes affecting the compressor and the engine. For instance, an integration of a low-fidelity 0-D gas-turbine performance simulator and a high-fidelity 2-D SLC compressor program (SOCRATES) [18,19], was used to obtain the overall engine and compressor performance under compressor inlet flow radial pressure distortion. The advantage of this integration technique is that the influence on engine performance due to physical phenomena arising in the compressor and analysed through SLC methods, can be represented. Equally, parallel compressor theory in the S1 surface was coupled to a SLC code in the S2 surface [171] to analyse fan inlet flow distortion and predict surge in the context of a quasi-3-D analysis. The effect of having a duct upstream of the compressor and consequently, boundary layer ingestion (BLI) and growth, was studied using a 2-D SLC code (SOCRATES) [66]. Moreover, this study addressed the lean angle variation to understand the effect on the compressor performance due to inlet-induced flow-distortion.

In short, SLC methods offer the advantage of analysing isolated gas-turbine engine components in detail, providing an accurate and inexpensive solution in terms of computational run-time against CFD. In terms of flexibility, SLC strategy allows to include empiricism in the form of all kind of deviation and loss models unlike CFD, where correlations are pre-defined and cannot be modified. Moreover, SLC analyses require less initial and boundary conditions in comparison with CFD. Even more, high-fidelity analyses from a 2-D SLC compressor performance simulator can be

incorporated into a low-fidelity entire 0-D engine solver. Through this amalgamation strategy, the influence of other engine components is considered to obtain detailed performance results of the SLC-analysed independent component, which is known as component zooming. On the other hand, engine performance prediction is more accurate as internal physical phenomena and a geometry-based approach are contemplated to compute component boundary conditions. Thus, component SLC analyses offer a good trade-off between accuracy and low computational cost and time; if coupled with a low-fidelity engine performance cycle simulator, a more accurate and cost-effective engine performance estimation can be obtained.

2.4 High-Speed Compressible Flow Aerodynamics

2.4.1 Normal Shock Waves

As a flow moves within a duct at lower speeds than the sound, the density of the fluid remains constant and the flow process can be considered as reversible. If the flow velocity increases towards speed of sound, compressibility effects start to become more significant. Shock waves appear when the flow transitions from supersonic to subsonic velocities as a result of an area change or a static-pressure gradient. Similar effect happens when instead of flow circulating inside of a duct, an object moves supersonically through a fluid. A shock wave can be considered as a sound wave with finite length and strength that compresses the flow and reduces its velocity. Discontinuous thermodynamic properties occur across the shock wave, causing dramatic temperature, pressure, density and velocity gradients, yielding to entropy production and making the process irreversible. Consequently, the total pressure of the flow is reduced, generating a loss. Therefore, isentropic relationships are valid upstream and downstream of the shock, but can no longer be used across of it [172]. A normal shock then is defined as that discontinuous step-change compression perpendicular to the flow direction.

Because the shock wave is assumed to be of zero thickness, a thin control volume is considered for the flow process as shown in Figure 2.15 , governed by the well-known thermofluid laws:

Continuity $$\rho_1 u_1 = \rho_2 u_2 \quad \textbf{(2.4.1)}$$

Momentum $$p_1 + \rho_1 u_1^2 = p_2 + \rho_2 u_2^2 \quad \textbf{(2.4.2)}$$

Energy $$h_1 + \frac{1}{2}u_1^2 = h_2 + \frac{1}{2}u_2^2 \quad \textbf{(2.4.3)}$$

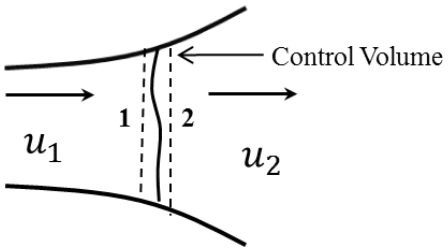

Figure 2.15 Control volume for a normal shock process.

Observe that the area change and viscous effects are neglected in the continuity and the momentum equations, respectively, as the shock thickness tends to zero. Sub-indices 1 and 2 represent the inlet and outlet states. If inlet conditions are known, the rest of the values from the governing equations can be found from the ideal gas relationships, giving the Rankine-Hugoniot relations. The perfect or ideal gas equation is

$$p = \rho R T \quad \textbf{(2.4.4)}$$

The total thermodynamic or static enthalpy h in a fluid is given by

$$h = C_p T \quad \textbf{(2.4.5)}$$

Where C_p is the specific heat at constant pressure, which can be expressed in terms of the heat specific ratio γ, giving

$$C_p = \frac{\gamma R}{\gamma - 1} \quad \textbf{(2.4.6)}$$

Substituting the perfect gas equation and C_p in the static enthalpy definition

$$h = \frac{\gamma R}{\gamma - 1}\frac{p}{\rho R} = \frac{\gamma p}{(\gamma - 1)\rho} \quad \textbf{(2.4.7)}$$

Therefore, the energy equation becomes

$$\frac{\gamma}{(\gamma-1)}\frac{p_1}{\rho_1}+\frac{1}{2}u_1^2=\frac{\gamma}{(\gamma-1)}\frac{p_2}{\rho_2}+\frac{1}{2}u_2^2 \quad \textbf{(2.4.8)}$$

Substituting continuity and momentum equation in Eq. 2.4.8 to replace u_2 and ρ_2, and solving for the pressure ratio across the shock

$$\frac{p_2}{p_1}=1+\frac{2\gamma}{\gamma+1}(\frac{\rho_1 u_1^2}{\gamma p_1}-1) \quad \textbf{(2.4.9)}$$

Besides the Mach number M can be expressed as

$$M^2=\frac{u^2}{a^2}=\frac{u^2}{\gamma RT}=\frac{\rho u^2}{\gamma p} \quad \textbf{(2.4.10)}$$

Thus, the velocity can be substituted for the Mach number in Eq. 2.4.9

$$\frac{p_2}{p_1}=1+\frac{2\gamma}{\gamma+1}(M_1^2-1) \quad \textbf{(2.4.11)}$$

Likewise, the Mach number expression is introduced in the momentum equation

$$p_1+M_1^2\gamma_1 p_1=p_2+M_2^2\gamma_2 p_2 \quad \textbf{(2.4.12)}$$

Solving for the outlet Mach number

$$M_2=\sqrt{\frac{(\gamma-1)M_1^2+2}{2\gamma M_1^2+1-\gamma}} \quad \textbf{(2.4.13)}$$

Static Temperature, density and velocity ratios can be similarly obtained as

$$\frac{T_2}{T_1}=1+\frac{(\gamma M_1^2+1)}{M_1^2}\frac{2(\gamma-1)}{(\gamma+1)^2}(M_1^2-1) \quad \textbf{(2.4.14)}$$

$$\frac{\rho_2}{\rho_1}=\frac{u_1}{u_2}=\frac{M_1^2(\gamma+1)}{(\gamma-1)M_1^2+2} \quad \textbf{(2.4.15)}$$

Since the shock process is adiabatic as there is no heat addition or rejection, the total-temperature remains constant, written as

$$T_{02}=T_{01} \quad \textbf{(2.4.16)}$$

And the total-pressure ratio or recovery across a normal shock is

$$P_{02} = \left[\frac{(\gamma+1)M_1^2}{(\gamma-1)M_1^2+2}\right]^{\frac{\gamma}{\gamma-1}} \left[\frac{\gamma+1}{2\gamma M_1^2-(\gamma-1)}\right]^{\frac{1}{\gamma-1}} \quad \textbf{(2.4.17)}$$

2.4.2 Oblique Shock Waves

When the flow exceeds the speed of sound and gets deflected by any obstacle it results in the formation of oblique shock waves. These kinds of shocks are not necessarily normal and the flow across them can no longer be considered 1-D. Instead, the flow is 2-D oriented at angle with respect of the shock wave. The flow changes across the shock are determined by the normal component of the velocity. A balance of conservation of momentum in the control volume containing the oblique shock, shows that the tangential velocity component remains unchanged. Hence, normal shock theory can be applied to oblique shocks but considering the perpendicular component of the velocity. If inviscid flow is assumed, compressible-flow theory establishes that the conditions immediately downstream of the shock are only a function of the free-stream Mach number and the shock angle ς. The relationship between the obstacle geometry and the shock angle is given by the inclination δ of the object surface. This relation has been well-documented for simple, but key, geometrical shapes as shown in Figure 2.16 a) for axially symmetric cones or wedges, and Figure 2.16 b) for inclined wall planes. As the oblique shock is at an angle ς with respect of the surface, the flow across the shock is turned by an amount δ, as shown in Figure 2.16. Consequently, the outlet velocity has a direction equals to the deflection angle δ. In fact, the normal shock is a particular case of the oblique shock theory with a $\varsigma = 90°$.

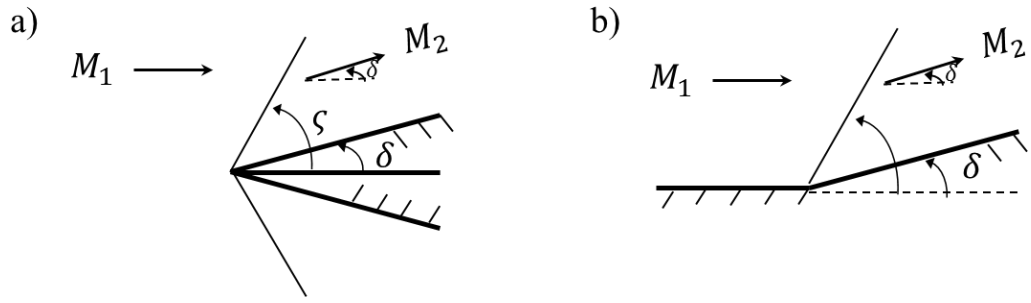

Figure 2.16 Oblique shock waves. a) Flow past a wedge. b) Flow past an inclined wall.

Therefore, the oblique-shock relations become [173]

$$\frac{p_2}{p_1} = 1 + \frac{2\gamma}{\gamma+1}(M_1^2 \sin^2 \varsigma - 1) \tag{2.4.18}$$

$$M_2 = \sqrt{\frac{(\gamma-1)M_1^2 \sin^2 \varsigma + 2}{2\gamma M_1^2 \sin^2 \varsigma + 1 - \gamma}} \Big/ \sin^2(\varsigma - \delta) \tag{2.4.19}$$

$$\frac{T_2}{T_1} = 1 + \frac{(\gamma M_1^2 \sin^2 \varsigma + 1)}{M_1^2 \sin^2 \varsigma} \frac{2(\gamma-1)}{(\gamma+1)^2}(M_1^2 \sin^2 \varsigma - 1) \tag{2.4.20}$$

$$\frac{\rho_2}{\rho_1} = \frac{u_1}{u_2} = \frac{M_1^2 \sin^2 \varsigma\,(\gamma+1)}{(\gamma-1)M_1^2 \sin^2 \varsigma + 2} = \frac{tan\varsigma}{\tan(\varsigma - \delta)} \tag{2.4.21}$$

$$T_{02} = T_{01} \tag{2.4.22}$$

$$\frac{P_{02}}{P_{01}} = \left[\frac{(\gamma+1)M_1^2 \sin^2 \varsigma}{(\gamma-1)M_1^2 \sin^2 \varsigma + 2}\right]^{\frac{\gamma}{\gamma-1}} \left[\frac{\gamma+1}{2\gamma M_1^2 \sin^2 \varsigma - (\gamma-1)}\right]^{\frac{1}{\gamma-1}} \tag{2.4.23}$$

Shock and deflection angle can be related through an expression derived from the oblique shock equations and trigonometric identities, giving

$$\delta = \operatorname{atan}\left\{2 \cot \varsigma \frac{M_1^2 \sin^2 \varsigma - 1}{M_1^2[\gamma + \cos(2\varsigma)] + 2}\right\} \tag{2.4.24}$$

The above oblique-shock relations have been presented in the form of charts [172,174,175] to conveniently determine the flow conditions downstream of an oblique shock for wedges and inclined wall surfaces. For instance, Eq. 2.4.24 is typically represented in a ς vs δ chart for constant inlet Mach numbers M_1, as shown in Figure 2.17. Observe that an increase in M_1at constant δ, reduces ς, and hence, the shock strength decreases with it. For a given inlet Mach number there is one maximum deflection angle δ_{max} and there is no attached straight oblique shock solution beyond this angle. Instead, a detached curved shock is obtained, explained later in Sec. 2.1.3, relevant for the physics principle of bow shocks in compressor rotor blades. Clearly it is noticed that for a $\varsigma = 90°$, namely a normal shock, $\delta = 0$ for any inlet Mach number. Two possible shock angle solutions are possible for a given M_1 and $\delta < \delta_{max}$: a weak

shock related to low shock angles, and a strong shock associated to high shock angles. For strong oblique shocks, the flow downstream is subsonic; whereas for weak shocks, which are more realistic to occur, the flow behind the shock generally remains supersonic.

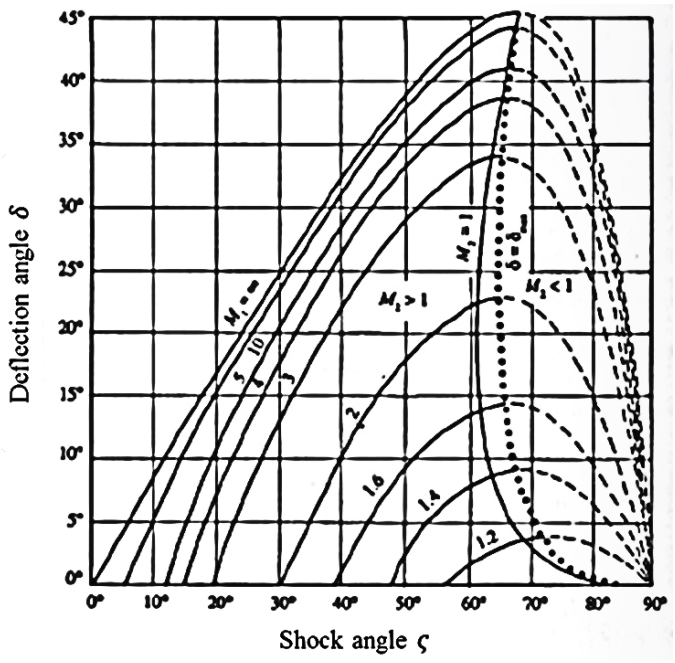

Figure 2.17 Shock angle vs deflection angle chart for oblique shock waves [173].

2.4.3 Detached Shock Waves

Early experimental investigations in objects moving at supersonic speeds showed a detached wave ahead of them, showing good agreement with theory in terms of shock strength and entropy generation across the shock system [176]. Crocco [177] initiated the first flow computations behind a detached shock by defining a stream function, highlighting the relationship between the streamlines and the shock curvature [178].

When there is a supersonic flow past a wedge with a wedge half-angle δ as in Figure 2.16 a) or past an inclined wall with a cone semivertex angle δ as in Figure 2.16 b), an oblique shock is formed ahead of the wall. As it was mentioned in Section 2.1.2, if $\delta > \delta_{max}$ for a particular M_1, the shock is no longer attached nor oblique. Alternatively, a detached curved shock wave stands in front of the sharp-nosed object as sketched in Figure 2.18. The supersonic flow passing across the central part of the

shock undergoes a strong compression, forming a subsonic flow pocket with $M_2 < 1$ in front of the body nose and behind the bow wave. This central portion of the shock can be considered as the strong solution in the ς vs δ chart due to the large shock angle. In fact, moving farther out of the central streamline, the shock angle keeps decreasing until is low enough to produce weak shock, resulting in supersonic flow behind it. As seen in Figure 2.18 , downstream of the detached shock there is a clear division between the subsonic flow originated from the large-shock-angle shock and the remaining weak shock called sonic line. Along the sonic line, the Mach number is unity.

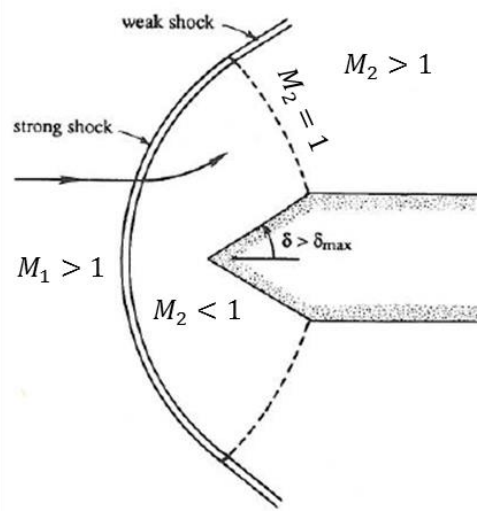

Figure 2.18 Detached shock wave ahead of a sharp-nosed body [173].

From the ς vs δ chart in Figure 2.17, it is evident that an increase in the inlet Mach number, extends the deflection angle margin, hence, if δ exceeds δ_{max}, an increment in M_1 produces shock re-attachment and obliquity. This is that for pointed bodies, there is a Mach number below which the bow wave is always detached but above which it is attached, and this is the detachment Mach number [179]. However for the case of blunt-nosed bodies as the blade profiles, the shock is always detached, regardless of any inlet free-stream Mach number increase and there is no detachment Mach number defined.

The detached wave DD' flow field is explained in Figure 2.19 for a blunt-nose body moving at supersonic speed. The bow shock leads up asymptotically to infinity whose angle with the flow velocity is the Mach angle. There is a stagnation point at p and the streamline passing through this point and aligned with the velocity direction, is the

stagnation streamline about the XX'-axis. The bow shock intersects the stagnation streamline at its vertex v, where only at this point the shock is completely normal. Farther out from the vertex in both directions, the shock becomes every time more or oblique with a particular shock angle ς at every point. Thus, the shock angle varies from zero at v to the Mach angle complement at infinity.

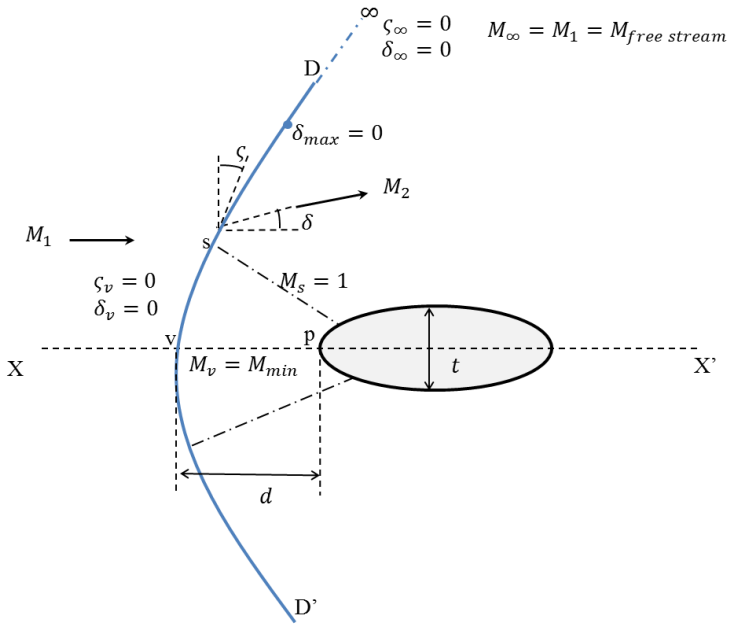

Figure 2.19 Bow shock-wave system in a blunt-nose body.

The shock system divides the flow in two parts in the direction of the velocity. Everywhere upstream of bow shock, the flow is uniform with constant total head or total pressure. Downstream of the shock, the flow field varies in the direction normal to the velocity having a different stagnation pressure due to a variation in entropy generation as a function of the free-stream Mach number and the shock angle. The deflection angle varies from zero at the bow vertex to a maximum deflection value at a finite distance out in the shock and gradually becomes zero again as the shock approaches its asymptote. This can be verified by ς vs δ plot of Figure 2.17, where for a given inlet free-stream Mach number, the deflection angle increases to a maximum on the strong side portion of the shock (dashed line), and decreases from the maximum value to zero on the weak shock section (solid line). Consequently, the downstream Mach number varies in the direction normal to the flow. The Mach number varies from

a minimum to unity on the sonic line and from unity progressively approaches to the free-stream Mach number as the shock angle approximates the Mach angle complement.

Laitone and Pardee [179] developed a method to obtain the bow shock location but for free-stream Mach numbers slightly above unity. This is an inlet Mach number of 1+ϵ, where ϵ is very small in comparison to one. To determine the detachment distance of the shock from the body nose, the problem was simplified to consider a normal shock plane, which is a relatively acceptable for Mach numbers just above sonic. Then, the entropy change across the bow-wave system is

$$\Delta s = C_v \ln\left(\frac{p_1/\rho_1}{p_{01}/\rho_{01}}\right) = C_v \frac{2\gamma(\gamma-1)}{3(\gamma-1)^2} \qquad \textbf{(2.4.25)}$$

Substituting in Eq. 2.4.25 the isentropic total-to-static relation for pressure and density in terms of Mach number and expanding it in powers of ${M_1}^2 - 1$ gives

$$\Delta s = C_v \frac{2\gamma(\gamma-1)}{3(\gamma-1)^2} ({M_1}^2 - 1)^3 + \cdots \qquad \textbf{(2.4.26)}$$

Since $M = 1 + \epsilon$, Eq. 2.4.26 becomes,

$$\Delta s = C_v \frac{16}{3} \frac{\gamma(\gamma-1)}{(\gamma+1)^2} \epsilon^3 + \cdots \qquad \textbf{(2.4.27)}$$

From the governing conservation equations of energy, continuity and momentum, the Mach number downstream of the bow is calculated assuming a normal shock using Eq. 2.4.13. Hence, the velocity ratio across the bow shock is expressed as

$$\frac{V_2}{V_1} = \frac{1}{\gamma+1}\left(\frac{2}{{M_1}^2} + \gamma - 1\right) \qquad \textbf{(2.4.28)}$$

As the incoming Mach number approaches unity from a supersonic value, the bow shock backs out of the body nose towards infinity, becoming weaker. Figure 2.20 shows a Schlieren photograph of an engine intake with a strong and weak bow shock on either side of the wedge-sharped cone tip. The dissymmetry of both systems allowed observing in the same photography a weaker solution when the shock recedes farther ahead and a stronger solution when the shock is more attached to the cone tip.

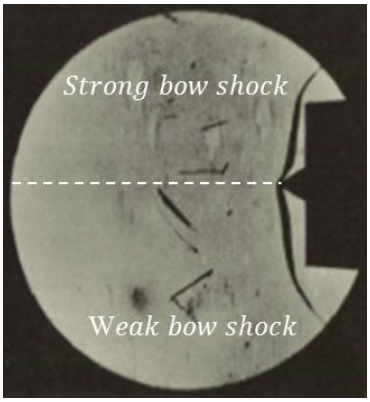

Figure 2.20 Weak and strong shock solutions for a detached wave in an engine intake (modified from [178]**).**

Thus, the thermodynamic properties the downstream of the shock between the bow-wave vertex and the body nose are a continuous function of the free-stream Mach number. Then, the velocity ratio along the stagnation streamline becomes a function of the inlet Mach number, detachment distance d, and the maximum body nose thickness t,

$$\frac{V_2}{V_1} = f(\frac{d}{t}, M_1) \tag{2.4.29}$$

For two-dimensional symmetrical bodies as the blade profiles, the thickness is twice the leading edge radius. As the flow is subsonic behind the bow shock, the flow is assumed to be incompressible, for which $\frac{V_2}{V_1}$ along the stagnation line for a two-dimensional symmetrical body is

$$\frac{V_2}{V_1} = 1 - \frac{0.1592}{\frac{d}{t} + 0.1592} \tag{2.4.30}$$

Equating Eq. 2.4.30 to the velocity ratio derived from conservation equations in Eq. 2.4.28, the bow-shock detachment distance becomes

$$d = t\left[\frac{0.0796(\gamma+1)}{\gamma + \frac{1}{{M_1}^2}} - 0.1592\right] \tag{2.4.31}$$

Busemann [178] reviewed different analytical techniques for detached-shock treatment, remarking the valuable shock polar application. The shock polar representation connects through a curve all the different supersonic velocity vectors for which a shock will appear. These polar diagrams obtain velocity magnitudes and angles for the inlet and outlet states, the deflection angle, and the shock angle. For the case of a two-dimensional flow, the shock polar information can be obtained at every streamline and plotted in the shock front as shown in Figure 2.21. This shock polar solution with streamlines identified the main flow points previously mentioned, except for the Crocco point which is the location on the bow shock where the streamline has a curvature of zero, even if the shock has a finite curvature.

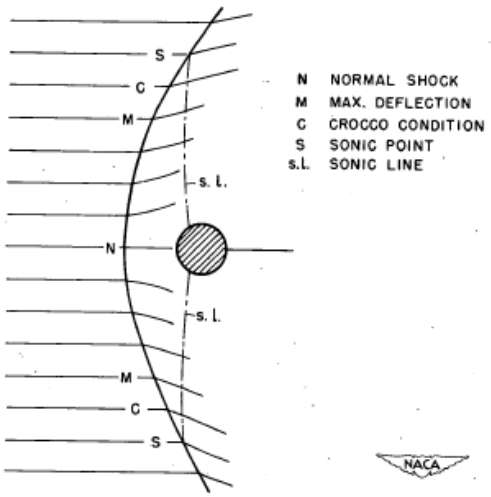

Figure 2.21 Detached shock solution through shock polar diagrams [178].

A fundamental hyperbola-approximation model was developed by Moeckel [180] to predict the detached bow-shock shape and location ahead of isolated bodies. This approximate method assumed the detached bow shock as a hyperbola asymptotic to the free-stream Mach wave and the sonic line to be straight and inclined. To determine the detached-shock location relative to the blunt-nosed body, a continuity and a geometric method were used, where the former showed a closer agreement with experiments. Under these assumptions, the overall bow wave location becomes a single-valued function of the free-stream Mach number.

If the inlet Mach number is large enough, the subsonic flow behind the bow wave becomes a significant part of the system; therefore, lengthy PDE-based numerical

methods can no longer be expected to return valid results. For such problem, simplifying the analysis to a hyperbola-shaped bow shock approximation along with the continuity equation for its location has laid the ground for all the successive shock model representations on transonic-compressor blade elements and infinite cascades.

2.4.4 Prandtl-Meyer Expansion

A supersonic flow compression process can be gradual over a wall as seen in Figure 2.22 a). As there is no wall corner as in the sudden compression of oblique shock theory, the shock is formed from emanating Mach waves or Mach lines that begin when the wall slope starts to change. These Mach lines are inclined at a Mach angle μ to the flow direction. Flow magnitude and direction are constant along the Mach lines. When an object moves faster than the speed of sound, the weak pressure disturbances (sound), form a Mach cone. The Mach cone half-wedge angle is the Mach angle, defined by

$$\mu = \text{asin}(\frac{1}{M}) \tag{2.4.32}$$

In Sec. 2.1.2, the wedge or inclined wall turn the flow inwards due to a concave shape. Conversely, if there is a convex profile submerged in a flow, the deflection of the flow is outwards and an expansion is generated. The expansion process is a series of infinite and continuous weak Mach waves that accelerate and turn the flow. If the expansion is gradual as sketched in Figure 2.22 b), every Mach line is inclined at an angle μ with respect of the flow direction. Similarly as in the gradual compression, the flow properties remain constant along the Mach waves.

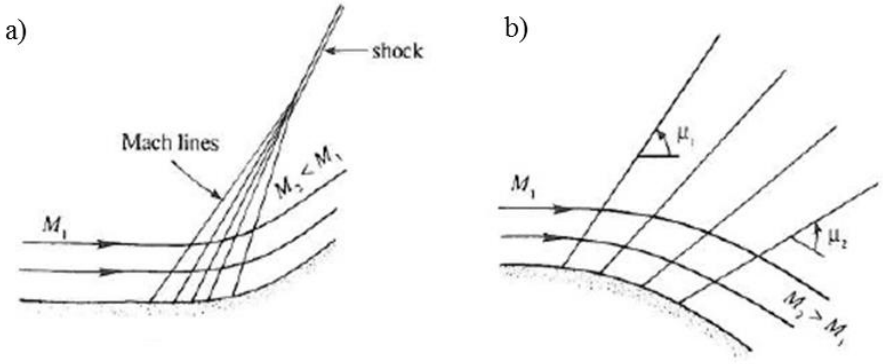

Figure 2.22 Supersonic flow past a gradually-inclined wall [173]**. a) Compression due to concave curvature. b) Expansion due to convex curvature.**

Nonetheless, if the expansion is not gradual and instead there is a sudden convex corner, the Mach waves coalesce in the corner point, as seen in Figure 2.23, generating an expansion fan or Prandtl-Meyer expansion. As in any expansion process, every Mach wave gradually accelerates the flow, causing continuous static pressure decay. In a similar manner as the gradual expansion, each Mach line is located at a μ with respect of the incoming flow, corresponding to every local Mach number. Near the wall, due to the coalescence of the waves, the flow does not undergo a smooth expansion, leading to a discontinuous drop of the static pressure.

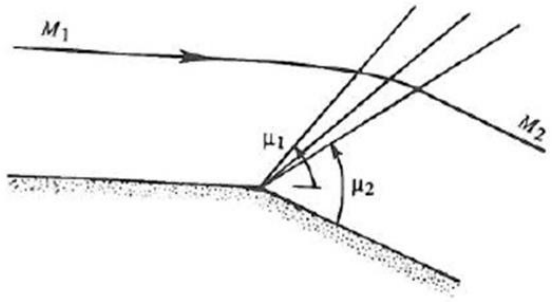

Figure 2.23 Supersonic flow expansion past a sudden convex corner causing a Prandtl-Meyer expansion [173]**.**

Using the method of characteristics, the flow magnitude and flow angle β downstream of the expansion process can be found. The Riemann's equation relates the flow angle and the Prandtl-Meyer angles between the inlet and the outlet through the Riemann's invariant K as follows

$$\beta \pm \nu = const = \mathrm{K} \tag{2.4.33}$$

Where ν is the Prandtl-Meyer angle, calculated as a unique function of the Mach number in the Prandtl-Meyer function expressed as

$$\nu(M) = \sqrt{\frac{\gamma+1}{\gamma-1}}\operatorname{atan}\left(\sqrt{\frac{\gamma+1}{\gamma-1}(M^2-1)}\right) - \operatorname{atan}(\sqrt{M^2-1}) \tag{2.4.34}$$

Depending on the Mach wave (characteristic) orientation the sign of Eq. 2.4.26 is chosen. For a right running characteristic, the Riemann's equation is:

$$\mathrm{K}_{-} = \mathrm{K}_{-1} = \mathrm{K}_{-2} \tag{2.4.35}$$

$$\beta_1 + \nu_1(M_1) = \beta_2 + \nu_2(M_2) \quad \textbf{(2.4.36)}$$

For a left running characteristic, the Riemann's identity becomes

$$\mathrm{K}_+ = \mathrm{K}_{+1} = \mathrm{K}_{+2} \quad \textbf{(2.4.37)}$$

$$\beta_1 - \nu_1(M_1) = \beta_2 - \nu_2(M_2) \quad \textbf{(2.4.38)}$$

Therefore, the flow turning ϑ is simply the difference in flow direction, turning to be the change in Prandtl-Meyer angle

K_- $$\vartheta = \beta_2 - \beta_1 = \nu_1(M_1) - \nu_2(M_2) \quad \textbf{(2.4.39)}$$

K_+ $$\vartheta = \beta_2 - \beta_1 = \nu_2(M_2) - \nu_1(M_1) \quad \textbf{(2.4.40)}$$

If analysis is concerned, a continuous expansion can be analysed as well using the Prandtl-Meyer expansion equations as the smooth turning can be considered to take place over a longer distance provided that the maximum turning angle is not exceeded.

2.5 Choking

2.5.1 One-Dimensional Isentropic Flow

To have a better understanding of choking phenomenon in transonic axial-flow compressor blading, a review in area-velocity relations is given for one-dimensional isentropic flows.

Isentropic flow acceleration or deceleration inside of a duct can be obtained by varying the area. In general, if the flow is subsonic ($M < 1$), a convergent duct or nozzle accelerates the flow; whereas a divergent duct or diffuser slows it down as shown in Figure 2.24 a). Conversely, if the flow is supersonic ($M > 1$), a divergent nozzle will accelerate the flow, while a convergent diffuser will decelerate the flow as shown in Figure 2.24 b).

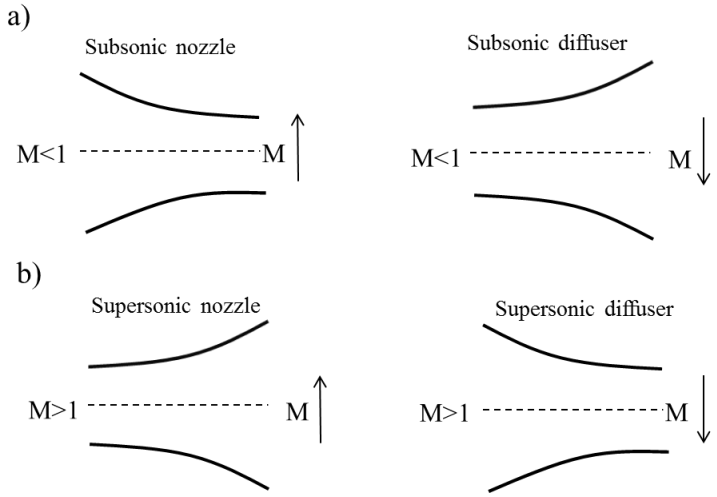

Figure 2.24 Flow Mach numbers for converging and diverging ducts. a) Subsonic inlet conditions. b) Supersonic inlet conditions.

This can be demonstrated through the mass conservation or continuity equation

$$\frac{D\rho}{Dt} + \rho \frac{\partial u_j}{\partial x_j} = 0 \qquad \textbf{(2.5.1)}$$

Where the sub index j represents the vectorial directions. Considering one-dimensional (1-D) flow, continuity equation can be expressed in the form

$$\frac{d\rho}{\rho} + \frac{du}{u} + \frac{dA}{A} = 0 \qquad \textbf{(2.5.2)}$$

If $\rho = const,$ namely, incompressible, the term $d\rho$ becomes zero. Thus, Eq. 2.5.2 becomes only dependent on the velocity and area. Thence, an area decrease will result in a velocity increase and vice versa. If $d\rho = 0$, Eq. 2.5.1 becomes the Boussinesq approximation that describes an incompressible flow

$$\rho \frac{\partial u_j}{\partial x_j} = \rho \nabla \overrightarrow{u_j} = \nabla \cdot \left(\rho \overrightarrow{u_j}\right) = 0 \qquad \textbf{(2.5.3)}$$

Expanding Eq. 2.5.3 in the three directions 1, 2, and 3, gives

$$\frac{\partial(\rho u_1)}{\partial x_1} + \frac{\partial(\rho u_2)}{\partial x_2} + \frac{\partial(\rho u_3)}{\partial x_3} = 0 \qquad \textbf{(2.5.4)}$$

For 1-D flow, Eq. 2.5.4 becomes

$$\frac{\partial(\rho u)}{\partial x} = \rho\frac{\partial u}{\partial x} + u\frac{\partial \rho}{\partial x} \quad \textbf{(2.5.5)}$$

Given a $M < 0.3$, incompressibility can be assumed, requiring that

$$u\frac{\partial \rho}{\partial x} \ll \rho\frac{\partial u}{\partial x} \quad \textbf{(2.5.6)}$$

or expressed in terms of ratio differentials

$$\frac{\delta \rho}{\rho} \ll \frac{\delta u}{u} \quad \textbf{(2.5.7)}$$

For $M \geq 0.3$, compressibility effects need to be considered as the density is not anymore constant. In compressible flow, the speed of sound a is a parameter of the compression level, defined as the square root of the pressure changes with respect to the density change at constant entropy

$$a^2 = (\frac{\partial p}{\partial \rho})_s \quad \textbf{(2.5.8)}$$

Besides, the conservation of momentum or the Euler's equation of motion of a continuum establishes

$$\rho\frac{Du_i}{Dt} = \frac{\partial \sigma_{ij}}{\partial x_j} + f_i \quad \textbf{(2.5.9)}$$

where σ_{ij} is the fluid stress tensor and f represents the body force per unit volume.

For a Newtonian viscous fluid, which is the case of air, the stress-strain relationship is specified by the Stokes formulation

$$\sigma_{ij} = -p\delta_{ij} + 2\mu e_{ij} + \lambda e_{kk}\delta_{ij} \quad \textbf{(2.5.10)}$$

In the case of inviscid assumption, the normal dynamic viscosity μ and the second viscosity term λ are neglected, meaning that there is no strain e and no shear stress, resulting in an isotropic stress tensor. Thus, the stress tensor is purely normal and only due to fluid pressure. Substituting Eq. 2.5.10 in Eq. 2.5.9 gives

$$\rho \frac{Du_i}{Dt} = -\frac{\partial(p\delta_{ij})}{\partial x_j} + f_i \quad \textbf{(2.5.11)}$$

Assuming there are no body forces, the conservation of momentum equation becomes

$$\rho \frac{Du_i}{Dt} = -\frac{\partial p}{\partial x_i} \quad \textbf{(2.5.12)}$$

For 1-D flow and re-arranging the terms from Eq. 2.5.12

$$\frac{du}{dt} = -\frac{1}{\rho}\frac{dp}{dx} \quad \textbf{(2.5.13)}$$

$$udu = -\frac{dp}{\rho} \quad \textbf{(2.5.14)}$$

which is the 1-D frictionless version of the Euler equation of motion of a continuum. Substituting then the speed-of-sound definition of Eq. 2.5.8 in Eq. 2.5.14

$$udu = -\frac{dp}{d\rho}\frac{d\rho}{\rho} = -a^2\frac{d\rho}{\rho} \quad \textbf{(2.5.15)}$$

Recalling that the Mach number is defined as

$$M = \frac{u}{a} \quad \textbf{(2.5.16)}$$

it is possible to substitute Eq. 2.5.16 into Eq. 2.5.15, giving

$$-M^2\frac{du}{u} = \frac{d\rho}{\rho} \quad \textbf{(2.5.17)}$$

This shows that for low Mach numbers ($M < 0.3$), the density change ratio is much less than the velocity change ratio, therefore, the density changes in the continuity equation can be neglected for incompressible flows. Whereas for high Mach numbers ($M > 0.3$),

the left-hand-side term of Eq. 2.5.17 becomes large enough, thus, the density change becomes significant and must be included in any conservation of mass equation for compressible flow. Because compressibility effects depend on the Mach number, flow is divided in different regimes as shown in Table 2.2.

Table 2.2 Flow regimes for incompressible and compressible flow depending on the Mach number.

Flow Regime	Mach Number Range
Incompressible	$M < 0.3$
Subsonic	$0.3 < M < 0.8$
Transonic	$0.8 < M < 1.2$
Supersonic	$1.2 < M < 3.0 \sim 4.0$
Hypersonic	$M > 3.0 \sim 4.0$

2.5.2 Convergent-Divergent Nozzle

It is evident then that an infinite convergent nozzle operating in subsonic conditions will accelerate the flow to $M = 1$, and further area reduction will eventually bring the flow to rest. If further velocity rise wants to be achieved, a convergent-divergent nozzle is required as sketched in Figure 2.25, having a minimum cross-sectional area where the duct slope changes, known as throat.

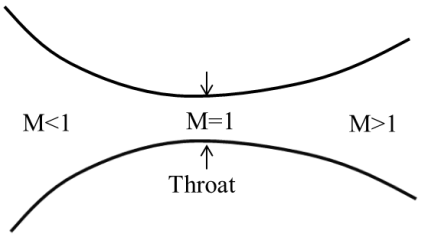

Figure 2.25 Convergent-divergent nozzle to continuously accelerate the flow from subsonic to supersonic speeds.

Typically, a convergent-divergent duct is controlled by reducing the back or outlet static-pressure p_{out} or by increasing the inlet mass flow $\dot{m}_{in}$. Through outlet static pressure reduction, the mass flow increases as the outlet velocity rises, up to a certain point. Further pressure decrease will not increase the mass flow, regardless of how low it is, even if it reaches vacuum. When no more mass flow can be passed through, the duct is said to become choked. Mass flow can be increased by opening the throat area, widening the mass flow range; however, choking will happen eventually. Choking occurs when $M = 1$ at the minimum cross-sectional area or throat, setting the flow

speed limit where no more mass flow can be passed. This limit is reached as lowering the back static pressure beyond the choking point will not accelerate the flow any more. Otherwise, it would involve the flow becoming supersonic upstream of the throat and the remaining converging section decelerating it, increasing the back static pressure, which is the opposite to the initial action of decreasing p_{out}, contradicting the nature of the physics.

Nonetheless, not always a $M = 1$ is obtained at the throat. In the case the flow is subsonic at the inlet of the convergent-divergent duct, the first section acts as a nozzle accelerating the flow. However, if the acceleration is not enough, the Mach number at the throat remains subsonic, and the diverging profile acts as a diffuser, slowing down the flow to low subsonic velocities, as sketched in Figure 2.26 a). Conversely, if the intake flow is supersonic, deceleration occurs in the converging section. Assuming the deceleration is not enough to bring the flow down to a unity Mach number at the throat, the rest of the convergent-divergent duct behaves as a nozzle, accelerating the flow to high supersonic speeds as seen in Figure 2.26 b).

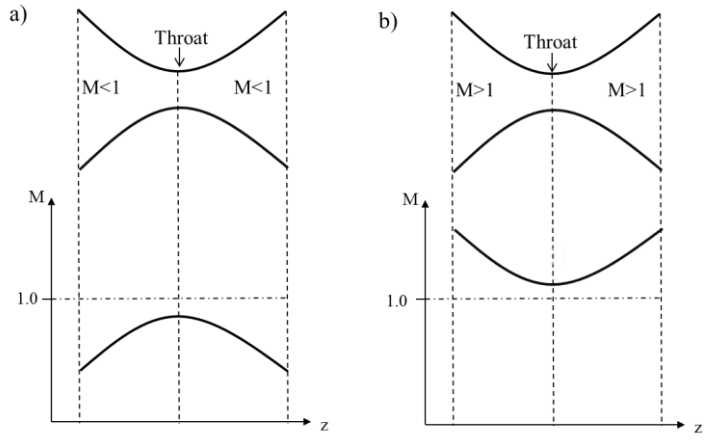

Figure 2.26 Convergent-divergent nozzle operating at different inlet conditions when Mach number is not unity at the throat. a) Subsonic inlet flow. b) Supersonic inlet flow.

Once choking is set, mass flow is fixed, but the flow downstream of the throat can change depending on the back static pressure variation. To represent different scenarios sketched in Figure 2.27 occurring in a convergent-divergent nozzle, let's consider a convergent-divergent nozzle connected to a chamber with a high static pressure p_{in}, subsonic inlet Mach number, and exhausting air into the ambient.

a) Flow is everywhere subsonic, meaning that the flow in the convergent portion is not accelerated enough to produce supersonic flow at the throat. Therefore, the flow in the divergent profile acts as a diffuser, decelerating the flow, as shown in Figure 2.27 a).
b) Eventual back static pressure reduction will produce $M = 1$ at the throat, as shown in Figure 2.27 b). The flow has become just choked and further outlet static pressure reductions could not increase the mass flow and the point of $M = 1$ remains fixed at the throat. Because the flow was just choked, the divergent portion behaves as a diffuser, decelerating the flow.
c) Once the flow is just choked, further p_{out} reduction will accelerate the flow in a portion of the divergent section, forming supersonic flow downstream of the throat. The supersonic flow region ends with a normal shock wave, as seen in Figure 2.27 c), producing flow discontinuities and deceleration to subsonic velocities. Provided that p_{out} is below the pressure to choke the flow, a pressure increase or decrease moves forward or backward the shock inside of the divergent portion, varying the supersonic flow streamwise extent.
d) Further p_{out} reduction causes the shock to be located at the nozzle exit, as observed in Figure 2.27 d), having supersonic flow in all the divergent section. As in case c), the flow downstream of the shock is subsonic.
e) If the outlet static pressure keeps dropping, the exit shock bends out and a complex shock pattern downstream of it is produced as illustrated in Figure 2.27 e). The shock is not anymore normal to the flow, originating a series of shocks and reflections bringing about mixed subsonic and supersonic flow, or just supersonic, if the p_{out} is low enough. In this case, the static pressure just at the exit is lower than the back static pressure, leading the flow to be overexpanded. Therefore a set of shocks outside of the nozzle are required to gradually increase the static pressure to match p_{out}.
f) Figure 2.27 f) shows the design condition for a convergent-divergent nozzle. Further back static pressure lowering will be equal to the exit static pressure caused by the shock pattern, weakening the shocks. Shock pattern disappears as

it not anymore needed and the flow is completely supersonic throughout all the divergent section.

g) Likewise case e), an inequality between the exit pressure and the back static pressure is produced if the latter is lowered even further. The difference is that now the exit pressure is greater than p_{out}, causing the flow to be underexpanded. A complex expansion-wave pattern is formed then downstream of nozzle outlet to increase the static pressure and match the boundary condition of p_{out}, as pictured in Figure 2.27 g), accelerating and turning the flow.

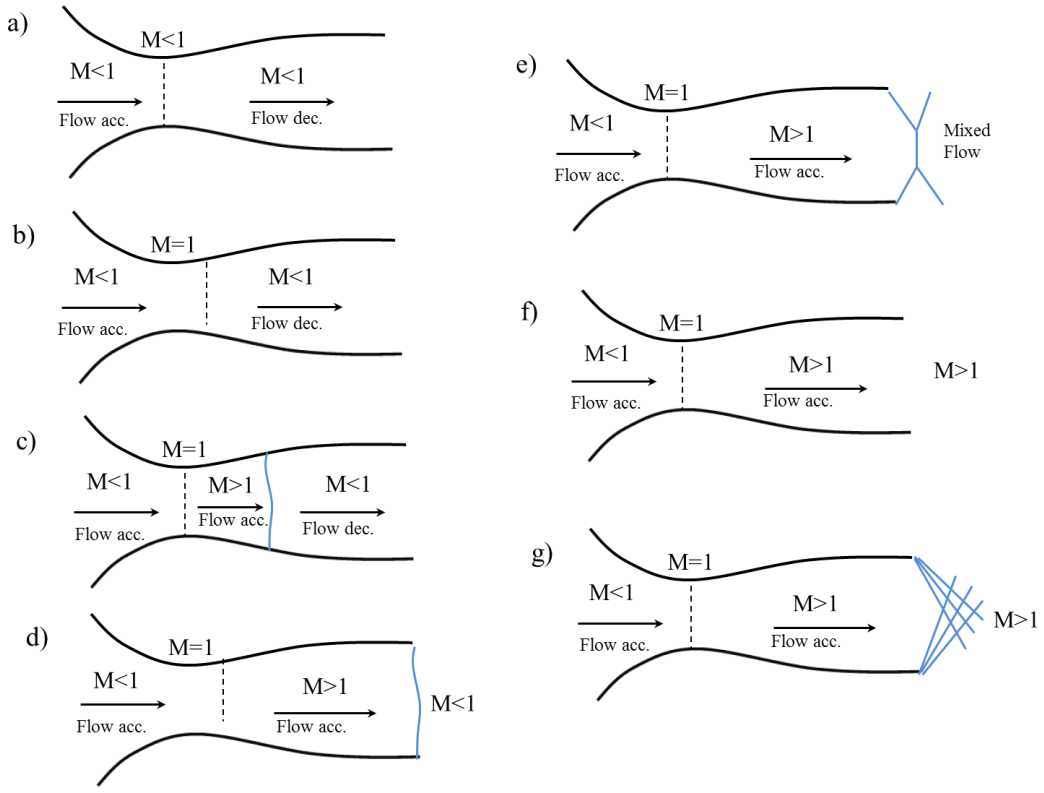

Figure 2.27 Flow patterns in a convergent-divergent nozzle. a) Subsonic flow. b) Flow just choked. c) Shock in nozzle. d) Shock at exit. e) Overexpanded flow. f) Design condition. g) Underexpanded flow.

As the flow is assumed to be isentropic along a convergent-divergent nozzle, the outlet total-pressure P_{02} is equals to that from the inlet total-pressure P_{01}, and thus, the stagnation condition at any point is simply p/P_0 as shown in Figure 2.28. Because the total-pressure remains unchanged throughout the nozzle, p/P_0 gets modified due to variations in the static pressure. In the converging section of the nozzle, the static pressure drops due to the flow acceleration. The static pressure drop in that first section

is higher as the conditions approach to choking, as the flow accelerates more rapid to reach $M = 1$. It is clearly observed that once the flow is choked, the flow thermodynamic properties remain unaffected upstream of the throat, as the flow cannot longer be accelerated more. Downstream of the throat, when the flow is entirely subsonic (a) there is a pressure rise as the flow keeps decelerating in the divergent section. Similarly, when the flow is just choked (b), the flow decelerates, increasing the static pressure which is lower than in case a). When there is a shock in the nozzle (c), the flow keeps accelerating behind it, reducing the static pressure and it is until the shock is encountered, that there is an instantaneous pressure rise across the shock. If the shock is standing at the nozzle exit (d), the static pressure keeps decreasing throughout the divergent section due to flow acceleration and the sudden pressure increment happens at the exit. Equally, in the overexpanded flow, the design condition, and the underexpanded flow, the static pressure drops until the exit inasmuch as the flow is supersonic in the divergent section, experiencing acceleration. When there is flow overexpansion (e), it is seen that the exit pressure is lower than p_{out}, requiring the complex shock structure to gradually increase the static pressure, decelerating the flow. When the exit pressure is equal to the back static pressure imposed (f), then no change in static pressure is observed after the nozzle exit. Finally in underexpansion conditions (g), the exit pressure is higher than p_{out} and eventually, the static pressure is reduced through the expansion-wave structure to match the outlet static pressure.

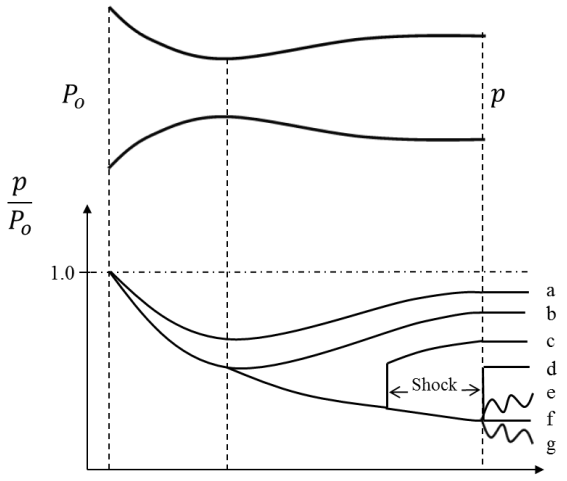

Figure 2.28 Static-to-total pressure-ratio distribution in a convergent-divergent nozzle for different outlet static pressure levels.

2.5.3 Area-Velocity Relationship

Given a convergent-divergent duct, the effect of area change on the Mach number can be obtained by comparing any point with an area A against the throat point with a critical area A^*, referring to the flow conditions when $M = 1$. Following the governing continuity equation, the mass flow entering at A is equals to that at A^*, thus

$$m^{\cdot} = \dot{m}^* = \rho u A = \rho^* u^* A^* \qquad \textbf{(2.5.18)}$$

Substituting the Mach number definition, Eq. 2.5.18 becomes

$$\frac{A}{A^*} = \frac{\rho^* u^*}{\rho u} = \frac{\rho^* a^* M^*}{\rho a M} \qquad \textbf{(2.5.19)}$$

However, $M^* = 1$ as is the sonic condition. Adding the stagnation or total density in both, numerator and denominator, Eq. 2.5.19 is written as

$$\frac{A}{A^*} = \frac{\rho^* \rho_0 a^*}{\rho_0 \rho a M} = \frac{\rho^*}{\rho_0} * \frac{\rho_0}{\rho} * \frac{a^*}{a} * \frac{1}{M} \qquad \textbf{(2.5.20)}$$

The speed-of-sound-to-critical-speed-of-sound ratio is the square root of its static-temperature ratio. And, if the stagnation temperature is added to the numerator and denominator, $\frac{a^*}{a}$ is given by

$$\frac{a^*}{a} = \sqrt{\frac{\gamma R T^*}{\gamma R T}} = \sqrt{\frac{T^*}{T}} = \sqrt{\frac{T^* T_0}{T_0 T}} \qquad \textbf{(2.5.21)}$$

Substituting Eq. 2.5.21 into the area-to-critical-area ratio gives

$$\frac{A}{A^*} = \frac{\rho^*}{\rho_0} \frac{\rho_0}{\rho} \sqrt{\frac{T^* T_0}{T_0 T}} \frac{1}{M} \qquad \textbf{(2.5.22)}$$

The area-to-critical-area ratio can be partially substituted by the isentropic relationship between stagnation and static conditions, expressed as

$$\frac{T_0}{T} = 1 + \frac{\gamma - 1}{2} M^2 \quad \textbf{(2.5.23)}$$

$$\frac{P_0}{p} = (1 + \frac{\gamma - 1}{2} M^2)^{\frac{\gamma}{\gamma - 1}} \quad \textbf{(2.5.24)}$$

$$\frac{\rho_0}{\rho} = (1 + \frac{\gamma - 1}{2} M^2)^{\frac{1}{\gamma - 1}} \quad \textbf{(2.5.25)}$$

For the terms $\frac{\rho^*}{\rho_0}$ and $\frac{T^*}{T_0}$, it is known that $M^* = 1$. Therefore, Eq. 2.5.22 transforms in

$$\frac{A}{A^*} = \frac{(1 + \frac{\gamma - 1}{2} M^2)^{\frac{1}{\gamma - 1}}}{(1 + \frac{\gamma - 1}{2})^{\frac{1}{\gamma - 1}}} \sqrt{\frac{1 + \frac{\gamma - 1}{2} M^2}{1 + \frac{\gamma - 1}{2}}} \frac{1}{M} \quad \textbf{(2.5.26)}$$

Re-arranging Eq. 2.5.26 for practicality,

$$\frac{A}{A^*} = \frac{1}{M} \left[\frac{1 + \frac{\gamma - 1}{2} M^2}{(1 + \frac{\gamma - 1}{2})^{\frac{1}{\gamma - 1}}} \right]^{\frac{\gamma + 1}{2(\gamma - 1)}} \quad \textbf{(2.5.27)}$$

Eq. 2.5.27 expresses the area-to-critical-area ratio as a function of the Mach number at any given point, and is a fundamental relation commonly found in tables [172,174] and charts. As observed in the chart for $\gamma = 1.4$ of Figure 2.29, there are two isentropic solutions for $\frac{A}{A^*}$. One solution accounts for the area A on the convergent portion of the duct, giving a subsonic flow solution on the LHS of $M^* = 1$. The other solution considers an area A on the divergeng duct section, where the flow is accelerated to a supersonic solution on the RHS of $M^* = 1$. It is then stated that a same area-to-critical-area ratio can be obtained either by subsonic flow acceleration to sonic conditions or by supersonic flow acceleration from sonic conditions.

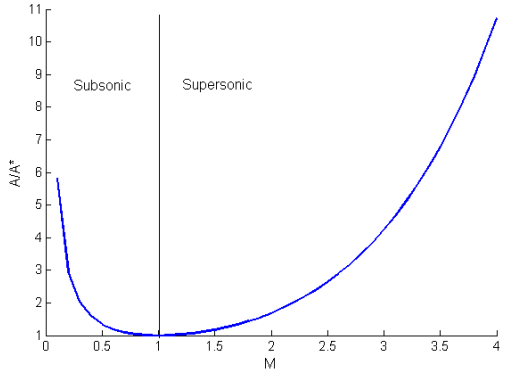

Figure 2.29 Area-Mach Number relationship chart for a $\gamma = 1.4$.

The mass flow per unit area or mass flux in a convergent-divergent duct can be expressed in terms of the equation of state or ideal gas law and the Mach number equation,

$$\frac{\dot{m}}{A} = \rho u = \frac{p}{RT} Ma = \frac{p}{RT} M\sqrt{\gamma RT} = \frac{p}{\sqrt{RT}} M\sqrt{\gamma} \qquad \textbf{(2.5.28)}$$

The static conditions in Eq. 2.5.28 are substituted by the stagnation conditions to write the mass flux as

$$\frac{\dot{m}}{A} = \frac{\dfrac{P_0}{(1+\frac{\gamma-1}{2}M^2)^{\frac{\gamma}{\gamma-1}}} M\sqrt{\gamma}}{\sqrt{R}\sqrt{\dfrac{T_0}{1+\frac{\gamma-1}{2}M^2}}} = \frac{P_0}{\sqrt{RT_0}} \frac{M\sqrt{\gamma}}{(1+\frac{\gamma-1}{2}M^2)^{\frac{\gamma+1}{2(\gamma-1)}}} \qquad \textbf{(2.5.29)}$$

For convenience, Eq. 2.5.29 can be written as well as

$$\frac{\dot{m}}{A} = \frac{P_0}{\sqrt{RT_0}} f(\gamma, M) \qquad \textbf{(2.5.30)}$$

Figure 2.30 shows the plot of $f(\gamma, M)$ with Mach number for $\gamma = 1.4$, with a maximum at $M = 1$. Therefore, for fixed total flow properties, there is always a maximum of $f(\gamma, M)$ when $M = 1$ that determines the maximum mass flux. This means that if the Mach number at the throat reaches unity, the mass flow cannot go any higher and yielding in choked flow. Likewise in the area-to-critical-area ratio equation, there are two solutions for $f(\gamma, M)$, corresponding to the subsonic flow in the convergent section

on the LHS of $M = 1$, and the supersonic flow in the divergent portion on the RHS of $M = 1$.

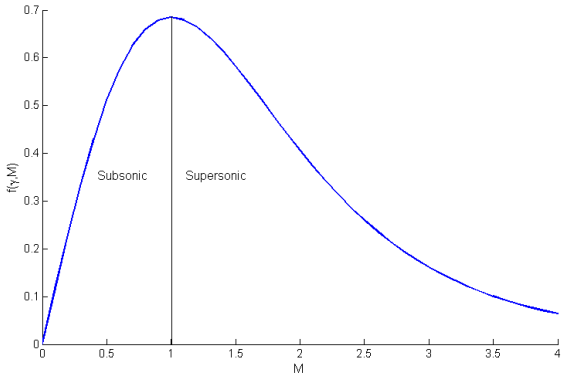

Figure 2.30 Variation of $f(\gamma, M)$ with Mach number for a $\gamma = 1.4$.

Using the critical flow conditions, the maximum mass flow or choked mass flow rate, turns in from Eq. 2.5.29 as

$$\dot{m}_{max} = \dot{m}_{ch} = A^* \frac{P_0}{\sqrt{RT_0}} \sqrt{\gamma} \left(1 + \frac{\gamma - 1}{2}\right)^{\frac{\gamma+1}{2(1-\gamma)}} \quad \textbf{(2.5.31)}$$

For $\gamma = 1.4$, the choked mass flow rate can be reduced to

$$\dot{m}_{ch} = 0.685 A^* \frac{P_0}{\sqrt{RT_0}} \quad \textbf{(2.5.32)}$$

2.6 Shock Waves in Transonic Compressors

2.6.1 Overview

As mentioned in Sec. 1.1 and Sec. 1.2, the main advantage of a fully supersonic axial-flow compressor is a higher pressure ratio per stage in a comparison to a subsonic system. Nevertheless, the shock-wave structures generated result in entropy generation, increasing the loss and reducing the isentropic efficiency. Shock losses owe to the total-pressure loss across the non-isentropic shock pattern, blade boundary layer separation due to the interaction with the shock (SWBLI), and other particular effects such as tip - clearance-flow/shock-wave interaction at the blade tip. For this reason, supersonic compressors have not been practical in aircraft gas turbines [181], apart from the

throughflow compression systems which result a promising technology due to the shock compression potential, but not to the capacity of superseding subsonic or the far-reaching transonic axial-flow compressor benefits. In contrast, transonic compressors, in which only the inlet relative velocity is supersonic towards the blade tip region, give a more satisfactory trade-off between the high single-stage pressure ratio and the shock losses.

The first experimental supersonic axial-flow compressors were tested around 1938 in Germany by Weise [182]. After the Second World War (1945) the growing interest of developing high-speed and more efficient flights became apparent. The work in high-speed axial-flow compressors was mainly continued by the NACA in the USA. One of the first investigations of the supersonic flow nature with a subsonic axial flow velocity in flat-plate cascades was conducted by Kantrowitz [183]. At low inlet relative velocities, expansion waves arise at the entrance region of every flat plate due to the convex profile between the entering air and the blade as shown in Figure 2.31 a). These infinity-extending expansion waves accelerate the flow until the relative velocity is parallel to the entrance region. In contrast, as the inlet relative velocity increases, a series of infinite oblique shocks are given off at the leading edge to decelerate the flow till is parallel to the flat plate entrance region as seen in Figure 2.31 b). Hence, the entrance region slope in a flat plate cascade controls and determines the flow to be passed through the limiting characteristic *a*-*b* or first-captured Mach wave. This limiting characteristic is also known in the literature as the last-captured Mach wave [184].

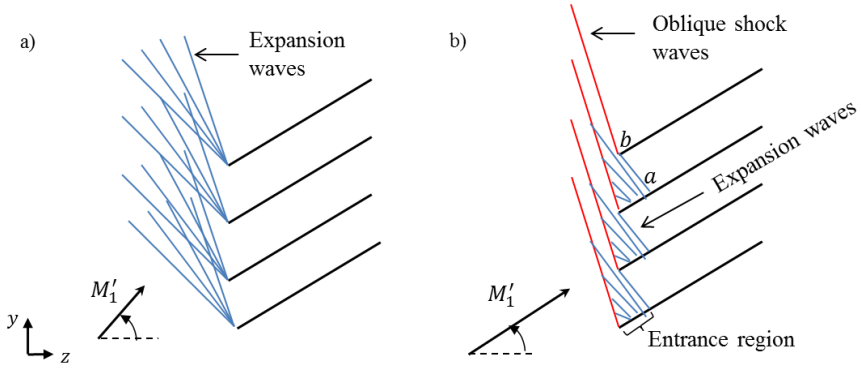

Figure 2.31 Expansion and shock system for an infinite flat plate cascade. a) Low supersonic inlet relative Mach number. b) High supersonic inlet relative Mach number.

The wave system for curved blades with a circular-arc profile for undisturbed and uniform upstream [185] is similar to that in Figure 2.31 b), except that the oblique shock wave becomes a detached bow-shock forasmuch as the surfaces are circular and ending in a blunt leading edge. To satisfy the disturbance-free and uniformity incoming flow condition, the net strength of the bow shocks and expansion waves must cancel each other out, resulting in no upstream influence. If any upstream-travelling wave was unbalanced, the axial velocity would be affected, changing the mass flow and violating continuity and steady-flow conditions.

The mass flow passing through a blade-row or entering the blade passage is determined by the flow velocity, area, and density along the first-captured Mach wave *a-b* sketched in Figure 2.31 b) [1]. Assuming that the leading edge is sharp with respect of the maximum blade thickness so that the upstream flow might be homentropic, the following relations must be satisfied between the limiting characteristic *a-b* and far upstream:

- Conservation of relative total-pressure
- Riemann's equation for the Prandtl-Meyer Expansion
- Corrected Mass flow per area, Corrected Mass Flux or Flow function

Levine [185] directly applied the continuity equation and the Riemann's equation for the Prandtl-Meyer expansion between the flow field far upstream and the limiting characteristic *a-b* in curved blades. Assuming the location of point *a* on the suction surface, the flow angle and flow area could be determined along the first-captured Mach wave. Thence, the solution of the two-equation system obtains the relative Mach number along the limiting characteristic. Analysis results evidenced that the entrance-region flow expansion depends on the inlet relative flow vector, and geometrically, on the spacing, stagger angle, and surface curvature.

A preliminary analysis on blade-passage shock-loss magnitudes conducted by Schwenk *et al*. [4], identified the variation of the shock structure and location with operating conditions. It was estimated that shock-losses represent 35 to 55% of the overall blade losses as a function of the supersonic inlet relative Mach number. Even at low inlet

relative Mach numbers, the suction-surface-camber-induced flow turning leads to a relative Mach number rise, increasing the shock loss.

In the design and off-design compressor performance prediction, gross-estimated losses or efficiencies do not suffice, as radial loss variations affect the radial equilibrium, modifying the flow velocity magnitudes and directions. Creagh [186] demonstrated the relevance of having an accurate methodology for loss calculations in transonic axial-flow compressor rotors. Early experiments in transonic axial-flow compressor rotors [187–191] showed that for inlet relative Mach numbers just below 1.1, shock effects were considerably small and simple diffusion-factor-based profile-loss models independent of M_1' were adequate enough. This consideration correlates with the assumptions made by Laitone and Pardee [179] covered in Sec. 2.4.3, where there was a significant amount of simplifications for inlet Mach numbers slightly above one in the detached-wave treatment.

Nonetheless, further experimental investigations [192,193] evidenced the shock effects even at a maximum of $M_1' = 1.3$ in that the measured minimum total losses were above the diffusion-factor-based correlation losses. Similarly validated, even at $M_1' = 1.1$ for low-solidity blade row tests [194,195], shock loss effects started to manifest. These investigations exposed the need to understand the transonic blade-row flow and to develop estimating models to predict the shock-loss magnitude.

2.6.2 Flow Description

Given a blade-profile row or a blade cascade, the shock-structure can be generally explained as consisting of two parts as shown in Figure 2.32: a) A shock-wave portion extending from the stagnation streamline to infinity, referred as bow wave. b) A shock segment entering and contained within the blade passage that extends from the suction surface to the stagnation streamline, known as the passage shock.

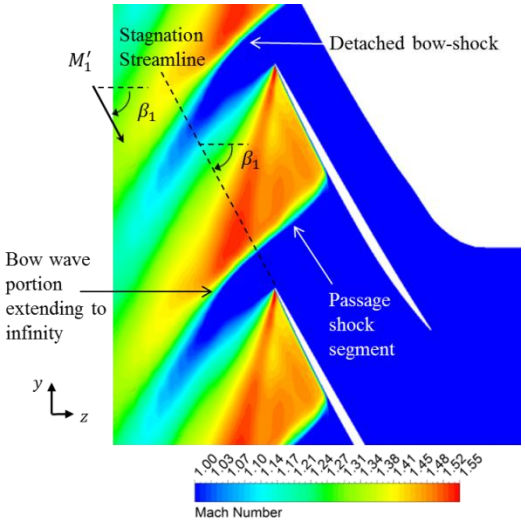

Figure 2.32 Shock-wave structure in a transonic compressor blade-element.

The bow wave is a portion of the fully detached bow-shock that stands in front of the blunt leading-edge as a result of the inlet relative flow moving at supersonic speed. As explained in Sec. 2.4.3, the detached shock shape and locations depends only on the free-stream Mach number and the thickness, which in the case of blade profiles, it is the inlet relative Mach number and the leading edge radius, respectively. For the particular case of moving or rotating objects with respect of a flow in motion, the orientation of the bow-shock depends as well on the inlet relative flow angle. Since the detached shock-front is normal to the inlet relative flow at the stagnation streamline, the whole bow-shock system is aligned with the inlet relative flow angle β_1.

The other detached bow-shock leg that penetrates and anchors into the blade passage is the passage shock. The passage shock form and location are a non-linear function of the inlet relative Mach number, inlet relative flow angle, blade suction surface curvature and the operating condition. However, the passage-shock situation might complicate even more. Since the blade passage is in the form of a convergent-divergent duct or De Laval nozzle, this can get choked depending on the operating point. When the passage is not choked, the operation is considered to be unstarted and the passage shock is a single structure. Conversely, in a choked passage the operation is referred as started and the structure becomes forked or dual. The different assumptions used to model the passage shock are provided in Sec. 2.6.4, while the current model used in this research is explained in Sec. 3.3

With the aid of understanding the compressible flow ahead of the passage shock, a shock-system configuration is sketched in Figure 2.33. The flow upstream of the detached bow-shock is everywhere uniform with supersonic relative velocity (zone I).The inlet relative flow traverses normal to the detached bow-shock at point *v*, which is the intersection of the bow-shock vertex and the stagnation streamline. The strong bow-shock central portion decelerates the flow to subsonic relative velocities till the sonic line *sb*-*s* (zone II). Depending on a low or high incidence, the flow is then expanded as a fan around the leading edge with less or more intensity, respectively (zone III). The first expansion wave originated at the leading edge is the sonic line, where the flow is at a relative Mach number of one all along the wave. The last leading-edge expansion wave *sb*-*s'* is such, that expands the flow parallel to the suction-surface leading-edge. The flow then continues expanding gradually for low incidences and suddenly for high incidences over the suction surface (zone IV). These expansion Mach waves intersect the bow-wave, reducing its strength even more and assisting it to asymptotically approach the Mach line.

It can be noted as well in Figure 2.33 that the stagnation streamline of the next adjacent blade interacts with the zone-IV flow expansion and even with the leading-edge flow expansion. At point *c*, the stagnation streamline intersects the bow wave, deflecting marginally the flow upwards, or in other words, increasing the relative flow angle. Consequently, the stagnation streamline is pushed downwards by a deflection *h* normal to the ideal stagnation streamline, aligned to the relative flow direction and passing through the leading edge camberline. The detached shock of the next adjacent blade has its vertex at the intersection with the deflected stagnation streamline at *b*, and the upstream airflow experiences the same process to that on the previous blade, satisfying flow periodicity.

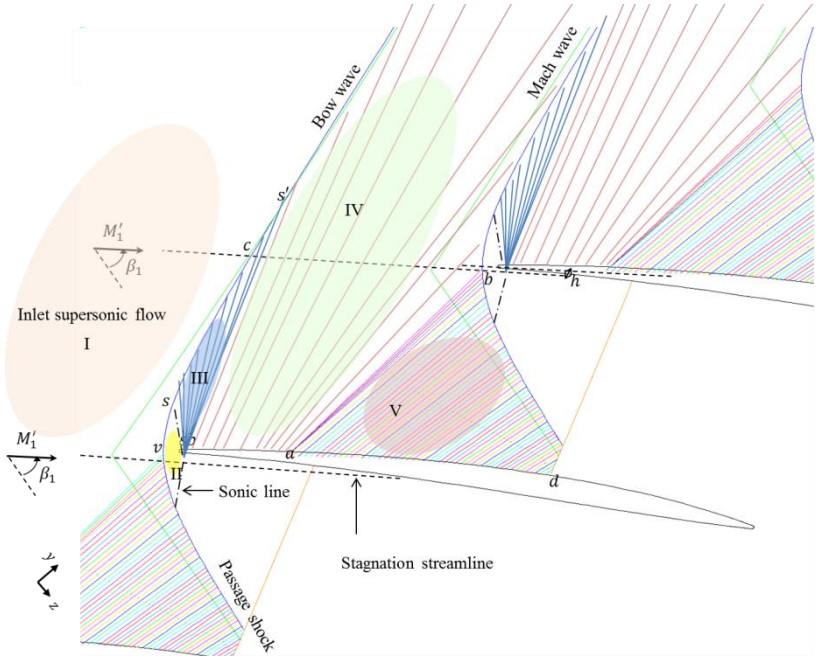

Figure 2.33 Flow field and shock-wave configuration around a blade cascade operating under supersonic upstream relative flow.

On the suction surface of the previous blade, the flow acceleration continues till the limiting characteristic *a*-*b* or first-captured Mach wave is encountered. The first-captured Mach wave is the first wave of a series of infinite weak waves over the suction-surface expansion that interacts with the passage shock. Hence the first captured Mach wave arises from a point *a* on the suction surface and extends till the first point of the adjacent-blade passage shock, which is the bow-shock vertex *b*. The flow gradually expands over the suction surface (zone V) until the passage shock impinges on the suction surface at point *d*. The zone-V expansion waves intersect the passage shock, which can be entirely the detached bow-shock or a fusion between the bow shock and choke-induce oblique shock.

The flow expansion downstream of the first-captured wave provides information of the flow properties along the characteristics, determining, for instance, the local relative Mach number on the passage shock, which is fundamental for the shock-loss estimation. As observed in Figure 2.33, the upstream flow entering a blade passage encounters two shock fronts, bow and passage shock, contributing both to the overall shock loss. Mentioned earlier in Sec. 2.6.1, there is no upstream influence of the wave system on the flow in order to satisfy continuity and steady-flow conditions.

2.6.3 Shock Losses

Similarly to the derivation of the total-loss factor in Sec. 2.2.2 from the overall relative total-pressure loss, a shock-loss coefficient can be defined as a function of the relative total-pressure drop due to shock-induced entropy generation only. Following Eq. 2.2.5, the shock-loss coefficient is expressed as

$$\overline{\omega_{sh}{}'} = \frac{P_{01}{}' - \overline{P_{02}{}'}}{P_{01}{}' - p_1} = \frac{1 - \overline{PR'}}{1 - (1 + \frac{\gamma - 1}{2} M_1{}'^2)^{\frac{\gamma}{1-\gamma}}} \qquad \textbf{(2.6.1)}$$

For a low-speed compressor rotor blade-element, the outlet total-pressure circumferential variation is as shown in Figure 2.34, observed using hot-wire anemometer measurements [196]. Due to the viscous effects of the blade boundary layer, there is an outlet total-pressure decay near the blade walls for both, suction and pressure surfaces. As there are no other effects, the outlet total-pressure remains constant in the free stream and relatively loss-free across the passage. The outlet total-pressure drop near the blade surfaces increases at high turnings as the wake extends since there is a diffusion process. Further turning increase can lead to stall, causing boundary layer separation and greatly increasing the magnitude and tangential extension of the outlet total-pressure loss coefficient.

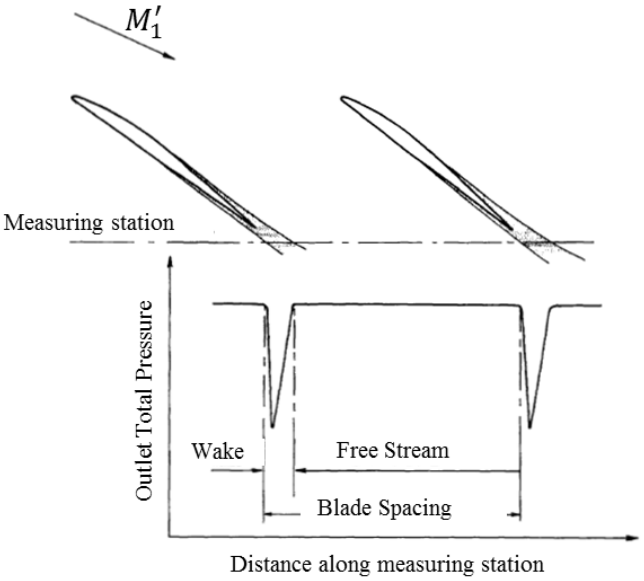

Figure 2.34 Outlet total-pressure distribution in the circumferential direction due to blade-profile viscous losses for low-speed compressor rotors (modified from [4]**).**

In high-speed or transonic rotor blading there are additional losses due to the shock-wave configuration. Because the passage shock decelerates the flow from supersonic to subsonic relative speeds, it contributes more to the shock-induced total-pressure loss than the bow wave. The higher the ratio of relative velocities at the end of the suction-surface flow expansion to relative subsonic velocities, the greater the shock-loss coefficient. Inasmuch as the shock process is non-isentropic, there is a relative total-pressure loss across the passage shock as seen in Figure a). In addition, the relative Mach number distribution ahead of the passage shock is not uniform, yielding to an outlet relative total-pressure circumferential variation. The major passage-shock loss or highest outlet relative total-pressure drop occurs near the suction surface and gradually recovers, as the flow expands to the highest relative Mach numbers near the suction surface and reduces towards the pressure surface of the adjacent blade. If both effects are added, subsonic diffusion and shock-wave losses, the outlet relative total-pressure distribution is as in Figure b), where the blade-profile wake significantly increases the relative total-pressure loss near the surfaces. Of course the challenge is to separate the shock and profile losses from the overall total-pressure loss coefficient.

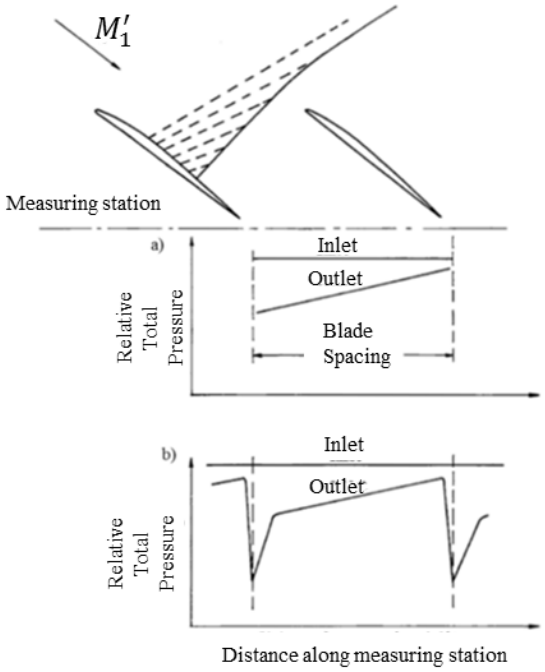

Figure 2.35 Circumferential outlet relative total-pressure distribution for high-speed compressor rotors (modified from [4]**). a) Shock-induced relative total-pressure drop. b) Profile-and-shock-induced relative total-pressure drop.**

Further hot-wire anemometer data [197] confirmed the profile of the total-loss coefficient measured in transonic compressor rotors as Figure 2.36 shows. In the blade-passage free-stream, loss is induced by the passage shock as a result of the discontinuous flow declaration, being higher on the suction surface as it reaches a peak relative Mach number immediately upstream of the shock. Additionally, the subsonic diffusion near the blade surfaces enlarges the boundary layer thickness, increasing the profile loss and adding to the total-loss coefficient. The blade-surface SWBLI stimulates even more the boundary layer growth, having a high-loss region observed as peak points in Figure 2.36

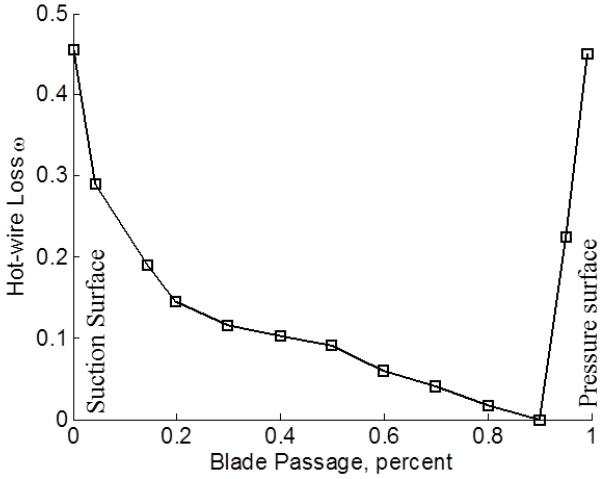

Figure 2.36 Circumferential total-loss coefficient distribution (replotted from [197]**).**

Transonic rotor-blade experimental data [197] conducted at different rotational speeds and various tip solidities showed the influence on the relative total-pressure loss coefficient. Shock and profiles losses increase with increasing tip speed. As solidity reduces, the intersection between the passage shock and suction surface shifts downstream, leading to a higher peak suction-surface Mach number and increasing the relative total-pressure loss.

The flow complexity increments even more when SWBLI is addressed [198–201]. An additional viscous loss is induced by the interaction of the passage shock with the blade boundary layer, causing the shock to adopt a λ-structure. Whereafter, the static-pressure rise through the shock is sensed back through the boundary layer. The overall static-pressure ratio of a λ-shock is considerably less than that for an oblique shock.

The more open the λ-shock limbs, the higher the SWBLI-induced subsonic diffusion losses. In turn, there is a momentum loss from the boundary-layer low-velocity flow to the free stream, augmenting the boundary-layer momentum thickness and form factor. These poor boundary-layer conditions increment the low-speed flow in the direction normal to the surface, thickening the boundary layer upstream of the shock and increasing the wake. Among different operating conditions, the SWBLI quickens the boundary layer growth, stimulating the flow separation and reducing the compressor working range. The SWBLI problem is out of the scope of this research; however, this does not represent a limitation to establish the effects of this phenomenon.

In the performance prediction of transonic axial-flow compressors, it is of great importance a detailed representation of the shock-wave-system structure to accurately calculate its associated losses. Yet, it is still nearly impossible to conduct a quantitative treatment without simplifications because of the highly-complex transonic flow [4]. Shock-system methods have employed a 2-D assumption on the S1 plane to simplify the problem [120]. This consideration excludes 3-D effects from the mixed subsonic and supersonic flows, and tip-clearance-flow/shock-wave interaction [196,202–205]. Dealing with 2-D flow analysis, however, permits a direct comparison against subsonic profiles and blade cascade data.

2.6.4 Shock Loss Models

From the beginnings of the transonic-compressor overall shock-loss modelling works in 1957, a shock configuration has been established beforehand any calculation. Apart from many simplifying assumptions, early works assumed the same shock configuration for the whole blade and not allowing the blade-elements to individually behave. For many decades, the succeeding shock models remained with the practice of imposing a given shock configuration. Along the years, the different shock models have tended to represent more realistically the shock physics. This section gives a profound review of the different shock models from its origins till the state-of-the-art methodologies with the purpose of not only explaining the compressible flow physics, but mainly, understanding the knowledge contribution of this research in terms of an analytical physics-based shock modelling.

Utilizing the hyperbolic approximation [180] to determine the form and location of a detached shock standing ahead of transonic blade profiles, Klapproth [206] estimated the approximate relative total-pressure loss incurred through this bow shock. A theoretical design and off-design performance analysis for a transonic rotor [207] revealed that bow-wave-associated losses were small compared to the overall losses. Other than the viscous-induced losses, the majority of the loss was attributed to the passage shock. This important investigation pushed forward to develop overall shock-loss models that consider the passage-shock effects.

Even though Schwenk *et al*. [4] identified that the shock configuration varies with operating conditions, the passage-shock shape was assumed to be that from the design point as seen in Figure 2.37 without any consideration for forked or dual-shock structure. Since the relatives Mach numbers vary across the passage, modifying the passage-shock strength, a mass-averaging process was considered at the midchannel streamline or mean camberline as depicted in Figure 2.37.

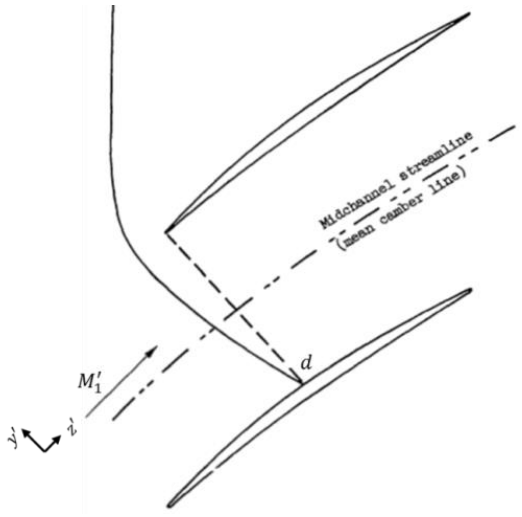

Figure 2.37 Assumed shock-configuration by Schwenk *et al.* [4] **for shock-loss estimation (modified from** [4]**).**

The passage shock impingement d on suction surface was assumed to be that on a line from the adjacent-blade leading edge and normal to the midchannel streamline as shown in Figure 2.37. Knowing the location of d as $z_{psh_{ss}}$, the distance between the leading edge and the intersection of the passage shock with the suction surface is $\Delta z_{LE-psh_{ss}}$. In practice, the location of d gets affected by the solidity. Nevertheless, as the solidity

reduces, point d moves farther back [3], resulting in a higher relative Mach number on the suction surface and an increased shock loss [197].

For DCA aerofoils, a geometry-based approach is given to compute the suction-surface angle. On a frame of reference parallel to the chord, the distance between the leading edge and suction-surface passage-shock impingement is

$$\Delta z'_{LE-psh_{ss}} = \Delta z_{LE-psh_{ss}}/cos\xi \quad \textbf{(2.6.2)}$$

Then, the suction-surface blade angle at point d becomes

$$\beta_{psh_{ss}} = \xi - \text{asin}\left[sin\theta_{ss}\left(\frac{\Delta z'_{LE-psh_{ss}}}{c-2r_{LE}} - 1\right)\right] \quad \textbf{(2.6.3)}$$

And the suction-surface camber angle is defined as

$$\theta_{ss} = 4\text{atan}\left(\frac{1-cos\frac{\theta}{2}}{sin\frac{\theta}{2}} + \frac{t_{max}}{c-2r_{LE}} + \frac{2r_{LE}}{c-2r_{LE}}\right) \quad \textbf{(2.6.4)}$$

However, a universal method is required to obtain the suction surface angle for any blade aerofoil contour. If the blade-element surface coordinates are obtained as in Sec. 3.2.2, the suction surface angle at any point is known.

Since the relative Mach number ahead of the passage shock is needed for the relative total-pressure loss coefficient, an equivalent relative Mach number M'_{eq} is obtained as an average between the ending points of the passage shock. This represents an approximated average Mach number at the midchannel streamline between the inlet relative Mach number hitting the detached-shock vertex and the peak suction-surface relative Mach number $M'_{psh_{ss}}$ resulting from the expansion,

$$M'_{eq} = \frac{M'_1 + M'_{psh_{ss}}}{2} \quad \textbf{(2.6.5)}$$

The peak suction-surface relative Mach number is obtained by means of the Prandtl-Meyer expansion equations. From Eq. 2.4.36, the Prandtl-Meyer expansion for a right-

running characteristic between leading edge and the passage-shock intersection on suction surface is

$$\beta_1 + \nu_1(M'_1) = \beta_{psh_{ss}} + \nu_{psh_{ss}}\left(M'_{psh_{ss}}\right) \quad \textbf{(2.6.6)}$$

The inlet relative Prandtl-Meyer angle ν_1 is obtained through the Prandtl-Meyer function in Eq. 2.4.34. Solving for the relative Prandtl-Meyer angle $\nu_{psh_{ss}}$ at the passage-shock intersection, $M'_{psh_{ss}}$ can then be obtained since the Prandtl-Meyer angle is a unique function of the Mach number.

Across the passage shock, the relative total-pressure ratio is determined using the normal-shock recovery factor, considering that the inlet Mach number ahead the passage shock is the average relative Mach number

$$PR'_{psh} = \left[\frac{(\gamma+1)M'^{2}_{eq}}{(\gamma-1)M'^{2}_{eq}+2}\right]^{\frac{\gamma}{\gamma-1}}\left[\frac{(\gamma+1)}{2\gamma M'^{2}_{eq}-(\gamma-1)}\right]^{\frac{1}{\gamma-1}} \quad \textbf{(2.6.7)}$$

Following Eq. 2.6.1, the shock-loss coefficient is written as

$$\omega_{sh}' = \frac{1 - PR'_{psh}}{1-(1+\frac{\gamma-1}{2}M_1'^{2})^{\frac{\gamma}{1-\gamma}}} \quad \textbf{(2.6.8)}$$

In spite of the agreement between the computed analysis and measured data in terms of passage-shock loss and location, it is not certain whether this apparent match is particular to the tested rotor or whether it would be generally applicable to any transonic compressor rotor geometry [208].

Lewis *et al*. [197] modified the shock model from Schwenk *et al*. [4] by moving upstream the intersection between the passage shock and the suction surface (point d) by a distance $\Delta z'$ as observed in Figure 2.38. Likewise, the model still assumed the minimum-loss shock configuration. Nevertheless, the forward shift $\Delta z'$ was based in correlating the computed circumferential total-losses against the hot-wire-measured distribution. Hence, a compressor-rig or transonic-cascade experimental test was required to predict the passage-shock location. Despite this approach was a semi-

empirical analysis, it set the ground to recognize that shock losses are mainly a function of the passage-shock position in the direction of the flow.

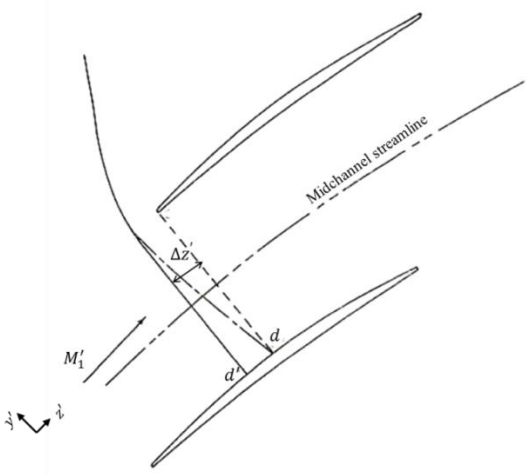

Figure 2.38 Shock-configuration established by Lewis *et al.* [197] **from experimental tests for shock-loss estimation (modified from** [197]**)**

A similar scheme was implemented by Miller and Hartmann [208], establishing the shock configuration from experimental investigations. Four different axial stations were placed over the blade tip to measure static-pressure variations over a range of operating conditions, setting the shock configuration and calculating the passage shock as per the previous methods [193,197]. In this approach, the passage-shock pattern was allowed to move as a function of the operating condition from open throat to stall and no longer using the design-point shock structure. However, the established shock configuration, and hence the shock losses, were limited to the blade tip and were not applicable to the rest of the transonic blade region. In terms of the bow wave, its form, location, and associated losses were analytically determined from Klapproth's approximation [206].

A more detailed shock model for DCA aerofoils was implemented by Miller *et al*. [3], consisting in the fusion of the analytical bow-wave structure and associated-loss model from Klapproth [206] and the approximate passage-shock direction (point *d* in Figure 2.37) suggested by Schwenk [4]. Instead of an averaged estimation of a relative Mach number to compute the relative total-pressure loss, the flow expansion was resolved ahead of the passage shock. The magnitude and direction of the relative Mach number

are thus determined everywhere in the expansion field and immediately upstream of the passage shock. Since the passage-shock configuration is already set, the relative total-pressure loss coefficient variation is computed and a mass-averaged value can be obtained.

Although the shock model from Miller *et al*. [3] was intended for blade-tip elements and design point, it was assessed at different radii and incidences. A consistent decrease in shock-loss magnitude was observed with lower radii; however, the passage-shock configuration was not altered to produce such results, which merits some further consideration. The shock-loss coefficient variation with incidence, and thus with operating condition, was found to be appreciably small as seen in Figure 2.39. This is the effect that as the incidence increases, the passage shock moves upstream in an intent to keep the same, and almost constant, relative Mach number distribution ahead of it. Thus, the significant total-loss coefficient increment observed with incidence is due to the profile frictional effects arising from the high flow turning and the inability of the boundary layer to remain attached at high pressure rises.

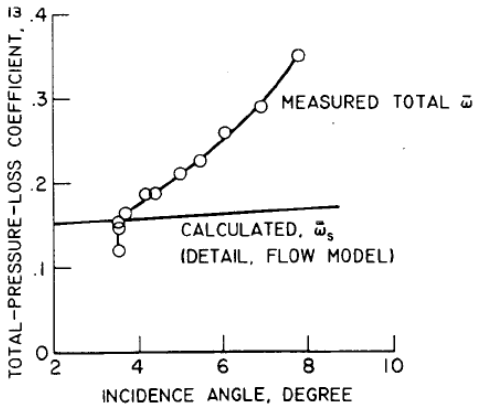

Figure 2.39 Relative total-pressure loss coefficient variation with incidence for measured total-losses and for an analytical shock model [3]**.**

An important review in through-flow calculations by Hirsch and Denton [90] demonstrated that if the inlet relative Mach number is in the subsonic regime and below the critical Mach number, the losses are independent of the inlet velocity. By definition, the inlet relative critical Mach number M'_{cr} is that for which the peak suction-surface relative Mach number reaches sonic conditions due to the surface turning. Thereby, a passage shock, and hence, shock losses of less magnitude than in the case of inlet

supersonic relative velocity are expected. Although Macchi [209] developed a SLC computer program for axial-flow turbines derived from Vavra's formulation [210] to the axisymmetric steady flow solution in turbomachines, a modified version of the shock-loss model from Miller *et al*. [3] was implemented into it. The modification consisted in accounting shock losses even for inlet relative Mach numbers below unity, in the range between the inlet relative critical Mach number and inlet relative sonic conditions.

In spite of its applicability only for DCA aerofoils, the shock-loss model from Miller *et al*. [3] has been broadly used among SLC solvers [20,31,45,66,90,114,149,162,163] due to its algorithm simplicity and reasonably acceptable loss prediction. Because of the model directness, it was simplified into a straight-forward correlation [162,163] as a function of the equivalent Mach number M'_{eq} that depends whether the inlet relative Mach number is fully supersonic or is between the critical value and unity, becoming

$$M'_{eq} = 0.5\left(M'_1 + M'_{psh_{ss}}\right) \qquad If \quad M'_1 \geq 1.0$$
$$M'_{eq} = 0.5M'_1\left(1 + M'_{psh_{ss}}\right) \qquad If \quad M'_{cr} \leq M'_1 < 1.0 \tag{2.6.9}$$

$$\omega_{sh}{}' = \frac{1 - \left[\frac{(\gamma+1)M'^{2}_{eq}}{(\gamma-1)M'^{2}_{eq}+2}\right]^{\frac{\gamma}{\gamma-1}}\left[\frac{(\gamma+1)}{2\gamma M'^{2}_{eq}-(\gamma-1)}\right]^{\frac{1}{\gamma-1}}}{1-(1+\frac{\gamma-1}{2}M_1{}')^{\frac{\gamma}{1-\gamma}}} \tag{2.6.10}$$

where $M'_{psh_{ss}}$ is calculated as per Eq. 2.6.6.

As mentioned in Sec. 2.3.2, during the 60's and early 70's, axisymmetric throughflow methods for compressors were developed. Some of these approaches were combined with blade-to-blade calculations defined for the number of streamlines determined in the meridional plane. For every individual blade-to-blade plane, a shock pattern was assumed, particularly with regard of the passage shock location. Besides the iterative approach for the REE and mass-flow continuity convergence, the meridional and blade-to-blade plane solutions were iteratively compared until an agreement of axial work-input distribution was achieved. In this case, blade designs obtained from these quasi-3D methods were dependant on the shock pattern assumed. Nonetheless, the main

drawback of this design approach was that every shock configuration for each streamline was assumed independently, whilst in real operation, the shock system moves continuously from one radial section to the other. Moreover, a SLC solution considers an axisymmetric pressure distribution in the meridional plane and does not consider the shock and expansion effects on the pressure. If the shock patterns are assumed, the equilibrium of pressures might not be consistent, producing misleading flow and performance. To assist the transonic compressor blading design, holographic studies of shock waves were conducted to understand and provide qualitative data of the actual shock patterns at the rotor blade tip.

At this stage, little success was obtained in generating an analytical model able to predict the shock configuration without the aid of experimental data, though several flow measurement and visualization techniques efforts were applied to understand the physics. Lichtfuss and Starken [11] provided a scholarly review upon supersonic relative flow at the inlet and outlet of semi-infinite flat-plate cascades, and cambered profiles with sharp and blunt leading edges. The entrance region flow was resolved as a Prandtl-Meyer expansion using Riemann's equations, while the shock losses were determined only for the bow shock using Klapproth's approach. Most notably, this comprehensive review contributed with a qualitative description of the starting and choking in blade cascades, which is fully discussed in Sec. 2.6.5

Flow expansion occurring along the cascade passage has been treated using the method of characteristics in different analyses [33,211–216]. However, the analysed blade cascades had been fully supersonic along the passage, apart from those where the small subsonic pocket around the leading edge was considered using a simple approach [211,213,214,216].

Notwithstanding there was an increasing belief that cascade shock dynamics could not follow the conventional shock theory, Prince [217] reconciled this relation by developing a supersonic flow procedure for compressor blade cascades. Flow expansion was resolved on the S1 surface up to a termination point along the passage, using the method of characteristics. Nevertheless, the expansion termination was arbitrary since the passage-shock location was assumed. This supersonic flow scheme

considered the leading-edge bluntness effect on the bow-shock front obliquity, measured on the S2 surface with respect of the chord. Having the shock structure in the S1 surface at different radii and following the bow-shock front obliquity profile in the S2 surface, permitted to think in a 3-D shock structure. Furthermore, a momentum-integral analysis from infinity to the leading edge was implemented to resolve the flow upstream of the bow-wave and determine bow-shock losses.

To improve the shape of leading-edge shock structure, York and Woodard [218] applied the Moeckel [180] model just to a small segment of the detached shock around the blade leading edge. Then, the remaining shape of the detached shock was computed through an extension method on a two-dimensional cascade. The extension method was successively resolved segment by segment using oblique-shock relations and the unit process of the method of characteristics as laid out in Figure 2.40. A first family of characteristics emanate from the suction surface, while a second family of characteristics on a known point of the detached shock intersects the former, providing the location for the next point on the detached-shock. The intersection process repeats until the detached shock reaches the suction surface of the adjacent blade on one side, and in the other, farther out towards infinity. Yaonan [219] approximated closer the detached shock to the real flow by computing its remaining shape through the extension method on a stream surface of revolution or S1 plane.

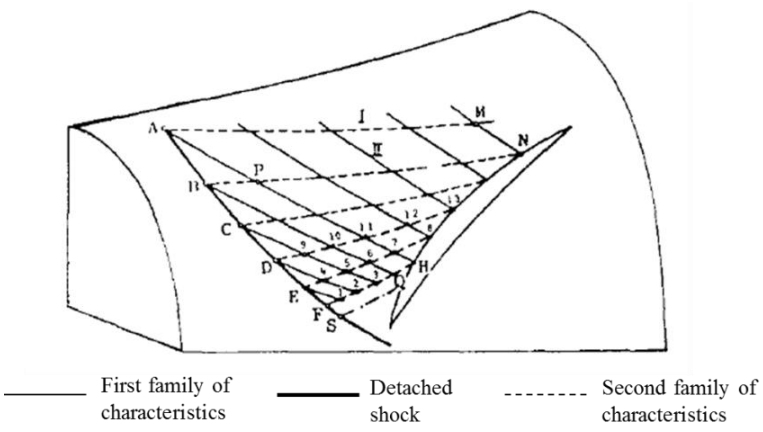

Figure 2.40 Extension method for the remaining part of the detached shock (modified from [219]**).**

On the basis of Levine's method [185], Hirsch and Denton [90] proposed a shock-loss model for relative supersonic inlet conditions. Such model consisted in the detached-

shock calculation using the Moeckel's model [180] and the flow expansion resolution through the method of characteristics to obtain the Mach number distribution upstream of the passage shock. Thus, the total-pressure loss across the shock is known. Yet once again, the passage shock location was assumed as in the models from Schwenk *et al*. and Miller *et al*. [3].

A method to calculate the position and shock losses within a through-flow approach was proposed by Sayari and Bolcs [24], where the passage shock was assumed to be normal to the stagnation streamline, being approximately normal to the passage for unstarted and started flows. Due to this assumption, the passage shock extends normal across the blade from point *b* to point *d* at the suction-surface intersection, as shown in Figure 2.41 a) for attached leading-edge oblique-shocks and in Figure 2.41 b) for detached bow-shocks. In attached leading-edge oblique-shocks, the end-point *b* is at the leading edge. Whereas in detached bow-shock, the same point is at the vertex of the bow wave, assumed to be hyperbolic, but not calculated with the Moeckel's method [180]. Instead, mass flow continuity is utilized to define the sonic point s of the bow wave by computing the sonic-line length $l_{s\,sb}$. Since the inlet mass flow is the same passing through the sonic line which has sonic conditions, a relation is set as

$$\dot{m}_1 = \dot{m}_{s\,sb} = \rho_{s\,sb} V_{ax_{s\,sb}} A_{s\,sb} = \rho^* a^* l_{s\,sb} \qquad \textbf{(2.6.11)}$$

Using the area-velocity relations presented in Sec. 2.5.3, the sonic conditions at the sonic line are calculated from the known total conditions as

$$\rho^* = \rho_0 \left(\frac{2}{\gamma+1}\right)^{\frac{\gamma}{\gamma-1}} \qquad \textbf{(2.6.12)}$$

$$a^* = \sqrt{\frac{2\gamma}{\gamma+1} R T_o} \qquad \textbf{(2.6.13)}$$

The bow-wave vertex is then defined by the intersection of a hyperbola shape that passes through the sonic point *s* and the stagnation streamline.

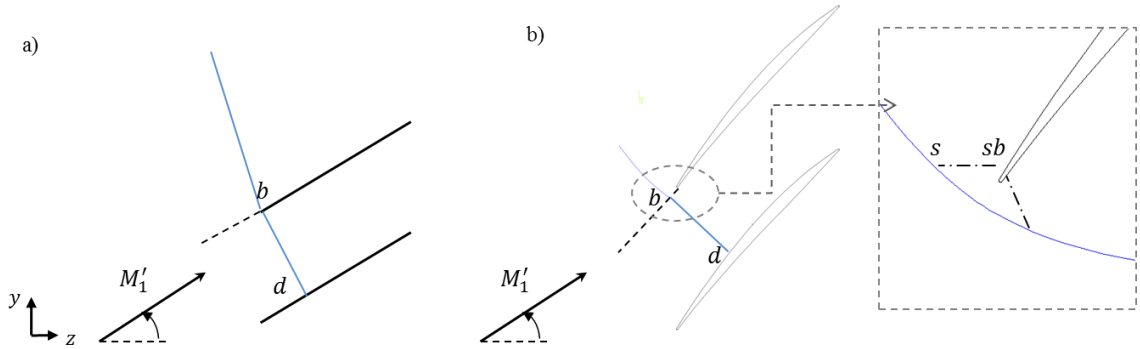

Figure 2.41 Shock model by Sayari and Bolcs [24] **assuming a normal passage-shock to the stagnation streamline. a) Attached leading-edge oblique-shock. b) Detached bow-wave**

Having point *b* for either of the detached or attached leading-edge shocks, a normal line from this point defines the shock impingement or point *d* on the suction surface, and hence, its angle is known. The rest of the calculations for the shock-loss coefficient computation proceed as in the model of Schwenk [4].

In contrast to the previously developed shock models where the passage-shock was assumed to be normal, Schobeiri [220] represented this for the first time as an oblique shock, whose position can change by the operating condition. Nevertheless, some necessary assumptions were made. The presence of any bow-shock, attached or detached, was disregarded; hence, its detrimental in total-pressure was neglected. To simplify the problem, the blading was assumed sufficiently sharp at the leading edge, so that the oblique passage-shock can be considered attached to the profile nose. The passage-shock obliqueness was introduced in the continuity requirement. Thereby, between far upstream and the passage shock the continuity relation is

$$\rho_1 V_1 A_1 = \rho_{sh} V_{sh} A_{sh} \qquad \textbf{(2.6.14)}$$

The inlet flow area A_1 is the frontal cross-section normal to the relative flow velocity with a streamtube height H_1 and a width equals to the staggered gap ϕ, written as

$$A_1 = H_1 \phi = H_1 s \cos\beta_1 \qquad \textbf{(2.6.15)}$$

Similarly, the flow area of the passage shock is that whose height is H_2 and width is the staggered pitch s_{sh} at that location tilted by the shock angle ς_{sh}, computed as

$$A_{sh} = H_{sh} = H_{sh}\varsigma_{sh}\cos(\beta_{sh} - \varsigma_{sh}) \quad \textbf{(2.6.16)}$$

The area ratios between the inlet and the passage shock can be defined through their critical area using the area-velocity relationships established in Sec. 2.5.3, as

$$\frac{A_1}{A_{sh}} = \frac{A_1}{A^*}\frac{A^*}{A_{sh}} = \frac{1}{M'_1}\left[\frac{1+\frac{\gamma-1}{2}M'_1{}^2}{(1+\frac{\gamma-1}{2})^{\frac{1}{\gamma-1}}}\right]^{\frac{\gamma+1}{2(\gamma-1)}} M'_{sh}\left[\frac{(1+\frac{\gamma-1}{2})^{\frac{1}{\gamma-1}}}{1+\frac{\gamma-1}{2}M'_{sh}{}^2}\right]^{\frac{\gamma+1}{2(\gamma-1)}} \quad \textbf{(2.6.17)}$$

Substituting the inlet and passage-shock critical area relation and their corresponding flow areas in the continuity equation,

$$\frac{A_1}{A_{sh}} = \frac{\rho_1 V_1}{\rho_{sh} V_{sh}} = \frac{H_1 s\cos\beta_1}{H_{sh}\varsigma_{sh}\cos(\beta_{sh}-\varsigma_{sh})} = \frac{M'_{sh}}{M'_1}\left[\frac{1+\frac{\gamma-1}{2}M'_1{}^2}{1+\frac{\gamma-1}{2}M'_{sh}{}^2}\right]^{\frac{\gamma+1}{2(\gamma-1)}} \quad \textbf{(2.6.18)}$$

The other condition to be satisfied between the inlet and the passage shock is of course the Riemann's equation for the Prandtl-Meyer expansion of a right running characteristic. According to Eq. 2.4.36, it yields to

$$\beta_1 + \nu_1(M'_1) = \beta_{sh} + \nu_{sh}(M'_{sh}) \quad \textbf{(2.6.19)}$$

The passage-shock angle might be computed from Eq. 2.4.24 corresponding to oblique-shock theory, where the deflection or expansion angle is the difference between the upstream and downstream angle. Thereon, the oblique passage-shock is

$$\delta_{sh} = \operatorname{atan}\left\{2\cot\varsigma_{sh}\frac{M'_1{}^2\sin^2\varsigma_{sh}-1}{M'_1{}^2[\gamma+\cos(2\varsigma_{sh})]+2}\right\} = \beta_1 - \beta_{sh} \quad \textbf{(2.6.20)}$$

Continuity equation, Prandtl-Meyer expansion and oblique-shock angle equations might be then numerically solved. Assuming a passage-shock flow angle β_{sh} in Eq. 2.6.19, the passage-shock Prandtl-Meyer angle ν_{sh} is known. Utilizing the Prandtl-Meyer function in Eq. 2.4.34, the upstream passage-shock relative Mach number M'_{sh} is computed, so that the passage-shock angle ς_{sh} is determined from Eq. 2.6.18. The calculated ς_{sh} needs to satisfy Eq. 2.6.20, in which any error in the expansion angle will determine the next value of β_{sh}.

In an attempt to address the variation of the passage-shock position with off-design conditions, Bloch *et al*. [34] introduced an engineering shock-loss to keep empiricism at its minimum. This model was limited to unchoked flow, where the shock is a single structure. The detached bow-shock was built as per the Moeckel's approximation [180], and its associated losses were calculated as suggested by Klapproth [206], with exception of the stagnation streamline position and the leading-edge radius for the bow-wave losses.

Because the infinite bow-wave interacts with the stagnation streamline, the flow undergoes a small upwards deflection that shifts the latter. As the back static pressure is increased, the detached bow-shock becomes more detached moving upstream by an amount of $\Delta z'$ and shifting the stagnation streamline towards the suction surface by an amount of $\Delta y'$. With the aid of unstarted CFD solutions for different cascades, the stagnation streamline shift was correlated as

$$\Delta z' = 6\Delta y' \tag{2.6.21}$$

Since most the flow traverses the central portion of the detached bow-shock, an extra loss increase was considered at this part by incrementing the radius to an effective leading-edge radius so that the incidence can increase. Once again, a CFD solution examination for the same cascades led to the following approximation

$$r_{LE_{eff}} = r_{LE} + \frac{\Delta y'}{2} \tag{2.6.22}$$

The CFD-based correlations developed by Bloch *et al*. [34] should be utilized with discretion, as they are not universal and might vary in some proportion for every blade profile and inlet relative Mach number combination considered.

As established by Levine [185], the flow information along the first-captured Mach wave was computed by applying continuity equation and the Riemann's equation for the Prandtl-Meyer expansion between the flow field far upstream and the limiting characteristic *a-b* in curved blades. Nonetheless, this time the bow-wave-induced losses were considered in the mass flow conservation.

In terms of the passage-shock position, the hyperbolic shape of the detached bow-shock was extended within the passage up to the sonic point *s*, as sketched in Figure 2.42. From this point *s*, the passage-shock was assumed to be a straight line normal to the stagnation streamline. This consideration is of relevant importance; since it is the first time that a shock-model considers a curved portion of the hyperbolic type for the passage shock, which is more realistic.

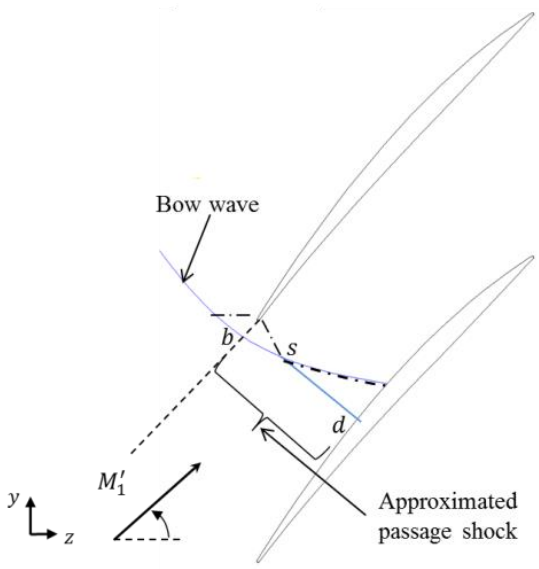

Figure 2.42 Shock model by Bloch *et al.* [34] **assuming a passage-shock with a hyperbolic and a straight portion, where the latter originates at the bow-shock sonic point.**

Given the pre-defined and approximated shock configuration in Figure 2.42, the passage shock was divided in 200 points to obtain every local relative Mach number upstream of the passage shock. The relative total-pressure losses are thus determined locally, which are mass-averaged in the circumferential direction to obtain the shock-loss coefficient.

In spite of the method presented by Bloch *et al*. [34] that modifies the shock configuration with the off-design condition, the model applies only for unstarted flows, namely between stall and slightly before peak-efficiency operating points. One of the most up-to-date shock-loss models was introduced by Boyer and O'Brien [13,35,36], as an extension of the method of Bloch *et al*. [34] for all operating conditions. Three different shock-wave patterns shown in Figure 2.43 were assumed for the three different reference operating conditions of a compressor or fan speedline: near stall at i_{norm}, peak efficiency or minimum loss at i_{min}, and near choke at i_{ch}.

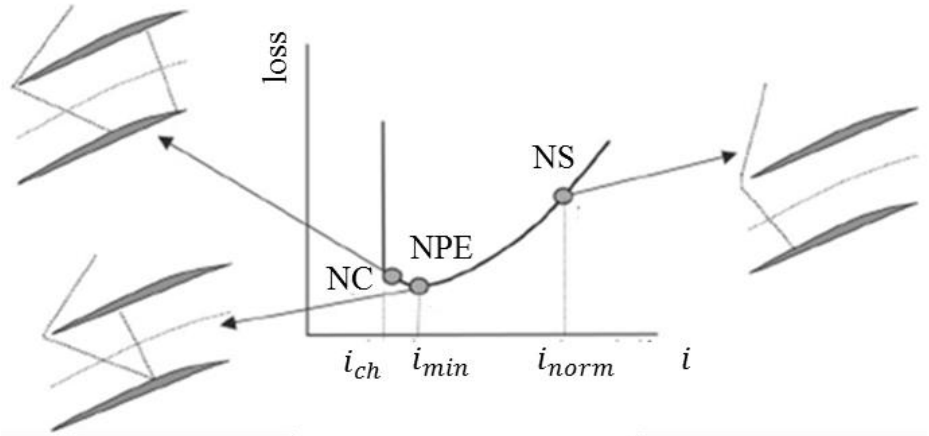

Figure 2.43 Shock configurations assumed by Boyer and O'Brien [13,35,36] **for near-stall, peak-efficiency, and near-choke operating conditions** [36]**.**

For near-stall condition, a single-shock structure was entirely defined by the hyperbola-approximated detached bow-shock [180]. Whereas for the minimum-loss at and near-choke conditions a dual-shock structure was assumed, compound by the detached bow-shock and a second passage shock inferred to be normal. At peak-efficiency point, the second passage-shock was considered to be just immediately behind of the detached bow-shock. While at near-choke condition, the second passage-shock was anchored at the trailing edge. Nevertheless, as the back static pressure (or incidence) increases from the minimum-loss point, the second passage-shock is supposed to coalesce with the first passage shock portion, which in fact, is not considered in this model. Despite these three shock configurations are given, the model does not explicitly moves the second passage-shock with the incidence as no analytical method was applied to find its location. Rather, the loss effect of the shock position and strength was accounted through empirical or simple representations as a function of the reference incidences: i_{norm}, i_{min}, i_{ch} . The minimum-loss incidence i_{min} might be computed with either of the empirical correlations by Chauvin and Weyer [149], Cetin *et al*., [141], or Aungier [136], presented in Table 2.1. The choking incidence i_{ch} can be obtained through the empirical model of Aungier [136] described in Sec. 3.4.2. The transition incidence i_{norm} between a single-shock and a dual-shock structure was calculated with the following simple representation

$$i_{norm} = i_{st} - 1.0° \qquad \textbf{(2.6.23)}$$

where i_{st} might be calculated again with the empirical correlation by Aungier [136] of Table 2.1.

Thereon, for high blade-section loadings or $i > i_{min}$, the loss-increase effect due to large incidence was accounted through a simulation-based correction in the overall-shock-loss coefficient as

$$\omega_{sh} = \omega_{bow} + \frac{0.015}{(i_{norm} - i_{min})^3}(i - i_{min}) \quad \textbf{(2.6.24)}$$

Likewise, in operating conditions where $i < i_{min}$, the effect of the second passage-shock was considered by introducing a loss-characteristics-based correction in the passage-shock loss coefficient as

$$\omega_{psh} = \omega_{psh_{min}} + \frac{\omega_{psh_{ch}} - \omega_{psh_{min}}}{(i_{ch} - i_{min})^4}(i - i_{min})^4 \quad \textbf{(2.6.25)}$$

which is then added to the bow-shock loss coefficient from the method of Klapproth [221] to compute the overall-shock losses.

Conventional methods have assumed the flow expansion to correspond to the suction-surface camber computed from the Prandtl-Meyer expansion, ignoring the boundary-layer thickness effect. Admittedly, the fluid expansion is less when the boundary layer is considered, as the flow is prevented from attaining its acceleration. For this reason, Balzer [222] presented a shock-loss model where the boundary-layer blockage effect was accounted by using the relative turning instead of the suction-surface camber angle for the flow expansion. Moreover, the use of the relative turning reflects the change in shock position as this varies with the inlet relative Mach number and incidence. The flow expansion was then determined by assuming that the flow turns from the inlet relative flow angle to the outlet relative flow angle as the surface flow path turns. However, this surface path was simplified to be two tangent circular arcs, limiting its applicability to only represent DCA and MCA blade section types. The assumed shock model was approximated to a single-shock normal to the midchannel stemmed from the leading edge of the pressure blade as sketched in Figure 2.44.

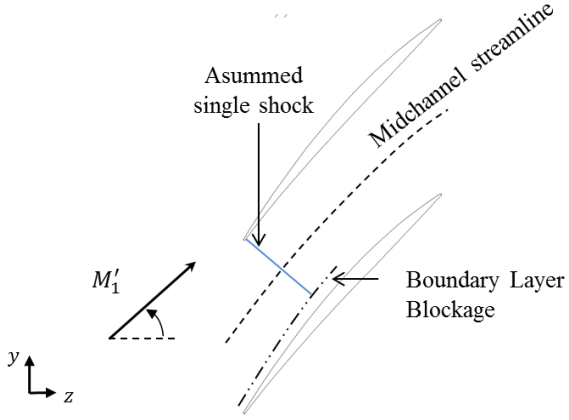

Figure 2.44 Shock model by Balzer [222] **assuming a single-shock configuration normal to the midchannel stramline and attached to the pressure blade leading-edge.**

This model by no means indicates the occurrence of a unique single shock, but it was considered that its associated loss was equivalent to that from the real shock system. The relative turning analysis obtains the relative Mach number upstream of the shock, and in turn, an equivalent Mach number encountering the normal shock is computed using Eq. 2.6.5. The usual procedure for relative total-pressure loss and shock-loss coefficient is then followed using Eq. 2.6.7 and Eq. 2.6.8, respectively. As seen from the single-shock model in Figure 2.44, the bow wave is neglected. Hence, the relative total-pressure loss accrued by the bow wave are not taken into account, and thus, assuming a constant relative total-pressure up to the shock location.

2.6.5 Empirical Shock-Loss Models

As discussed in Sec. 2.3.2, the computation of the total-pressure loss or entropy generation from cascade measured data to establish an empirical shock-loss correlation generally considers the effects from the shock strengthening and the SWBLI. However, Koch and Smith presented an empirical expression for the entropy rise to account only for the bow-wave and passage-shock strengthening as a function of the leading-edge bluntness, given by

$$\frac{\Delta S}{R} = -ln\left\{1 - \frac{r_{LE}}{scos\beta_1}[1.28(M'_1 - 1) + 0.96(M'_1 - 1)^2]\right\} \qquad \textbf{(2.6.26)}$$

Eq. 2.6.26 represents the so-called leading-edge bluntness loss model, reviewed as well by York and Woodard [216]. These empirical shock-loss correlations are one of the

few that consider the shock-only loss as isolated. The associated subsonic diffusion process is then calculated using another empirical correlation.

The following empirical shock-loss models within this section consider merged shock-strengthening and SWBLI losses. By no means is the purpose of this thesis to resolve the SWBLI problem, however it results unavoidably to mention it if further shock loss models are addressed. In an attempt to understand the differences against the state-of-the art and the currently developed analytical shock-loss models a brief review of these important empirical shock-loss models implemented in SLC programs for transonic axial-flow compressors is provided below. The following review skips the mention of the SWBLI losses if they are detached from the shock-loss coefficient.

Considering that SWBLI inevitably occurs in a transonic viscous flow, Gustafson [223] assumed an arbitrary λ-shock structure and position for the passage shock in DCA aerofoils. In a similar manner as the assumption in the model of Schwenk *et al*. [4], an equivalent Mach number was defined at the mid-channel camberline as in Eq. 2.6.27. Instead of a $M'_{psh_{ss}}$ at point *d* just immediately before the passage shock, the maximum relative Mach number $M'_{dwsl_{ss}}$ was considered to be at the downstream limb of the assumed λ-shock, obtained through a Prandtl-Meyer expansion.

$$M'_{eq} = \frac{M'_1 + M'_d}{2} = \frac{M'_1 + M'_{dwsl_{ss}}}{2} \qquad \textbf{(2.6.27)}$$

Having M'_{eq}, an empirical correlation based on experimental results [154,224,225] was established to compute the relative total pressure loss in the form of

$$PR'_{psh} = f(M'_{eq}) \qquad \textbf{(2.6.28)}$$

A second shock standing near the trailing edge was observed through Schlieren visualization. Its location was obtained directly from the observations as there was no method available to obtain predict it. This shock was assumed to be normal to the flow, and its relative total pressure was found from normal shock relations.

The two-shock model from Gustafson was modified by Koning *et al*. [153,155] to be applied not only to DCA aerofoils but also to low-cambered (MCA and wedge-type)

and pre-compression concave blade profiles. The passage-shock location x_d with respect to the chord was approximated as per the following empirical correlation

$$\frac{x_d}{c} = \frac{1}{\sigma} cos\xi \quad \textbf{(2.6.29)}$$

The flow angle for low-cambered profiles at point *d* is merely the blade angle, which can be computed as

$$\beta_d = \kappa_d + \xi \quad \textbf{(2.6.30)}$$

Where κ is the angle between a tangent at a given blade surface point and the chord, and ξ is the stagger angle. For pre-compression blades the angle between the tangent at point *d* and the chord was assumed to be twofold, thus

$$\beta_d = 2\kappa_d + \xi \quad \textbf{(2.6.31)}$$

Since the inlet conditions are known, the Riemanns's equation for a right running characteristic from Eq. 2.4.36 solves the Prandtl-Meyer angle at point *d* in the form

$$\nu_d = \nu_1 + \beta_1 - \beta_d \quad \textbf{(2.6.32)}$$

The relative Mach number at point *d* M'_d is then computed using the Prandtl-Meyer function from Eq. 2.4.34, so that the equivalent Mach number ahead of the passage is obtained as in Eq. 2.6.27. Given M'_{eq}, the downstream Mach number, static-pressure ratio, and the relative total-pressure ratio $\frac{P_{0_{d2}}{}'}{P_{0_{d1}}{}'}$ can be calculated with normal shock equations given in Sec. 2.4.1. The relative total-pressure ratio and the equivalent Mach number determines thus the passage-shock-loss coefficient using Eq. 2.6.1.

Additional empiricism was introduced to this model in the calculation of the total-to-static pressure ratio downstream of the passage shock using a correction factor q that reflects the pressure rise weakening due to the SWBLI, being

$$\frac{p_2}{p_1} = 1 + \frac{2\gamma}{\gamma + 1}(M_1^2 - 1) * q \quad \textbf{(2.6.33)}$$

The correction factor q was correlated to the relative Mach number at point *d* as

$$q = -0.5(M'_d - 1) + 0.64 \quad \textbf{(2.6.34)}$$

The rest of the shock-model from Koning *et al*. [153,155] considers the occurrence of a second compression shock downstream of the passage shock and close to the exit, which accounts for the choke-induced shock. However, this second passage-shock was always considered regardless of the flow starting situation. Thereby, an empirical relationship between the outlet or jet area A_J and the area at point *d* was set as

$$\frac{A_J}{A_d} = 0.4993M'_q + 0.5007 + C \quad \textbf{(2.6.35)}$$

The upstream relative Mach number of the second passage-shock is M'_q. The parameter C is a function of the blade section type, taking a value of 0.774 for low-cambered blading and a value of 0.0351 for pre-compression profiles.

Fottner [226] defined an empirical shock loss coefficient at the blade leading-edge that considered both, the local-shock compressibility and its effect on the profile losses for subsonic supercritical inlet conditions, expressed as

$$\omega_{bow} = \omega_{prof}\left[A\left(M'_1 - M'_{1_{cr}}\right) + 1\right] \qquad If \quad M'_{cr} \leq M'_1 < 1.0 \quad \textbf{(2.6.36)}$$

where ω_{prof} accounts for the incompressible profile losses, and A is a coefficient set to 2.0 based on cascade evaluations. Hirsch and Denton [90] improved Eq. 2.6.36 to provide a more accurate agreement against test data, expressed as

$$\omega_{bow} = \omega_{prof}\{14[M'_1 - (M'_1 - 0.4)^3] + 1\} \qquad If \quad M'_{cr} \leq M'_1 < 1.0 \quad \textbf{(2.6.37)}$$

Besides the SWBLI, Eq. 2.6.36 and Eq. 2.6.37 consider only the bow-wave entropy generation. To account for the passage-shock losses within inlet supercritical conditions, Hirsch and Denton [90] resolved the shock-loss coefficient as

$$\omega_{psh} = \Omega_{eq}\left[\frac{1 - \frac{\gamma - 1}{\gamma + 1}\Omega_{eq}{}^2}{1 - \frac{\gamma - 1}{\gamma + 1}\frac{1}{\Omega_{eq}{}^2}}\right]^{\frac{1}{\gamma - 1}} \qquad If \quad M'_{cr} \leq M'_1 < 1.0 \quad \textbf{(2.6.38)}$$

Where Ω_{eq} is the Laval number at the midchannel camberline, which can be calculated through an iterative method from

$$M'_{eq} = \frac{\Omega_{eq}}{\sqrt{0.5[1+\gamma-(\gamma-1){\Omega_{eq}}^2]}} \quad \textbf{(2.6.39)}$$

and the equivalent relative Mach number M'_{eq} is computed as in Eq. 2.6.9.

An experimental investigation on a transonic two-stage fan by Cunnan *et al*. [38] provided an empirical shock-loss correlation based on several transonic rotor tests [227–229]. A shock-loss parameter Π_{sh} was empirically defined as a function of the inlet relative Mach number as seen in the chart of Figure 2.45.

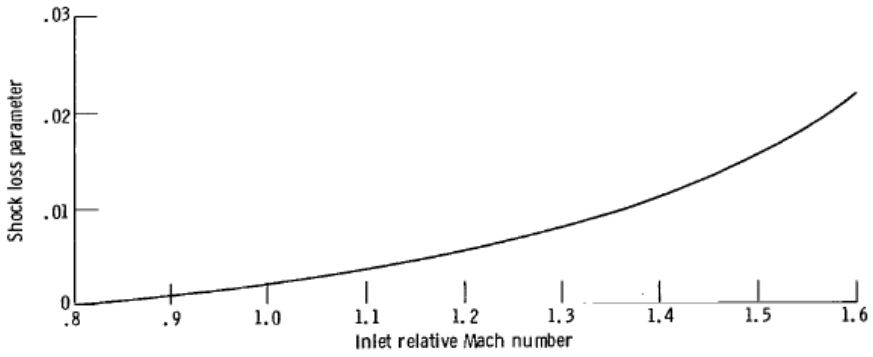

Figure 2.45 Empirical shock-loss parameter correlation [38]**.**

Thus, the shock-loss coefficient is correlated to the shock-loss parameter Π_{sh} as

$$\omega_{sh} = \frac{2\sigma\Pi_{sh}}{cos\beta_2} \quad \textbf{(2.6.40)}$$

In a very simplified empirical model for DCA blading, Haslam-Jones [230] separated the shock losses in inlet and outlet. The inlet shock losses emulate the inlet shock-system and were calculated as the total-pressure loss across a normal shock with an equivalent upstream Mach number of

$$M'_{eq} = M'_1 + 0.2 \quad \textbf{(2.6.41)}$$

The outlet shock losses were just considered for started-flow conditions since they tend to represent the shock and SWBLI losses from the choke-induce second shock. The

outlet shock-loss coefficient was thus approximated to be the scaled profile losses by a factor that depends on the choking margin Ξ, defined in Eq. 2.7.8, such that

$$\omega_{out} = \omega_{prof}[1 + 40(\Xi - 1)] \quad \textbf{(2.6.42)}$$

2.7 Transonic Axial-flow Compressor Blading Choking

2.7.1 Loss-Incidence Relation

Expertise in blade profiles has led to design high-speed compressor rotor blades with metal inlet angles k_1 between 35 and 70° [40,132,238,229,231–237] from hub to tip. Ideally in the rotor design intent, the inlet relative flow angle β_1 is desired to be as close as possible to the blade inlet angle to minimize profile losses. The difference between the inlet flow angle and the blade inlet angle is the incidence i, written as

$$i = \beta_1 - \kappa_1 \quad \textbf{(2.7.1)}$$

In design process of a compressor rotor there is a design incidence i^* for which the total losses are minimum, quantified as the design total-loss coefficient ω^*, as observed in Figure 2.46. Nevertheless, in real operations, the design point slightly shifts from the design intent, leading to a higher inlet relative Mach number. Thus, at this real design condition, there is a different incidence for which the losses are the lowest possible, known as the minimum-loss incidence i_{min}. Correspondingly, the total-loss coefficient at i_{min} is the minimum-loss total-loss coefficient ω_{min}. Figure 2.46 shows the displacement of the curve ω vs i when the inlet relative Mach number increases at design point, raising the total losses and the incidence at which these occur. This means that even at off-design conditions, either lower or higher inlet relative flows, the total losses and their corresponding incidences decrease or increase, respectively. Note that not only is the abscissa and ordinate translation of $\omega = f(i)$ when $M_1{}'$ is varied, but also the working range W is modified. At high inlet relative Mach numbers, the working range narrows; whereas at low inlet flow velocities W broadens.

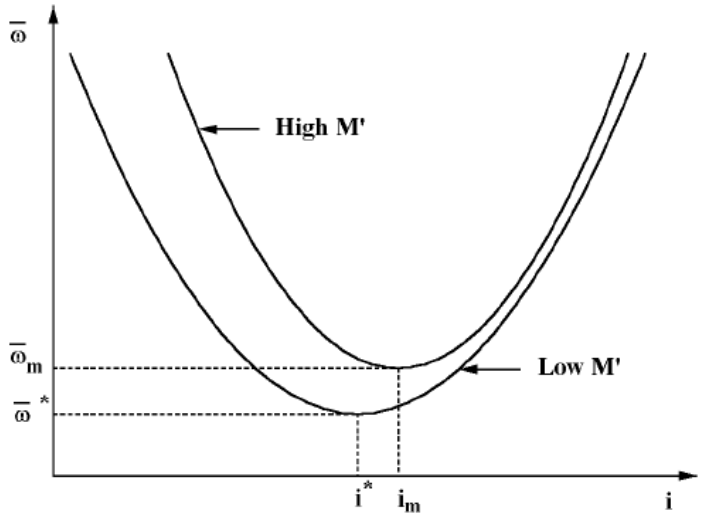

Figure 2.46 Loss coefficient vs incidence plot for different inlet relative Mach numbers [136]**.**

The working range is bounded for high inlet relative flow angles at the stall incidence i_{st} and for low inlet relative flow directions at the choking incidence i_{ch}, as seen in the plot of Figure 2.47. Even if the stall incidence is reached, the inlet relative flow angle can still be further increased till surge at the expense, of course, of a profile loss increment due to boundary layer separation and a reduction in rotor stability. Surge onset is preceded by stall, and it can be understood as a severe blade row stalling. Physically, surge is an event in which the energy contained in the compressed flow becomes greater than the imparted energy by the blade rows. Since stall and specially surge occur at very high incidences within the stall regime, they are out of the scope of the present investigation and no additional discussion is provided upon these two phenomena.

In contrast, the choking incidence occurs when no more mass flow can be passed through the choked blade passage, fixing the inlet axial velocity, and hence, the inlet relative angle. Therefore, for a given inlet relative Mach number, the choking incidence is the minimum value of incidence that can be attained. Blade passage choking develops progressively in the spanwise direction as the incidence reduces instead of being a sudden effect along the blade height. Due to the presence of dual-shock structures during blade-element choking, its complex physics have remained unclear and are yet to be understood. The blade-row choking phenomenon is key element of this research and is treated in detail in Sec. 2.7.2.

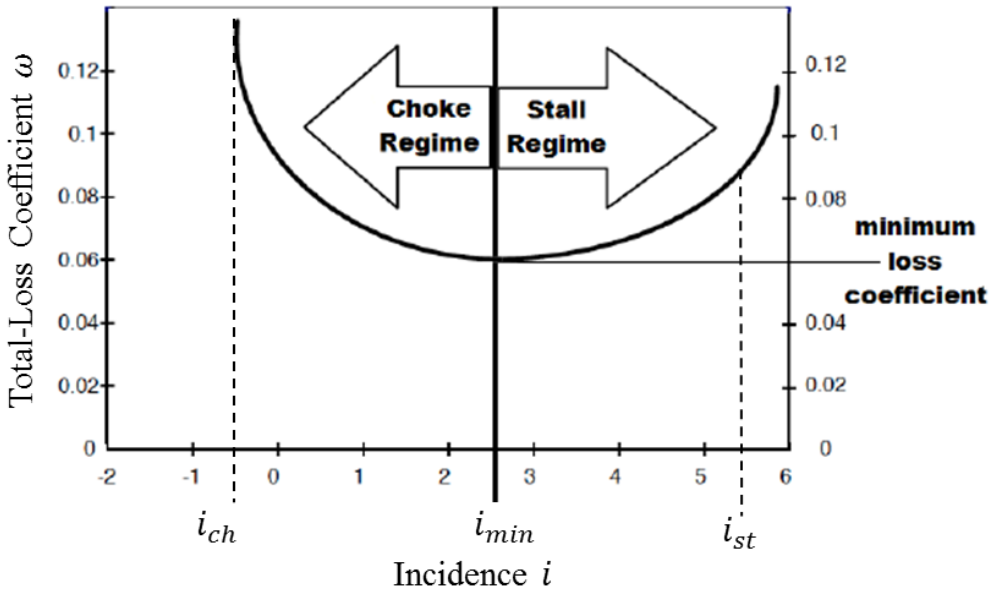

Figure 2.47 Loss coefficient variation with incidence (modified from [239]**).**

2.7.2 Blade-Passage Choking Models

As mentioned earlier, a transonic axial-flow compressor operating with an inlet relative Mach number above the critical value leads to a shock-system. As discussed in Sec. 2.5.2, the diffusing blading passages are in the form of a convergent-divergent duct. Since the blade passage flow is transonic, there is a potential for the flow to become choked. When choking is reached, the mass flow is fixed, causing the transonic compressor performance to be limited by a loss increase and a working range reduction. In Sec. 2.6.2, the distinction between unstarted and started inlet flows was established. During unstarted flow operations, the inlet passage flow is still affected by downstream throttling. Conversely, at started flow operations a second shock within the passage occurs to meet the back conditions. Having the shock discontinuity avoids any communication of the downstream throttle with the inlet flow, leading then to fixed inlet conditions, and hence, a constant mass flow.

The blade-cascade flow is described to be analogous to that in a double-throat nozzle, where the second throat acts as a throttle [11]. The first throat is considered to be the blade inlet area, while the second throat existing at the smallest passage cross-section. Contrary to a nozzle, the area in a blade-row cannot be altered. Instead, the inlet flow

angle is not fixed and can be modified. Hence, for every blade throat area, a functional relation of $\beta_1 = f(M_1{}')$ can be established. As long as the blade-inlet area remains larger than the blade-throat area, the flow is unstarted. Any further increase of the blade throat area beyond the blade inlet area chokes the passage and the unique incidence is attained. This is that for every inlet flow angle there is an inlet relative Mach number at which the blade cascade chokes. In other words, when the inlet relative Mach number is fixed there is a unique flow angle or incidence that simultaneously satisfies the Riemann's equation for the Prandtl-Meyer expansion and mass flow continuity [1,2].

The fact of having started conditions leads to mixed subsonic and supersonic fields. As the flow equations involved are no longer elliptic but hyperbolic, an approximate solution for the mixed flow can be found through numerical methods, such as, time-dependent difference [240], multistrip integral [241,242] or hodograph [243] methods. For instance, the unstarted and started cascade flows for different back static pressures were determined through a finite difference scheme including an artificial viscosity [240]. Nevertheless, the inconvenience of these methods is the exact determination of the shock wave.

Horlock [244] used actuator-disc theory to analyse the flow in zero-stagger-and-zero-cambered profiles and staggered blade rows when the mass flow is just choked. The choking was assumed to arise from three different sources: throat area variation, back pressure variation, and entry shear. Several assumptions were implied in the actuator-disc analysis which merit further consideration. For instance, the flow was considered to be locally choked at all blade sections and to be isentropic from the leading edge up to the throat. Despite these considerations, the inlet flow readjusted itself so that a unity relative Mach number was attained at the throat. It was resolved that the throat area must be reduced to keep the mass flow choked and hence, fixed. For this, the mass flow was reduced fractionally by C/s, where C is a coefficient that depends on the inlet Mach number.

To emulate the passage choking situation happening at high inlet relative Mach numbers, Starken [184] applied the Moeckel's method [180] and Levine procedure [185], assuming the point a of the limiting characteristic stands on the suction-surface

leading-edge. In this manner the length l_{ab} of the characteristic *a-b* is known since point *a* is on the leading edge and point *b* is the vertex of the hyperbola-approximated detached-shock. Mass flow conservation was applied between the far inlet field and the limiting characteristic *a-b* as

$$\rho_1 V_1 A_1 = \rho_{ab} V_{ab} A_{ab} \tag{2.7.2}$$

Contrary to Schobeiri [220], the streamtube height contraction H_1/H_{ab} was disregarded in the area ratio for the mass flow conservation. Thereupon, the inlet flow area A_1 simplifies to

$$A_1 = \phi = s \cos \beta_1 \tag{2.7.3}$$

Similarly, the flow area of the limiting characteristic, whose angle is the Mach angle μ_{ab}, is normal to the incoming flow, such that

$$A_{ab} = l_{ab} \sin \mu_{ab} \tag{2.7.4}$$

Thence, the continuity equation between far upstream and the first-captured Mach wave becomes

$$\rho_1 V_1 s \cos \beta_1 = l_{ab} \sin \mu_{ab} \tag{2.7.5}$$

Accordingly, the Riemann's equation for the Prandtl-Meyer expansion needs to be satisfied. Using Eq. 2.4.36 for a right-running characteristic gives

$$\beta_1 + \nu_1 = \beta_{ab} + \nu_{ab} \tag{2.7.6}$$

Since the limiting characteristic is assumed to impinge on the suction-surface leading edge, its flow angle β_{ab} is approximately the blade leading edge k_1. Whereupon, the continuity equation and Prandtl-Meyer expansion might be numerically solved for a given inlet relative flow velocity to determine a unique β_1. This unique inlet relative flow angle is considered to be the choking flow angle, inasmuch as the limiting characteristic location corresponds to a choke case representation.

Although the formulation of the two relations is correct, total-pressure losses due to the detached bow-shock were neglected in the mass flow conservation. More important to

consider is that imposing the limiting wave to the suction-surface leading-edge deserves some further attention as the suction surface has no more influence on the relative Mach number upstream of the first-captured Mach wave. Later investigations demonstrated [13,34,36,205,245] that even at choked conditions, the point *a* of the first-captured Mach wave can lie anywhere on the suction-surface entrance region depending on the geometry.

Haslam-Jones [230] introduced choking calculations within a through-flow method for $M'_1 \geq 0.8$. For started-flow blades, the maximum mass flow rate that can be passed through the passage was obtained through a cascade-based empirical correlation as a function of the inlet relative Mach number, given by

$$\dot{m}_{max} = \frac{\dot{m}_{theory}}{(1 + \frac{M'_1 - 0.8}{20})(1 + \frac{\beta_1 - \beta_{thr}}{100})} \quad \textbf{(2.7.7)}$$

where the $\dot{m}_{theory}$ is the theoretical mass flow calculated as in Sec. 2.5.31 and the term $\beta_1 - \beta_{thr}$ represents the turning angle between the inlet and throat. Following the composition of a though-flow simulation, the actual and maximum mass flow rates are computed at every streamline, where a ratio between them defined as the choking margin Ξ can be obtained as

$$\Xi = \frac{\dot{m}}{\dot{m}_{max}} \quad \textbf{(2.7.8)}$$

Consequently, the losses and deviation angles are proportionally scaled to the choking margin. Being that not all the streamlines are choked, relaxation factors were applied to those in order to assure stability.

Tiwari *et al*. [23] implemented a new technique for SLC methods to handle choked flow across the flowpath. The treatment was divided in annular choking to account for all the stream tubes choked from hub to tip and local choking for few stream tubes choked. In the seldom cases of annular choking, a maximum value of mass flow is reached for the entire flowpath. Conversely, localized choking is encountered regularly.

To treat annular choking in SLC, a pressure ratio is defined as target for which the target mass flow rates per stream tube are calculated. After full REE is satisfied, mass flow continuity determines the stream tube mass flow. The ratio of mass flow rates between the target and the calculated values adjusts the upstream target pressure for the next iteration. Eventually, all the stream tubes attain the target mass flow and pressure ratio, achieving convergence.

The local choked mass flow was fixed by setting the required spanwise distribution of average throat turning $rC_\theta|_{th}$. However, this is unknown in the analysis mode of SLC program. Instead, the average meanline throat turning can define a radial distribution. The average throat turning at the meanline was assumed to be almost proportional to that at the tip $rC_\theta|_{tip_{th}}$, defined as

$$rC_\theta|_{tip_{th}} = rC_\theta|_{tip_{in}} + \left(\frac{\overline{rC_\theta}|_{th} - \overline{rC_\theta}|_{in}}{\overline{rC_\theta}|_{out} - \overline{rC_\theta}|_{in}}\right)\left(rC_\theta|_{tip_{out}} - rC_\theta|_{tip_{in}}\right) \quad \textbf{(2.7.9)}$$

Given the average tip throat turning, the spanwise throat turning distribution is computed to assign an average throat turning to the rest of the stream tubes. The distribution is based on a linear equation whose slope depends on the flow condition and vortexing behaviour.

2.8 Summary

Transonic axial-flow compressors need to guarantee high single-stage pressure ratio at high efficiencies and working ranges, at least comparable to those from the subsonic systems. Shock-induced losses in transonic compressors arise from the shock strength, SWBLI, shock and tip-leakage vortex interaction, blockage, corner stall and upstream wake destabilization. Shock losses represent 35 to 55% of the overall blade losses. Blade-profile shaping through maximum-thickness location increase, maximum thickness reduction, and solidity increment, reduces the shock losses. For the rest of the blade, cambered profiles are desired to still offer flow turning and increase the pressure ratio.

2-D blade-profile studies have resulted in low-thickness profile sections at the tip. 3-D blade-shaping has shown that the shock structure can be controlled by sweep and lean

with different influence along the span, leading to S-shaped blades. A compound forward-sweep blade increases the isentropic efficiency but shortens the working range due to a reduction in both, secondary flows effects and entropy generation. On the other hand, a compound backward-sweep blade provides a lower efficiency enhancement but improves the working range since the shock-loss intensity is lessened.

Because of the transonic-flow complexity in compressors, the preferred method is 3-D CFD RANS. Nonetheless, these simulations are computationally expensive and still can show deviations due to the numerical approach or the turbulence/transition modelling. In contrast, 2-D throughflow SLC methods provide acceptable solution for the full compressor map in a quicker manner. 2-D SLC methods provide the flow field solution on the meridional plane by numerically resolving the full REE, which estimates the gradient of the meridional velocity in the spanwise direction.

Previously published shock-loss models for 2-D SLC have oversimplified the shock configuration, assuming an equivalent passage-shock structure from design point with the inability of being sensitive to off-design conditions. This condition has limited the analytical shock-loss models to unstarted blade passages. The pioneer model of Schwenk *et al*. [4], cornerstone of successive models, assumed only a normal passage shock from the detached bow-shock vertex to an arbitrary suction-surface location to calculate the peak relative suction-surface Mach number. The widely used model from Miller *et al*. [3], combined the model of Schwenk *et al*. [4] with the detached bow-shock approximation from Moeckel [180] and resolved the flow expansion ahead of the assumed passage-shock. Sayari and Bolcs [24] assumed a passage-shock normal to the stagnation streamline. Schobeiri [220] modelled for the first time the passage shock as oblique but only for sharp-nosed profiles with no bow shock. Bloch *et al*. [34] assumed the passage shock normal to the flow and emanating from the bow-shock sonic point. Although the flow expansion was resolved analytically, the stagnation streamline and geometric leading-edge radius were altered based on CFD correlations. The most recent state-of-the-art model by Boyer and O'Brien [13,35,36] assumed three different reference shock systems for NS, NPE and NC. Any other off-design shock-loss computation different from the standard configurations was corrected using CFD-based correlations, which were not universal.

Choking-process within 2D- SLC tools has remained as a challenge. Horlock [244] used actuator-disc theory and reduced the mass flow at all blade sections by a fraction that depends on the inlet Mach number. Starken [184] used mass flow conservation and a Prandtl-Meyer expansion between far upstream and an assumed limiting characteristic that impinges on the leading edge, and neglecting any detached bow-shock. Haslam-Jones [230] calculated the maximum mass flow in a choked passage suing a cascade-based empirical correlation. The most recent choked-flow treatment in throughflow method by Tiwari *et al*. [23] assumed a spanwise distribution of the required average thoat turning to fix the local choked mass flow.

3 METHODOLOGY

3.1 Introduction

This chapter offers a thorough description of the four key implementations in the 2-D SLC methodology that focus in improving the axial-flow compressor modelling and its flow solution to account for a more accurate transonic-flow performance prediction, as shown in Figure . Concerning the axial-flow compressor modelling discussed in Sec. 3.2, a blade-element-layout method and a modification to the 2-D SLC fundamental equation were implemented. The main contribution to knowledge focuses in the flow solution, where a novel analytical physics-based shock-loss model was developed and incorporated into the 2-D SLC program, described in Sec. 3.3. This shock-loss model can be used in both unstarted and started operations, where the later required the development of a radial mass flow redistribution model due to the choking effect, reviewed in Sec 3.4. For the shock-loss mode to operate in started conditions, an iterative method was implemented as an outer loop to the algorithm to correctly predict the overall passage-shock structure. In order to provide the highlights and key points of the overall methodology, a summary is provided in Sec. 3.5.

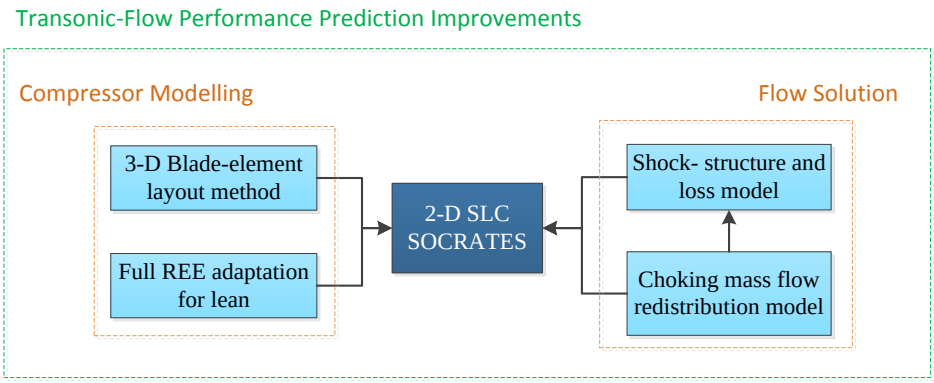

Figure 3.1 Structure of the incorporated modules into the 2-D SLC simulation strategy to improve the transonic-flow performance prediction.

The theory behind the blade-element-layout method consisting in projecting the blade-element parameters on a conical surface of revolution to later sweep and lean the blade sections individually is presented in Sec. 3.2.1. The adaptation of the full-REE second-order differential equation to account for lean effects in the 2-D SLC strategy is examined in Sec. 3.1

Central to this research, the physics-based shock-loss model obtains a relative shock-loss coefficient at both, relative subsonic supercritical and relative supersonic span. The shock-loss computation for the relative subsonic supercritical conditions is given in Sec. 3.2.3. The complex shock-structure for the relative supersonic span is discussed from Sec. 3.3.3 to Sec. 3.3.9. Sec. 3.3.3 intends to give a description of the supersonic flow traversing the shock configuration so that further discussions on the methodology can be easily digested by the reader. Inasmuch as the detached bow-shock is a significant percentage of the shock-structure skeleton, its modelling is given in Sec. 3.3.4. The associated shock-loss corresponding to that portion of the detached shock that extends to infinity, namely the bow wave, are calculated in Sec. 3.3.5.

With respect of the passage shock, its situation is a function of the choking incidence and choking margin calculated in Sec. 3.4.2 and Sec. 3.4.3, respectively, establishing the passage-shock configuration in Sec. 3.3.6. If the blade passage is identified as unstarted, the passage-shock is fully determined by the detached bow-shock. Nevertheless, if the blade-passage is started, the passage-shock location and shape are assumed in Sec. 3.3.6. Having an established passage shock, the flow expansion ahead is calculated in Sec. 3.3.7, by first identifying the limiting characteristic using mass flow conservation in Sec. 3.3.7.1 and then developing the full flow-field expansion through the method of characteristics in Sec. 3.3.7.2. The algorithm was developed is such that any potential expansion fan or pre-compression shocks are determined and accounted for the over-all expansion process. The full expansion provides flow information in the circumferential direction which is mass-averaged to obtain the associated passage-shock losses in Sec. 3.3.8. Forasmuch as the passage-shock form and position were assumed during choking, the iterative method of Sec. 3.3.9 is required to find the correct location and angle for the choke-induced passage-shock. For the started cases, a second flow-expansion is computed accordingly to consider the relative total-pressure recovery from the second passage-shock.

The started blade passages are required to limit the incidence to the already computed choking incidence, affecting the streamtube mass flow at those choked blade-profiles. For this reason, a novel numerical mass flow redistribution model was developed and presented in Sec. 3.4.4.

3.2 Compressor Blade Modelling

3.2.1 Overview

A blade-element-layout method based on the approach of Crouse *et al*. [107] was generated in FORTRAN90 and implemented into the 2-D SLC axial-flow fan/compressor performance simulation software (SOCRATES) [14,17,31] to compose the blading on conical surfaces. The flow chart in Figure 3.2 defines the subroutines created for the conical blade-element-layout method. This method requires the parameters at the leading edge, trailing edge, maximum thickness point and transition point (if any) as reference to be projected on a conical stream surface. The camberline is defined by assuming a constant rate of change of blade angle with respect to the profile path. Given the camberline, the thickness distribution is defined normal to it so that the suction and pressure surfaces can be modelled. For each blade-element section the stacking point might be computed accordingly to establish the stacking line so that any sweep or lean angle can be implemented with respect of this reference line. The swept and leaned blading sections are transformed from conical to Cartesian coordinates and fed back to the 2-D SLC simulation.

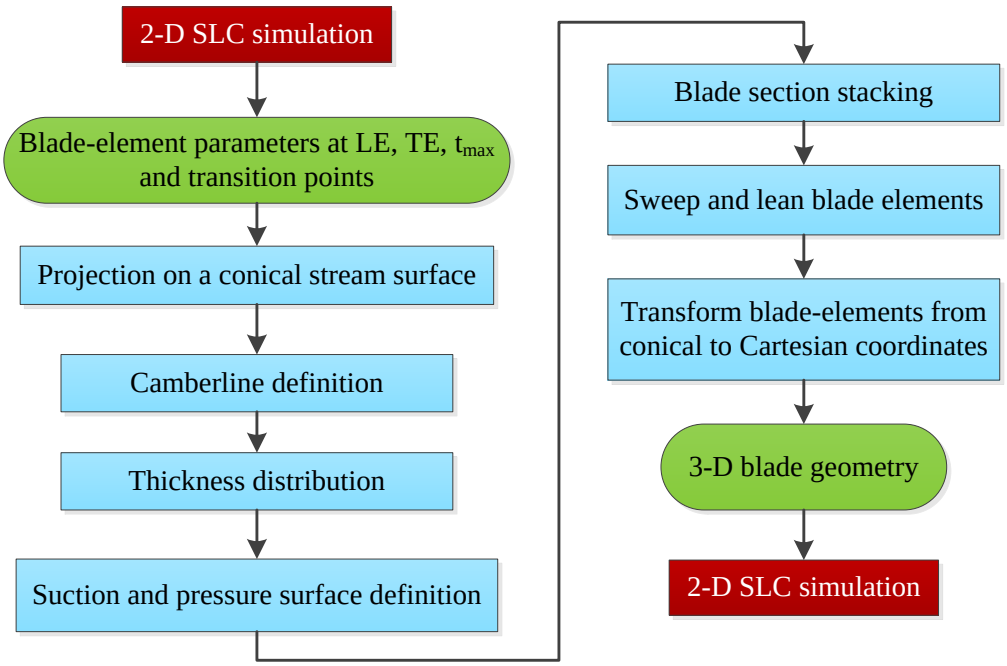

Figure 3.2 Blade-element-layout method to compose blade profiles on conical stream surfaces, implemented in the 2-D SLC axial-flow fan/compressor performance software.

3.2.2 Blade-Element-Layout Method Definition

In each blade profile section, the parameters that define its geometry are known as blade elements. Each blade profile section is conveniently projected on a conical surface to approximate the stream flow surfaces, which are considered to be axisymmetric. Due to the axisymmetric assumption, the stream surfaces can be represented in a 2-D plane as streamlines. When the streamline slopes are low, the conical approach can be considered accurate; however when the streamline slopes are high there are discrepancies between the blade-profile conical representation and the stream surfaces. Due to the blade-profile conical projection inability to capture all the blade element parameters, there are several approaches of blade shape modelling on a conical surface [107]: blade-element direct layout on the conical surface, and blade element projection that lay out on plane or cylindrical surface onto a cylindrical surface.

Flow across the blades is influenced by several interacting forces; however, the most direct factor driving the local flow is the surface curvature, which is the rate of change-of-surface-angle with respect to the streamline. Therefore, a blade-element-layout method by Crouse *et al*. [107] was developed accordingly, to keep constant the angle change along the blade surface, so that less flow changes can be expected due to blade layout. In other words, the blade-layout method consists in maintaining a constant rate of change-of-angle with respect to the path distance at every defined arc segment of the camberline, suction surface and pressure surface. Subsequently, the complete blade geometry is obtained by stacking the different blade profile sections along the stacking axis.

In particular, the present blade-element layout method is suitable to sketch multiple-circular-arc (MCA) -type blade profile sections. As explained in Sec. 2.1, the demand for an increase in aircraft speeds has led to have higher entry-flow velocities at the compressor, reaching transonic regime and therefore, shock wave presence. The need to control shock losses at the throat area, and regulate chordwise flow turning, has resulted in MCA-type blade profile sections. An MCA-type blade profile consists of two circular arcs that outline the suction surface and other two circular arcs for the pressure surface, thus, camberline is defined as well by two circular arcs. For any of

both surfaces, suction and pressure, and camberline, the boundary of every circular arc is delimited by the transition point; namely, the first circular arc goes from leading edge to transition point, and second arc joins transition point with trailing edge.

More important, the implemented blade-element layout method in this research allows to find the blade profile centre of area in a convenient manner, so that further sweep λ and lean angle η variations can be introduced with respect of the stacking axis. Based on Crouse *et al*. [107], the following blade-element-layout method was programmed and implemented in SOCRATES for blade profile modelling; its validation can be found in Sec. 4.2. To project the blade elements in a conical surface, an R-ε conical coordinate system is defined, where R is the ray from the cone vertex to a certain point, and ε is the angle between a certain ray with respect to a reference ray as shown in Figure 3.3. The cone half-angle α of every conical coordinate system is defined and fixed for every blade profile section.

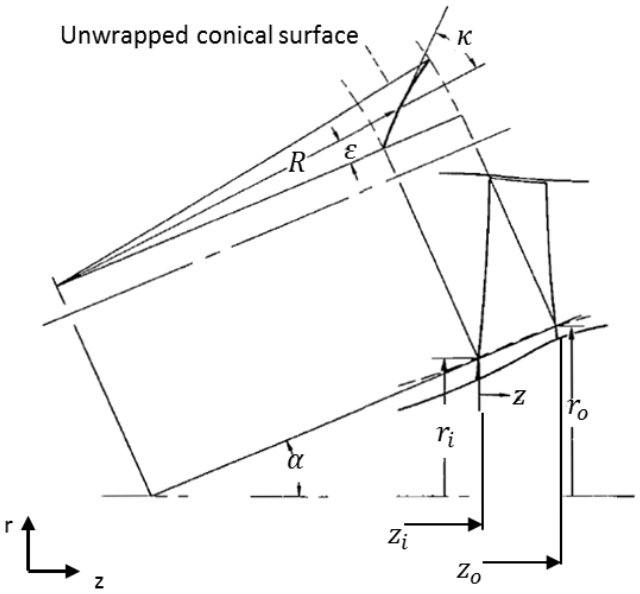

Figure 3.3 Unwrapped view of the conical coordinate system used for the constant turning blade-element-layout method (obtained and modified from Crouse *et al.* [107]).

From Figure 3.3, r_{LE} and r_{TE} define the blade leading edge and trailing edge radius, respectively on the radial direction r. In the axial direction or rotation axis z, the blade leading and trailing edge coordinate are given by z_{LE} and z_{TE}. The blade inlet and outlet angles are defined by k_{LE} and k_{TE}, respectively.

The rate of change of blade angle with respect to the blade profile path S is defined by the turning rate C. If a constant turning rate is established as in this method, the blade metal angle k decreases as the surface path S increases. This is,

$$\frac{dk}{dS} = -C \tag{3.2.1}$$

The camberline laid out on a conical surface is defined as seen in Figure 3.5.

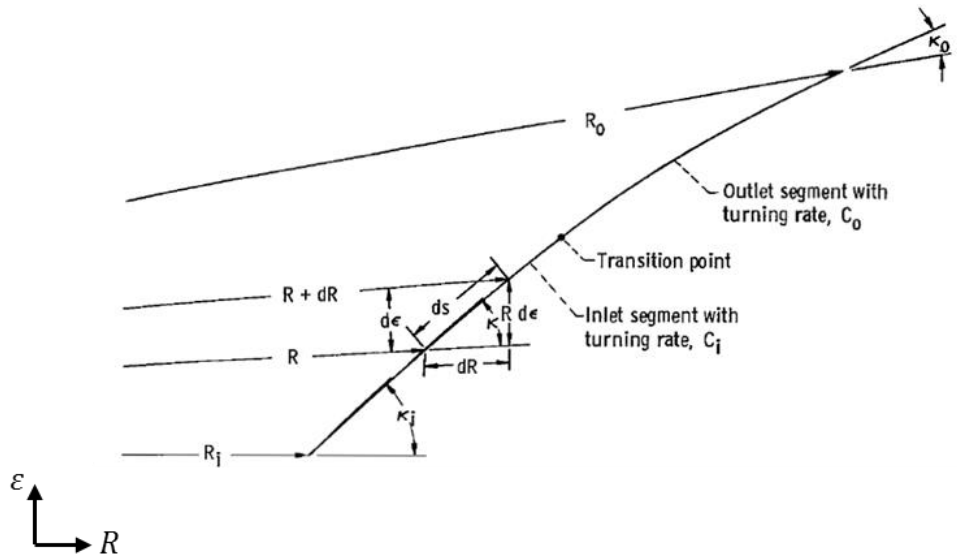

Figure 3.4 Camberline blade elements on a conical coordinate system (obtained and modified from Crouse *et al.* [107])

From Figure 3.4, the following trigonometric relations are derived

$$dR = dS \cos k \tag{3.2.2}$$

$$Rd\varepsilon = dS \sin k \tag{3.2.3}$$

Substituting Eq. 3.2.1 in Eq. 3.2.2 and Eq. 3.2.3, respectively,

$$dR = -\frac{\cos k}{C} dk \tag{3.2.4}$$

$$d\varepsilon = -\frac{\sin k}{RC} dk \tag{3.2.5}$$

Integrating Eq. 3.2.4 from a point 1 where R and k are known to the point of interest on the camberline,

$$\int_{R_1}^{R} dR = \int_{k_1}^{k} -\frac{\cos k}{C} dk$$

$$-R_1 = \frac{1}{C}(\sin k_1 - \sin k) \quad \textbf{(3.2.6)}$$

Rearranging Eq. 3.2.6 to have one side the known variables and on the other the unknown variable, defines the constant ζ as

$$RC + \sin k = R_1 C + \sin k_1 = \zeta \quad \textbf{(3.2.7)}$$

Substituting Eq. 3.2.7 in Eq. 3.2.5, gives the solution for ε,

$$d\varepsilon = \frac{\sin k}{\sin k - \zeta} dk \quad \textbf{(3.2.8)}$$

Eq. 3.2.8 is a differential equation that is complex to solve and the solution is a function of k, k_1 and ζ, expressed as

$$\varepsilon = \varepsilon_1 + f(k, k_1, \zeta) \quad \textbf{(3.2.9)}$$

Nevertheless, if the blade angle k does not change, it results in $k = const$ and $C = 0$. Therefore, the term dk from Eq. 3.2.5 can be substituted from that in Eq. 3.2.4,

$$d\varepsilon = -\frac{\sin k}{RC} dk = \frac{\sin k}{RC} \frac{C}{\cos k} dR = \tan k \frac{dR}{R} \quad \textbf{(3.2.10)}$$

To define the R- ε coordinates on the camberline, the following equation can be deduced from the trigonometric relation in Figure 3.1,

$$\alpha = \arctan\left(\frac{r_{c_{TE}} - r_{c_{LE}}}{z_{c_{TE}} - z_{c_{TE}}}\right) \quad \textbf{(3.2.11)}$$

Where the subscript c accounts for the camberline. In the case of the R- ε coordinates for the blade surfaces, the subscript n is later used.

The ray conical-coordinates for the leading edge LE, transition point T, trailing edge TE are given respectively by

$$R_{c_{LE}} = \frac{r_{c_{LE}}}{\sin \alpha} \tag{3.2.12}$$

$$R_{c_T} = R_{c_{LE}} + \frac{z_T - z_{LE}}{\cos \alpha} \tag{3.2.13}$$

$$R_{c_{TE}} = R_{c_{LE}} + \frac{z_{TE} - z_{LE}}{\cos \alpha} \tag{3.2.14}$$

For the rest of the blade profile axial points R is equals to

$$R_{c_n} = R_{c_{LE}} + \frac{z_n - z_{LE}}{\cos \alpha} \tag{3.2.15}$$

Where z_n is the axial coordinate for a point n, defined as

$$z_n = \frac{n}{N_{ap} - 1}(z_{TE} - z_{LE}) + z_{LE} \tag{3.2.16}$$

where N_{ap} is the total number of axial points defined for the blade profile.

Since the turning rate in Eq. 3.2.7 is constant, it can be defined for each camberline segment: from the leading edge to transition point, and from the transition point to trailing edge, respectively as

$$C_{LET} = \frac{\sin k_{c_{LE}} - \sin k_{c_T}}{R_{c_T} - R_{c_{LE}}} \tag{3.2.17}$$

$$C_{TTE} = \frac{\sin k_{c_T} - \sin k_{c_{TE}}}{R_{c_{TE}} - R_{c_T}} \tag{3.2.18}$$

The solution for the ε coordinate can be broken down in special cases as follows

a) If $k = k_1$ or $C = 0$

When the blade angle does not change along the surface path, meaning $k = k_1$, the turning ratio becomes $C = 0$. Thus, Eq. 3.2.10 can be solved for ε by simple integration,

$$\int_{\varepsilon_{c_1}}^{\varepsilon_c} d\varepsilon_c = \int_{R_{c_1}}^{R_c} \tan k_c \frac{dR_c}{R_c} \tag{3.2.19}$$

$$\varepsilon - \varepsilon_{c_1} = \tan k(lnR - lnR_1) = \tan k_c ln(\frac{R}{R_1})$$

$$\varepsilon = \varepsilon_{c_1} + \tan k_c ln(\frac{R}{R_1})$$

For the rest of the cases, as $k \neq k1$, ε needs to be solved through the solution of the differential Eq. 3.2.8, which has the general form Eq. 3.2.9. Due to the complexity to solve this differential equation, only the solution for it is presented below for each of the particular cases,

b) If $k \neq k_1$ or $\zeta^2 > 1$

$$\varepsilon_c = \varepsilon_{c_1} + k_c - k_{c_1}$$

$$+\frac{2\zeta}{\sqrt{\zeta^2-1}}\left\{arctan\left[\frac{1-\zeta\tan\left(\frac{k_c}{2}\right)}{\sqrt{\zeta^2-1}}\right] - arctan\left[\frac{1-\zeta\tan\left(\frac{k_{c_1}}{2}\right)}{\sqrt{\zeta^2-1}}\right]\right\} \quad \textbf{(3.2.20)}$$

c) If $k \neq k_1$ or $\zeta^2 > 1$

$$\varepsilon_c = \varepsilon_{c_1} + k_c - k_{c_1} + \frac{\zeta}{\sqrt{1-\zeta^2}}$$

$$\left[ln\left|\frac{1-\zeta\tan\left(\frac{k_c}{2}\right)-\sqrt{1-\zeta^2}}{1-\zeta\tan\left(\frac{k_c}{2}\right)+\sqrt{1-\zeta^2}}\right| - ln\left|\frac{1-\zeta\tan\left(\frac{k_{c_1}}{2}\right)-\sqrt{1-\zeta^2}}{1-\zeta\tan\left(\frac{k_{c_1}}{2}\right)+\sqrt{1-\zeta^2}}\right|\right] \quad \textbf{(3.2.21)}$$

d) If $k \neq k_1$ or $\zeta^2 \pm 1$

$$\varepsilon_c = \varepsilon_{c_1} + k_c - k_{c_1} \pm \left[\tan\left(\frac{\pi}{4} \pm \frac{k_1}{2}\right) - \tan\left(\frac{\pi}{4} \pm \frac{k_{c_1}}{2}\right)\right] \quad \textbf{(3.2.22)}$$

The above equations, Eq. 3.2.19 to Eq. 3.2.22, can be applied for all blade-profile axial points, including leading edge, transition point and trailing edge.

The solution of Eq. 3.2.12 to Eq. 3.2.15 and the generic Eq. 3.2.9 determines R and ε coordinates for the blade-profile camberline. Therefore, the blade-element surface R- ε coordinates can be computed from the calculated camberline. The initial surface points

are determined by adding the thickness to the camberline leading-edge, maximum-thickness point *m* and trailing-edge. Similarly to the camberline, the blade-surface conical coordinates can be obtained from Eq. 3.2.2 and Eq. 3.2.3 by substituting the camberline path *s* changes for the surface path $\mathcal{s}$, as shown in Figure 3.5. Additionally, the camberline blade-angle k_c is shifted 90° for the suction surface and -90° for the pressure surface becoming k_n, expressed as

$$k_n = k_c \pm \frac{\pi}{2} \quad \textbf{(3.2.23)}$$

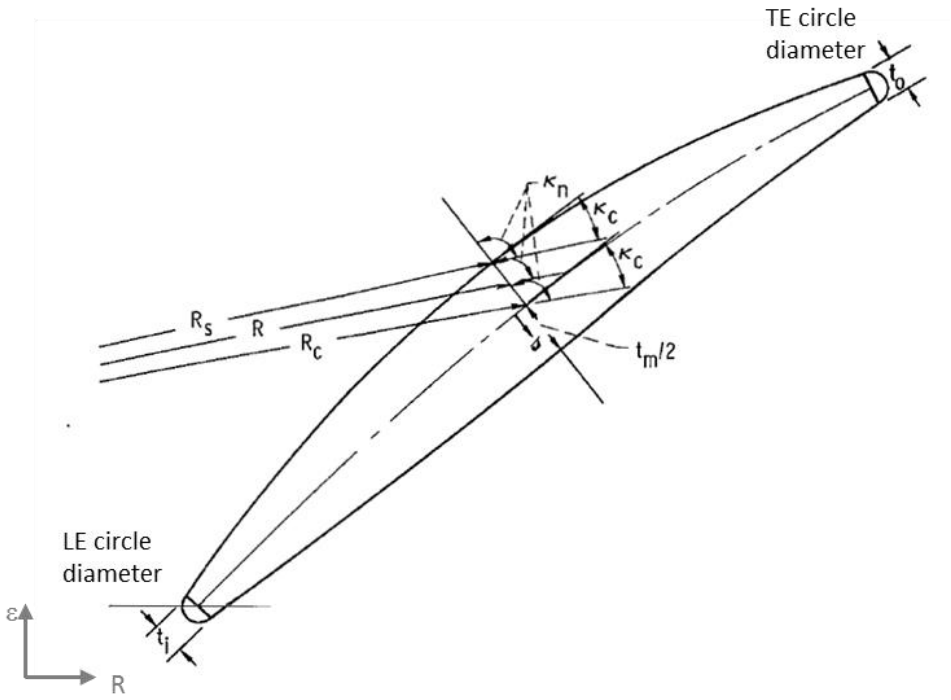

Figure 3.5 Surface blade-elements on a conical coordinate system (obtained and modified from Crouse *et al.*, [107]**).**

It can be seen in Figure 3.5 that thickness *t* is defined from surface to surface, thus, the half-thickness goes from the camberline to one surface.

From Figure 3.5, Eq. 3.2.2 and Eq. 3.2.3 become

$$dR = d\mathcal{s}\cos k_n \quad \textbf{(3.2.24)}$$

$$Rd\varepsilon = d\mathcal{s}\sin k_n \quad \textbf{(3.2.25)}$$

Integrating Eq. 3.2.24,

$$\int_{R_c}^{R} dR = \int_{0}^{t/2} d\mathcal{s}\cos k_n$$

$$R - R_c = (\frac{t}{2})\cos k_n \quad \textbf{(3.2.26)}$$

Substituting Eq. 3.2.24 in Eq. 3.2.25 gives,

$$Rd\varepsilon = \frac{dR}{cosk_n}\sin k_n = \tan k_n \frac{dR}{R} \quad \textbf{(3.2.27)}$$

Integrating Eq. 3.2.27,

$$\int_{\varepsilon_c}^{\varepsilon} d\varepsilon = \int_{R_c}^{R} \tan k_n \frac{dR}{R}$$

$$\varepsilon_c - \varepsilon = \tan k_n(lnR - lnR_c) = \tan k_n \ln(\frac{R}{R_c}) \quad \textbf{(3.2.28)}$$

For the special case of $k_c = 0$, which means $k_n = \pm\frac{\pi}{2}$, Eq. 3.2.26 becomes

$$R = R_c \quad \textbf{(3.2.29)}$$

Consequently, ε can be directly computed from Eq. 3.2.25, as $\sin k_n = \pm 1$

$$Rd\varepsilon = d\mathcal{s}$$

$$\int_{\varepsilon_c}^{\varepsilon} d\varepsilon = \int_{0}^{t/2} \pm\frac{d\mathcal{s}}{R} \quad \textbf{(3.2.30)}$$

$$\varepsilon = \varepsilon_c \pm \frac{t/2}{R} \quad \textbf{(3.2.31)}$$

where the positive solution for ε accounts for the suction surface, whilst the negative solution determines ε for the pressure surface.

The conical coordinates might be computed for every axial point on both surfaces, suction and pressure, from Eq. 3.2.26 and Eq. 3.2.28, respectively. Thus, R_n and ε_n are defined for the leading edge as

$$R_{n_{LE}} = R_{c_{LE}} + (\frac{t_{LE}}{2})\cos k_{n_{LE}} \quad \textbf{(3.2.32)}$$

$$\varepsilon_{n_{LE}} = \varepsilon_{c_{LE}} + \tan(k_{n_{LE}}) \ln(\frac{R_{n_{LE}}}{R_{c_{LE}}}) \quad \textbf{(3.2.33)}$$

for the trailing edge as

$$R_{\ \ TE} = R_{c_{TE}} + (\frac{t_{TE}}{2})\cos k_{n_{TE}} \quad \textbf{(3.2.34)}$$

$$\varepsilon_{n_{TE}} = \varepsilon_{c_{TE}} + \tan(k_{n_{TE}}) \ln(\frac{R_{n_{TE}}}{R_{c_{TE}}}) \quad \textbf{(3.2.35)}$$

and for the axial points *ap* as

$$R_{n_{ap}} = R_{c_{ap}} + (\frac{t_{ap}}{2})\cos k_{n_{ap}} \quad \textbf{(3.2.36)}$$

$$\varepsilon_{n_{ap}} = \varepsilon_{c_{ap}} + \tan\left(k_{n_{ap}}\right) \ln(\frac{R_{n_{ap}}}{R_{c_{ap}}}) \quad \textbf{(3.2.37)}$$

And for the case of maximum thickness point mt, blade angle at this point is unknown; however it can be calculated using Eq. 3.2.37, thus

$$k_{c_{mt}} = \arcsin(\zeta - R_{c_{mt}} C) \quad \textbf{(3.2.38)}$$

Where ζ and C depend on the camberline segment where the maximum thickness point is located, either between leading edge and transition point or between transition point and trailing edge. R_{c_m} is similarly obtained as in Eq. 3.2.15, while ε_{c_m} is computed from Eq. 3.2.9. Once the R- ε coordinates are known for the maximum thickness point on the camberline, R_n and ε_n for this point are defined as

$$R_{n_{mt}} = R_{c_{mt}} + (\frac{t_{mt}}{2})\cos k_{n_{mt}} \quad \textbf{(3.2.39)}$$

$$\varepsilon_{n_{mt}} = \varepsilon_{c_{mt}} + \tan(k_{n_{mt}}) \ln(\frac{R_{n_{mt}}}{R_{c_{mt}}}) \quad \textbf{(3.2.40)}$$

The above procedure can be repeated for a specified number of blade profile sections and for a number of blade rows. Thence, the whole blade is described in conical coordinates. The following step is to translate the conical coordinates into Cartesian. It results convenient to already consider in this step, the deviation introduced by the sweep and lean angles, if any. For this purpose, other two coordinate systems are defined to describe the stacking line and account for the angle variations. A cartesian coordinate system is defined as observed in Figure 3.6, and a cylindrical coordinate is used as shown in Figure 3.7. In both figures, it is observed that sweep and lean angle can be defined in both, *z-x* and r-θ planes.

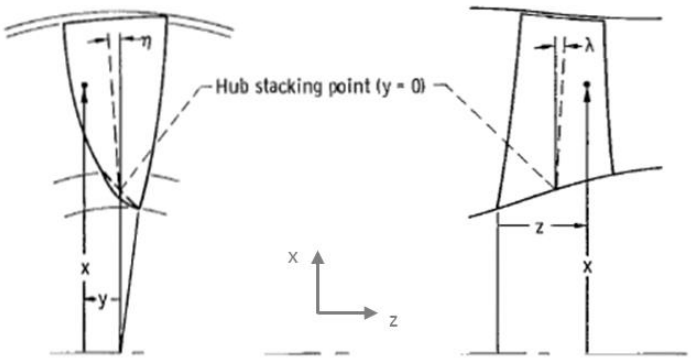

Figure 3.6 Sweep and lean angle definition on a cartesian coordinate system.

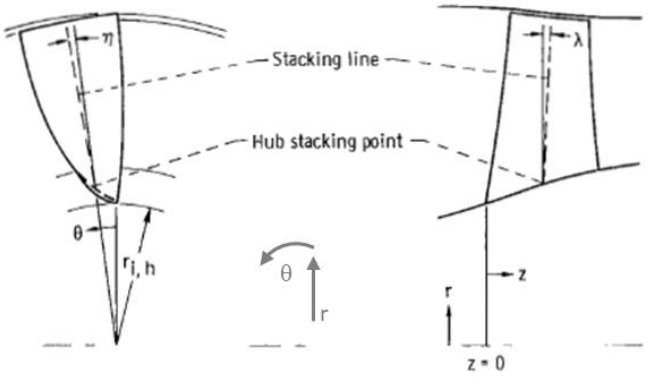

Figure 3.7 Sweep and lean angle definition on a cylindrical coordinate system.

The blade profile sweep and lean, as explained in Sec. 2.6, is with respect to the centre-of-area CA of that particular blade profile. The imaginary axis that passes through all the blade profile centre-of-areas is the stacking line. The intersection between the

stacking axis and the conical surface where the blade profile lies is called stacking point sp. For this reason, the conical coordinates for the centre-of-areas are calculated. Recalling that the centre of area is defined as the moment of area J divided by the total area A_{tot}:

$$CA = \frac{J}{A_{tot}} \tag{3.2.41}$$

The centre-of-area conical coordinates for a blade profile section become:

$$R_{sp} = \frac{\int R dA}{\int dA} \tag{3.2.42}$$

$$\varepsilon_{sp} = \frac{\int \varepsilon dA}{\int dA} \tag{3.2.43}$$

The total area is the region comprised between the leading edge and trailing edge rays at the camberline, and their respective ε angles at the suction surface ss and pressure surface ps. Thus, the above integrals can be independently described as

$$\int dA = \int_{R_{c_{LE}}}^{R_{c_{TE}}} dR \int_{\varepsilon_{ps}(R)}^{\varepsilon_{ss}(R)} R d\varepsilon = \int_{R_{c_{LE}}}^{R_{c_{TE}}} R\left[\varepsilon_{ss}(R) - \varepsilon_{ps}(R)\right] dR \tag{3.2.44}$$

$$\int R dA = \int_{R_{c_{LE}}}^{R_{c_{TE}}} R dR \int_{\varepsilon_{ps}(R)}^{\varepsilon_{ss}(R)} R d\varepsilon = \int_{R_{c_{LE}}}^{R_{c_{TE}}} R^2\left[\varepsilon_{ss}(R) - \varepsilon_{ps}(R)\right] dR \tag{3.2.45}$$

$$\int \varepsilon dA = \int_{R_{c_{LE}}}^{R_{c_{TE}}} dR \int_{\varepsilon_{ps}(R)}^{\varepsilon_{ss}(R)} \varepsilon R d\varepsilon = \frac{1}{2}\int_{R_{c_{LE}}}^{R_{c_{TE}}} R\left[{\varepsilon_{ss}}^2(R) - {\varepsilon_{ps}}^2(R)\right] dR \tag{3.2.46}$$

The above integrals are complex to solve analytically; hence, numerical integration is employed to solve them. Two numerical integration procedures were used and implemented in the 2-D SLC code, a 3- and 5-point formulas, called Simpson's rule and Boole's rule. Simpson's rule assumes a third-degree polynomial ($n = 2$) that passes through 3 points, while Boole's rule considers a fourth-degree polynomial ($n = 4$) across 5 points. It was found that there is no significant difference between these formulations; nonetheless, both numerical integration approaches were coded for robustness purposes. Recalling Simpson's rule:

$$\int_a^b f(x) = \frac{b-a}{6}(F_o + 4F_1 + F_2) = \frac{b-a}{6}[F(x_o) + 4F(x_1) + F(x_2)] \quad \textbf{(3.2.47)}$$

Where $F(x_i)$ represent the Newton-Cotes formula, evaluated at every discretization point, which is calculated as

$$x_i = a + i\frac{(b-a)}{n} \quad \textbf{(3.2.48)}$$

Therefore, the solution of Eq. 3.2.44 to Eq. 3.2.46 using Simpson's rule gives

$$\int_{R_{c_i}}^{R_{c_o}} f(R)dR = \frac{R_{c_o} - R_{c_i}}{6}\left[F(R_{c_i}) + 4F(\frac{R_{c_i} + R_{c_o}}{2}) + F(R_{c_o})\right] \quad \textbf{(3.2.49)}$$

In terms of the Boole's rule, the formulation is

$$\int_a^b f(x) = \frac{(b-a)}{90}(7F_0 + 32F_1 + 12F_2 + 32F_3 + 7F_4) = \frac{(b-a)}{90} \quad \textbf{(3.2.50)}$$

$$[7F(x_o) + 32F(x_1) + 12F(x_2) + 32F(x_3) + 7F(x_4)]$$

Likewise, every Newton-Cotes formula is evaluated at every discretization point, calculated using Eq. 3.2.48. Hence, the solution of Eq. 3.2.44 to Eq. 3.2.46 using Boole's rule is

$$\int_{R_{c_i}}^{R_{c_o}} f(R)dR = \frac{R_{c_o} - R_{c_i}}{90}\left[F(R_{c_i}) + 32F\left(\frac{3R_{c_i} + R_{c_o})}{4}\right) + 12F\left(\frac{R_{c_i} + R_{c_o}}{2}\right) + 32F\left(\frac{R_{c_i} + 3R_{c_o})}{4}\right) + 7F(R_{c_o})\right] \quad \textbf{(3.2.51)}$$

Given the numerical integrations in Eq. 3.2.44 to Eq. 3.2.46 and using Eq. 3.2.42 and Eq. 3.2.43, the R-ε coordinates for the stacking point at each blade-profile section are determined.

In the case the blading is to be swept and leaned, it results convenient to apply the corresponding sweep and lean angles with respect of the each stacking line. This 3-D blade-profile shaping consists in sweeping the stacking points in the z-x plane of the

Cartesian system and leaning them in the r-θ plane of the cylindrical system. Both the sweep and lean angles, as discussed in Sec. 2.2.4, are measured with respect to the hub stacking point. The convention used herein is that the sweep angle is positive in the positive direction of the z-axis, whereas the lean angle is positive in the positive direction of the θ-axis, as shown in Figure 3.6 and Figure 3.7, respectively.

Thus, the stacking point z-coordinate with the deviation from sweep angle is

$$z_{sp} = z_{sp_h} + \left(r_{sp} - r_{sp_h}\right)\tan\lambda \quad \textbf{(3.2.52)}$$

where the subscript *h* accounts for hub. Then, z_{sp_h} and r_{sp_h} are the stacking-point radial and axial coordinates defined as

$$z_{sp_h} = R_{sp_h}\cos\alpha_h \quad \textbf{(3.2.53)}$$

$$r_{sp_h} = R_{sp_h}\sin\alpha_h \quad \textbf{(3.2.54)}$$

For the rest of the blade-elements apart from the hub, the stacking-point radial coordinate r_{sp} is

$$r_{sp} = R_{sp}\sin\alpha \quad \textbf{(3.2.55)}$$

To account for the stacking-point displacement in the circumferential direction, the lean angle causes a tangential deflection δ expressed as

$$\delta = \arcsin\left\{\frac{r_{sp_h}}{r_{sp}}\left(\frac{\tan\eta}{1+\tan^2\eta}\left[\sqrt{\left(\frac{r_{sp}}{r_{sp_h}}\right)^2(1+\tan^2\eta) - \tan^2\eta} - 1\right]\right)\right\} \quad \textbf{(3.2.56)}$$

Hence, the stacking-point θ-coordinate deviated by the lean-induced tangential deflection is

$$\theta_{sp} = \theta_{sp_h} + \delta \quad \textbf{(3.2.57)}$$

where θ_{sp_h} is the stacking point θ-coordinate at the hub determined as

$$\theta_{sp_h} = \frac{\varepsilon_{sp_h}}{\sin\alpha_h} \quad \textbf{(3.2.58)}$$

The final x-y-z coordinates for the blade-element camberline and surfaces are fully determined with the following transformation relationship between Cartesian and conical system

$$x = R\sin\alpha\cos\left(\frac{\varepsilon}{\sin\alpha} + \theta_{c_i} - \theta_{sp_h}\right) \quad \textbf{(3.2.59)}$$

$$y = R\sin\alpha\sin\left(\frac{\varepsilon}{\sin\alpha} + \theta_{c_i} - \theta_{sp_h}\right) \quad \textbf{(3.2.60)}$$

$$z = z_{sp} - \left(R_{sp} - R\right)\cos\alpha \quad \textbf{(3.2.61)}$$

Where θ_{c_i} is the θ-coordinate of the camberline leading edge defined as

$$\theta_{c_i} = \theta_{sp_h} + \delta - \frac{\varepsilon_{sp}}{\sin\alpha} \quad \textbf{(3.2.62)}$$

Figure 3.8 a) displays the meridional projection of the blade rows in the 2-D SLC compressor simulator for the NASA two-stage fan [246], whilst Figure 3.8 b) shows the 3-D blade-element geometry resulted from the conical blade-element-layout method for the NASA two-stage fan. A mid-span section for the two fan stages can be observed in Figure 3.9, where the blade-element camberlines and surfaces are laid out on a conical surface that approximates the stream surface.

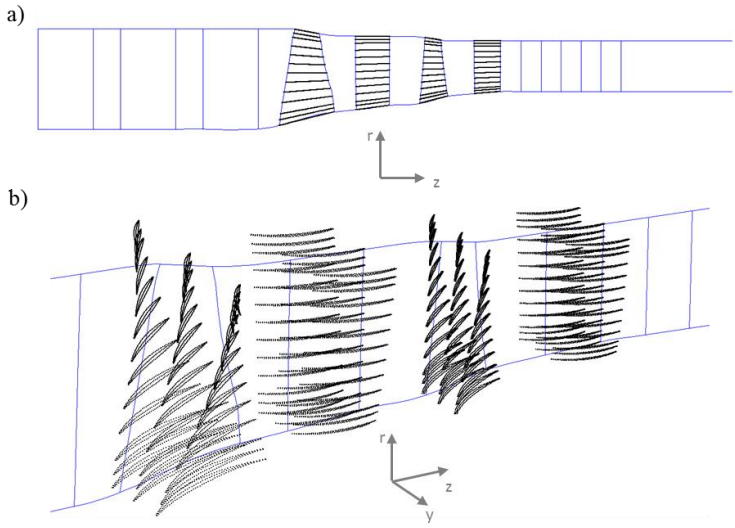

Figure 3.8 Blade profile sections determined with the conical blade-element-layout method implemented into the 2-D SLC code for the NASA two-stage fan [246]**. a) Meridional view. b) 3-D view.**

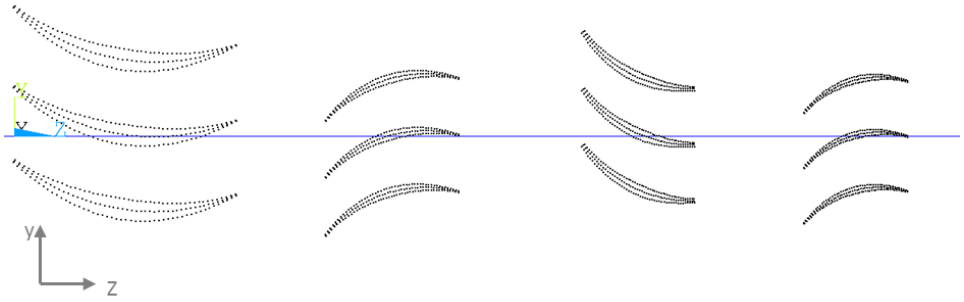

Figure 3.9 Blade-to-blade projection for mid-span blade-element sections obtained with the conical blade-element-layout method implemented into the 2-D SLC code for the NASA two-stage fan [246].

3.2.3 Streamline Curvature Modification

In Sec. 2.3.2 the effect of the blade body forces in the REE was discussed. Because of the inherent two-dimensionality of the SLC methodology, any geometrical blade lean in the r-θ plane is not visible in the meridional r-z plane. The introduction of the blade lean in SLC requires the REE to consider an additional body force induced by the lean itself to capture its effects. When the blade, and hence the blade-elements on the streamlines, are swept by angle λ, the quasi-orthogonal lines are shifted from the radial direction by the same amount. If the quasi-orthogonal lines are swept, the leaned blade surface intersection with the r-θ plane deviates from η to $\breve{\eta}$, expressed as

$$\breve{\eta} = \operatorname{atan}(\tan\eta + \tan\breve{\alpha}\tan\lambda) \tag{3.2.63}$$

Since the absolute flow angle α on a stream surface is not the same as the projected absolute flow angle $\breve{\alpha}$ on a blade-to-blade plane, the relationship between both angles is given by

$$\breve{\alpha} = \operatorname{atan}\left(\frac{\tan\alpha - \sin\varphi\tan\eta}{\cos\varphi}\right) \tag{3.2.64}$$

Provision was made so that every quasi-orthogonal has an individual sweep and lean angle depending on the blade geometric values. Following Jackson *et al*. [247] and Templalexis [118] aspects upon force terms implementation within the REE, the lean-induced body forces F were divided in normal pressure F_p and drag forces D as presented in Eq. 2.3.34. The pressure forces act normal to the blade surfaces in the

three directions of any coordinate system. The drag force acts opposite to the absolute flow vector representing the dissipative force from the surface shear. As stated in Sec. 2.3.2, it is the circumferential normal-pressure force F_{p_θ} the component affecting the REE. Then, the components in a cylindrical-coordinate system of the resultant lean-induced body-force from the whirl normal-pressure and drag forces are

$$F_r = -F_{p_\theta} \tan\eta - D\cos\alpha\sin\varphi \quad \textbf{(3.2.65)}$$

$$F_z = -F_{p_\theta} \tan\breve{\alpha} - D\cos\alpha\cos\varphi \quad \textbf{(3.2.66)}$$

$$F_\theta = F_{p_\theta} - D\sin\alpha \quad \textbf{(3.2.67)}$$

The whirl normal-pressure force from Eq. 3.2.67 is substituted in the radial and axial body-force components, giving

$$F_r = -F_\theta \tan\eta - D(\sin\alpha\tan\eta + \cos\alpha\sin\varphi) \quad \textbf{(3.2.68)}$$

$$F_z = -F_\theta \tan\breve{\alpha} - D(\sin\alpha\tan\breve{\alpha} + \cos\alpha\cos\varphi) \quad \textbf{(3.2.69)}$$

The whirl component of the body force remains unchanged in a streamline coordinate system, whereas the body-force component transformations to the streamline m and quasi-orthogonal q directions are given by

$$F_m = F_z\cos\varphi + F_r\sin\varphi \quad \textbf{(3.2.70)}$$

$$F_q = F_r\cos\lambda + F_z\sin\lambda \quad \textbf{(3.2.71)}$$

Substituting Eq. (3.2.68 and Eq. (3.2.69 in the meridional transformations of Eq. (3.2.70 gives

$$_m = -F_\theta\tan\alpha - D\csc\alpha \quad \textbf{(3.2.72)}$$

Similarly, substituting Eq. (3.2.68, Eq. (3.2.69, and the relation between η and $\breve{\eta}$ given in Eq. 3.2.63 into Eq. (3.2.71, the quasi-orthogonal transformation is

$$F_q = -F_\theta\tan\breve{\eta}\cos\lambda - D[\sin\alpha\tan\breve{\eta}\cos\lambda + \cos\alpha\sin(\varphi+\lambda)] \quad \textbf{(3.2.73)}$$

Following the procedure established in Sec. 2.3.2, the quasi-orthogonal body-force is algebraically added to the coefficient C of the solution of the second-order differential equation that describes the full REE. Therefore, C gets redefined as

$$C = \left[-\frac{V_\theta}{r}\frac{d(rV_\theta)}{ds} - 2\omega V_\theta \cos\lambda + \frac{dI}{ds} - T\frac{dS}{ds} \right.$$
$$+ T\frac{dS}{dm}(\sin(\varphi-\lambda)\cos^2\beta - \tan\lambda \sin\beta\cos\beta) \qquad \textbf{(3.2.74)}$$
$$\left. - F_\theta \tan\breve{\eta}\cos\lambda - D[\sin\alpha\tan\breve{\eta}\cos\lambda + \cos\alpha\sin(\varphi+\lambda)] \right]$$

Substituting Eq. 3.2.67 in Eq. 3.2.74 to express C in terms of the whirl normal-pressure force, gives

$$C = \left[-\frac{V_\theta}{r}\frac{d(rV_\theta)}{ds} - 2\omega V_\theta \cos\lambda + \frac{dI}{ds} - T\frac{dS}{ds} \right.$$
$$+ T\frac{dS}{dm}(\sin(\varphi-\lambda)\cos^2\beta - \tan\lambda \sin\beta\cos\beta) \qquad \textbf{(3.2.75)}$$
$$\left. - F_{p_\theta} \tan\breve{\eta}\cos\lambda - D\cos\alpha\sin(\varphi+\lambda) \right]$$

3.3 Shock- Structure and Loss Model

3.3.1 Overview

Previous empirical and simplified shock models could not accurately estimate the passage-shock position, yielding to an incorrect peak suction-surface relative Mach number and deviation in the flow field expansion, and hence, an inaccurate shock-loss estimation. For this reason, a novel physics-based shock- structure and loss model was developed in FORTRAN90 and implemented into the 2-D SLC axial-flow fan/compressor performance simulation software (SOCRATES) [14,17,31]. The current shock model illustrated in the flow chart of Figure 3.10 analytically solves the shock-system structure to accurately predict the associated losses at unstarted and

started flow for arbitrary blade-row sections using an iterative method. In this way, the relative total pressure losses due to the shock-configuration strength are calculated for design and off-design conditions, offering a more realistic fan and compressor performance prediction for the transonic working range.

The analytical shock model developed in this research works by laying out the bow wave and the passage shock. As the bow-wave is fully defined from the detached-bow shock, its relative total-pressure losses can be integrated to find a corresponding bow-wave loss-coefficient. The choking-incidence method in Sec. 3.4.2 determines whether the blade passage is choked or not to establish the corresponding dual passage-shock pattern compound of the first passage-shock and a choked-induced oblique-shock. A comprehensive flow expansion that considers potential expansion fan and pre-compression is computed ahead of the passage-shock, calculating the relative Mach numbers upstream of it and determining the mass-averaged relative total pressure loss. Depending on the second passage-shock location, a second flow-expansion is computed accordingly, determining the associated relative total-pressure loss. The overall relative pressure loss is then conveyed to an iterative approach to calculate the location of the second passage-shock as a function of the back stagnation condition. Utilizing a secant method, an updated axial location for the choked-induced shock is established to start a new iteration cycle that replays the overall process until the error tolerance is satisfied.

Not only was the transonic span with inlet relative supersonic conditions resolved, but also the blade section with subsonic inlet relative supercritical conditions in contrast to the historical shock models that did not consider this region. A simple analytical but useful model was coupled to the previous physics-based transonic shock and structure - loss model within the context of the 2-D SLC axial-flow fan/compressor performance simulation software [14,17,31], as shown in the flow chart of Figure 3.10.

On the whole, the overall shock-wave losses are determined per streamline for that blade-row span that undergoes relative subsonic supercritical and relative supersonic velocities at the inlet. The predicted overall shock-wave-induced relative total-pressure decay per streamline is then added up to each profile-loss coefficient to compute the overall total-loss coefficient $\overline{\omega'}$ at every radial position.

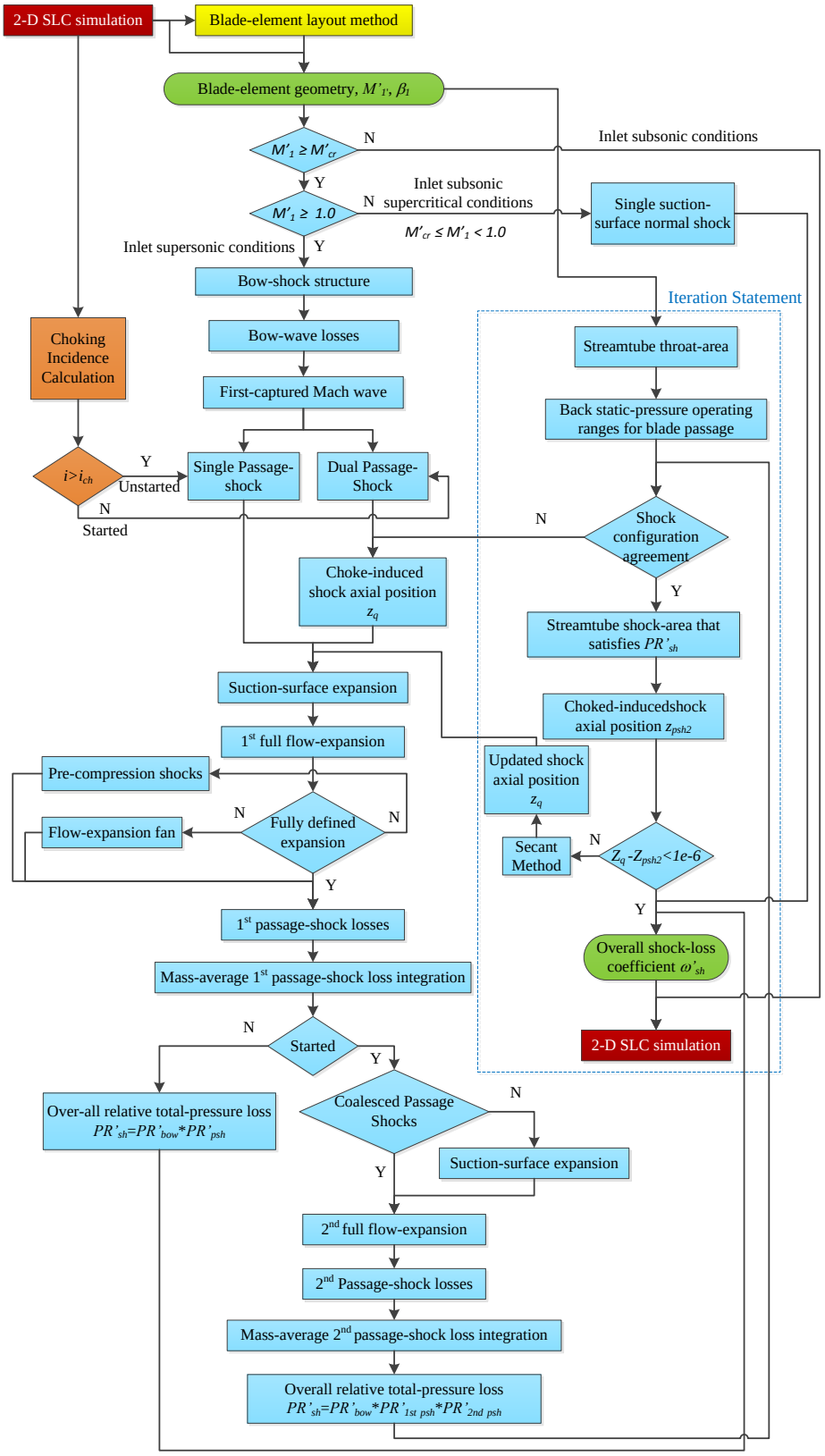

Figure 3.10 Flow-chart diagram for the current shock- loss and structure model developed and implemented into the 2-D SLC axial-flow fan/compressor performance simulator.

3.3.2 Subsonic Supercritical Conditions

Even at inlet relative subsonic speeds, shock-wave formation can develop on the blade suction surface. Because of inlet relative subsonic Mach numbers close to unity, somewhere on the suction surface and near the leading edge, the relative Mach number can become sonic due to the curvature-induced turning that accelerates the flow. Further increase of the free-stream relative subsonic Mach number forms forthwith a pocket of relative supersonic flow that eventually terminates in a normal shock-wave producing a loss in relative total-pressure, as illustrated in Figure 3.11. From compressible-flow theory [248], the free-stream Mach number for which sonic flow is first encountered on an aerofoil surface is the critical Mach number M'_{cr}.

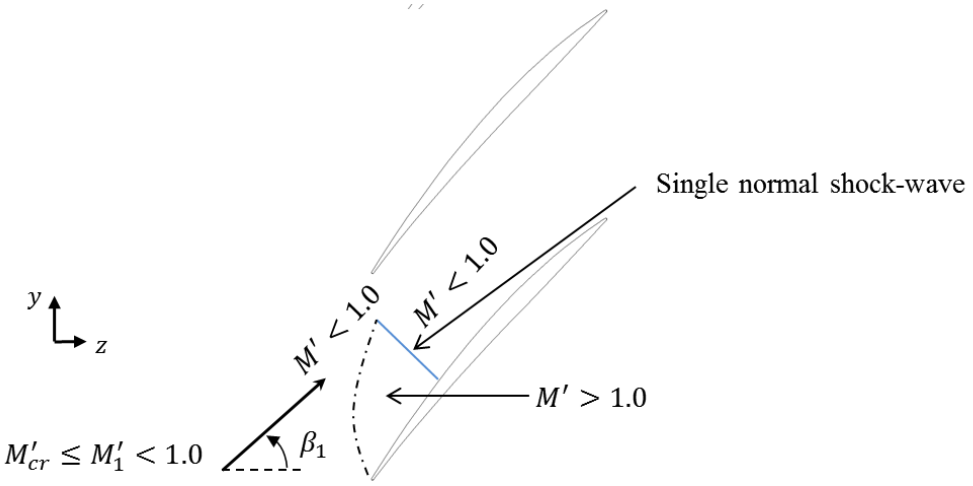

Figure 3.11 Inlet relative subsonic supercritical condition for blade rows.

Conventional aerofoil theory resolves a pressure coefficient Cp at every surface point, which becomes negative when the flow velocity is non-zero. The pressure coefficient at any surface point for a given inlet relative Mach number is

$$Cp = \frac{2}{\gamma {M'_1}^2}\left\{\left[\frac{1+\frac{1}{2}(\gamma-1){M'_1}^2}{1+\frac{1}{2}(\gamma-1)M'^2}\right]^{\frac{\gamma}{\gamma-1}} - 1\right\} \qquad \textbf{(3.3.1)}$$

The surface point with the maximum local Mach number has as well the minimum local static-pressure. Similarly to M'_{cr}, a critical pressure Cp_{cr} coefficient can be defined for the case of the flow becoming sonic for the first time.

The overall shock-loss model in Figure 3.10 identifies the type of inlet conditions at every streamline with respect of the inlet relative critical Mach number so that the appropriate model to resolve the flow can be established. Thus, the method by Anderson [248] to determine the critical Mach number in aerofoils was implemented and adapted for blade-row profiles.

If a local Mach number equals to unity is used in Eq. 3.3.1, the pressure coefficient corresponds to the critical condition for which the flow accelerate to sonic conditions on the suction surface, becoming

$$Cp_{cr} = \frac{2}{\gamma {M'_{cr}}^2}\left\{\left[\frac{2+(\gamma-1){M'_{cr}}^2}{\gamma-1}\right]^{\frac{\gamma}{\gamma-1}} - 1\right\} \quad \textbf{(3.3.2)}$$

The relation $Cp_{cr} = f(M'_{cr})$ from Eq. 3.3.2 is solved by using any of the compressibility-corrections available in the literature to determine the compressible Cp from known incompressible pressure distributions, such as

$$Cp = \frac{Cp_0}{\sqrt{1-{M'_1}^2}}\ ; Prandtl - Glauert \quad \textbf{(3.3.3)}$$

$$Cp = \frac{Cp_0}{\sqrt{1-{M'_1}^2} + \frac{Cp_0}{2}\left(\frac{{M'_1}^2}{1+\sqrt{1-{M'_1}^2}}\right)}\ ; Karman - Tsien \quad \textbf{(3.3.4)}$$

$$Cp = \frac{Cp_0}{\sqrt{1-{M'_1}^2} + Cp_0\left\{\frac{{M'_1}^2\sqrt{1-{M'_1}^2}}{2}\left[1+\left(\frac{\gamma-1}{2}\right){M'_1}^2\right]\right\}}\ ; Laitone \quad \textbf{(3.3.5)}$$

where Cp_0 is the minimum pressure coefficient at zero lift. According to selected NACA-aerofoil experimental distributions, Cp_0 is determined as a function of the profile relative thickness (t_{max}/c). Forasmuch as the fan-blade and compressor-blade profiles are relatively slender in comparison to those from the NACA wing-aerofoils, an almost-constant value of -0.2 is obtained for every blade-row section. Nevertheless, the actual relative thickness was computed for every blade section defined on the computed

streamlines to determine the specific zero-lift pressure-coefficient based on NACA experimental data for thin aerofoils.

The three compressibility-correction rules from Eq. 3.3.3 to Eq. 3.3.5 were programmed and compared without any significant final impact on the shock-loss coefficient radial distribution for the inlet relative subsonic super-critical span. Nonetheless, the Prandtl-Glauert and Karman-Tsien rules underpredict the experimental data, despite the latter attempts to consider the non-linearity of the flow. Being more conservative, Laitone's rule was the preferred equation to be used in the computation of M'_{cr} since it takes into account the non-linear flow aspects resulting in a slight overprediction of the measured data.

Substituting Cp_{cr} in Laitone's rule and in set with Eq. 3.3.2 yields to a two-equation system reduced to

$$\frac{Cp_0}{\sqrt{1-{M'_{cr}}^2}+Cp_0\left\{\frac{{M'_{cr}}^2\sqrt{1-{M'_{cr}}^2}}{2}\left[1+\left(\frac{\gamma-1}{2}\right){M'_{cr}}^2\right]\right\}} = \frac{2}{\gamma{M'_{cr}}^2}\left\{\left[\frac{2+(\gamma-1){M'_{cr}}^2}{\gamma-1}\right]^{\frac{\gamma}{\gamma-1}}-1\right\} \quad \textbf{(3.3.6)}$$

Eq. 3.3.6 is solved using an iterative secant-method to determine M'_{cr}. In other words, the iterative secant-method finds the critical Mach number by intersecting the critical pressure coefficients from Eq. 3.3.2 and the compressibility correction.

For an arbitrary blade-row profile on a streamline, if $M'_1 < M'_{cr}$, the flow is subsonic everywhere in the passage and no shock-loss computation is carried out to continue normally with the 2-D SLC analysis continues normally.

In the case of $M'_{cr} \leq M'_1 < 1.0$, the inlet relative conditions are still subsonic but supercritical. To resolve the flow within this regime, the blade row is discretized in axial intra-stations, for which the relative Mach number is determined in the meridional plane, assuming that the flow traverses parallel to the suction surface with zero-

deviation. The peak relative suction-surface Mach number is recognized and a normal shock-wave is placed at this location. The relative total-pressure recovery is thence calculated using Eq. 2.4.17 from normal-shock theory to compute the shock-loss coefficient as in Eq. 2.6.1.

For the fully inlet relative supersonic conditions, namely $M'_1 \geq 1.0$, the flow and shock-wave situation complicates substantially. The following sections from Sec. 3.3.3 to Sec. 3.3.9 propose a methodology that resolves the shock-wave structures and its associated losses for a more accurate fan and compressor performance prediction.

3.3.3 Supersonic Flow Description

To simplify the shock-system analysis, a 2-D blade-element approach is used as in the common practice for transonic-compressor shock-wave modelling [120], which is applied to every SLC compressor stream surface computed. The main intention of this model is to provide a physics-based shock-system structure in its entirey to compute more accurately the overall-shock-induced relative total-pressure loss. By no means this shock-loss model neither attempts to resolve the blade boundary-layer blockage effect nor intends to include the SWBLI-induced viscous losses. However, due to the physical ground of the shock-loss model developed herein, it can set the foundations to be coupled in the future with blade boundary-layer models.

The current analytical shock-loss model resolves the shock structure and associated losses for every transonic stream surface at design and off-design operating conditions from stall to choke, applicable to any arbitrary cascade or blading aerofoil geometry. This means that this shock model is not only limited to unchoked operations as the model of Bloch *et al*. [34], but also computes the shock configuration and losses at choked operating conditions. The shape, location and losses of the shock configuration are not only sensitive to the streamline inlet conditions and blade-element geometry, but also get updated within the 2-D SLC method for every REE and mass flow conservation iteration loops.

Insomuch as the upstream flow is moving at supersonic speeds in a relative frame of reference, the required detached bow-shock was considered for both, unchoked and

choked flows. The detached bow-shock is analytically modelled utilizing the hyperbola-approximation method from Moeckel [180]. The detached bow-shock is aligned with the inlet relative flow angle with vertex on the stagnation streamline. Because the infinite bow-wave portion interacts with the stagnation streamline, the flow undergoes a small upwards deflection that shifts the latter as a function of the operating point. In contrast to the shock-loss model by Bloch *et al*. [34] where the stagnation-streamline deflection was treated empirically, the current model uses an analytical model suggested by Miller and Hartmann [208]. The bow-wave-induced losses are calculated as per the method by Klapproth [206] without any correction for the leading-edge radius, as the discretization method used suffices to capture the required loss across the bow-wave central part.

During unstarted flows, a single-shock structure is considered consisting in the detached bow-shock, with a bow-wave portion extending to infinity and a passage-shock segment confined between the stagnation streamline and the suction blade profile as seen in Figure 3.12.

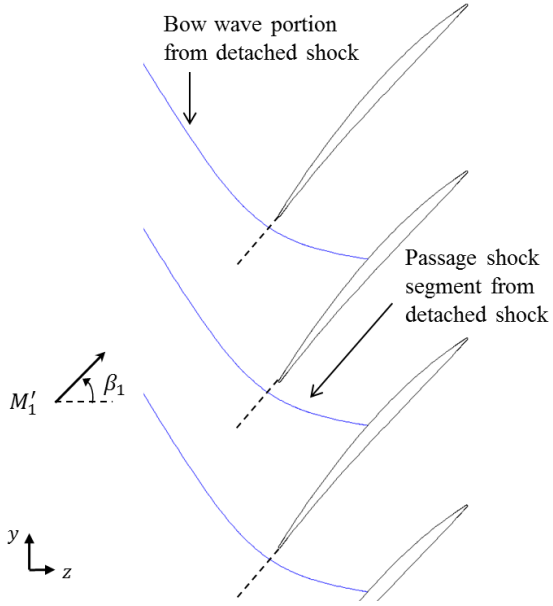

Figure 3.12 Single-shock structure for unchoked blade-elements or unstarted blade-passages consisting only in the detached bow-shock.

The blade passage was assumed to be an isentropic convergent-divergent nozzle which can potentially choke, leading to a second shock that produces a step change in the flow

properties to match the boundary conditions. Hence, during started flows, a dual-shock configuration is considered compound of the detached bow-shock with the bow-wave extending to infinity, the remaining passage-shock portion and a second choke-induce shock-wave. Koning *et al*. [152,153], and Boyer and O'Brien [13,35,36] considered this second shock to be normal to the flow. However, 3-D CFD RANS simulations for the NASA Rotor 67 [40] evidenced that the second shock is not necessarily normal to the relative flow direction as seen in Figure 3.13 for different radial positions. Since the passage is not a symmetric channel with respect to the midchannel camberline and the relative velocity is not constant in the normal direction to the flow, it is not surprising that any shock arising to decelerate the flow is oblique to the flow. For this reason, the current shock-loss model considered the choke-induce shock as oblique at an angle that depends on the operating condition.

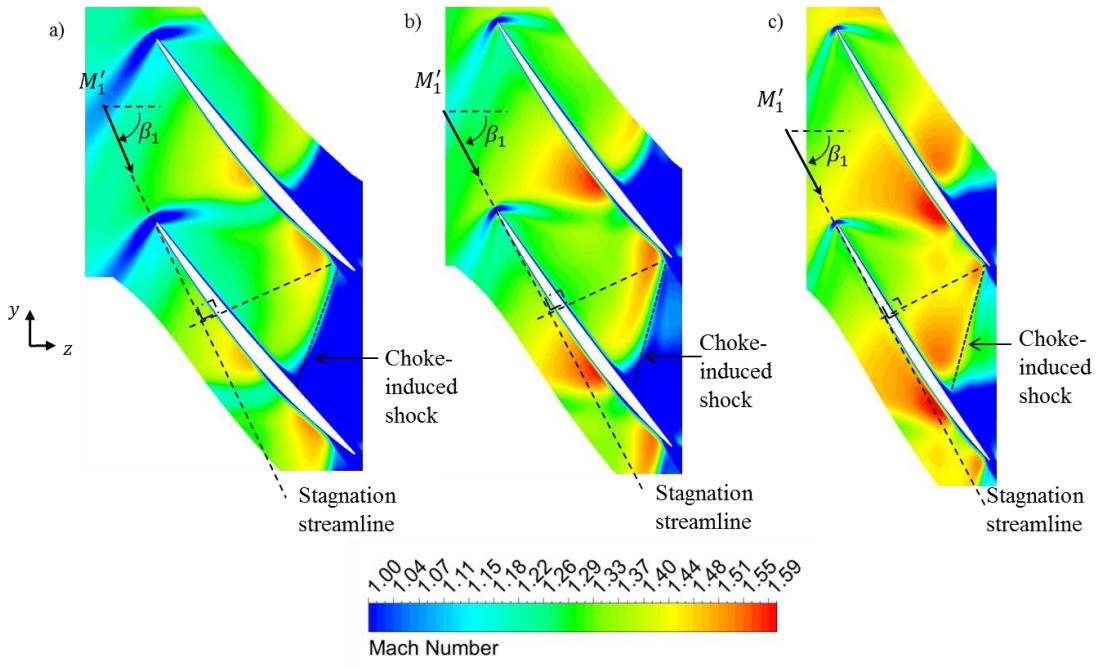

Figure 3.13 3-D CFD RANS simulation for the NASA Rotor 67 [40] **at 100% of design speed and w=34.45 kg/s. a) 60% hub-to-tip span. b) 70% hub-to-tip span. c) 80% hub-to-tip span.**

Conversely to the most recent state-of-the-art model by Boyer and O'Brien [13,35,36], the second shock position is not imposed in the current shock-loss model. Rather, the back static pressure determines the location of the choke-induced oblique shock within a domain limited by the trailing edge and the throat. As the operating point moves from

choke to stall, the back static-pressure (and incidence) increases, pushing the second shock upstream towards the throat as less flow acceleration is required to meet the outlet condition. Eventually, the second passage-shock might intersect the detached-shock passage-shock portion, depending on the form, location and orientation of the latter. Boyer and O'Brien [13,35,36] completely discarded this effect, whereas the present shock-loss model takes into account the coalescence of the detached shock passage-shock portion with the second oblique-shock.

It is prominent to consider this phenomenon as this coalescing effect defines the correct shape of the first passage shock, and hence the expansion extension with accurate relative Mach numbers upstream of the compound passage-shock. Having a correct velocity distribution in the circumferential direction certainly leads to a more accurate shock-loss estimation. The importance of capturing this effect becomes even greater as its occurrence is more often than is thought as a result of the combination between inlet and outlet conditions.

If the choke-induced shock does not intersect the first passage shock, this prolongs till the suction surface as shown in Figure 3.14 a). As the back static-pressure increases, the second shock moves upstream and can stand just immediately behind of the first passage-shock impingement on the suction surface. Further outlet static-pressure rise makes the choke-induced shock to intersect the first passage-shock at a finite distance out as seen in Figure 3.14 b). Both passage shocks, first and second, coalesce so that the hyperbolic shape of the first passage-shock ends in a nearly-normal strong shock that extends till the suction blade.

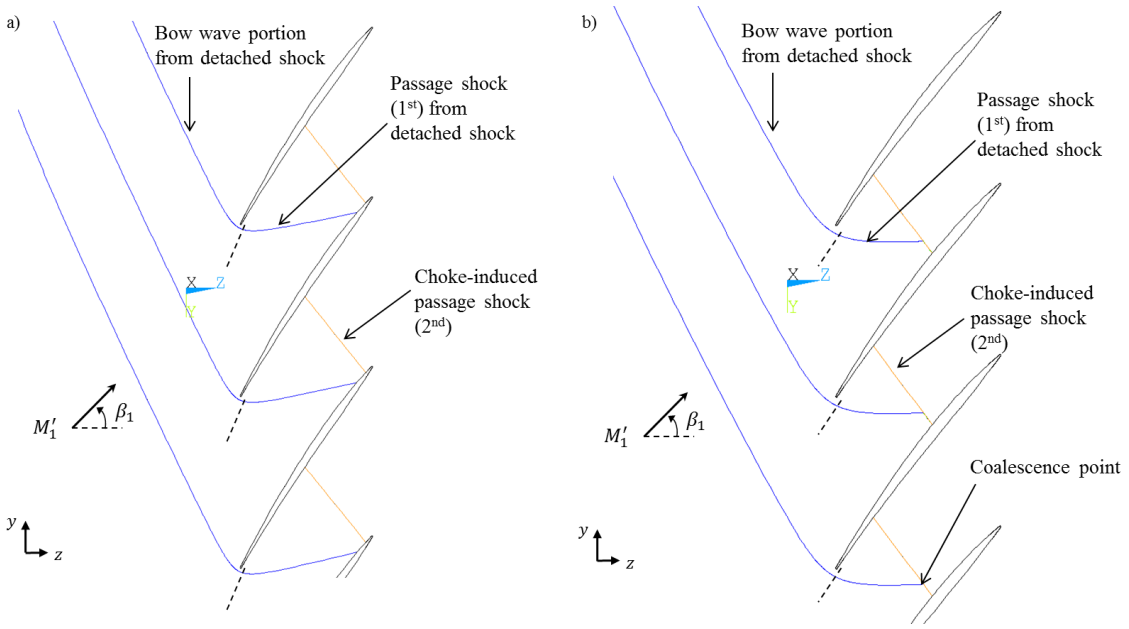

Figure 3.14 Dual-shock structure for choked blade-elements or started blade-passages consisting in a detached bow-shock and a choke-induce shock. a) No intersection between the first and second passage-shocks b) Intersection between the first and second passage-shocks.

Once the shock configuration is established, the gradual flow expansion of zone V (as seen in Figure 2.33 is resolved to obtain the circumferential distribution of relative Mach numbers upstream of the passage. The implementation of the expansion model is such that it is detected if there is any fan expansion or pre-compression arising at zone V that can affect the relative velocity distribution upstream of the passage shock. If so, the fan expansion or pre-compression is computed accordingly along their corresponding characteristics. Fan expansion occurring at zone V for high blade-loadings is an extension of the fan expansion from zone III, as a result of the waves trying to expand the flow parallel to the suction surface over a very short chord length. The pre-compression shocks occur after the first expansion wave extending over a suction-surface ramp, coalescing in the leading-edge of the adjacent blade. Pre-compression can take place intentionally due to pre-defined pre-compression aerofoils or it can develop over a very little region as an effect from the suction-surface curvature. The intent of the pre-compression blade-profile sections is to minimize shock losses by introducing a series of weak shocks instead of a strong passage shock.

Having the relative Mach number profile upstream of the passage shock and utilizing oblique shock-theory, the relative total-pressure drop distribution across the passage shock is computed. These values are then mass-averaged in the tangential direction to calculate then the passage shock-loss coefficient. This methodology works straight as discussed for blade-elements or operating conditions where the incidence is higher than the choking incidence, whose computation is given in Sec 3.4.2. Nonetheless, for choked blade-elements, the same methodology is conducted within a novel iterative method, detailed in Sec. 3.3.9, to correctly position the second passage-shock. If a stream surface, however, is identified as choked within a 2-D SLC analysis, its incidence and mass flow need to be adjusted to the choking values while still satisfying the full REE and mass flow conservation. This was attained with a novel numerical algorithm presented in Sec. 3.4.3 and Sec. 3.4.4.

3.3.4 Detached Bow-Shock

The detached bow-shock is essential to represent the overall shock configuration. The complete detached bow-shock is laid out by approximating its shape and location according to the Moeckel's method [180]. The detached bow-shock structure approximation relies on 2 fundamental assumptions: (1) The bow shock is assumed to be hyperbolic and asymptotic to the free-stream Mach wave. (2) The sonic line that divides the pocket of subsonic flow and the outer supersonic flow is considered to be straight and inclined as a function of the inlet relative Mach number. Figure 3.15 sketches the hyperbolic representation for the detached bow-shock and the free-stream Mach waves on a blade-row stream surface. Note that the detached bow-shock has its vertex on the stagnation streamline that is parallel to the velocity direction, dividing the detached bow-shock in an infinite bow wave and a confined passage shock.

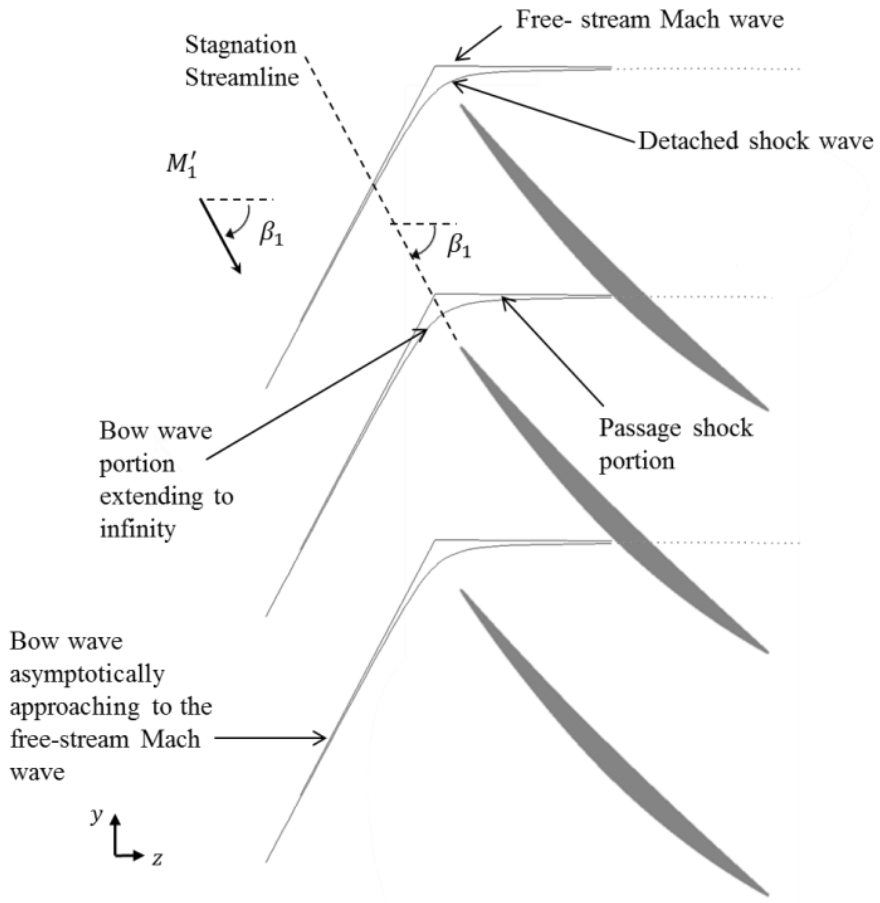

Figure 3.15 Hyperbolic approximation for a detached bow-shock on a blade-row stream surface.

The hyperbola approximation describing the detached bow-shock structure is shown in Figure 3.16, where the flow field and parameters considered are detailed. Forasmuch as the detached shock is normal to the incoming flow, the hyperbola-shaped bow-shock is assumed to lie on a local frame of reference aligned to the flow. In consequence, the overall shock-system model is rotated by an angle β_1 around the hyperbola centre, which is the intersection point of its asymptotes. Thus, the hyperbola centre and vertex are situated at $y_o' = 0$ and $y_v' = 0$, respectively, on the relative frame of reference. For convenience all the shock structures herein are represented in a local coordinate system aligned with the inlet flow with z'-axis origin at $z_o' = 0$.

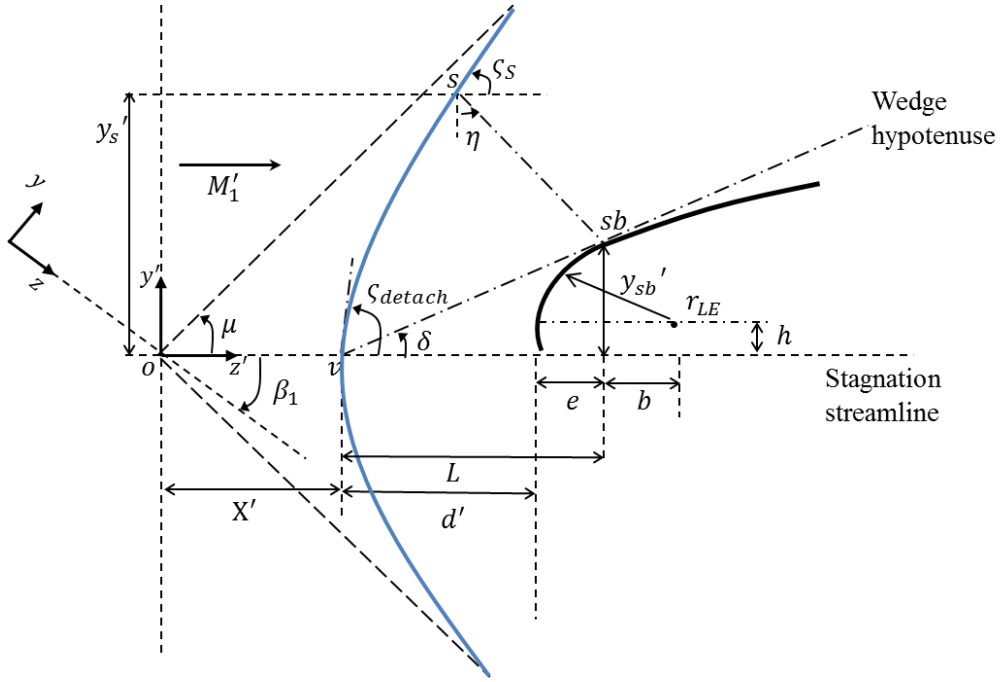

Figure 3.16 Hyperbolic approximation for a detached bow-shock ahead of a blade-profile leading-edge.

As discussed in Sec. 2.4.3, the central part of a detached shock gives a strong shock solution, while farther out the shock is considered to be weak. The shock angle that corresponds to the central part of a detached hyperbola-shaped bow-shock is

$$\varsigma_{detach} = \frac{1}{2}\operatorname{acos}\left\{\frac{1}{\gamma}\left[\frac{\gamma+1}{2} - \cos 2\mu - \sqrt{\gamma+1}\sqrt{\left(\frac{\gamma+1}{2} - \cos 2\mu\right)^2 + \frac{\gamma(3-\gamma)}{4}}\right]\right\} \qquad \textbf{(3.3.7)}$$

The detached bow-shock shape is a unique function of the inlet relative Mach number M_1'. As described in Sec. 2.4.3, a shock-wave that is detached is not anymore a straight oblique-shock as the deflection angle caused by the blade profile exceeds the maximum deflection angle. Thus, the maximum deflection angle for which the bow shock becomes detached is

$$\delta_{detach} = \operatorname{atan}\left\{\tan\varsigma_{detach}\left[\frac{(\gamma+1)M_1'^2}{2(M_1'^2\sin^2\varsigma_{detach} - 1)} - 1\right]\right\}^{-1} \qquad \textbf{(3.3.8)}$$

For detached-shock analysis, a wedge is assumed to exist such that the detached bow-shock is attached to it, as drawn in Figure 3.16 . The wedge sharp nose is located at the middle of the central portion of the shock, which is the hyperbola vertex. The wedge

hypotenuses are required to be tangent to the blade-profile leading edge circle with a radius r_{LE}. The wedge tip moves upstream or downstream in the flow direction always tangent to the blade leading edge so that the wedge half-angle δ is the maximum deflection angle to detach the bow shock. Yet, to guarantee that the bow shock is fully detached, the wedge half-angle is assumed to be [180]

$$\delta = \delta_{detach} + 1° \tag{3.3.9}$$

Even if the inlet relative Mach number is increased as an intent of extending the maximum deflection-angle limit, the bow wave never attaches to the blade-element profile due to its finite leading-edge bluntness. Though, as the inlet relative Mach number turns larger, the detachment distance shortens and the bow wave approaches to the leading edge, reducing the shock angle and strength, and thus, increasing its obliqueness. If $M_1{}'$ is further increased, eventually the passage-shock segment of the hyperbola-approximated detached bow-shock does not intersect anymore the suction surface of the adjacent blade, as observed in Figure 3.17. Admittedly, at these high-speed cases, it is very likely for the passage to become choked, resulting in a dual-shock structure, where the first passage-shock is truncated by the choke-induced shock as seen in Figure 3.17. The shock angle and location of the choke-induced shock is treated separately in Sec. 3.3.9

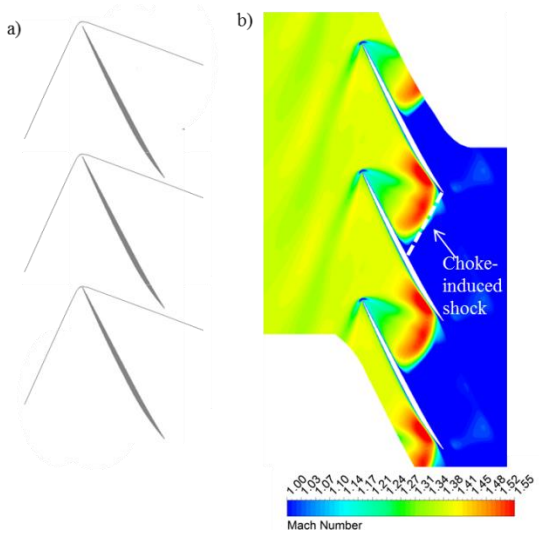

Figure 3.17 Hyperbolic approximation for a highly-oblique detached bow-shock of the NASA Rotor 67 [40] **at 95% span at 100% of design speed and near-choke operating point. a) 2-D SLC simulation. b) 3-D CFD simulation.**

The intersection between the wedge and leading edge gives the sonic point sb. A normal line to the tangent at point sb forms the sonic line. The sonic line in set with the bow-shock central part bounds the region to contain the subsonic flow, whereafter, the flow becomes supersonic. Thus, as mentioned in Sec. 2.4.3, the relative Mach number on the sonic line is unity, and this characteristic is the first wave of the leading-edge expansion

The y'-axis distance between the bow-wave vertex and the point sb is calculated from Figure 3.18, resulting in the following trigonometric relation

$$y_{sb}{}' = \cos\delta = \cos(\delta_{detach} + 1°) \qquad \textbf{(3.3.10)}$$

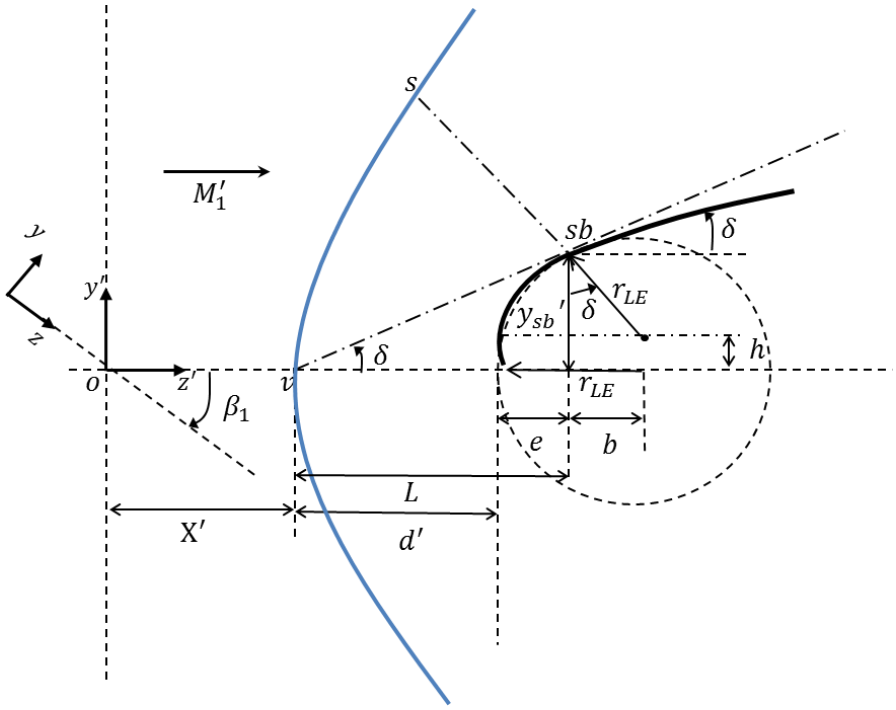

Figure 3.18 Parameters for the calculation of the detachment distance in a hyperbolic approximation for a bow wave.

The intersection between the sonic line and the bow-shock gives the sonic point s. The shock angle at point s for which the downstream flow becomes sonic is determined by

$$\varsigma_s = \operatorname{asin}\sqrt{\frac{1}{2\gamma}\left[\frac{\gamma-3}{2}\sin^2\mu + \frac{\gamma+1}{2} + \sqrt{4\gamma\sin^4\mu + \left(\frac{\gamma-3}{2}\sin^2\mu + \frac{\gamma+1}{2}\right)^2}\right]} \qquad \textbf{(3.3.11)}$$

Therefore, the deflection angle at point s becomes

$$\delta_s = \operatorname{atan}\left\{\tan\varsigma_s\left[\frac{(\gamma+1)M_1'^{\,2}}{2(M_1'^{\,2}\sin^2\varsigma_s - 1)} - 1\right]\right\}^{-1} \quad \textbf{(3.3.12)}$$

To obtain the relative total-pressure ratio at the sonic point, the sonic line slope needs to be determined. The sonic line inclination is equal to the shock angle at the sonic line centroid of mass c, computed as

$$\varsigma \quad = \operatorname{atan}\sqrt{\frac{4\left(M_1'^{\,2} - 1\right)\operatorname{atan}^2\varsigma_s - 3}{M_1'^{\,2} - 1}} \quad \textbf{(3.3.13)}$$

Using Eq. 2.4.23 for the total-pressure ratio of an oblique shock wave and given the shock angle at the centroid of mass, the relative total-pressure recovery between the inlet and the sonic line at the sonic point *s* is

$$\Pi'_{s1_c} = \left.\frac{P'_s}{P'_1}\right|_c = \left[\frac{(\gamma+1)M_1'^{\,2}\sin^2\varsigma_c}{(\gamma-1)M_1'^{\,2}\sin^2\varsigma_C + 2}\right]^{\frac{\gamma}{\gamma-1}}\left[\frac{(\gamma+1)}{2\gamma M_1'^{\,2}\sin^2\varsigma_c - (\gamma-1)}\right]^{\frac{1}{\gamma-1}} \quad \textbf{(3.3.14)}$$

Having the relative total-pressure recovery at the sonic point, the distance y_S between the z'-axis and point s is determined through the continuity relation for the flow traversing the sonic line. Inasmuch as the total temperature and total pressure are constant along every streamline downstream of the bow shock, the simplified version of the continuity can be written as

$$y_s{}' = y_{sb}{}'\frac{1}{1 - \dfrac{\cos\eta}{\Pi'_{s1_c}\dfrac{A_1}{A^*}}} \quad \textbf{(3.3.15)}$$

where η is the angle between the sonic line and the y'-axis calculated as the arithmetic mean between the deflection angle to detach the bow-shock and the deflection angle at the sonic point s; this is

$$\eta = \frac{1}{2}(\delta + \delta_s) = (\delta_{detach} + 1° + \delta_s) \quad \textbf{(3.3.16)}$$

The ratio A_1/A^* is the area contraction to isentropically decelerate the supersonic free-stream to sonic conditions calculated using the area-velocity relationship from Eq. 2.5.27 as,

$$\frac{A_1}{A^*} = \frac{1}{M_1'}\left[\frac{1+\frac{\gamma-1}{2}M_1'^{\,2}}{(1+\frac{\gamma-1}{2})^{\frac{1}{\gamma-1}}}\right]^{\frac{\gamma+1}{2(\gamma-1)}} \quad \textbf{(3.3.17)}$$

To determine the distance in the z'-axis between the hyperbola vertex v and its centre, a function of the height and shock angle at the sonic point and the inlet relative Mach number is used [208], expressed as

$$\mathrm{X}' = y_s{}'\sqrt{M_1'^{\,2}-1}\sqrt{\left(M_1'^{\,2}-1\right)\tan^2\varsigma_S - 1} \quad \textbf{(3.3.18)}$$

Hence, the hyperbola vertex z'-axis location is

$$z_v' = z_o' + \mathrm{X}' \quad \textbf{(3.3.19)}$$

The detachment distance between the hyperbola vertex and the blade leading-edge foremost point is d', while the distance between the point sb and the hyperbola vertex is L, as seen in Figure 3.17. The distance L is related to the wedge half-angle and the height of point sb by the following trigonometric relation

$$L = \frac{y_{sb}{}'}{\tan\delta} = \frac{y_{sb}{}'}{\tan(\delta_{detach}+1°)} \quad \textbf{(3.3.20)}$$

Alternatively, the distance L is computed as well from the continuity method as

$$L = y_s(C+\tan\eta) - y_{sb}{}'\tan\eta \quad \textbf{(3.3.21)}$$

Where C is just a convenient parameter to group the following equation

$$C = \sqrt{M_1'^{\,2}-1}\left[\sqrt{M_1'^{\,2}-1}\tan\varsigma_S - \sqrt{(M_1'^{\,2}-1)\tan^2\varsigma_S - 1}\right] \quad \textbf{(3.3.22)}$$

Experimental data from supersonic flow past various bodies (i.e. inclined planes or axially symmetric cones) [175,249,250] revealed that the ratio of $L/y_{sb}{}'$ agreed more

with the values obtained by the continuity method. Rather, the geometric method tended to maximize $L/{y_{sb}}'$, whereas the continuity formulation leaded to a ratio average. Nonetheless, the geometric method appeared to match closer against experimental data for body leading-edges just slightly blunter than the wedge required for shock detachment. Therefore, an assessment of both methods is performed to select the lowest value of L, used in the forthcoming calculations.

Inasmuch as the infinite bow-wave segment from the full detached shock interacts with the stagnation streamline, the flow undergoes a slight deflection that displaces the stagnation streamline towards the suction surface in a direction normal to the flow. The calculation of the stagnation streamline deflection h is crucial as it determines the location of the hyperbola-shaped detached bow-shock vertex relative to the blading. Inasmuch as the variation of the dimensionless ratio ${h/y_{sb}}'$ increases with the back static pressure or incidence, a method based on isolated-bodies theory using M_1' as constant is used to compute the stagnation streamline deflection as follows

$$\frac{L}{{y_{sb}}'} = \frac{h}{{y_{sb}}'}\left(\frac{C + \frac{A^*}{A_1}{\Pi'_{s1}}_c^{\,-1}\sin\delta_s}{1 - \frac{A^*}{A_1}{\Pi'_{s1}}_c^{\,-1}\cos\delta_s}\right) \tag{3.3.23}$$

$$h = L\frac{1 - \frac{A^*}{A_1}\frac{P_1'}{P_s'}\Big|_c\cos\delta_s}{C + \frac{A^*}{A_1}\frac{P_1'}{P_s'}\Big|_c\sin\delta_s} \tag{3.3.24}$$

From Figure 3.18, the leading-edge circle centre forms a triangle with the point sb, for which opposite side b is

$$b = r_{LE}\sin\delta \tag{3.3.25}$$

Then, the length e between the leading-edge foremost point and the point sb is

$$e = r_{LE} - b = r_{LE}(1 - \sin\delta) \tag{3.3.26}$$

Having computed the previous two lengths and L, the detachment distance becomes

$$d' = L - e = L - r_{LE}(1 - \sin\delta) \tag{3.3.27}$$

Noting that the detachment distance d' is calculated in the relative frame of reference, the projection of in the absolute frame of reference is then

$$d = d' \cos \beta_1 \quad \textbf{(3.3.28)}$$

Similarly, the distance X' is project in the absolute frame of reference as

$$\mathrm{X} = \mathrm{X}' \cos \beta_1 \quad \textbf{(3.3.29)}$$

The z and y coordinates in the absolute frame of reference for the foremost point of the leading edge circle that is aligned with the flow direction may be expressed as

$$z_{LE} = z_{in} - r_{LE} \cos \beta_1 \quad \textbf{(3.3.30)}$$

$$y_{LE} = y_{in} + r_{LE} \cos \beta_1 \quad \textbf{(3.3.31)}$$

Where z_{in} and y_{in} represent the blade inlet camberline axial and tangential coordinates, respectively, obtained from the blade-element layout method of Sec. 3.2.2.

Given the leading edge coordinates and the detachment distance, the absolute coordinates for the hyperbola-shape bow shock vertex are given by

$$z_v = z_{LE} - d \quad \textbf{(3.3.32)}$$

$$y_v = y_{LE} - d \sin \beta_1 \quad \textbf{(3.3.33)}$$

Thus, the hyperbola centre o coordinates in the absolute frame of reference are written as

$$z_o = z_v - \mathrm{X} \quad \textbf{(3.3.34)}$$

$$y_o = y_v - \mathrm{X} \sin \beta_1 \quad \textbf{(3.3.35)}$$

The hyperbola equation is defined by its centre, vertices and co-vertices. Given the vertex from Eq. 3.3.18 and the inlet relative Mach number, the co-vertex is

$$\Upsilon' = \mathrm{X}' \tan \mu \quad \textbf{(3.3.36)}$$

Whereupon, the detached bow-shock equation in the relative frame of reference becomes

$$\frac{{z_{bow}}'^2}{\mathrm{X}'^2} - \frac{{y_{bow}}'^2}{\mathrm{Y}'^2} = \frac{{z_{bow}}'^2}{\mathrm{X}'^2} - \frac{{y_{bow}}'^2}{(\mathrm{X}'\tan\mu)^2} = 1 \qquad \textbf{(3.3.37)}$$

Thereupon, for any given z' in Eq. 3.3.37, the bow-shock axial coordinate in the relative frame is computed Solving for y', gives a positive and negative solution, which correspond to the side of the bow shock that penetrates into the passage and the bow shock side that extends to infinity, respectively.

The free-stream Mach-wave straight lines forming the Mach cone depend on the inlet relative Mach number and run asymptotically to the bow wave. Thus, the Mach-wave lines equation is

$$\frac{y_\mu}{z_\mu} = \pm\frac{\mathrm{Y}'}{\mathrm{X}'} = \tan\mu \qquad \textbf{(3.3.38)}$$

Note as well in Eq. 3.3.38 that there are two solutions for the asymptotes, where the positive solution corresponds to the passage side and the negative belongs to the infinity-side bow wave.

As discussed in Sec. 1.2, not all the blade span is subjected to inlet relative supersonic flow. For this reason, the shock-loss model was properly setup to identify the streamlines with inlet relative subsonic flow, so that neither bow shocks nor Mach waves are generated at those stream surfaces as shown in Figure 3.19. It is observed that as the span increases, the detached bow-shock and its corresponding free-stream Mach-wave shrink in the axial direction due to the effect of the high inlet relative Mach number.

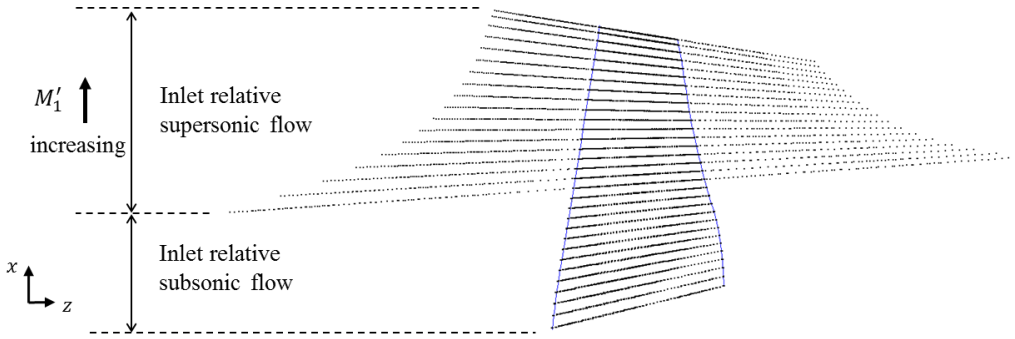

Figure 3.19 Detached bow-shock and free-stream Mach wave projections on the meridional plane for a blade row using the 2-D SLC compressor simulator

Naturally, as the inlet relative Mach number increases from the first streamline with inlet supersonic relative flow towards the tip, the free-stream Mach angle lowers, reducing the detachment distance and increasing the obliquity of the bow-shock, as seen in Figure 3.20. Hence, as the span is reduced and $M_1' \geq 1$, the bow-shock in set with the free-stream Mach wave become wider and more open, tending to become normal.

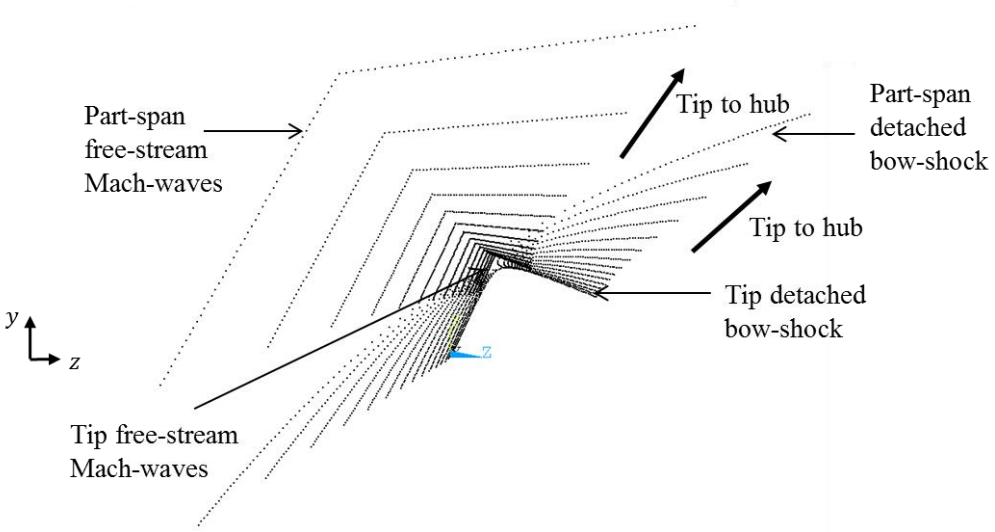

Figure 3.20 Detached bow-shocks and free-stream Mach waves in the blade-to-blade plane for the set of transonic blade-elements using the 2-D SLC compressor simulator

The calculated detached bow-shock and free-stream Mach-wave coordinates are rotated from the relative to the absolute coordinate system through the conventional rotation matrix,

$$\begin{bmatrix} z_{bow} \\ y_{bow} \end{bmatrix} = \begin{bmatrix} \cos(-\beta_1) & \sin(-\beta_1) \\ \sin(\beta_1) & \cos(-\beta_1) \end{bmatrix} \begin{bmatrix} z' \\ y' \end{bmatrix} + \begin{bmatrix} z_0 \\ y_0 \end{bmatrix} \quad \textbf{(3.3.39)}$$

The full three-dimensional Cartesian coordinates are found through the cylindrical radial coordinate, which is

$$r_{bow} = r_{in} - (z_{in} - z_{bow})\tan\alpha \quad \textbf{(3.3.40)}$$

where r_{in} represents the inlet radial coordinate and α is the cone angle for a given blade-profile element. Finally, the x cartesian coordinate is given as

$$x_{bow} = \sqrt{{r_{bow}}^2 + {y_{bow}}^2} \quad \textbf{(3.3.41)}$$

3.3.5 Bow-Wave Losses

Given the full detached bow-shock shape and stagnation streamline from Sec. 3.3.4, the bow-wave portion extending to infinity is known, and its associated losses can be determined.

The relative total-pressure loss calculated in Eq. 3.3.14 applies only at the sonic line inasmuch as the shock angle is at its centroid of mass. Along the bow wave, however, the shock angle changes due to the hyperbola curvature. Thus, the shock angle for a detached wave at any point n in the y'-axis (perpendicular to the flow) is

$$\varsigma_n = \text{atan}\left(\frac{\sqrt{\mathrm{X}'^2 + \left({M_1'}^2 - 1\right)y}}{\left({M_1'}^2 - 1\right)y}\right) \quad \textbf{(3.3.42)}$$

Therefore, the relative total-pressure ratio becomes at a given point *n* becomes

$$\mathrm{PR}'_{n1} = \frac{P_n'}{P_1'} = \left[\frac{(\gamma+1){M_1'}^2\sin^2\varsigma_n}{(\gamma-1){M_1'}^2\sin^2\varsigma_n + 2}\right]^{\frac{\gamma}{\gamma-1}}\left[\frac{(\gamma+1)}{2\gamma{M_1'}^2\sin^2\varsigma_n - (\gamma-1)}\right]^{\frac{1}{\gamma-1}} \quad \textbf{(3.3.43)}$$

Eq 3.3.43 demonstrates that every point on the bow wave produces a different relative total-pressure downstream of it. Therefore, an integration of infinitesimal P_n'/P_1' is required along the hyperbola from the stagnation streamline to infinity. Insomuch as the mass flow entering every passage undergoes a bow-wave-induced loss process

similar to that of a shock wave from the stagnation streamline to infinity, the average bow wave relative total-pressure loss approximated by Klapproth [206] is

$$1-\left(\frac{P_2'}{P_1'}\right)_{bow}=\frac{y}{y_{SB}}\int_{y_g/h}^{y_\infty/h}\left(1-\frac{P_n'}{P_1'}\right)\left(\frac{y}{h}-\frac{y_g}{h}\right) \quad \textbf{(3.3.44)}$$

In Eq. 3.3.44, g represents the distance perpendicular to the flow direction between the bow-shock and stagnation streamline. As explained in Sec. 3.3.4, the detached bow-shock was positioned so that its y'-axis was coincident with the deflected stagnation streamline and hence $h=0$. Therefore, Eq. 3.3.44 can be simplified to have a lower integration limit of $y'=0$, becoming

$$\left(\frac{P_2'}{P_1'}\right)_{bow}=1-\frac{\int_0^\infty\left(1-\frac{P_n'}{P_1'}\right)dy}{\int_0^\infty dy} \quad \textbf{(3.3.45)}$$

Because the bow wave has its strongest part in its vertex, the highest relative total-pressure decay is expected at $y'=0$, coincident with the calculated stagnation streamline location. Farther away from the hyperbola vertex, the bow wave loses strength, until P_n'/P_1' becomes unity. For this reason, the integration domain of Eq. 3.3.45 ranges between 0 and ∞. For implementation purposes in a numerical code, however, the upper integration limit is defined as the sonic point s, as farther out beyond this point, the bow shock becomes weak with negligible contribution to the overall bow-wave loss [34]. Thence, the bow-wave relative total-pressure ratio of Eq. 3.3.45 becomes

$$\left(\frac{P_2'}{P_1'}\right)_{bow}=1-\frac{\int_0^S\left(1-\frac{P_n'}{P_1'}\right)dy}{\int_0^s dy} \quad \textbf{(3.3.46)}$$

The term $\int_0^S\left(1-\frac{P_2'}{P_1'}\right)dy$ is solved through numerical integration using Simpson's rule. The integration domain between 0 and s is discretized in equally spaced integration points as follows

$$\Delta y=\frac{y_S-y_0}{N} \quad \textbf{(3.3.47)}$$

Where Δy is the increment in the y'-axis dependant on the number of integration points N. As every integration segment is approximated by three points in the Simpson's rule, the Newton-Cotes functions become:

$$\mathrm{F}_0 = f(y_0) = 1 - \frac{P_n'}{P_1'}\bigg|_y \tag{3.3.48}$$

$$\mathrm{F}_1 = f(y + \Delta y/2) = 1 - \frac{P_n'}{P_1'}\bigg|_{y+\Delta y/2} \tag{3.3.49}$$

$$\mathrm{F}_2 = f(y + \Delta y) = 1 - \frac{P_n'}{P_1'}\bigg|_{y+\Delta y} \tag{3.3.50}$$

Hence, the numerical integration of the term $1 - \frac{P_n'}{P_1'}$ for a segment between y and $y + \Delta y$ is

$$\int_y^{y+\Delta y} \left(1 - \frac{P_n'}{P_1'}\right) dy = \frac{\Delta y}{6}[\mathrm{F}_0 + 4\mathrm{F}_1 + \mathrm{F}_2] = \frac{\Delta y}{6}\left[\left(1 - \frac{P_n'}{P_1'}\right)_y + 4\left(1 - \frac{P_n'}{P_1'}\right)_{y+\Delta y/2} + \left(1 - \frac{P_n'}{P_1'}\right)_{y+\Delta y}\right] \tag{3.3.51}$$

The integration of the term $1 - \frac{P_n'}{P_1'}$ over the whole domain from the computed stagnation streamline and the sonic point becomes a summation of Eq. 3.3.51 on every integration segment, expressed as

$$\int_0^S \left(1 - \frac{P_n'}{P_1'}\right) dy = \sum_{i=1}^{N} \frac{\Delta y_i}{6}\left[\left(1 - \frac{P_n'}{P_1'}\right)_{y_i} + 4\left(1 - \frac{P_n'}{P_1'}\right)_{y_i+\Delta y_i/2} + \left(1 - \frac{P_n'}{P_1'}\right)_{y_i+\Delta y_i}\right] \tag{3.3.52}$$

To optimize the code in the 2D SLC compressor software, if a value for $\frac{P_n'}{P_1'}$ is found to be unity before the sonic point, the cumulative summation of Eq. 3.3.52 stops to avoid

further redundant calculations that do not contribute to the pressure decay. Having Eq. 3.3.52 solved, the overall bow-wave losses are computed through Eq. 3.3.46, giving

$$\mathrm{PR}'_{bow} = \left(\frac{P'_2}{P'_1}\right)_{bow} = 1 - \frac{\int_0^S \left(1 - \frac{P'_n}{P'_1}\right) dy}{y_S - y_0} \qquad \textbf{(3.3.53)}$$

3.3.6 Passage-Shock Location

Prior to computing any flow field expansion, the different passage-shock impingement points on the blade surfaces are calculated to have information of the flow angle at those points. Because the entire blade-surfaces geometry is known from the blade-element-layout method in Sec. 3.2.2, the blade angle is known at any point. Thus, the flow angle is also known at any point as is equal to its blade angle according to the wall-point unit process from the method of characteristics.

The passage-shock segment from the detached bow-shock is extended to find the intersection at a point k with the blade suction-surface as shown in Figure 3.21. Using an iterative secant-method, a z_k value was assumed to be interpolated in the suction-surface and passage-shock geometry distribution so that the corresponding values of $y_{k_{ss}}$ and $y_{k_{hy}}$, and its difference Δy_k are determined. The process repeats for a second assumption of z_k. The secant method establishes a linear function between the assumed z_k values with corresponding Δy_k to find the root of the next z_k. The secant method is iteratively solved until Δy_k is below a tolerance of 1e-6 to determine an accurate z_k and y_k. Given these coordinates, the blade angle k_k is computed using a cubic-spline interpolation within the blade-metal-angle distribution obtained from the blade-element-layout method. Thence, the full 3-D Cartesian coordinates for point k are obtained as in Eq. 3.3.40 for r_k and Eq.3.3.41 for x_k.

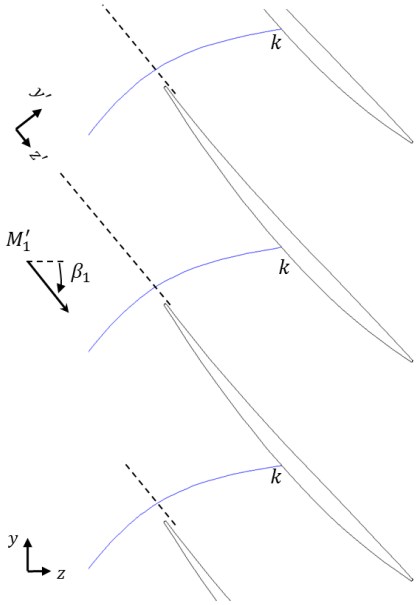

Figure 3.21 Passage-shock impingement-point definition for a single-shock configuration in unstarted flows.

In the case there is no intersection between the passage-shock segment due to high obliquity of the detached bow-shock, the case is considered to be choked since the passage shock needs to impinge unequivocally somewhere on the suction surface. Hence this scenario is treated no more as a single shock, but rather as a flow-started case with a dual-shock pattern.

Following the choking-incidence calculation in Sec. 3.4.2, if the current streamline incidence is greater than the unique incidence for those conditions, a single-shock structure is considered and the entire only passage-shock shape location is defined. Alternatively, if the incidence is equal or less than the unique incidence for the streamline conditions, the passage is choked and a dual-shock needs to be implemented. Before any computation on the S1 surface for the shock configuration, the actual incidence is fixed to be choking value at the started streamlines, since the incidence cannot be less than the unique incidence for a given inlet relative Mach number. Admittedly, the procedure for limiting the incidence to the choking value in a 2-D SLC simulation is not as straight as it sounds, as the REE and mass-flow conservation need to be satisfied at all times. The solution for this problem is presented in Sec. 3.4.3 and Sec. 3.4.4 consisting in a choking margin definition and a novel mass flow redistribution model, respectively.

The estimation of the passage-shock shape and location is solved iteratively for started flows. At first, a point q is assumed to represent the impingement of the choke-induced shock on the suction surface. The point q is first estimated to be that impingement point from a normal shock to the flow stemming at the sonic point of the first passage shock as displayed in Figure 3.22. This is different from Bloch *et al*. [34] in that no normal angularity is being imposed to the second shock; rather the point q is in a normal direction to the flow but it can lead to an oblique shock. Furthermore the point q is just a first assumption which will be later modified by the iterative method of Sec. 3.3.9, whereas Bloch *et al*. [34] set this passage-shock location and angle as final.

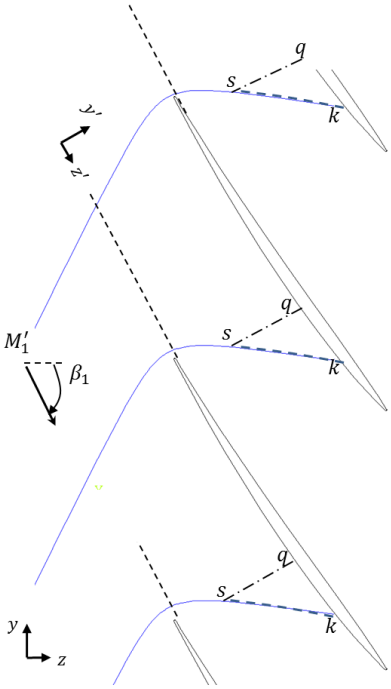

Figure 3.22 Second passage-shock impingement-point assumption for a dual-shock configuration in started flows.

The z'-coordinate for the sonic point s on the hyperbola is calculated from Eq. 3.3.37 as,

$$z_s{}' = \sqrt{\mathrm{X}'^2\left[1+\frac{y_s{}'^2}{(\mathrm{X}'\tan\mu)^2}\right]} \qquad \textbf{(3.3.54)}$$

Using the relative-to-absolute rotation matrix from Eq. 3.3.39, z_s and y_s are determined, from where a straight line is extended till the suction surface to find the impingement

coordinates z_q and y_q. Thus, the full 3-D Cartesian coordinates for point q are determined as in Eq. 3.3.40 for r_q and Eq.3.3.41 for x_q.

The coordinate information points k and q defines the second passage-shock situation. If point k is in front of point q, there is no intersection of the second oblique-shock with the first passage-shock, yielding in a dual-shock structure as noticed in Figure 3.23 a). On the other hand, if point q is upstream of point k, there is coalescence between both passage shocks, truncating the hyperbola and the dual-shock structure is merged as seen in Figure 3.23 b). Since the hyperbola is truncated by the second passage-shock and does not impinge anymore on the suction surface, the intersection between both shocks is at the transition point t. Note that in most of the cases, the first assumption of the impingement point q leads to a merged pattern as in Figure 3.23 b) resulting in a second passage-shock too forward (and relatively proximate to the leading-edge) in the chordwise direction. Whether a the merged or unmerged choked situation occurs, the second passage-shock extends across the passage shock, intersecting the pressure side of the next adjacent blade at point u.

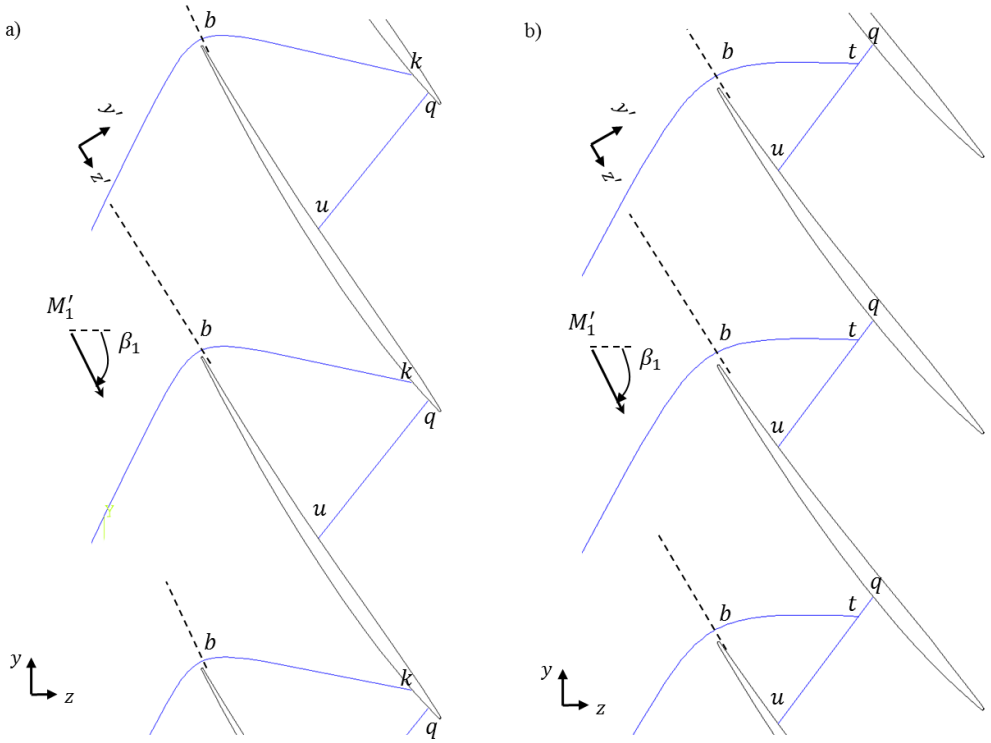

Figure 3.23 Dual-shock configuration situation depending on the choke-induced passage-shock location. a) No intersection between both passage shocks. b) Coalescence of both passage shocks.

3.3.7 Flow Expansion

3.3.7.1 First-Captured Mach wave

The flow expansion affecting the upstream velocity distribution ahead of the passage shock is that occurring in zone V of Figure 2.33. The first wave of this flow acceleration process is the limiting characteristic *a-b* or the first captured Mach wave, running from a suction surface point *a* upstream of the passage shock to the detached bow-shock vertex at *b*, as seen in Figure 3.24.

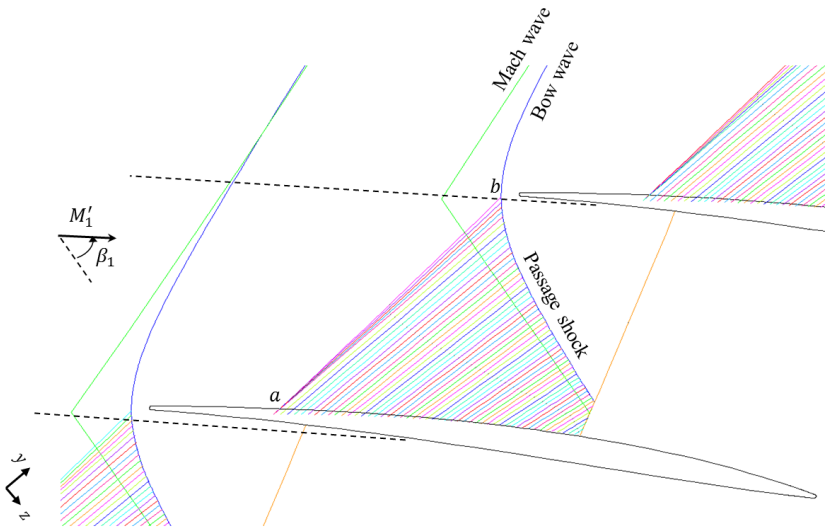

Figure 3.24 First-captured Mach or limiting wave for the flow expansion that interacts with the passage shock.

The required relations of corrected mass flow per unit area and Prandtl-Meyer expansion between far upstream and the limiting characteristic *a-b* are applied in an iterative scheme to determine the position of the first-captured Mach wave. In contrast to the continuity formulation of Levine [185] and Starken [184], the relative total-pressure loss due to the bow-wave system is considered in the current expansion model. Moreover, the streamtube height contraction is accounted in the normal-flow area ratio in contrast to the model of Bloch *et al*. [34] and Boyer and O'Brien [13,35,36]. The corrected mass flow per unit area or flow function is by definition,

$$F(M) = \frac{\dot{m}\sqrt{C_p T_0}}{A P_0} \qquad \textbf{(3.3.55)}$$

Therefore, the mass flow conservation between the inlet and the limiting wave *a-b* yields to the following expression

$$\dot{m}_1 = \dot{m}_{ab} = \dot{m} = \frac{F(M_1')A_1 P_{0_1}}{\sqrt{C_p T_{0_1}}} = \frac{F(M_{1_{ab}}')A_{ab} P_{0_{ab}}}{\sqrt{C_{p_{ab}} T_{0_{ab}}}} \qquad \textbf{(3.3.56)}$$

Since, the process is adiabatic, C_p and T_0 are exactly constant, thus, the continuity relation is reduced to

$$\dot{m} = F(M_1')A_1 = F(M_{1_{ab}}')A_{ab}\frac{P_{0_{ab}}}{P_{0_1}} \qquad \textbf{(3.3.57)}$$

where $P_{0_{ab}}/P_{0_1}$ is the bow-wave total-pressure ratio Π_{bow}' obtained from Eq. 3.3.53. The flow areas A_1 and A_{ab} in Figure 3.25 are the frontal areas normal to the relative flow velocity with a streamtube height H.

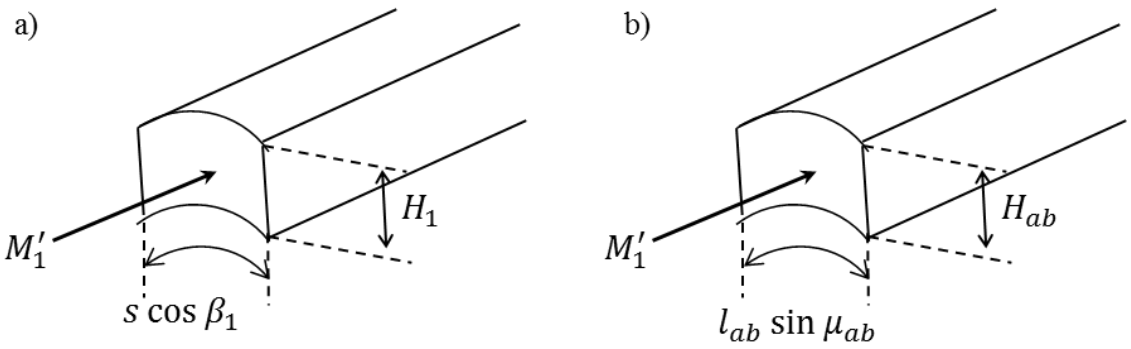

Figure 3.25 Normal cross-sectional area to the inlet relative flow. a) Far upstream or inlet. b) First-captured Mach wave.

The width of the flow areas is determined as that length perpendicular to the inlet relative flow on a blade-to-blade surface as displayed in Figure 3.26. Similarly to Eq. 2.6.15, the inlet flow area is

$$A_1 = H_1\phi = H_1 s\cos\beta_1 \qquad \textbf{(3.3.58)}$$

and the flow area for the limiting characteristic *a-b* becomes

$$A_{ab} = H_{ab} l_{ab}\sin\mu_{ab} \qquad \textbf{(3.3.59)}$$

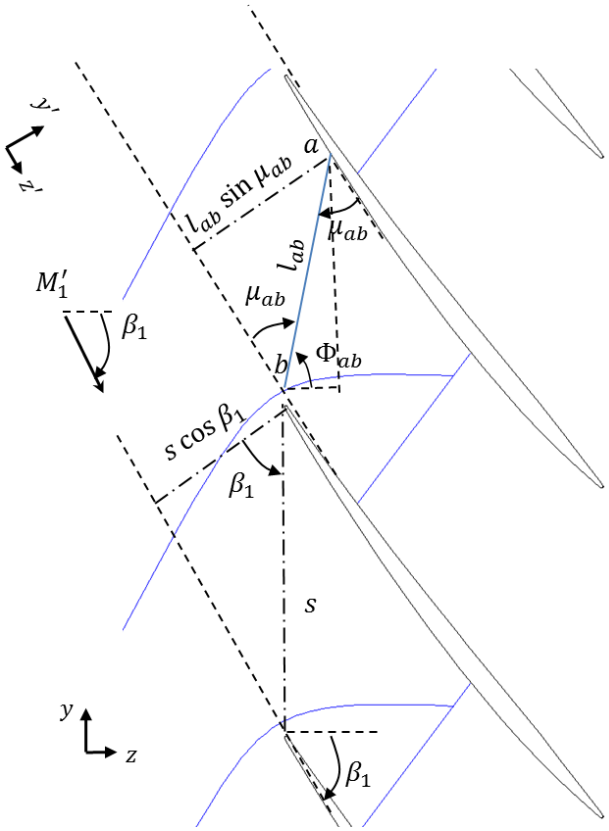

Figure 3.26 Width definition for the flow areas at the inlet and at the first-captured Mach wave.

Then, the mass flow conservation of Eq. 3.3.57 might be rewritten as

$$F(M_1')\frac{H_1}{H_{ab}}s\cos\beta_1 = F(M_{ab}')l_{ab}\sin\mu_{ab}\,\Pi_{bow}' \qquad \textbf{(3.3.60)}$$

The streamtube height H for a mean streamline j is determined through its area as

$$A = \pi\left({R_{j+1/2}}^2 - {R_{j-1/2}}^2\right) = 2\pi R_j H_j \qquad \textbf{(3.3.61)}$$

Solving for H_j,

$$H_j = \frac{{R_{j+1/2}}^2 - {R_{j-1/2}}^2}{R_j} \qquad \textbf{(3.3.62)}$$

In the case, the streamline j is at an intermediate location between hub and tip, a central difference scheme is used to find the average radii as

$$R_{j+1/2} = \frac{R_{j+1} + R_j}{2} \qquad \textbf{(3.3.63)}$$

$$R_{j-1/2} = \frac{R_j + R_{j-1}}{2} \tag{3.3.64}$$

For the hub streamlines, a backward difference is used to approximate the lower average radius, becoming

$$R_{j-1/2} = R_j \tag{3.3.65}$$

Likewise, for the tip streamlines, a forward difference is used to estimate the upper average radius as

$$R_{j+1/2} = R_j \tag{3.3.66}$$

Thence, the streamtube height contraction H_1/H_{ab} can be expressed as

$$\frac{H_1}{H_{ab}} = \frac{{R_{j+1/2}}_{LE}^{\,2} - {R_{j-1/2}}_{LE}^{\,2}}{R_{j_{LE}}} \frac{R_{j_{ab}}}{{R_{j+1/2}}_{ab}^{\,2} - {R_{j-1/2}}_{ab}^{\,2}} \tag{3.3.67}$$

Thereon, the mass flow conservation between the inlet and the first-captured Mach wave for a given streamline *j* becomes

$$F(M_{j_1}') \frac{{R_{j+1/2}}_{LE}^{\,2} - {R_{j-1/2}}_{LE}^{\,2}}{R_{j_{LE}}} \frac{R_{j_{ab}}}{{R_{j+1/2}}_{ab}^{\,2} - {R_{j-1/2}}_{ab}^{\,2}} s_j \cos\beta_{j_1} = F(M_{j_{ab}}') l_{j_{ab}} \sin\mu_{j_{ab}} \Pi_{j_{bow}}' \tag{3.3.68}$$

The complete solution of the continuity relation in Eq. 3.3.68 requires to know the impingement point *a* of the first-captured Mach wave on the suction surface, which is determined by an iterative method. Initially, an axial coordinate z_a for point *a* is assumed, for which a blade angle k_a is determined from the blade-element-layout method.

At the inlet, all conditions are known and the Prandtl-Meyer angle is determined using the Prandtl-Meyer function in Eq. 2.4.34. Then, the Riemann's equation for the Prandtl-Meyer expansion of a right-running characteristic in Eq. 2.4.36 determines the flow angle of the limiting characteristic *a*-*b* as

$$\nu_{ab}(M_{ab}) = \beta_{ab} + \nu_1(M_1') - \beta_1 \quad \textbf{(3.3.69)}$$

Given ν_{ab}, M'_{ab} is known using the Prandtl-Meyer function in Eq. 2.4.34 and the Mach angle μ_{ab} is determined as per Eq. 2.4.32. The relative Mach numbers at both inlet and limiting wave *a*-*b* determine their respective flow functions as

$$F(M') = \frac{\gamma}{\sqrt{\gamma-1}} M' \left[1 + \frac{\gamma-1}{2} M'^2\right]^{\frac{-(\gamma+1)}{2(\gamma-1)}} \quad \textbf{(3.3.70)}$$

The assumed location z_a resolves the distance l_{ab} between the suction-surface impingement point of the first-captured Mach wave and the detached bow-shock vertex, whose slope angle Φ_{ab} is

$$\Phi_{ab} = \text{atan}\left(\frac{y_b - y_a}{z_b - z_a}\right) \quad \textbf{(3.3.71)}$$

From Figure 3.26, l_{ab} is determined by trigonometry as

$$l_{ab} = \frac{z_b - z_a}{\cos \Phi_{ab}} \quad \textbf{(3.3.72)}$$

Thereby, the continuity equation determines the mass flow error per streamline *j* that results from the assumed value of z_a as

$$E = F\left(M_{j_1}'\right) \frac{R_{j+\frac{1}{2}_{LE}}{}^2 - R_{j-\frac{1}{2}_{LE}}{}^2}{R_{j_{LE}}} \frac{R_{j_{ab}}}{R_{j+\frac{1}{2}_{ab}}{}^2 - R_{j-\frac{1}{2}_{ab}}{}^2} s_j \cos \beta_{j_1} - F(M'_{j_{ab}}) \frac{z_{j_b} - z_{j_a}}{\cos\left[\text{atan}\left(\frac{y_{j_b} - y_{j_a}}{z_{j_b} - z_{j_a}}\right)\right]} \sin \mu_{j_{ab}} \Pi'_{j_{bow}} \quad \textbf{(3.3.73)}$$

A next value of z_a is assumed for which the respective error is obtained. Having two z_a values and their corresponding errors, the next approximation for z_a is given by a secant method. The secant equation is iteratively solved until the error is lower than a tolerance set to 1e-6, resulting in an accurate impingement point for the limiting characteristic *a*-*b*.

3.3.7.2 Full Flow-Field Expansion

The full flow-expansion is gradual and computed first by discretizing a finite suction-surface domain that extends from point a till the intersection of the passage shock with the suction surface, whether it is point *k* or q. At every discretization point n_{ss}, there is a gradual-expansion wave or characteristic Ch_n defined. The axial-coordinate $z_{n_{ss}}$ of every discretization point is placed equidistant on the suction surface determined by the maximum number of discretization points N, expressed as

$$z_{n_{ss}} = \sum_{n_{ss}=1}^{N} z_a + \frac{(n_{ss}-1)z_{psh_{ss}} - z_a}{N-1} \quad \begin{matrix} z_{psh_{ss}} = z_k \; ; \; unstarted \\ z_{psh_{ss}} = z_q \; ; started \end{matrix} \qquad \textbf{(3.3.74)}$$

The number of discretization points *N* determines the number of integration points to be used in the circumferential mass-averaged passage-shock loss computation. A value of $N = 50$ suffices for convergence and accuracy without compromising the computational solution-speed of the 2-D SLC code. Increasing *N* by 10% beyond 50 modifies the shock-loss coefficient precision by 0.002%, and instead it increases the solution time by 0.1%.

For every discretization point n_{ss} with axial coordinate $z_{n_{ss}}$, the blade angle $k_{n_{ss}}$ and tangential coordinate $y_{n_{ss}}$ are calculated from the blade-element-layout method. According to the wall-point unit process from the method of characteristics, the blade angle at any surface point is equal to the characteristic flow angle arising from such location. Thus, the gradual flow-expansion over the suction surface of zone V can be computed successively using the Prandtl-Meyer expansion for a right-running characteristic from Eq. 2.4.36 to determine the Prandtl-Meyer angle ν_n of every characteristic Ch_{n-} as

$$\nu_n(M_n) = \beta_n + \nu_{n-1}(M'_{n-1}) - \beta_{n-1} = k_{n_{ss}} + \nu_{n-1}(M'_{n-1}) - \beta_{n-1} \qquad \textbf{(3.3.75)}$$

The relative Mach number M_n of each characteristic Ch_{n-} is then determined by the Prandtl-Meyer function of Eq. 2.4.34. To determine the characteristic slope, a successive field-point calculation from the method of characteristics as illustrated in Figure 3.27 is necessary. A left-running characteristic Ch_{n+} is set between a suction-

surface point n_{ss} and a corresponding point n'' on the field, whose location is to be determined but flow conditions are known. Additionally, a right-running characteristic Ch_{n-} is established between the field points n'', for which the first point of that sequence is the detached bow-shock vertex b with known conditions. Knowing the relative Mach number at n_{ss} and b, the Prandtl-Meyer angle and the Mach angle for both characteristics can be computed as usual with the Prandtl-Meyer function in Eq. 2.4.34 and Eq. 2.4.32, respectively. For the left-running characteristic Ch_{n+}, the Riemann's equation in Eq. 2.4.38 gives

$$\mathrm{K}_{+} = \mathrm{K}_{+n_{ss}} = \mathrm{K}_{+n''} = \beta_{n_{ss}} - \nu_{n_{ss}}\left(M'_{n_{ss}}\right) = \beta_{n''} - \nu_{n''}\left(M'_{n''}\right) \quad \textbf{(3.3.76)}$$

In the case of the right-running characteristic Ch_{n-}, the Prandtl-Meyer expansion is as per Eq. 2.4.36, thus

$$\mathrm{K}_{-} = \mathrm{K}_{-b} = \mathrm{K}_{-n''} = \beta_1 + \nu_1(M'_1) = \beta_{n''} + \nu_{n''}\left(M'_{n''}\right) \quad \textbf{(3.3.77)}$$

The simultaneous solution of Eq. 3.3.76 and Eq. 3.3.77 leads to the following equations to find the Prandtl-Meyer angle $\nu_{n''}$ and flow angle $\beta_{n''}$.

$$\nu_{n''}\left(M'_{n''}\right) = \frac{\beta_1 + \nu_1(M'_1) + \nu_{n_{ss}}\left(M'_{n_{ss}}\right) - \beta_{n_{ss}}}{2} \quad \textbf{(3.3.78)}$$

$$\beta_{n''} = \beta_1 + \nu_1(M'_1) - \nu_{n''}\left(M'_{n''}\right) \quad \textbf{(3.3.79)}$$

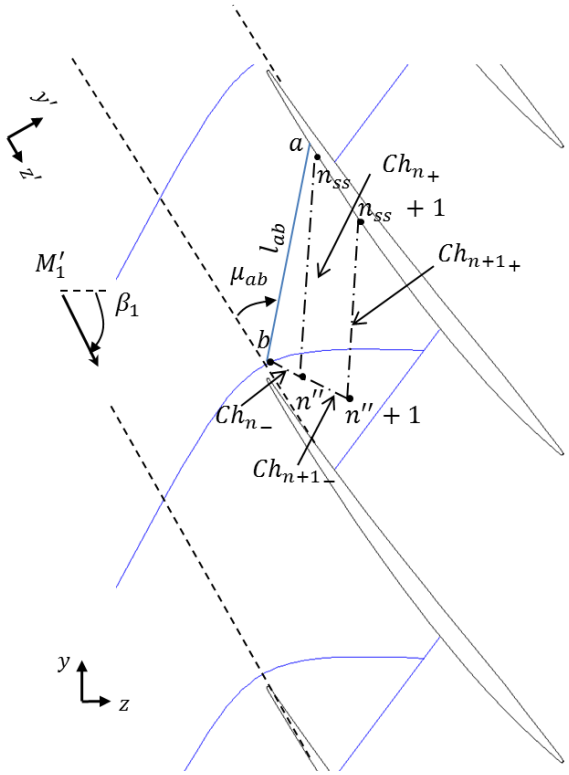

Figure 3.27 Field-point calculation to determine the characteristic slopes of the zone-V flow expansion.

An iterative secant-method that solves the Prandtl-Meyer function is applied to obtain $M'_{n''}$, and thus, determining $\mu_{n''}$ using Eq. 2.4.32. Inasmuch as all the flow information is known at b, n_{ss} and n'', the slope $\mathcal{S}$ for both characteristics, left-running and right-running, is computed respectively as

$$\mathcal{S}_{n_{ss}n''} = \tan\left[\frac{\left(\beta_{n_{ss}} + \mu_{n_{ss}}\right) + \left(\beta_{n''} + \mu_{n''}\right)}{2}\right] \tag{3.3.80}$$

$$\mathcal{S}_{bn''} = \tan\left[\frac{\left(\beta_1 - \mu_1\right) + \left(\beta_{n''} - \mu_{n''}\right)}{2}\right] \tag{3.3.81}$$

Thus, having both characteristic slopes, the coordinates for point n'' are thus determined from their straight-line equations as

$$z_{n''} = \frac{\mathcal{S}_{bn''}z_b - y_b + y_{n_{ss}} - \mathcal{S}_{nn''}z_{n_{ss}}}{\mathcal{S}_{bn''} - \mathcal{S}_{nn''}} \tag{3.3.82}$$

$$y_{n''} = \mathcal{S}_{bn''}(z_{n''} - z_b) + y_b \tag{3.3.83}$$

The process repeats successively for the rest of the discretization points n_{ss} by substituting the subindex 1 for $n'' - 1$ from Eq. 3.3.77 to Eq. 3.3.83. In this way, the full expansion field of zone V is determined. Nonetheless, this is an over-extended gradual expansion-field as the passage-shock must truncate the expansion characteristics.

For the choked operations, the choked-induced passage-shock intersection with the suction surface at point q is an assumed value with unknown shock angle. Furthermore, the suction-surface expansion from Eq. 3.3.75 determines the flow parameters at this point q. The passage-shock angle is assumed to be constant throughout the oblique shock and is thus computed utilizing an iterative secant-method that solves the shock-point unit process from the method of characteristics. A shock angle for the second shock ς_{psh} is first assumed. The deflection angle δ_{psh} and outlet relative Mach number M'_{2_q} for the choked-induced passage shock are calculated then from oblique-shock theory using Eq. 2.4.24 and Eq. 2.4.19, respectively as

$$\delta_{psh} = \operatorname{atan}\left\{2\cot\varsigma_{psh}\frac{{M'_{1_q}}^2\sin^2\varsigma_{psh} - 1}{{M'_{1_q}}^2\left[\gamma + \cos\left(2\varsigma_{psh}\right)\right] + 2}\right\} \tag{3.3.84}$$

$$M'_{2_q} = \sqrt{\frac{(\gamma-1){M'_{1_q}}^2\sin^2\varsigma_{psh} + 2}{2\gamma{M'_{1_q}}^2\sin^2\varsigma_{psh} + 1 - \gamma}\frac{}{\sin^2(\varsigma_{psh} - \delta_{psh})}} \tag{3.3.85}$$

The deflection angle is the flow turning and thus determines the flow angle β_{2_q} downstream of the second passage-shock as

$$\beta_{2_q}\Big|_{\vartheta} = \beta_{1_q} - \delta_{psh} \tag{3.3.86}$$

Given M'_{2_q}, the Prandtl-Meyer Function in Eq. 2.4.34, resolves the outlet Prandtl-Meyer angle ν_{2_q}. Alternatively, a Prandtl-Meyer expansion for a right-running characteristic from Eq. 2.4.36 resolves as well the outlet flow angle β_{2_q} for the second passage-shock as

$$\beta_{2_q}\Big|_{PM} = \beta_{1_q} + \nu_{1_q}\left(M'_{1_q}\right) - \nu_{2_q}\left(M'_{2_q}\right) \quad \textbf{(3.3.87)}$$

As a result, an error in the second passage-shock outlet flow angle is determined as

$$E = \beta_{2_q}\Big|_{PM} - \beta_{2_q}\Big|_{\vartheta} \quad \textbf{(3.3.88)}$$

Similarly to the aforementioned iterative methods, a second value ς_{psh} is assumed to obtain a corresponding error so that a secant method determines the next approximated ς_{psh}. The secant method is iteratively solved until the error is lower than the typical tolerance used of 1e-6 to determine an accurate choked-induced passage-shock angle.

The second passage-shock is then extended at an angle ς_{psh} across the passage till it intercepts the passage-shock portion of the detached bow-shock to find point t. The interception is resolved again using an iterative secant-method similar to that in Sec. 3.3.6, by solving a cubic-spline interpolation of the extended second-passage shock onto the first-passage shock determining z_t and y_t. Equally to the previous key points, the full 3-D Cartesian coordinates for point t are obtained as in Eq. 3.3.40 for r_t and Eq.3.3.41 for x_t.

As discussed in Sec. 3.3.6, the first assumption of point q yields in the majority of the cases to a point t. However, if no interception is found between both passage shocks, the second passage-shock is simply extended till the pressure surface with the same angle ς_{psh} and the expansion process of zone V is treated as in the unstarted-flow situation. Whether the dual-shock configuration for the started operations is coalesced or not, the second passage-shock is extended till it intersects the pressure blade at point u. Likewise its coordinates z_u and y_u, are determined using the same iterative secant-method by solving a cubic-spline interpolation of the extended second-passage shock onto the pressure surface, and x_u and r_u are given by Eq. 3.3.40 and Eq.3.3.41, correspondingly.

Either flow condition, unstarted with a unique passage-shock, started with an unmerged first passage-shock or started with coalesced passage-shocks, the full-passage shock structure interacting with the zone-V flow expansion is given. The over-extended

gradual expansion-waves from zone V are then intercepted with the passage shock to find the right intersection coordinates for any case. The usual iterative secant-method is applied to resolve a cubic-spline interpolation of the gradual expansion-waves onto the passage shock to find the intersecting points $n_{g,psh}$ with coordinates $z_{n_{g,psh}}$ and $y_{n_{g,psh}}$, whose $x_{n_{g,psh}}$ and $r_{n_{g,psh}}$ are given by Eq. 3.3.40 and Eq.3.3.41, respectively. The intersecting points $n_{g,psh}$ are resolved in such manner that intersects both hyperbolic and straight portions of any passage shock configuration.

3.3.7.3 Expansion Fan and Pre-Compression

The flow expansion described in Sec. 3.3.7.2 is such that resolves the relative Mach number $M_n{}'$ and relative flow angle $\beta_n{}'$ as constant along the characteristics. Further, the absolute 3-D gradual expansion-wave coordinates intercepting the passage-shock configuration were determined accordingly. In spite of the suction-surface discretization for the gradual flow-expansion and regardless of its resolution, there might be a passage region where there is no influence of the calculated characteristics, as displayed in Figure 3.28 a).

Such cases occur for highly-loaded bladings or high incidences, forcing the flow to turn faster over a reduced suction surface and leading to an expansion fan extending from zone III up to the onsets of zone V. Therefore, for those high-turning situations where the gradual expansion does not suffice to describe the entire flow field, an expansion fan emanating from the first-captured Mach-wave impingement on the suction surface is assumed, as shown in Figure 3.28 b). Naturally, the expansion fan intruding in zone V occurs generally for single-shock structures, when the flow is unstarted due to high incidences and low mass flow rates.

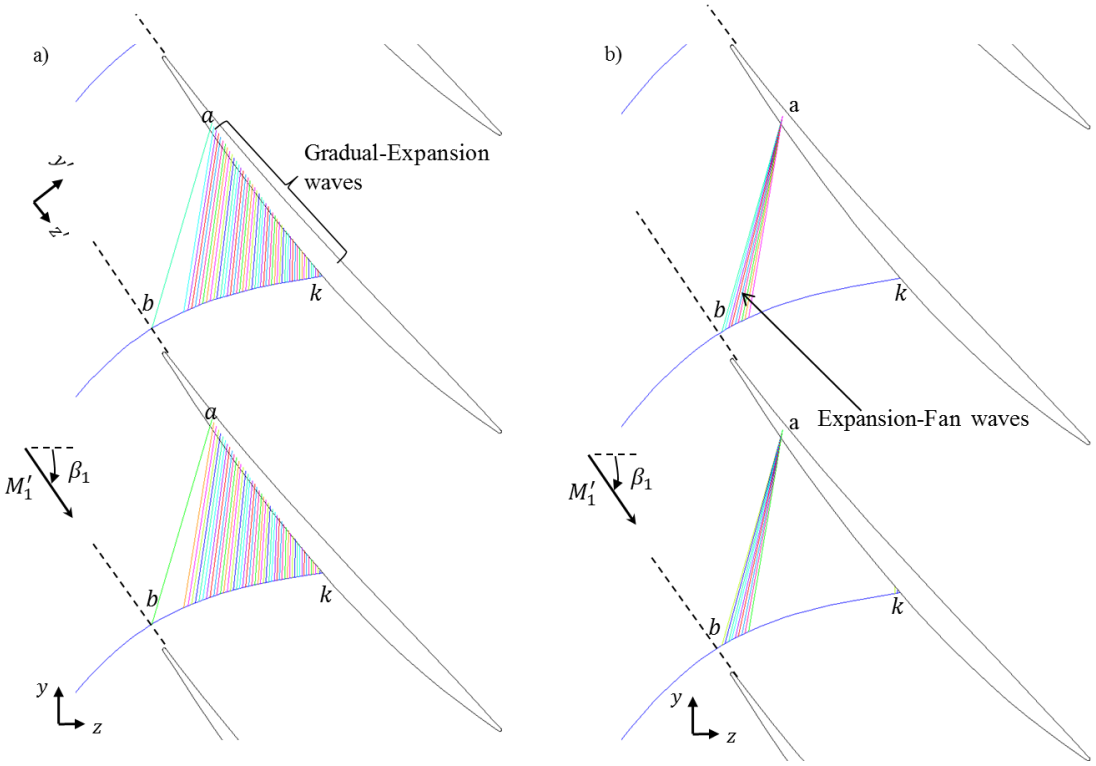

Figure 3.28 Highly-loaded blading for which there is an expansion fan intruding in the zone-v expansion field. a) Gradual-expansion characteristics. b) Expansion-fan waves arising from the limiting wave impingement on the suction surface

To further determine a potential expansion-fan, it is convenient to rotate-back the gradual-expansion intersecting points $n_{g,psh}$ with the passage-shock to the local frame of reference using the following rotation matrix

$$\begin{bmatrix} z_{n_{g,psh}}{}' \\ y_{n_{g,psh}}{}' \end{bmatrix} = \begin{bmatrix} \cos(\beta_1) & \sin(\beta_1) \\ \sin(-\beta_1) & \cos(\beta_1) \end{bmatrix} \begin{bmatrix} z_{n_{g,psh}} - z_o \\ y_{n_{g,psh}} - z_o \end{bmatrix} \quad \textbf{(3.3.89)}$$

Similarly, the point t, if any, is rotated back to the relative coordinate system using Eq 3.3.89, to find $z_t{}'$ and $y_t{}'$.

The domain extent along the y'-axis where a expansion-fan might develop is established by the extremity passage-shock points at the detached bow-shock vertex and point k or q, depending on the flow situation. The domain is discretized with equidistant points $n_{f,psh}$ determined by a maximum number of discretization points N_f, which is independent of the number of gradual-expansion characteristics established in Sec. 3.3.7.2. For every point $n_{f,psh}$ there is a corresponding expansion-fan

characteristic Ch_{n_f} rising from point a. Hence, the passage shock discretization in the y'-axis to intercept the expansion-fan characteristics is as follows

$$y_{n_{f,psh}}{}' = \sum_{n_{f,psh}=1}^{N_f} y_{1_{g,psh}}{}' + \frac{(n_{f,psh}-1)y_{N_{g,psh}}{}' - y_{1_{g,psh}}{}'}{N_f - 1}$$
$$= \sum_{n_{f,psh}=1}^{N_f} y_v{}' + \frac{(n_{f,psh}-1)y_{psh_{ss}}{}' - y_v{}'}{N_f - 1} \quad \textbf{(3.3.90)}$$

$$y_{psh_{ss}}{}' = y_k{}' \; ; \; unstarted \; and \; unmerged \; started$$
$$y_{psh_{ss}}{}' = y_q{}' \; ; \; coalesced \; started$$

Although it is acknowledged that the expansion fan will not extend till points *k* or *q*, the discretization to capture the expansion fan is performed until these points to account for robustness. The corresponding z'-coordinates for the expansion-fan discretization are calculated for the hyperbolic or straight passage-shock portion as a function of the shock configuration as follows

$$z_{n_{f,psh}}{}' = \begin{cases} \sqrt{\mathrm{X}'^2\left[1 + \frac{y_{n_{f,psh}}{}'^2}{(\mathrm{X}'\tan\mu)^2}\right]} & ; unstarted \\ & ; unmerged \; started \\ & ; coalesced \; stared \; y_{n_{f,psh}} \le y_t{}' \end{cases}$$

$$z_{n_{f,psh}}{}' = \left(y_{n_{f,psh}}{}' - y_{N_{g,psh}}{}'\right)\frac{z_t{}' - z_{N_{g,psh}}{}'}{y_t{}' - y_{N_{g,psh}}{}'} + z_{N_{g,psh}}{}' \; ; \; coalesced \; started \; y_{n_{f,psh}} > y_t{}' \quad \textbf{(3.3.91)}$$

Given the expansion-fan point coordinates, the rotation matrix from Eq. 3.3.39 is applied to transform from the relative to the absolute coordinate system to compare $z_{n_{f,psh}}$ and $y_{n_{f,psh}}$against those intersecting point coordinates of the gradual expansion. $x_{n_{f,psh}}$ and $r_{n_{f,psh}}$ are given by Eq. 3.3.40 and Eq.3.3.41, correspondingly. Thereupon, a transition point between the expansion fan and the gradual expansion on the passage shock can be identified. The only expansion-fan waves to be included in the overall expansion field are just those extending till the inception of the gradual-

expansion as noted in Figure 3.28. For those expansion-fan characteristics Ch_{n_f} upstream of the gradual expansion, the flow properties are solved within an iterative secant-method that solves the wall-point unit process between point a and points n_f on the passage shock. For every characteristic Ch_{n_f}, the geometric slope between their extremity points is

$$\mathcal{S}_{an_{f,psh}} = \frac{y_{n_{f,psh}} - y_a}{z_{n_{f,psh}} - z_a} \quad \textbf{(3.3.92)}$$

To determine the expansion, a relative Mach number M'_{n_f} is assumed for the characteristics Ch_{n_f}, for which ν_{n_f} is given by the Prandtl-Meyer function in Eq. 2.4.34 and μ_{n_f} as per Eq. 2.4.32. Thus, the Prandtl-Meyer expansion for a left-running characteristic from Eq. 2.4.38 determines the flow angle β_{n_f} for the expansion-fan characteristic as

$$\beta_{n_f} = \beta_a - \nu_a(M'_a) + \nu_{n_f}\left(M'_{n_f}\right) \quad \textbf{(3.3.93)}$$

The resultant characteristic slope from the expansion fan is

$$\mathcal{S}_{an_{f,psh}}\Big|_{PM} = \tan\left[\frac{(\beta_a - \mu_a) + \left(\beta_{n_f} - \mu_{n_f}\right)}{2}\right] \quad \textbf{(3.3.94)}$$

An error in the characteristic slopes is obtained as follows

$$E = \mathcal{S}_{an_{f,psh}} - \mathcal{S}_{an_{f,psh}}\Big|_{PM} \quad \textbf{(3.3.95)}$$

The process repeats for another assumption of M'_{n_f} with a corresponding error, so that secant method can be solved iteratively until the error reaches the tolerance set to 1e-6.

The algorithm established to layout the characteristics for the fan-expansion and gradual expansion permits the identification of any Prandtl-Meyer expansion of opposite sign, if any, accounting thus for pre-compression. The pre-compression is a series of weak shocks extending over a suction-surface ramp and coalescing all in the leading-edge of the next adjacent blade as seen in Figure 3.29. This method is then applicable to pre-

compression aerofoils that intend to reduce the passage-shock strength and losses, and also conventional aerofoils that might develop a localized pre-compression region due to the suction-surface curvature. The pre-compression process is resolved similarly to the fan-expansion process in terms of the discretization, but this time along the suction surface. Oblique shock theory from Sec. 2.4.2 is then applied successively to each weak oblique-shock to find the downstream flow properties till the onset of the gradual-expansion.

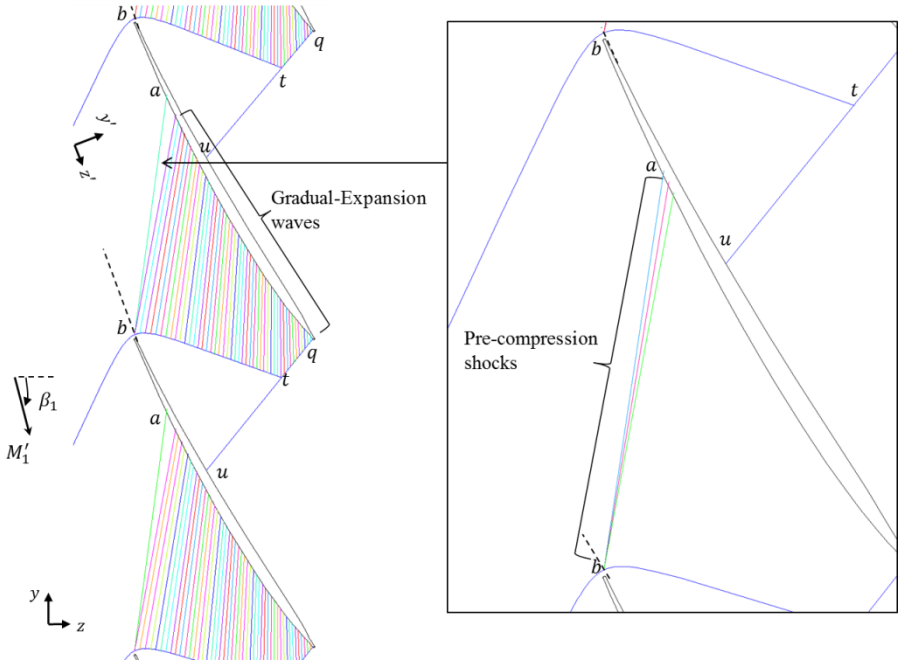

Figure 3.29 Pre-compression shocks arising from the suction-surface ramp and coalescing at the leading edge of the next adjacent blade

The solution of the gradual expansion, and potential expansion fan and pre-compression determines the overall flow process at zone V. This method provides the entire circumferential distribution of the relative Mach number upstream of any shape of passage-shock, whether is unstarted or started. In turn, the total-pressure ratio can be computed at every point along the passage-shock for which a final circumferential mass-averaged shock-loss coefficient is obtained as discussed in the following section.

3.3.8 Passage-Shock Losses

The integration points on the passage-shock (unstarted or started) are established by the intersecting points $n_{g,psh}$ with the gradual-expansion characteristics in Sec. 3.3.7.2. In

the case of expansion-fan characteristics for highly-loaded blade-elements, their intersecting points $n_{f,psh}$ with the passage shock are contemplated accordingly in Sec. 3.3.7.3. All these passage-shock points n_{psh} contain the upstream flow information for the computation of the passage-shock relative total-pressure loss. Even though there is no transition point *t* in the unstarted and unmerged started shock-configurations by definition, the passage-shock impingement on the suction surface is considered as the point *t* for algorithm-convenience purposes. Thus, the next rule can be established

$$y_t = y_{N_{g,psh}} = y_{psh_{ss}} = y_k \quad ; \ unstarted\ and\ unmerged\ started \tag{3.3.96}$$

Clearly, the passage-shock configuration shape portion, hyperbolic or straight (if any), dictates the upstream Mach number and shock angle to be used. For hyperbolic portion, the upstream relative Mach number $M'_{1_{n_{psh}}}$ is considered to be M'_1 due to the formulation of the shock angle for this region. In the case of the straight-section, the upstream relative Mach number $M'_{1_{n_{psh}}}$ is $M'_{n_{psh}}$ as is the local value ahead of the discretized oblique-shock point. The shock angle is defined for the hyperbolic section of the passage-shock as that from a detached bow-shock in Eq. 3.3.42. For the straight-portion the shock angle is constant and is that computed from the iterative-method error of Eq. 3.3.88, projected on the relative frame of reference. Both shock angle expressions are hence written as

$$\varsigma_{n_{psh}} = \operatorname{atan}\left(\frac{\sqrt{X'^2 + \left(M_1'^2 - 1\right)y_{n_{psh}}}}{\left(M_1'^2 - 1\right)y_{n_{psh}}}\right) \quad ; \ y_{n_{psh}} \leq y_t$$

$$\varsigma_{n_{psh}} = \left|-\varsigma_{psh} - \beta_1 - \frac{\pi}{2}\right| \quad ; \ y_{n_{psh}} > y_t{}' \tag{3.3.97}$$

The flow properties downstream of the passage-shock, are computed using the oblique-shock theory from Sec. 2.4.2, expressed as

$$\delta_{n_{psh}} = \operatorname{atan}\left\{2\cot\varsigma_{n_{psh}}\frac{M'^2_{1_{n_{psh}}}\sin^2\varsigma_{n_{psh}} - 1}{M'^2_{1_{n_{psh}}}\left[\gamma + \cos\left(2\varsigma_{n_{psh}}\right)\right] + 2}\right\} \tag{3.3.98}$$

$$M'_{2_{n_{psh}}} = \sqrt{\frac{(\gamma-1){M'_{1_{n_{psh}}}}^2 \sin^2 \varsigma_{n_{psh}} + 2}{(2\gamma {M'_{1_{n_{psh}}}}^2 \sin^2 \varsigma_{n_{psh}} + 1 - \gamma)\sin^2(\varsigma_{n_{psh}} - \delta_{n_{psh}})}} \quad \textbf{(3.3.99)}$$

$$tr_{n_{psh}} = \frac{T_{2_{n_{psh}}}}{T_{1_{n_{psh}}}}$$

$$= 1 + \frac{(\gamma {M'_{1_{n_{psh}}}}^2 \sin^2 \varsigma_{n_{psh}} + 1)}{{M'_{1_{n_{psh}}}}^2 \sin^2 \varsigma_{n_{psh}}} \frac{2(\gamma-1)}{(\gamma+1)^2} ({M'_{1_{n_{psh}}}}^2 \sin^2 \varsigma_{n_{psh}} - 1) \quad \textbf{(3.3.100)}$$

$$pr_{n_{psh}} = \frac{p_{2_{n_{psh}}}}{p_{1_{n_{psh}}}} = 1 + \frac{2\gamma}{\gamma+1}({M'_{1_{n_{psh}}}}^2 \sin^2 \varsigma_{n_{psh}} - 1) \quad \textbf{(3.3.101)}$$

$$\mathrm{PR'}_{n_{psh}} = \frac{{P'}_{2_{n_{psh}}}}{{P'}_{1_{n_{psh}}}} =$$

$$\left[\frac{(\gamma+1){M'_{1_{n_{psh}}}}^2 \sin^2 \varsigma_{n_{psh}}}{(\gamma-1){M'_{1_{n_{psh}}}}^2 \sin^2 \varsigma_{n_{psh}} + 2}\right]^{\frac{\gamma}{\gamma-1}} \left[\frac{\gamma+1}{2\gamma {M'_{1_{n_{psh}}}}^2 \sin^2 \varsigma_{n_{psh}} - (\gamma-1)}\right]^{\frac{1}{\gamma-1}} \quad \textbf{(3.3.102)}$$

where M'_1 in Eq. 3.3.98 to Eq. 3.3.102 is expressed for every section of the passage shock as

$$M'_{1_{n_{psh}}} = M'_1 \quad y_{n_{psh}} \leq y_t$$

$$M'_{1_{n_{psh}}} = M'_{n_{psh}} \quad y_{n_{psh}} > y_t \quad \textbf{(3.3.103)}$$

The computation of the mass-averaged values from Eq. 3.3.99 to Eq. (3.3.103 in the circumferential direction is performed by integrating all the weight-flow-averaged values at every discretization point n_{psh} from the detached bow-shock vertex till the passage-shock impingement on the suction surface (point k or point q) as

$$\overline{M'_{1_{psh}}} = \frac{\int_{y_{1_{psh}}}^{y_{N_{psh}}} M'_{n_{psh}} \left(1 + \frac{\gamma - 1}{2} M'_{n_{psh}}\right)^{\frac{-\gamma}{\gamma-1}+\frac{1}{2}} M'_{1_{n_{psh}}} \cos(\frac{\pi}{2} - \varsigma_{n_{psh}}) ds}{\int_{y_{1_{psh}}}^{y_{N_{psh}}} M'_{n_{psh}} \left(1 + \frac{\gamma - 1}{2} M'_{n_{psh}}\right)^{\frac{-\gamma}{\gamma-1}+\frac{1}{2}} \cos(\frac{\pi}{2} - \varsigma_{n_{psh}}) ds} \quad \textbf{(3.3.104)}$$

$$\overline{M'_{2_{psh}}} = \frac{\int_{y_{1_{psh}}}^{y_{N_{psh}}} M'_{n_{psh}} \left(1 + \frac{\gamma - 1}{2} M'_{n_{psh}}\right)^{\frac{-\gamma}{\gamma-1}+\frac{1}{2}} M'_{2_{n_{psh}}} \cos(\frac{\pi}{2} - \varsigma_{n_{psh}}) ds}{\int_{y_{1_{psh}}}^{y_{N_{psh}}} M'_{n_{psh}} \left(1 + \frac{\gamma - 1}{2} M'_{n_{psh}}\right)^{\frac{-\gamma}{\gamma-1}+\frac{1}{2}} \cos(\frac{\pi}{2} - \varsigma_{n_{psh}}) ds} \quad \textbf{(3.3.105)}$$

$$\overline{tr_{psh}} = \frac{\int_{y_{1_{psh}}}^{y_{N_{psh}}} M'_{n_{psh}} \left(1 + \frac{\gamma - 1}{2} M'_{n_{psh}}\right)^{\frac{-\gamma}{\gamma-1}+\frac{1}{2}} tr_{n_{psh}} \cos(\frac{\pi}{2} - \varsigma_{n_{psh}}) ds}{\int_{y_{1_{psh}}}^{y_{N_{psh}}} M'_{n_{psh}} \left(1 + \frac{\gamma - 1}{2} M'_{n_{psh}}\right)^{\frac{-\gamma}{\gamma-1}+\frac{1}{2}} \cos(\frac{\pi}{2} - \varsigma_{n_{psh}}) ds} \quad \textbf{(3.3.106)}$$

$$\overline{pr_{psh}} = \frac{\int_{y_{1_{psh}}}^{y_{N_{psh}}} M'_{n_{psh}} \left(1 + \frac{\gamma - 1}{2} M'_{n_{psh}}\right)^{\frac{-\gamma}{\gamma-1}+\frac{1}{2}} pr_{n_{psh}} \cos(\frac{\pi}{2} - \varsigma_{n_{psh}}) ds}{\int_{y_{1_{psh}}}^{y_{N_{psh}}} M'_{n_{psh}} \left(1 + \frac{\gamma - 1}{2} M'_{n_{psh}}\right)^{\frac{-\gamma}{\gamma-1}+\frac{1}{2}} \cos(\frac{\pi}{2} - \varsigma_{n_{psh}}) ds} \quad \textbf{(3.3.107)}$$

$$\overline{\mathrm{PR}'_{psh}} = \frac{\int_{y_{1_{psh}}}^{y_{N_{psh}}} M'_{n_{psh}} \left(1 + \frac{\gamma - 1}{2} M'_{n_{psh}}\right)^{\frac{-\gamma}{\gamma-1}+\frac{1}{2}} \mathrm{PR}'_{n_{psh}} \cos(\frac{\pi}{2} - \varsigma_{n_{psh}}) ds}{\int_{y_{1_{psh}}}^{y_{N_{psh}}} M'_{n_{psh}} \left(1 + \frac{\gamma - 1}{2} M'_{n_{psh}}\right)^{\frac{-\gamma}{\gamma-1}+\frac{1}{2}} \cos(\frac{\pi}{2} - \varsigma_{n_{psh}}) ds} \quad \textbf{(3.3.108)}$$

The mass-average integrals from Eq. 3.3.104 to Eq. 3.3.108 are resolved using numerical integration. The Newton-Cotes functions are calculated as follows

$$F_{wf}(n) = F_{wf_n} = M'_{n_{psh}} \left(1 + \frac{\gamma - 1}{2} M'_{n_{psh}}\right)^{\frac{-\gamma}{\gamma-1}+\frac{1}{2}} \cos(\frac{\pi}{2} - \varsigma_{n_{psh}}) \quad \textbf{(3.3.109)}$$

$$F_{M_1'}(n) = F_{M_1'_n} = M'_{1_{n_{psh}}} F_{wf}(n) \quad \textbf{(3.3.110)}$$

$$F_{M_2'}(n) = F_{M_2'_n} = M'_{2_{n_{psh}}} F_{wf}(n) \quad \textbf{(3.3.111)}$$

$$F_{tr}(n) = F_{tr_n} = tr_{n_{psh}} F_{wf}(n) \quad \textbf{(3.3.112)}$$

$$F_{pr}(n) = F_{pr}{}_n = tr_{n_{psh}} F_{wf}(n) \tag{3.3.113}$$

$$F_{\mathrm{PR}'}(n) = F_{\mathrm{PR}'}{}_n = \mathrm{PR}'_{n_{psh}} F_{wf}(n) \tag{3.3.114}$$

Using the trapezoid rule, the passage-shock mass-averaged values are integrated as

$$\overline{M'_{1_{psh}}} = \frac{\sum_{n=1}^{N} \frac{y_{n+1_{psh}} - y_{n_{psh}}}{2} \left[F_{M_1}{}'(n) + F_{M_1}{}'(n+1)\right]}{\sum_{n=1}^{N} \frac{y_{n+1_{psh}} - y_{n_{psh}}}{2} \left[F_{wf}(n) + F_{wf}(n+1)\right]} \tag{3.3.115}$$

$$\overline{M'_{2_{psh}}} = \frac{\sum_{n=1}^{N} \frac{y_{n+1_{psh}} - y_{n_{psh}}}{2} \left[F_{M_2}{}'(n) + F_{M_2}{}'(n+1)\right]}{\sum_{n=1}^{N} \frac{y_{n+1_{psh}} - y_{n_{psh}}}{2} \left[F_{wf}(n) + F_{wf}(n+1)\right]} \tag{3.3.116}$$

$$\overline{tr_{psh}} = \frac{\sum_{n=1}^{N} \frac{y_{n+1_{psh}} - y_{n_{psh}}}{2} \left[F_{tr}(n) + F_{tr}(n+1)\right]}{\sum_{n=1}^{N} \frac{y_{n+1_{psh}} - y_{n_{psh}}}{2} \left[F_{wf}(n) + F_{wf}(n+1)\right]} \tag{3.3.117}$$

$$\overline{pr_{psh}} = \frac{\sum_{n=1}^{N} \frac{y_{n+1_{psh}} - y_{n_{psh}}}{2} \left[F_{pr}(n) + F_{pr}(n+1)\right]}{\sum_{n=1}^{N} \frac{y_{n+1_{psh}} - y_{n_{psh}}}{2} \left[F_{wf}(n) + F_{wf}(n+1)\right]} \tag{3.3.118}$$

$$\overline{\mathrm{PR}'_{psh}} = \frac{\sum_{n=1}^{N} \frac{y_{n+1_{psh}} - y_{n_{psh}}}{2} \left[F_{\mathrm{PR}'}(n) + F_{\mathrm{PR}'}(n+1)\right]}{\sum_{n=1}^{N} \frac{y_{n+1_{psh}} - y_{n_{psh}}}{2} \left[F_{wf}(n) + F_{wf}(n+1)\right]} \tag{3.3.119}$$

Eq. 3.3.119 gives the circumferential mass-averaged relative total-pressure loss induced by the passage shock. Since the only shock-loss mechanisms are the bow-shock and the passage-shock for unstarted flows, the overall relative total-pressure ratio between inlet and outlet can thus be calculated for these conditions as

$$\mathrm{PR}'_{sh_{uch}} = \mathrm{PR}'_{bow} * \overline{\mathrm{PR}'_{psh}} = \left(\frac{P'_2}{P'_1}\right)_{bow} \overline{\left(\frac{P'_2}{P'_1}\right)_{psh}} \tag{3.3.120}$$

Following Eq. 2.6.1, the overall shock-loss coefficient for unstarted operations becomes

$$\overline{\omega_{sh'_{uch}}} = \frac{1 - \mathrm{PR}'_{sh_{uch}}}{1 - (1 + \frac{\gamma - 1}{2} M_1{}')^{\frac{\gamma}{1-\gamma}}} \quad \textbf{(3.3.121)}$$

In contrast, the overall relative total-pressure ratio in started flows needs to consider the additional loss-source from the second passage-shock. This calculation is incorporated within an iterative method to correctly position this choke-induced oblique-shock, discussed in Sec. 3.3.9

3.3.9 Iterative Method for Started-Flow Shock Configurations

The choke-induced oblique-shock location that decelerates the flow to subsonic conditions was assumed in Sec. 3.3.6, for whose shock angle was calculated in Sec. 3.3.7.1 according to the gradual expansion ahead. This second passage-shock can intersect or not the passage-shock portion of the detached bow-shock as illustrated in Figure 3.23. The flow conditions downstream of the first-passage shock were computed accordingly in Sec. 3.3.8 from the expansion system upstream. Nevertheless, in the presence of a second passage-shock, a second expansion needs to be resolved to determine the flow conditions upstream. For that operating case where the second passage-shock does not coalesce with the first, the expansion is computed between points *b-k-u-q*. Similarly to the expansion process discussed in Sec. 3.3.7.2, a wall-unit process is applied on the suction-surface segment between the first and second passage shocks; whereafter, a field-point calculation determines the full flow-field expansion comprised between both shocks. In a like manner, the expansion field for those cases where the second oblique-shock coalesces with the first is determined between points *b-t-u* and is resolved using the field-point calculation reviewed in Sec. 3.3.7.2. The field-point calculation for any of the started shock-configurations determines the relative Mach number $M'_{n_{psh2}}$ upstream of the second passage-shock at the established discretization points n_{psh2}. Equally to Sec. 3.3.8, the flow conditions downstream of the choke-induced shock are computed using oblique-shock theory from Sec. 2.4.2. In this case, the shock angle for all the discretization points is the same as there is no composition of different shapes, becoming a constant ς_{psh} and calculated as the straight

portion of Eq. 3.3.97. Thence, the relative total-pressure ratio for the second passage-shock can be written as,

$$\mathrm{PR'}_{n_{psh2}} = \frac{{P'}_{2_{n_{psh2}}}}{{P'}_{1_{n_{psh2}}}} = \left[\frac{(\gamma+1){M'_{n_{psh2}}}^{2}\sin^2\varsigma_{psh}}{(\gamma-1){M'_{n_{psh2}}}^{2}\sin^2\varsigma_{psh}+2}\right]^{\frac{\gamma}{\gamma-1}} \left[\frac{\gamma+1}{2\gamma{M'_{n_{psh2}}}^{2}\sin^2\varsigma_{psh}-(\gamma-1)}\right]^{\frac{1}{\gamma-1}} \quad \textbf{(3.3.122)}$$

The circumferential mass-average values for the flow properties upstream and downstream of the second passage-shock are obtained as in Sec. 3.3.8 and solved with the numerical-integration approach described therein. For instance, the mass-averaged values for the inlet relative Mach number and relative total-pressure ratio corresponding to second passage-shock are respectively

$$\overline{M'_{1_{psh2}}} = \frac{\int_{y_{1_{psh2}}}^{y_{N_{psh2}}} M'_{n_{psh2}}\left(1+\frac{\gamma-1}{2}M'_{n_{psh2}}\right)^{\frac{-\gamma}{\gamma-1}+\frac{1}{2}} M'_{n_{psh}}\cos(\frac{\pi}{2}-\varsigma_{psh})ds}{\int_{y_{1_{psh2}}}^{y_{N_{psh2}}} M'_{n_{psh2}}\left(1+\frac{\gamma-1}{2}M'_{n_{psh2}}\right)^{\frac{-\gamma}{\gamma-1}+\frac{1}{2}}\cos(\frac{\pi}{2}-\varsigma_{psh})ds} \quad \textbf{(3.3.123)}$$

$$\overline{\mathrm{PR'}_{psh2}} = \frac{\int_{y_{1_{psh2}}}^{y_{N_{psh2}}} M'_{n_{psh2}}\left(1+\frac{\gamma-1}{2}M'_{n_{psh2}}\right)^{\frac{-\gamma}{\gamma-1}+\frac{1}{2}} \mathrm{PR'}_{n_{psh2}}\cos(\frac{\pi}{2}-\varsigma_{psh})ds}{\int_{y_{1_{psh2}}}^{y_{N_{psh2}}} M'_{n_{psh2}}\left(1+\frac{\gamma-1}{2}M'_{n_{psh2}}\right)^{\frac{-\gamma}{\gamma-1}+\frac{1}{2}}\cos(\frac{\pi}{2}-\varsigma_{psh})ds} \quad \textbf{(3.3.124)}$$

The additional relative total-pressure loss in Eq. 3.3.123 caused by the second passage-shock during started flows, modifies the overall relative total-pressure ratio between inlet and outlet to be

$$\mathrm{PR'}_{sh_{ch}} = \mathrm{PR'}_{bow} * \overline{\mathrm{PR'}_{psh}} * \overline{\mathrm{PR'}_{psh2}} = \left(\frac{P'_2}{P'_1}\right)_{bow} \overline{\left(\frac{P'_2}{P'_1}\right)_{psh}} \overline{\left(\frac{P'_2}{P'_1}\right)_{psh2}} \quad \textbf{(3.3.125)}$$

Using Eq. 2.6.1, the overall shock-loss coefficient for started operating conditions becomes

$$\overline{\omega_{sh}{}'_{ch}} = \frac{1 - \mathrm{PR}'_{sh_{ch}}}{1 - (1 + \frac{\gamma - 1}{2} M_1{}')^{\frac{\gamma}{1-\gamma}}} \tag{3.3.126}$$

Yet, the overall shock-loss coefficient in Eq. 3.3.126 is based on an assumed position for the choke-induced passage-shock which is corrected by the iterative second-passage-shock-location method described below.

The blade outlet-to-throat area-ratio defines the choking situation. The blade-throat area is calculated as that streamtube cross-sectional area normal to the flow with the minimum width. By interpolating the suction-surface axial-coordinates $y_{n_{ss}}$ into the pressure-surface coordinate distribution, the corresponding suction-surface tangential coordinate $y_{n_{ss,on,ps}}$ on the pressure surface is found. The difference between the tangential coordinates of the pressure surface and the suction surface of the adjacent blade in the relative coordinate-system might be expressed as

$$w_n = \left| y_{n_{ss}} - y_{n_{ss,on,ps}} \right| \cos \beta_1 \tag{3.3.127}$$

The streamtube area corresponding to the minimum width from Eq. 3.3.127 located at $z_{w,min}$ gives the blade-throat area as

$$A_{thr} = w_{min} H_{z_{w,min}} \tag{3.3.128}$$

Likewise, the streamtube area at the outlet of a blade-element is

$$A_{out} = w_{ap} H_{z_{ap}} = w_{ap} H_{out} \tag{3.3.129}$$

Similarly to Sec. 2.5.3, an area-to-critical-area ratio can be found as

$$\frac{A}{A^*} = \frac{A_{out}}{A_{thr}} = \frac{w_{ap} H_{out}}{w_{min} H_{z_{w,min}}} \tag{3.3.130}$$

where the streamtube height contraction between outlet and throat is calculated as in the procedure described from Eq. 3.3.61 to Eq. 3.3.67, resulting in

$$\frac{H_{out}}{H_{z_{w,min}}} = \frac{{R_{j+1/2}}_{TE}^{\,2} - {R_{j-1/2}}_{TE}^{\,2}}{R_{j_{TE}}} \frac{R_{j_{w,min}}}{{R_{j+1/2}}_{w,min}^{\,2} - {R_{j-1/2}}_{w,min}^{\,2}} \tag{3.3.131}$$

From Eq. 2.5.27, the area-to-critical-area ratio as a unique function of the relative Mach number at the outlet has both solutions subsonic and supersonic, and is expressed as

$$\frac{A_{out}}{A_{thr}} = \frac{1}{M'_{out}} \left[\frac{1 + \frac{\gamma - 1}{2} {M'_{out}}^2}{(1 + \frac{\gamma - 1}{2})^{\frac{1}{\gamma - 1}}} \right]^{\frac{\gamma + 1}{2(\gamma - 1)}} \tag{3.3.132}$$

The solution for Eq. 3.3.132 is obtained by independent iterative secant-methods that resolves both for $M'_{out}|_{sub}$ and $M'_{out}|_{sup}$. The stagnation conditions corresponding to the subsonic and supersonic solutions define the operation ranges of the blade passage. The outlet total-to-static pressure ratio for which the flow is everywhere subsonic between the throat and the outlet corresponds to the solution of the outlet relative subsonic Mach number, given by

$$\left. \frac{{P'}_{0_{out}}}{p_{out}} \right|_{sub} = \left[1 + \frac{\gamma - 1}{2} \left({M'_{out}}^2 |_{sub} \right) \right]^{\frac{\gamma}{\gamma - 1}} \tag{3.3.133}$$

On the other hand, the supersonic solution of the outlet relative Mach number corresponds to that outlet total-to-static pressure ratio for which the flow is shock-free within the same domain, expressed as

$$\left. \frac{{P'}_{0_{out}}}{p_{out}} \right|_{sup} = \left[1 + \frac{\gamma - 1}{2} \left({M'_{out}}^2 |_{sup} \right) \right]^{\frac{\gamma}{\gamma - 1}} \tag{3.3.134}$$

In contrast to the convergent-divergent nozzle in Figure 2.28 of Sec. 2.5.2, the flow in a blade passage is not isentropic as it traverses the bow-shock and the passage-shock system (merged or not coalesced), inducing a relative total-pressure loss. Thence, the stagnation conditions at the outlet by no means consider the inlet relative total-pressure, instead it uses the actual relative total-pressure loss.

The range limit for which the choking-induced shock stands at the exit requires $M'_{out}|_{sup}$ to be the upstream relative Mach number to be resolved using oblique shock theory. The deflection angle δ_{psh} induced by this oblique shock is calculated from Eq. 2.4.24 as

$$\delta_{psh} = \operatorname{atan}\left\{2\cot\varsigma_{psh}\frac{(M'^{2}_{out}|_{sup})\sin^2\varsigma_{psh}-1}{(M'^{2}_{out}|_{sup})[\gamma+\cos(2\varsigma_{psh})]+2}\right\} \quad \textbf{(3.3.135)}$$

Thence, the downstream relative Mach number at the outlet is determined using Eq. 2.4.19, given by

$$M'_{2_{out}} = \sqrt{\frac{(\gamma-1)(M'^{2}_{out}|_{sup})\sin^2\varsigma_{psh}+2}{[2\gamma(M'^{2}_{out}|_{sup})\sin^2\varsigma_{psh}+1-\gamma]\sin^2(\varsigma_{psh}-\delta_{psh})}} \quad \textbf{(3.3.136)}$$

The static pressure-ratio for the choking-induced shock standing at the exit is computed from Eq. 2.4.18 as

$$\frac{p_{2_{out}}}{p_{1_{out}}} = 1+\frac{2\gamma}{\gamma+1}[(M'^{2}_{out}|_{sup})\sin^2\varsigma_{psh}-1] \quad \textbf{(3.3.137)}$$

The stagnation condition downstream of the shock standing at the blade-passage exit is obtained from the definition of the total-to-static pressure ratio for the supersonic solution, which is written as

$$\left.\frac{P'_{0_{out}}}{p_{out}}\right|_{sup} = \frac{p_{2_{out}}}{p_{1_{out}}} * \left.\frac{P'_{02_{out}}}{p_{2_{out}}}\right|_{sh@ex} \quad \textbf{(3.3.138)}$$

The total-to-static pressure ratios $(P'_{02_{out}}/p_{2_{out}})_{sub}$, $(P'_{02_{out}}/p_{2_{out}})_{sh@exit}$, $(P'_{0_{out}}/p_{out})_{sup}$, establish the operation ranges for the blade passage. The current stagnation condition at every stream surface is known as the full REE establishes the outlet relative Mach number. Nevertheless, this expression for the stagnation condition must include the total-pressure loss from the bow-shock and the passage-shock mechanisms. Therefore, the total-to-static pressure ratio at the back is given from the assumed shock-loss configuration as

$$\left(\frac{\widetilde{P'_{02_{out}}}}{p_{2_{out}}}\right) = \mathrm{PR}'_{sh_{ch}}\left[1+\frac{\gamma-1}{2}{M'}_{out}^{2}\right]^{\frac{\gamma}{\gamma-1}}$$

$$= \left(\frac{P'_2}{P'_1}\right)_{bow}\overline{\left(\frac{P'_2}{P'_1}\right)}_{psh}\overline{\left(\frac{P'_2}{P'_1}\right)}_{psh2}\left[1+\frac{\gamma-1}{2}{M'}_{out}^{2}\right]^{\frac{\gamma}{\gamma-1}} \quad \textbf{(3.3.139)}$$

To guarantee that the assumption of the shock configuration is consistent, the current stagnation condition at the outlet is compared against the range limits as shown in Table 3.1 and Figure 3.30.

Table 3.1 Range of total-to-static pressure ratios at the blade-element exit to validate the situation of the assumed passage-shock pattern.

Range	Operating Condition	Flow situation downstream of the blade-passage throat
$\left(\frac{\widetilde{P'_{02_{out}}}}{p_{2_{out}}}\right) < \left.\frac{P'_{0_{out}}}{p_{out}}\right\|_{sub}$	Unstarted	a) No Shock. Flow is everywhere subsonic
$\left(\frac{\widetilde{P'_{02_{out}}}}{p_{2_{out}}}\right) = \left.\frac{P'_{0_{out}}}{p_{out}}\right\|_{sub}$	Started	b) Second passage-shock at blade throat
$\left.\frac{P'_{0_{out}}}{p_{out}}\right\|_{sub} > \left(\frac{\widetilde{P'_{02_{out}}}}{p_{2_{out}}}\right) < \left.\frac{P'_{02_{out}}}{p_{2_{out}}}\right\|_{sh@ex}$	Started	c) Second passage-shock between blade throat and exit
$\left(\frac{\widetilde{P'_{02_{out}}}}{p_{2_{out}}}\right) = \left.\frac{P'_{02_{out}}}{p_{2_{out}}}\right\|_{sh@ex}$	Started	d) Second passage-shock standing at blade exit
$\left.\frac{P'_{02_{out}}}{p_{2_{out}}}\right\|_{sh@ex} > \left(\frac{\widetilde{P'_{02_{out}}}}{p_{2_{out}}}\right) < \left.\frac{P'_{0_{out}}}{p_{out}}\right\|_{sup}$	Started	e) Over-expanded
$\left(\frac{\widetilde{P'_{02_{out}}}}{p_{2_{out}}}\right) = \left.\frac{P'_{0_{out}}}{p_{out}}\right\|_{sup}$	Started	f) Shock-free

$\left(\frac{P'\widetilde{_{02_{out}}}}{p_{2_{out}}}\right) > \left.\frac{P'_{0_{out}}}{p_{out}}\right|_{sup}$ Started g) Under-expanded

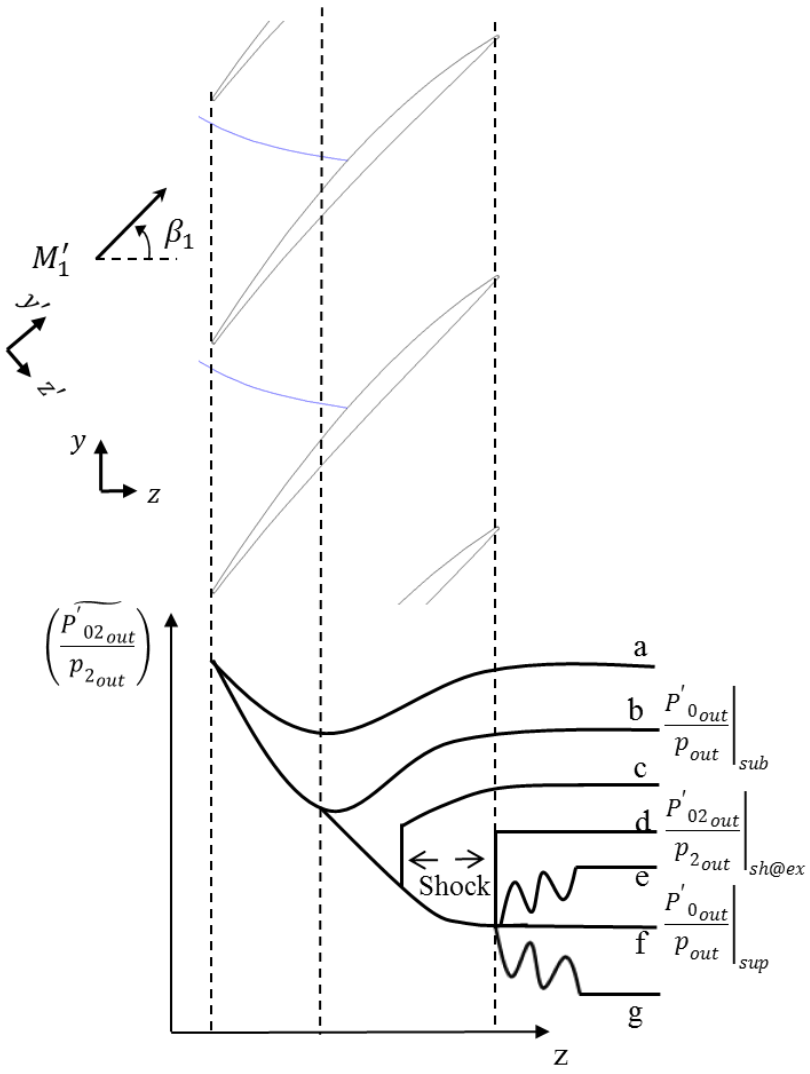

Figure 3.30 Choke-induced passage-shock situation in a blade-element passage as a function of the current total-to-static pressure ratio.

If there is no agreement between the passage-shock configuration assumed to obtain the overall shock-induced relative total-pressure loss and the corresponding range of total-to-static pressure ratios at the back, a new computation starts with a different location assumption for the choke-induced passage-shock. The new location for the second passage-shock is defined by moving it downstream just after the blade throat for the current flow conditions so that the complete procedure can be re-started all over again

from Sec 3.3.7.2. The second passage-shock cannot go more upstream than the sonic point or the blade throat; otherwise it would mean that there is a shock in the convergent portion of the passage, violating the compressible-flow physics. If this would be the case, then no passage-shock is required, and the operating condition becomes unstarted, where the only relative total-pressure loss-mechanism is the detached bow-shock and the portion of it that penetrates into the passage.

Conversely, if the assumed passage-shock configuration agrees with the corresponding range of the current back stagnation-condition, a new position for the choke-induced shock corresponding to $(P'_{02_{\widetilde{out}}}/p_{2_{out}})$ can be calculated to estimate a new relative total-pressure loss coefficient. Provided the agreement is satisfied, the free-jet or outlet relative Mach number that matches $(P'_{02_{\widetilde{out}}}/p_{2_{out}})$ is obtained from the stagnation condition as

$$\widetilde{M'_{2_{out}}} = \sqrt{\frac{2}{\gamma-1}\left[\left(\frac{P'_{02_{\widetilde{out}}}}{p_{2_{out}}}\right)^{\frac{\gamma-1}{\gamma}} - 1\right]} \tag{3.3.140}$$

The ratio between the outlet area and the area where the second passage-shock forms can be defined through their critical area using the area-velocity relationship from Eq. 2.5.27, as

$$\frac{A_{out}}{A_{psh2}} = \frac{A_{out}}{A_{out}^{*}}\frac{A_{psh2}^{*}}{A_{psh2}}$$

$$= \frac{1}{\widetilde{M'_{2_{out}}}}\left[\frac{1+\frac{\gamma-1}{2}\widetilde{M'_{2_{out}}}^{2}}{(1+\frac{\gamma-1}{2})^{\frac{1}{\gamma-1}}}\right]^{\frac{\gamma+1}{2(\gamma-1)}} \overline{M'_{1_{psh2}}}\left[\frac{(1+\frac{\gamma-1}{2})^{\frac{1}{\gamma-1}}}{1+\frac{\gamma-1}{2}\overline{M'_{1_{psh2}}}^{2}}\right]^{\frac{\gamma+1}{2(\gamma-1)}} \tag{3.3.141}$$

Substituting the outlet area from Eq. 3.3.129, the choke-induced passage-shock area is

$$A_{psh2} = \tag{3.3.142}$$

$$\frac{w_{ap}\dfrac{{R_{j+1/2}}_{TE}^{\,2}-{R_{j-1/2}}_{TE}^{\,2}}{{R_j}_{TE}}}{\dfrac{1}{\widetilde{M'_{2_{out}}}}\left[\dfrac{1+\dfrac{\gamma-1}{2}\widetilde{M'_{2_{out}}}^{\,2}}{(1+\dfrac{\gamma-1}{2})^{\frac{1}{\gamma-1}}}\right]^{\frac{\gamma+1}{2(\gamma-1)}}\overline{M'_{1_{psh2}}}\left[\dfrac{(1+\dfrac{\gamma-1}{2})^{\frac{1}{\gamma-1}}}{1+\dfrac{\gamma-1}{2}\overline{M'_{1_{psh2}}}^{\,2}}\right]^{\frac{\gamma+1}{2(\gamma-1)}}}}$$

Since the axial location and streamtube height are unknown for A_{psh2}, the streamtube area is calculated at every axial point on the blade is

$$A_n = w_n H_n = w_n = \left|y_{n_{ss}} - y_{n_{ss,on,ps}}\right| \cos\beta_1 \frac{{R_{j+1/2}}_n^{\,2} - {R_{j-1/2}}_n^{\,2}}{{R_j}_n} \quad \textbf{(3.3.143)}$$

Hence, the choked-induced passage-shock area A_{psh2} is interpolated into the distribution of flow areas A_n along the axial axis using a cubic-spline approximation, to find the corresponding axial coordinate z_{psh2} that corresponds to such shock area. In this manner, the first error for the first assumed axial position of the choke-induced shock is determined by

$$E_i = {z_q}_i - {z_{psh2}}_i \quad \textbf{(3.3.144)}$$

For the next iteration, a second axial-position ${z_q}_{i+1}$ is assumed for the second passage-shock, establishing a different shock-configuration to the initial assumption. The selection of ${z_q}_{i+1}$ is arbitrary, provided that is between the detached bow-shock point and the blade outlet. The overall methodology is thence re-started again in its entirety from Sec. 3.3.7.2. A gradual-expansion is computed over the suction surface till the new position of the second passage-shock, where its shock angle is determined using the shock-point unit process. This new second passage-shock angle produces such pattern that might intersect or not the first passage-shock. The full expansion is then determined to obtain the flow properties ahead of the new passage-shock, resolving for any potential expansion-fan waves or pre-compression shocks accordingly. The relative total-pressure loss is thus computed circumferentially, for which a mass-averaged value is determined. Similarly, the expansion between the first and second passage shock is resolved, calculating the mass-averaged relative total-pressure loss due to the choke-

induced shock. Theb, the overall shock-induced relative total-pressure loss is known due to the accrued relative total-pressure losses from the bow shock and both passage shocks, determining the total-to-static pressure ratio at the back. Provided there is agreement in the type of shock-configuration used, a new passage-shock axial location $z_{psh2}{}_{i+1}$ is computed to satisfy the stagnation condition at the back. Whereupon, the corresponding error for this second iteration cycle is

$$E_{i+1} = z_{q}{}_{i+1} - z_{psh2}{}_{i+1} \tag{3.3.145}$$

In a likewise manner to the previously mentioned iterative approaches, a secant-method is utilized to find the root of the linear function and estimate the next approximation for the axial location z_q of the choked-induced passage-shock. This results of results in a new z_{psh2} , for which the corresponding error is calculated. The secant method is solved iteratively until the error becomes lower than a tolerance set to 1e-6, determining an accurate value for the choked-induced passage-shock location that satisfies mass flow conservation, continuity and the back total-to-static pressure-ration condition.

3.4 Choking Mass Flow Redistribution

3.4.1 Overview

As reviewed in Sec. 2.1.5, when the outlet static pressure decreases, the inlet meridional velocity, and hence the meridional Mach number, increases. As a consequence, the mass flow rises. For the blade passage to accommodate more mass flow, the flow angle, and thus the incidence angle, reduces. An incidence reduction means that the flow becomes more normal to the passage in the blade-to-blade plane. Nevertheless, there is a minimum value for the incidence to decrease, as the flow has reached a maximum velocity within the passage, and no further flow acceleration can be accomplished. As no lower incidence value is possible, the inlet velocity triangle remains constant, fixing the mass flow. This maximum mass flow case is known as choke condition, corresponding to a minimum or choking incidence. The choke condition is often referred in the literature as leading edge choke or unique incidence [13], where the latter is a misnomer [1]. The term “unique incidence” is related to the two independent equations between upstream conditions and the first-captured wave.

As the Prandtl-Meyer expansion and continuity must be satisfied, it follows that for a given the inlet relative Mach number, there is one unique inlet flow angle that satisfies both equations, hence, a unique incidence [2].

A flow-physics examination explains the mass flow limitation in choke conditions. Inasmuch as the incidence is not allowed to further decrease, no more mass flow can be accommodated within the passage, remaining constant. In this choke conditions, the upstream conditions remain unchanged, and it is the passage-shock which displaces forward or backwards to increase or decrease the back static pressure, respectively, and match the boundary condition. For this reason, a comprehensive choke-prediction code consisting in an analytical choking incincende model, a choking margin calculator, and a numerical mass flow redistribution algorithm were developed in FORTRAN90 and implemented into the 2-D SLC axial-flow fan/compressor performance simulation software (SOCRATES) [14,17,31]. As a result, the minimum possible incidence i_{ch} and maximum mass flow $\dot{m}_{max}$ are computed and fixed for those stream surfaces identified as started.

Figure 3.31 displays the intervention of the choke-prediction method in its full within the 2-D SLC algorithm of SOCRATES. The iterative full REE and mass flow conservation solutions establish the flow properties at every streamline. After which, the choking incidence is computed by simultaneously solving the laws of continuity, conservation of total enthalpy and conservation of momentum between the inlet and a station on the chord. A comparison between the choking and actual incidences determines a coefficient denominated as choking margin. This parameter serves as a reference for the mass flow redistribution algorithm to limit the stream tube mass flow so that the choking margin becomes unity, and the incidence is matched to be that from the choking condition. Even though the mass flow redistribution model requires of the choking margin to operate, it was intentionally placed before any choke calculation so that the mass flow is corrected for the current iteration as a function of the choking margin determined in the previous iteration. Evidently, the mass flow redistribution model is activated after the very first full REE iteration so as to have a computed choking margin.

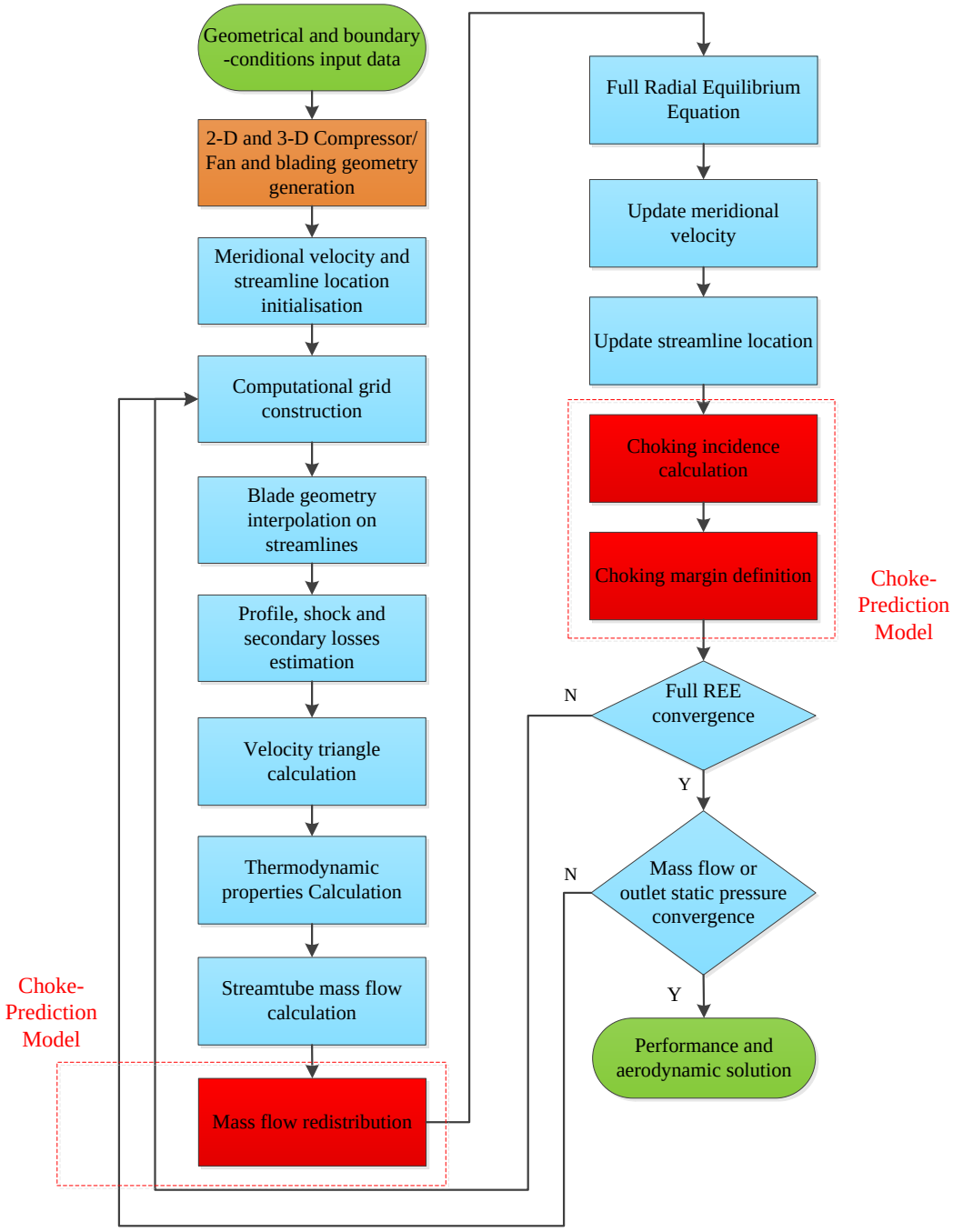

Figure 3.31 Implementation of the full choke-prediction model in the 2-D SLC axial-flow fan/compressor performance simulator (SOCRATES) [14,17,31]**.**

3.4.2 Choking Incidence

A 1-D supersonic flow model for unstarted cascade operation developed by Freeman and Cumpsty [1,2] was modified, adapted and implemented in the 2-D SLC code to arrive to the prediction of the choking inception. The modification consisted in

including the streamtube height contraction for the control volume established. The analysis defines a periodic control volume of one pitch, aligned with the flow direction so that the frontal area to the relative velocity vector is the staggered gap ϕ, starting upstream of the blade-row inlet and finishing somewhere along the passage, as shown diagrammatically in Figure 3.32.

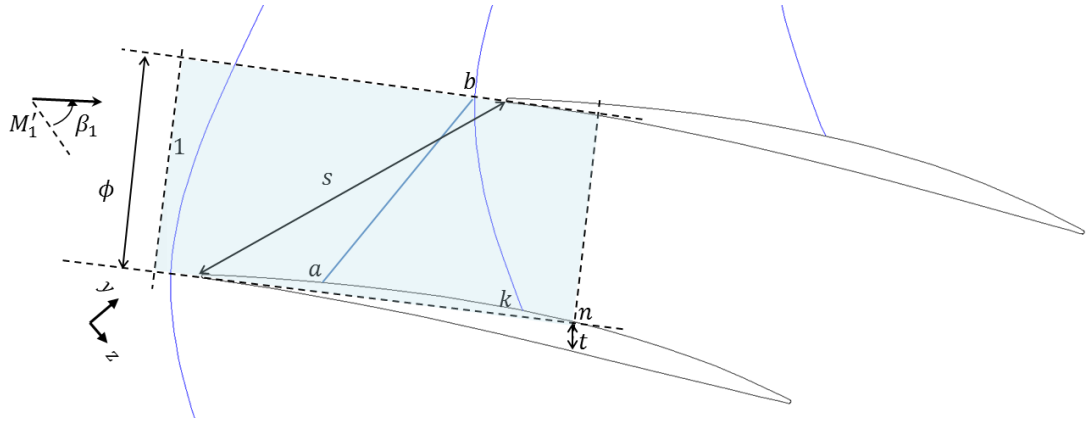

Figure 3.32 Control volume definition for a blade-element passage to predict the onset of the choking incidence.

For the domain in Figure 3.32, the governing relations of continuity, conservation of stagnation enthalpy and conservation of momentum must be satistfied.

The streamtube flow area for the domain inlet is as defined in Eq. 2.6.15 and Eq. 3.3.58. At the domain outlet, the flow direction is unknown as it depends on the diffusion magnitude. Yet, choking occurs more often and is more critical at the blade tip sections, where the blade-element profiles have a thin leading edge and a little curvature, and hence, a small camber. For this reason, it results reasonable to approximate the flow parallel to the blade surface so that the flow angle β_n at any surface point is the blade inlet angle k_1. Using the expression for the streamtube height in Eq. 3.3.62, the flow area at the domain outlet is thus

$$A_n = H_n(s - t_n)\cos k_1 = \frac{{R_{j+1/2}}_n^{\,2} - {R_{j-1/2}}_n^{\,2}}{R_{j_n}}(s - t_n)\cos k_1 \qquad \textbf{(3.4.1)}$$

Establishing conservation of mass flow between the domain inlet and outlet and substituting the streamtube height contraction ratio from Eq. 3.3.67, gives

$$H_1 \mathrm{scos}\,\beta_1 = H_n(s - t_n)\cos k_1$$

$$\frac{{R_{j+1/2}}_{LE}^{\,2} - {R_{j-1/2}}_{LE}^{\,2}}{R_{j_{LE}}} \frac{R_{j_n}}{{R_{j+1/2}}_n^{\,2} - {R_{j-1/2}}_n^{\,2}} = \frac{\cos k_1}{\cos \beta_1} \frac{(s - t_n)}{s} \quad \textbf{(3.4.2)}$$

The conservation of relative stagnation enthalpy h_0 for the control volume implies that

$$h_{01}{}' = h_{0n}{}'$$

$$CpT_{01} = CpT_{0n} \quad \textbf{(3.4.3)}$$

Substituting the total-to-static isentropic relationship from Eq. 2.5.23 in the conservation of stagnation enthalpy,

$$T_1 \left(1 + \frac{\gamma - 1}{2} {M_1}'^2\right) = T_n \left(1 + \frac{\gamma - 1}{2} {M_n}'^2\right) \quad \textbf{(3.4.4)}$$

Along the blade-chord direction, the momentum is conserved through the following relationship [1,2]

$$p_1 s + p_1 \gamma {M_1}'^2 s \frac{\cos \beta_1 \cos(k_1 - \beta_1)}{\cos k_1} = p_n s + p_n \gamma {M_n}'^2 (s - t_n) \quad \textbf{(3.4.5)}$$

The governing equations of conservation of mass, conservation of relative total-enthalpy, and conservation of momentum are simultaneously resolved. The system of equations can be algebraically manipulated to combine in a single expression the inlet conditions on the LHS and the outlet conditions on the RHS as

$$\frac{\frac{\cos k_1}{\cos \beta_1} + \gamma {M_1}'^2 \cos(\beta_1 - k_1)}{{M_1}' \sqrt{1 + \frac{\gamma - 1}{2} {M_1}'^2}} = \frac{1 + \gamma {M_n}'^2 (1 - \frac{t_n}{s})}{{M_n}' (1 - \frac{t_n}{s}) \sqrt{1 + \frac{\gamma - 1}{2} {M_n}'^2}} \quad \textbf{(3.4.6)}$$

Note that Eq. 3.4.6 establishes that for a blade profile with a given inlet angle, pitch, and thickness, there is a distribution with a minimum inlet flow direction or unique incidence for every inlet relative Mach number. Geometrically, the three blade-element parameters define the choking; however, it is the thickness distribution the more influential as this determines the blade-throat width for the stream tube area.

Forasmuch as this analysis is only valid for inlet flow angles greater than or equal to that for which the passage chokes, the flow beyond started operations is undetermined. Nevertheless, this model suffices to obtain the minimum value of β_1 from the LHS of Eq. 3.4.6. The choking flow angle is computed by specifying a set of values that solve the LHS so that β_1 is found using an iterative secant-method. The distribution of inlet flow angles as a function of the LHS $\beta_1 = f(LHS)$ permits to identify a minimum value, corresponding to the choking flow angle β_{ch}, determining in this way the choking incidence i_{ch}.

Alternatively, the 2-D SLC simulation framework already calculates the positive and negative angles of attacks, and working ranges required for the minimum-loss incidence computation using cascade rig-test correlations as discussed in Sec. 2.3.2. Despite its empirical nature, these parameters can be used to obtain an estimation of the choking incidences and compare it against those from the analytical method previously described.

In Sec. 2.7.1, the relationship between the incidence and the total-loss coefficient and the choking incidence definition was established. It is observed in Figure 2.46 the working-range narrowing as the inlet relative Mach number increases. This results critical for high-speed axial-flow compressors since the incidence range, and hence mass-flow range, shorten significantly, particularly in the choking regime. A measure of the operating range at started flows can be determined through the choking low-loss working range W_{ch}, designated as [136]

$$W_{ch} = \alpha^* - \alpha_{nst} = i^* - i_{ch} \quad \textbf{(3.4.7)}$$

where α is the angle for attack. The corresponding angles of attack calculation is based in a systematic methodology for 2-D NACA 65-series cascade tests [143], described in Aungier [136] and implemented in SOCRATES by Pachidis [14].

An equivalent stall low-loss working range can be also defined as $(i_{st} - i^*)$. For low-speed cascades both low-loss working ranges, choke and stall decrease at the same rate as the inlet relative Mach number increases [121]. In contrast, for high-speed blade profiles, the choke low-loss working range $(i^* - i_{ch})$ reduces faster than $(i_{st} - i^*)$ as

the M_1' is increased. Thus, the choking incidence i_{ch} becomes a function of M_1' and W_{ch}, expressed as [136]

$$i_{ch} = \frac{i^* - W_{ch}}{1 + 0.5{M_1'}^3} \quad \textbf{(3.4.8)}$$

Eq. 3.4.8 sets the lowest possible for the incidence for a cascade and no incidence value should be below it, since this is the operating condition where no further mass flow increase can be attained.

Although the choking incidence values between the analytical and empirical method differed about 0.5%, the ultimate impact of these discrepancies on the mass flow redistribution, and hence, in the passage shock-losses was negligible. Therefore, the blade-row relative total-pressure recovery and isentropic efficiency remain essentially unaffected.

Nonetheless, both analytical and empirical choking-incidence models were programmed and implemented within the 2-D SLC performance simulator so that their outcome is constantly compared during run-time. The robustness of the choking-incidence prediction implies the identification of any major discrepancy between the analytical and empirical models, so that the LHS-value assumption of Eq. 3.4.8 in the iterative secant-method is redefined. An outer iterative secant-method calculates the next assumption for the LHS of Eq. 3.4.8, until the difference between both choking-incidence values is within the proved error of 0.5%. In this way, the analytical prediction of the choking incidence is guaranteed to be within the expected limits to avoid any false local minimum of β_{ch}.

3.4.3 Choking Margin

The choking incidence estimation allows the flow field calculation for the choke condition. The inlet choking relative flow angle for a rotor becomes

$$\beta_{1_{ch}} = i_{ch} + k_1 \quad \textbf{(3.4.9)}$$

For a stator, Eq. 3.4.9 applies to the absolute flow angle, being

$$\alpha_{1_{ch}} = i_{ch} + k_1 \quad \textbf{(3.4.10)}$$

To evaluate whether a blade profile at each streamline is choked or not, a comparison is needed between the inlet choking flow angle calculated in Eq. 3.4.9 and the current SLC inlet flow angle obtained from radial equilibrium equation (REE) for all the blading components, i.e., rotor, stator, inlet guide vane (IGV), outlet guide vane. If $\beta_1 > \beta_{1_{ch}}$ for a rotor or $\alpha_1 > \alpha_{1_{ch}}$ for a stator streamline, choking condition has not been reached and the REE-estimated inlet flow angle is well enough. Conversely, if $\beta_1 \leq \beta_{1_{ch}}$ or $\alpha_1 \leq \alpha_{1_{ch}}$, the REE-estimated inlet flow angle needs to corrected to be $\beta_{1_{ch}}$ or $\alpha_{1_{ch}}$, respectively, as the choking condition has been reached at those streamlines.

Given $\beta_{1_{ch}}$ or $\alpha_{1_{ch}}$ for the identified choked streamlines, an inverse design scheme is implemented to obtain the flow conditions that satisfy the choking incidence. In choke condition, the inlet relative whirl velocity is conserved as the blade speed remains constant and the swirl or inlet absolute angle α_1 condition does not change, keeping the inlet absolute whirl velocity unaffected. In the particular case of no swirl ($\alpha_1 = 0$), the inlet relative whirl velocity is equals to the blade speed at a given streamline radius. Therefore, inlet meridional relative velocity for a rotor in choke condition becomes

$$V_{1_{ch}} = \frac{V_{\theta_1}}{\sin \beta_{1_{ch}}} \quad \textbf{(3.4.11)}$$

It follows, that the inlet meridional choking velocity is

$$V_{m_{1_{ch}}} = \sqrt{{V_{1_{ch}}}^2 - {V_{\theta_1}}^2} \quad \textbf{(3.4.12)}$$

Hence, the inlet meridional absolute choking velocity is expressed as

$$C_{1_{ch}} = \sqrt{{C_{\theta_1}}^2 + V_{m_{1_{ch}}}} \quad \textbf{(3.4.13)}$$

In the absence of a relative velocity triangle for a static components (stator, IGV, OGV), $C_{1_{ch}}$ is directly computed from the inlet absolute choking flow angle,

$$C_{1_{ch}} = \frac{C_{\theta_1}}{\sin \alpha_{1_{ch}}} \quad \textbf{(3.4.14)}$$

Knowing $C_{1_{ch}}$, the inlet static temperature $T_{1_{ch}}$ and inlet specific ratio $\gamma_{1_{ch}}$ for choking operations are calculated through a secant iteration method. A value for $T_{1_{ch}}$ is assumed based on the given absolute total-temperature T_{01} to satisfy the adiabatic steady flow energy equation, which is

$$\frac{\widetilde{T_{01}}}{T_{1_{ch}}} = 1 + \frac{\gamma_{1_{ch}} - 1}{2}\left(\frac{C_{1_{ch}}}{\gamma_{1_{ch}} R T_{1_{ch}}}\right)^2 \quad \textbf{(3.4.15)}$$

Where $\gamma_{1_{ch}}$ is calculated as a function [251] of the assumed $T_{1_{ch}}$. Hence, the error function becomes:

$$E = T_{01} - \widetilde{T_{01}} \quad \textbf{(3.4.16)}$$

Similar to the secant iteration methods described in Sec. 3.1, a second value for $T_{1_{ch}}$ is assumed to obtain a second error that will approximate the next secant-based estimation for $T_{1_{ch}}$ until the error is below the tolerance set of 1e-6.

Having the inlet choking static temperature, the inlet speed of sound in choke condition is

$$a_{1_{ch}} = \sqrt{\gamma_{1_{ch}} R T_{1_{ch}}} \quad \textbf{(3.4.17)}$$

Hence, the inlet meridional relative Mach number is obtained for the rotor,

$$M'_{1_{ch}} = \frac{V_{1_{ch}}}{a_{1_{ch}}} \quad \textbf{(3.4.18)}$$

For static components (stator, IGV, OGV), the inlet meridional absolute Mach number becomes

$$M_{1_{ch}} = \frac{C_{1_{ch}}}{a_{1_{ch}}} \quad \textbf{(3.4.19)}$$

Having the above calculated flow parameters for the started flow, a comparison is needed to determine how far the current flow field is from the choke conditions. As mentioned in Sec. 2.6.1, the flow function or corrected mass flow per unit area need to be satisfied between far upstream and the characteristic *a*-*b*. The flow function is used to establish a compatibility equation to satisfy continuity such that a ratio between the unique incidence condition and the current flow defines a choking margin Ξ. Using Eq. 3.3.70 as a unique function of the Mach number, the flow functions for the current and started flows for both, rotor and stator, are solved as

$$F(M) = \frac{\gamma}{\sqrt{\gamma - 1}} M \left[1 + \frac{\gamma - 1}{2} M^2\right]^{\frac{-(\gamma+1)}{2(\gamma-1)}} \quad \textbf{(3.4.20)}$$

In Eq. 3.3.55, the flow function was defined as well as the corrected mass flow per unit area, which applies to both current and started flow conditions. The flow area at the inlet is that as derived from Figure 3.26, thus, the corrected mass flow per unit area becomes

$$F(M) = \frac{\dot{m}\sqrt{C_p T_0}}{A P_0} = \frac{\dot{m}\sqrt{C_p T_0}}{Hs \cos\beta \, P_0} \quad \textbf{(3.4.21)}$$

Even at started flow conditions, the net strength of the expansion waves travelling upstream cancel out with the bow-wave system. Whereupon, there is no choking influence upstream of the blade-row leading-edge and the conditions at this station are considered to be those from the inlet flow. As mass conservation is satisfied between the upstream domain and a potentially choked blade inlet, it is therefore valid to establish continuity between the current and choked flows as

$$\dot{m} = \dot{m}_{ch} \quad \textbf{(3.4.22)}$$

Substituting Eq. 3.4.21 in Eq. 3.4.22, the mass flow conservation in a rotor becomes

$$\frac{F(M_1') Hs \cos\beta_1 \, P_{01}}{\sqrt{C_p T_{01}}} = \frac{F\left(M_{1_{ch}}'\right) Hs \cos\beta_{1_{ch}} \, P_{01_{ch}}}{\sqrt{C_{p_{ch}} T_{01_{ch}}}} \quad \textbf{(3.4.23)}$$

In the case of static components (stator, IGV, OGV), the continuity gives

$$\frac{F(M_1)Hs\cos\alpha_1 P_{01}}{\sqrt{C_p T_{01}}} = \frac{F(M_{1_{ch}})Hs\cos\alpha_{1_{ch}} P_{01_{ch}}}{\sqrt{C_{p_{ch}} T_{01_{ch}}}} \quad \textbf{(3.4.24)}$$

The choking-margin is computed for every given streamline for which the blade-element pitch s and streamtube height H do not vary. Moreover, between the immediate upstream domain and the blade inlet angle, the inlet total-temperature and inlet total-temperature are the same, and the specific heat ratio at constant pressure remains approximately constant. Thence, the mass flow conservation equation is reduced to

Rotor $$\frac{F(M_1')}{F(M_{1_{ch}}')} = \frac{\cos\beta_{1_{ch}}}{\cos\beta_1} \quad \textbf{(3.4.25)}$$

Stator, IGV, OGV $$\frac{F(M_1)}{F(M_{1_{ch}})} = \frac{\cos\alpha_{1_{ch}}}{\cos\alpha_1} \quad \textbf{(3.4.26)}$$

The above equations establish a fundamental relationship between the current-flow and choke conditions. Moreover, it is noticed that for the flow function, which is dependant only on the Mach number there is only one value of flow angle that can satisfy the equations; hence, the flow angle is unique. If the right-hand side (RHS) in Eq. 3.4.25 or Eq. 3.4.26 is passed to the left-hand side (LHS), or viceversa, it is clear that if the current-flow blade inlet angle is the same as the inlet choking angle, the inlet Mach numbers are the same, and hence, the flow functions, giving a unity ratio. In the case, that the inlet flow angle is higher or lower from the inlet choking flow angle, the ratio would be other than one. To determine how far the current flow field from the choke state is, the ratio of both sides of Eq. 3.4.25 and Eq. 3.4.26 is defined as the choking margin Ξ. The choking margin for the rotor and static components are formally presented,

Rotor $$\Xi = \frac{F(M_1')}{F(M_{1_{ch}}')}\frac{\cos\beta_1}{\cos\beta_{1_{ch}}} \quad \textbf{(3.4.27)}$$

Stator, IGV, OGV $$\Xi = \frac{F(M_1)}{F(M_{1_{ch}})}\frac{\cos\alpha_1}{\cos\alpha_{1_{ch}}} \quad \textbf{(3.4.28)}$$

It is evident from Eq. 3.4.27 and Eq. 3.4.28 that if the inlet flow angle is lower than the inlet choking flow angle, the choking margin is greater than one, meaning a choked streamline blade-profile. This is the case for the tip and high-span blade locations, as the inlet velocities are higher at these radii, increasing the mass flow and reducing the inlet flow angle at a higher rate than in lower blade span locations. The choking starts at the blade tip and gradually decreases towards the hub. If a blade-profile is identified as choked, it is required for β_1 to be fixed to the value of $\beta_{1_{ch}}$, to obtain a unity choking margin.

In contrast, if the inlet flow angle exceeds the inlet choking flow angle, the choking margin is less than unity, resulting in an unchoked blade-profile. In the case, the blade-profile is unchoked, the 2-D SLC REE-estimated flow angle does not need direct correction; however, due to the choking at higher streamlines, the mass flow that is not passing by, needs to be redistributed to lower unchoked streamlines, where the choking margin is less than one. As a result of this mass flow accommodation from the choked streamlines into the unchoked streamlines, the flow angle gets reduced in those streamlines where $\Xi < 1$, as there is still *room* to fit the extra mass flow. To fix the mass flow at the choked streamlines and redistribute it into the unchoked streamlines, in the context of the 2-D SLC compressor performance simulator, a mass flow redistribution model was devised to work in parallel with the choking prediction model.

3.4.4 Mass Flow Redistribution

As discussed in Sec. 3.2.3, when a streamline is identified as choked based on the criteria covered in Sec. 3.2.2 and Sec. 3.2.3, the mass flow needs to be limited to bring the choking margin down to unity, leading in the inlet flow angle to be $\beta_{1_{ch}}$. To satisfy mass flow continuity between the upstream domain and the blade inlet, the extra mass flow that is not allowed to pass through the choked blade-profiles, needs to be redistributed into the unchoked blade-profiles. When more mass flow is *sent* to the unchoked blade-profiles, the choking margin is brought up, reducing the inlet flow angle. Therefore, a mass-flow redistribution numerical model among the streamtubes was developed and implemented in the 2-D SLC compressor performance simulator.

A choking margin tolerance of 0.1% is set to activate the mass flow limitation module. In other words, if the choking margin is greater than 1.001, the mass flow limitation for the streamtubes starts. When the streamtube is choked, the inlet streamtube mass flow gets reduced by a mass flow choking coefficient Λ_{ch}, this is

$$\dot{m}_{1_{ch}} = \dot{m}_1 + \Lambda_{ch} \tag{3.4.29}$$

In the case the streamtube is choked, Λ is negative in order to reduce and limit the mass flow. The mass flow choking coefficient is defined as a function of the choking margin ($\Xi > 1.001$), expressed as

$$\Lambda_{ch} = \Lambda_{ch} - f_{ch} \left(\frac{\Xi - 1}{\Xi}\right) \tag{3.4.30}$$

where f_{ch} is a factor for the choked streamtubes that modulates the severity of the choking level. Values for f_{ch} were found to be in the order of 1e-1 or less. In sec. 4.3, the f_{ch} influence is demonstrated. In general, as f_{ch} is decreased, a more accurate solution is expected, however the solution time increases considerably. A value of $f_{ch\ i} = 0.1$ was found to be a good trade-off between accuracy and solution speed.

To account for mass flow continuity across the choked streamtube, the outlet mass flow is equals to the adjusted inlet mass flow:

$$\dot{m}_{2_{ch}} = \dot{m}_{1_{ch}} \tag{3.4.31}$$

The total extra mass flow from the choked streamtube is the summation of all their mass flow choking coefficients, given as follows

$$\dot{m}_{ch} = \sum_{i=1}^{N_{ST_{ch}}} \Lambda_{ch_i} \tag{3.4.32}$$

where $N_{ST_{ch}}$ is the number of choked streamtubes.

Nevertheless, the extra mass flow withdrawn for the extra mass flow needs to be placed in the other unchoked streamtubes depending on their choking margin. Similarly as for the choked streamtubes, a mass flow choking coefficient Λ_{uch} is defined as a function of the choking margin ($\Xi \leq 1.001$), defined as

$$\Lambda_{uch} = \Lambda_{uch} - f_{uch}\left(\frac{\Xi - 1}{\Xi}\right) \quad \textbf{(3.4.33)}$$

Λ_{uch} represents the mass flow that is added from the choked to the unchoked streamtubes. Hence, the mass flow choking coefficient for the unchoked streamtubes needs to be correlated to that coefficient from choked streamtubes. For this, the factor f_{uch} for unchoked streamtubes is found through a secant iteration method, previously reviewed in Sec. 3.1 and Sec. 3.2.4. Given f_{uch}, the inlet mass flow for the unchoked streamtubes becomes

$$\dot{m}_{1_{uch}} = \dot{m}_1 + \Lambda_{uch} \quad \textbf{(3.4.34)}$$

And the outlet mass flow for the unchoked streamtube to guarantee mass flow contuinity is

$$\dot{m}_{2_{uch}} = \dot{m}_{1_{uch}} \quad \textbf{(3.4.35)}$$

To find the factor for the unchoked streamtubes that satisfies the withdrawn mass flow from the choked streamtubes, a factor $\widetilde{f_{uch}}$ is assumed to calculate a mass flow choking coefficient, as follows

$$\widetilde{\Lambda_{uch}} = \widetilde{\Lambda_{uch}} - \widetilde{f_{uch}}\left(\frac{\Xi - 1}{\Xi}\right)$$

Then, the total added mass flow rates to the unchoked streamtubes is the summation of all their mass flow choking coefficients, given by

$$\dot{m}_{uch} = \sum_{i=1}^{N_{ST_{uch}}} \widetilde{\Lambda_{uch_i}} \quad \textbf{(3.4.36)}$$

where $N_{ST_{uch}}$ is the number of unchoked streamtubes.

As the total mass flow added to the unchoked streamtubes must be equal to the total mass flow extracted from the choked streamtubes, the error function is given by

$$E = \dot{m}_{uch} - \dot{m}_{ch} \quad \textbf{(3.4.37)}$$

To complete the iterative method, a second value for $\widetilde{f_{uch}}$ is assumed for which a corresponding error is obtained. Having two values for the mass flow choking coefficient and their respective errors, the next approximation for $\widetilde{f_{uch}}$ is obtained by a secant method. The process repeats until the error is lower than at tolerance set to 1e-6, resulting in a solved mass flow choking coefficient for the unchoked streamtubes.

Once the corresponding streamtube are adjusted, either with a restriction or addition in mass flow rate, the downstream component streamtubes follow the same mass flow distribution. The overall mass flow rate redistribution model finishes whenever a choking is encountered in a component, to avoid influence of the mass flow modifications in further downstream components. In the case further downstream component streamtube are choked, the model provides with the versatility of independent choking and mass flow redistribution treatment.

3.5 Summary

The methodology reviewed in this chapter involves four main improvements to obtain a more accurate transonic-flow performance prediction in 2-D SLC simulations: a blade-element-layout method, an adaptation to the full-REE second order differential equation, a novel analyitical physics-based shock-loss model for unstarted and started conditions, and a choking mass flow redistribution model. One of the major contributions of the shock-loss model developed in this research is the incorporation of an iterative method to correctly predict the passage-shock shape and location, in contrast to previously published models which assumed and oversimplified its structure.

The blade-element-layout method was introduced to correctly model the sweep and lean at every blade profile section, and capture the influence of these geometric variations on the shock behaviour. This blading-modelling strategy projects the blade-element parameters on a conical surface, which approximates a stream surface of revolution, leading to a more accurate blade-section representation in the blade-to-blade plane. Insomuch of the two-dimensionality of the SLC method in the S2 plane, the lean effect on any blade section is not *seen* in the full-REE formulation. For this reason, the full-REE second-order differential equation was modified in its coefficient C to reflect the lean effect at the blade sections.

More important is the progress done in developing a novel physics-based shock-loss model and a choking model to simulate the radial mass flow redistribution occurring during started operations. A significant contribution of the current shock-loss model is the solution of the shock-loss coefficient throughout all the blade span. In the subsonic inlet relative supercritical region, the shock losses are determined using conventional aerofoil theory to calculate the critical relative Mach number and the corresponding relative total-pressure loss induced by the entrance turning. In the supersonic span region, the shock structure is divided into a bow-wave and a passage shock to ease the calculation. The modelling starts by laying out the detached bow-shock, since its shape and location are a function only of the inlet relative Mach number and its orientation is given by the inlet relative angle. Given the bow-shock form, the shock-losses corresponding to the bow-wave portion are computed. However, the computation for the passage-shock shape, location, and hence, losses, complicates more depending on the choking status.

To determine whether the blade passage is choked or not, a choking model was developed to calculate the choking incidence and a choking margin as a ratio of the current incidence against that from the started condition. In the case the blade passage is unchoked, the passage shock-structure is given only by the remaining part of the detached bow-shock that penetrates into the passage. Having the passage-shock location, the flow expansion ahead of it is resolved through the method of characteristics to obtain a circumferential relative Mach number distribution ahead of the passage shock, determining the relative total-pressure recovery, and computing the its mass-average value. The passage-shock-induced relative total-pressure ratio is then added to that from the bow-wave to obtain an over-all relative total-pressure drop that leads to the relative shock-loss coefficient calculation.

If the blade passage is identified as choked, a second passage-shock appears, whose location and shape are assumed in the first place. The choking-shock can intersect or not the bow passage-shock, and depending on the coalescence a second flow expansion is calculated accordingly, for which a relative total-pressure loss is computed and added to the overall relative total-pressure ratio.

The iterative method to correctly position the choke-induced passage-shock compares then the current stagnation condition penalized by the computed overall relative total-pressure drop from the assumed passage-shock against the stagnation-condition operating ranges determined from the streamtube throat-area calculation. In the case there is no agreement between the assumed shock-configuration and the operating range that correspond to the current overall relative total-pressure recovery, a new choke-induced shock axial position is established to re-start the algorithm by assuming another location for the second passage shock. In contrast, if there is an agreement of shock patterns between the assumed and that from the operating range, the streamtube shock-area that satisifies the current overall relative total-pressure loss is computed, for which the axial position along the chord is determined. This choke-induced passage-shock axial location is compared against that from the assumption within a secant method to determine a new axial postion for the second passage-shock, and re-start the process all over again from the suction-surface flow-expansion ahead of the first passage-shock. The algorithm iteratively repeats until the axial locations between the assumed and calculated second passage-shocks agree within a tolerance established. The overall relative total-pressure can then be applied as is to determine the overall shock-loss coefficient.

4 VALIDATION & VERIFICATION

4.1 Introduction

The purpose of this section is to evidence the authenticity of the flow-solution models (shock-loss and mass flow redistribution schemes) developed in this research and implemented in SOCRATES.

To demonstrate the operation of the current shock-loss and mass flow redistribution simulation strategies in SLC, a 2-D SLC model for the NASA Rotor 67 [40] was built and used as a case study. The validation of the NASA Rotor 67 2-D SLC against measured data is given in Sec. 4.2 for design and off-design speedlines. Inasmuch as new variable-pitch fan was re-designed and optimised having as a reference the NASA ADP Fan [252–254], the baseline geometry of the fan was reproduced and simulated in 2-D SLC for which the corresponding validation against test data is shown in Sec. 4.3

The verification of the mass flow redistribution model, including the verification of the off-design point for the choking onset, is given in Sec. 4.4. Similarly, a thorough verification of the current shock-loss model against the most notable state-of-the-art models for design point is provided in Sec. 4.5. The verification at design condition suffices, since the previous models are only limited to this operating point. Furthermore, the verification of the shock-loss model demonstrates its sensitivity for off-design conditions and the overall impact in the compressor performance maps. The shock-wave structure in terms of its shape and location is qualitatively verified against 3-D CFD simulation results on the blade-to-blade plane and presented in Sec. 4.6.

4.2 2-D SLC NASA Rotor 67 Validation

4.2.1 Model Generation

The well-known NASA Rotor 67 [40] is a single-stage transonic compressor, modelled according to manufacturing specifications. The NASA Rotor 67 2-D SLC model was generated in SOCRATES and validated against experimental results [255]. Particular interest in this rotor was generated as it experiences transonic behaviour in the single rotor blades, with a tip inlet relative Mach number equals to 1.38, allowing to do further

3-D blading optimisation studies that consider shock wave effects. Table 4.1 shows the design specifications of the NASA Rotor 67 [40].

Table 4.1 NASA Rotor 67 [40] **design specifications.**

Parameter	
Number of Rotor Blades	22
Rotational speed [rpm]	16043
Pressure ratio	1.63
Mass flow [kg/s]	33.25
Rotor tip speed [m/s]	429
Inlet Tip Relative Mach Number	1.38

Flow path, blade row, and blade profile data, were used as input to model the geometry in SOCRATES. The NASA Rotor 67 [40] flow path dimensions are presented in Table 4.2.

Table 4.2 NASA Rotor 67 [40] **flow path dimensions.**

Parameter	
Max. Radius [cm]	25.6982
Min. Radius [cm]	8.8618
Radius Length [cm]	16.8364
Max. Z-coordinate [cm]	35.4423
Min. Z-coordinate [cm]	-18.0598
Length [cm]	53.5022

4.2.2 Model Validation

The NASA Rotor 67 2-D SLC model was calibrated accordingly by adjusting the blockage factors to match the inlet and outlet meridional velocity against experimental results [255]. This procedure was applied for the maximum efficiency point at every rotational velocity so that the whole speedline is run with the tuned blockage factors. The best meridional velocity match of the 2-D SLC NASA rotor 67 model against experimental results [255] for 100% NRT case, shown in Figure 4.1 a), was obtained with the blockage factors listed on Table 4.3.

A consistent trend in meridional velocity and meridional Mach number is obtained at the inlet and outlet between experimental and SLC simulation data, having an acceptable match at the hub and tip, where the blockage factors were applied, as observed in Figure 4.1. Further, the calibration of the SOCRATES model is confirmed by obtaining an acceptable agreement at the inlet and outlet between measured and 2-D SLC simulation results for the meridional absolute and meridional relative velocity in Figure 4.2, and for the absolute and relative flow angles in Figure 4.3.

Table 4.3 Blockage factors for 100% NRT applied to NASA Rotor 67 model.

Location	Blockage Factor
InletTip Leading Edge	0.8000
Inlet Hub Leading Edge	1.5000
Outlet Tip Trailing Edge	0.0000
Outlet Hub Leading Edge	0.0000

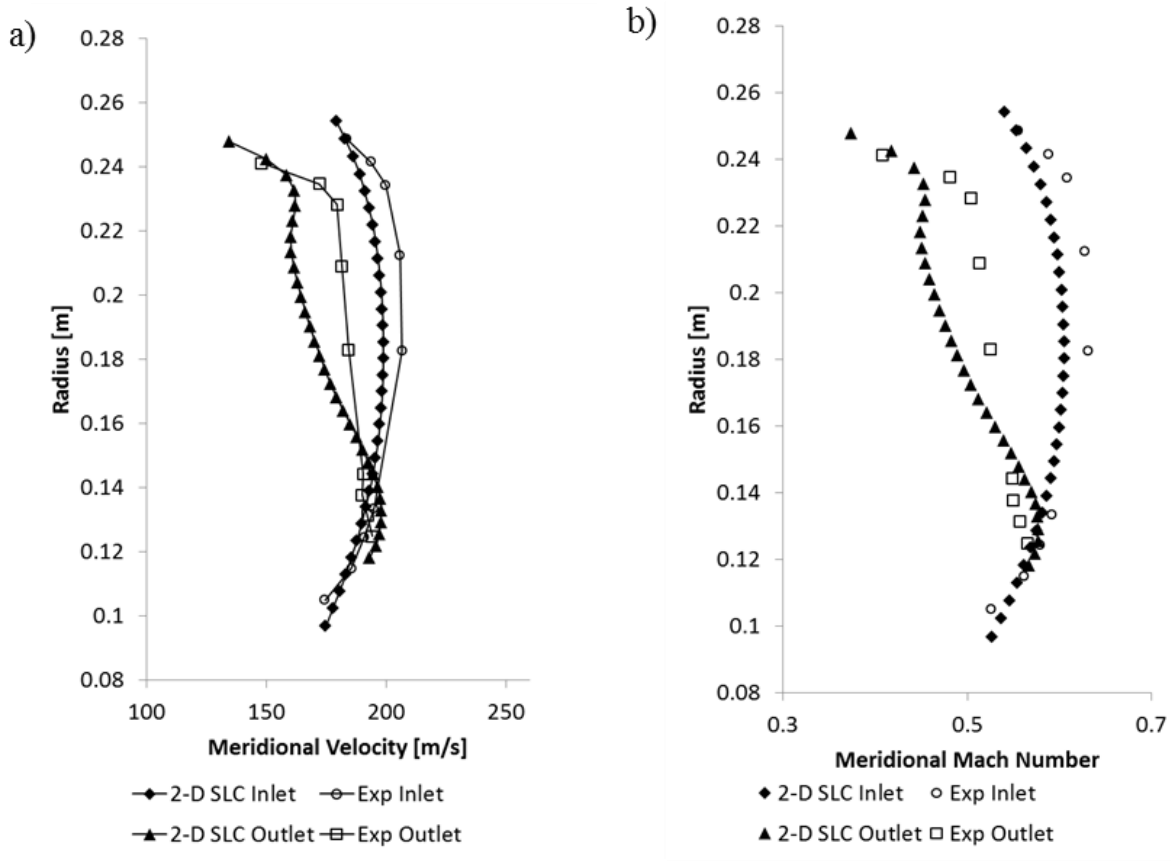

Figure 4.1 NASA Rotor 67 blade inlet and outlet comparison between 2-D SLC simulation and test data at 100% NRT and *w*=34.56 kg/s. a) Meridional velocity. b) Meridional Mach number.

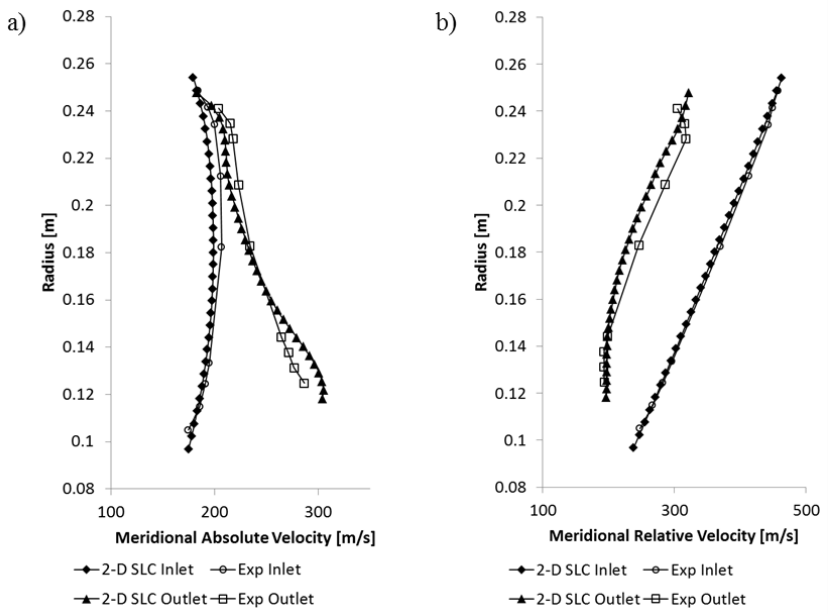

Figure 4.2 NASA Rotor 67 blade inlet and outlet comparison between 2-D SLC simulation and test data at 100% NRT and *w*=34.56 kg/s. a) Meridional absolute velocity. b) Meridional relative velocity.

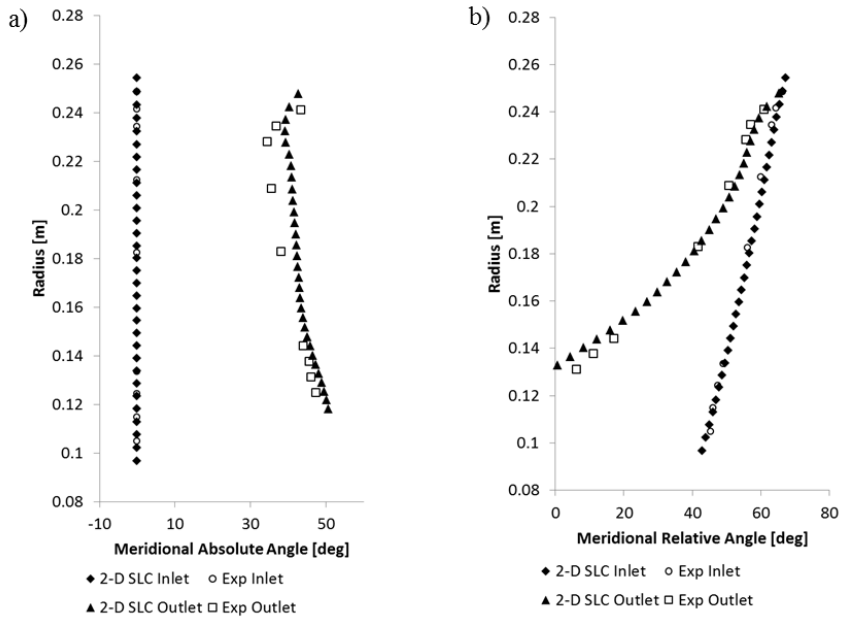

Figure 4.3 NASA Rotor 67 blade inlet and outlet comparison between 2-D SLC simulation and test data at 100% NRT and *w*=34.56 kg/s. a) Meridional absolute angle. b) Meridional relative angle.

The 2-D SLC incidence and deviation angle trend observed in Figure 4.4 appears to agree well with that from the test data, considering that the incidence and deviation values were determined from statistics-based empirical correlation. Despite of this

necessary empiricism, the difference is within 0.2% along the spanwise direction. As expected, the incidence values are lower at the tip than at the hub due to higher relative velocities as the blade speed increases with radius. In the case of the deviation angle, the values are lower at the tip than at the hub due to the lower turning produced by a less cambered blade profile.

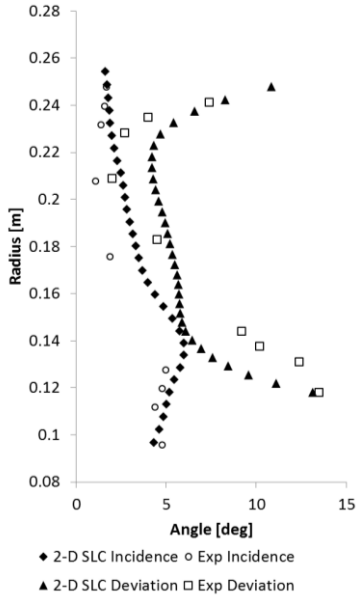

Figure 4.4 NASA Rotor 67 blade incidence and deviation angle comparison between 2-D SLC simulation and test data at 100% NRT and *w*=34.56 kg/s.

In terms of the performance characteristics, an acceptable agreement between experimental data and 2-D SLC results throughout the different percentage of rotational speeds is observed in Figure 4.5 and Figure 4.6 for pressure ratio and temperature ratio, respectively. Forasmuch as the NASA Rotor 67 [40] is the same as the firs-stage rotor of the NASA two-stage fan [246], experimental results from the latter are used in the 80% NRT, 70% NRT and 50% NRT cases. The isentropic efficiency comparison in Figure 4.7 shows a consistent trend between test data and the 2-D SLC results. The difference observed between the experimental and 2-D SLC curves is less than 1.1%, and reducing towards the peak-efficiency point of every rotational speed. The overestimation of the isentropic efficiency in 2-D SLC is mostly due to the empiricism introduced in the profile-loss calculation; however, the discrepancy is almost constant along the operating range and across the angular speeds, allowing the use of a correction factor.

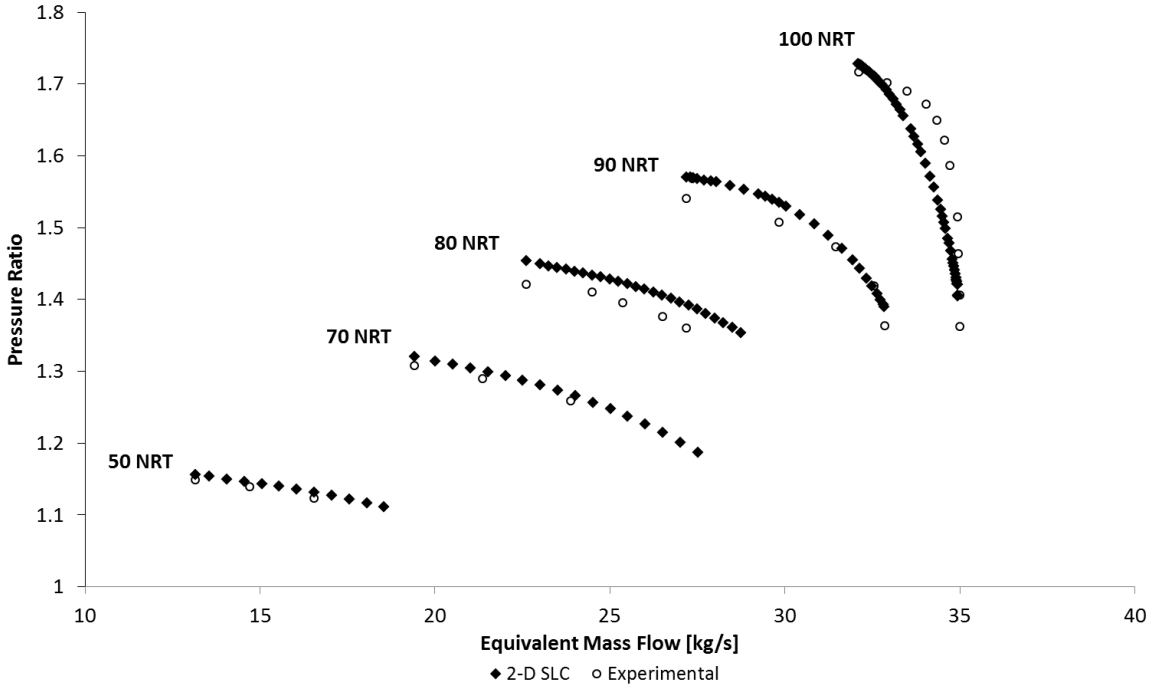

Figure 4.5 NASA Rotor 67 SLC pressure ratio compressor map verification against experimental results.

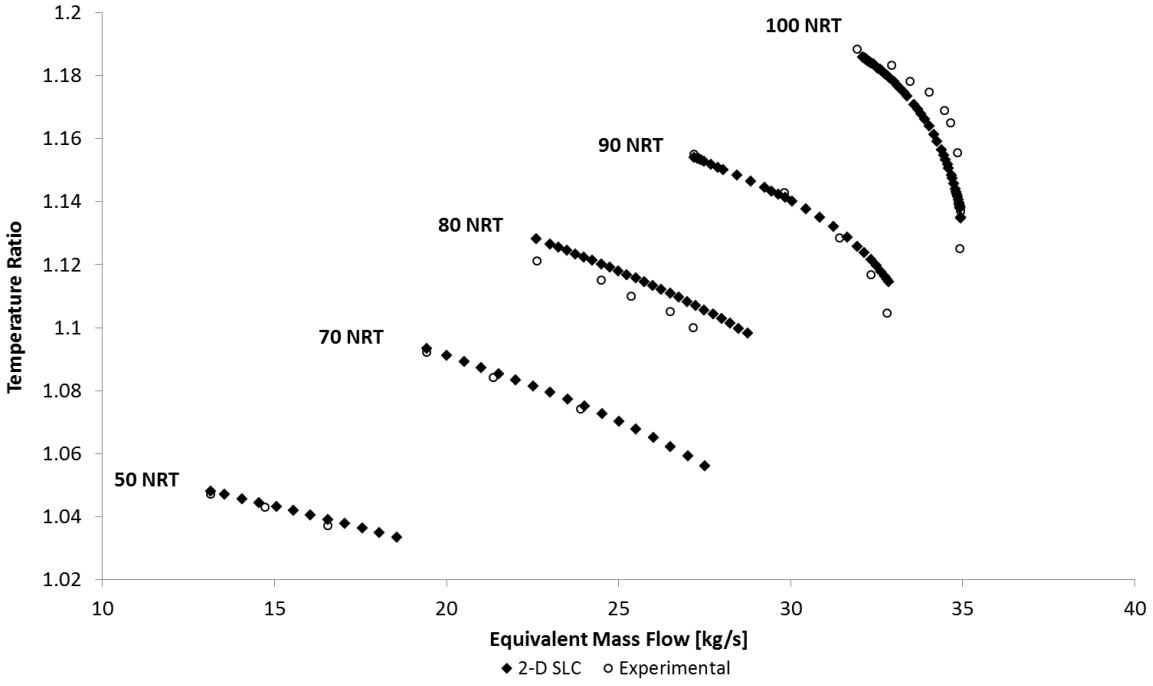

Figure 4.6 NASA Rotor 67 SLC temperature ratio compressor map verification against experimental results.

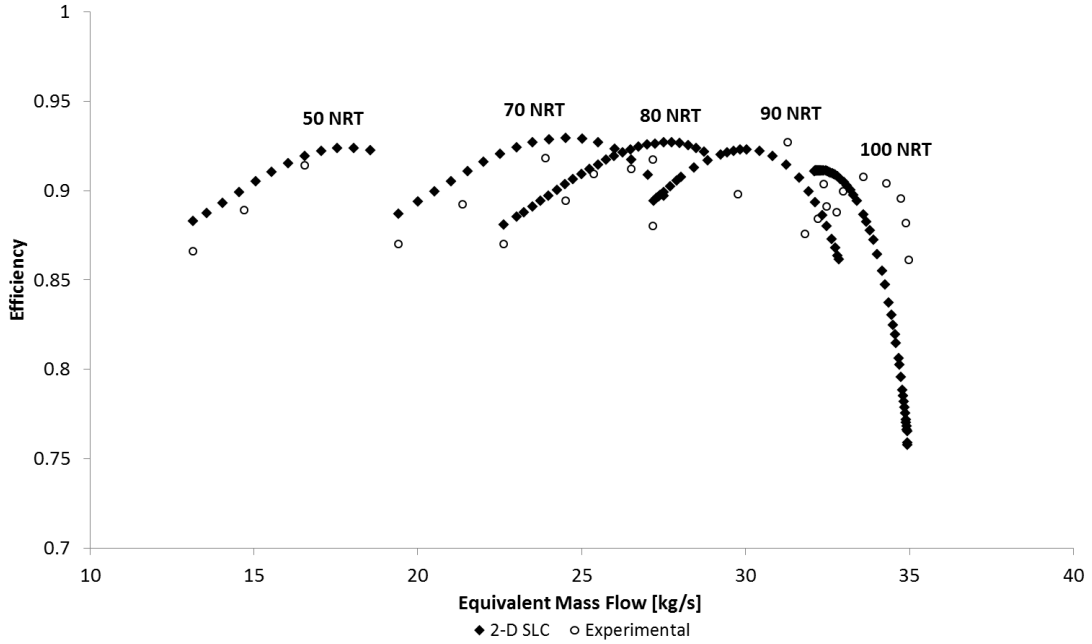

Figure 4.7 NASA Rotor 67 SLC isentropic efficiency compressor map verification against experimental results and SLC NASA Two-stage fan first-stage rotor.

4.3 2-D SLC NASA ADP Fan Validation

4.3.1 Model Generation

A 2-D SLC model was created for the NASA ADP Fan [252–254] based on the geometry input from the Cambridge Whittle Laboratory as shown in Figure 4.8. The purpose of this geometry generation was the application of the shock- structure and loss model in set with the choking mass flow redistribution model within an optimisation scheme reviewed in Sec. 5.4.3. The NASA ADP Fan [252–254] served then as a reference geometry to design a new variable-pitch fan (VPF) and further optimise it as seen in Sec. 5.4.

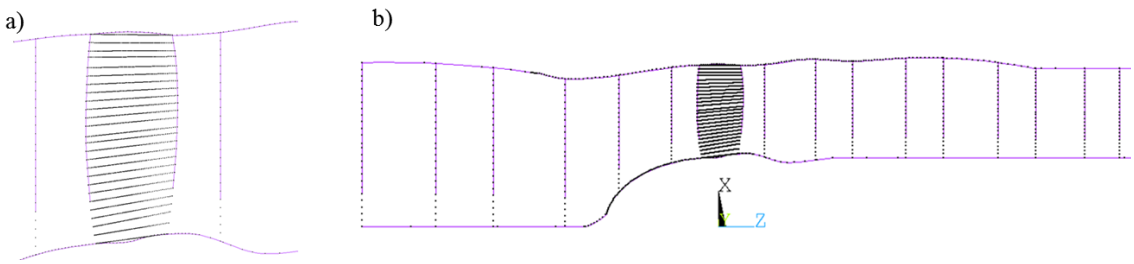

Figure 4.8 2-D SLC model for the NASA ADP Fan. a) Blade sections definition. b) Flowpath and fan blade definition.

The NASA ADP Fan [252–254] design parameters are listed in Table 4.4

Table 4.4 NASA ADP Fan [252] design parameters.

Fan Design Parameters	
PR	
SLTO	1.284
Cruise	1.294
Approach	1.077
Cutback	1.209
RPM	
SLTO	8750
Cruise	8400
Approach	5000
Cutback	7740
Blade Number	18
Hub/Tip Radius	0.426
Diameter	22

4.3.2 Model Validation

The 2-D SLC NASA ADP Fan model was calibrated and validated against experimental rig-test data, so that any further modification to this baseline fan geometry is consistent and reliable.

The 2D-SLC model for the NASA ADP Fan [252–254] was then run at cruise condition at 8396.5 rpm and 0 deg stagger angle setting. The design point was matched acceptably against measured data [252] within 0.2% of difference for the pressure and temperature ratios, and in 0.9% of deviation for the isentropic efficiency, as seen in the fan maps of Figure 4.9, Figure 4.10, and Figure 4.11.

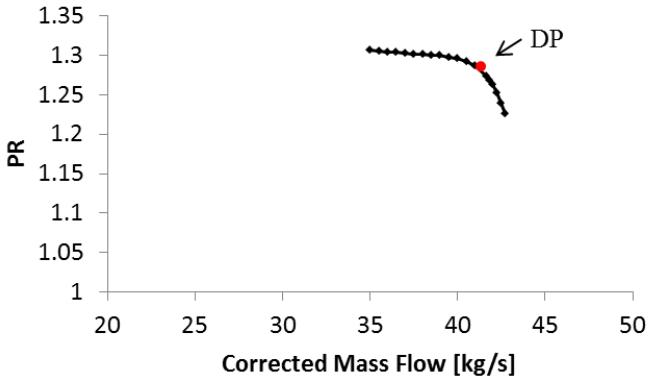

Figure 4.9 Pressure-ratio comparison between the 2-D SLC NASA ADP Fan model and measured data [252] **at design point and cruise speed of 8396.5 rpm.**

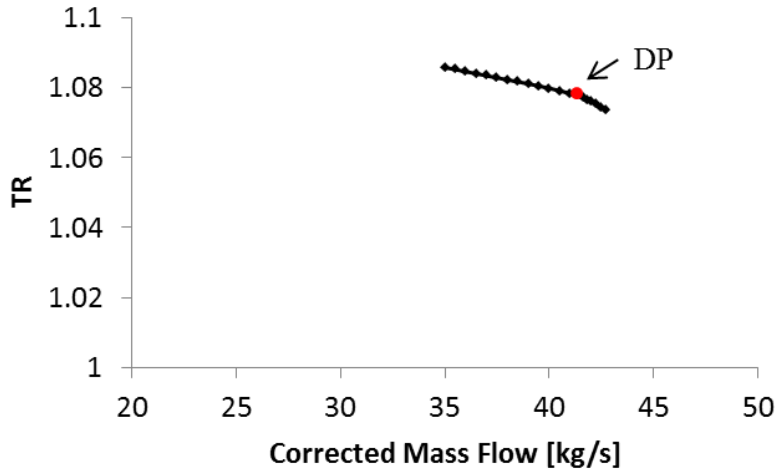

Figure 4.10 Temperature-ratio comparison between the 2-D SLC NASA ADP Fan model and measured data [252] **at design point and cruise speed of 8396.5 rpm.**

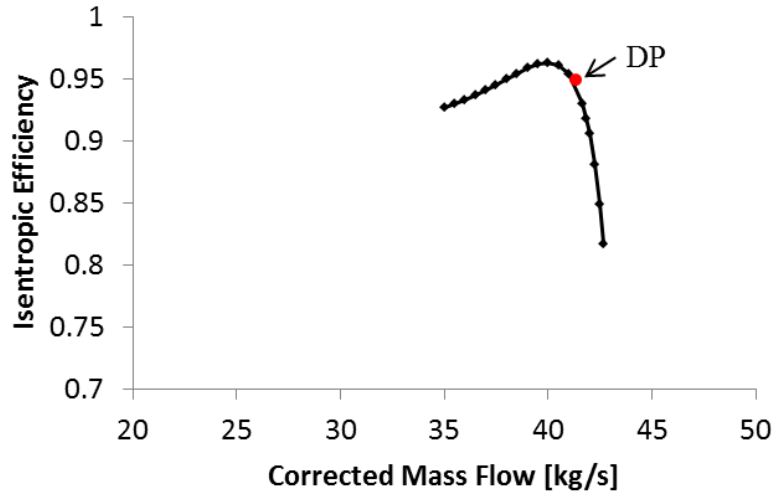

Figure 4.11 Isentropic-efficiency comparison between the 2-D SLC NASA ADP Fan model and measured data [252] **at design point and cruise speed of 8396.5 rpm**

The 2-D SLC NASA ADP Fan model proved to work well for different flight mission speeds within acceptable differences. The pressure-ratio comparison between the predicted results and measured data [252] for the design conditions at part-speeds is given in the map of Figure 4.12.

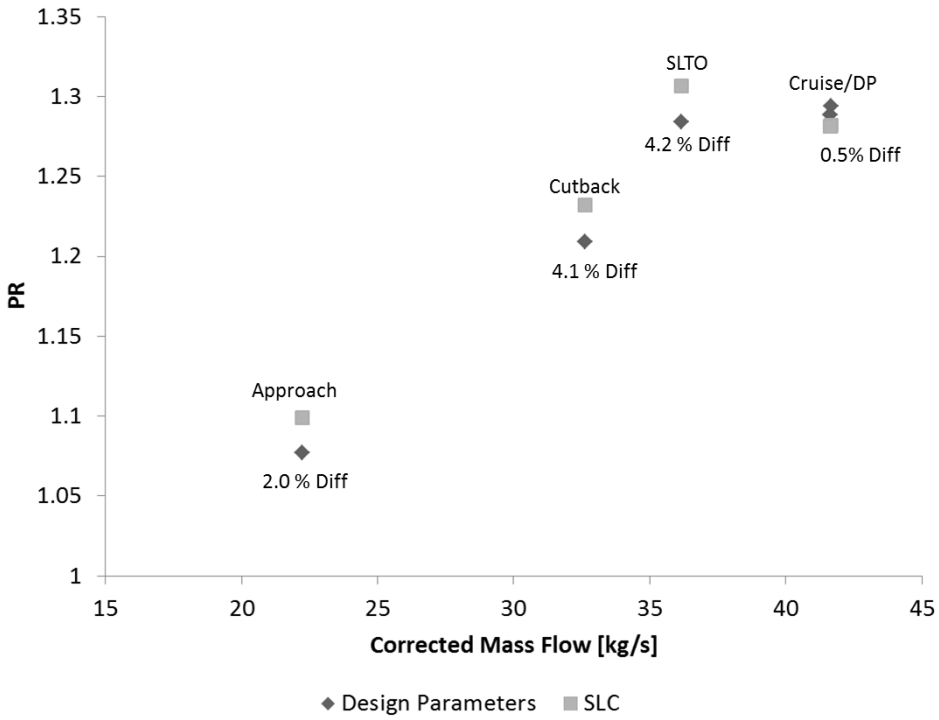

Figure 4.12 Pressure ratio map for different flight conditions: Approach, cutback, SLTO and cruise.

The 2-D SLC NASA ADP Fan model was calibrated in such a way that the differences in terms of the total-pressure, total-temperature ratio, and isentropic efficiency remain around 1.0% for the whole working range at design and part-speeds. The comparison of the 2-D SLC NASA ADP Fan model results against the reported data by Jeracki [256] for the performance characteristics is given in Figure 4.13, Figure 4.14, and Figure 4.15.

In terms of the performance characteristics, the 2-D SLC NASA ADP Fan model proved to work well, showing its adequate calibration, since the maximum average deviation in pressure ratio against measured data is 0.69% at design speed for the whole working range. Similarly, the total-temperature ratio agrees satisfactory along the entire operating range for all the engine speeds with discrepancies less than 0.55% .

The highest differences observed are in the isentropic efficiency, due to the empirical correlations used for the profile losses that might not be adequate for the NASA ADP Fan blade-profile geometry. The 2-D SLC model shows differences less than 1.9% throughout the speedlines, while keeping the same trend and consistent deviation as in the measured data. To correct this difference, a scaling factor might be used to cover

any deficiency from the empirical loss and deviations models. On the whole, the 2-D SLC NASA ADP Fan model compared well against experimental results and is acceptable to use for analysis and design.

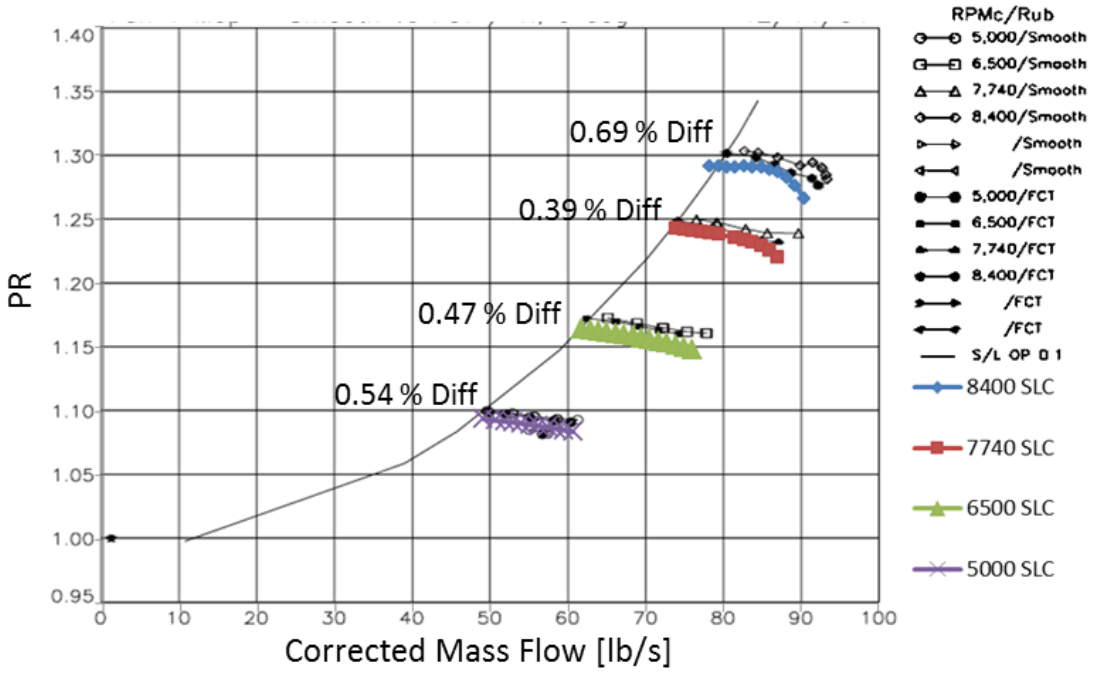

Figure 4.13 Pressure ratio map for a 0 deg stagger configuration.

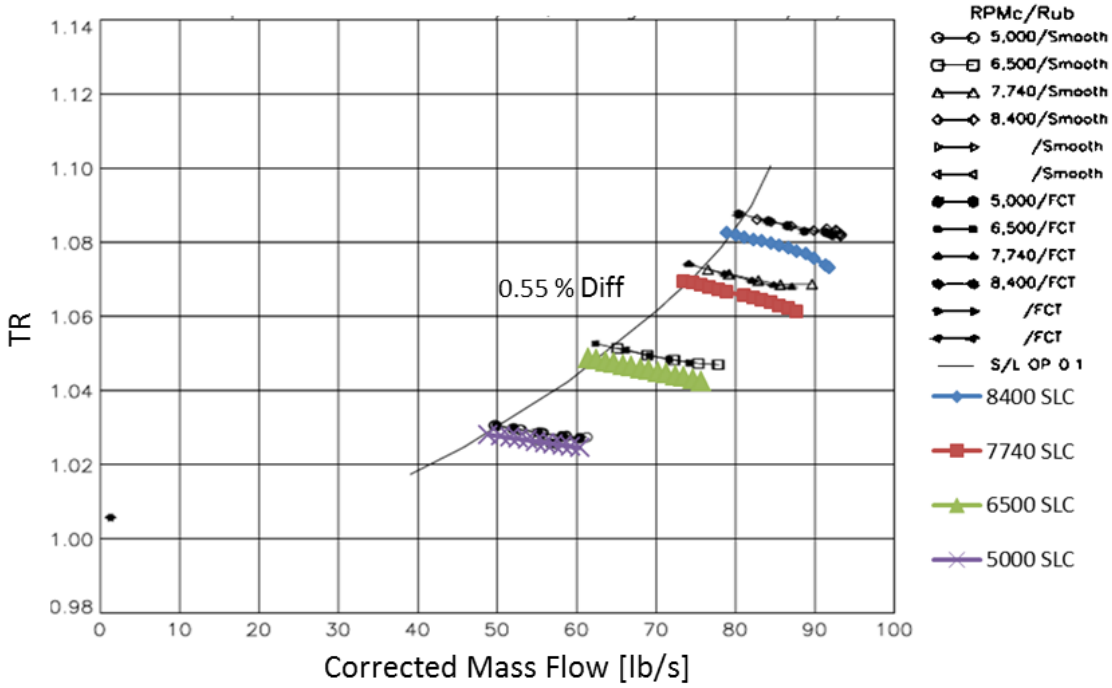

Figure 4.14 Temperature ratio map for a 0 deg stagger configuration

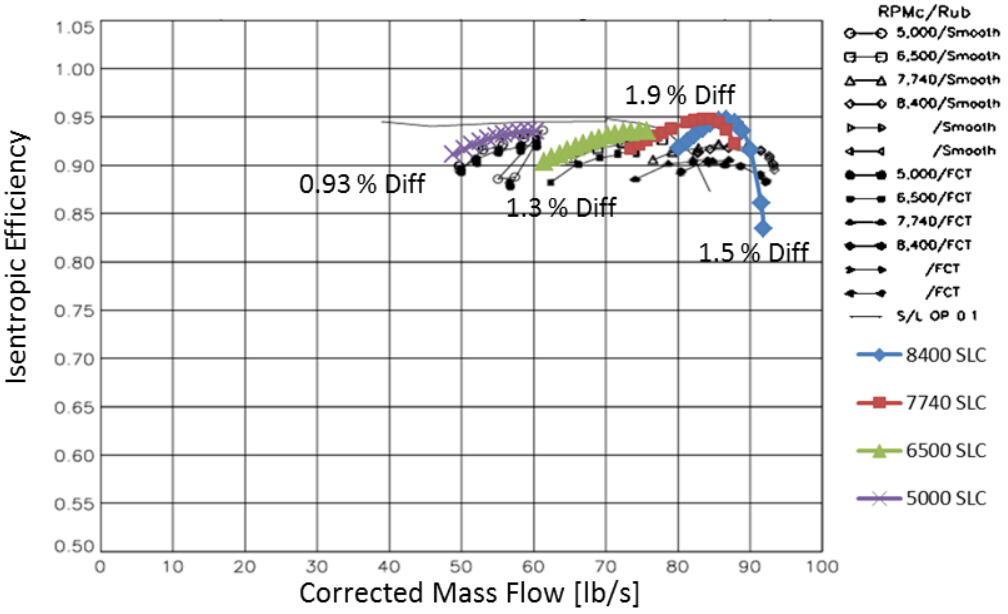

Figure 4.15 Adiabatic efficiency map for a 0 deg stagger configuration.

4.3.3 Model Generation

To understand the complex compressible-flow phenomena occurring in transonic axial-flow compressor rotors, a 3-D CFD Reynolds-Averaged Navier-Stokes (RANS) investigation for the NASA Rotor 67 was carried out for 16 different off-design points at 100% of design speed. The 3-D CFD RANS model was leveraged from Mehdi [257] and DiCugno [258] and re-run for the cases of interest, as the simulation was further throttled beyond choking. The overall model in terms of geometry and mesh was the same, with exception of the domain, which was further extended at the inlet and outlet to avoid direct influence of the boundary conditions, as displayed in Figure 4.16. The inlet and outlet extended duct-length was matched to that from the 2-D SLC model, for further research in the development of a spanwise mixing model.

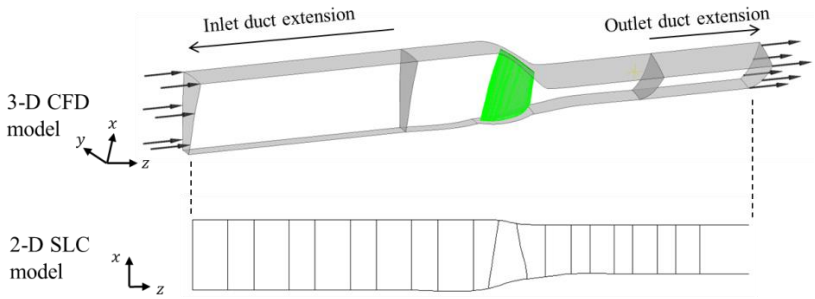

Figure 4.16 Extended inlet and outlet duct domains for the 3-D CFD and 2-D SLC models.

The mesh generation for the compressor was created by Mehdi [257] in ANSYS CFX-Turbogrid 15.0, and the inlet and outlet extension were meshed in ANSYS CFX-Turbogrid. Model options, wall, symmetry and periodic boundaries, and analysis and solution settings were used as is from the leveraged model [257]. A summary of the assumed settings is presented in Table 4.5.

Table 4.5 Solution settings for the 3-D CFD RANS NASA Rotor 67 model.

Option	
Analysis Type	Steady State
Domain Motion	Rotating
Frame Type	Stationary
Number of Mesh Nodes	968 072
Number of Mesh Elements	921 968
Turbulence	k-ε
Advection Scheme	High Resolution
Turbulence Numerics	First Order
Residual Type	RMS

The boundary condition type set for the model was uniform total-temperature and total-pressure at the inlet, and average outlet static pressure at the outlet. Inlet boundary condition values are shown in Table 4.6.

Table 4.6 Inlet boundary conditions for the 3-D CFD RANS NASA Rotor 67 model.

Boundary Condition	
Inlet Total Temperature	288.15 K
Inlet Total Pressure	101.333 kPa

The average outlet static pressure was modified for 16 different off-design cases, which range from stall to deep-choke condition, presented in Table 4.7.

Table 4.7 Outlet boundary conditions for the 3-D CFD RANS NASA Rotor 67 model.

Off-design case	Outlet Static Pressure [kPa]	Off-design case	Outlet Static Pressure [kPa]
TS1	90	TS9	121
TS2	94.1	TS10	121.5
TS3	104.86	TS11	121.75
TS4	109.5	TS12	122
TS5	112	TS13	123
TS6	114	TS14	124
TS7	118	TS15	125
TS8	120	TS16	126

4.4 Choking Model Verification

4.4.1 Choke Condition

To understand the flow field in choked operating conditions, a 3-D CFD RANS investigation was conducted for the NASA Rotor 67 [40] for the 16 different off-design points listed in Table 4.7. No inlet flow distortion was introduced at the inlet domain. Near choking, the rotor was further throttled by lowering the outlet static pressure to observe the flow behaviour in choke operations. Flow readings were captured at the blade leading edge, and at 25, 50, 75 and 100% of the chord upstream of the blade leading edge. In addition, to know the current situation of the 2D-SLC flow prediction, the same 16 off-design cases were run in SOCRATES with the outlet static pressure as boundary condition to account for comparison fairness against the 3-D CFD simulation. The SOCRATES results here presented were obtained with a SLC method that does not include the choking incidence prediction and mass flow redistribution models.

Figure 4.17 shows the resultant mass flow for the given outlet static pressures. For the 3-D CFD simulation, it can be argued that in the three points circled, which correspond to the first three cases of Table 3.3, choke condition is found as the mass flow is not significantly changing. Nonetheless, a deeper examination reveals that the mass flow is still changing between those off-design cases. For instance, the mass flow rate difference between the 4^{th} and the 3^{rd} point is 0.09%, between the 3^{rd} and the 2^{nd} is 0.02%, and between the 2^{nd} and the 1^{st} point is 0.002%. In fact choking phenomenon is not a sudden condition, but a progressive operation. Even before the maximum mass flow, the blade tip is choked. As the back static pressure is dropped, the mass flow gradient gets reduced, resulting in more span locations near the tip to be choked. If the outlet static pressure is further decreased, the choke condition can potentially exist from the tip to mid-span locations.

About the 2-D SLC curve in Figure 4.17, it is clear that the mass flow is not limited when choking approaches. As there is no model to restrict the mass flow or the inlet flow angle, the mass flow is allowed to increased. For this reason, a choking prediction and a mass flow redistribution model were developed and implemented into SOCRATES.

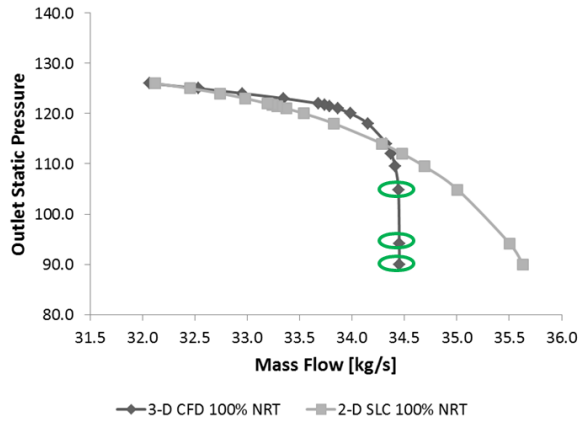

Figure 4.17 Outlet static pressure vs mass flow comparison for the NASA Rotor 67 at 100% of design speed between and 2-D and 3-CFD simulation results.

The compressor maps in Figure 4.17, Figure 4.18, and Figure 4.19 show the small mass flow change for the first three off-design points in the 3-D CFD simulation. In the case of the 2-D SLC, the mass flow is not limited, requiring models that were later implemented. It can be observed that the experimental data shows choking in the first 2 off-design cases of the pressure ratio and temperature ratio map, with a mass flow rate difference between the points of 0.002%, and .02%, respectively. The compressor maps display a difference between the 3-D CFD results and the experimental data for the complete speed line. In fact, the mass flow difference increases towards choking, being of 1.58% at a pressure ratio of 1.34. In fact the 2-D SLC results compare better against experimental results at near-stall and design conditions due to the treatment of the empirical loss models in the former.

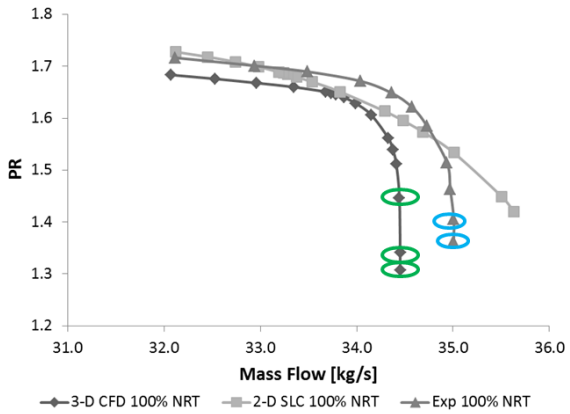

Figure 4.18 Pressure ratio compressor map comparison for the NASA Rotor 67 at 100% of design speed between experimental data, and 2-D and 3-CFD simulation results.

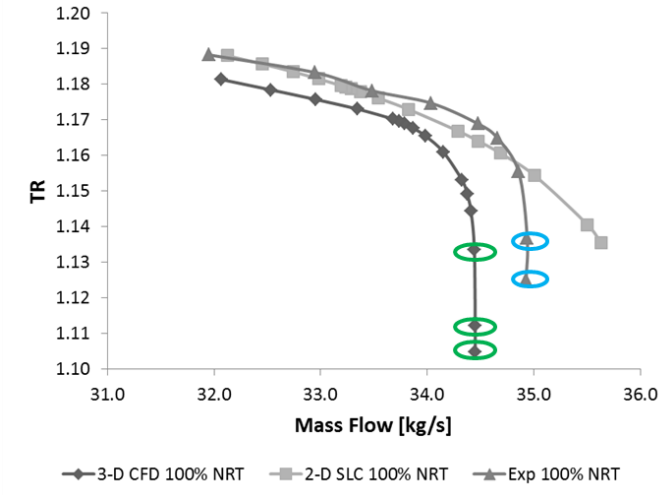

Figure 4.19 Temperature ratio compressor map plot for the NASA Rotor 67 at 100% of design speed between experimental data, and 2-D and 3-CFD simulation results.

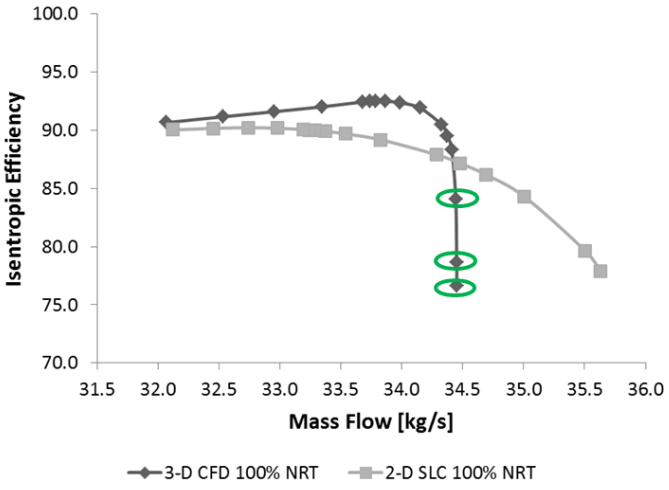

Figure 4.20 Isentropic efficiency compressor map plot for the NASA Rotor 67 at 100% of design speed between experimental data, and 2-D and 3-CFD simulation results.

Figure 4.21 shows that the relative flow angle is not affected upstream. Nonetheless, it evidences how the relative flow angle reduces with an increase in mass flow, particularly at low-span locations. Figure 4.22 zooms into the relative flow angle at the leading edge, where it can be seen how the relative flow angle decreases with mass flow at high-span locations. Further pressure drop brings the relative flow angle gradient to be every time smaller up to a point where it remains constant, as the relative choking flow angle is reached, fixing the mass flow at those streamlines. At low-span locations, especially at the hub, the relative flow angle significantly reduces as the mass flow

increases due to the mass flow redistribution from the tip to the hub. Inasmuch as more mass flow needs to pass at the hub, the relative flow angle becomes smaller, increasing the meridional velocity. Figure 4.23 exhibits the inlet relative flow angle for the first six off-design cases, cover the near-choking and choking. For the 3-D CFD curves, the inlet relative flow angle is almost fixed, hence, choked streamlines. At the hub, the relative flow angle drops to accommodate the extra mass flow that was withdrawn from the tip radii. In terms of the 2-D SLC curves, although close to the 3-D CFD curves, a correction to account for the relative flow angle restriction at the tip and the decrease in flow angle at the hub is required.

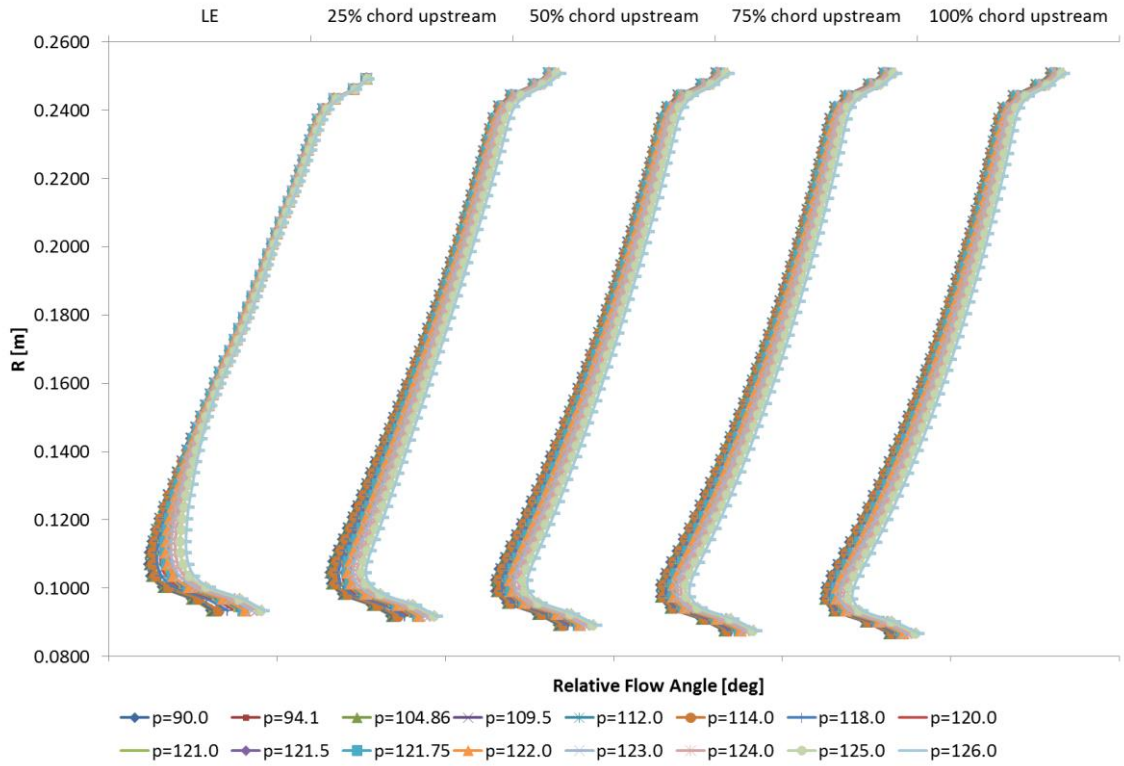

Figure 4.21 Relative flow angle spanwise distribution for the NASA Rotor 67 at 100% of design speed for the leading edge, and 25, 50, 75 and 100% of chord upstream of the leading edge.

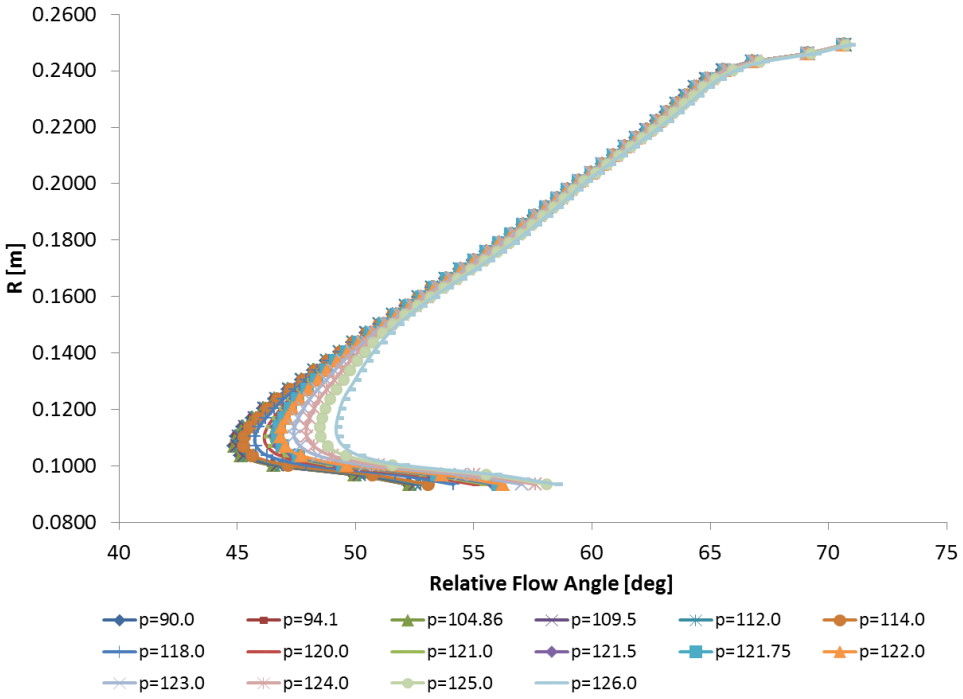

Figure 4.22 Relative flow angle spanwise distribution for the NASA Rotor 67 at 100% of design speed for the leading edge.

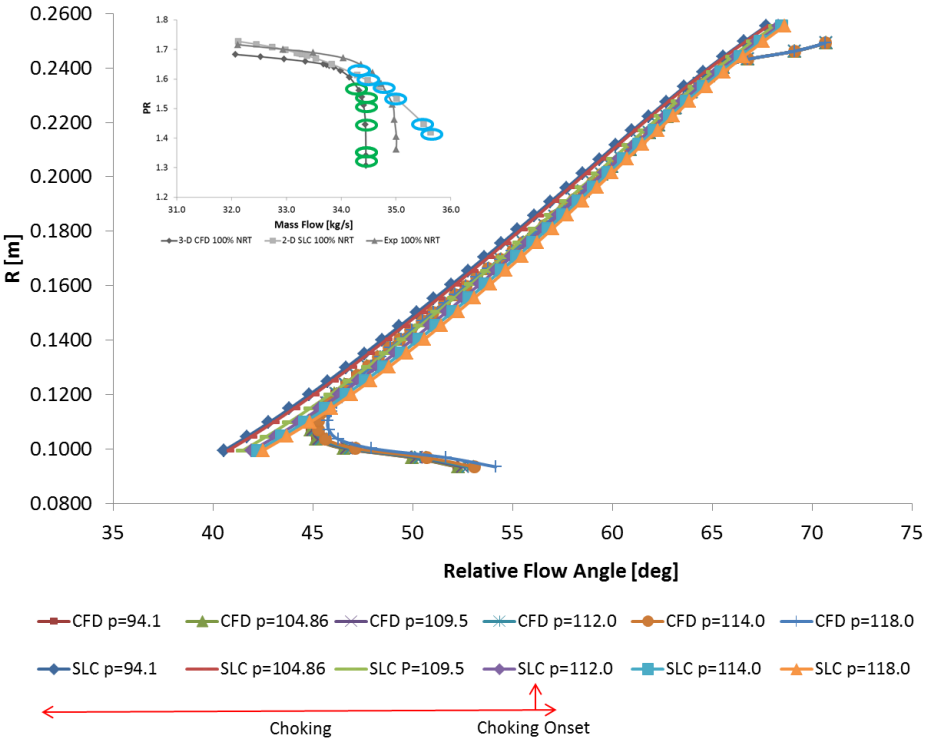

Figure 4.23 Relative flow angle spanwise distribution for the NASA Rotor 67 at 100% of design speed for the leading edge.

The meridional velocity plots confirm the findings in the relative flow angle. Figure 4.24 shows a direct correlation with Figure 4.21, as there are small meridional velocity gradients at the tip and higher meridional velocity gradients at the hub as a result of the extra mass flow allocated at this region. As the meridional velocity is proportional to the mass flow, this significant velocity increase at the hub is not surprising. Figure 4.25 zooms into the meridional velocity profile at the inlet, observing a direct correlation between the relative flow angle and the meridional velocity. Figure 4.26 evidences the necessary corrections that are required in the 2-D SLC code to redistribute the mass flow, leading in a velocity increase at the hub that matches the 3-D CFD results.

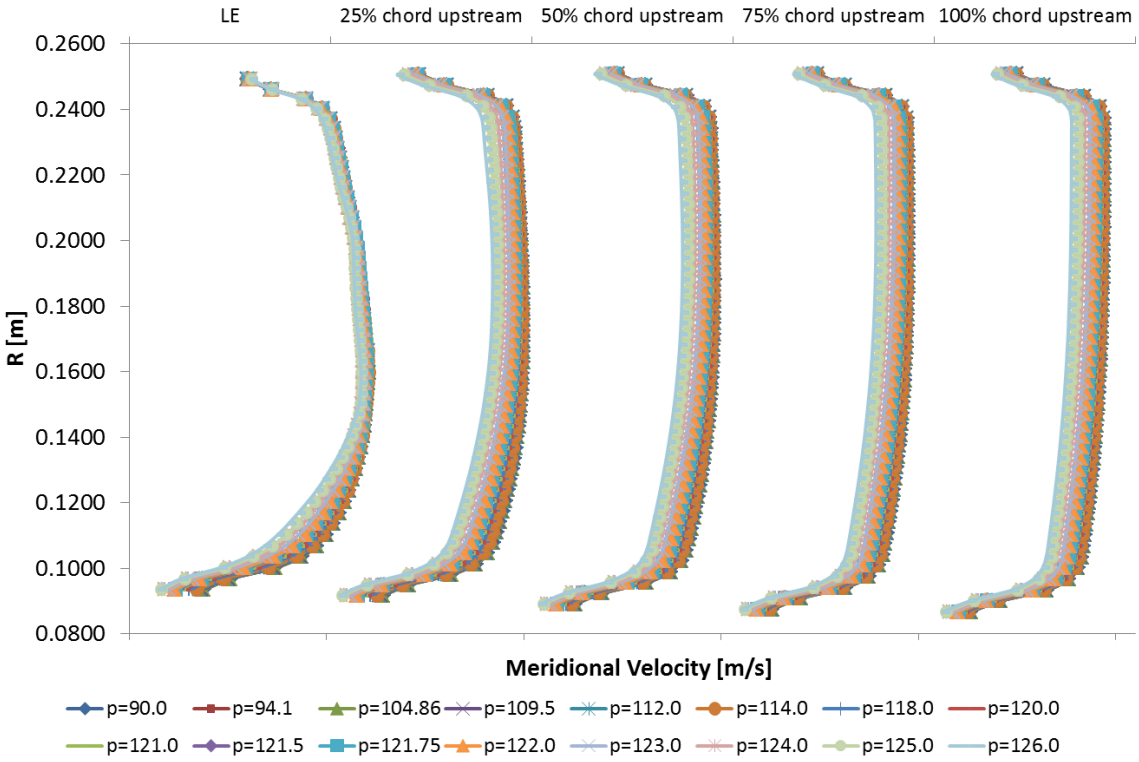

Figure 4.24 Meridional velocity spanwise distribution for the NASA Rotor 67 at 100% of design speed for the leading edge, and 25, 50, 75 and 100% of chord upstream of the leading edge.

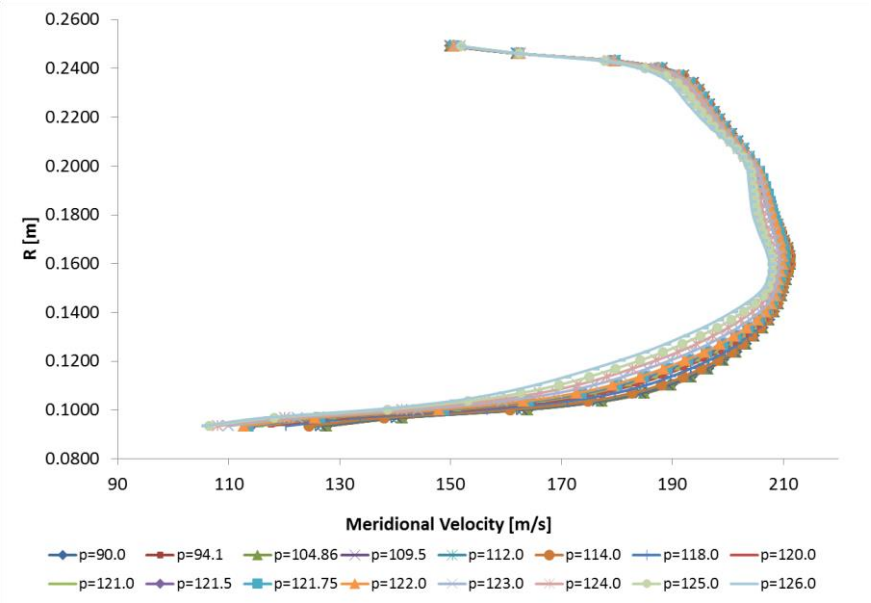

Figure 4.25 Meridional velocity spanwise distribution for the NASA Rotor 67 at 100% of design speed for the leading edge.

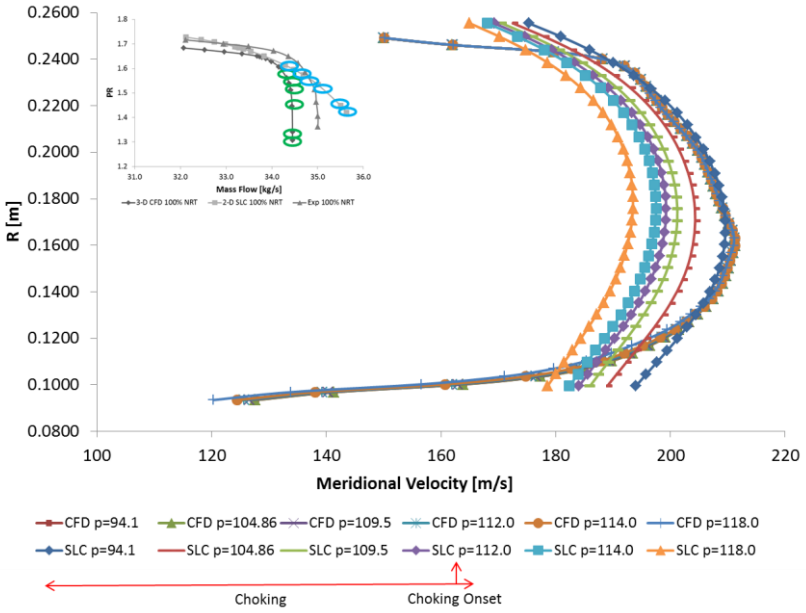

Figure 4.26 Meridional velocity spanwise distribution for the NASA Rotor 67 at 100% of design speed for the leading edge.

4.4.2 Mass Flow Redistribution

The streamtube mass flow radial distribution for various operating conditions from stall towards choking is plotted in Figure 4.27, comparing the 3-D CFD RANS and the 2-D SLC without any choked-induced mass flow correction. The streamtube mass flow

prediction in 2-D SLC without any mass flow redistribution induced by choking is allowed to increase at the tip.

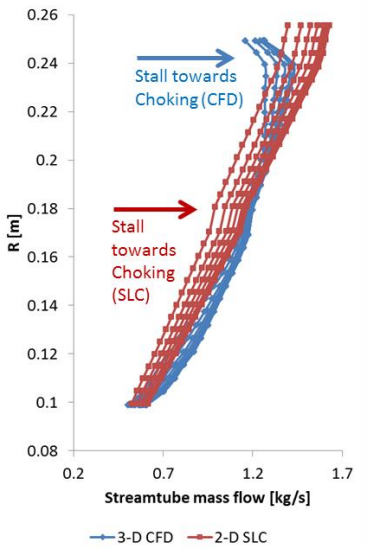

Figure 4.27 Streamtube mass flow radial distribution for the uncorrected choke conditions in 2-D SLC.

The choking mass flow redistribution model implemented within the 2-D SLC compressor performance simulator fixes the mass flow at the tip and redistributes successively the mass flow downwards as seen in Figure 4.28. Note that the reduction at the tip in the 2-D SLC simulation replicates that from the 3-D CFD analysis.

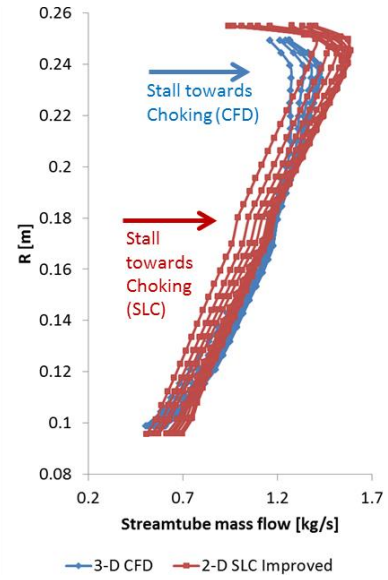

Figure 4.28 Stream tube mass flow radial distribution with the mass flow redistribution model activated in 2-D SLC for choking conditions.

Figure 4.29 compares the redistributed mass flow in the 2-D SLC analysis in choke conditions against a 3-D RANS CFD simulation for the NASA Rotor 67. Spanwise mass flow distributions between the analyses show minimum differences throughout all the span and for all the off-design cases at 100% of design speed. As expected, maximum differences are present in the choked cases at the blade tip, with values ranging around 1.3%.

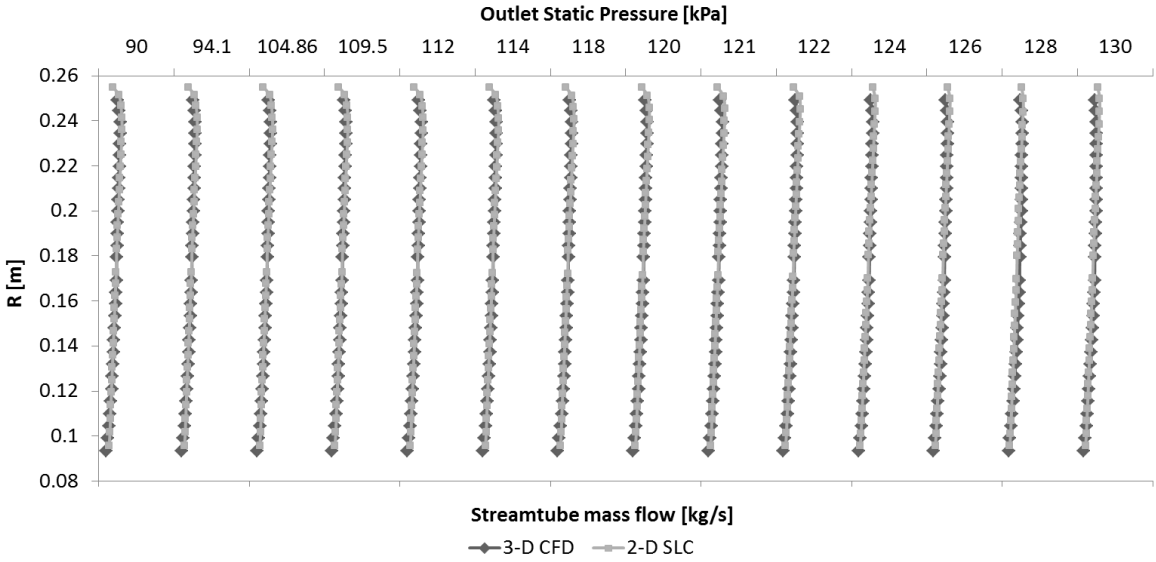

Figure 4.29 Spanwise mass flow distribution comparison between 2-D SLC and 3-D CFD simulations for the NASA Rotor 67 at 100% NRT.

The streamtube mass flow and inlet relative flow angle at the tip show an acceptable agreement between 3-D CFD and 2-D SLC as seen in Figure 4.30, with a difference of 0.9% and 0.3%, respectively. The streamtube mass flow prediction in Figure 4.30 a) was improved by 11% at the tip and by 14% at the hub with respect of the previous version of the 2-D SLC code due to the implementation of the choking mass flow redistribution model. Figure 4.30 b) exhibits that the 2-D SLC simulation fixes those choked locations at the high-span regions to the value of the choking incidence. Farther down, the blade-elements start to choke and are well above the choking incidence.

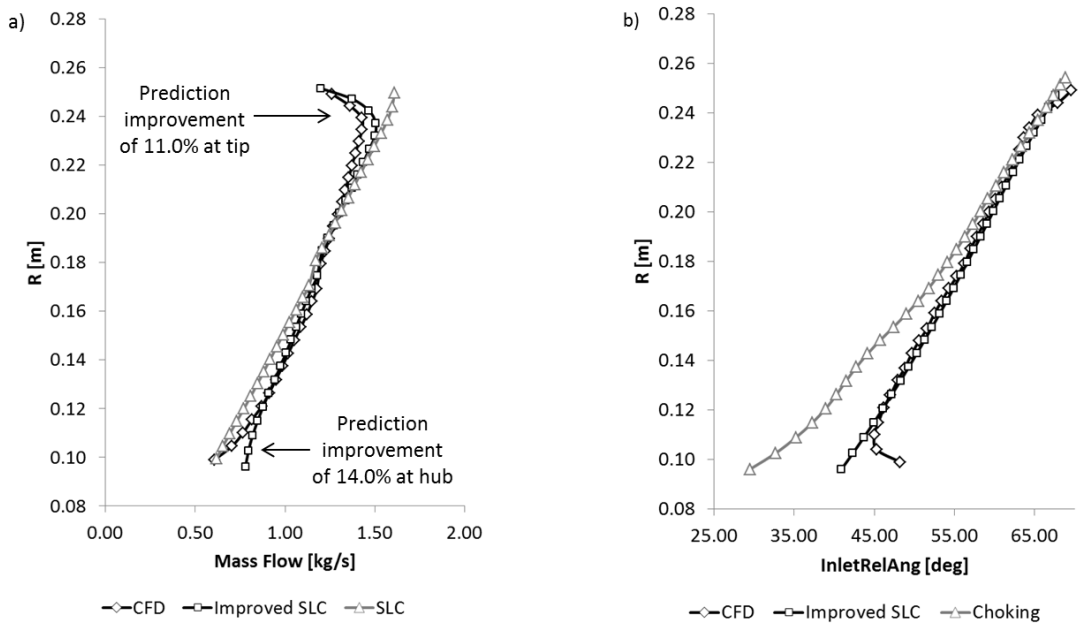

Figure 4.30 Spanwise comparison for the choking prediction between the 2-D SLC and 3-D CFD simulation. a) Mass flow distribution. b) Inlet relative flow angle.

4.5 Shock-Loss Model Validation and Verification

4.5.1 Design Shock-Losses

The present shock- structure and loss model described in Sec. 3.3 was applied to the NASA Rotor 67 [40] in the context of the 2-D SLC compressor performance simulation and compared against experimental data [246,255] for validation purposes. According to the practice in the NASA technical reports for transonic-compressor performance rig tests and analogous to the shock-loss coefficient defined in Eq. 2.6.40, the experimental shock-loss coefficient distribution is obtained by calculating first the profile-loss coefficient as follows

$$\omega_{prof} = \frac{2\sigma\Pi_{prof}}{cos\beta_2} \qquad \textbf{(4.5.1)}$$

where the profile-loss parameter Π_{prof} is corre-lated to the diffusion factor using the annular cascade rig-test data from Figure 4.31 for different blade spans. The diffusion factor is calculated using Lieblein's equation as in Eq. 2.3.32. Thus, the profile-loss coefficient is subtracted from the measured relative total-pressure loss coefficient to determine ω_{sh} from experimental data.

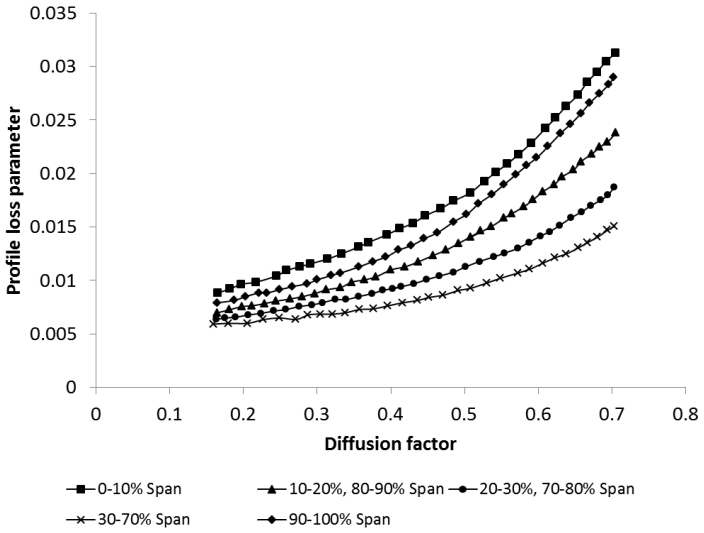

Figure 4.31 Annular cascade rig-test correlation [38] **for the profile-loss parameter as a function of the diffusion factor for experimental measurements.**

As discussed in Sec. 3.3.4, the transonic flow regime is not present in the whole span. For the NASA Rotor 67, the transonic phenomenon extends ~90% from tip to hub. Henceforth, choking is expected to develop progressively from the tip towards mid-span through the working range. Even at near peak-efficiency, 20% of the top blade-sections are already choked. These physics were properly captured by the choking-incidence model of Sec. 3.4.2 and the mass flow redistribution scheme of Sec. 3.4.4 to fix the mass flow, and hence the incidence, at the identified started blade-elements of the 2-D SLC simulation.

The most notable state-of-the-art shock-loss models used in SLC methods were programmed accordingly and ran for the NASA Rotor 67 in order to validate the current shock-loss model and understand its accuracy improvement. Forasmuch as the previously published models are intended mainly for design point and assuming the entire blade operation is unstarted, it results unfair to compare their outcome at off-design points. Figure 4.32 shows the shock-loss coefficient comparison along the spanwise direction for the NASA Rotor 67 at 100% of design speed and near peak-efficiency ($w = 34.03\ kg/s$) between the test data, and the historical, and current models. The shock-loss coefficients from the simplified analytical models of Schwenk *et al*. [4], Miller *et al*. [3], Sayari and Bolcs [24], and Bloch *et al*. [34] were determined without any alteration to the models, as described in Sec 2.6.4. Although its

empiricism, the shock-loss formulation of Koning *et al.* [153,155] resulted interesting for comparison due to the consideration of the second passage-shock. Additionally, the empirical model reported by Cunnan *et al.* [38] was also compared to set a basis for reference.

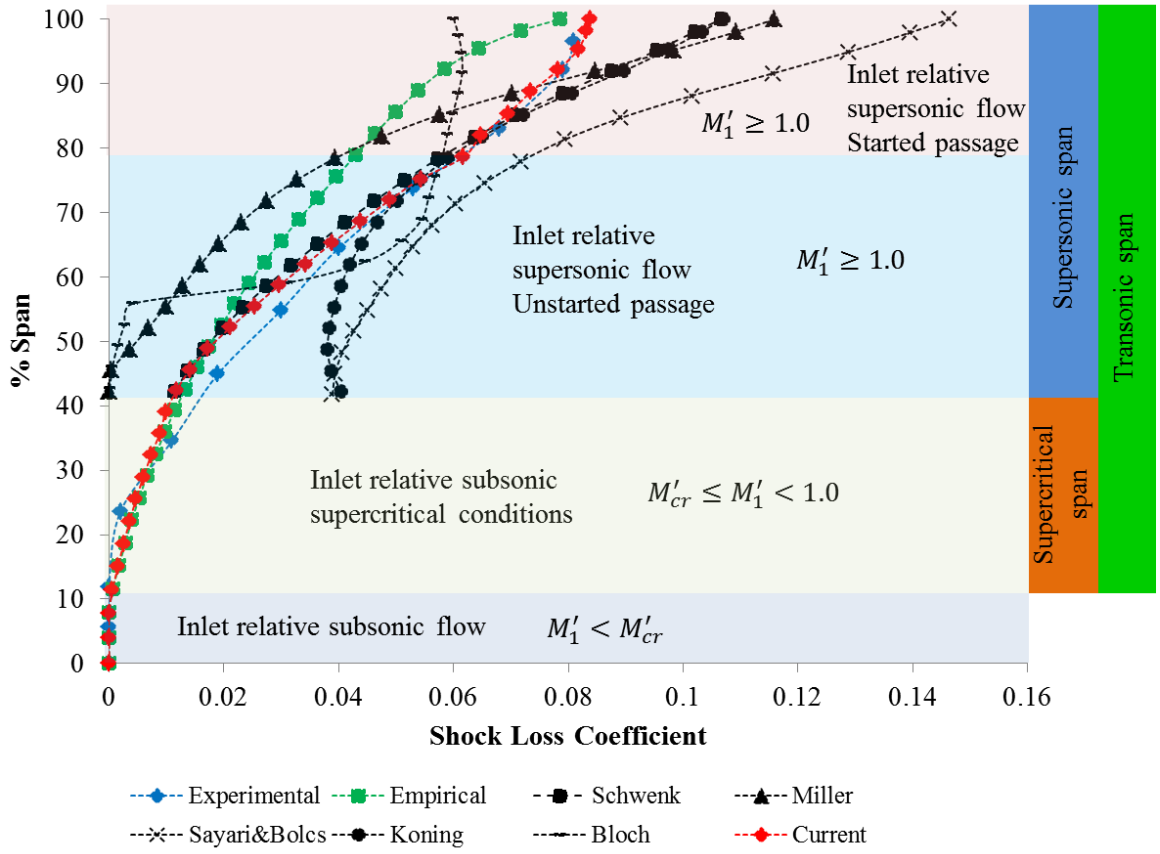

Figure 4.32 Shock-loss coefficient radial distribution comparison for the NASA Rotor 67 [40] **at 100% of design speed and w=34.03 kg/s (NPE) between test data, and historical and current models.**

Because of the simplifications considered in the historical models, there is a significant deviation of the relative total-pressure loss coefficient along the entire span against experimental data as observed in Figure 4.32. Conversely, the current shock-loss model reduces considerably this difference and follows the same trend as the measurements all along the blade span. The current shock-loss prediction improvement is more remarkable at the top 20%, where the historical models fail to predict the choking. Instead, these models assume a normal passage-shock standing almost at the leading

edge, extending from suction to pressure surface, and resulting in an overestimation of shock losses.

Note as well the inability of the previous analytical models to resolve the flow in the subsonic supercritical span region, as they rely on the Prandtl-Meyer expansion, which is not defined for Mach numbers less than a unity value. In contrast, the current shock-loss model does resolve the shock losses at the supercritical span using the model described in Sec. 3.3.2, yielding in a satisfactory agreement against experimental data and the empirical model of Cunnan *et al*. [38]. In fact, it can be seen that the shock-loss distributions from these three sources agree for the supercritical-span initiation at ~9%, sign that the critical relative Mach number was accurately predicted in the current shock-loss model.

The widely used model of Miller *et al*. [3] in SLC shows an absolute deviation of 43.1% at the tip, while the model of Sayari and Bolcs [24] overestimates the shock loss by 80.5%. The error at the tip slightly reduces to 32.0% in the models of Schwenk *et al*. [4] and Koning *et al*. [153,155].

At the supersonic-span inception, the shock-induced relative total-pressure losses are relatively low, however, the model of Miller *et al*. [3] under predicts the loss by 78.7%, while the models of Sayari and Bolcs [24] and Koning *et al*. [153,155] increases the loss in 103%. The model of Bloch *et al*. [34] shows the larger average radial deviation against experimental data, underestimating the loss by 25.9% at the tip and predicting an almost-zero loss at low supersonic-spans, representing a difference of 96.8%. These intolerable discrepancies are not surprising, as the overall passage-shock structure is oversimplified represented by an equivalent shock normal to the flow, which does not represent the true configuration.

On the contrary, the iterative method implemented in the current model guarantees the correct position and angle of the second passage-shock to intercept or not the passage-shock portion of the detached bow-shock. This formulation leads to an accurate passage-shock pattern to resolve the proper flow-expansion mechanisms, yielding in an accurate relative total-pressure loss distribution in the pitchwise direction. The current shock-loss methodology significantly improves the agreement against the measured data

by 42.4% at the tip and by 54.9% at the lower supersonic sections with respect of the model of Miller *et al*. [3]. This means that the absolute error is reduced to a maximum of 0.6% at the tip, and shock-loss coefficient discrepancies of 5e-4 and 4.8e-3 at mid and mid supersonic-spans, respectively.

At mid supersonic-span, the current shock-loss model yielded a satisfactory prediction of the flow physics, translated to differences around 0.3%. The largest deviation observed between the current shock-loss prediction and experimental results occurs at low supersonic-spans, immediately after the transition from the inlet relative subsonic supercritical conditions. The final effect of these discrepancies on the isentropic efficiency can be considered minimal, as the shock-loss coefficients are underestimated in the order 1e-3 within a relatively small region of about 10% of span.

Even though at the low supersonic-spans there is only a single passage-shock as a portion of the detached bow-shock, the assumption of a hyperbolic approximation for it might need further refinement. In fact, as the span reduces, the hyperbola-approximation starts to lose accuracy since the inlet relative Mach number decreases, incrementing the free-stream Mach angle, and forcing the detached bow-shock to become less oblique. In other words, at the supersonic-span initiation, the assumption of a nearly normal detached-shock to increase the shock loss would appear more appropriate than a hyperbolic shape that reduces its shock angle outwards from the vertex.

The models of Schwenk *et al*. [4] and Sayari and Bolcs [24] were modified and improved up to some extent in an attempt to increment their accuracy, but mainly, to validate, and appreciate the importance and complexity of the current shock-loss model. Special attention is brought to the shock model of Schwenk *et al*. [4], since it is, in some way, the essence for the other previous models and because of its good agreement against measured data, at least at mid-span locations (~42-68% span). To demonstrate the validity of the current shock-loss model, two other shock-loss models were derived from Schwenk *et al*. [4]. Instead of using the geometric formulation as a function of a DCA surface , Schwenk's *et al*. [4] model is fully coupled with the blade-element-layout method (BELM) of Sec. 3.2.2 to estimate the passage-shock impingement flow

angle for any arbitrary surface shape. The other model consists of replacing the assumption of the passage-shock location by that assumed by Bloch *et al*. [34] at the sonic point of the hyperbolic detached bow-shock.

Two other further variations were introduced to these models in terms of the relative total-pressure coefficient computation. The variation M1 considers the baseline model by computing the shock-loss coefficient as a function of the inlet relative Mach number M'_1 as in Eq. 2.6.8. Inasmuch as the normal-shock placement tends to be an equivalent of the complex passage-shock situation, it is not entirely true that the upstream Mach number is M'_1. The variation in the model M2 uses the peak suction-surface relative Mach number $M'_{psh_{ss}}$ to calculate the relative total-pressure loss coefficient since the equivalent passage-shock is then assumed to be the only loss mechanism. Nevertheless the bow-wave-loss influence must be considered. Therefore the model variation M3 considers the bow-wave-induced relative total-pressure ratio in addition to the equivalent passage-shock losses as in Eq. 3.3.120.

Given the overall relative total-pressure loss, the overall shock-loss coefficient is thus determined as in Eq. 3.3.121, using the inlet relative Mach number upstream of the loss system. Table summarizes the matrix of the evaluated historical analytical shock-loss models and their modifications. Such emphasis in this evaluation raises the understanding level of the disparities of the current and measured data against those from the previous models at design point.

Table 4.8 Matrix of the assessed historical shock-loss models and their modifications.

Shock-loss models	**Variations**		
Schwenk *et al*.	M1 (original)	M2	M3
Schwenk *et al*./BELM	M1 (original)	M2	M3
Schwenk *et al*./Bloch	M1 (original)	M2	M3
Sayari and Bolcs	M1 (original)	M2	M3
Miller *et al*.	Original		
Koning *et al*.	Original		
Bloch *et al*.	Original		

Despite of its simplicity, the model of Schwenk *et al*. [4] shows the best agreement against experimental data among the historical approximations especially at low and mid sections of the supersonic span as seen in Figure 4.33. This is explained since the

passage-shock simplification approximates to the presence of the nearly-normal detached bow-shock at low supersonic-spans. The shock losses predicted by the present model are consistent with those from the model of Schwenk *et al*. [4] at these radial locations, with differences less than 2e-3 in the relative total-pressure loss coefficient.

At high supersonic-spans, there is an average overestimation of ~20%, since Schwenk's *et al*. [4] simplification considers a very strong equivalent passage-shock. In contrast, the current shock loss is significantly less than that from Schwenk *et al*. [4], since the shock strength reduces due to the physics-based solution of the choked-induced shock obliqueness in the relative frame of reference. More important is the correct location of the second passage-shock computed utilizing the iterative approach. In case there is a coalescence of passage shocks, the shock loss is reduced as just a portion of the configuration consists of the straight shock. If there is no intersection of passage shocks, the shock loss still reduces as the first passage-shock is weak due to its hyperbolic shape, reducing slightly the downstream relative Mach number. Although small, this reduction in the relative Mach number magnitude helps for the second passage-shock not to be that dramatic. This is equivalent to having different weak compression waves instead of a unique strong shock.

In terms of the variations, the model M2 corrects the loss deviation at the tip 15.4% at the expense of losing accuracy for the rest of the resolved transonic span. This is a clear indication that the current shock-loss model operates accordingly at low and mid supersonic-spans, and increases the upstream relative Mach number of the passage shock towards the tip. The variation M3 to the model of Schwenk *et al*. [4] considers the bow-wave losses, resulting in a slight increase of loss towards the blade tip with respect of the model M1 in 1.9%. This shock-loss increase agrees with the current model when the bow-wave losses are removed, following the same trend and reducing the shock-loss coefficient at the tip by 1.1%.

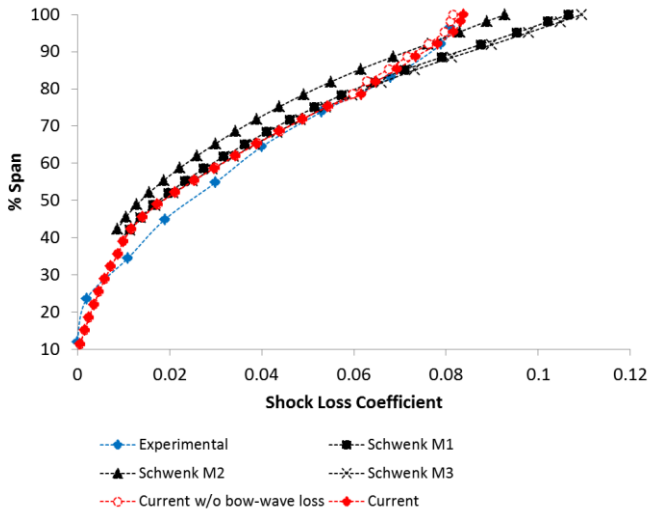

Figure 4.33 Shock-loss coefficient radial distribution comparison for the NASA Rotor 67 [40] **at 100% of design speed and w=34.03 kg/s (NPE) between test data, current model, and variations of Schwenk *et al.*** [4]**.**

Although the blade-element-layout method accurately resolves the surface angles required for the flow direction in the Prandtl-Meyer expansion, its coupling with the model of Schwenk *et al.* [4] results in a shock-loss over prediction as seen in Figure 4.34 a). Similar effect is observed in Figure 4.34 b) if the passage-shock location is then moved downstream to be at the sonic point as suggested by Bloch *et al.* [34], raising $M'_{psh_{ss}}$ and increasing the shock strength. This indicates that Schwenk's *et al.* [4] model itself suffices with its assumptions and any other attempt of introducing an improvement, for more analytical that this could be, would deviate the agreement against measured data. Even if the assumed passage-shock is translated to the leading edge as in the Sayari and Bolcs [24], the flow-expansion process extends, increasing $M'_{psh_{ss}}$ and raising the shock losses as plotted in Figure 4.34 c).

In terms of the variations, a similar trend to that in Figure 4.33 is seen across the shock-loss models of Figure 4.34, where the variation M2 reduces the shock-loss magnitude. However, this time the consideration of the peak suction surface Mach number in the shock-loss coefficient produces a better match against experimental data. This apparent agreement is more as a result of a compensation of the passage-shock loss over prediction rather than a physical behaviour. The variation M3 in the models of Figure 4.34 confirms the findings in Figure 4.33 and being consistent with the trend and

percentage of shock-loss detrimental in the current shock-loss model when the bow-wave losses are removed.

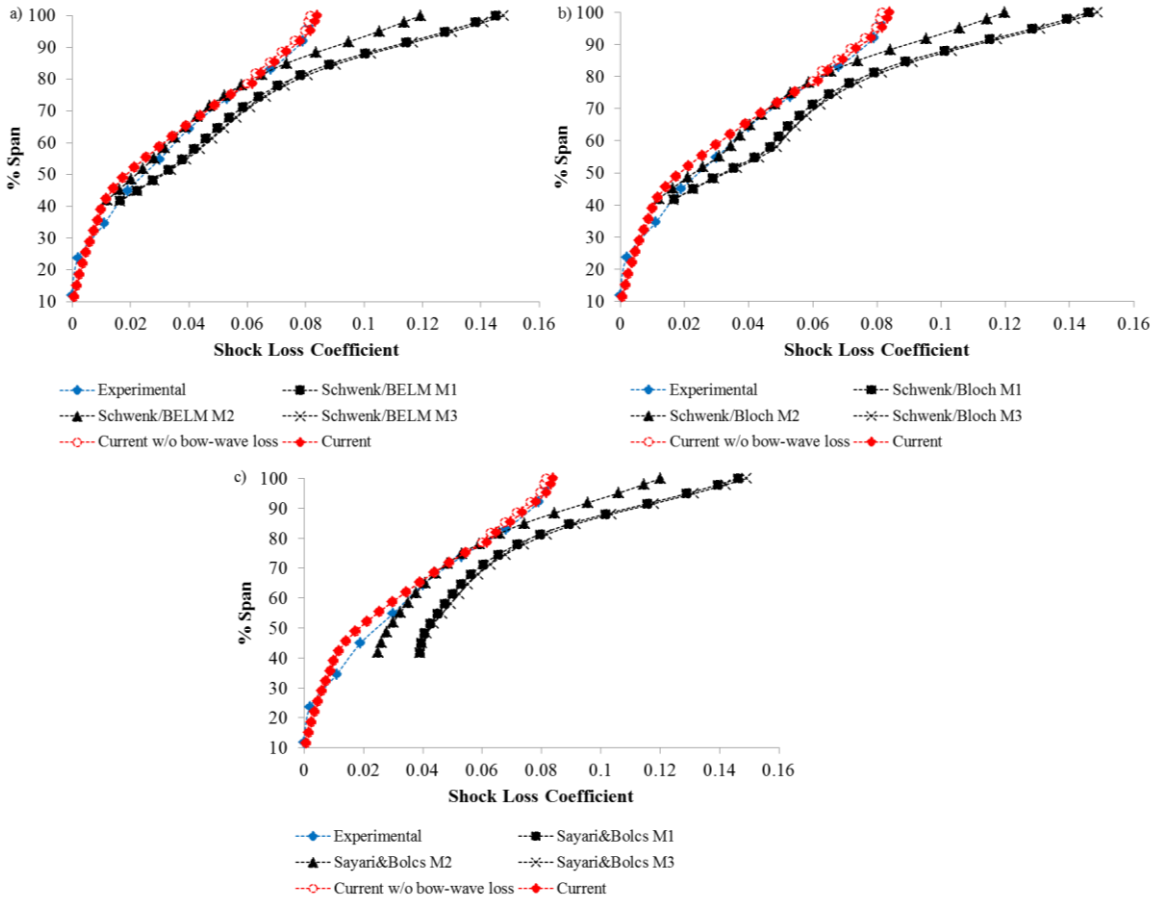

Figure 4.34 Shock-loss coefficient radial distribution comparison for the NASA Rotor 67 [40] **at 100% of design speed and w=34.03 kg/s (NPE) between test data, current model, and historical-model variations. a) Schwenk *et al.*** [4]**/BELM. b) Schwenk *et al.*** [4]**/ Bloch *et al.*** [34]**. c) Sayari and Bolcs** [24]**.**

The circumferential mass-average integration of relative Mach numbers in the model of Miller *et al*. [3] upstream of the assumed passage-shock, produces less shock losses rather than having a higher equivalent Mach number from Eq. 2.6.5, as viewed in Figure 4.35 a) Nonetheless, the shock-loss coefficient at low and mid supersonic-sections is underestimated inasmuch as the passage shock is too upstream of what it should be. Conversely, the current shock-loss model uses the same circumferential-loss-integration approach but at an accurate axial location. At the blade tip, the typical overestimation of the historical models is observed due to the inability of segmenting

the passage shock in the hyperbolic passage-shock portion and the choked-induced shock as is executed in the present shock-loss methodology.

The lack of discrimination between unstarted and started passages from the model of Koning *et al*. [153,155] fixes the second-passage shock-loss all along the transonic span, overestimating the shock losses at low and mid supersonic-regions as seen in Figure 4.35 b). Even at the top locations, where there is definitely a second passage-shock, the shock-loss magnitude is over predicted. The previous models have demonstrated that one of the main difficulties is to match the blade tip shock-losses, which in part is understandable since they do not model explicitly the choke-induced passage shock. One of the highlights of the present shock-loss model is its ability to attain a good agreement at the blade top sections. A full substitution of the empirical second-passage shock-loss effect from Koning *et al*. [153,155] in the current model at the top sections, proves the inaccuracy of a simple empirical correlation. Rather, the current shock-model suffices in its prediction accuracy through the implemented analytical iterative-approach, resulting in the same trend as the experimental results. As expected, the incapability of Koning *et al*. [153,155] model to adjust gradually the choked-induced passage-shock loss towards the hub, causes a significant increase in the shock-loss coefficient for mid and low supersonic-span heights.

Although the composite nature of the passage-shock consisting in a hyperbolic portion and a straight-shock section in the model of Bloch *et al*. [34], the shock losses are underestimated as noticed in Figure 4.35 c). This is as a consequence of placing always the straight passage-shock at the bow-shock sonic point, which is close to the hyperbola vertex regardless of the flow conditions, yielding in a very upstream straight passage-shock. In turn, the flow expansion ahead of the passage shock shrinks, decrementing the local relative Mach numbers in the circumferential direction, and hence, inducing lower relative total-pressure losses. The current shock-loss model uses the same principle of intercepting both passage shocks; however, the correct placement of the straight shock produces a much better agreement in comparison to the rig-test measurements. Despite the discrepancies in Bloch's *et al*. [34] model, there is a similar tendency of the rate-of-change of shock-loss coefficient with radius at the tip as in the current shock-loss model and test data.

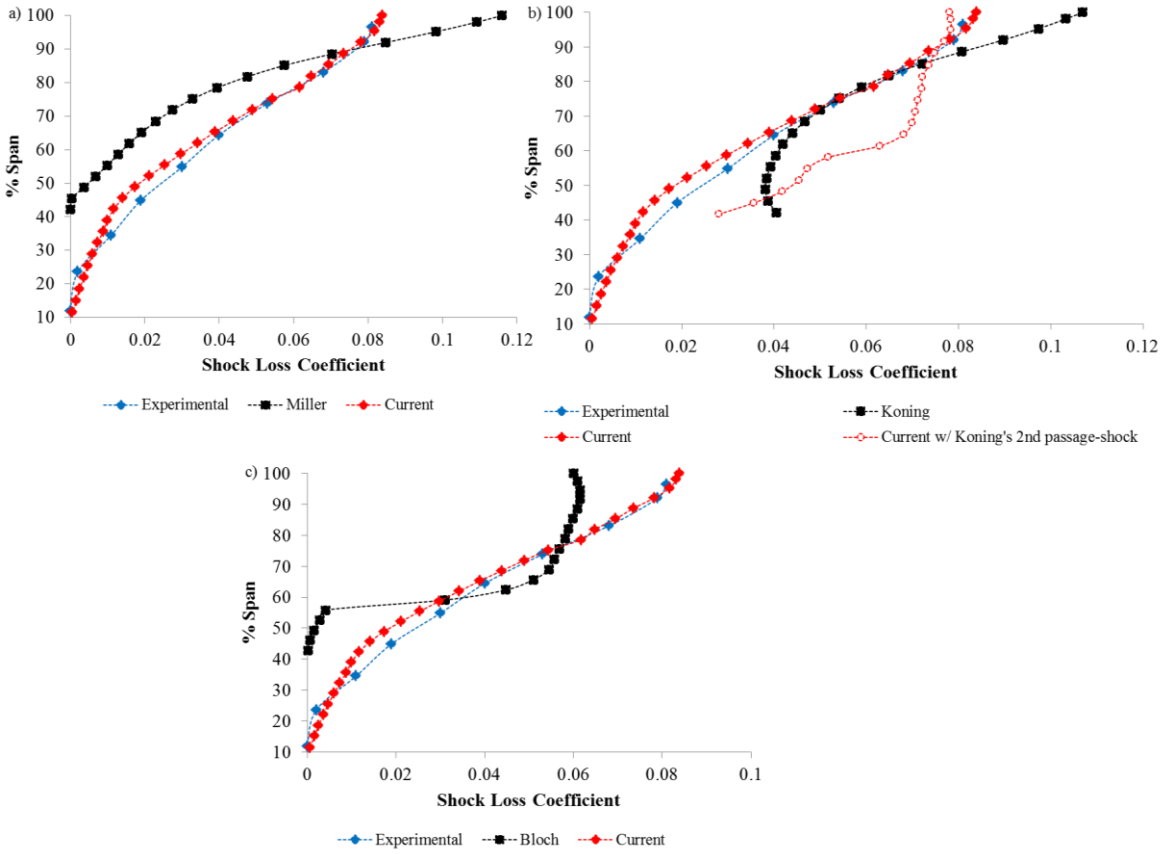

Figure 4.35 Shock-loss coefficient radial distribution comparison for the NASA Rotor 67 [40] **at 100% of design speed and w=34.03 kg/s (NPE) between test data, current model, and historical models. a) Miller *et al.*** [3]**. b) Koning *et al.*** [153,155]**. c) Bloch *et al.*** [34]**.**

The outcome examination of the empirical correlation of Cunnan *et al*. [38] permits to situate the prediction of the current shock-loss model. As mentioned earlier, there is an accurate agreement between test data, and the current and empirical models, when the inlet relative conditions are subsonic supercritical. As the inlet relative flow becomes supersonic, the empirical model under predicts the shock losses forming a concave gradient as seen in Figure 4.36. Rather, the currently estimated shock losses follow the convex gradient of the experimental data. Observe how the empirical model tries to approximate the real results particularly at the very tip of the blade, where the difference is 3.3%. In this respect, the current shock-loss model works adequately at the top regions, as it agrees satisfactory against experimental data at the very tip and downward profiles with an average difference of 0.4%.

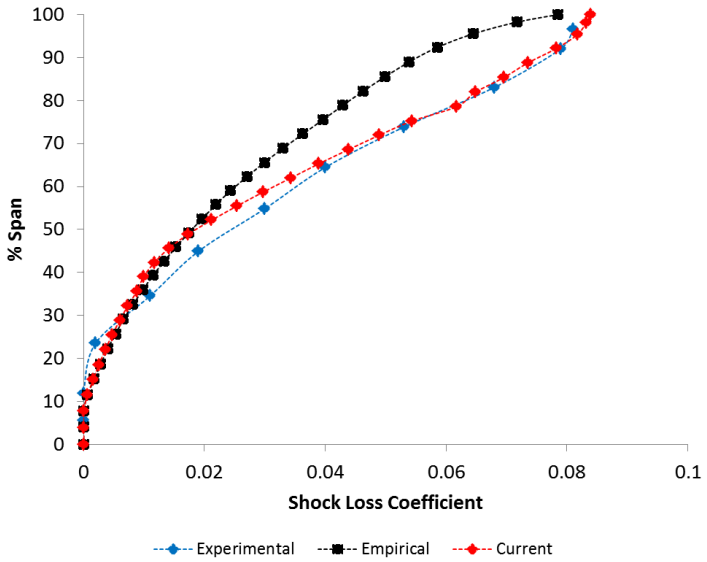

Figure 4.36 Shock-loss coefficient radial distribution comparison for the NASA Rotor 67 [35] at 100% of design speed and w=34.03 kg/s (NPE) between test data, current model, and empirical model of Cunnan *et al.* [38].

4.5.2 Off-design Shock-Loss Performance

As mentioned in Sec. 4.5.1, the previously published shock-loss models are intended to operate at design point by assuming that the entire blade operation is unchoked. Nonetheless, the NASA Rotor 67 reveals that even at design point, there can be a certain percentage of blade-span choked at the tip. As reviewed in Sec. 2.7.1, the mass flow is increased, the choking develops progressively from tip towards hub, until the entire transonic span is choked and no further mass flow can be passed. Henceforth, a change in the passage-shock configuration, and hence in shock losses, is expected as the mass flow is increased across the off-design operating points.

The historical simplified shock-loss models fail to predict the off-design shock-losses since the assumption of the design-point passage-shock location is anchored for other operating conditions as a consequence of the lack of a mechanism to modify the passage-shock pattern. The model of Boyer and O'Brien [13,35,36] does apply corrections for the off-design shock-loss estimation, however, it is an empirical model that is not universal for arbitrary aerofoil geometries. Figure 4.37 evidences the inability of the models of Schwenk *et al.* [4], Miller *et al.* [3] and Cunnan *et al.* [38], for instance, to adjust the passage-shock configuration and shock-loss for off-design

operations. Equally, the other historical models reviewed in Sec. 4.5.1 show an absence of shock-loss effect with the reduction in incidence.

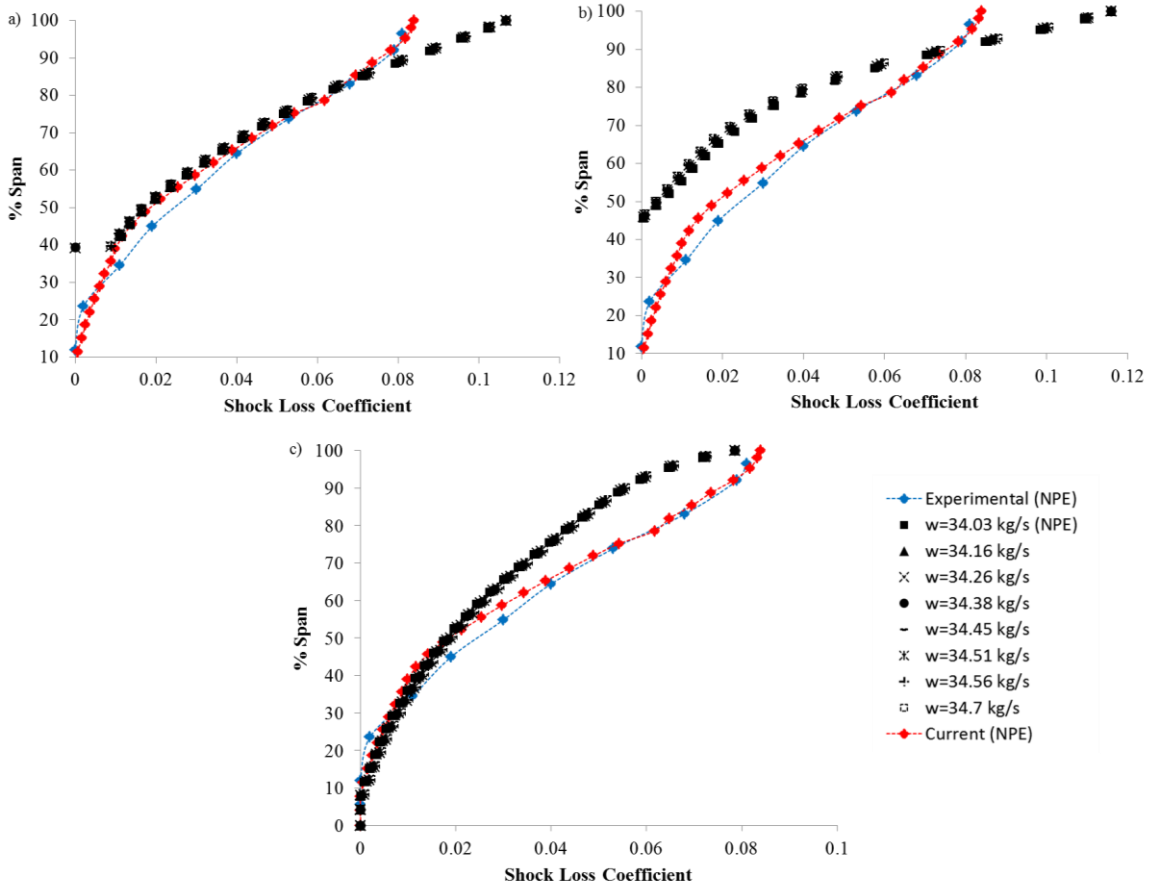

Figure 4.37 Shock-loss coefficient radial distribution comparison for the NASA Rotor 67 [40] **at 100% of design speed for different off-design points. a) Schwenk *et al.*** [4]**. b) Miller *et al.*** [3]**. c) Cunnan *et al.*** [38]**.**

In contrast, the current analytical shock-loss model modifies the passage-shock system according to the implemented iterative approach by displacing upstream and downstream the choked-induced shock along the chord. During this process, both passage shocks might coalesce, for which the appropriate flow-expansion systems are set and resolved, resulting in a passage-shock loss, and hence overall shock-loss adjustment through the successive iterations. The ruggedized iterative approach to locate the choked-induced shock, which constantly checks the flows status for unstarted or started situations, converges until the back static-pressure condition is satisfied. The converged dual passage-shock configuration composed of the hyperbolic portion from

the detached bow-shock and the straight choked-induced shock yields to the off-design shock-loss evolution shown in Figure 4.38. As expected, as the incidence reduces the passage shock-loss increases. The supercritical span and the low supersonic sections get little affected with incidence since the flow is unstarted at those passages. In the case of the supercritical portion, any mass flow variation induces a slightly different flow turning but does not substantially modify the normal-shock relative total-pressure recovery. For the low supersonic-spans, the variation of incidence modifies the single passage-shock pattern, which is just affected by the detached bow-shock shape as a function of the inlet relative Mach number.

On the other hand, at mid and high supersonic-sections, the passages are expected to be choked. Henceforth, any change of incidence will modify the location of the second passage-shock, re-shaping the passage-shock shape, and producing different relative total-pressure decays. Yet, the affection of the choking with an increase in mass flow travels towards the hub, resulting every time in more dual passage-shock structures spanwise, and thence, an overall shock-loss augmentation at mid and low transonic-spans. At the blade tip, the passage-shock loss increase as the incidence decreases is greater as a result of the low back static pressure, demanding higher peak suction surface Mach numbers. To augment the peak suction surface Mach number, the flow-expansion extends chordwise, displacing downstream the straight portion of the passage shock, leading to a more dramatic and stronger shock that generates more relative total-pressure decay. It can be deduced then that the major shock-loss increment occurs at the top sections, where it appears to be almost constant throughout the operating points with a value of 1.2% of shock-loss increase per 0.1 kg/s of change.

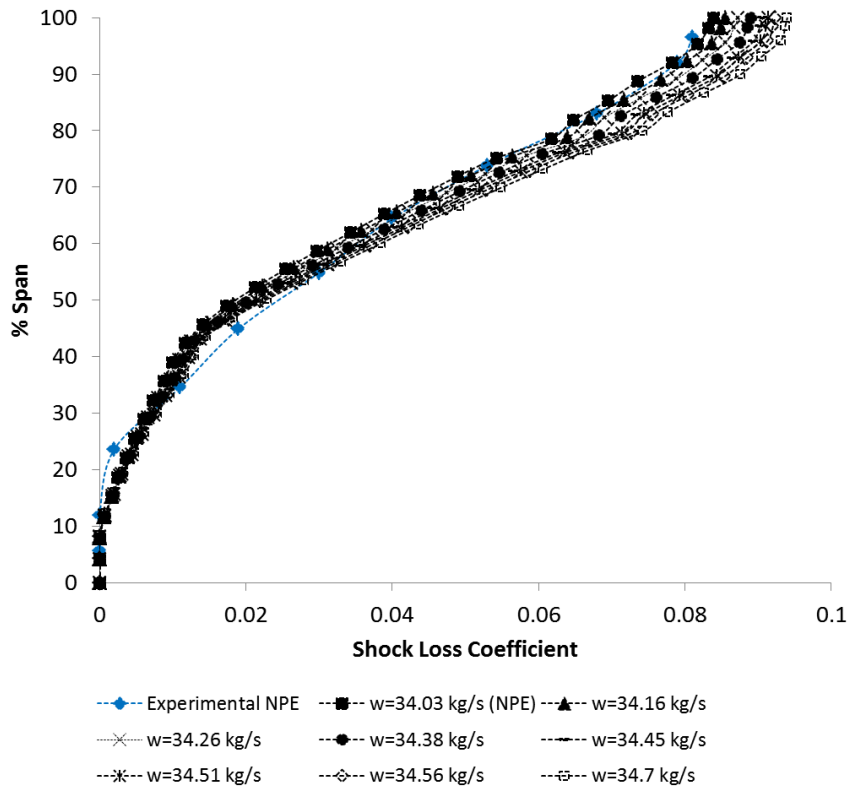

Figure 4.38 Off-design evolution of the shock-loss coefficient radial distribution for the NASA Rotor 67 [35] at 100% of design speed.

Figure 4.39 shows the comparison of the off-design overall shock-loss coefficient radial distributions against measured data to evidence the adequacy of the current analytical and physics-based model. For the top 85% of the supersonic span, there is an accurate agreement and consistency between both experimental and computed data, where absolutes differences are less than 2.5% at the high sections and less than 0.5% for the mid-section of the transonic span. As discussed before in Sec. 4.5.1 this represents an outstanding improvement of ~40-50% with respect of the previously published shock-loss models, considering even more that this enhancement was obtained utilizing a fully physics-based model free of empiricism.

Notwithstanding that there are differences between both experimental and predicted data within the remaining 15% at the bottom of the supersonic span; there is consistency in the shock-loss coefficient trend. More important, however, is that the shock-loss magnitudes at the low supersonic-heights are relatively small in comparison to those from the tip. Whereupon, the underestimations within such blade span have a

maximum shock-loss coefficient difference of 0.01 at the supersonic-span bottom and reducing to 2e-3 towards the tip. Likewise the design point, these deviations might be due to the hyperbola-approximation for the nearly-normal and highly-detached bow-shock that is formed at these heights. Thence, the small shock-loss differences at the supersonic span bottom, might be considered of little effect on the isentropic efficiency as evidenced in the compressor isentropic-efficiency map of Figure 4.41.

Note as well that for every off-design point and near the tip, the predicted shock-loss coefficient increases with the same gradient as the experimental results. Similarly as to the near peak-efficiency point, the average difference at the tip profile-sections is ~0.4% between the current shock-loss model and test data.

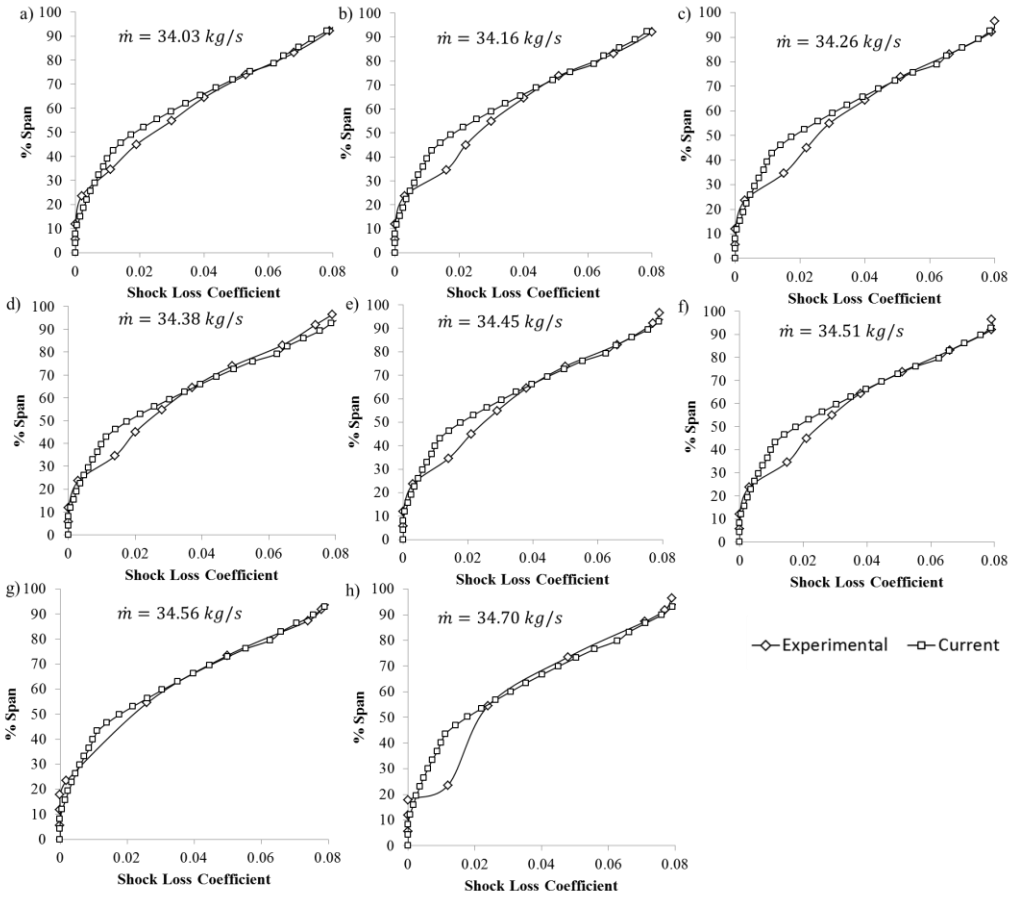

Figure 4.39 Off-design comparison of shock-loss coefficient radial distribution between experimental and current shock-loss model data for the NASA Rotor 67 [35] at 100% of design speed. a) $\dot{m} = 34.03 \frac{kg}{s}$ (NPE) b) $\dot{m} = 34.16 \frac{kg}{s}$ c) $\dot{m} = 34.26 \frac{kg}{s}$ d) $\dot{m} = 34.38 \frac{kg}{s}$ e) $\dot{m} = 34.45 \frac{kg}{s}$ f) $\dot{m} = 34.51 \frac{kg}{s}$ g) $\dot{m} = 34.56 \frac{kg}{s}$ g) $\dot{m} = 34.70 \frac{kg}{s}$ (NC).

4.5.3 Compressor Performance

The NASA Rotor 67 [40] compressor maps in Figure 4.40 and Figure 4.41 compare the performance prediction from the previous 2-D SLC simulator against that from the updated version with the incorporation of both novel physics-based shock-loss and choking mass flow redistribution models. The empirical shock-loss model from Cunnan *et al*. [38] was used in the previous version of the 2-D SLC software. Besides, the characteristics at 100% of design speed from the 3-D CFD RANS simulation are compared as well for reference.

Overall, there is a consistent agreement between the updated 2-D SLC simulations and measured data, where the major isentropic-efficiency prediction improvement of ~1.1% is attained at 100% of design speed due to the high relative velocities leading to impacting shock-losses. In fact, a closer agreement against experiments is obtained with the updated 2-D SLC simulation than with 3-D CFD. Although the CFD results show the same trend as the test data, they show a deviation about 2.5% in pressure ratio and 1.9% in isentropic efficiency, and underestimating the choking mass flow by 1.5%.

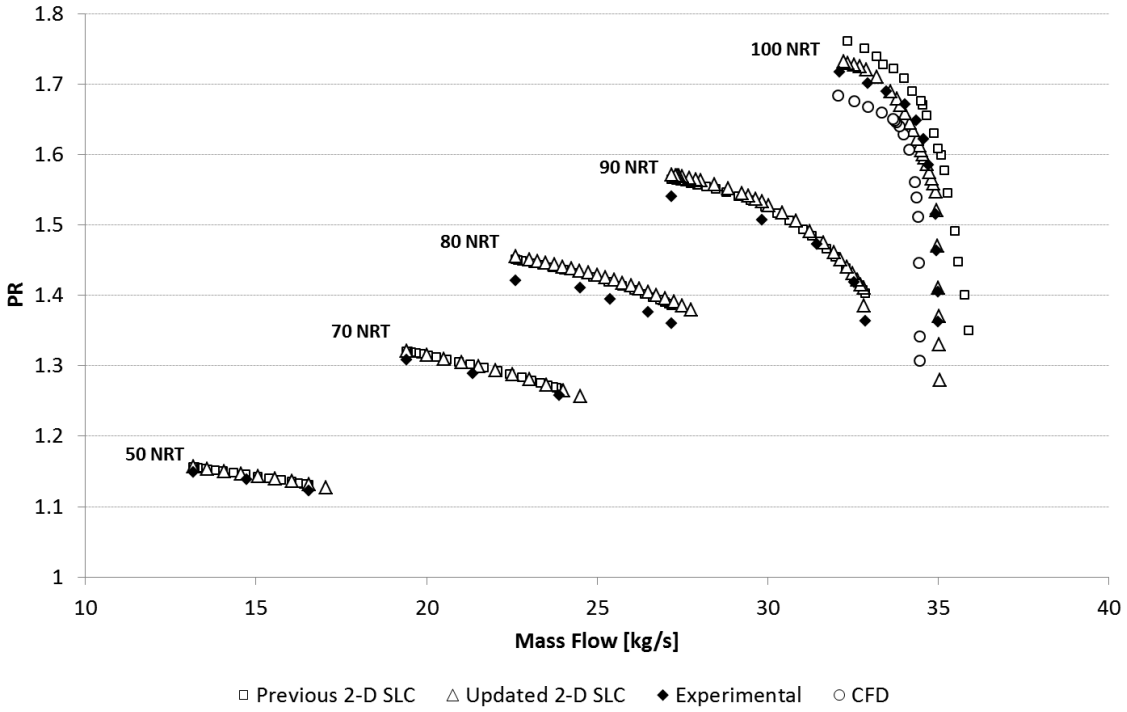

Figure 4.40 NASA Rotor 67 [35] compressor total-pressure ratio map comparison between experiments, and the previous and updated 2D-SLC performance simulation codes.

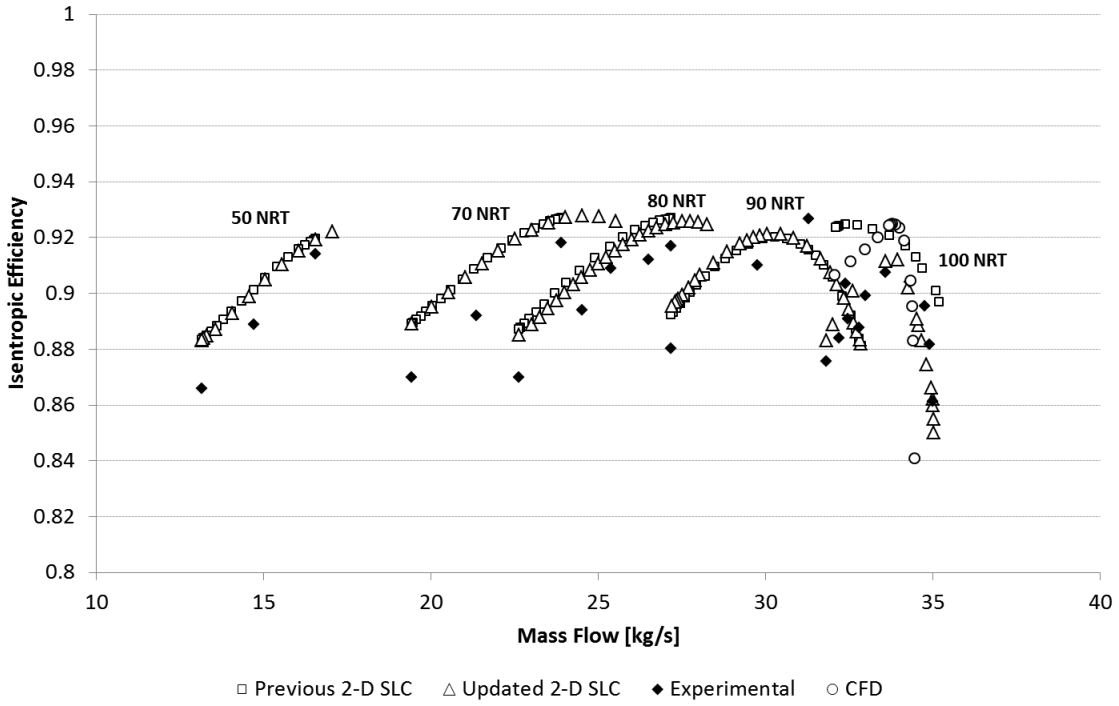

Figure 4.41 NASA Rotor 67 [35] compressor isentropic-efficiency ratio map comparison between experiments, and the previous and updated 2D-SLC performance simulation codes.

As expected, at 50% and 70% of design speed the performance between the previous and updated models is the same since the supersonic solution of the current shock-loss model did not have any participation on the analysis. Although at 70% of design speed, the top 26% of the blade span has subsonic supercritical conditions and the supercritical strategy was used, the shock loss generated was too small to produce a noticeable change in the overall pressure ratio and isentropic efficiency.

Even at 80% and 90% of design speeds and near their peak-efficiency, there are inlet relative supersonic conditions for the 17% and 40% of the blade span from tip to hub, respectively, where the shock-loss model was applied accordingly. Nevertheless the shock-loss influence on total-pressure ratio and isentropic efficiency is minimal along their working range, since the highest suction-surface Mach numbers are low values of 1.09 and 1.27 at design speed for 80% and 90%, correspondingly. These Mach numbers reduce progressively pitchwise towards the pressure surface, resulting in an even lower mass-averaged upstream relative Mach number of the single passage-shock systems formed, and thus, a low mass-averaged relative total-pressure loss. For a high

mass flow of 32.8 kg/s at 90% of design speed, choking appears for the first time at the very tip just for a unique streamline, identified by the choking model to redistribute the mass flow. This suffices for the shock-loss model to structure a dual-shock configuration and estimate the corresponding mass-averaged relative total-pressure recovery. The accrued shock losses from the supersonic span and that from the started flow at the tip add up to drop the total pressure ratio of the highest mass flow rate at 90% of design speed as seen in Figure 4.40.

The same phenomenon of the highest mass flow at 90% is extrapolated to a wider working range at 100% of design speed. Previous 2-D SLC underpredicted the isentropic efficiency throughout the working range and shifting the peak-efficiency point to a lower mass flow rate. This is explained as the empirical shock-loss model underestimates the shock-loss coefficient by a radial average of 26.5% within the relative supersonic span, producing an over prediction of the isentropic efficiency by 1.4% at design point. The current shock-loss prediction improvement by 25% with respect of the empirical model within the relative supersonic span, results in a satisfactory agreement against test data with an over prediction of 0.4% at design point. A further SWBLI model might even bring down the efficiency to enhance the agreement. Similarly, the overall pressure ratio is improved by an average of 1.5% throughout the working range. Because of the inability of the empirical shock-loss model to react to off-design conditions where the shock-loss coefficient becomes greater as the incidence reduces, the isentropic efficiency in the previous 2-D SLC does not get lower. Conversely, the current shock-loss coefficient increments with incidence, particularly between NPE and NC, where there are choke-induced dual shock-configurations that contribute more to the loss. In this way, the isentropic efficiency suffers a significant detrimental effect at a fixed mass flow determined by the redistribution model implemented, that adequately agrees with the asymptotic distribution near the maximum mass flow of the measured results, as observed in Figure 4.40 and Figure 4.41. The predicted maximum mass flow differs from that of the experiment by 0.1%, which represents an improvement of 1.4% compared to the 3-D CFD RANS estimation.

4.6 Shock-Structure Verification

4.6.1 Detached Bow-Shock

To validate the shock-pattern model, a 2-D SLC run was performed for the NASA Rotor 67. The validation of the shock data was done against charts as function of the inlet relative Mach number presented by Moeckel [180] and Miller and Hartmann [208]. The corresponding shock angles, $\varsigma_{detach}, \varsigma_S, \varsigma_C$ are presented in Figure 4.42. It can be observed that towards an inlet relative Mach number of one, the shock angles tend to coalesce to the value of 90 degrees.

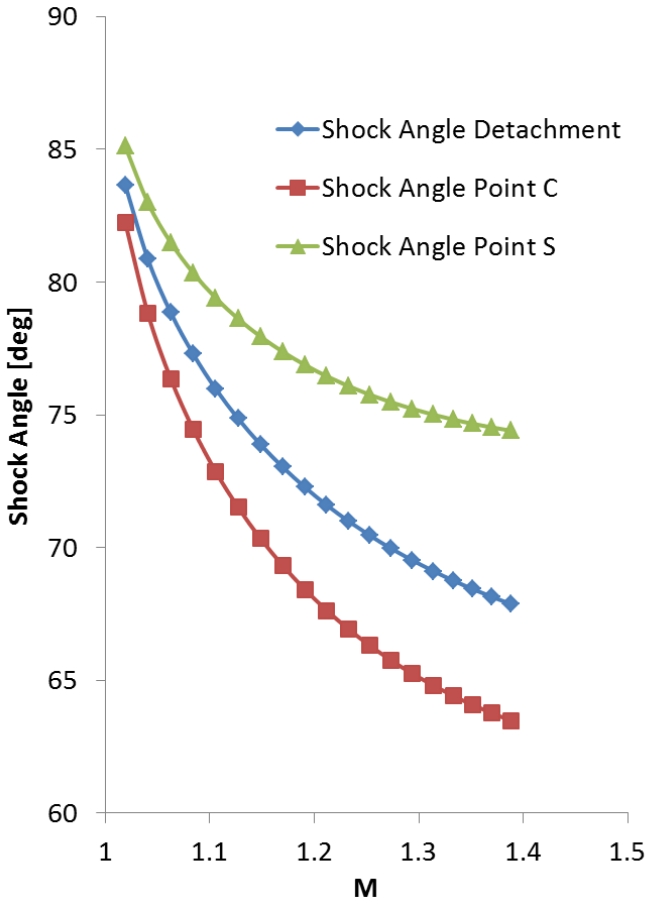

Figure 4.42 2-D SLC-estimated bow shock angles for the NASA Rotor 67.

A comparison of $\varsigma_{detach}, \varsigma_S, \varsigma_C$ against those obtained by Moeckel as a function of M_1', is displayed in Figure 4.43. A satisfactory comparison is found between the 2-D SLC shock-structure angles and the ones presented in the chart. Maximum difference for the three shock angles was 0.12%.

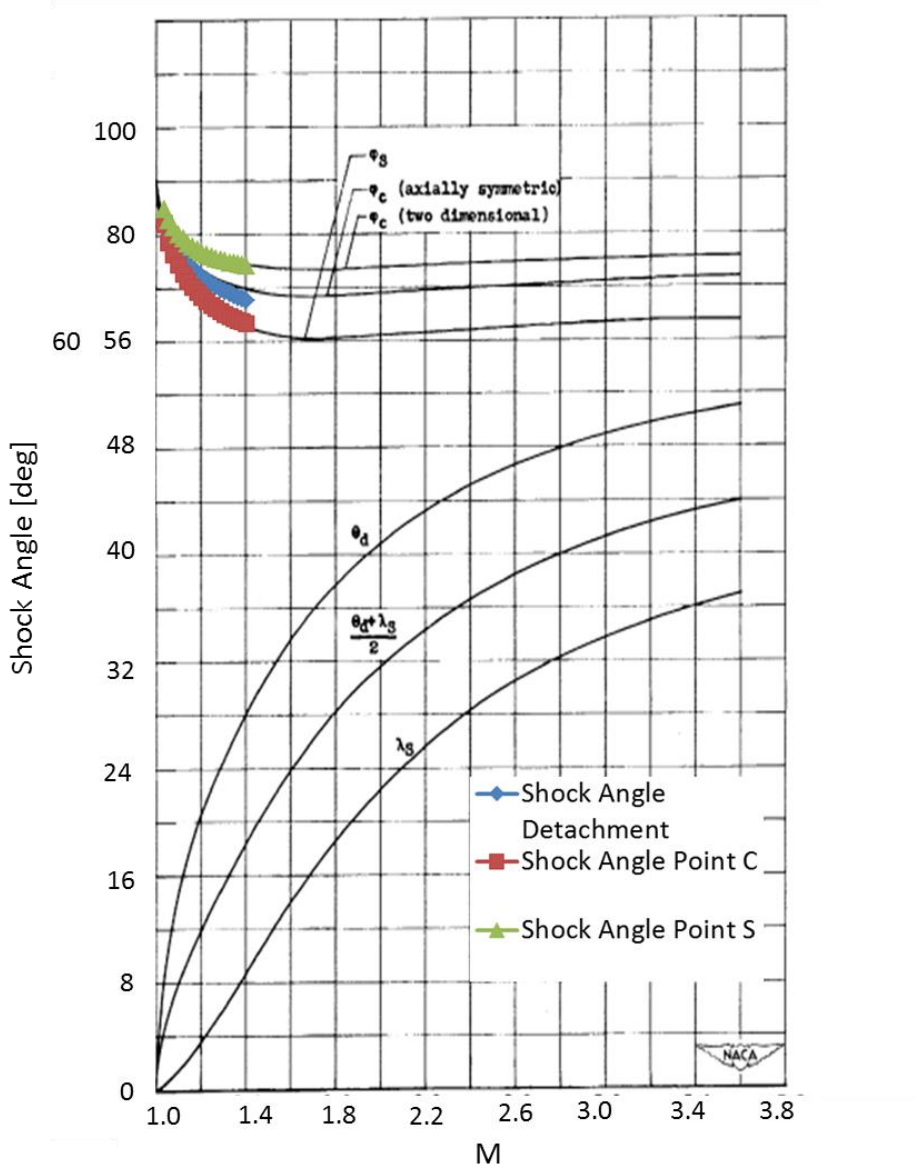

Figure 4.43 Bow-wave angles comparison as a function of the inlet relative Mach number against chart presented by Moeckel [180]**.**

Similarly, the ratio of X'/y_{SB} and y_S/y_{SB} or non-dimensional detachment distance and sonic point height are plotted against M_1' in Figure 4.44. It can be seen that for high Mach numbers, the detachment distance and the height of the sonic point are too small, resulting in close bow waves to the leading edge. As the inlet relative Mach number is decreased, the curves tend to infinity, as the bow wave becomes highly detached. This is confirmed by the 2-D SLC shock structures plot shown in Figure 3.19 and Figure 3.20, where it is evident that as the blade span reduces, the inlet relative Mach number decreases, increasing exponentially the bow-wave extension.

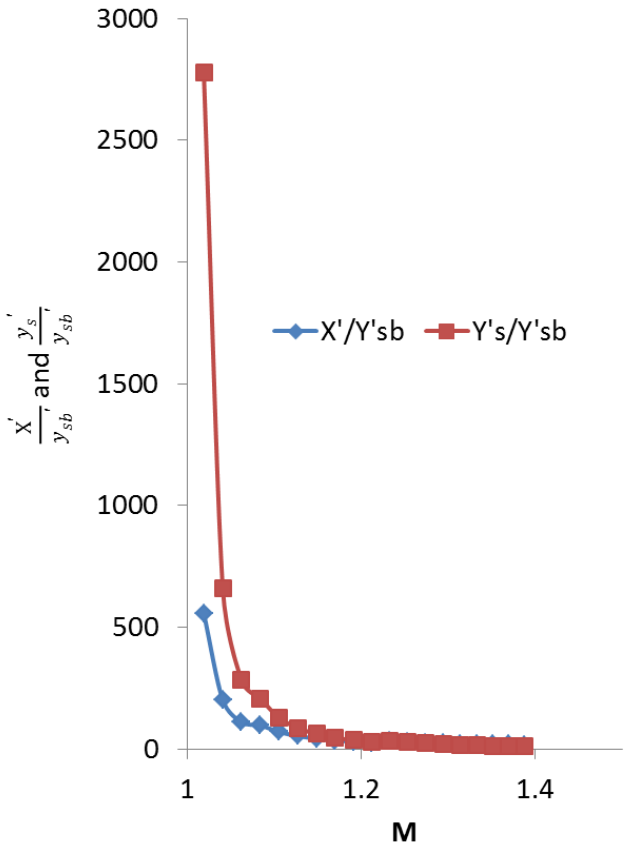

Figure 4.44 2-D SLC bow-wave non-dimensional detachment distance and non-dimensional sonic point height for the NASA Rotor 67.

The comparison of the ratios X'/y_{SB} and y_S/y_{SB} against the chart reported by Moeckel, is presented in Figure 4.45. The y_S/y_{SB} ratio is found to compare fairly reasonable, with a maximum error of 0.35% for the highest Mach numbers. A maximum difference of 1.1% was found for the X'/y_{SB} ratio, however, it is for the two scattered points observed. Apart from this noticeable difference, a maximum difference of 0.62% is found at the highest Mach number.

The local-axial distance L between the sonic point and the bow-wave vertex is typically found as a ratio with respect of the point SB, which is the point that forms the wedge tangency. Figure 4.46 shows the comparison of L/y_{SB} as a function of the inlet Mach number against a corresponding chart obtained by Miller and Hartmann [208]. The L/y_{SB} ratios estimated by the 2-D SLC fall around the curve, with a maximum difference of 1.7% and a minimum of 0.43%.

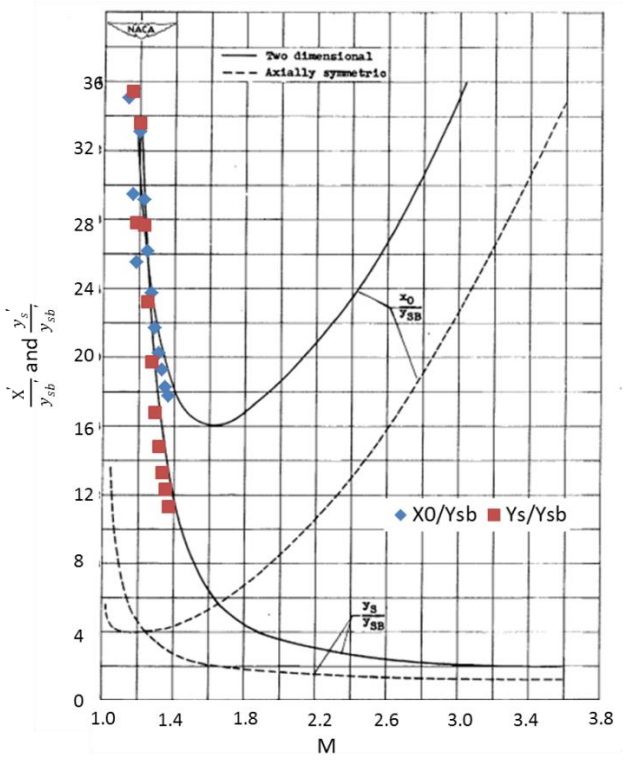

Figure 4.45 Bow-wave non-dimensional detachment distance and non-dimensional sonic point height comparison as a function of the inlet relative Mach number against chart presented by Moeckel [180]**.**

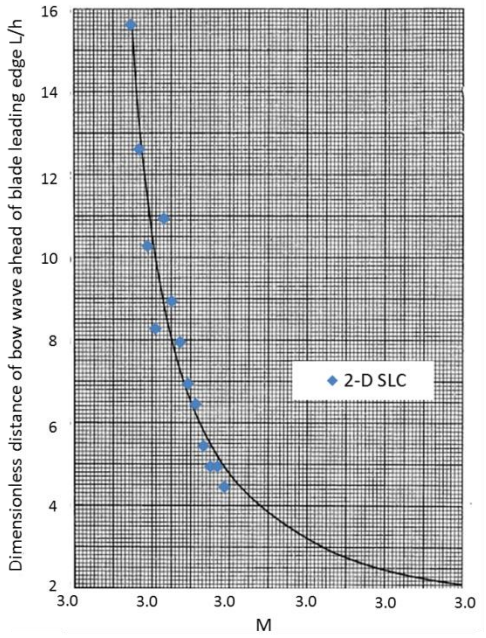

Figure 4.46 Comparison for the bow-wave non-dimensional distance from the wedge tangency point as a function of the inlet relative Mach number against chart presented by Miller and Hartmann [208]**.**

4.6.2 Passage-Shock Configuration

The accurate relative total-pressure recovery across the different waves of the shock system for an adequate shock-loss determination by the current model relies on predicting the appropriate shock configuration. Figure 4.47 compares the shock-configuration structure for different blade heights between a 3-D CFD RANS simulation and the current shock-loss model within the context of a 2-D SLC performance simulation for the NASA Rotor 67 at 100% and near peak-efficiency ($w = 34.03\ kg/s$). On the whole, there is a consistent and satisfactory agreement of shock patterns between 3-D CFD and 2-D SLC simulations for both, detached bow-shock and passage-shock configuration. Even though the detached bow-shock shape was validated in Sec. 4.6.1, its location and detachment distance from the leading edge are confirmed with 3-D CFD as well. Most important for a correct shock-loss coefficient is the prediction of the form and location of the passage shock in any of its forms.

One of the main features of the shock-loss model is its capacity for plotting the overall shock structure itself along with the expansion waves or characteristics from zone V interacting with the passage shock. The expansion processes observed in Figure 4.47 and Figure 4.48 extends the first-captured Mach wave till the impingement point either of the first passage-shock (point k) or the choke-induced passage shock (point q). For each characteristic, the flow information is computed and determined in this way, the properties ahead of the passage shock for the relative total-pressure loss calculation.

For the near peak-efficiency point, between the supersonic-span initiation and 58% of span, the passage-shock structure is single as seen in Figure 4.47 a). Above this height, the second passage-shock appears due to choking, intercepting the first passage-shock for the rest of the top span due to the proximity of the latter to the blade throat, yielding in coalesced passage shocks. The location of the estimated second passage-shock differs from 3D-CFD by approximately 0.9% of the chord, while its angle deviates by 0.4%. This satisfactory agreement yields in a good estimation of the transition point (point t).

Because the relative Mach number increases with the span, the incidence reduces, displacing the second passage shock downstream, and extending the flow expansion to attain highest peak suction-surface Mach numbers. The distribution of the suction-surface relative Mach number in the current shock-loss model deviates from that in the 3D-CFD results of Figure by ~1.3%, having a peak suction surface Mach number of 1.52.

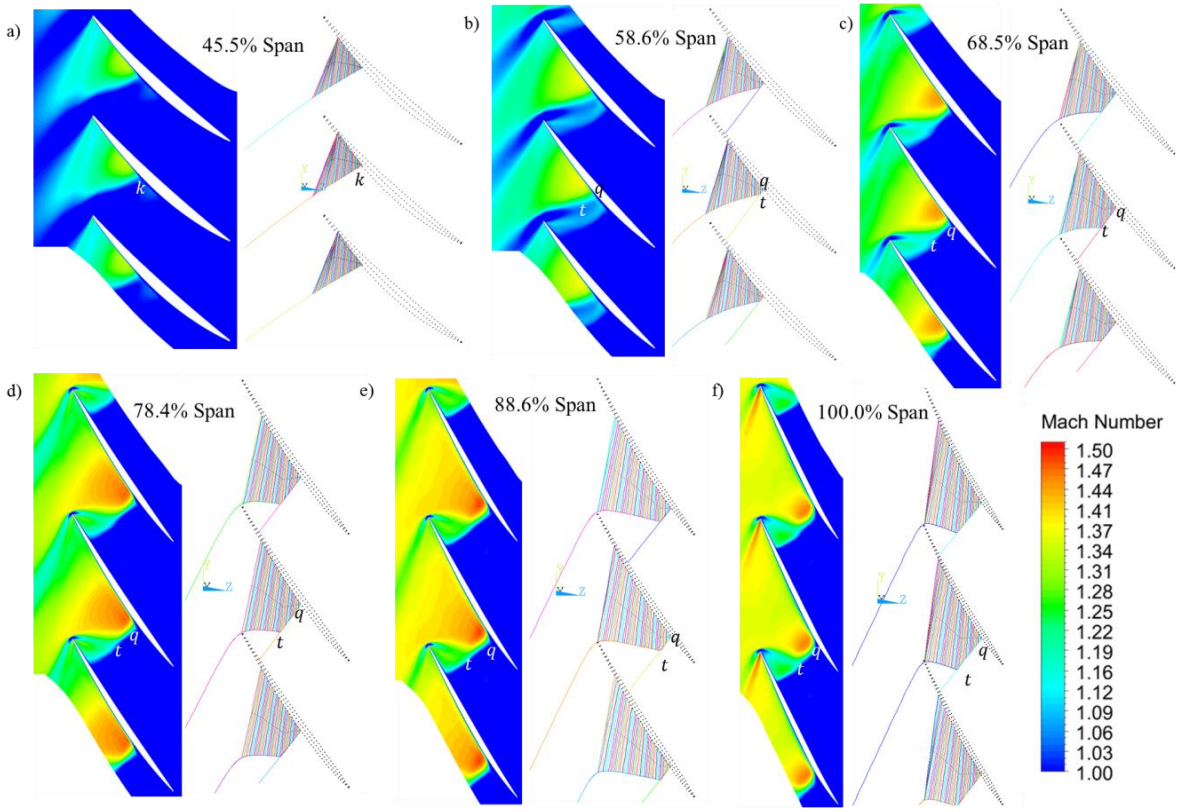

Figure 4.47 Overall shock configuration comparison between 2-D SLC with the current shock model and 3-D CFD RANS simulations for the NASA Rotor 67 [35] at 100% of design speed and near peak-efficiency ($\dot{m} = 34.03 \frac{kg}{s}$). a) 45.5% Span. b) 58.6% Span. c) 68.5% Span. d) 78.4% Span. e) 88.6% Span. f) 100.0% Span.

The current shock-loss model reacts to the off-design conditions in such a manner that it modifies the passage-shock pattern accordingly as seen in Figure 4.48 for near-choking ($w = 34.45\ kg/s$). The prediction of the second passage-shock location is a function of the iterative method incorporated to the overall shock- structure and loss model, and deviating from 3-D CFD by the same amount as in the design operating point. For this high mass flow point, the whole supersonic span is choked without any regions of

single-shock structures. Further mass flow increase will just extend the supersonic span towards the hub. Insomuch as the back static pressure is low, the second passage-shock is pushed downstream making this not to intersect anymore the first passage-shock, in agreement with the 3-D CFD results. However, at the very tip both passage shocks coalesce due to the high obliqueness of that passage-shock segment from the detached bow-shock as seen in Figure 4.48 d).

Similarly, the current prediction of the flow expansion on the suction-surface within zone V has its highest relative Mach number immediately ahead of the first passage-shock with a value of 1.62, deviating from 3-D CFD by 1.2%.

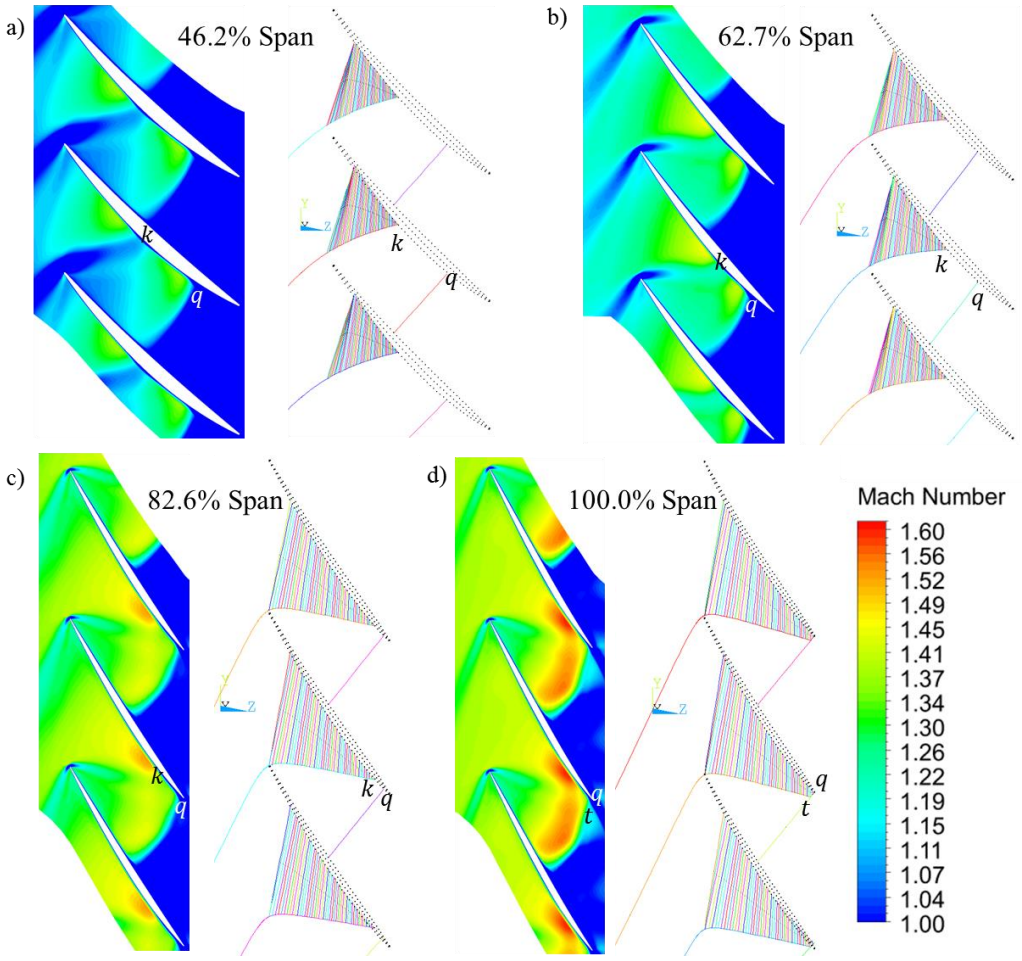

Figure 4.48 Overall shock configuration comparison between 2-D SLC with the current shock model and 3-D CFD RANS simulations for the NASA Rotor 67 [35] at 100% of design speed and near peak-choking ($\dot{m} = 34.45 \frac{kg}{s}$). a) 46.2% Span. b) 65.7% Span. c) 82.6% Span. d) 100.0% Span.

The spanwise evolution of the NASA Rotor 67 shock-system at design point for the relative supersonic span is displayed in Figure 4.49 a), where it can be noticed the crescent extension of the zone-V expansion with radius that leads to higher peak suction-surface Mach numbers towards the tip. Figure 4.49 b) models the resolved 3-D interaction of the shock-system in its totality for the whole 22 passages of the NASA Rotor 67 computed by the current shock- structure and loss model within a 2-D SLC simulation. Note how the incoming flow traverses the series of bow-waves that extend to infinity, which cancel with the expansion waves of zone IV in terms of magnitude to avoid any upstream influence.

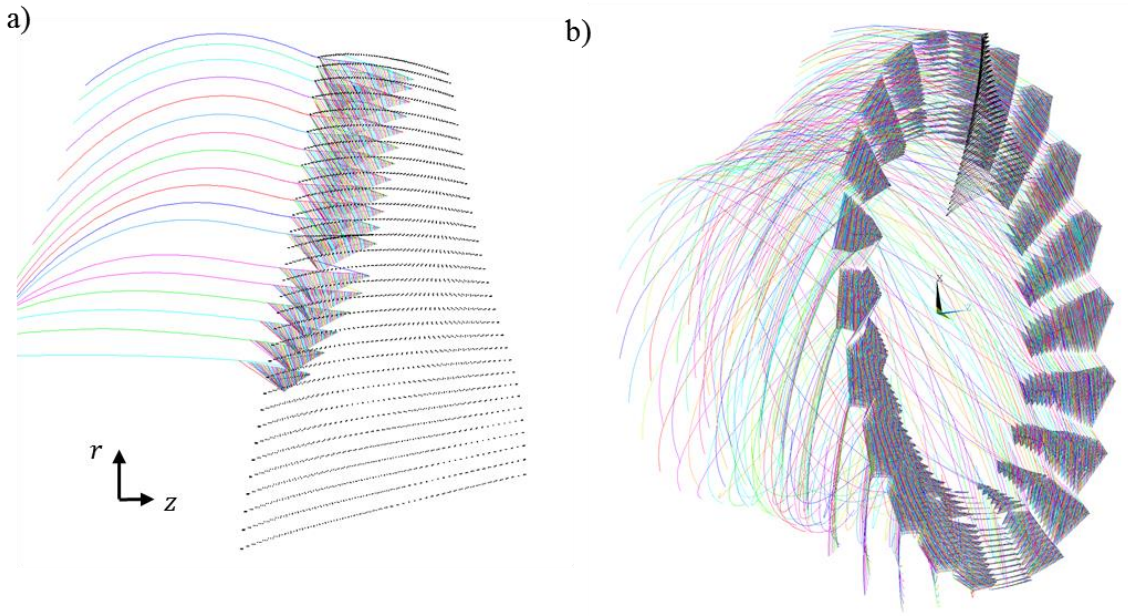

Figure 4.49 Shock-configuration radial evolution determined by the current shock- structure and loss model in the context of a 2-D SLC simulation for the NASA Rotor 67. a) Meridional view. b) 3-D projection view for the entire compressor rotor.

5 RESULTS & DISCUSSION

5.1 3-D CFD NASA Rotor 67 Shock Physics

Results from the 3-D CFD simulation allowed to understand the complex shock-wave-associated phenomena as described in this section. The incidence-induced inlet meridional velocity for a streamline determines the amount of mass flow passing through the blade-element passage corresponding to a specific streamline. For high outlet static pressures, the blade passage is not choked.

As the back static pressure lowers, mass flow increases, and hence, the inlet meridional velocity rises. Because the blade speed remains constant, the inlet relative velocity increases with the meridional velocity, reducing the flow angle, and thus, the incidence. It is precisely the flow direction the parameter that lowers in order to accommodate and allow for more mass flow rate. Due to the incidence change, the Prandtl-Meyer expansion gets affected. At high incidences or low mass flow rates, the convex corner formed between the flow direction and the wall is more pronounced, leading to a more abrupt expansion fan, resulting in a limited suction surface for the flow acceleration as shown in Figure 5.1 a) b). Conversely, at low incidences or high mass flow rates, the suction surface turning is more gradual with respect of the flow direction, obtaining a smoother Prandtl-Meyer expansion fan, thus, a larger suction surface extension for the flow to accelerate, as displayed in Figure 5.1 i) j). The flow acceleration in both cases, high and low incidences, cause a static pressure drop. For the flow to catch up with the outlet static pressure imposed, a strong shock is needed within the passage to raise the pressure to produce the sudden gradient in Figure 5.1. The passage shock evolution from high to low incidence values in Figure 5.1 for the NASA Rotor 67 tip [40] at 100% of design speed, shows how the flow acceleration region extends more over the suction surface as the mass flow is increased. Thereupon, the shock moves upstream or downstream depending on the flow acceleration extension, determined by the incidence-induced expansion fan.

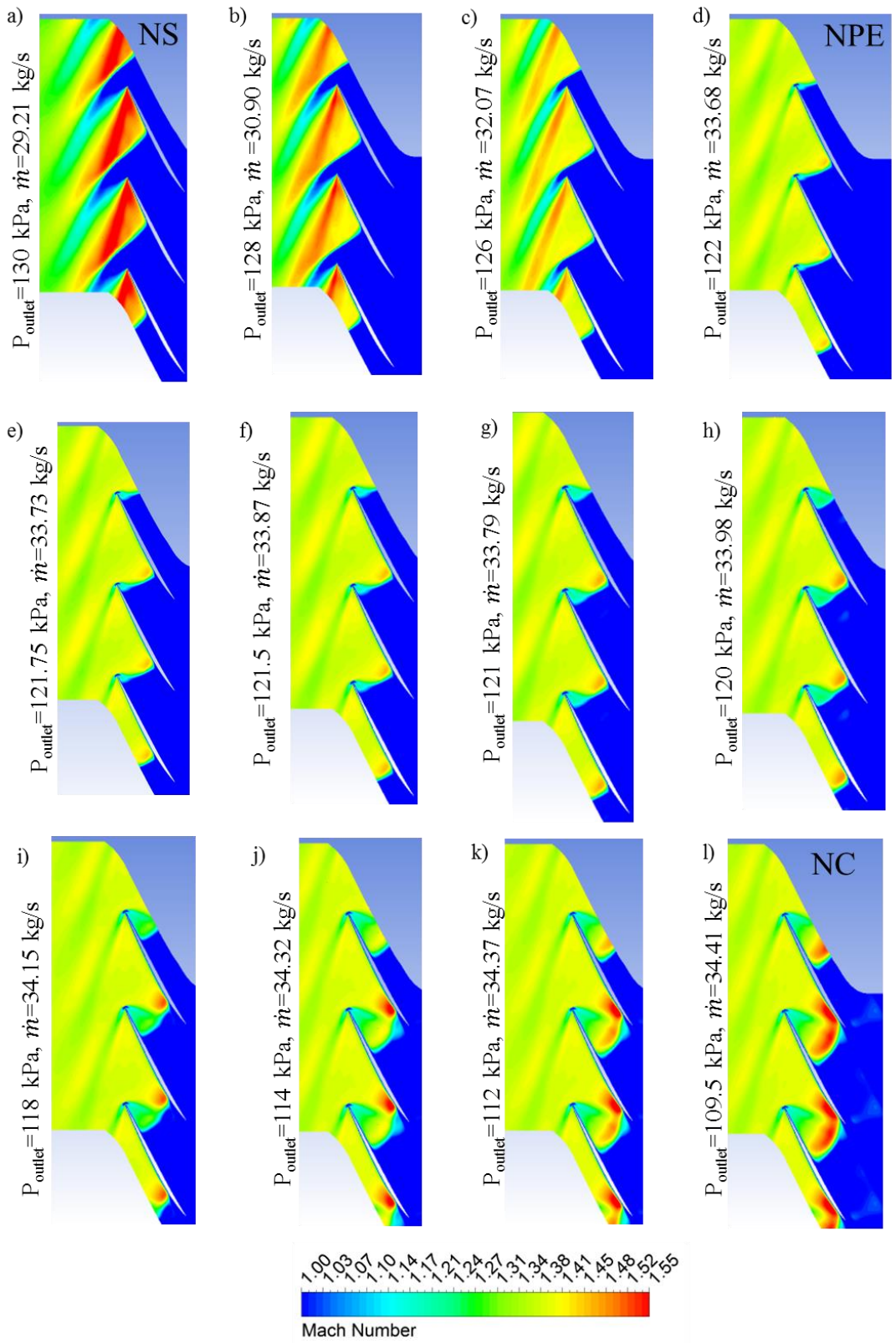

Figure 5.1 3-D CFD NASA Rotor 67 simulation for 100% of design speed at 95% span from hub to tip.

For this reason, when the Prandtl-Meyer expansion is short but abrupt due to a high incidence, the bow shock is almost normal, as a strong shock is required to drop the pressure. As discussed before, for low incidences, the inlet relative Mach number is high, yielding in a highly-oblique bow shock with weak shock-extremity strength. By the time the expansion fan starts to dissipate and encounters the weak bow-shock extremity, its strength is not enough to produce a pressure rise, thus, a normal shock appears. This normal shock fusions with the bow shock at the transition point, to conform together the passage shock. Nevertheless, further outlet static pressure drop corresponding to lower incidences, causes higher flow acceleration, forcing the normal shock to be farther downstream and not intersecting the bow shock as observed from Figure 5.1 d) to l). In fact, the normal shock for these cases extends up to the pressure side of the adjacent blade profile. In fact, this extension is explained as the shock necessitates to be stronger to produce the pressure rise that the highly-oblique shock, even with its strongest central part, cannot provide.

Figure 5.1 k) and l) show the particular duct-flow cases d) and e) explained in Sec. 2.2. The former corresponds for which the shock stands at the passage exit. The later shows overexpanded flow, as the passage length is not enough for the static pressure rise, requiring a complex shock structure at the outlet to gradually decelerate the flow and increase the static pressure.

Farther down from the tip, same flow phenomenon occurs at lower inlet velocities due to lower blade speeds and lower mass flow rates as a result of the blade-throat area reduction with the solidity increase. Figure 5.2 shows the NASA Rotor 67 at 80% span from hub to tip, where the passage shock moves downstream as the mass flow increases. For the lowest back static pressure in Figure 5.2 l), the shock stands at the exit, without overexpansion, inasmuch as the passage shock is strong enough to produce the required pressure.

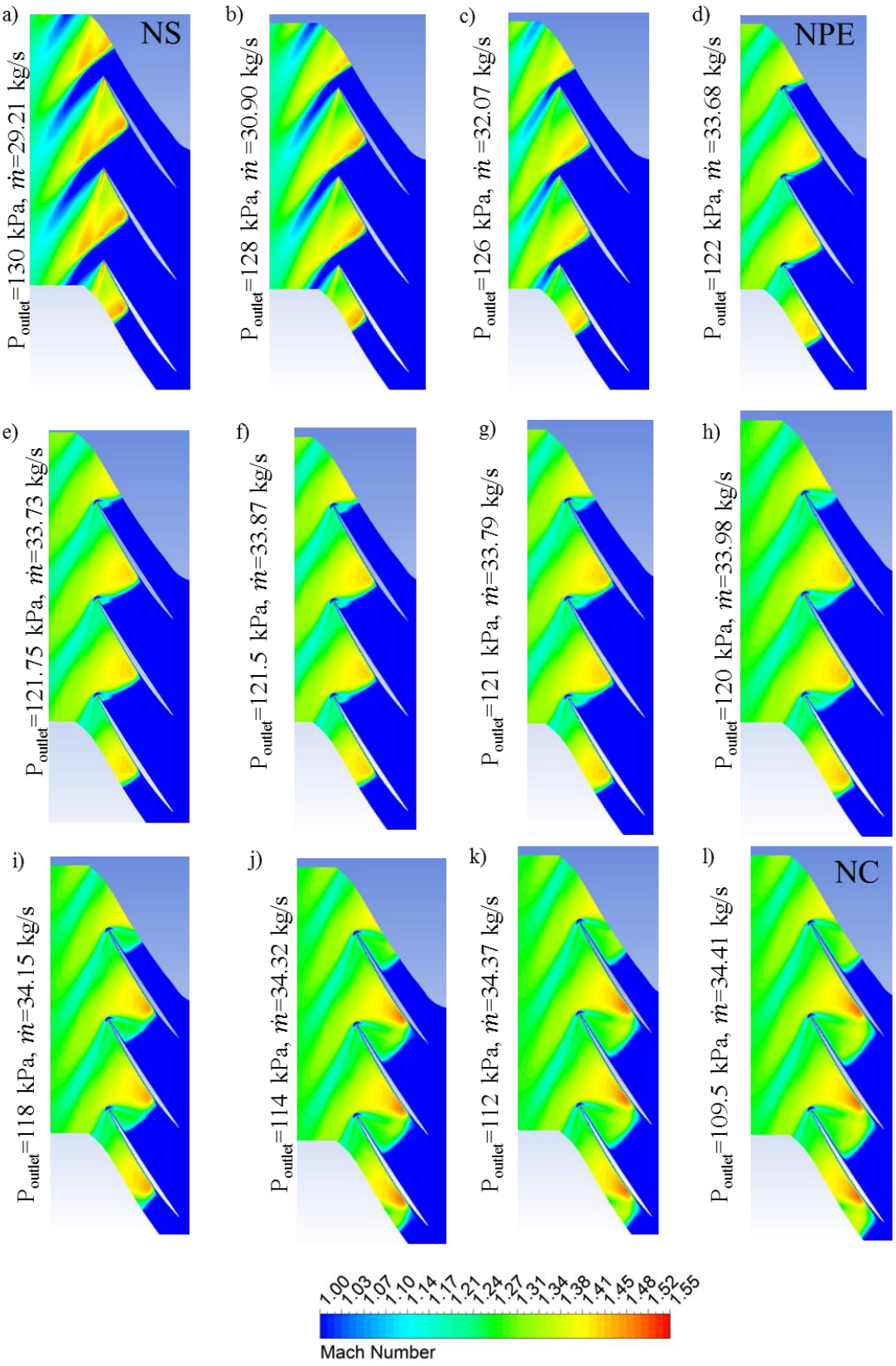

Figure 5.2 CFD NASA Rotor 67 simulation for 100% of design speed at 80% span from hub to tip.

Farther down at 70%, Figure 5.3 displays same behaviour but not as severe as for the higher span locations. Observing the lowest outlet static pressure in Figure 5.3 l), the passage shock never reaches the passage exit, as the flow acceleration imposed by the Prandtl-Meyer expansion is dissipated slightly upstream with a small bow-wave contribution near the suction end-wall.

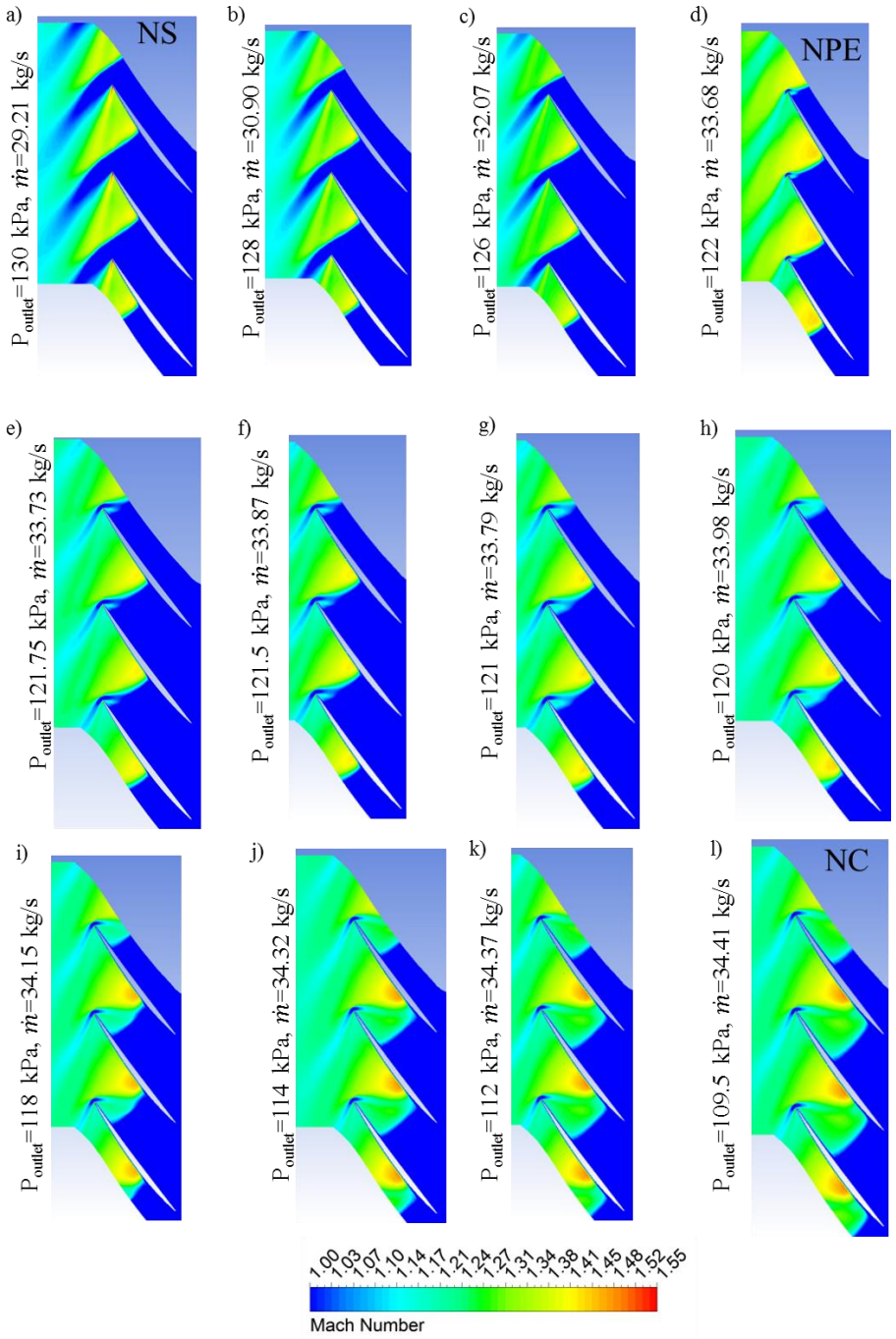

Figure 5.3 CFD NASA Rotor 67 simulation for 100% of design speed at 70% span from hub to tip

5.2 Shock-Loss Parametric Studies

5.2.1 Overview

A parametric study was conducted for the NASA Rotor 67 to assess the 2-D and 3-D geometry variables that impact the shock-wave losses using the 2-D SLC compressor performance with the current shock-loss model developed. Since the bow-shock is a unique function of the inlet relative Mach number, it is the passage-shock configuration and its strength the mechanisms that get affected when the 2-D or 3-D profile geometry are altered. The influence on shock-loss was evaluated at 100% of design speed and near peak-efficiency, in both radial and circumferential direction to raise the understanding.

It is interesting to analyse the difference between modifying the blade-element parameters just in 2-D or performing a 3-D blade-shaping. For this reason, the purpose of this parametric study is to demonstrate design trends between these two design strategies, and to show the applicability of the physics-based shock-loss model in the context of 2-D SLC methods.

5.2.2 Influence of 2-D Blade-Element Parameters

The 2-D parametric study consisted in varying the maximum-thickness location z_{mt}, maximum thickness t_{max} and solidity σ. For convenience, the maximum-thickness location and maximum thickness were normalized with respect of the chord c. Besides the baseline geometry, a lower and a higher variation were introduced for these parameters. Although it is expected no influence on shock losses below the choked span since there are only single passage-shock configurations, the 2-D parameters were varied constant for the entire blade span to guarantee a smooth and continuous spanwise distribution. Except for the case of $\frac{z_{mt}}{c}$% and $\frac{t_{max}}{c}$%, where the blade profile at the root was unaltered inasmuchas as there is no transonic effect, and hence, any 2-D profile modification would contribute to an alteration of the diffusion factor and potentially modifying the full REE. The non-dimensional maximum-thickness location and maximum thickness were reduced and increased in 5% as seen in Figure 5.4 a) and Figure 5.4 b), respectively. The solidity modification was achieved by reducing and

increasing one blade count, from the baseline value of 22, resulting in a solidity reduction and increase of 4.5%, respectively, as shown in Figure 5.4 c).

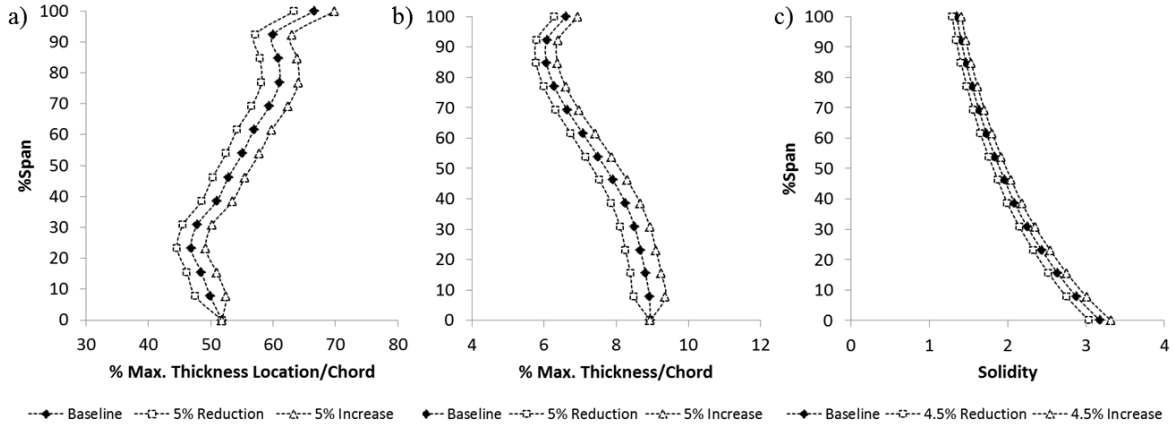

Figure 5.4 2-D blade-element parameter variation for the NASA Rotor 67 [40] **baseline geometry. a) %Maximum-Thickness Location/Chord. b) %Maximum Thickness/Chord. c) Solidity.**

The 2-D blade-element parameters variations yielded to the radial shock-loss coefficient modification in Figure 5.5. As expected, there is no major influence on the shock losses at the supercritical span, since the normal shock wave formed there is just a function inlet relative Mach number and the leading-edge turning. The variation of $\frac{z_{mt}}{c}$% and $\frac{t_{max}}{c}$% did not cause major alteration in shock losses at the unstarted passages since the only existing passage shock is that segment from the detached bow-shock.

At high-span locations, there is a slight modification in the shock-loss coefficient. Displacing the maximum-thickness point upstream and increasing the maximum thickness have the same effect in increasing the passage-shock losses since the suction-surface turning is increased. As a result, the flow-expansion magnitude rises, incrementing the peak suction-surface relative Mach number $M'_{psh_{ss}}$ ahead of the passage shock and leading to higher relative total-pressure losses. The 5% variation of $\frac{z_{mt}}{c}$ reduction and $\frac{t_{max}}{c}$ increase produced a shock-loss coefficient increment of 2.5% and 4.5% at the tip, respectively.

In contrast, the $\frac{z_{mt}}{c}$% increase and $\frac{t_{max}}{c}$% reduction make the blade-elements less susceptible to the passage-shock effects. This is because the expansion of zone V is less

severe, leading to lower suction-surface relative speeds, and hence, a higher relative total-pressure recovery. The improvement in shock-loss coefficient is 1.1% and 2.9% at the tip for a 5% variation of $\frac{z_{mt}}{c}$ increase and $\frac{t_{max}}{c}$ reduction, correspondingly. It can be argued then that the maximum thickness has slightly more impact on the shock losses than its axial location. However, proof of the non-linearity of the physics is that even with the same percentage of variation of any of these parameters, the shock-loss increment is higher than the reduction.

A modification in the thickness parameters results in modest shock loss variations, particularly at the mid-span. Noticeable shock-loss reductions can be obtained by using even lower maximum thicknesses; however, of course, this would significantly compromise the loading and negatively affecting the pressure ratio.

The influence of solidity produces more an offset of the baseline shock-loss radial distribution. Increasing the solidity reduces the shock-loss coefficient even at the unstarted passages. Despite the blade throat decreases with solidity and stimulating choking, the pitch shortening causes the passage-shock segment from the detached bow-shock to intersect faster the suction surface, leading to unmerged passage-shocks if the passage is choked. This shock-pattern acts more as a gradual compression so that the choked-induced shock process becomes less dramatic. Increasing the solidity in 4.5% brings an improvement in shock-loss coefficient of ~4.2% for the entire supersonic span and not only at the tip as the thickness parameters.

Conversely, the solidity reduction makes the detached bow-shock to penetrate more into the passage, intersecting the choked-induced shock very upstream in the passage, leading to a coalesced passage-shock where the majority is a straight shock. As a consequence, a stronger passage-shock is formed, leading to higher relative total-pressure losses. This is evidenced in the parametric study, where the 4.5% of solidity increases raises the shock-loss coefficient by 7.7% throughout the supersonic span.

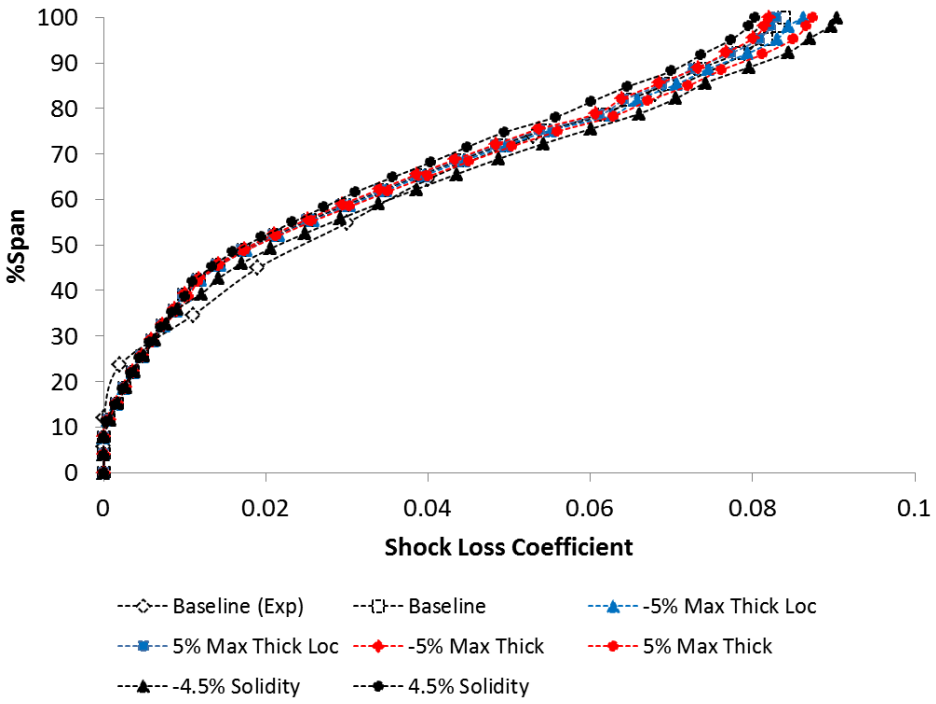

Figure 5.5 Influence of 2-D blade-element parameters in the shock-loss coefficient radial distribution.

5.2.3 Influence of 3-D Blade-Element Parameters

The 3-D blade-element parameters varied for the parametric study were the sweep λ and lean η angles. Similar to the 2-D parametric study, a lower and a higher modification to the baseline variables was introduced. The sweep and lean angle variation was constant for all the blade profiles, except for that at the hub, which remains fix as it sets the stacking-axis reference for the upward sections to be swept and leaned. Even though modern transonic fans are designed with a compound or S-shaped sweep and lean, this study assumes a constant radial distribution of the angles with the only purpose of identifying design trends. The sweep angle was reduced and increased in 5^{o}, where a positive value indicates a backward sweep in the direction of the flow as seen in Figure 5.6. The lean angle was reduced and increased in 1.5^{o}, being positive in the direction of rotation as observed in Figure 5.7.

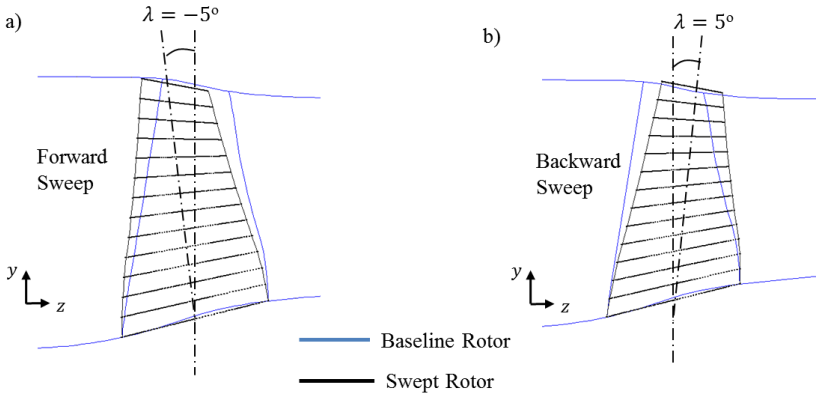

Figure 5.6 Sweep angle variation for the NASA Rotor 67 parametric study. a) Forward sweep. b) Backward sweep.

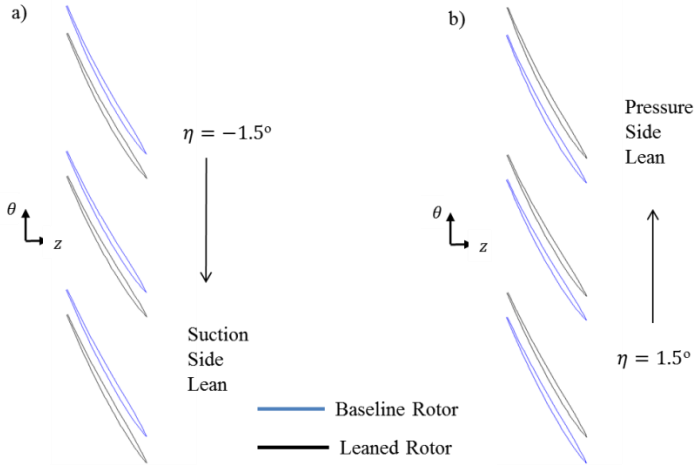

Figure 5.7 Lean angle variation for the NASA Rotor 67 parametric study. a) Suction side lean. b) Pressure side lean.

The sweep and lean angle variations resulted in the shock-loss coefficient radial distributions plotted in Figure 5.8. Similar to the 2-D parametric study, the major influence of the 3-D parameters is at the high-span profiles. Besides the higher velocities and more expected impact at the top, since the sweep and lean angles are varied constant along the span, the geometry variation decreases towards the bottom resulting every time in less influence. Thereupon, the tip sections are where a noticeable effect is observed. The lean angle variation showed little variations in shock-loss coefficient less than 1%, however, there is an appreciable trend at the tip.

A forward sweep and a suction-side lean, namely when their values are reduced, have the same effect of increasing the shock losses. The forward sweep and suction-side lean

produced a shock-loss coefficient increase of 3.9% and 0.8% at the tip, respectively. On the other hand, a backward sweep and a pressure-side lean reduce the shock losses at the tip by 3.8% and 0.5%. Similar to the non-linearity remarked in the 2-D parametric study, the same angle variation either for sweep or lean, generates a slightly higher detrimental than the improvement in relative total-pressure recovery.

Because none of the 2-D blade-element parameters are modified but translated in the space, the passage-shock shape was conserved for all the blade sections, confirmed by the shock-structure resolved by the current shock-loss model. The shock-loss difference instead is the consequence of a shift of the overall shock-configuration due to the sweep or lean. This translation causes the passage shock to see a different peak suction-surface relative Mach number $M'_{psh_{ss}}$ ahead, resulting in a different relative total-pressure loss at an unchanged passage-shock pattern.

Figure 5.8 also shows that if a higher shock-loss improvement is desired, greater variations in sweep and lean angle at the tip and mid –span might need to be introduced to produce a significant change. At the blade bottom and subsonic supercritical regions, sweep and lean might not be required, however, they should be introduced to shape a continuous curvature (see Appendix A).

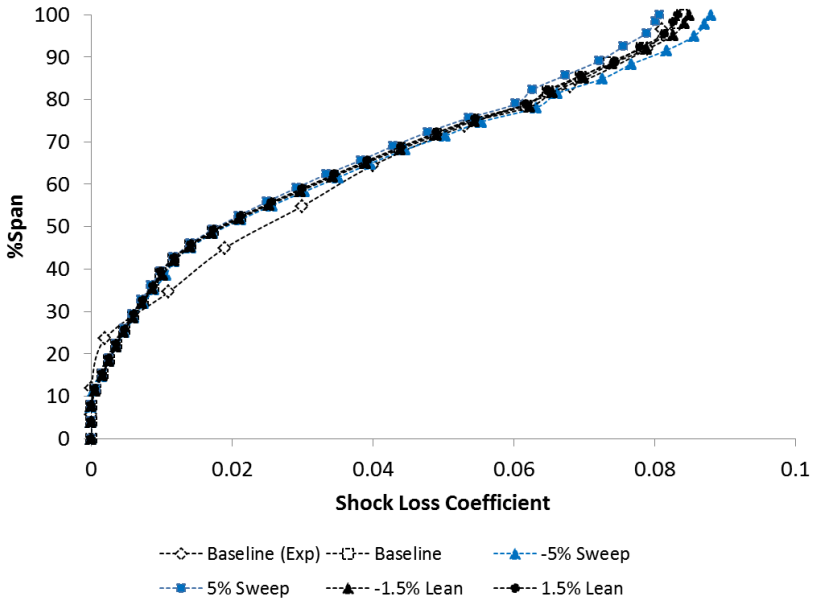

Figure 5.8 Influence of 3-D blade-element parameters in the shock-loss coefficient radial distribution.

5.2.4 Influence on Relative Total-Pressure Loss

The relative total-pressure recovery across the passage determined with Eq. 3.3.102 was examined at the blade tip to obtain further information on the modification of the passage shock structure and strength. Forasmuch as detached bow-wave, and hence its passage-shock segment are not modified with the 2-D and 3-D blade element parameters, the relative total-pressure loss in Figure 5.9 and Figure 5.10 is only plotted for that straight portion of the passage shock. Observe that the relative total-pressure loss $\mathrm{PR}'_{n_{psh}}$ is higher in the suction-surface vicinity as expected since the peak relative Mach number $M'_{psh_{ss}}$ of the passage shock is located there as a result of the expansion process of zone V. All the pitchwise distributions agree with the findings in Figure 5.5 and Figure 5.8 in that there is a decrease in shock-loss coefficient when there is an improvement in the relative total-pressure recovery, and vice versa.

In terms of the 2-D blade-element parameters variation of Figure 5.9, the thickness-parameters modification do not produce a significant change near the pressure side since the maximum-thickness location and maximum thickness affect mainly the suction surface. Henceforth, the flow expansion of zone V gets modified due to a different turning, leading to different $M'_{psh_{ss}}$ that produce other values for $\mathrm{PR}'_{n_{psh}}$. A maximum-thickness location increase and reduction of 5%, results in a 0.3% increment and a 0.22% decrease of PR'_{psh} at the suction surface, respectively. The same percentage variation in maximum thickness, either for increase or reduction, modifies by 0.4% the PR'_{psh} at the suction surface.

In the case of the solidity, there is an offset of the relative total-pressure loss, meaning that even $\mathrm{PR}'_{n_{psh}}$ is improved at the pressure side when the spacing is reduced, apart from that larger enhancement at the suction surface. In fact, there is a reduction of 2.0% in the pitchwise extension of the straight passage-shock, proving that the coalescence between both shocks occurs more downstream along the passage. Thereon, 4.5% of solidity increase leads to have a 2.0% more of the detached bow-shock as a passage shock, sufficing to have a mass-averaged relative total-pressure loss reduction of 0.9%. Alternatively, if solidity is reduced by the same percentage, the straight shock enlarges

1.7% due to the early interception of this with the first passage-shock and increasing the mass-averaged relative total-pressure loss in 0.8%.

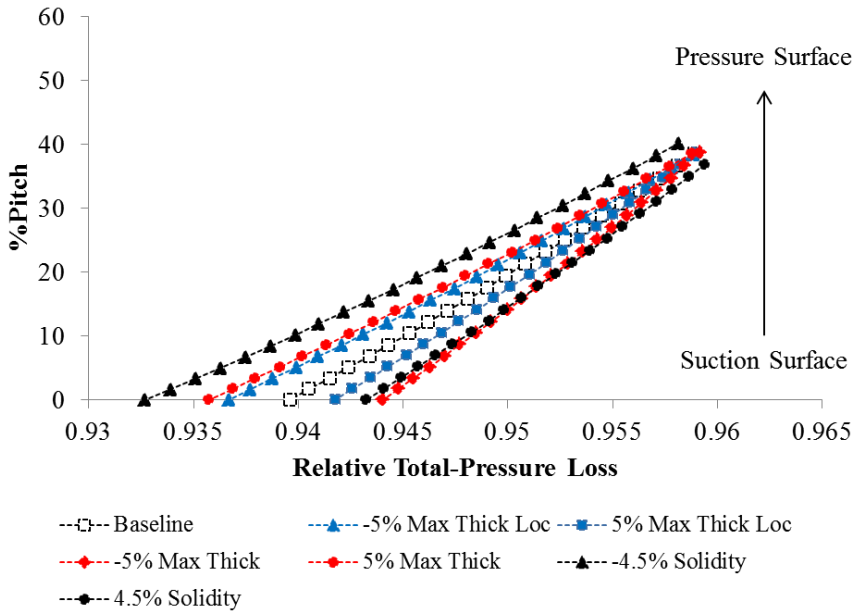

Figure 5.9 Pitchwise distribution of relative total-pressure along the passage shock for the 2-D blade-element parameters variation.

With respect of the 3-D blade-element parameters in Figure 5.10, the $PR'_{n_{psh}}$ distribution along the pitch for that portion of the choking-induced shock is shifted with a tendency of keeping the same rate-of-change. Unlike the 2-D blade-element parameters, where the $PR'_{n_{psh}}$ improvements are minimal at the pressure surface and growing towards the suction surface, the $PR'_{n_{psh}}$improvement for the 3-D blade-element parameters remains almost constant throughout the pitch. This is a proof that the overall shock-structure remains with the same shape as in the baseline geometry, and any change in sweep or lean just shifts the structure axially or tangentially, respectively.

Variations in $PR'_{n_{psh}}$ induced by the lean are small due to the small angle modification, but still a tendency can be deduced. Backward sweep and a pressure-side lean induce an interception of the shock system with lower relative Mach numbers and reducing the shock strength. The variations of 5^o and 1.5^o introduced for sweep and lean, decrease the relative total-pressure throughout the passage shock in 1.2% and 1.0%, respectively,

yielding to the improvement in shock-losses. The same percentage variations in forward sweep and suction-side lean displace the entire shock-system to intercept a higher relative Mach number distribution, producing a variation of relative total-pressure loss of 1.1%, almost constant throughout the passage shock.

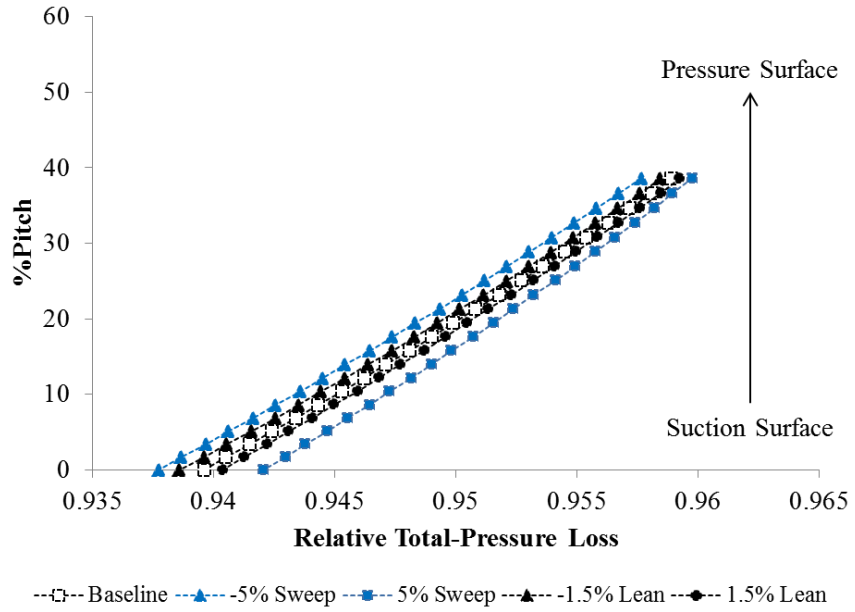

Figure 5.10 Pitchwise distribution of relative total-pressure along the passage shock for the 3-D blade-element parameters variation.

5.2.5 Influence on Isentropic Efficiency

The 2-D blade-element parameter variations induce a different diffusion, modifying the loading and profile loss, and eventually the overall pressure ratio and isentropic efficiency. For this reason, it is unfair to compare the performance characteristics between the baseline and the modified models if the influence of shock losses is to be addressed.

In contrast, a variation of sweep and lean maintains the 2-D blade-profile shapes without significantly modifying the diffusion, profile loss and loading. This guarantees to keep the same pressure ratio while obtaining a modification in the isentropic efficiency due to shock losses only.

Figure 5.11 shows the change in the isentropic efficiency with the variations of sweep and lean at design point, where the overall pressure ratio remained essentially

unchanged with variations within 0.08% due to the numerical solution of the full REE in 2-D SLC. Note that there is consistency between the shock-loss coefficient modification and its impact on the isentropic efficiency. Forward sweep and suction-side lean produce efficiency reduction of 0.2% with respect of the baseline rotor; whereas a backward sweep and pressure-side lean improve the isentropic efficiency by 0.2% and 0.1%, respectively.

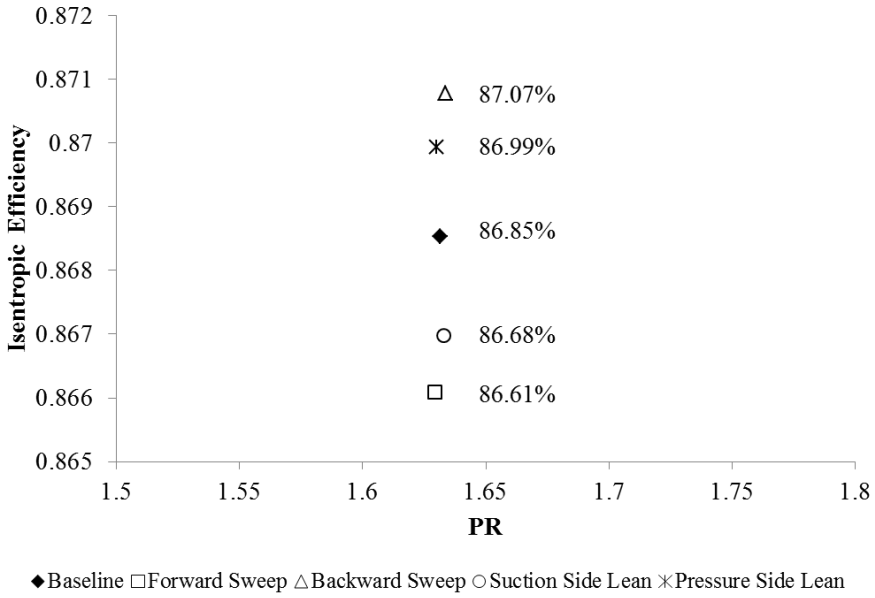

Figure 5.11 Influence of sweep and lean variations on the overall isentropic efficiency.

5.3 Choking Prediction and Mass flow limitation

The choking prediction model implemented in the 2-D SLC model, obtains a choking incidence for each blade-span streamline section, indicating the minimum value for the inlet relative flow angle at a given inlet Mach number. If the current-flow incidence is less than the choking incidence, a mass flow redistribution is required. Figure 5.12 shows the current-flow and choking incidence values for the well-known NASA Rotor 67 [40], from an off-design point of low outlet static pressure towards peak efficiency. Figure 5.12 a) shows that the current-flow incidence is lower than the choking incidence limit at high-span locations. When this is the case, choke condition can be established for those streamtubes. As the back static pressure is increased, the blade span starts to unchoke until the off-design case observed in Figure 5.12 h), where the tip streamline is slightly above the choke limit.

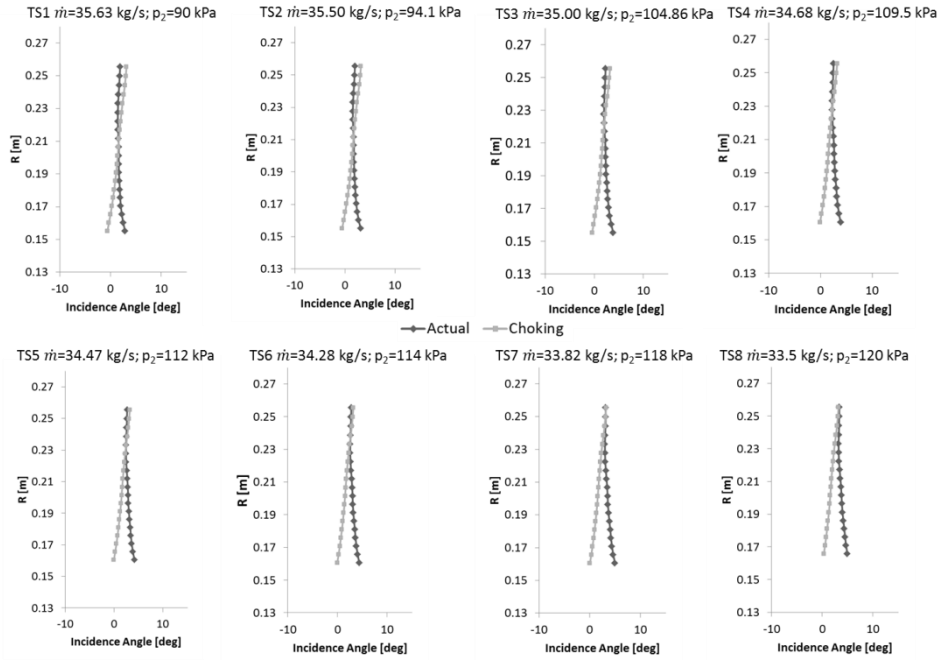

Figure 5.12 Current-flow and choking incidence angles from choking to peak efficiency for the NASA Rotor 67 2-D SLC simulation.

Figure 5.13 displays off-design points from peak efficiency towards stall. As the current-flow incidence is always higher than the choking incidence, the whole blade span remains unchoked.

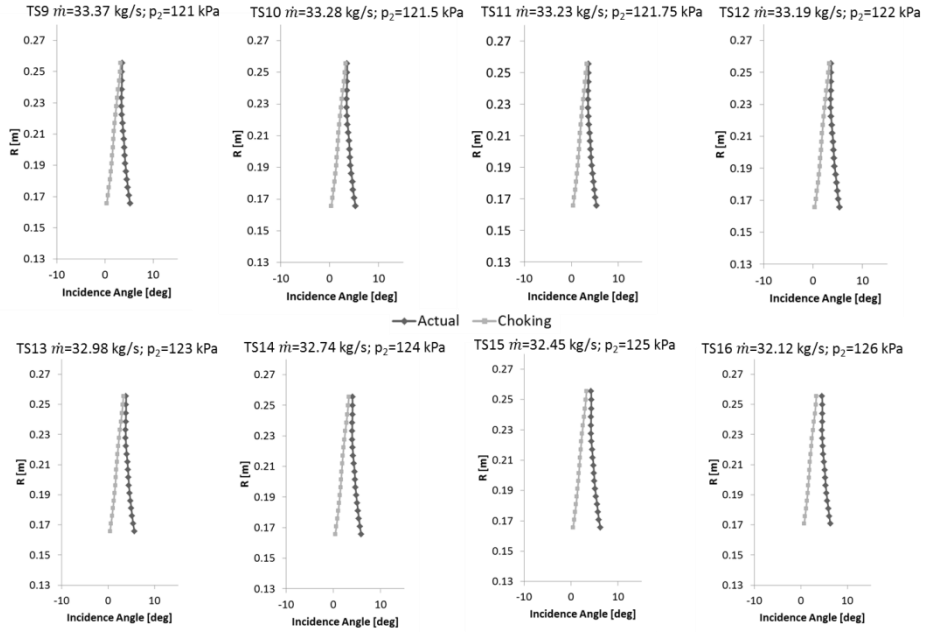

Figure 5.13 Current-flow and choking incidence angles from peak efficiency to stall efficiency for the NASA Rotor 67 2-D SLC simulation.

This is confirmed by examining the inlet flow angle in Figure 5.14. In choke conditions, the inlet flow angle is less than the inlet choking angle as observed in Figure 5.14 a), where almost half of the blade span is choked. Further outlet static pressure increase, decreases the mass flow, reducing the meridional velocity, and hence, increasing the inlet flow angle. Figure 5.14 h) shows the off-design point, where the inlet flow angle is just higher than the choking flow angle. Figure 5.15 shows the cases from near peak efficiency to stall, where the whole blade span remains unchoked due to a low inlet mass flow.

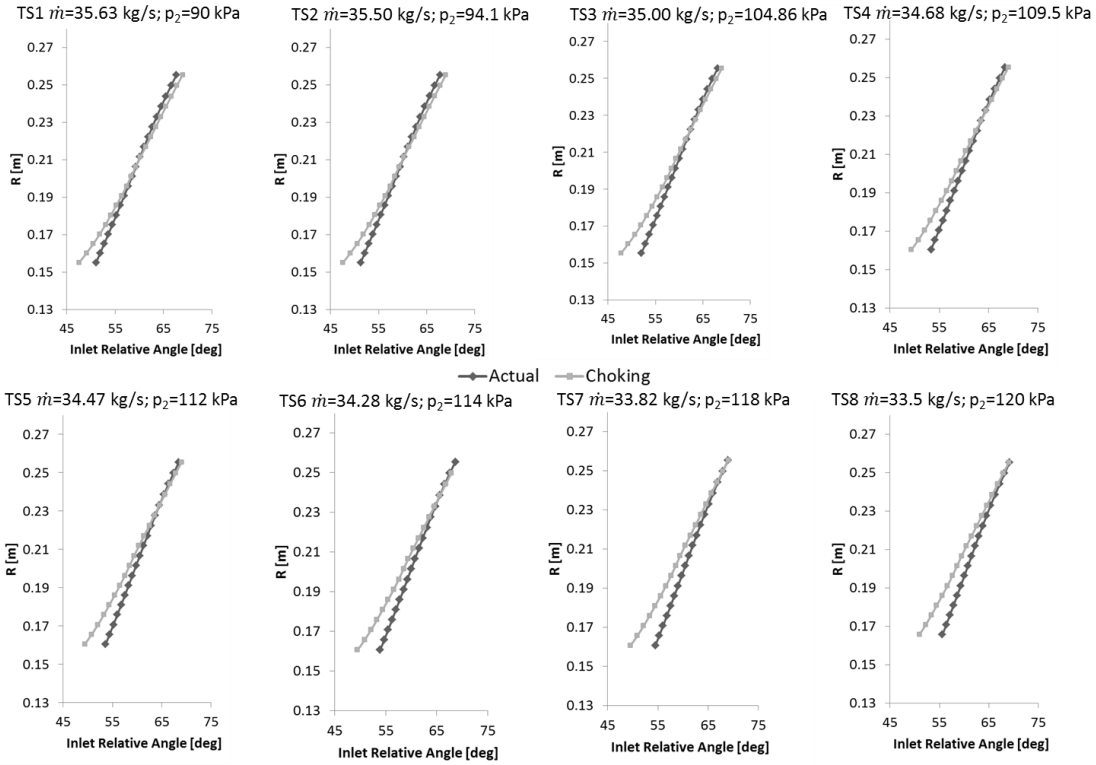

Figure 5.14 Current-flow and choking inlet flow angles from choking to peak efficiency for the NASA Rotor 67 2-D SLC simulation.

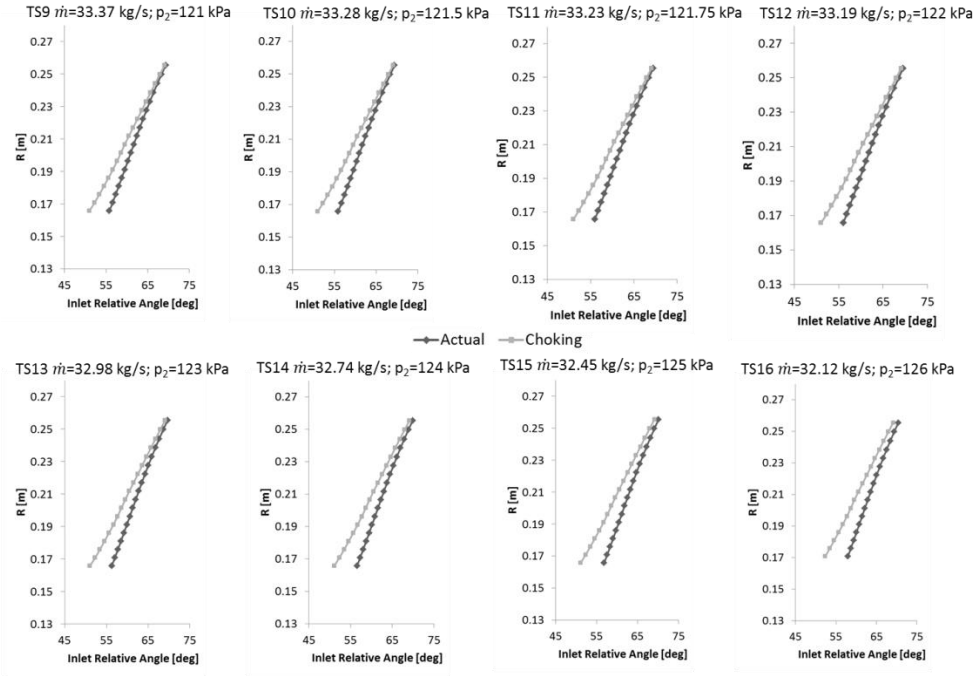

Figure 5.15 Current-flow and choking inlet flow angles from peak efficiency to stall for the NASA Rotor 67 2-D SLC simulation.

The evolution of the incidence angle with respect to the outlet static pressure is displayed in Figure 5.16, which demonstrates that the choking (or unchoking) process is gradual. Likewise, Figure 5.17 shows the progressive choking development in terms of the inlet flow angle.

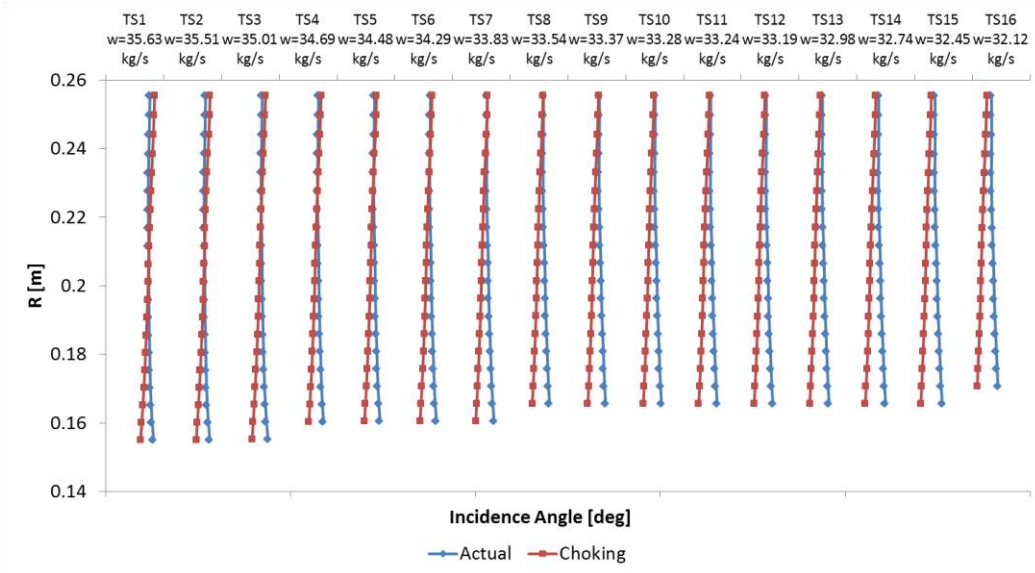

Figure 5.16 2-D SLC-estimated incidence and choking incidence evolution for the NASA Rotor 67 speedline at 100% NRT.

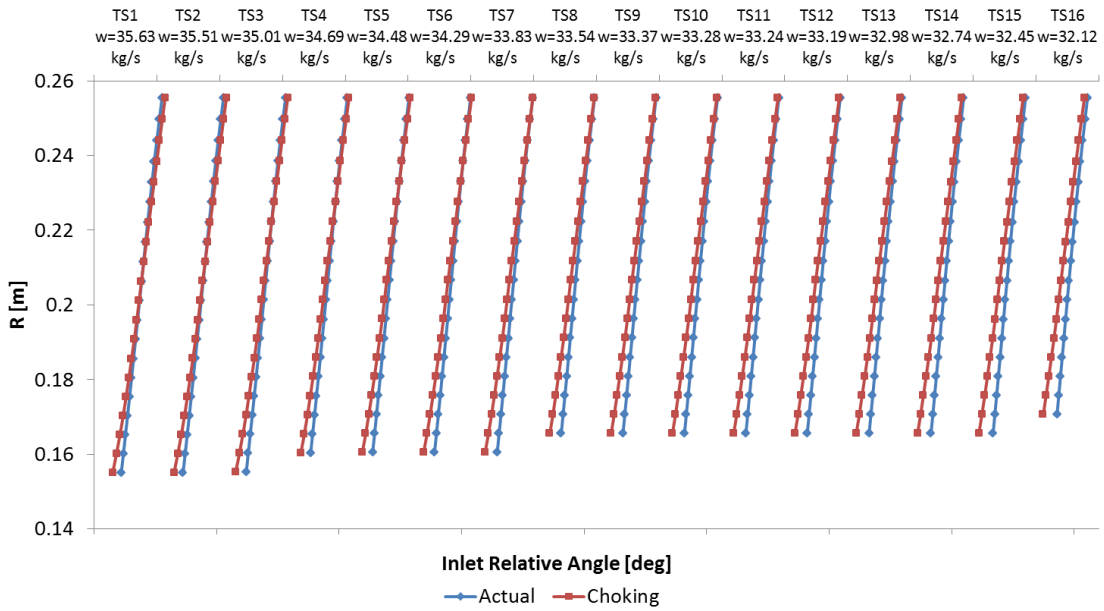

Figure 5.17 2-D SLC-estimated inlet flow angle and inlet choking flow angle evolution for the NASA Rotor 67 speedline at 100% NRT.

By compiling the incidence radial distributions from Figure 5.16 into Figure 5.18, it is noted that the choking incidence limit does not significantly change across the off-design points, as is more a function of the blade throat area and the inlet relative Mach number. Conversely, the current incidence grows faster than the choking incidence with the outlet static pressure. It is evident that the incidences that are on the LHS of the choking curve need to be limited to adopt the choking incidence value. Similarly, the compilation of inlet flow angle radial distributions from Figure 5.17 into Figure 5.19 results in an almost constant value for the inlet relative flow angle, whilst the inlet relative flow angle is permitted to go below the inlet relative choking flow angle.

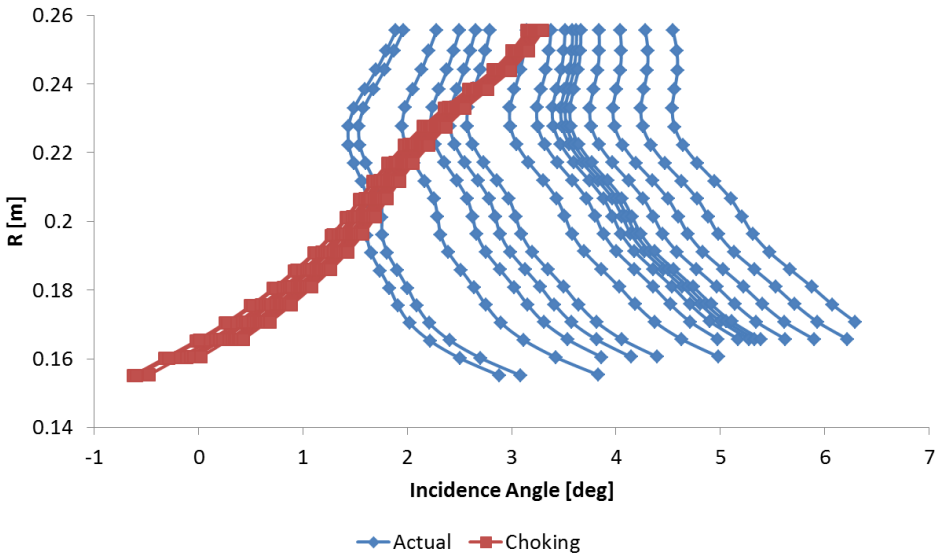

Figure 5.18 2-D SLC-estimated incidence and choking incidence for the NASA Rotor 67.

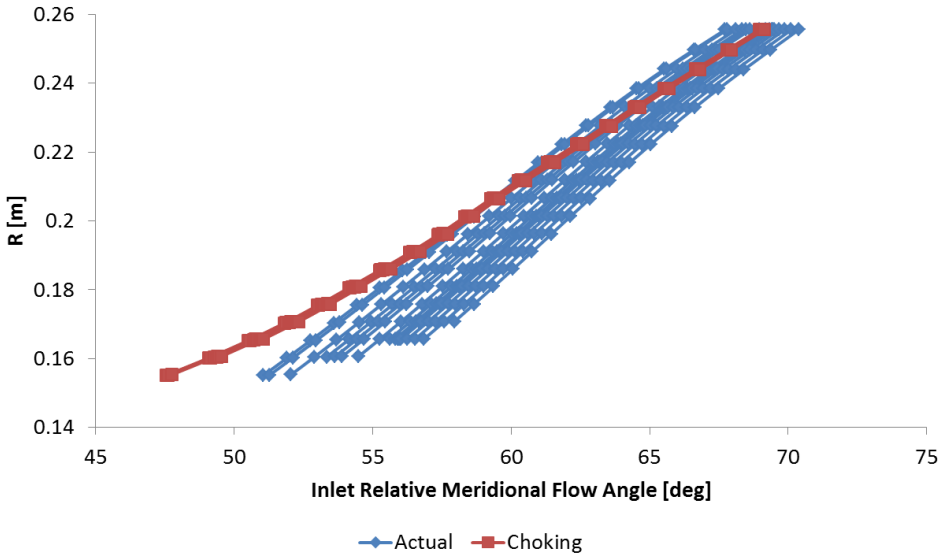

Figure 5.19 2-D SLC-estimated inlet flow angle and inlet choking flow angle for the NASA Rotor 67.

The mass flow redistribution model led to the results shown in Figure 5.20, where the inlet flow angle that was previously exceeding the choking limit is now limited by the choking flow angle. Observe that at high mass flow rates, more blade span is choked due to the high meridional velocities, coinciding within a tolerance with the choking flow angle. Nevertheless, as the extra mass flow is retired from the tip locations, the hub allocates that extra mass flow by reducing its incidence angle. Therefore, the inlet

flow angle at the hub its expected to be closer to the choking limit than without any restriction model.

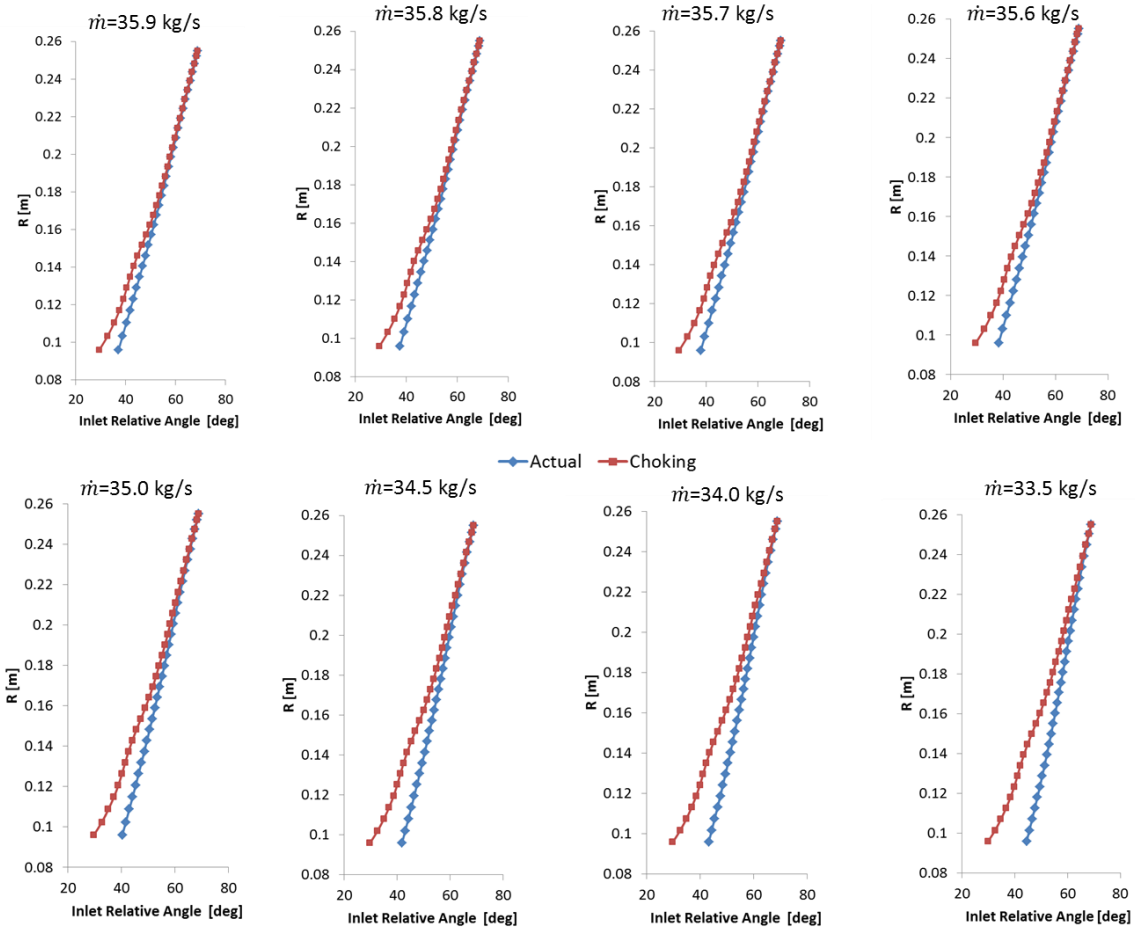

Figure 5.20 Inlet flow angle correction for choke conditions through a mass flow redistribution.

In terms of the choking margin λ, Figure 5.21 sketches the evolution of the choking index from stall to choking conditions. As the mass flow is limited at those choked streamtubes, the choking margin is expected to be unity within the tolerance set of 0.1%. It is clear that at the hub, the choking margin is still far from the choking limit, however, any outlet static pressure deficit will bring the choking margin closer to unity. Additionally, it is seen that the inlet flow angle is never lower than the choking flow angle, causing a coalescence at the tip of the flow angles which are stopped to be the choking flow angle due to a choking margin-based mass flow redistribution.

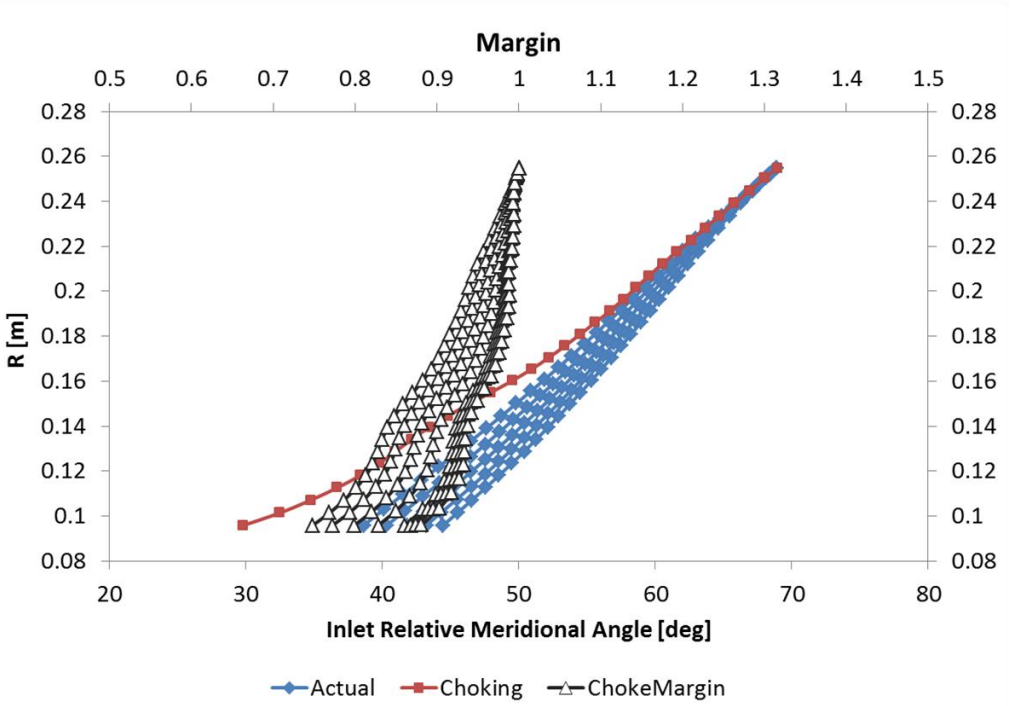

Figure 5.21 Radial distribution of the inlet relative flow angle and choking margin compared to the limiting values of choking.

5.4 Single-Objective Variable-Pitch Fan Optimisation

5.4.1 Variable-Pitch Fan Dynamics

High-bypass-ratio turbofans are more efficient than conventional turbojets at the expense of high noise production due to the fan-compressed bypass flow. The recent demand for noise reduction in long-, but mainly in short-haul aircrafts, with under-the-wing engine installation has imposed to have low-pressure-ratio fans [259]. One of the earliest programs to investigate the variable-pitch-fan aerodynamics research was the NASA Quiet Clean Short-Haul Experimental Engine (QCSEE) [260]. It was demonstrated that the use of a variable-pitch fan instead of a fixed-pitch fan controls the pressure ratio and even offers the potential of reverse thrust by means of rapid response. Blade-pitch-induced reverse thrust replaces the conventional thrust reversers, reducing weight, maintenance, and improving reverse-flow response time. From the baseline forward-thrust blade position, the blade passes through a transient state to arrive to the steady-state reversed aerodynamics.

The blade can be rotated in both directions: through-flat-pitch, resulting in zero lift, or through-feather-pitch, generating flow separation and stall. In the case the blade is turned through-flat-pitch, the chord becomes perpendicular to the axial axis, requiring the solidity to be less than unity along the entire blade span to avoid clashing. This represents a constraint for the blade design. In contrast, solidity can be greater than one when the blade is turned through feather as the chord never reaches perpendicularity with respect of the engine axis, permitting more flexibility for the blade design [259]. At through-flat-pitch configuration, there is a moment when the blade inlet angle is equal to the inlet relative flow angle, resulting in no reverse thrust. This can be corrected in the through-feather-pitch setting. Nonetheless, in the latter, flow separates during the transition and reattaches for reverse thrust. As the angle increases toward through-feather-pitch, the aerodynamic loads increase on the blade, generating more torque, hence more thrust. Due to the energy used for thrust increment, the rotational speed reduces. Further pitch angle increase eventually stalls the blade, dropping the thrust zero and increasing the fan rotor speed [259]. At stalled blade, the flow is mainly tangential with a tendency of rotating with the fan. Whereas in reverse thrust, the blade is unstalled, generating axial flow primarily.

5.4.2 Variable-Pitch Fan Design

As part of the variable-pitch fan (VPF) design program for the Rolls-Royce UTC, the NASA ADP fan model [252] was leveraged as reference to re-design a new geometry. The baseline 2-D SLC NASA ADP fan model was scaled up 3.9 times to meet the original equipment manufacturer (OEM) requirement of a fan diameter equals to 2.735 m. to satisfy under-the-wing installation purposes. The 2-D SLC model scaling was carried out from a nominal NASA ADP fan diameter of 0.2794 m as shown in Figure 5.22.

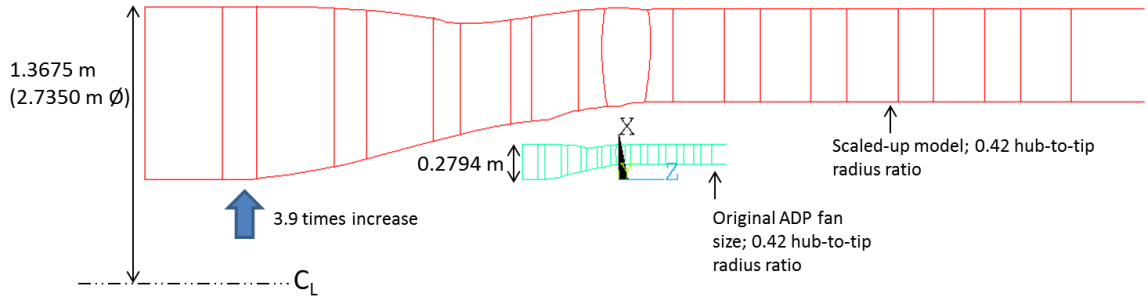

Figure 5.22 Scaling for the NASA ADP fan 2-D SLC geometry to a fan diameter of 2.735 m for the variable-pitch fan.

Therewithal, the hub-to-tip fan radius was decreased from a nominal value of 0.42 to a value of 0.3 to meet the OEM requirement for structural integrity, as depicted in Figure 5.23. The fan blade-element geometry was scaled proportionally to keep the same ratio of 2-D profile parameters.

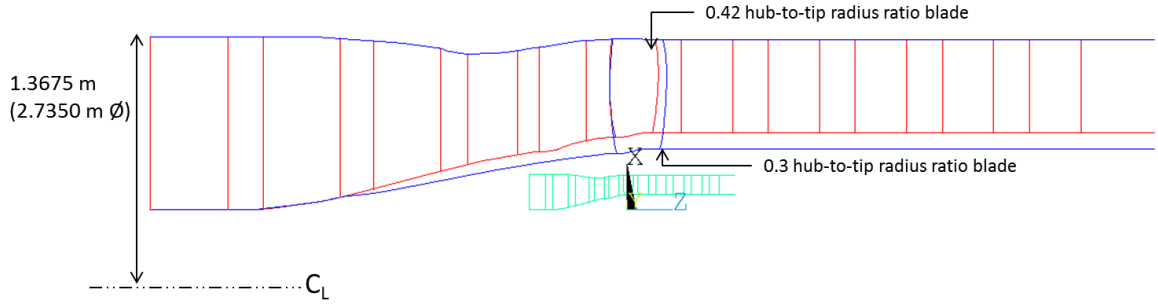

Figure 5.23 Hub-to-tip radius ratio decrease for the NASA ADP fan 2-D SLC model from 0.42 to 0.3 to build up the variable-pitch fan geometry.

Because the flowpath shroud was fixed to match the required diameter, the flowpath hub section was shifted downwards to satisfy the hub-to-tip radius ratio of 0.3. Nonenetheless, the flowpath hub section at the inlet identified as I in Figure 5.24. was kept constant to concide with the already designed spinner. Henceforth, the flowpath section between the spinner and the fan blade was modified and smoothed out in such a way that it can satisfy the hub-to-tip radius ratio of 0.3, as displayed in Figure 5.24.

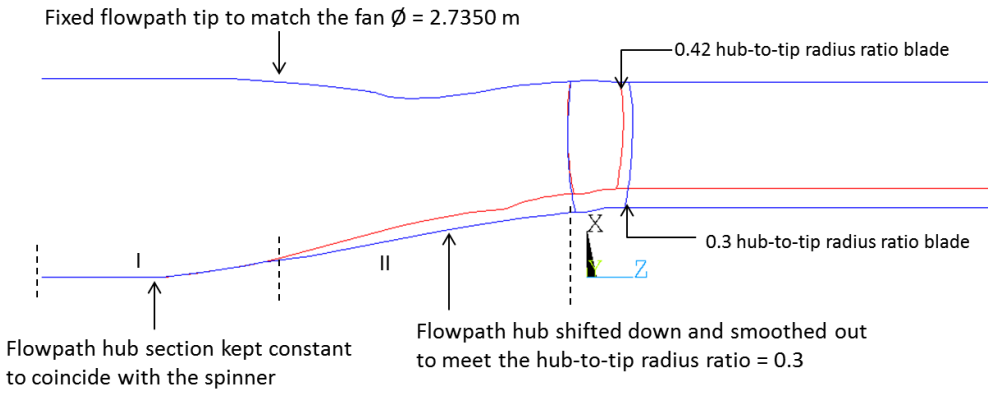

Figure 5.24 Flowpath hub modification to match the required hub-to-tip radius ratio of 0.3 for the variable-pitch fan geometry.

The stretched fan geometry increases the span region for inlet relative supersonic velocities at the hub. To avoid choking at the hub profile sections, the maximum-thickness-location-to-chord ratio was increased by 8% at the hub, whereas the maximum-thickness-to-chord ratio was reduced in 3.9% at the hub, as plotted in Figure 5.25. The variations of these 2-D blade-element parameters were gradually diminished towards the tip, to satisfy the baseline profile geometry at the top sections, using a cubic B-spline approximation (see Appendix A). Provision was made to maintain the modified maximum-thickness-location-to-chord ratio between 40 and 52%, since data provided from the Cambridge Whittle Laboratory specified this range for the NASA ADP Fan [252].

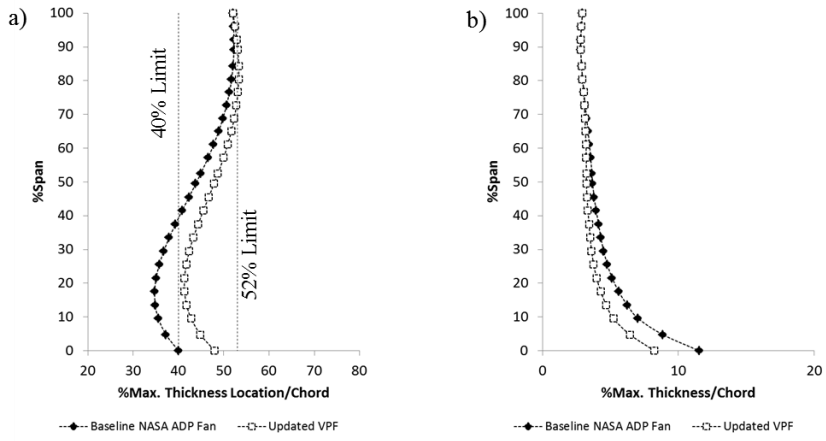

Figure 5.25 2-D blade-element parameter modification for the NASA ADP Fan [252] **to compose the variable-pitch fan. a) Maximum-thickness-location-to-chord ratio. b) Maximum-thickness-to-chord ratio.**

Additionally, the fan-blade inlet angles were adjusted accordingly using axial-flow compressor design theory for the entire span to match the incidence from the NASA ADP Fan [252], and guarantee the same profile losses.

5.4.3 Optimisation Strategy

5.4.3.1 Overall Framework

With the aim of a full-design exploration, the updated version of the 2-D SLC fan/compressor performance was fully coupled to an evolutionary genetic algorithm (EGA) for an aerodynamic design-optimisation as shown in the flow chart of Figure 5.26. The updated version of SOCRATES includes all the improvements developed and presented herein, consisting of: 3-D blade-element layout method, full REE adaptation for sweep and lean effects, shock- structure and loss model, and the choking mass flow redistribution scheme.

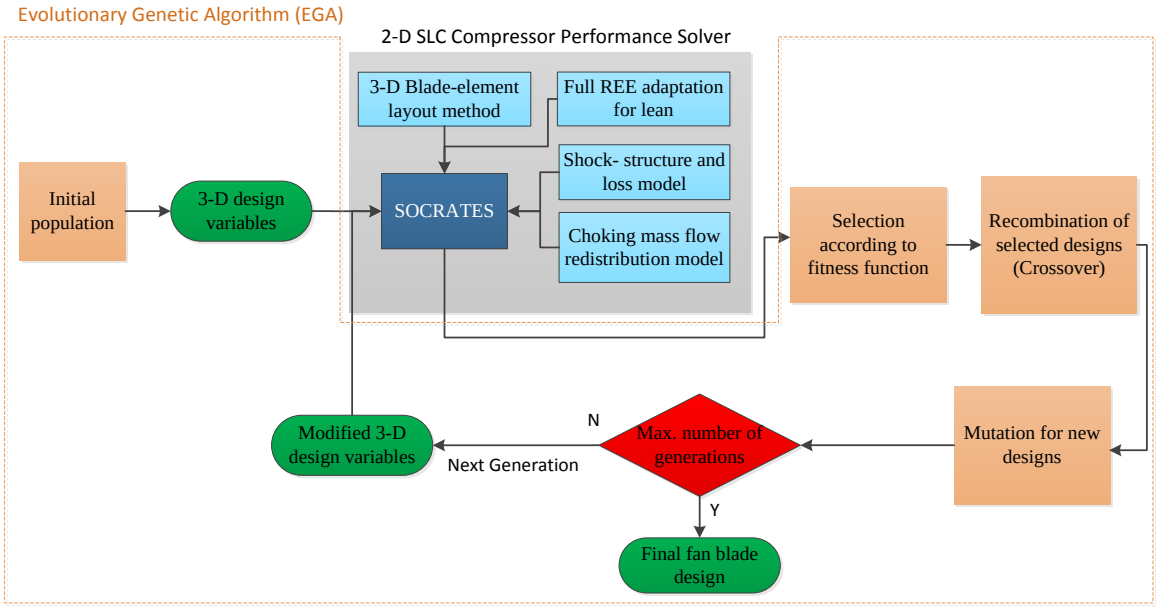

Figure 5.26 Evolutionary genetic algorithm design -optimisation strategy using a 2-D SLC fan/compressor performance simulator as solver.

Since the parametric studies of Sec. 5.2 established the isolated effect of shock losses on the isentropic efficiency when the 3-D blade-element parameters are varied, this design optimisation intents to find the most efficient VPF blade by just varying the sweep and

lean angles. In this manner, the effect on the shock-losses due to sweep and lean can be addressed.

The EGA optimiser works as displayed in Figure 5.27. An initial population of 3-D design variables are specified within the limits determined to be analysed by SOCRATES, which computes the performance solution for the various fan-blade models. Whereafter, a fitness function discriminates to select the best solutions, so that a crossover is performed between them to recombine the variables and mutate for a new generation of designs. The modified 3-D design variables form a new set of fan-blade individuals that are analysed again by SOCRATES, starting a new generation cycle. The process repeats iteratively until the maximum limit of 50 generations is satisfied, which suffice for convergence, determining the most optimum fan-blade design.

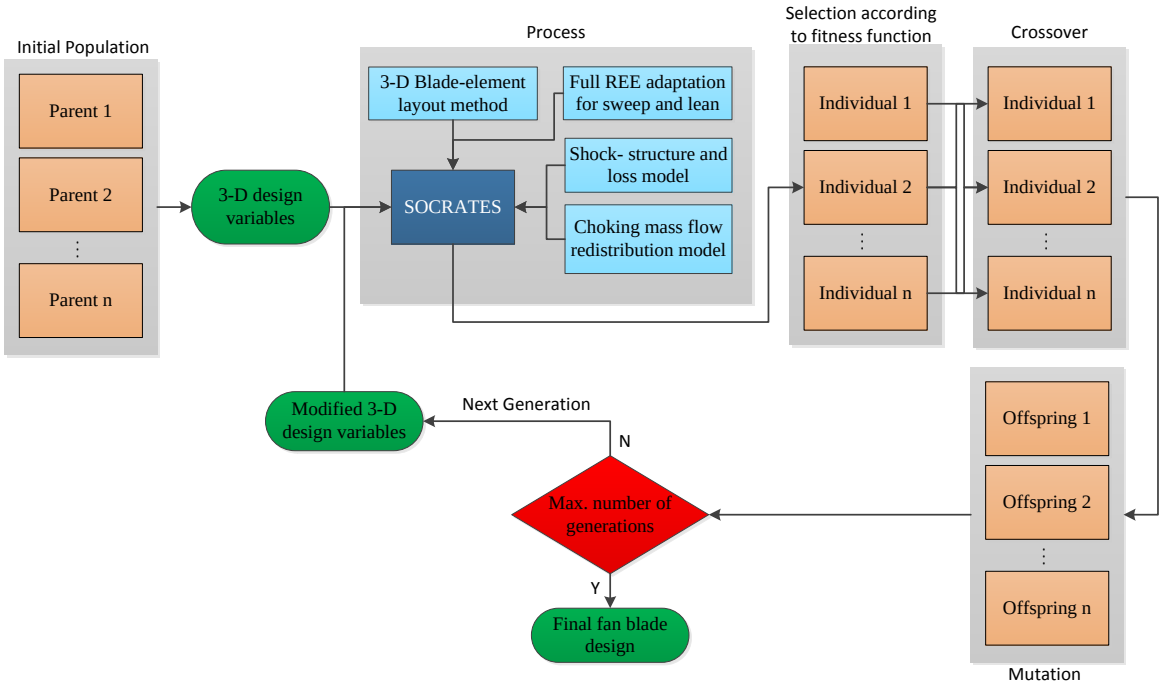

Figure 5.27 Flow chart for the 3-D variable-pitch fan design optimisation using an evolutionary genetic algorithm coupled to a 2-D SLC fan/compressor software as solver.

5.4.3.2 Objective Function and Design Variables

The single-objective function set for the design optimisation was to maximize isentropic efficiency at 100% of design speed and design-point condition.

As mentioned earlier, the purpose of this effort is to attain the objective by varying the sweep and lean angle for every blade-profile section, obtaining in this way a compound radial distribution. To assure a continuous curvature (G2 continuity) radial distribution, the sweep and lean angle were varied along the mid-span and at the tip, as shown in Figure 5.28. The mid-span radius for the sweep and lean angle was also considered to be a design variable. Therefore, 6 decision variables were introduced to the design-optimisation framework: λ_{tip}, λ_{mid}, R_{mid_λ}, η_{tip}, η_{mid}, and R_{mid_η}. The radial distribution of sweep and lean angles is determined by control points located at the 6 decision variables, the hub and tip radii, and the known zero-sweep and zero-lean at the hub. A Bezier-curve approximation is then used to curve-fit these control points, so that an interpolation at the desired radial positions computes the corresponding values for sweep and lean along the blade span.

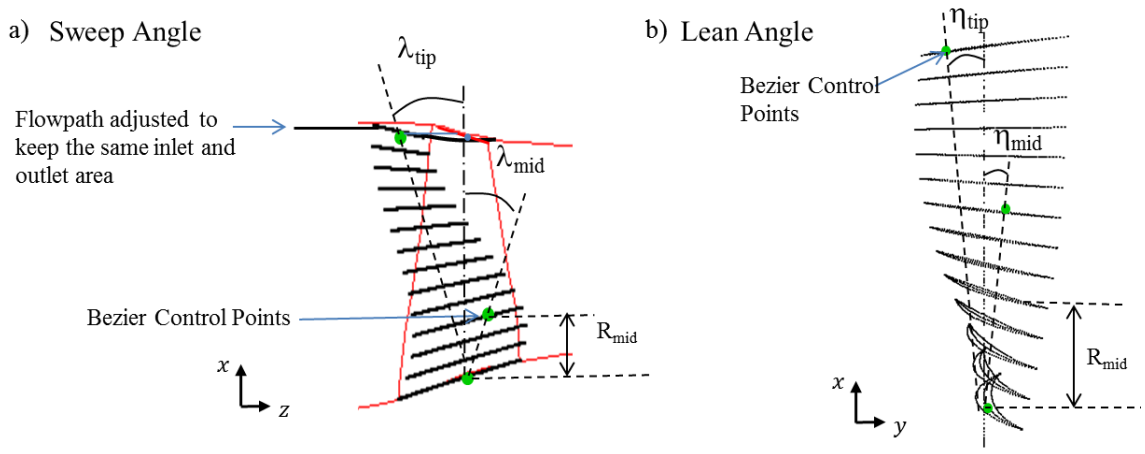

Figure 5.28 Decision-variable structure for the sweep and lean angle variation for the 3-D VPF EGA design-optimisation.

The tip and mid-span sweep decision-variable was limited to keep the same inlet and outlet area, although the flowpath was adjusted accordingly to do this. The decision variable that corresponds to lean at the mid-span and tip was limited by the through-flat-pitch rotation mode, since the blade-profile chord might become perpendicular to the axial axis leading to potential blade interference. To avoid this, a solidity less than unity with a tolerance gap of 0.5% of the pitch was established to limit the sweep and

lean angles. The design-variable limits are listed in Table 5.1, where these ranges suffice for a full design-exploration.

Table 5.1 Decision variable limits for the 3-D variable-pitch fan design-optimisation.

Decision Variable	Variable Limits
Tip Sweep Angle	-17.8 deg ≤ λ ≤ 22.5 deg
Mid-Span Sweep Angle	-17.8 deg ≤ λ ≤ 22.5 deg
Tip Lean Angle	-8.2 deg ≤ η ≤ 17.7 deg
Mid-Span Lean Angle	-6.4 deg ≤ η ≤ 15.4 deg

5.4.3.3 Constraint Function

Forasmuch as the fan working range must not be affected with any blade modification, a constraint was set to keep an unchanged surge margin. Maintaining the surge margin at design speed assures that the working range for part-speeds remain unaffected since the working range at 100% NRT is narrower. To maintain an unchanged surge margin, the percentage of stalled blade-span of the NASA ADP fan [252] is calculated for various stalled operating points to establish a reference. Henceforth, the 2-D SLC performance analysis used in the EGA not only solves the design operating condition, but also simulates operating conditions on the stall regime of the working range. In this way, the constraint is set to be no more than the stalled blade-span of Table 5.2 at the analysed operating or mass flow points of the fan map in Figure 5.29. The percentage of stalled blade-span was calculated for the baseline geometry at every computed streamline where the aerodynamic velocity ratio is compared against the geometric velocity ratio, according to Aungier's method [136].

Table 5.2 Percentage of stalled blade-span for the NASA ADP fan [252] **at 100% of design speed and near-stall and stall operating conditions.**

Operating Point	Mass Flow [kg/s]	%Stalled Blade-Span
1	29.00	35.48
2	29.50	32.26
3	30.00	29.03
4	30.50	22.58
5	31.00	19.35
6	31.50	16.13
7	32.00	12.90
8	32.50	9.68
9	33.00	6.45
10	33.50	3.23
11	34.00	3.23
12	34.50	0.00
13	35.00	0.00
14	35.50	0.00

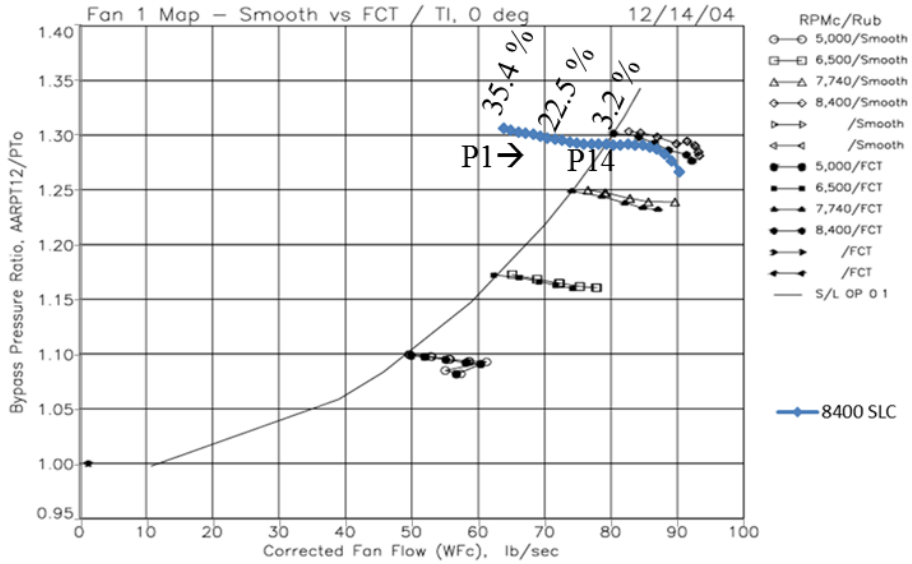

Figure 5.29 Percentage of stalled blade-span at 0 degrees pitch-setting for the NASA ADP fan [252] **at 100% of design speed.**

5.4.4 Optimised Variable-Pitch Fan Geometry

The EGA single-objective optimisation evaluated 2000 individuals across 50 generations. For instance, Figure 5.30 show the different design modifications for sweep and lean angle, respectively, for the 40th generation, where the decision variables are within the limits established. The qualitative plots in Figure 5.31 show the cumulative full design-space exploration of sweep and lean angle for the 45th generation. Figure 5.31 demonstrates that the design-space exploration from the 40th

generation is covered with similar distributions that vary in less than 0.01%, proving the convergence at early generations.

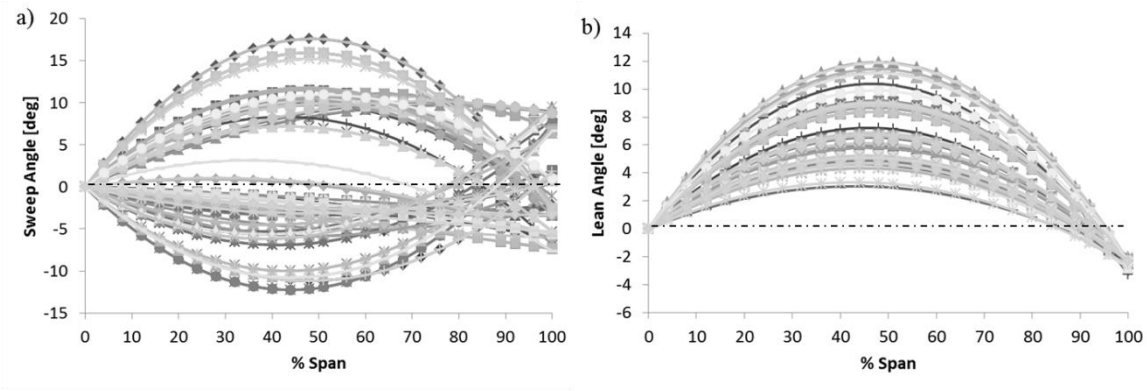

Figure 5.30 Modified design variables along the span for the 40th generation cycle of the 3-D VPF EGA design-optimisation. a) Sweep angle variation. b) Lean angle variation.

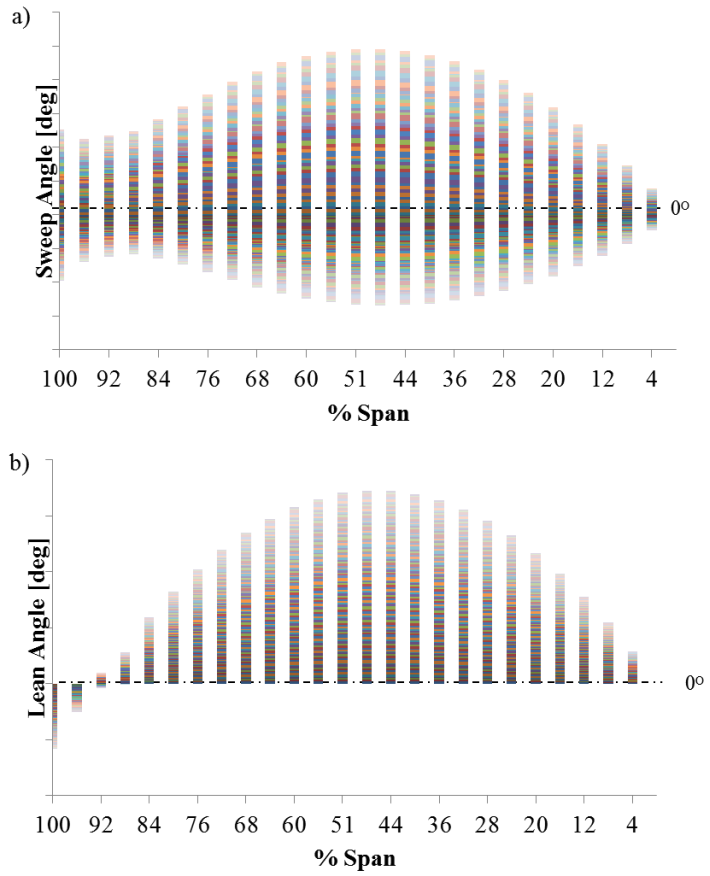

Figure 5.31 Full design-space exploration for the cummulative decision variables from the 45th generation cycle of the 3-D VPF EGA design-optimisation. a) Sweep angle variation. b) Lean angle variation.

After 50 evaluated generations, the converged solution for the optimised geometry for which the isentropic efficiency is maximum within the explored design space, results in the sweep and lean radial distribution of a) and b), respectively. The optimised VPF increases the isentropic efficiency by 0.47% with respect of the baseline geometry at the optimised design point.

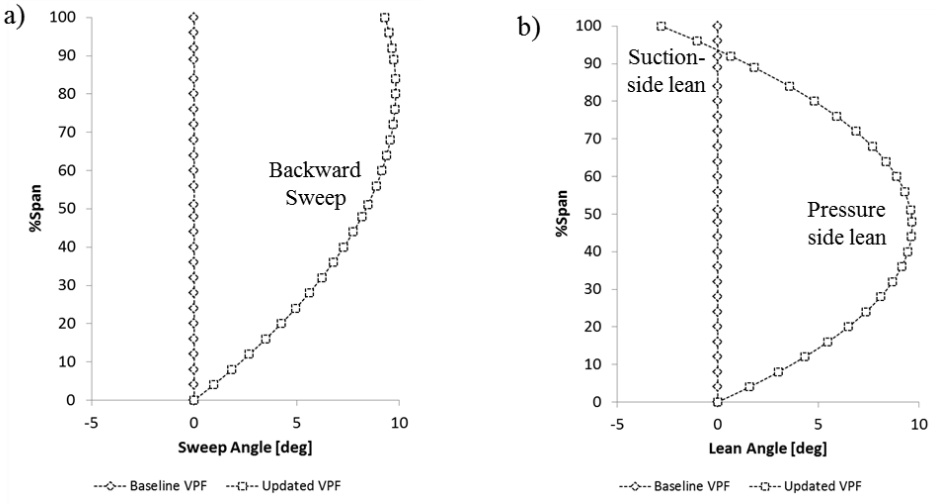

Figure 5.32 Radial distribution of the optimised 3-D blade-element parameters for the variable-pitch fan. a) Sweep angle. b) Lean angle.

The meridional projection of the optimised VPF in comparison to the baseline reveals the compound backward-sweep for the entire span as shown in Figure 5.33 a). A fwd-looking-aft (FLA) view in Figure 5.33 b), shows the radial distributions of the swept and leaned blade sections. Further, a 3-D comparison between the baseline VPF and the optimised geometry is displayed in Figure 5.34.

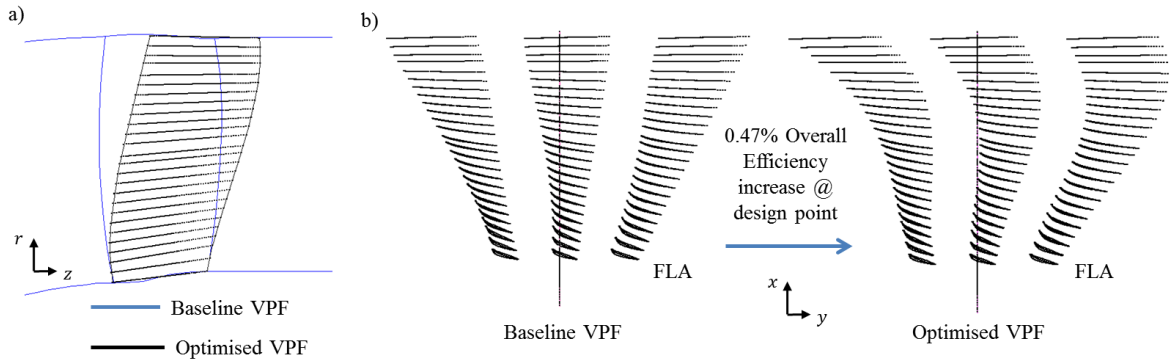

Figure 5.33 Variable-pitch fan comparison between the baseline and optimised geometry models. a) Meridional view. b) Forward-looking-aft view.

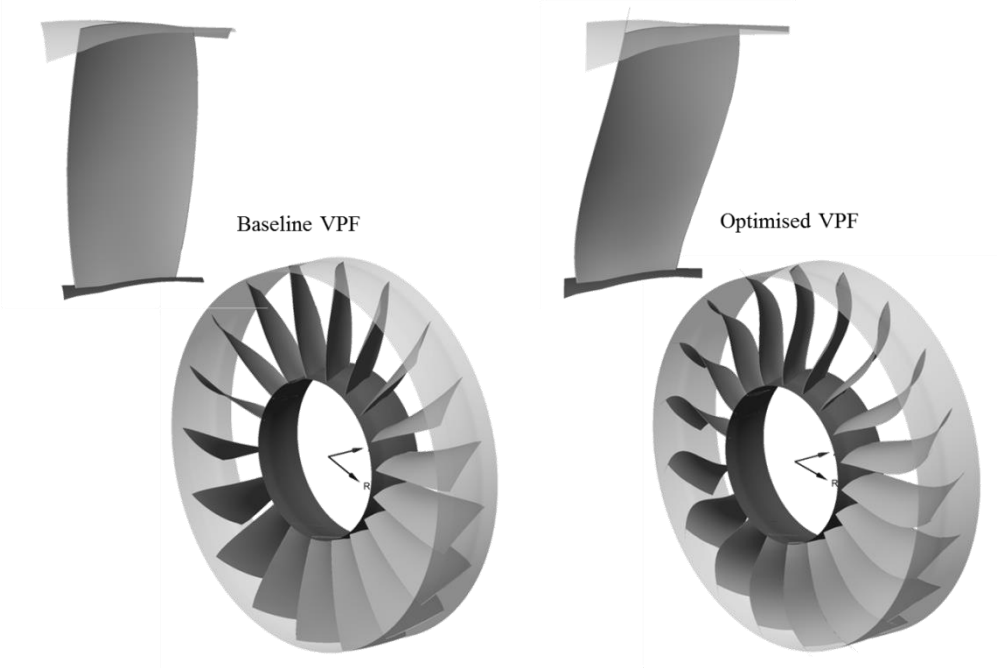

Figure 5.34 3-D variable-pitch-fan model comparison between the baseline and optimised geometries.

The rotational speeds for which there was a change in isentropic efficiency were cutback at 7740 RPM and cruise at 840 RPM as shown in the fan map of Figure 5.35. Along all the unchanged working ranges, there was an improvement in the isentropic efficiency about 0.1% for the cutback speed and 0.4% for the cruise speed. Note as well, the tendency of the cruise speedline to asymptotically approach the choking mass flow, indicating an acceptable operation of the 2-D SLC mass flow redistribution model.

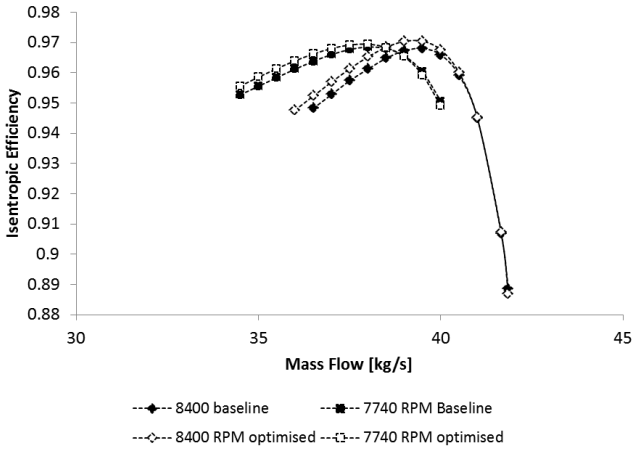

Figure 5.35 Isentropic efficiency map comparison for the baseline and optimised variable-pitch fan at cutback and cruise (design) speed.

Since no 2-D profile modifications were introduced, the diffusion magnitude remained the same throughout the span, without affecting neither the profile loss nor the loading. For this reason, the overall total-pressure ratio remains approximately unchanged with a difference of 0.03% at design point that might be due to the SLC numerical formulation.

A closer examination into the shock losses reveal that the isentropic-efficiency enhancement originates from the effect of the shock-loss coefficient radial distribution in Figure 5.36, obtained from the output of the current shock-loss model. In contrast to the NASA Rotor 67, where the tip shock-loss coefficients were close to 0.080, the baseline VPF has a shock-loss coefficient of 0.055 at 100% of span. This is explained since the tip inlet relative Mach number for the NASA Rotor 67 at design point is 1.37, accelerating to a peak suction-surface Mach number ahead of the passage shock of 1.52. Conversely, the tip inlet relative Mach number for the VPF is 1.21 rising to a $M'_{psh_{ss}} = 1.32$. Henceforth, the passage-shock strength is less than in the NASA Rotor 67, leading to have lower relative total-pressure losses.

The optimised VPF geometry with both variations in sweep and lean angle throughout the span, reduces the shock-loss coefficient in 5.5% in comparison to the baseline VPF geometry. In contrast to the variation only of sweep and lean in the parametric study where no major improvement was obtained at mid-span, the combined effect of sweep and lean angle variation decreases the shock-loss coefficient at mid-sections by 6.5%.

This percentage should be looked with modesty since shock-loss coefficient values are relatively low at mid-span ranging around 0.03. Towards the hub, the shock-loss coefficient improvement diminishes since the shock effects are less severe due to reduced relative Mach numbers and the 3-D geometry variation is less at those radial profiles. Below 9% of the VPF-blade span, the shock-loss coefficient remains zero due to the inlet relative subsonic speeds that even a small sweep or lean variation would not induce any additional loss.

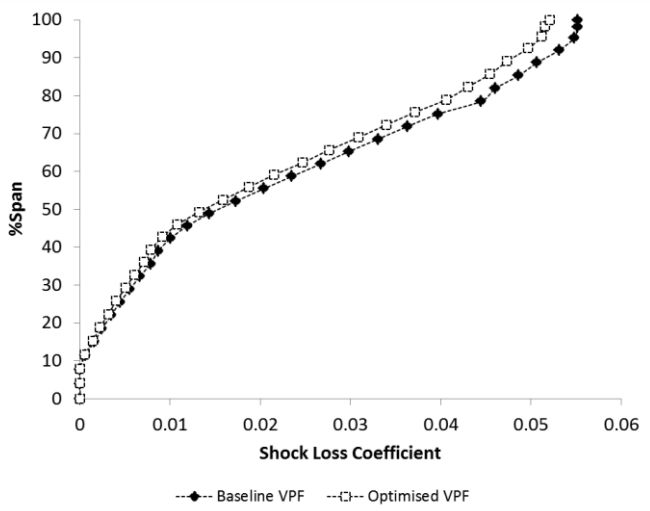

Figure 5.36 Shock-loss coefficient radial distribution comparison between the baseline and optimised geometries for the variable-pitch fan.

Because of the VPF low solidity with a blade count of 18 and low inlet relative Mach numbers in comparison to those from the NASA Rotor 67, the bow-shock is less oblique and more detached, and thus, extending more across the passage and reducing the passage-shock length. In consequence, the relative total-pressure loss reduces since there is less influence of the passage shock. While the tip passage-shock straight portion extends about 40% of the pitch in the NASA Rotor 67, the extension of the same in the VPF is confined within 30% as seen in Figure 5.37 a), contributing to have a reduced shock-loss coefficient. Figure 5.37 b) shows the 3-D shock-system interaction in 3-D, including the compressible-flow mechanisms of detached-bow shock, flow expansion and passage shock for the VPF-blade tip.

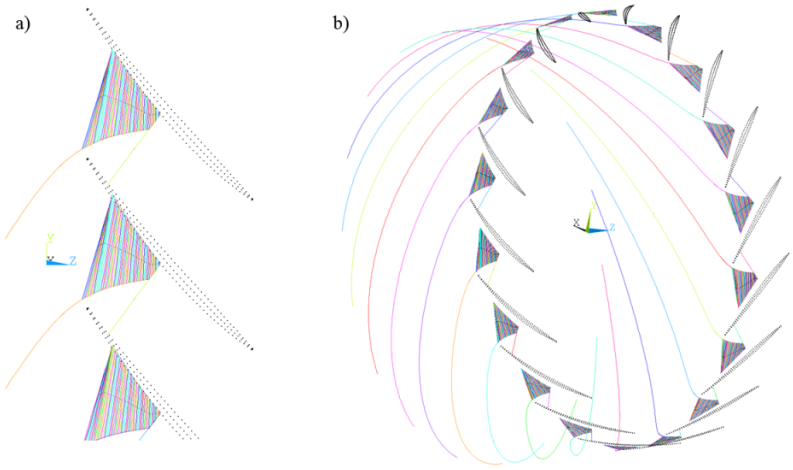

Figure 5.37 Overall shock-configuration for the variable-pitch fan blade tip. a) 2-D cascade view. b) 3-D projection view.

Observe in Figure 5.38 that the pitch-averaged relative total-pressure recovery determined by the current shock-loss model for the baseline VPF is about 0.98 while in the NASA Rotor 67 is ~0.95%, signal of a less severe passage-shock for the VPF due to a reduced relative Mach number pitchwise distribution. The optimised VPF shifts the $PR'_{n_{psh}}$ pitchwise distribution to higher values by an average of 0.4%, improving the recovery at the suction surface in 0.6%. Similar to the discussion in Sec. 5.2.4, the rate-of-change of $PR'_{n_{psh}}$ with the spacing is maintained, indicating that the shock-system shape is not changed, but it is rather shifted by the sweep and lean to intercept a lower distribution of relative Mach numbers. An unmodified shock-configuration form is expected since none of the 2-D blade-element parameters are varied.

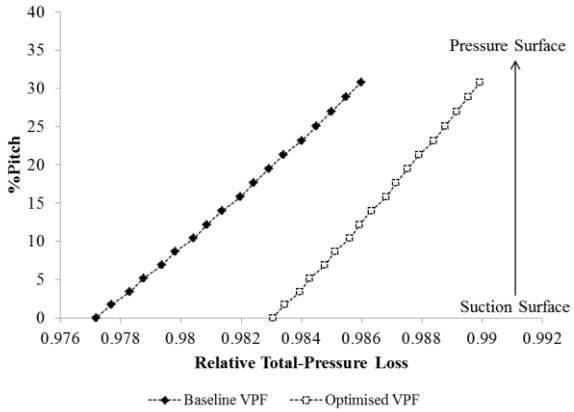

Figure 5.38 Relative total-pressure loss pitchwise distributon comparison between the baseline and optimised geometries for the variable-pitch fan.

6 CONCLUSIONS AND CONTRIBUTION TO KNOWLEDGE

6.1 General Conclusions

Modern aircraft gas turbine engines demand to be light and compact whilst being highly efficient to reduce fuel consumption. Transonic axial-flow fans and compressors respond to these needs due to the additional loading generated by the shock structure at the expense of an overall shock loss increment. The challenge, however, is to design a transonic compressing system such that its efficiency and working range is comparable to that from a subsonic compressor.

Traditionally, in the turbomachinery design and analysis process, 3-D CFD RANS tools are used due to their high level of fidelity. Nevertheless, their huge solution times make them expensive apart from the inability to incorporate loss and deviation models since the flow is solved numerically using the Navier-Stokes equations. In contrast, 2-D SLC methods provide fast and reasonably accurate solutions. If the 2-D SLC performance-prediction simulation fidelity is further improved, a more detailed component-level blading study can be achieved. The usage of 2-D SLC methods can be potentially exploited even more if coupled with an optimiser framework to conduct paramount full-design-space explorations in the optimisation process, yielding in more detailed product designs at low cost.

Transonic-flow analysis for axial-flow fans and compressors is complex due to the shock structures involved and the associated phenomena. One of the key elements to compute the overall shock-induced losses is to estimate the correct location and shape of the shock system composed by a detached bow-shock and a choke-induced passage-shock. Previously published models have failed in an accurate prediction of shock losses, lacking of the ability to establish a solution for off-design and started blade passages, resulting in unreliable estimations for the total-loss coefficient and isentropic efficiency. State-of-the-art models have shown intolerably-high deviations ranging around 50% at the blade tip. This is not surprising since the tip of a conventional transonic axial-flow compressor at design point is choked, for which the shock-system employed is that as in the unstarted flow cases.

For this reason, a comprehensive analytical transonic-flow package was developed in the present research to address the main aspects of the compressible flow in axial-flow transonic compressor blading. The core of this innovative toolkit relies on a physics-based shock-wave model to estimate its structure and relative total-pressure losses using an iterative method that positions the second passage-shock. To make this shock-loss model fully functional, additional methods and schemes were required, such as an explicit blade-element-profile definition, a 3-D-blade-element incorporation for the 2-D SLC full REE, and a choking mass flow redistribution model. These systems were conjugated accordingly to handle transonic flow for an accurate compressible-flow solution and were fully implemented and integrated into a 2-D SLC compressor performance simulation software (SOCRATES).

The improved version of the 2-D SLC code was tested and validated against experimental and CFD data. To prove the ability of and the application of the shock-structure and –loss model, a 2-D and 3-D blade-element parametric study, and an EGA optimisation fully-coupled with the enhanced 2-D SLC software were conducted to examine the impact on shock losses. The single-objective optimisation varied the sweep and lean angle to maximize the isentropic efficiency by 0.4% while maintaining the surge margin for a new design of a variable-pitch fan leveraged from the NASA ADP Fan [252].

In Sec. 6.2, remarkable conclusions upon the novel incorporations to the 2-D SLC performance prediction framework and its application in the design of transonic axial-flow compressors are given to highlight the contributions to knowledge.

6.2 Main Conclusions

6.2.1 State-Of-the-Art

Heretofore, published shock-loss models assumed an over-simplified fixed shock structure for design point and unstarted conditions, without the capability of adapting and reacting to off-design conditions. For instance, one of the early shock-loss models developed by Schwenk *et al*. [4] consists in only a passage shock modelled as a normal shock emanating from the detached bow-shock vertex to an assumed location for the

peak suction-suction Mach number location. Despite this model works acceptably at the mid-span of the relative supersonic region, there is an average overestimation at top locations of ~20% due to the equivalent passage-shock used.

The use of an equivalent structure has been the case for the successive shock-loss models where essentially the main variation has been the passage-shock impingement on the suction surface. Even the most widely used model to capture shock losses by Miller *et al*. [3] among 2-D SLC codes, the shock-loss coefficient differs at the very tip by 43%. One of the most recent state-of-the-art models by Bloch *et al*. [34], uses a more sophisticated procedure to resolve the flow expansion ahead of the passage shock. Nevertheless, the inaccurate estimation of the passage shock, assumed to be normal to the flow and standing at the sonic point of the detached bow-shock, producing differences against test data of 26% at the tip, and losing the better match that was achieved at mid-span with other historical models. Even if the flow expansion ahead of the passage shock (for more complicated that this could be) is resolved, it can lead to unacceptable shock-loss coefficient estimations if there is no an accurate prediction of the passage-shock location.

Owing to the imposition of a passage-shock, the previously published models show an inability of adapting and reacting to off-design conditions. Even more, if the conditions are choked, the shock-configuration complicates in such a way that the oversimplification of the historical models is not enough to represent the real physics. This explains the higher discrepancy at the high-span profiles, since the passage-flow is expected to be choked at those sections. Further, state-of-the-art shock-loss models were not able to predict a loss in the subsonic relative supercritical span, since the Prandtl-Meyer-based methodology used in there does not have definition when the relative Mach number is less than unity.

Under these circumstances, the aim of this research work was to improve the performance prediction of transonic axial-flow compressors in the context of 2D through-flow SLC methods. To this end, a fully-integrated analytical package to predict shock losses at design and off-design conditions (even at choking) was developed and implemented into an existing in-house 2-D SLC performance simulator.

6.2.2 3-D Blade-Element-Definition & Full-REE Adaptation

Inasmuch as the flow field for the shock- structure and loss model is solved in the blade-to-blade plane, an explicit blade-element-layout method on a conical surface was implemented to account for the solution of any arbitrary aerofoil geometry. The projection of the blade-elements on a conical surface of revolution results appropriate as it approximates a streamsurface projected as an axisymmetric streamline on the meridional plane of the 2-D SLC simulation.

The blade-element-layout considers a constant blade-surface turning for each arc defined along the chord. In this way, not only DCA and MCA –camberline aerofoils can be accurately modelled, but also CDA –camberline aerofoils with known spline arcs. This enhances the capabilities of the shock-loss model, since the surface geometry is known in its plenitude in terms of 3-D coordinates and blade angle, which is pre-requisite in the solution of the flow expansion through the method of characteristics.

More important, is the capability of the method to introduce 3-D blade-element parameters in terms of sweep and lean angle and translate the blade-profiles in the space with respect of the stacking axis, defined at the stacking points or centre-of-areas. The method itself then replaces the Cartesian-system-based blade-geometry method used in the 2-D SLC for conventional blade-profile shapes.

Forasmuch of the two-dimensionality of the 2D-SLC flow field solution, additional body forces such as pressure and drag were introduced to account for the lean-angle-induced effects in the circumferential axis. In the presence of sweep, the lean angle deviates from the original value, leading to different pressure forces that act normal to the blade surfaces. The whirl component of the normal pressure is then added as a body force acting on the quasi-orthogonal direction to the second-order differential equation solution that represents the full REE. The adaptation of the full REE in 2-D SLC allows thus to include the effect of the lean angle itself, and the combined effect of lean and sweep angles for a more accurate flow solution.

6.2.3 Shock- Structure and Loss Model

The correct location and shape of the shock-system is a pre-requisite for an accurate shock-loss prediction. The physics-based shock- structure and loss model computes analytically the detached bow-shock approximating it to a hyperbola. Relative total-pressure losses were computed for the segment of the detached bow-shock that extends to infinity to account for bow-wave losses. Thereupon, information from the choking mass flow redistribution scheme is communicated to determine if a blade-element is choked to determine whether it is a single or dual passage-shock. For unstarted operations, the single passage-shock is simply the limb of the detached bow-shock that penetrates into the passage. In the case the passage is started, a first assumption for the choke-induced passage-shock location is done, which might intercept that segment from the detached bow-shock, forming a coalesced dual-shock configuration. The shock angle for this second passage-shock is calculated as oblique instead of a normal assumption as the previous models since 3-D CFD analysis demonstrated the obliquity in the relative frame of reference.

Having established the passage-shock shape and location, the upstream flow expansion that interacts with it is determined using the method of characteristics to compute the flow properties immediately ahead of the passage shock. The fidelity of the implemented shock methodology is such that any potential expansion fan and pre-compression shocks are detected and computed as a function of the blade geometry computed in the 3-D BELM. This innovative implementation is unique in its class, affecting slightly the flow field ahead of the passage shock. Given the circumferential distribution of flow properties immediately ahead of the passage shock, an integration of shock losses determines the mass-averaged relative total-pressure recovery. The overall relative total-pressure loss, and shock-loss coefficient is then defined for started-flow passages.

Nonetheless for started flows, the analysis requires more detail. In the case both passage shocks are not merged in the dual-shock system, an additional suction-surface is resolved. Whether the passage shocks coalesce or not, the expansion in between them

is resolved to compute in a similar fashion as the first expansion, the corresponding mass-averaged relative total-pressure ratio and the overall relative total-pressure decay.

The successive steps establish the key for the prediction improvement of the shock losses as a function of the choke-induced shock location. An outer iterative method computes the streamtube throat-area to establish the operating ranges for the blade passage to find agreement against the computed passage situation. In the case of a different operation range, the second-passage shock location is redefined to repeat the expansion process. If the choke-induce passage shock location complies this sanity filter, an appropriate streamtube shock-area and shock location are calculated to satisfy the calculated relative total-pressure loss. The difference in shock locations determines an error, so that an inner iterative secant method repeats the process for a second error to update the choke-induced axial location. The process replays iteratively in its entirety for a new shock location, until an agreement is found between the second passage-shock location analysed and that required to satisfy the computed relative total-pressure loss. This complicated arrangement of nested loops comes without extra cost in the execution of a 2-D SLC simulation.

To aid in the complete solution of the shock losses for the entire span and in contrast to the historical models, the current shock-loss model calculates the inlet relative critical Mach number to solve for relative subsonic critical conditions. The relative velocities are solved for the blade-row intra-stations to find the highest, where a normal shock-wave is placed to compute the associated losses.

The current shock- structure and loss model proved to work well and yielded to a very satisfactory agreement against the NASA Rotor 67 experimental data, decreasing the error to a maximum of 0.6% at the tip and 0.3% at the mid-span of the supersonic span. This represents a significant prediction enhancement of 40-50% with respects of the historical models. For instance, the prediction is improved in the critical region of the tip by 42% and by 55% at low-span supersonic regions in comparison to the model of Miller *et al*. [3]. The major discrepancies against test data were found at a reduced transition region between the subsonic supercritical and the supersonic span in the order of 1e-3. However, these differences are of minimal effect on the isentropic efficiency,

since the shock-loss coefficients at these regions are small. At relative subsonic supercritical regions, the model behaves accurately in its prediction of the inlet relative critical Mach number and leads to shock-loss differences of 0.1% against measured data.

6.2.4 Choking Mass Flow Redistribution Scheme

A fully detailed and exhaustive 3-D CFD RANS analysis evidenced the close relationship between choking phenomenon and shock waves within the blade passages. As a matter of fact, the passage shock is the responsible of the relative total-pressure decay at choke conditions.

For this reason, a novel choking scheme was developed and implemented to establish a reference of the current-flow conditions with respect of the choking limits, fix the angle and mass flow where it is pertinent, and redistribute the mass flow spanwise. In this sense, the whole choking mass flow redistribution scheme consists of: (1) a choking incidence calculation; (2) a choking margin definition: (3) a numerical method to redistribute the mass flow along the entire blade span.

The choking incidence is calculated using a 1-D supersonic flow model for an unstarted cascade, where the governing equations of continuity, conservation of stagnation enthalpy, and conservation of momentum are solved. The algebraic manipulation of the simultaneous solution of these relations, establishes a minimum for the inlet flow angle, indicating the choking value. However, this minimum value can be false along the distribution of flow angles. For this reason, an iterative method was devised to compare such analytical inlet flow angle against that obtained from empirical correlations as a function of the choking low-loss working range. In this way, the analytical method is guided to convey to an accurate value for the choking flow angle.

Given the choking flow angle at the inlet, velocity triangles are solved for this condition to establish mass flow conservation between the current and choked conditions, using the corrected mass flow per unit area. Thereby, a ratio between both conditions establishes the choking margin, which is a non-dimensional parameter that serves a reference to measure the magnitude of the choked flow.

At those streamlines where the choking margin is above unity, a numerical method extracts mass flow to bring the margin parameter to a value of one, leading the inlet flow angle to be fixed to the choke value. Nevertheless, to still satisfy mass flow conservation, the removed mass flow from the choked top sections is redistributed downwards. The streamtube mass flow withdrawal from the started sections and the allocation of it on the unchoked streamtubes is performed according to the choking margin defined for every streamline. This scheme is executed iteratively for every full-REE iteration within a 2-D SLC simulation. Provision was made not to cause any significant impact on the time to find a converged solution.

The overall choking mass flow redistribution model proved to work adequately by fixing the inlet flow angles to the choking values were applicable, while fixing their streamtube mass flow and redistributing it into unstarted streamtubes. Validation against a 3-D CFD RANS simulation for the NASA Rotor 67 showed the adequacy of the model by bringing down the steamtube mass flow at the tip while being consistent in the mass flow spanwise distribution for the entire span. Mass flow discrepancy at the tip was 0.9%, while the span-averaged mass flow difference at mid and low –spans was about 1.3%. This represents an improvement in the mass flow prediction of 11% at the tip and 14% at hub sections against previous 2-D SLC simulators that do not correct the mass flow at the started passages. For the started passages, the estimated choking flow angle and hence, choking incidence, showed a difference of 0.3% against 3-D CFD results.

Not less important to note, is the sensitivity of the choking mass flow redistribution of reacting to off-design conditions. Insomuch as the choking margin gets more severe towards choking, the implemented models extend the started region towards the hub as the mass flow increases. Consequently, more radial locations are fixed to have the corresponding choking incidence and choking mass flow. This feature permits to observe the evolution of choking in 2-D SLC throughout the operating conditions.

6.2.5 2-D and 3-D Parametric Studies

To demonstrate the functionality of the transonic-flow package on its whole and recognize design trends, a parametric study to assess the impact of 2-D and 3-D blade-

element parameter variation was conducted for the NASA Rotor 67 at 100% of design speed and design point condition.

In terms of the 2-D blade-element parameters, maximum-thickness location, maximum thickness, and solidity were varied by ±5.0% for the thickness parameters and by ±4.5% for the solidity from the baseline parameters. As expected none of the three parameters caused an impact at low and mid –spans, since the single shock-structure there owed to the unstarted conditions, is entirely the detached bow-shock which is a function of the inlet relative Mach number and not of the blade geometry. The major influence observed was at the top profiles, where the flow is started. Although marginal, an increase in maximum-thickness location and reduction of maximum thickness have almost the same effect of decreasing the shock losses by 1.1 and 2.9%, respectively. In this case the turning is reduced and a lower peak suction-surface Mach number is attained, resulting in a less severe relative total-pressure ratio across the passage-shock.

A greater improvement of 4.2% in shock-loss coefficient is obtained with a 4.5% increase in solidity increase for the entire choked span. A closer examination into the pitchwise distribution of the relative total-pressure losses exhibited that there is more penetration of the detached bow-shock into the passage, moving downstream the coalescence, and having a lower magnitude of relative speeds. In fact, the straight portion of the passage shock shortens by 2.0%, since there is more composition of the bow-shock, sufficing to generate a mass-averaged relative total-pressure loss reduction of 0.9%.

The 3-D blade-element parameters were varied in $\pm 5^{o}$ for the sweep angle and $\pm 1.5^{o}$ for the lean angle, being constant throughout the span. Although is known that a compound sweep and lean offer a more significant improvement, the purpose of a constant blade inclination was to identify design tendencies using the treatment of the current shock-loss model. Because the 2-D profile is unaltered but translated in the space, the passage-shock shape does not get modified. Instead, the entire shock configuration is shifted in the direction of the sweep or lean, intercepting the flow expansion at different relative Mach numbers, leading to a different shock-loss coefficient. In fact, the shape of the relative total-pressure drop pitchwise distribution remains almost the same but

displaced to a different magnitude. Despite a higher impact in the shock-loss coefficient was observed at the tip, the rest of the span suffered a gradual modification towards the hub, since there is also a sweep and lean introduced that generate the same effects as in the tip. Thus, a combined sweep and lean can potentially further increase the isentropic efficiency, as small improvements along the span and not only at the tip can be achieved.

A backward and a pressure-side lean showed a shock-loss decrease at the tip of 3.8% and 0.5%, leading to an isentropic-efficiency enhancement of 0.2%. Conversely, a forward and a suction-side lean increase the shock losses by 3.9% and 0.8%, reducing the isentropic efficiency by 0.2% and 0.1%, respectively. The marginal improvement in lean is due to the small variation introduced; however, further improvements can be obtained for higher variations of lean angle.

Henceforth, the variation of sweep and lean angles, proved to influence the shock loss coefficient. A combined backward and a pressure-side lean can potentially increase the isentropic efficiency since the shock system is displaced to intersect lower magnitudes of relative Mach numbers upstream of the passage shock. These observations were confirmed in the EGA single-objective optimisation carried out.

6.2.6 Single-Objective Variable-Pitch Fan Optimisation

A cutting-edge variable-pitch fan was designed as scale-up in 3.9 times from the NASA ADP Fan to meet the OEM required diameter for under-the-wing installation purposes. The hub-to-tip radius ratio was increased for which the flowpath hub was adapted. To avoid choking at the hub sections, the maximum thickness location was increased and the maximum thickness decreased, while maintaining the same spanwise distribution proportion. Since the new geometry developed is different from the original NASA ADP Fan, the blade inlet angles were adjusted accordingly to match at least the incidence from the NASA ADP Fan and assure the same scale of profile losses.

In the aim of demonstrating the practical application and benefits of the entire transonic-flow toolkit (shock-loss model and mass flow redistribution scheme), an EGA was

coupled to the 2-D SLC code to conduct a single-objective optimisation for the new VPF designed.

The objective function was to maximize efficiency, while the decision variables were assigned to be the sweep and lean angle at tip and mid-span locations. The location of the decision variables established the control points to curve fit and approximate a Bezier curve to layout the compound spanwise distribution of sweep and lean. The design variables were limited by the through-flat-pitch rotation mode, inasmuch as the blade chord becomes normal to the axis at some point during the rotation. This required a solidity less than unity, setting the limiting ranges for the sweep and lean angle rotation. The optimisation was constrained by an unchanged surge margin, calculated as a percentage of the stalled blade-span for various operating points. This constraint function required SOCRATES to run a multi-point simulation for every design tested, to assure that the same percentage of stalled blade-span is less or at least equal as in the baseline VPF.

The EGA single-objective optimisation ran 2000 individual designs across 50 generations, which converged at the 40^{th} generation. The resulting optimised geometry, confirms the observations of the parametric study. The optimised VPF consists of a backward sweep along the entire span and mostly a pressure-side lean. The backward sweep increases progressively from the hub, reaching its maximum at about 81%. To generate a significant impact, the lean angles at mid-span are about 9^{o}, while reducing gradually towards the tip and hub. A close examination to the shock losses revealed that the combination of sweep and lean contributes to a higher reduction of the shock loss coefficient for the supersonic relative span, leading to an isentropic efficiency increase of 0.4% at cruise speed (8400 rpm). Even at a lower cutback speed (7740 rpm), there is still an improvement of 0.1%, despite the lower relative Mach numbers occurring.

In spite of the relatively low shock losses in the baseline VPF due to low relative Mach numbers, the combination of sweep and lean angle along the entire span reduces the shock-loss coefficient in 5.5%. In contrast to the 3-D parametric study, there is as well

an improvement at mid-sections of 6.5% owed to the combined effect of higher variations of sweep and lean and a higher variation of lean.

The fact that the blade count is lower in the VPF than in the NASA Rotor 67, the straight portion of the passage shock is just about 30% of the pitch. In conformity, with the 3-D blade parametric study, the gradient of the relative total-pressure distribution is approximately maintained but displaced to higher magnitudes by an average of 0.4%, improving the recovery at the suction surface in 0.6%.

All of the above proves the adequacy and full universality for arbitrary designs of the trasonic-flow package to respond to geometry variations and any effect from the adaptation of sweep and lean in the solution of the full REE. This practical application evidences the potential for a rapid and accurate design optimisation using high-fidelity 2-D SLC methods.

7 FUTURE RECOMMENDATIONS

Inasmuch as the core of the transonic-flow treatment is the shock- and loss model, which proved to work adequately, the following future recommendations are given in this direction.

- The shock-loss coefficient was calculated for every radial location of the span. Nevertheless, this coefficient just considers the effects from the shock strength as a function of the severity of the relative total-pressure loss across mainly the passage shock. Since the shock-loss model proved to work well and it is sophisticated in its class, a blade boundary-layer model can be implemented and fully coupled to it, to compute the SWBLI-induced losses. Should this is the case; a further modification to the shock-configuration modelling might be required to include the lambda-foot, which highly interacts with the boundary layer.
- The overall shock-system, flow expansion and associated losses were computed within the passage. However, at very high mass flows there is an overexpansion or even an underexpansion which results in a series of reflecting compression and expansion waves that might add to the shock losses. An analytical model to capture this reflecting wave-system and its associated losses at the jet area would increase the fidelity for the applicable cases.
- In the shock-loss computation for the relative subsonic supercritical conditions, a deviation of zero was assumed for the suction-surface turning to determine the peak suction-surface Mach number. Nonetheless, a deviation model can be implemented to calculate the actual deviation and obtain a more accurate estimation of the suction-surface relative Mach number distribution for a better prediction of the shock loss.
- In the radial distribution of the shock-loss coefficient there were discrepancies at the initiation of the relative supersonic span, where the hyperbola-approximation method for the detached bow-shock appears to be slightly inaccurate. The high incidence values at these radii increase the Mach angle and forces the detached bow-shock to lose that obliquity that approximates to a hyperbola. A different

approximation method to represent the detached bow-shock at these low-span locations can lead to better agreements in terms of shock-loss coefficient. Perhaps a simple normal shock at least as a first attempt would produce a more realistic representation.

- The close examination to the relative total-pressure loss pitchwise distribution revealed a step change between the choking-induced straight shock and the hyperbola-shaped passage-shock. 3-D CFD RANS evidenced that there is a smooth transition between these passage shocks. A blending model for the properties at the transition point would assure a smooth transition between the passage-shock portion of the detached bow-shock and the choke-induced passage-shock.
- The 3-D EGA optimisation for the VPF showed a marginal improvement in efficiency, due to the low relative Mach numbers for which the shock-loss model was operating. If the fan is further throttled for the design-optimisation process, a different geometry might be obtained, leading to even higher isentropic efficiency improvements.
- The 3-D optimisation conducted for the VPF using a 2-D SLC compressor performance simulator merits some consideration, since the decision variables of sweep and lean induce 3-D effects that trigger a circumferential flow fluctuation. Because of the two-dimensionality of the solver, these effects are not currently captured in the present framework. These 3-D effects are of particular importance at the tip. As a first attempt, a simple empirical correlation can be introduced to the 2-D SLC code to account for the 3-D impact of sweep and lean, in the aim of investigating how different the optimised geometry is.

REFERENCES

1. Freeman C., Cumpsty NA. A Method for the Prediction of Supersonic Compressor Blade Performance. ASME 1989 Int. Gas Turbine and Aeroengine Congress and Exposition. 4-8 June, Toronto, Ontario, Canada: 89-GT-326; 1989. pp. 1–13.

2. Cumpsty NA. Compressor Aerodynamics. 5th edn. Malabar, Florida, United States of America: Krieger Publishing Company; 2004. 517 p.

3. Miller GR., Lewis Jr. GW., Hartmann MJ. Shock Losses in Transonic Compressor Blade Rows. Trans. ASME J. Engineering for Power. 1961; 60(WA-77): 1–7.

4. Schwenk FC., Lewis GW., Hartmann MJ. A Preliminary Analysis of the Magnitude of Shock Losses in Transonic Compressors. Research Memorandum. Lewis Flight Propulsion Laboratory, Cleveland, Ohio, United States of America: NACA RM E57A30; 1957. pp. 1–49.

5. Wilcox WW., Tysl ER., Hartmann MJ. Resume of the supersonic compressor research at NACA Lewis Laboratory. Trans. ASME Series D J. of Basic Engineering. 1959; 81(1): 559–569.

6. Bullock RO. Critical Highlights in the Development of the Transonic Compressor. Trans. ASME J. Engineering for Power. 1961; 83(1): 1–243.

7. Calvert WJ., Ginder RB. Transonic fan and compressor design. Proceedings IMechE Part C: J. Mechanical Engineering Science. 1999; 213(C1 & C2): 419–436.

8. Benini E., Biollo R. Aerodynamics of Swept and Leaned Transonic Compressor-Rotors. J. Applied Energy. 2007; 84(10): 1012–1027.

9. Wilson DG., Korakianitis T. The Design of High-Efficiency Turbomachinery and Gas Turbines. 2nd edn. London, United Kingdom: MIT Press; 2014. 1-593 p.

10. Becker B., Kwasniewski M., von Schwerdtner O. Transonic Compressor

Development for Large Industrial Gas Turbines. Trans. ASME J. Engineering for Power. 1981; 105(3): 5.

11. Lichtfuss H-J., Starken H. Supersonic Cascade Flow. Progress in Aerospace Sciences. 1974; 15(376): 37–149.

12. Law CH., Wadia AR. Low Aspect Ratio Transonic Rotors : Part 1 — Baseline. ASME Int. Gas Turbine & Aeroengine Congress & Exposition. 1-4 June, Cologne, Germany: 92-GT-185; 1992. pp. 1–11.

13. Boyer KM. An Improved Streamline Curvature Approach for Off-Design Analysis of Transonic Axial Compression Systems. PhD Thesis. Virginia Polythenic Institute and State University, Blacksburg, Virginia, United States of America; 2001. pp. 1–168.

14. Pachidis V. Gas Turbine Advanced Performance Simulation. PhD Thesis. Cranfield University, School of Engineering, Cranfield, United Kingdom; 2006. pp. 1–384.

15. Denton JD., Dawes WN. Computational Fluid Dynamics for Turbomachinery Design. Proceedings IMechE Part C: J. Mechanical Engineering Science. 1998; 213(2): 107–124.

16. Denton JD. Some Limitations of Turbomachinery CFD. ASME Turbo Expo 2010: Power for Land, Sea and Air. 14-18 June, Glasglow, United Kingdom: GT2010-22540; 2010. pp. 1–11.

17. Pachidis V., Pilidis P., Marinai L., Templalexis I. Towards a Full Two Dimensional Gas Turbine Performance Simulator. Aeronautical J. 2007; 111(1121): 433–442.

18. Pachidis V., Pilidis P., Templalexis I., Alexander T., Kotsiopoulos P. Prediction of Engine Performance Under Compressor Inlet Flow Distortion Using Streamline Curvature. ASME Turbo Expo 2006: Power for Land, Sea and Air. 8-11 May, Barcelona, Spain: GT2006-90806; 2006. pp. 1–17.

19. Pachidis V., Pilidis P., Templalexis I., Korakianitis T., Kotsiopoulos P.

Prediction of Engine Performance Under Compressor Inlet Flow Distortion Using Streamline Curvature. ASME J. Engineering for Gas Turbines and Power. 2007; 129(1): 97–103.

20. Templalexis I., Pilidis P., Pachidis V., Kotsiopoulos P. Development of a Two-Dimensional Streamline Curvature Code. ASME J. Turbomachinery. 2011; 133(1): 1–7.

21. Smith Jr. LH. The Radial-Equilibrium Equation of Turbomachinery. Trans. ASME J. Engineering for Power. 1966; 88(1): 1–12.

22. Marsh H. A digital computer program for the through-flow fluid mechanics in an arbitrary turbomachine using a matrix method. Aeronautical Research Council Reports and Memoranda. Ministry of Technology; National Gas Turbine Establishment, London, United Kingdom: R. & M. No. 3509; 1968. pp. 1–34.

23. Tiwari P., Stein A., Lin Y-L. Dual-Solution and Choked Flow Treatment in a Streamline Curvature Throughflow Solver. ASME J. Turbomachinery. 2013; 135(4): 1–11.

24. Sayari N., Bolcs A. A New Throughflow Approach For Transonic Axial Compressor Stage Analysis. ASME 1995 Int. Gas Turbine and Aeroengine Congress and Exposition. 5-8 June, Houston, Texas, United States of America: 95-GT-195; 1995. pp. 1–12.

25. Reed JA., Afjeh AA. Development of a Protoype Simulation Executive with Zooming in the Numerical Propulsion System Simulation. NASA Contract Report. University of Toledo, Mechanical Engineering Deparment, Toledo, Ohio, United States of America: NASA CR-200613; 1995. pp. 1–66.

26. Reed JA., Turner MG., Norris A., Veres JP. Towards an Automated Full-Turbofan Engine Numerical Simulation. NASA Technical Memorandum; XVI Int. Symposium on Air Breathing Engines 2003. Glenn Research Center, Cleveland, Ohio, United States of America; 31 August-5 September, Cleveland, Ohio, United States of America: NASA/TM-2003-212494; 2003. pp. 1–16.

27. Turner MG., Reed JA., Ryder R., Veres JP. Multi-Fidelity Simulation of a Turbofan Engine With Results Zoomed Into Mini-Maps for a Zero-D Cycle Simulation. NASA Technical Memorandum; ASME Turbo Expo 2004: Power for Land, Sea and Air. Glenn Research Center, Cleveland, Ohio, United States of America; 14-17 June, Vienna, Austria: NASA TM-2004-213076; GT2004-53956; 2004. pp. 1–18.

28. Pachidis V., Pilidis P., Talhouarn F., Kalfas A., Templalexis I. A Fully Integrated Approach to Component Zooming Using Computational Fluid Dynamics. ASME J. Engineering for Gas Turbines and Power. 2006; 128(3): 579–584.

29. Pachidis V., Pilidis P., Texeira J., Templalexis I. A comparison of component zooming simulation strategies using streamline curvature. Proceedings IMechE Part G: J. Aerospace Engineering. 2006; 221(5): 1–15.

30. Adamczyk JJ. Aerodynamic Analysis of Multistage Turbomachinery Flows in Support of Aerodynamic Design. ASME Int. Gas Turbine & Aeroengine Congress & Exhibition. 7-10 July, Indianapolis, Indiana, United States of America: PP-GT-80; 1999. pp. 1–40.

31. Templalexis I., Pilidis P., Pachidis V., Kotsiopoulos P. Development of a 2-D Compressor Streamline Curvature Code. ASME Turbo Expo 2006: Power for Land, Sea and Air. 8-11 May, Barcelona, Spain: GT2006-90867; 2006. pp. 1–10.

32. Biollo R., Benini E. Recent Advances in Transonic Axial Compressor Aerodynamics. Progress in Aerospace Sciences. 2013; 56(1): 1–18.

33. Wright LC., Vitale NG., Ware TC., Erwin JR. High-Tip-Speed Low-Loading Transonic Fan Stage. NASA Contract Report. NASA Lewis Research Center, Cleveland, Ohio, United States of America: NASA CR-121095; 1973. pp. 1–171.

34. Bloch GS., Copenhaver WW., O'Brien WF. A Shock Loss Model for Supersonic Compressor Cascades. Trans. ASME J. Turbomachinery. 1999; 121(1): 28–35.

35. Boyer KM., O'Brien WF. An Improved Streamline Curvature Approach for Off-Design Analysis of Transonic Axial Compression Systems. ASME Turbo Expo

2002: Power for Land, Sea and Air. 3-6 June, Amsterdam, The Netherlands: GT-2002-30444; 2002. pp. 1–9.

36. Boyer KM., O'Brien WF. An Improved Streamline Curvature Approach for Off-Design Analysis of Transonic Axial Compression Systems. Trans. ASME J. Turbomachinery. 2003; 125(3): 475–481.

37. Wennerstrom AJ., Frost GR. Design of a 1500 Ft/Sec, Transonic, High-through-Flow, Single-Stage Axial-Flow Compressor with Low Hub/Tip Ratio. Technical Report. Air Force Aero Porpulsion Laboratory, Wright-Patterson Air Force Base, Ohio, United States of America: AFAPL-TR-76-59; 1974. pp. 1–298.

38. Cunnan WS., Stevans W., Urasek DC. Design and Performance of a 427-Meter-Per-Second-Tip-Speed Two-Stage Fan Tip-Speed Two-Stage Fan Having a 2.40 Pressure Ratio. NASA Technical Paper. Lewis Research Center, Cleveland, Ohio, United States of America: NASA TP-1314; 1978. pp. 1–94.

39. Morris AL., Halle JE., Kennedy E. High-Loading, 1800 ft/sec Tip Transonic Compressor Fan Stage I. Aerodynamic and Mechanical Design. NASA Contract Report. NASA Lewis Research Center, Cleveland, Ohio, United States of America: NASA CR-120907; 1972. pp. 1–114.

40. Strazisar AJ., Wood JR., Hathaway MD., Suder KL. Laser Anemometer Measurements in a Transonic Axial-Flow Fan Rotor. NASA Technical Paper. Lewis Research Center, Cleveland, Ohio, United States of America: NASA TP-2879; 1989. pp. 1–214.

41. Pachidis V., Pilidis P., Templalexis I., Marinai L. An Iterative Method for Blade Profile Loss Model Adaptation Using Streamline Curvature. ASME J. Engineering for Gas Turbines and Power. 2008; 130(1): 1–8.

42. Smith Jr. LH. Axial Compressor Aerodesign Evolution at General Electric. ASME J. Turbomachinery. 2002; 124(3): 321–330.

43. Gallimore SJ. Axial Flow Compressor Design. Proceedings IMechE Part C: J. Mechanical Engineering Science. 1998; 213(C1 & C2): 437–449.

44. Hah C., Shin H-W. Study of Near-Stall Flow Behavior in a Modern Transonic Fan with Compound Sweep. ASME J. Fluids Engineering. 2012; 134(7): 1–7.

45. Creveling HF., Carmody RH. Axial Flow Compressor Computer Program for Calculating Off-Design Performance (Program IV). NASA Contract Report. Lewis Research Center, Cleveland, Ohio, United States of AmERICA: CR-72427; EDR-5898; 1968. pp. 1–258.

46. Barbosa JR. A Streamline Curvature Computational Programme for Axial Compressor Performance Prediction. PhD Thesis. Cranfield Institute of Technology, School of Mechanical Engineering, Cranfield, United Kingdom; 1987. pp. 1–183.

47. Sena de Jesus G., Barbosa JR., Ramsden KW. A Comparison of Loss Models Using Different Radial Distribution of Loss in an Axial Turbine Streamline Curvature Program. ASME Turbo Expo 2007: Power for Land, Sea and Air. 14-17 May, Montreal, Canada: GT2007-27641; 2007. pp. 1–8.

48. Pachidis V., Pilidis P., Templalexis I., Marinai L. An Iterative Method for Blade Profile Loss Model Adaptation Using Streamline Curvature. ASME Turbo Expo 2007: Power for Land, Sea and Air. 14-17 May, Montreal, Canada: GT2007-27402; 2007. pp. 1–11.

49. Chung J., Shim J., Lee KD. Design of 3D Transonic Compressor Blades using Numerical Optimization. AIAA 38th Aerospace Sciences Meeting & Exhibit. 10-13 January, Reno, Nevada, United States of America: AIAA-2000/0227; 2000. pp. 1–10.

50. Wadia AR., Copenhaver WW. An investigation of the Effect of Cascade Area Ratios on Transonic Compressor Performance. Trans. ASME J. Turbomachinery. 1996; 118(4): 760–770.

51. Chen N., Zhang H., Xu Y., Huang W. Blade Parameterization and Aerodynamic Design Optimization for a 3D Transonic Compressor Rotor. J. Thermal Science. May 2007; 16(2): 105–114.

52. Suder KL., Chima R V., Strazisar AJ., Roberts WB. The Effect of Adding Roughness and Thickness to a Transonic Axial Compressor Rotor. NASA Technical Memorandum. Lewis Research Center, Cleveland, Ohio, United States of America: NASA TM-106958; 1994. pp. 1–22.

53. Burguburu S., Toussaint C., Bonhomme C., Leroy G. Numerical Optimization of Turbomachinery Bladings. ASME J. Turbomachinery. 2004; 126(1): 91–100.

54. Lian Y., Liou M-S. Multi-Objective Optimization of Transonic Compressor Blade using Evolutionary Algorithm. AIAA J. Propulsion and Power. 2005; 21(6): 979–987.

55. Luo J., Zhou C., Liu F. Multipoint Design Optimization of a Transonic Compressor Blade by Using an Adjoint Method. Trans. ASME J. Turbomachinery. 2014; 136(5): 1–10.

56. Wang XD., He L., Li YS., Wells RG. Adjoint Aerodynamic Design Optimization for Blades in Multistage Turbomachines - Part II: Validation and Application. Trans. ASME J. Turbomachinery. 2010; 132(2): 1–11.

57. Oyama A., Liou M-S., Shigeru O. Transonic Axial-Flow Blade Optimization: Evolutionary Algorithms/Three-Dimensional Navier-Stokes solver. AIAA J. Propulsion and Power. 2004; 20(4): 612–619.

58. Prince Jr. DC. Three-Dimensional Shock Structures for Transonic/Supersonic Compressor Rotors. AIAA J. Of Aircraft. 1980; 17(1): 28–37.

59. Gui X., Zhu F., Wan K., Jin D. Effects of Inlet Circumferential Fluctuation on the Sweep Aerodynamic Performance of Axial/Fans Compressors. J. Thermal Science. 2013; 22(5): 383–394.

60. Yamaguchi N., Tominaga T., Hattori S., Misuhashi T. Aerodynamic Effects of Blade Swep and Skew in Low-Speed Axial Flow Rotors at the Design Flow Rate: An Overview. Proceesdings of Yokohama Int. Gas Turbine Congress. N/A: N/A; 1991. pp. 61–68.

61. Gallimore SJ., Bolger JJ., Cumpsty NA., Taylor MJ., Wright PI., Place JMM.

The Use of Sweep and Dihedral in Multistage Axial Flow Compressor Blading: Part II — Low and High Speed Designs and Test Verification. ASME Turbo Expo 2002: Power for Land, Sea and Air. 3-6 June, Amsterdam, The Netherlands: GT-2002-30329; 2002. pp. 49–59.

62. Gallimore SJ., Bolger JJ., Cumpsty NA., Taylor MJ., Wright PI., Place JMM. The Use of Sweep and Dihedral in Multistage Axial Flow Compressor Blading—Part I: University Research and Methods Development. ASME J. Turbomachinery. 2002; 124(4): 521–532.

63. Passrucker H., Engber M., Kablitz S., Hennecke DK. Effect of Forward Sweep in a Transonic Compressor Rotor. Proceedings IMechE Part A: J. Power and Energy. 2003; 217(A4): 357–365.

64. Wadia AR., Szucs PN., Crall DW. Inner Workings of Aerodynamic Sweep. Trans. ASME J. Turbomachinery. 1998; 120(1): 671–682.

65. Hah C., Puterbaugh SL., Wadia AR. Contol of Shock Structure and Secondary Flow Field Inside Transonic Compressor Rotors Through Aerodynamic Sweep. ASME Int. Gas Turbine & Aeroengine Congress & Exhibition. 2-5 June, Stockholm, Sweden: 98-GT-561; 1998. pp. 1–15.

66. Templalexis I., Pachidis V., Pilidis P., Kotsiopoulos P. The Effect of Upstream Duct Boundary Layer Growth and Compressor Blade Lean Angle Variation on an Axial Compressor Performance. Proceedings IMechE Part G: J. Aerospace Engineering. 1 August 2010; 224(8): 927–935.

67. Denton JD., Xu L. The Efects of Lean and Swep on Transonic Fan Performance. ASME Turbo Expo 2002: Power for Land, Sea and Air. 3-6 June, Amsterdam, The Netherlands: GT-2002-30327; 2002. pp. 23–32.

68. Denton JD. The effects of lean and sweep on transonic fan performance: a computational study. Task Quarterly. 2002; 6(1): 7–23.

69. Ramakrishna P V., Govardhan M. On Loading Corrections and Loss Distributions in Low-Speed Forward Swept Axial Compressor Rotors.

Proceedings IMechE Part A: J. Power and Energy. 2010; 225(1): 120–130.

70. Vad J. Aerodynamic Effects of Blade Sweep and Skew in Low-Speed Axial Flow Rotors at the Design Flow Rate: An Overview. Proceedings IMechE Part A: J. Power and Energy. 2008; 222(A1): 69–85.

71. Ramakrishna P V., Govardhan M. Study of Sweep and Induced Dihedral Effects in Subsonic Axial Flow Compressor Passages - Part I: Design Considerations - Changes in Incidence, Deflection, and Streamline Curvature. Int. J. Rotating Machinery. 2009; 2009(ID 787145): 1–11.

72. Chen NX., Zhang HW., Huang WG. Aerodynamic Sweeping Study and Design for Transonic Compressor Rotor Blades. J. Thermal Science. 2010; 19(4): 295–299.

73. Razavi SR., Boroomand M. Numerical and Performance Analysis of One Row Transonic Rotor with Sweep and Lean Angle. J. Thermal Science. 2014; 23(5): 438–445.

74. Reid L., Moore RD. Design and Overall Performance of Four Highly Loaded, High-Speed Inlet Stages for an Advanced High-Pressure-Ratio Core Compressor. NASA Technical Paper. Lewis Research Center, Cleveland, Ohio, United States of America: nasa tp-; 1978.

75. Jang C-M., Li P., Kim K-Y. Optimization of Blade Sweep in a Transonic Axial Compressor Rotor. JSME Int. J. Series B. 2005; 48(4): 793–801.

76. Jang C-M., Samad A., Kim K-Y. Optimal Design of Swept, Leaned and Skewed Blades in a Transonic Axial Compressor. ASME Turbo Expo 2006: Power for Land, Sea and Air. 8-11 May, Barcelona, Spain: GT2006-90384; 2006. pp. 1–10.

77. Okui H., Verstraete T., Van den Braembussche RA., Alsalihi Z. Three-Dimensional Design and Optimization of a Transonic Rotor in Axial Flow Compressors. ASME J. Turbomachinery. 2013; 135(3): 1–11.

78. Copenhaver WW. The Effect of Tip Clearance on a Swept Transonic Compressor Rotor. Trans. ASME J. Turbomachinery. 1996; 118(2): 230–229.

79. Puterbaugh SL., Copenhaver WW., Hah C., Wennerstrom AJ. A Three-Dimensional Shock Loss Model Applied to an Aft-Swept , Transonic Compressor Rotor. ASME J. Turbomachinery. 1997; 119(3): 452–459.

80. Gümmer V., Wenger U., Kau H-P. Using Sweep and Dihedral to Control Three-Dimensional Flow in Transonic Stators of Axial Compressors. Trans. ASME J. Turbomachinery. 2001; 123(1): 40–48.

81. Hah C., Shin H-W. Study of Near-Stall Flow Behavior in a Modern Transonic Fan with Composite Sweep. XX Int. Symposium on Air Breathing Engines 2011. 12-16 September, Gothenburg, Sweden: ISABE-2011-1220; 2011. pp. 1–11.

82. Gui X., Zhu F., Wan K., Jin D. Effects of Inlet Circumferential Fluctuation on the Sweep Aerodynamic Performance of Axial Fans/Compressors. J. Thermal Science. 2013; 22(5): 383–394.

83. Corsini A., Rispoli F. Using Sweep to Extend the Stall-free Operational Range in Axial Fan Rotors. Proceedings IMechE Part A: J. Power and Energy. 2004; 218(A3): 129–139.

84. Breugelmans FAH., Carels Y., Demuth M. Influence of Dihedral on the Secondary Flow in a Two-Dimensional Cascade. Trans. ASME J. Turbomachinery. 1984; 106(3): 578–584.

85. Sasaki T., Breugelmans FAH. Comparison of Sweep and Dihedral Effects on Compressor Cascades. ASME 1997 Int. Gas Turbine and Aeroengine Congress and Exhibition. 2-5 June, Orlando, Florida, United States of America: 97-GT-2; 1997. pp. 1–12.

86. Pachidis V., Pilidis P., Templalexis I., Barbosa JB., Nantua N. A De-Coupled Approach to Component High-Fidelity Analysis Using Computational Fluid Dynamics. Proceedings IMechE Part G: J. Aerospace Engineering. 2007; 221(G1): 105–113.

87. Follen G., AuBuchon M. Numerical Zooming Between a NPSS Engine System Simulation and a One-Dimensional High Compressor Analysis Code. NASA

Technical Memorandum; Computational Aerosciences Workshop 2000. Glenn Research Center, Cleveland, Ohio, United States of America; 15-17 February, Moffett Field, California, United States: NASA TM-2000-209913; 2000. pp. 1–18.

88. Adamczyk JJ. Simulation of Dynamic Models. NASA Report. NASA Lewis Research Center, Cleveland, Ohio, United States of America: N91-21069; 2013. pp. 119–126.

89. Wu C-H. A General Theory of Three-Dimensional Flow in Subsonic and Supersonic Turbomachines of Axial, Radial and Mixed-Flow Types. NACA Technical Note. Lewis Flight Propulsion Laboratory, Cleveland, Ohio, United States of America: NACA TN 2604; 1952. pp. 1–93.

90. Hirsch C., Denton JD. Through Flow Calculations in Axial Turbomachines. NATO Advisory Group for Aerospace Research and Development Report. Neuilly sur Seine, France: AGARD-AR-175; 1981. pp. 1–342.

91. Dawes WN. Computation of Viscous Compressible Flow in Blade Cascades Using an Implicit Iterative Replacement Algorithm. Proceedings IMechE Conference Computational Methods in Turbomachinery. 1984; 3: 157–164.

92. Davis RL., Hobbs DE., Weingold HD. Prediction of Compressor Cascade Performance Using a Navier-Stokes Technique. Trans. ASME J. Turbomachinery. 1988; 110(4): 520–531.

93. Hansen EC. Blade-Surface Boundary Layer and Wake Computational Models for Estimation of Axial-Flow Compressor and Fan Blade-Row Fluid Turning Angles and Losses. PhD Thesis. Iowa State University, Iowa, United States of America; 1978. pp. 1–140.

94. Drela M., Giles MB. Viscous-Inviscid Analysis of Transonic and Low Reynolds Number Airfoils. AIAA Journal. 1987; 25(10): 1347–1355.

95. Adamczyk JJ. Model Equation for Simulating Flows in Multistage Turbomachinery. NASA Technical Memorandum. Lewis Research Center,

Cleveland, Ohio, United States of AmERICA: NASA TM 86869; 1984. pp. 1–35.

96. Denton JD. The Calculation of Three Dimensional Viscous Flow Through Multistage Turbomachines. Trans. ASME J. Turbomachinery. 1992; 114(1): 1–10.

97. Rhie CM., Gleixner AJ., Spear DA., Fischberg CJ., Zacharias RM. Development and Application of a multistage Navier-Stokes solver. Part I: multistage modelling using body forces and deterministic stresses. ASME 1995 Int. Gas Turbine and Aeroengine Congress and Exposition. 5-8 June, Houston, Texas, United States of America: 95-GT-342; 1995. pp. 1–14.

98. Howell AR. Fluid dynamics of axial compressors. Proceedings of the IMechE. 1945; 153(1): 441–452.

99. Wu CH., Wolfenstein L. Application of radial-equilibrium condition to axial-flow compressor and turbine design. NACA Report. Lewis Flight Propulsion Laboratory, Cleveland, Ohio, United States of America: NACA Report 955; 1949. pp. 1–31.

100. Hamrick JT., Ginsburg A., Osborn WM. Method of Analysis for Compressible Flow Through Mixed-Flow Centrifugal Impellers of Arbitrary Design. NACA Technical Report. Lewis Flight Propulsion Laboratory, Cleveland, Ohio, United States of America: NACA TR 1082; 1952. pp. 513–522.

101. Wright LC., Kovach K. Design Procedure and Limited Test Results for a High Solidity, 12-inch Transonic Impeller with Axial Discharge. NACA Research Memorandum. Lewis Flight Propulsion Laboratory, Cleveland, Ohio, United States of America: NACA RM E53B09; 1953. pp. 1–37.

102. Wright LC., Novak RA. Aerodynamic Design and Development of the General Electric CJ805-23 Aft-Fan. ASME Conference Proceedings. ASME Paper 60-WA-270; 1960.

103. Swan WC. A Practical Method of Predicting Transonic-Compressor

Performance. Trans. ASME J. Power. 1961; 83(3): 322–330.

104. Silvester MD., Hetherington R. A numerical solution of the three-dimensional compressible flow through axial turbomachinery in numerical analysis. Numerical Analysis - an Introduction. Oxford Academic Press; 1966.

105. Frost GR., Hearsey RM., Wennerstrom AJ. A Computer Program for the Specification of Axial Compressor Airfoils. ARL Report. Aerospace Research Laboratories, Air Force Systems Command, Wright-Patterson Air Force Base, Dayton, Ohio, United States of America: ARL 72-0171; NTIS AD-785 879; 1972. pp. 1–158.

106. Novak RA. Streamline Curvature Computing Procedures for Fluid-Flow Problems. Trans. ASME J. Engineering for Gas Turbines and Power. 1967; 89(4): 478–490.

107. Crouse JE., Junetzke DC., Schwirian RE. A Computer Program for Composing Compressor Blading from Simulated Circular-Arc Elements on Conical Surfaces. NASA Technical Note. Lewis Research Center, Cleveland, Ohio, United States of America: NASA TN D-5437; 1969. pp. 1–82.

108. Hearsey RM. A computer Program for Axial Compressor design, Vol. 1: Theory Descriptions, and users Instructions. Technical Report. Dayton University, Cincinnati, Ohio, United States of America: AFAPL-TR-73-66-VOL-1; 1973.

109. Hearsey RM. A Computer Program for Axial Compressor Design, Vol. 1: Theory Descriptions, and User Instructions. Technical Report. Dayton University, Cincinnati, Ohio, United States of America: AD-A 009273; 1975.

110. Glenny DE. An Application of Streamline Curvature Methods to the Calculations of Flow in a Multistage Axial Compressor. Mechanical Engineering Note. Australian Defense Scientific Service, Aeronautical Research Laboratories: ARL/ME 346; 1974.

111. Denton JD. Through-flow calculations for transonic axial flow turbines. Trans. ASME J. Engineering for Power. 1978; 100(2): 212–218.

112. Jennions IK., Stow P. The Quasi-Three-Dimensional Turbomachinery Blade Design System, Part I: Through-Flow Analysis. Trans. ASME J. Engineering for Gas Turbines and Power. 1985; 107(2): 308–314.

113. Ucer AS., Shreeve RP. A Viscous Axisymmetric Throughflow Prediction Method for Multi-Stage Compressors. ASME Int. Gas Turbine & Aeroengine Congress & Exposition. 1-4 June, Cologne, Germany: 92-GT-293; 1992. pp. 1–11.

114. Zhu XC., Hu JF., Ou-Yang H., Tian J., Qiang XQ., Du ZH. The Off-Design Performance Prediction of Axial Compressor Based on a 2D Approach. J. Theoretical and Applied Mechanics. 2013; 51(3): 523–531.

115. Limited R-R. A Suite of Programs for the Aerodynamic Design Analysis of Axial Flow Turbomachines. Program Logic Manuals. Derby, United Kingdom: Volume III; pp. 1–51.

116. Pachidis V., Templalexis I., Pilidis P., Kotsiopoulos P. A Dynamic Convergence Control Scheme for the Solution of the Radial Equilibrium Equation in Through-flow Analyses. Proceedings IMechE Part G: J. Aerospace Engineering. 2009; 224(G7): 803–815.

117. Pachidis V., Templalexis I., Pilidis P., Kotsiopoulos P. A dynamic convergence control scheme for the solution of the radial equilibrium equation in through-flow analyses. Proceedings of the Institution of Mechanical Engineers, Part G: Journal of Aerospace Engineering. 1 July 2010; 224(7): 803–815.

118. Templalexis I. The Importance of Force Terms Modeling Within the Streamline Curvature Through-Flow Method. Proceedings IMechE Part A: J. Power and Energy. 20 June 2014; 228(7): 825–835.

119. Lieblein S., Schwenk FC., Broderick RL. Diffusion Factor for Estimating Losses and Limiting Blade Loadings in Axial-Flow Compressor Blade Elements. NACA Research Memorandum. Lewis Flight Propulsion Laboratory, Cleveland, Ohio, United States of America: NACA RM E53D01; 1953. pp. 1–43.

120. Lieblein S. Review of High-Performance Axial-Flow-Compressor Blade-Element Theory. NACA Research Memorandum. Lewis Flight Propulsion Laboratory, Cleveland, Ohio, United States of America: NACA RM E53L22; 1954. pp. 1–34.

121. Johnsen IA., Bullock RO. Aerdoynamic Design of Axial-Flow Compressors. NASA Single Research Memorandum Volume. Lewis Research Center, Cleveland, Ohio, United States of America: NASA SP-36; 1965. pp. 1–508.

122. Lieblein S. Aerodynamic Design of Axial-Flow Compressors. NASA Special Publication. Washington, D.C., United States of America: NASA SP-36 Chapter VI; 1965. pp. 183–226.

123. Wennerstrom AJ. Highly Loaded Axial Flow Compressors : History and Current Developments. ASME J. Turbomachinery. 1990; 112(4): 567–578.

124. Deutsch S., Zierke WC. The Measurement of Boundary Layers on a Compressor Blade in Cascade at High Positive Incidence Angle II - Data Report. NASA Contract Report. Applied Research Laboratory, Pennsylvania State University, Stage College, Pennsylvania, United States of America: NASA CR-179492; 1986. pp. 1–113.

125. Zierke WC., Deutsch S. The Measurement of Boundary Layers on a Compressor Blade in Cascade Volume II - Data Tables. NASA Contract Report. Applied Research Laboratory, Pennsylvania State University, Stage College, Pennsylvania, United States of America: NASA CR-185118; 1989. pp. 1–209.

126. Fuchs R., Steinert W., Starken H. Transonic Compressor Rotor Cascade With Boundary-Layer Separation Experimental and Theoretical Results. ASME 1993 Int. Gas Turbine and Aeroengine Congress and Exposition. 24-27 May, Cincinnati, Ohio, United States of America: 93-GT-405; 1993. pp. 1–9.

127. Deutsch S., Zierke WC. The Boundary Layer on Compressor Cascade Blades. NASA Contract Report. Applied Research Laboratory, Pennsylvania State University, Stage College, Pennsylvania, United States of America: NASA CR-173514; 1983. pp. 1–76.

128. Deutsch S., Zierke WC. The Measurement of Boundary Layers on a Compressor Blade in Cascade at High Positive Incidence Angle I - Experimental Techniques and Results. NASA Report. Applied Research Laboratory, Pennsylvania State University, Stage College, Pennsylvania, United States of America: NASA CR-179491; 1986. pp. 1–61.

129. Deutsch S., Zierke WC. The Boundary Layer on Compressor Cascade Blades. Semi-Annual Progress Report. Applied Research Laboratory, Pennsylvania State University, Stage College, Pennsylvania, United States of America; 1986. pp. 1–20.

130. Hoheisel H., Seyb NJ. The Boundary Layer Behaviour of Highly Loaded Compressor Cascade at Transonic Flow Conditions. Report. Defense Technical Information Center, Fort Belvoir, Virginia, United States of America: ADP005508; 1987. pp. 1–17.

131. Deutsch S., Zierke WC. The Measurement of Boundary Layers on a Compressor Blade in Cascade Volume I - Experimental Technique, Analysis and Results. NASA Contract Report. Applied Research Laboratory, Pennsylvania State University, Stage College, Pennsylvania, United States of America: NASA CR-185118; 1988. pp. 1–223.

132. Suder KL. Experimental Investigation of the Flow Field in a Transonic, Axial Flow Compressor with Respect to the Development of Blockage and Loss. NASA Technical Memorandum. Lewis Research Center, Cleveland, Ohio, United States of AmERICA: NACA TM 107310; 1996. pp. 1–269.

133. Suder KL. Blockage Development in a Transonic, Axial Compressor Rotor. Trans. ASME J. Turbomachinery. 1998; 120(3): 465–476.

134. Wennerstrom AJ. A Review of Predictive Efforts for Transport Phenomena in Axial. 1991; 113(2): 175–179.

135. Cahill JE. Identification and Evaluation of Loss and Deviation Models for Use in Transonic Compressor Stage Performance Prediction. MSc Thesis. Virginia

Polythenic Institute and State University, Blacksburg, Virginia, United States of America; 1997. p. 83.

136. Aungier RH. Axial-Flow Compressors. 1st edn. New York, New York, United States of America: ASME Press; 2003. 368 p.

137. Lieblein S. Analysis of Experimental Low-Speed Loss and Stall Characteristics of Two-Dimensional Compressor Blade Cascades. NACA Research Memorandum. NACA RM E57A28; 1957. pp. 1–32.

138. Jansen W., Moffatt WC. The Off-Design Analysis of Axial-Flow Compressors. Trans. ASME J. Engineering for Power. 1967; 89(4): 453–462.

139. Dettmering W. Machzahleninfluss aur fie Verdichterscharakteristik. Z. Flujwiss. 1971; 19(1): 145–150.

140. Koch CC., Smith Jr. LH. Loss Sources and Magnitudes in Axial-Flow Compressors. Trans. ASME J. Engineering for Power. 1976; 98(3): 411–424.

141. Cetin M., Ucer AS., Hirsch C., Serovy GK. Application of Modified Loss and Deviation Correlations to Transonic Axial Compressors. NATO Advisory Group for Aerospace Research and Development Report. Neuilly sur Seine, France: AGARD-R-745; 1987. pp. 1–74.

142. Lieblein S. Incidence and Deviation-Angle Correlations for Compressor Cascades. Trans. ASME J. of Basic Engineering. 1960; 82(3): 575–584.

143. Herrig JL., Emery JC., Erwin JR. Systematic Two-Dimensional Cascade Tests of Naca 65-Series Compressor Blades at Low Speeds. NACA Technical Note. Langley Aeronautical Laboratory, Langley Field, Virginia, United States of America: NACA TN 3916; 1957. p. 226.

144. Constant H. Performance of Cascades of Aerofoils. Note. British RAE: No. E3696; 1939.

145. Carter ADS. The Low Speed Performance of Related Aerofoils in Cascades. Aeronautical Research Council Current Papers. Ministry of Supply; National Gas

Turbine Establishment, London, United Kingdom: CP No. 29, Report No. R.55; 1949. pp. 1–44.

146. Carter ADS., Hughes HP. A Theoretical Investigation Into the Effect of Profile Shape on the Performance of Aerofoils in Cascade. Aeronautical Research Council Reports and Memoranda. Ministry of Supply; National Gas Turbine Establishment, London, United Kingdom: R. & M. No. 2384; 1946.

147. Pollard D., Gostelow JP. Some Experiments at Low Speed on Compressor Cascades. Trans. ASME J. Engineering for Power. 1967; 89(3): 427–436.

148. Lieblein S. Loss and Stall Analysis of Compressor Cascades. Trans. ASME J. of Basic Engineering. 1959; 81(1): 387–400.

149. Chauvin J., Weyer H. Through-flow Calculations in Axial Turbomachinery. NATO Advisory Group for Aerospace Research and Development Report. Neuilly sur Seine, France: AGARD-CP-195; 1977. pp. 1–242.

150. Koning WM., Hennecke DK., Fottner L. Improved Blade Profile Loss and Deviation Angle Models for Advanced Transonic Compressor Bladings : Part I — A Model for Subsonic Flow. ASME 1994 Int. Gas Turbine and Aeroengine Congress and Exposition. 13-16 June, The Hague, Netherlands: 94-GT-335; 1994. pp. 1–9.

151. Koning WM., Hennecke DK., Fottner L. Improved Blade Profile Loss and Deviation Angle Models for Advanced Transonic Compressor Bladings : Part I — A Model for Subsonic Flow. ASME J. Turbomachinery. 1996; 118(1): 73–80.

152. Koning WM., Hennecke DK., Fottner L. Improved Blade Profile Loss and Deviation Angle Models for Advanced Transonic Compressor Bladings : Part II — A Model for Supersonic Flow. ASME 1994 Int. Gas Turbine and Aeroengine Congress and Exposition. 13-16 June, The Hague, Netherlands: 94-GT-336; 1994. pp. 1–8.

153. Koning WM., Hennecke DK., Fottner L. Improved Blade Profile Loss and Deviation Angle Models for Advanced Transonic Compressor Bladings : Part II

— A Model for Supersonic Flow. ASME J. Turbomachinery. 13-16 June, The Hague, Netherlands; 1996; 1(118): 81–87.

154. Fottner L. A Semi-Empirical Approach of the Transonic Flow Past Cascades Including Shock and Viscous Effects. NATO Advisory Group for Aerospace Research and Development Report. Neuilly sur Seine, France: AGARD-CP-34; 1968. pp. 1–101.

155. Koning WM., Hennecke DK. Improved Blade Profile Loss and Deviation Angle Models for Advanced Transonic Compressor Bladings: PART II - A Model for Supersonic Flow. ASME 1994 Int. Gas Turbine and Aeroengine Congress and Exposition. 13-16 June, The Hague, Netherlands: 94-GT-336; 1994. pp. 1–8.

156. Hearsey RM. Program HT0300 NASA. Report. Boeing Company: D6-81569TN; 1994.

157. Howard MA., Gallimore SJ. Viscous Throughflow Modeling for Multistage Compressor Design. ASME Int. Gas Turbine & Aeroengine Congress & Exposition. 1-4 June, Cologne, Germany: 92-GT-302; 1992. pp. 1–10.

158. Dunham J. A New Endwall Model for Axial Compressor Throughflow Calculations. Journal of Turbomachinery. 1995; 117(October 1995): 533.

159. Dunham J. Modelling of Spanwise Mixing in Compressor Through-Flow Computations. Proceedings IMechE Part A: J. Power and Energy. 1997; 211(3): 243–251.

160. Dunham J. Modelling of spanwise mixing in compressor through- flow computations. Journal of Power and Energy. 1997; 211(3): 243–251.

161. Dunham J. CFD Validation for Propulsion System Components. NATO Advisory Group for Aerospace Research and Development Report. Neuilly sur Seine, France: AGARD-AR-355; 1998. pp. 1–96.

162. Hu JF., Ou-Yang H., ZHu XC., Qiang XQ., Du ZH. An Improved Streamline Curvature Approach for Transonic Axial Compressor Performance Prediction. Proceedings IMechE Part G: J. Aerospace Engineering. 2010; 225(5): 575–584.

163. Hu JF., Zhu XC., OuYang H., Qiang XQ., Du ZH. Performance prediction of transonic axial compressor based on streamline curvature method. J. Mechanical Science and Technology. 2011; 25(12): 3037–3045.

164. Griepentrog H. Secondary Flow Losses in Transonic Compressors. NATO Advisory Group for Aerospace Research and Development Report. AGARD-LS-39-70; 1970. p. N/A.

165. Came PM. Streamline Curvature Throughflow Analysis. VDI-BER. Report 1185; 1975. pp. 1–291.

166. Horlock JH. On Entropy Production in Adiabatic Flow in Turbomachines. ASME J. Basic Engineering. 1971; 93(4): 587–593. Available at: http://fluidsengineering.asmedigitalcollection.asme.org/article.aspx?articleid=1435973

167. Horlock JH., Marsh H. Flow models for turbomachines. J. Mechanical Engineering Science. 1971; 13(5): 358–368.

168. Katsanis T. Use of Arbitrary Quasi-Orthogonals for Calculating Flow Distribution in the Meridional Plane of a Turbomachine. NASA Technical Note. Lewis Research Center, Cleveland, Ohio, United States of AmERICA: NASA TN D-2546; 1964. pp. 1–46.

169. Wilkinson DH. Stability, Convergence, and Accuracy of Two-Dimensional Streamline Curvature Methods Using Quasi-Orthogonals. Proceedings IMechE Conference Proceedings. 1969; 184(7): 108–126.

170. Shan P. A Mass Addition Approach to the Bypass Turbomachine Through Flow Inverse Design Problem. J. Mechanical Science and Technology. 2008; 22(10): 1921–1925.

171. Doulgeris GC., Khaleghi H., Kalfas A., Pilidis P. Development of a Method for Enhanced Fan Representation in Gas Turbine Modeling. Int. J. Rotating Machinery. 2011; 2011(ID 182906): 1–8.

172. Staff AR. Equations, Tables, and Charts for Compressible Flow. NACA Report.

AMES Aeronautical Laboratoy, Moffett Field, California, United States of America: Report 1135; 1953. p. 69.

173. Kundu PK., Cohen IM. Fluid Mechanics. 3rd edn. San Diego, Calfironia, United States of America: Elsevier Academic Press; 2004.

174. Staff AR. Notes and Tables for Use in the Analysis of Supersonic Flow. Technical Note. AMES Aeronautical Laboratoy, Moffett Field, California, United States of America: NACA TN 1428; 1947. pp. 1–86.

175. Moeckel WE., Connors JF. Charts for the Determination of Supersonic Air Flow Against Inclined Planes and Axially Symmetric Cones. NACA Technical Note. Flight Propulsion Research Laboratory, Cleveland, Ohio, United States of America: NACA TN 1373; 1947. pp. 1–38.

176. Ladenburg R., Van Voorhis CC., Winckler J. Interferometric Study of Supersonic Phenomena. Part I. A Supersonic Air Jet at 60 lb/sq in Tank Pressure. Report. Defense Technical Information Center, Fort Belvoir, Virginia, United States of America: AD0604112; 1946. pp. 1–132.

177. Crocco L. Singolarita della corrente gassosa iperacustica nell'intorno di una prora a diedro. L'Aerotecnica. 1937; 17(6): 519–534.

178. Busemann A. A Review of Analytical Methods for the Treatment of Flows with Detached Shocks. NACA Technical Note. Langley Aeronautical Laboratory, Langley Field, Virginia, United States of America: NACA TN 1858; 1949. pp. 1–23.

179. Laitone E V., Pardee OO. Location of Detached Shock Wave in Front of a Body Moving at Supersonic Speeds. AMES Aeronautical Laboratoy, Moffett Field, California, United States of America: NACA RM A7B10; 1947. pp. 1–20.

180. Moeckel WE. Approximate Method for Predicting Form and Location of Detached Shock Waves Ahead of Plane or Axially Symmetric Bodies. NACA Technical Note. Lewis Flight Propulsion Laboratory, Cleveland, Ohio, United States of America: NACA TN 1921; 1949. pp. 1–32.

181. Hawthorne WR. Aerodynamics of Turbines and Compressors. 1st edn. Princeton, New Jersey, United States of America: Princeton University Press; 1964. 1-616 p.

182. Weise A. Uberschallaxialverdichter. Bericht 171 der Lilienthal-Gesellschaft. 1939. pp. 92–109.

183. Kantrowitz A. The Supersonic Axial-Flow Compressor. NACA Report. Langley Memorial Aeronautical Laboratory, Hampton, Virginia, United States of America: NACA ACR L6D02; Report 974; 1946. pp. 473–481.

184. Starken H., Yongxing Z., Schreiber H-A. Mass Flow Limitation of Supersonic Blade Rows due to Leading Edge Blockage. ASME 1984 Int. Gas Turbine Conference and Exhibit. 4-7 June, Amsterdam, The Netherlands: 84-GT-233; 1984. pp. 1–7.

185. Levine P. The Two Dimensional Inflow Conditions for a Supersonic Compressor with Curved Blades. Technical Report. Wright Air Development Center, Aeronautical Research Laboratory, Wright-Patterson Air Force Base, Ohio, United States of America: WADC TR 55-387; 1956. pp. 1–27.

186. Creagh JWR. Performance Characteristics of an Axial-Flow Transonic Compressor Operating up To Tip Relative Inlet Mach Number of 1.34. NACA Research Memorandum. Lewis Flight Propulsion Laboratory, Cleveland, Ohio, United States of America: NACA RM E56D27; 1956. pp. 1–61.

187. Schwenk FC., Lieblein S., Lewis Jr. GW. Experimental Investigation of an Axial-Flow Compressor Inlet Stage Operating at Transonic Relative Inlet Mach Numbers III - Blade-Row Performance of Stage with Transonic Rotor and Subsonic Stator at Corrected Tip Speeds of 800 and 1000 feet per second. NACA Research Memorandum. Lewis Flight Propulsion Laboratory, Cleveland, Ohio, United States of America: NACA RM E53G17; 1953. pp. 1–69.

188. Sandercock DM., Lieblein S., Schwenk FC. Experimental Investigation of an Axial-Flow Compressor Inlet Stage Operating at Transonic Relative Inlet Mach

Numbers IV - Stage and Blade-Row Perfromance of Stage with Axial-Discharge Stators. NACA Research Memorandum. Lewis Research Center, Cleveland, Ohio, United States of America: NACA RM E54C26; 1954. pp. 1–51.

189. Montgometry JC., Glaser FW. Experimental Investigation of a 0.4 Hub-Tip Diameter Ratio Axial-Flow Compressor Inlet Stage at Transonic Inlet Relative Mach Numbers II - Stage and Blade-Element Performance. NACA Research Memorandum. Lewis Flight Propulsion Laboratory, Cleveland, Ohio, United States of America: NACA RM E54I29; 1955. pp. 1–48.

190. Lewis Jr. GW., Schwenk FC. Experimental Investigation of a Transonic Axial-Flow-Compresor Rotor with Double-Circular-Arc Airfoil Blade Sections II - Blade-Element Performance. NACA Research Memorandum. Lewis Flight Propulsion Laboratory, Cleveland, Ohio, United States of America: NACA RM E54J08; 2018. pp. 1–34.

191. Schwenk FC., Tysl ER. Experimental Investigation of a Transonic Compressor Rotor with a 1.5-Inch Chord Length and an Aspect Ratio of 3.0 II - Blade-Element Performance. NACA Research Memorandum. Lewis Flight Propulsion Laboratory, Cleveland, Ohio, United States of America: NACA RM E55F10; 1955. pp. 1–23.

192. Wright LC., Wilcox WW. Investigation of Two-Stage Counterrotating Compressor II - First-Rotor Blade-Element Performance. NACA Research Memorandum. Lewis Flight Propulsion Laboratory, Cleveland, Ohio, United States of America: NACA RM E56G09; 1956. pp. 1–37.

193. Schwenk FC., Lewis GW., Lieblein S. Experimental Investigation of an Axial-Flow Compressor Inlet Stage Operating at Transonic Relative Inlet Mach Numbers V - Rotor Blade-Element Performance at A Reduced Blade Angle. NACA Research Memorandum. Lewis Flight Propulsion Laboratory, Cleveland, Ohio, United States of America: NACA RM E56J17; 1957. pp. 1–45.

194. Schwenk FC., Lewis Jr. GW. Experimental Investigation of a Transonic Axial-Flow-Compressor Rotor with Double-Circular-Arc Airfoil Blade Sections III -

Comparison of Blade-Element Performance with Three Levels o Solidity. NACA Research Memorandum. Lewis Flight Propulsion Laboratory, Cleveland, Ohio, United States of America: NACA RM E55F01; 2018. pp. 1–46.

195. Tysl ER., Schwenk FC. xperimental Investigation of a Transonic Compressor Rotor with a 1.5-Inch Chord Length and an Aspect Ratio of 3.0 III - Blade-Element and Over-All Performance at Three Solidity Levels. NACA Research Memorandum. Lewis Flight Propulsion Laboratory, Cleveland, Ohio, United States of America: NACA RM E56D06; 2018. pp. 1–40.

196. Fessler TE., Hartmann MJ. Preliminary Survey of Compressor Rotor-Blade Wakes and Other Flow Phenomena with a Hot-Wire Anemometer. NACA Research Memorandum. Lewis Flight Propulsion Laboratory, Cleveland, Ohio, United States of America: NACA RM E56A13; 2018. p. 1959.

197. Lewis GW., Tysl ER., Fessler TE. Analysis of Transonic Rotor-Blade Passage Loss with Hot-Wire Anemometers. Research Memorandum. Lewis Flight Propulsion Laboratory, Cleveland, Ohio, United States of America: NACA RM E58C04; 1958. pp. 1–28.

198. Song DJ., Hwang HC., Kim YI. A Numerical Study of Shock Wave/Boundary Layer Interaction in a Supersonic Compressor Cascade. KSME Int. J. 2001; 15(3): 366–373.

199. Hilgenfeld L., Cardamone P., Fottner L. Boundary Layer Investigations on a Highly Loaded Transonic Compressor Cascade with Shock/Laminar Boundary Layer Interactions. Proceedings IMechE Part A: J. Power and Energy. 2003; 217(A4): 349–356.

200. Calvert WJ. An Inviscid-Viscous Interaction Treatment to Predict the Blade-to-Blade Performance of Axial Compressors with Leading Edge Normal Shock Waves. ASME 1982 Int. Gas Turbine Conference and Exhibit. 18-22 April, London, United Kingdom: 82-GT-135; 1982. pp. 1–12.

201. Song B., Song B. Experimental and Numerical Investigations of Optimized High-

Turning Supercritical Compressor Blades. PhD Thesis. Virginia Polythenic Institute and State University, Mechanical Engineering Department, Blacksburg, Virginia, United States of America; 2003. pp. 1–154.

202. Hah C., Wennerstrom AJ. Three-Dimensional Flowfields Inside a Transonic Compressor with Swept Blades. ASME 1990 Int. Gas Turbine and Aeroengine Congress and Exposition. 11-14 June, Brussels, Belgium: 90-GT-359; 1990. pp. 1–12.

203. Rabe DC., Wennerstrom AJ., O'Brien WF. Characterization of Shock Wave-Endwall Boundary Layer Interactions in a Transonic Compressor Rotor. Trans. ASME J. Turbomachinery. 1988; 110(3): 386–392.

204. Clark KP., Gorrell SE. Analysis and Prediction of Shock-Induced Vortex Circulation in Transonic Compressors. Trans. ASME J. Turbomachinery. 2015; 137(12): 1–10.

205. Schobeiri MT. Advanced Compressor Loss Correlations, Part II: Experimental Verifications. Int. J. Rotating Machinery. 1997; 3(3): 179–187.

206. Klapproth JF. Approximate Relative-Total-Pressure Losses of an Infinite Cascade of Supersonic Blades with Finite Leading-Edge Thickness. NACA Research Memorandum. Washington, D.C., United States of America: NACA RM E9L21; 1950. pp. 1–8.

207. Graham RC., Klapporth JF., Barina FJ. Investigation of Off-Design Performance of Shock-In-Rotor Type Supersonic Blading. NACA Research Memorandum. Lewis Flight Propulsion Laboratory, Cleveland, Ohio, United States of America: NACA RM E51C22; 1951. pp. 1–25.

208. Miller GR., Hartmann MJ. Experimental Shock Configurations and Shock Losses in a Transonic-Compressor Rotor at Design Speed. NACA Research Memorandum. Washington, D.C., United States of America: RM E58A14b; 1958. pp. 1–55.

209. Macchi E. Computer Program for Prediction of Axial Flow Turbine Performance.

Report. U.S. Naval Post-Graduate School: NPS-57Ma 70081a; 1970.

210. Vavra MH. Aero-thermodynamics and Flows in Turbomachines. 1st edn. New York, New York, United States of America: John Wiley & Sons, Inc.; 1960. 1-609 p.

211. Lichtfuss HJ., Starken H. Supersonic Exit Flow of Two-Dimensional Cascades. ASME 1972 Int. Gas Turbine and Fluids Engineering Conference and Products Show. 26-30 March, San Francisco, California, United States of America: 72-GT-49; 1972. pp. 1–17.

212. Simon H. A Contribution to the Theoretical and Experimental Examination of the Flow Through Plane Supersonic Deceleration Cascades and Supersonic Compressor Rotors. Trans. ASME J. Engineering for Power. 1973; 95(3): 233–243.

213. Hantman RG., Mikolajczak AA., Camarata FJ. Application of a Two-Dimensional Supersonic Passage Analysis to the Design of Compressor Rotors. ASME 1974 Int. Gas Turbine Conference and Products Show. 30 March-4 April, Zurich, Switzerland: 74-GT-97; 1974. pp. 1–12.

214. Gostelow JP. Review of Compressible Flow Theories for Airfoil Cascades. Trans. ASME J. Engineering for Power. 1973; 95(4): 281–292.

215. Lichtfuss HJ., Starken H. Supersonic Cascade Interaction. ASME 1974 Int. Gas Turbine Conference and Products Show. 30 March-4 April, Zurich, Switzerland: 74-GT-76; 1974. pp. 1–12.

216. York RE., Woodard HS. Supersonic Compressor Cascades-An Analysis of the Entrance Region Flow Field Containing Detached Shock Waves. Trans. ASME J. Engineering for Power. 1976; 98(2): 247–254.

217. Prince Jr. DC. Three-Dimensional Shock Structures for Transonic/Supersonic/ Compressor Rotors. 17th AIAA Aerospace Sciences Meeting. 15-17 January, New Orleans, Lousiana, United States of America: AIAA-79-0043; 1979. pp. 1–15.

218. York RE., Woodard HS. Flow in the Entrance Region of Supersonic Compressor Cascades. Final Report. DDA: EDR 8224; 1974.

219. Yaonan H. Computation of the Detached Shock and the Entrance Flow Field in a Supersonic or Transonic Cascade. ASME 1985 Gas Turbine Conference and Exhibit. 18-21 March, Houston, Texas, United States of America: 85-GT-7; 1985. pp. 1–8.

220. Schobeiri MT. Advanced Compressor Loss Correlations, Part I: Theoretical Aspects. Int. J. Rotating Machinery. 1997; 3(3): 163–177.

221. Klapproth JF. General Considerations of Mach Number Effects on Compressor-Blade Design. NACA Research Memorandum. Lewis Flight Propulsion Laboratory, Cleveland, Ohio, United States of America: NACA RM E53L23a; 1954. pp. 1–24.

222. Balzer RL. A Method for Predicting Compressor Cascade Total Pressure Losses When the Inlet Relative Mach Number is Greater Than Unity. Trans. ASME J. Engineering for Power. 1971; 93(1): 119–124.

223. Gustafson B-A. A Simple Method for Supersonic Compressor Cascading Performance Prediction. ASME 1976 Int. Gas Turbine and Fluids Engineering Conference Show. 21-25 March, New Orleans, Lousianaa, United States of America: 76-GT-64; 1976. pp. 1–10.

224. Love ES. Pressure Rise Associated with Shock-Induced Boundary-Layer Separation. NACA Technical Note. Langley Aeronautical Laboratory, Langley Field, Virginia, United States of America: NACA TN 3601; 1955. pp. 1–32.

225. Starken H. Untersuchung der Strömung in ebenen Überschallverzögerungsgittern. DLR FB. Cologne, Germany; 1970. pp. 71–99.

226. Fottner L. Ein halempirisches Verfahren zur Bestimmung der reibungabehafteten transsonischen Schaufelgitterstromung mit Einschluss von Uberschallefeldern und Verdichtungastossen. Dissertation Thesis. TH Munchen, Munich, Germany; 1970.

227. Urasek DC., Moore RD., Qsborn WM. Performance of a Single-Stage Transonic Compressor with a Blade-Tip Solidity of 1.3. NASA Technical Memorandum. Lewis Research Center, Cleveland, Ohio, United States of America: NASA TM X-2645; 1972. pp. 1–106.

228. Ball CL., Janetzke DC., Reid L. Performance of 1380 foot per second Tip-Speed Axial-Flow Compressor Rotor Blade Tip Solidity of 1.5. NASA Technical Memorandum. Lewis Research Center, Cleveland, Ohio, United States of America: NASA TM X-2379; 1972. pp. 1–99.

229. Osborn WM., Urasek DC., Moore RD. Performance of a Single-Stage Transonic Compressor with a Blade-Tip Solidity of 1.5 and Comparison with 1.3- and 1.7-Solidity Stages. NASA Technical Memorandum. Lewis Research Center, Cleveland, Ohio, United States of America: NASA TM-X-2926; 1973. pp. 1–98.

230. Haslam-Jones TF. The Application of a subsonic throughflow analysis method to axial compressors with some transonic blade rows. Proceedings IMechE Conference Computational Methods in Turbomachinery. N/A: Paper C60/84; 1984. pp. 19–24.

231. Moore RD., Reid L. Performance of Single-Stage Axial-Flow Transonic Compressor with Rotor and Stator Aspect Ratios of 1.63 and 1.77, Respectively, and with Design Pressure Ratio of 2.05. NASA Technical Paper. Lewis Research Center, Cleveland, Ohio, United States of America: NASA TP-2001; 1982. pp. 1–115.

232. Urasek DC., Kovich G., Moore RD. Performance of Transonic Fan Stage with Weight Flow per Unit Annulus Area of 208 Kilograms per Second per Square Meter (42.6 (lb/sec)/ft^2). NASA Technical Memorandum. Lewis Research Center, Cleveland, Ohio, United States of America: NASA TM X-2903; 1973. pp. 1–96.

233. Reid L., Tysl ER. Performance of a Transonic Compressor Rotor with an Aspect Ratio of 6.5. NASA Technical Note. Lewis Research Center, Cleveland, Ohio, United States of America: NASA TN D-7662; 1974. pp. 1–66.

234. Urasek DC., Steinke RJ., Lewis GW. Performance of Inlet Stage of Transonic Compressor. NASA Technical Memorandum. Lewis Research Center, Cleveland, Ohio, United States of America: NASA TM X-3345; 1976. pp. 1–71.

235. Moore RD., Lewis Jr. GW., Osborn WM. Performance of a Transonic Fan Stage Designed for a Low Meridional Velocity Ratio. NASA Technical Paper. Lewis Research Center, Cleveland, Ohio, United States of America: NASA TP-1298; 1978.

236. Hathaway MD. Unsteady Flows in a Single-Stage Transonic Axial-Flow Fan Stator Row. NASA Technical Memorandum. Lewis Research Center, Cleveland, Ohio, United States of America: NASA TM-88929; USAAVSCOM-TR 86-C-29; 1986. pp. 1–200.

237. Schwenk FC., Lewis GW., Lieblein S. Experimental Investigation of an Axial-Flow Compressor Inlet Stage Operating at Transonic Rel Inlet Mach No. NASA Research Memorandum. Lewis Flight Propulsion Laboratory, Cleveland, Ohio, United States of America: RM E56J17; 1957. pp. 1–45.

238. Moore RD., Reid L. Performance of Single-Stage Axial-Flow Transonic Compressor with Rotor and Stator Aspect Ratios of 1.63 and 1.77, Respectively, and with Design Pressure Ratio of 2.05. NASA Technical Paper. Lewis Research Center, Cleveland, Ohio, United States of America: NASA TP-1659; 1980. pp. 1–102.

239. Cahill JE. Identification and Evaluation of Loss and Deviation Models for use in Transonic Compressor Stage Performance Prediction Identification and Evaluation of Loss and Deviation Models for use in Transonic Compressor Stage Performance Prediction. 1997;

240. Gopalakrishnan S., Bozzola R. A Numerical Technique for the Calculation of Transonic Flows in Turbomachinery Cascades. ASME 1971 Int. Gas Turbine and Fluids Engineering Conference and Products Show. 28 March - 1 April, Houston, Texas, United States of America: 71-GT-42; 1971. pp. 1–10.

241. Belotserkovskii OM. On the calculation of flow past axisymmetric bodies with detached shock waves using an electronic computing machine. J. Applied Mathematics and Mechanics. 1960; 24(3): 511–517.

242. Der Jr. J., Mullings BN., Hoffman GH., Pridmore Brown BN. Numerical Analysis of Supersonic Flow Through Curved Channels. ARL Report. Aerospace Research Laboratories, Air Force Systems Command, Wright-Patterson Air Force Base, Dayton, Ohio, United States of America: ARL 63-117; 1963. pp. 1–280.

243. Rigaut F. A Numerical Technique for the Calculation of Transonic Flows in Turbomachinery Cascades. NATO Advisory Group for Aerospace Research and Development Report. Neuilly sur Seine, France: AGARD-CP-35; 1971.

244. Horlock JH. Choking Effects in the Blade Rows of Turbomachines. J. Mechanical Engineering Science. 1980; 22(4): 161–173.

245. Boyer KM., O'Brien WF. An Improved Streamline Curvature Approach for Off-Design Analysis of Transonic Axial Compression Systems. ASME Turbo Expo 2002: Power for Land, Sea and Air. 3-6 June, Amsterdam, The Netherlands: GT-2002-30444; 2002. pp. 1–9.

246. Urasek DC., Gorrell WT., Cunnan WS. Performance of Two-Stage Fan Having Low-Aspect Ratio, First-Stage Rotor Blading. NASA Technical Paper. Lewis Research Center, Cleveland, Ohio, United States of America: NASA TP-1493; AVRADCOM TR 78-49; 1979. pp. 1–131.

247. Jackson R., W NB., Boston A. The efficient modeling of blade lean effects within the turbomachinery throughflow method. Int. J. Heat and Fluid Flow. 1989; 10(1): 32–39.

248. Anderson JD. Modern compressible flow: with historical perspective. 3rd edn. New York, New York, United States of America: McGraw-Hill; 2002. 1-776 p.

249. Maccoll JW., Codd J. Theoretical Investigations of the Flow around Various Bodies in the Sonic Region of Velocities. Min. of Supply Theoretical Research

Report. Armament Research Department, United Kingdom: No. 17; 1945. pp. 1–45.

250. Liepmann HW., Ashkenas H., Cole JD. Experiments in Transonic Flow. U.S. Air Force Technical Report. Wright-Patterson Air Force Base, United States of America: TR 5667; 1947.

251. Walsh PP., Fletcher P. Gas Turbine Performance. 1st edn. Oxford, United Kingdom: Blackwell Sciende; 1998. 628 p.

252. Hobbs DE., Neubert RJ., Malmborg EW., Philbrick DH., Spear DA. Low Noise Research Fan Stage Design. NASA Contract Report. Lewis Research Center, Cleveland, Ohio, United States of America: NASA CR-195382; 1995. pp. 1–60.

253. Holcombe V. Aero-Propulsion Technology (APT) Task V-Low Noise ADP Engine Definition Study. NASA Contract Report. Washington, D.C., United States of America: NASA CR-2003-212521; 2003. pp. 1–74.

254. Tweedt DL. Computational Aerodynamic Simulations of an 840 ft / sec Tip Speed Advanced Ducted Propulsor Fan System Model for Acoustic Methods Assessment and Development. NASA Contract Report. Washington, D.C., United States of America: NASA CR-2014-218129; 2014. pp. 1–60.

255. Gelder TF., Schmidt JF., Suder KL., Hathaway MD. Design and performance of Controlled-Diffusion Stator Compared with Original Double-Circular-Arc Stator. NASA Technical Paper. Lewis Research Center, Cleveland, Ohio, United States of America: NASA TP-2852; AVSCOM TR-88-C-013; 1989. pp. 1–80.

256. Jeracki RJ. Comprehensive Report of Fan Performance From Duct Rake Instrumentation on 1.294 Pressure Ratio, 806 ft/sec Tip Speed Turbofan Simulator Models. NASA Technical Memorandum. Glenn Research Center, Cleveland, Ohio, United States of America: NASA TM-2006-213863; 2006. pp. 1–147.

257. Mehdi A. Effect of Swirl Distortion on Gas Turbine Operatbility. PhD Thesis. Cranfield University, School of Engineering, Cranfield, United Kingdom; 2014.

pp. 1–256.

258. Dicugno D. Inlet Swirl Distortion in Gas Turbine Fan S-Duct Inlets. PhD Thesis. Cranfield University, School of Engineering, Cranfield, United Kingdom; 2014. pp. 1–258.

259. Schaefer JW., Sagerser DA., Stakolich EG. Dynamics of High-Bypass-Engine Thrust Reversal Using a Variable-Pitch Fan. NASA Technical Memorandum. Washington, D.C., United States of America: NASA TM X-3524; 1977. pp. 1–34.

260. Neitzel R., Lee R., Chamay AJ. QCSEE Task II Final Report: Engine and Installation Preliminary Design. NASA Contract Report. Lewis Research Center, Cleveland, Ohio, United States of America: NASA CR-134738; 1973. pp. 1–351.

261. Zanenga ES. Design and Engineering Methods for Open-Rotor Nacelle Shaping. PhD Thesis. Cranfield University, School of Engineering, Cranfield, United Kingdom; 2010. pp. 1–231.

262. Salomon D. The Computer Graphics Manual Volume 2. 1st edn. London, United Kingdom: Springer; 2011. 1-1496 p.

263. Turner MG., Merchant A., Bruna D. A Turbomachinery Design Tool for Teaching Design Concepts for Axial-Flow Fans, Compressors, and Turbines. ASME J. Turbomachinery. 2011; 133(3): 1–12.

264. Genrup M., Carlsson I., Engdar U., Assadi M. A Reduced-Order Through-Flow Program for Choked and Cooled Axial Turbines. ASME Turbo Expo 2005: Int. Gas Turbine & Aeroengine Congress. 6-9 June, Reno, Nevada, United States of America: GT2005-68716; 2005. pp. 1161–1168.

265. Mattingly JD., Heiser WH., Pratt DT. Aircraft Engine Design. 2002.

266. Mattingly JD. Elements of Gas Turbine Propulsion. AIAA Education Series; 2005.

267. Gelder TF., Soltis RF. Inlet Noise of 0.5-Meter-Diameter NASA QF-1 Fan as

Measured in an Unmodified Compressor Aerodynamic Test Facility and in an Anechoic Chamber. NASA Technical Note. Lewis Research Center, Cleveland, Ohio, United States of America: NASA TN D-8121; 1975. pp. 1–97.

268. Gelder TF., Lewis Jr. GW. Aerodynamic Performance of 0.5-Meter-Diameter, 337-Meter-per-Second Tip Speed, 1.5-Pressure-Ratio, Single-Stage Fan Designed for Low Noise Aircraft Engines. NASA Technical Note. Lewis Research Center, Cleveland, Ohio, United States of America: NASA TN D-7836; 1974. pp. 1–182.

269. Steinke RJ. Design of 9.271-Pressure-Ratio Five-Stage Core Compressor and Overall Performance for First Three Stages. NASA Technical Paper. Lewis Research Center, Cleveland, Ohio, United States of America: NASA TP-2597; 1986. pp. 1–34.

270. Urasek DC., Cunnan WS., Stevans W. Performance of Two-Stage Fan with Larger Dampers on First-Stage Rotor. NASA Technical Paper. Lewis Research Center, Cleveland, Ohio, United States of America: NASA TP-1399; 1979. pp. 1–78.

BIBLIOGRAPHY

Brown N., Royce. (1986). Compressors Selection and Sizing. 2nd Ed. *Gulf Publishing Company*. Houston. pp. 552.

Cohen H., Rogers G. F. C., Saravanamuttoo H. I. H. (1996). 4th Ed. *Longman Group Limited*. London. pp. 442.

Horlock, J. H. (1958). Axial Flow Compressors. 1st Ed. *Butterworths Scientific Publications*. London. pp. 189.

Lakshminarayana B.. (1996). Fluid Dynamics and Heat Transfer of Tubomachinery. 1st Ed. *AIAA, Inc*. New York. pp. 551.

McKenzie, A. B. (1997). Axial Flow Fans and Compressors. 1st Ed. *Ashgate Publishing Limited*. Suffolk. pp. 267.

Oates G. O. (1985). Aerothermodynamics of Aircraft Engine Components. 1st Ed. *John Wiley & Sons Inc*. New York. pp. 809.

Whittle, F. (1981). Gas Turbine Aero-Thermodynamics. 1st Ed. *Pergamon Press*. Oxford. pp. 261.

APPENDICES

Appendix A Approximation Methods for the Geometry Layout in Analysis and Optimisation

A.1 Overview

As part of a sanitization process of SOCRATES for further enhancement, the generated compressor flow path geometry modelling was reviewed. Before describing the approximating curves used to model the flow path, it is attempted to provide the reader with a brief overview on innovative curve-geometry shaping in Sec. Curve Geometric Shaping A.2. Later, the curve-fitting techniques implemented in SOCRATES, Bezier curve and cubic B-spline approximations, are detailed in Sec. A.3.

A.2 Curve Geometric Shaping

When the shape of parametric curves or surfaces is designed smooth or fair manner, it is said that geometric continuity exists. A spline is a set of polynomial curves of degree *k* that are smoothly connected at certain points, where each single curve is a parametric function. A parametric function only exists between 0 and 1. The equations that join these segments to form the spline, which provide different levels of smoothness, are called geometric continuity constraints. The geometric continuity degrees are:

- G0 - connection
- G1 - tangency
- G2 - curvature
- G3 - rate of change of curvature

Functions to express a curve can be expressed as a parameter. Similar to geometric continuity degrees, the parametric continuity levels are C0, C1, C2 and C3, which correspond to the geometric continuity description. In fact, parametric continuity implies geometric continuity; nonetheless, geometric continuity does not imply parametric continuity.

The maximum order of parametric continuity that can be achieved is *k*-1, where *k* is the polynomial degree. For instance, to have a C1 continuity in a curve, a second-degree

polynomial is required. To create a C2 continuity, the typical methods to use are: Cubic, Cubic Hermite spline (obtain the derivatives at each interpolated point), Cardinal spline (evaluate the derivatives at each interpolated point), Kochanec-Bartels (Cardinal spline special case), Catmull-Rom (Kochanec/Bartels special case). In theory if a third-order polynomial is used in a curve, a C2 parametric continuity can be achieved, however, this is not always true for the case of a 4^{th} order or higher polynomial, where a C3 parametric continuity cannot always be obtained. The ability to obtain a C3 depends on the values of the positional and derivational conditions entered by the user.

For aerodynamics, a high order geometric continuity is desired to obtain flow smoothness, and hence, reduce drag and energy losses, particularly at high velocities. For an aerofoil, a G0 and G1 are acceptable near the stagnation point; however, moving downstream from stagnation point, G2 and G3 are more desired.

The most common parametric curves used in Computer Aided Geometry Design (CAGD) are the Non-Uniform Rational B-Spline (NURBS), Bezier curves and B-Splines. In general, Bezier curves are a special case of the B-splines curves, while NURBS curves are an extension of the B-Spline curves that cope the Bezier curve limitations of inaccurately representing conic curves. To shape a geometry in CAGD, the software code uses two methods: curve-fitting techniques and approximation techniques. In the former, points are set to be fitted through a cubic spline approximation, leading in a misplacement of the resultant curve with respect of the original points. In the latter, three main elements are involved: control points, knots and weights.

Any of the aforementioned geometry shaping methods can be modified through its parameters to achieve a smooth line, which can result in a significant difference between the approximated curve and the actual curve that must pass through the points. In other words, curve smoothness and accuracy are two contradictory concepts for which a trade-off should be found. For this reason, Zanenga [261] developed an interpolation technique to overcome the above limitations, consisting in setting and controlling the tangency and constraints of the defined control points. The interpolation consists in connecting two points by creating a segment, where the segment is a

polynomial curve or function, which can be linear, quadratic, cubic, quartic, quantic, cardinal, Catmull-Rom or Kochanec-Bartels.

A.3 Bezier Curve and Cubic B-spline Approximation

A.3.1 Cubic B-Spline Approximation

Originally, SOCRATES flow path geometry interpolation was represented using a cubic spline approximation. Computer Aided Design (CAD) software mostly uses the cubic B-spline curve approximation to join scattered points through a visually-smooth path, which guarantees G2 and C2 without introducing complex wiggling shapes from G3 and C3 [262]. For this reason, the cubic B-spline curve approximation was used to compare and validate the cubic spline approximation implemented in SOCRATES.

To describe a cubic B-spline in a parametric manner, the third-degree polynomial curve *P* of the parameter *t* that approximates to the points to be fitted is defined as:

$$P_i(t) = [t^3\ t^2\ t\ 1]M\begin{pmatrix} P_{i-1} \\ P_i \\ P_{i+1} \\ P_{i+2} \end{pmatrix} = [t^3\ t^2\ t\ 1]\begin{bmatrix} a_3 & b_3 & c_3 & d_3 \\ a_2 & b_2 & c_2 & d_2 \\ a_1 & b_1 & c_1 & d_1 \\ a_0 & b_0 & c_0 & d_0 \end{bmatrix}\begin{pmatrix} P_{i-1} \\ P_i \\ P_{i+1} \\ P_{i+2} \end{pmatrix} =$$

$$[a(t) \quad b(t) \quad c(t) \quad d(t)]\begin{pmatrix} P_{i-1} \\ P_i \\ P_{i+1} \\ P_{i+2} \end{pmatrix} \quad 0 \le t \le 1 \tag{A.3.1}$$

Where the subscript *i* represents the curve point and *M* is the Hermite basis matrix. To get $P_i(t)$, the terms $a(t) \quad b(t) \quad c(t) \quad d(t)$, need to be found. As it can be seen from Eq. A.3.1, a cubic B-spline needs of four points to be built. To guarantee C2 continuity while connecting these points, position, first derivative, and second derivative constraints are set for two adjacent points:

$$P_i(1) = P_{i+1}(0) \tag{A.3.2}$$

$$P_i'(1) = P_{i+1}'(0) \tag{A.3.3}$$

$$P_i''(1) = P_{i+1}''(0) \tag{A.3.4}$$

The above constraints make possible the solution of Eq. A.3.1, resulting in 16 equations, which can be summarized as:

$$P_i(t) = \frac{1}{6}[t^3\ t^2\ t\ 1]\begin{bmatrix} -1 & 3 & -3 & 1 \\ 3 & -6 & 3 & 0 \\ -3 & 0 & 3 & 0 \\ 1 & 4 & 1 & 0 \end{bmatrix}\begin{pmatrix} P_{i-1} \\ P_i \\ P_{i+1} \\ P_{i+2} \end{pmatrix} \quad 0 \le t \le 1 \quad \text{(A.3.5)}$$

Eq. A.3.5 represents the parametric cubic B-spline approximation, which was programmed in SOCRATES to be used as .dll and .lib files, to interpolate between given points; for instance, between the given flow path point coordinates. The above equation is only to define one single cubic B-spline curve, hence, if there are more than four points to be joined, a set of cubic B-spline polynomial segments will be required.

A.3.2 Bezier Curve Approximation

A Bezier curve is a parametric curve *P*(*t*), that is a polynomial function of the parameter *t*. Control points are set to shape the curve; however the curve does not pass through these points as they only "pull" the curve towards them as observed in Figure A.1. Consequently, the curve (Bezier) that is generated and controlled by the control points is smooth.

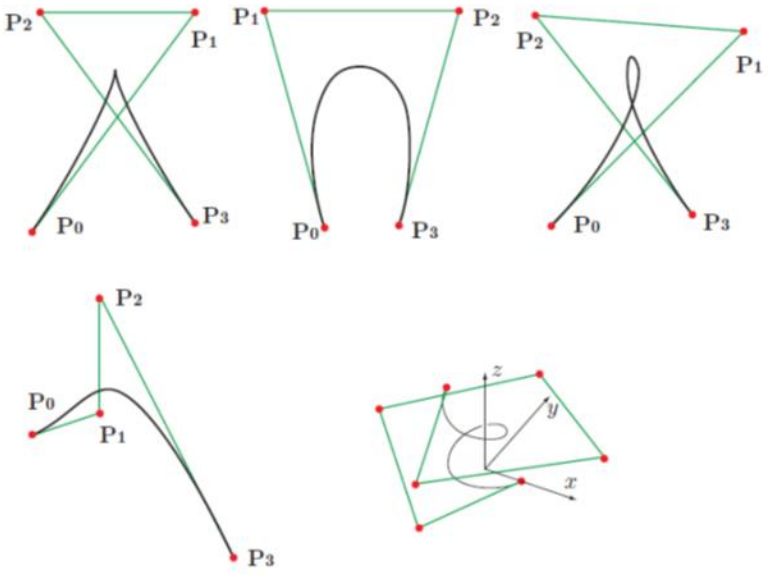

Figure A.1 Control points defining a Bezier curve [262].

The number of control points determines the polynomial degree *n* through,

$$n = control\ points - 1 \tag{A.3.6}$$

There are 2 approaches to model the Bezier curve: Bernstein polynomial and mediation operator. The Bernstein polynomial consists that every control point P_i is multiplied by a weight function B_i that acts as blending,

$$P(t) = \sum_{i=0}^{n} P_i B_i(t) \quad 0 \le t \le 1 \tag{A.3.7}$$

The maximum of the weight function depends on the number of control points, and hence, on the polynomial degree. Hence, $B_i(t)$ becomes $B_{n,i}(t)$, which represents the Bernstein polynomial. Thus, Eq. 3.2.7 becomes,

$$P(t) = \sum_{i=0}^{n} P_i \binom{n}{i} t^i (1-t)^{n-i} \quad 0 \le t \le 1 \tag{A.3.8}$$

If a shift operator is defined as

$$E^i P_i = P_{i+1} \tag{A.3.9}$$

Then, Bezier curve definition from Eq. 3.2.8 becomes

$$P(t) = [tE + (1-t)]^n P_0 \tag{A.3.10}$$

Eq. A.3.10 is the general Bezier polynomial equation. For instance, for a case of n=1 or two control points, the Bezier curve polynomial gives

$$P(t) = (tE + 1 - t)P_0$$

$$P(t) = P_0(1-t) + P_1 t \tag{A.3.11}$$

In the case of n=2, Bezier curve polynomial is defined by

$$P(t) = (tE + 1 - t)^2 P_0$$

$$P(t) = P_0(1-t)^2 + 2P_1 t(1-t) + P_2 t^2 \tag{A.3.12}$$

Flexibility can be obtained through Bezier curves. For instance, instead of having a single large curve with several control points as in Figure A.2 a), the curve can be split into small segments as shown in Figure A.2 b).

a)

$$P(t) = P_0(1-t)^4 + 4P_1t(1-t)^3 + 6P_2t^2(1-t)^2 + 4P_3t^3(1-t) + P_4t^4$$

$n = 4$
5 control points

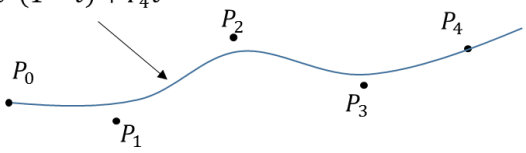

b)

$$P(t) = P_0(1-t)^2 + 2P_1t(1-t) + P_2t^2$$

$n = 2$
3 control points

$$P(t) = P_2(1-t)^2 + 2P_3t(1-t) + P_4t^2$$

$n = 2$
3 control points

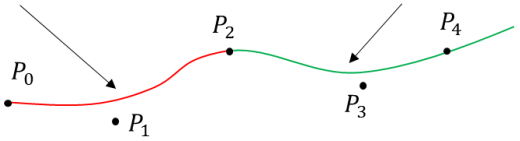

Figure A.2 Curve fitting through Bezier curve polynomial approximation. a) Single 4th-order Bezier curve. b) Two 2th-order Bezier curve segments.

The second approach for the Bezier curve is the mediation operator, consisting in the creation of an envelope from a set of lines as depicted in Figure A.3.

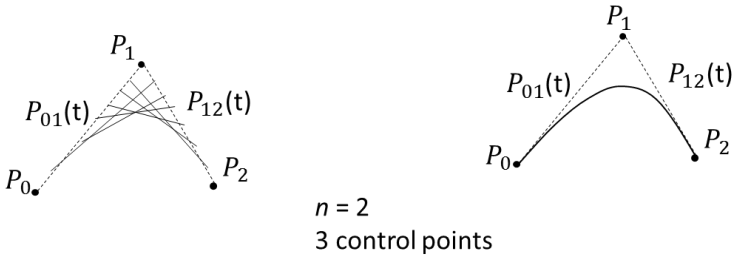

Figure A.3 Mediation operator approach for Bezier curve polynomial approximation.

Each segment from Figure A.3, is a linear parametric function which is described as

$$P_{01}(t) = P_0(1-t) + P_1t \tag{A.3.13}$$

$$P_{12}(t) = P_1(1-t) + P_2t \tag{A.3.14}$$

Then, the mediation operator is introduced to represent a linear parametric function between 2 control points:

$$t[[P_0, P_1]] = P_0(1-t) + P_1t \tag{A.3.15}$$

If there are more points, the mediation operator in a general form is

$$t\left[[P_0, \dots, P_n]\right] = t[[t\left[[P_0, \dots, P_{n-1}]\right], t\left[[P_0, \dots, P_{n-1}]\right]]] \quad \text{(A.3.16)}$$

Thus, for *n*=2 or three control points, the mediation operator gives the following Bezier curve polynomial:

$$t\left[[P_0, P_1, P_2]\right] = t\left[[P_{01}, P_{12}]\right] = t[[t\left[[P_0, P_1]\right], t\left[[P_1, P_2]\right]]] = t\left[[P_0(1-t) + P_1, P_1(1-t) + P_2 t]\right] = P_0(1-t)^2 + 2P_1 t(1-t) + P_2 t^2 \quad \text{(A.3.17)}$$

It can be seen that Eq. A.3.17 gives the same result as Eq. A.3.12, validating in this manner, the two approaches. Thence, Eq. A.3.16, as well as Eq. A.3.10, represents the general form of the Bezier curve polynomial equation.

In short, Bezier curve approximation provides smoothness for curve fitting. Nevertheless if given points are fit through Bezier approximation, the curve will not be passing through them, as they will function as control points. On the other hand, any kind of B-spline, either quadratic or cubic, overcome the Bezier-curve disadvatanges by offering the following features:

a) The polynomial degree do not depend on the number of control points
b) Offer local control instead of global control
c) High-continuity degrees can be achieved, while Bezier only gives C1 continuity.

Appendix B NASA Rotor 67 3-D CFD Simulation

Figure B.1 and Figure B.2 show the boundary conditions, absolute total pressure and absolute temperature, imposed to the 3-D CFD model. Despite of the choke conditions reached at the three lowest pressures, there is no upstream influence.

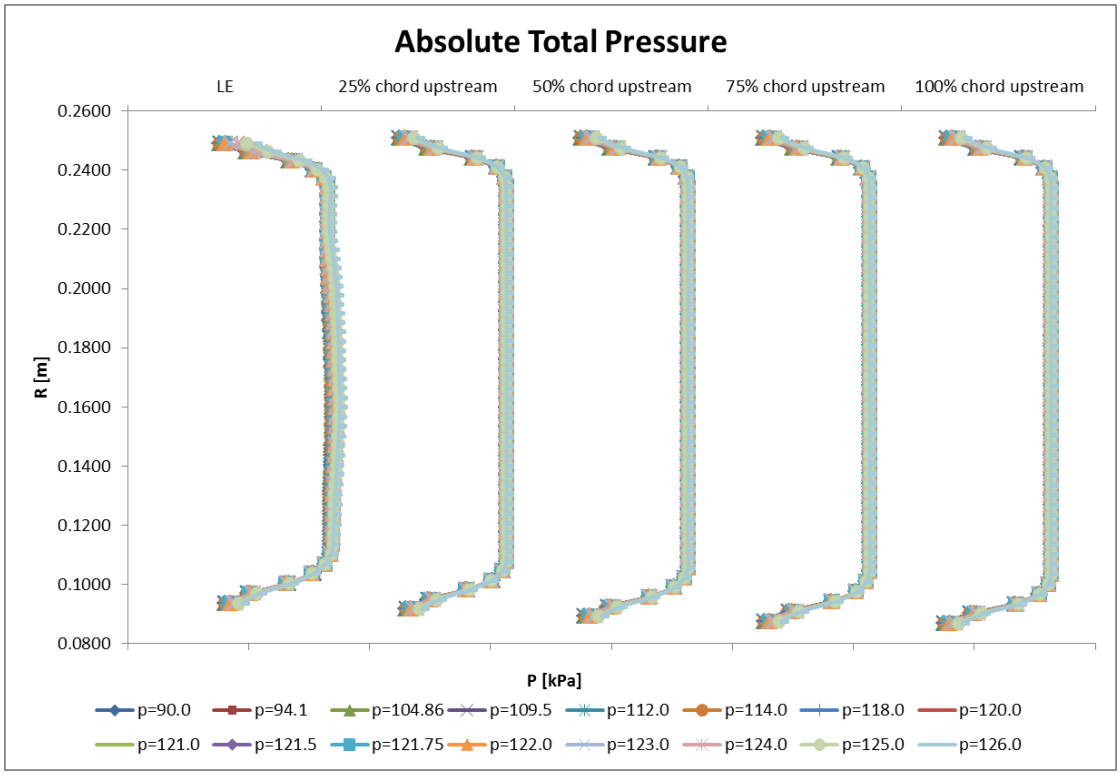

B. 1 Absolute total-pressure spanwise distribution for the NASA Rotor 67 at 100% of design speed for the leading edge, and 25, 50, 75 and 100% of chord upstream of the leading edge.

Figure B.3 and Figure B.4 demonstrate that there is no upstream influence due to choking operations, as the relative velocity and relative Mach number, respectively, remain unaffected. A closer look to the leading edge curves, shown in Figure B.5 and Figure B.6, reveal that the relative velocity and Mach number, respectively, increase with the mass flow at the tip up to a certain point where the mass flow do not change significantly, fixing the velocities. Moving farther down from tip to hub, the velocities are slightly increased due to the relative flow angle reduction to pass the mass flow withdrawn from the tip. Finally, Figure B.7 and Figure B.8 exhibit the necessity of mass flow redistribution to increase the velocities and Mach numbers, respectively, at the hub and fix them at the tip when choking is encountered.

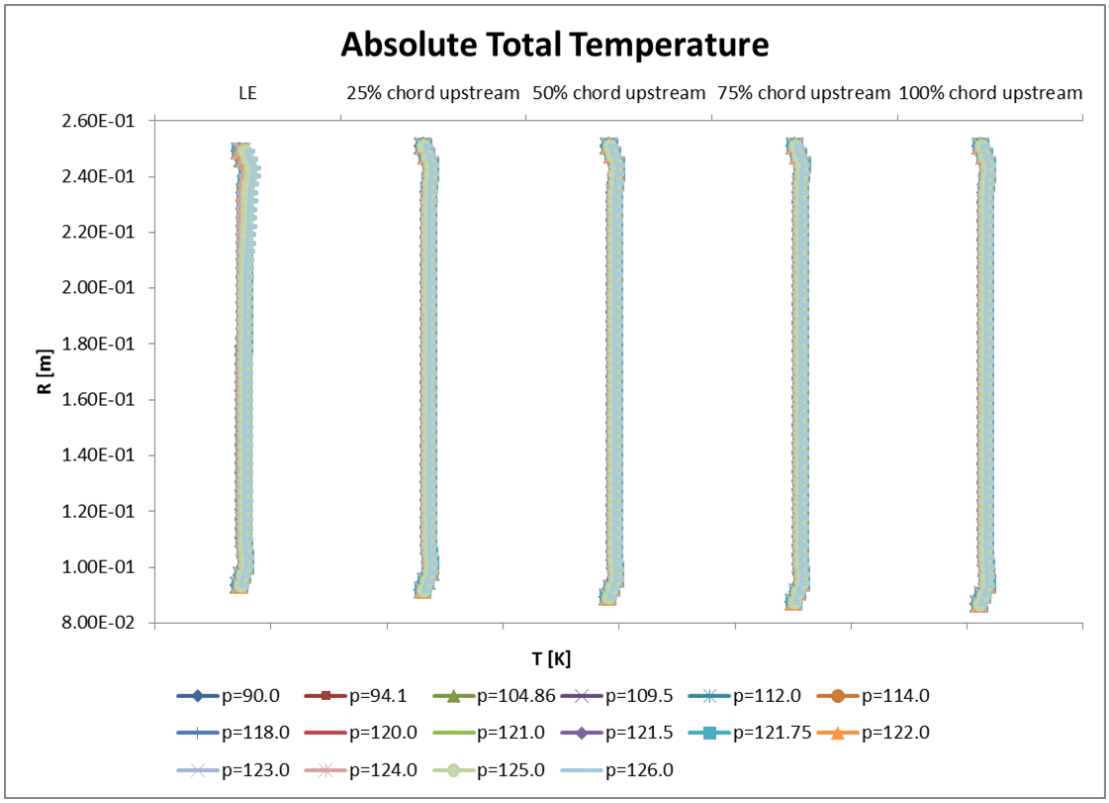

B. 2 Absolute total-temperature spanwise distribution for the NASA Rotor 67 at 100% of design speed for the leading edge, and 25, 50, 75 and 100% of chord upstream of the leading edge.

Similarly, Figure B.9 and Figure B.10 demonstrate that there is no upstream influence for those streamlines that are choked. Perturbations due to choking in the relative total-pressure and relative total-temperature are minimum. The relative total-pressure decay observed at the hub and the tip in Figure B.11 and Figure B.12 is due to the endwall boundary layer effect. Figure B.12 provides a closer look into the relative pressure deficit observed at the leading edge just below the tip, due to high-separated flow as a consequence of the near-stall condition, as is only present in high outlet static pressure off-design points.

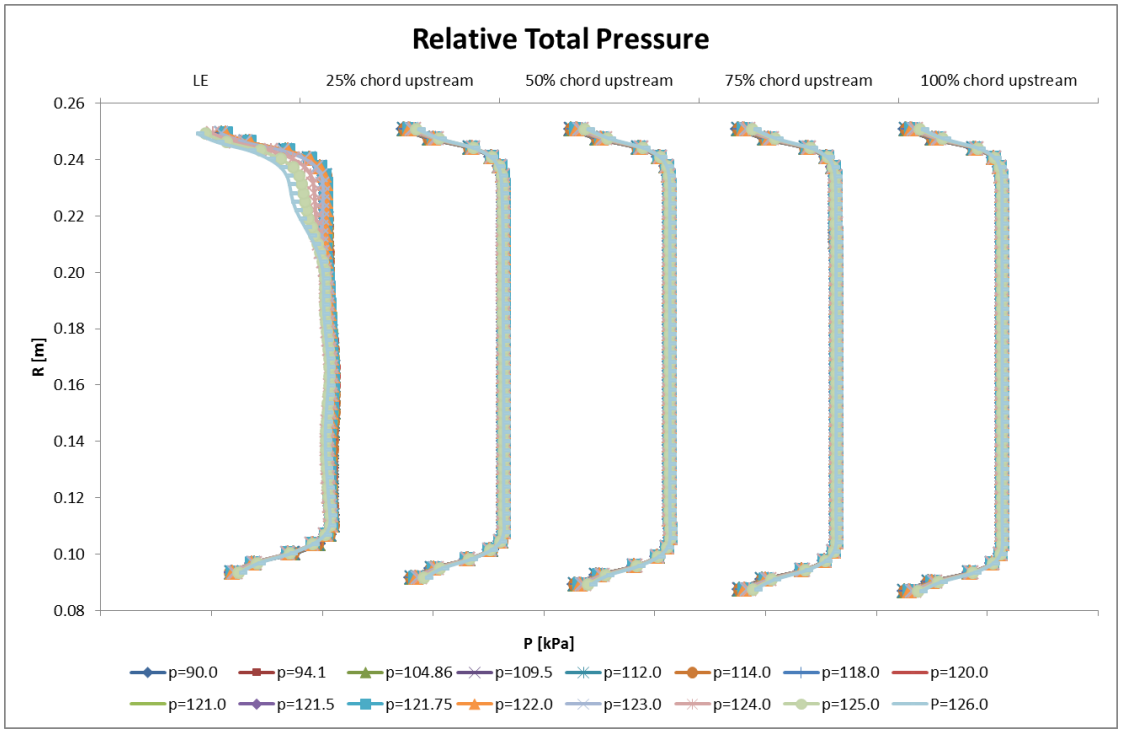

B. 3 Relative total-pressure spanwise distribution for the NASA Rotor 67 at 100% of design speed for the leading edge, and 25, 50, 75 and 100% of chord upstream of the leading edge.

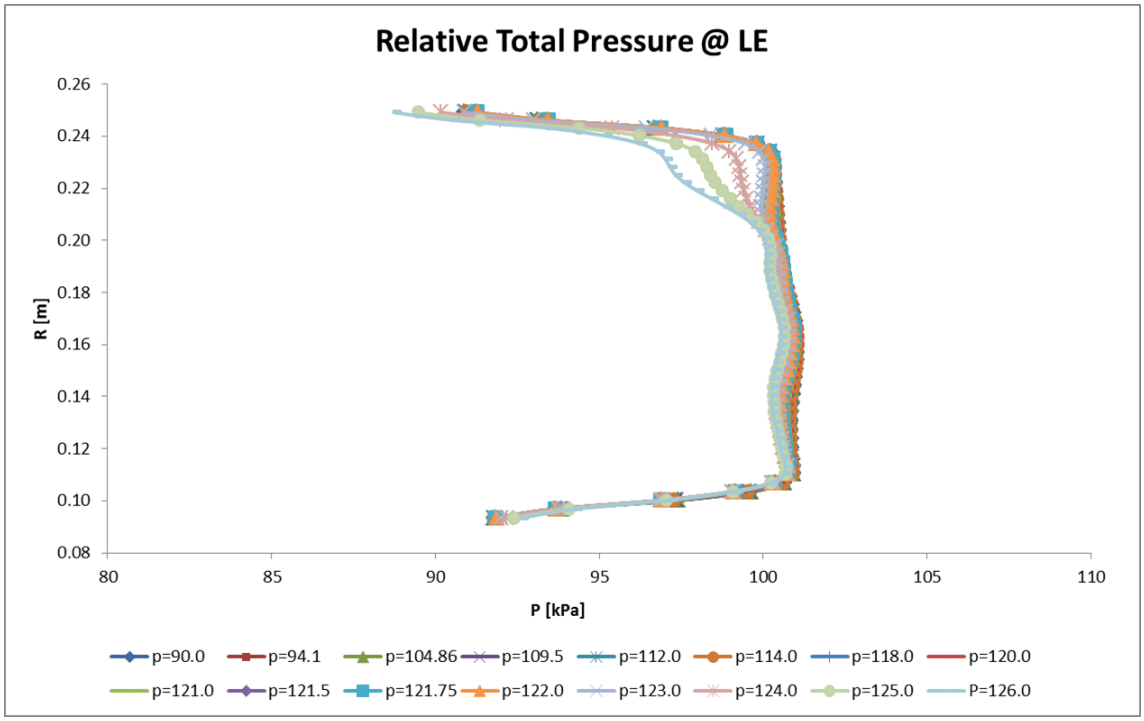

B. 4 Relative total-pressure spanwise distribution for the NASA Rotor 67 at 100% of design speed for the leading edge.

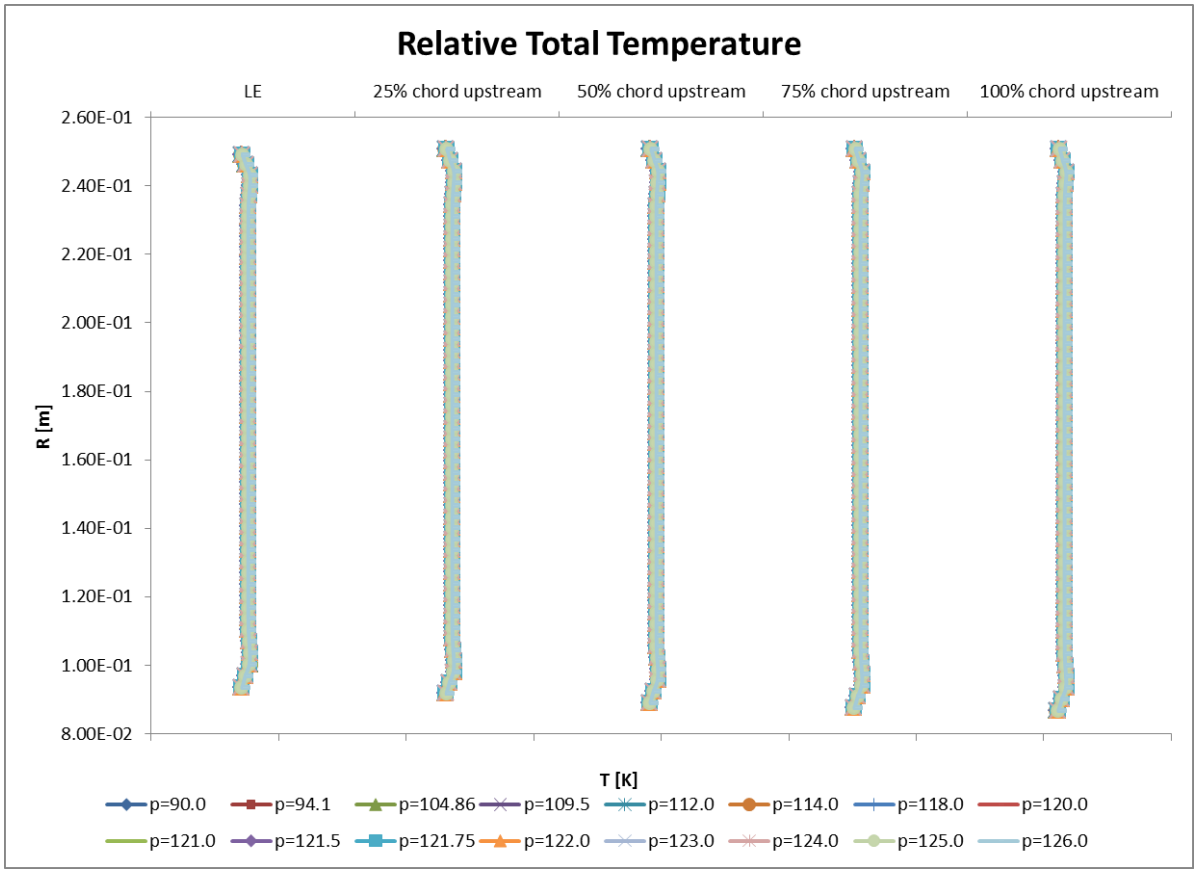

B. 5 Relative total-temperature spanwise distribution for the NASA Rotor 67 at 100% of design speed for the leading edge, and 25, 50, 75 and 100% of chord upstream of the leading edge.

As the 3-D CFD simulation was run with clean inlet conditions, the absolute flow angle is fixed around zero with small perturbations as seen in Figure B.12. In spite of the choking at the first three off-design points, the upstream absolute flow angle is unaffected, hence, there is no upstream influence as shown in Figure B.13.

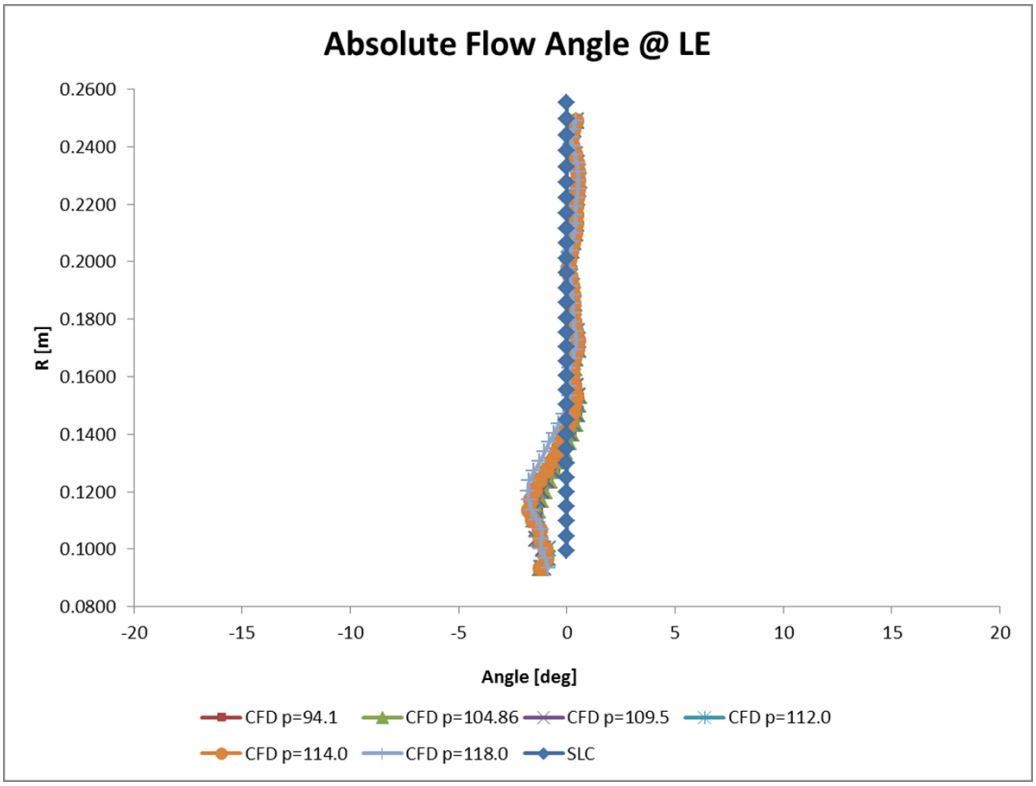

B. 6 Absolute flow angle spanwise distribution for the NASA Rotor 67 at 100% of design speed for the leading edge.

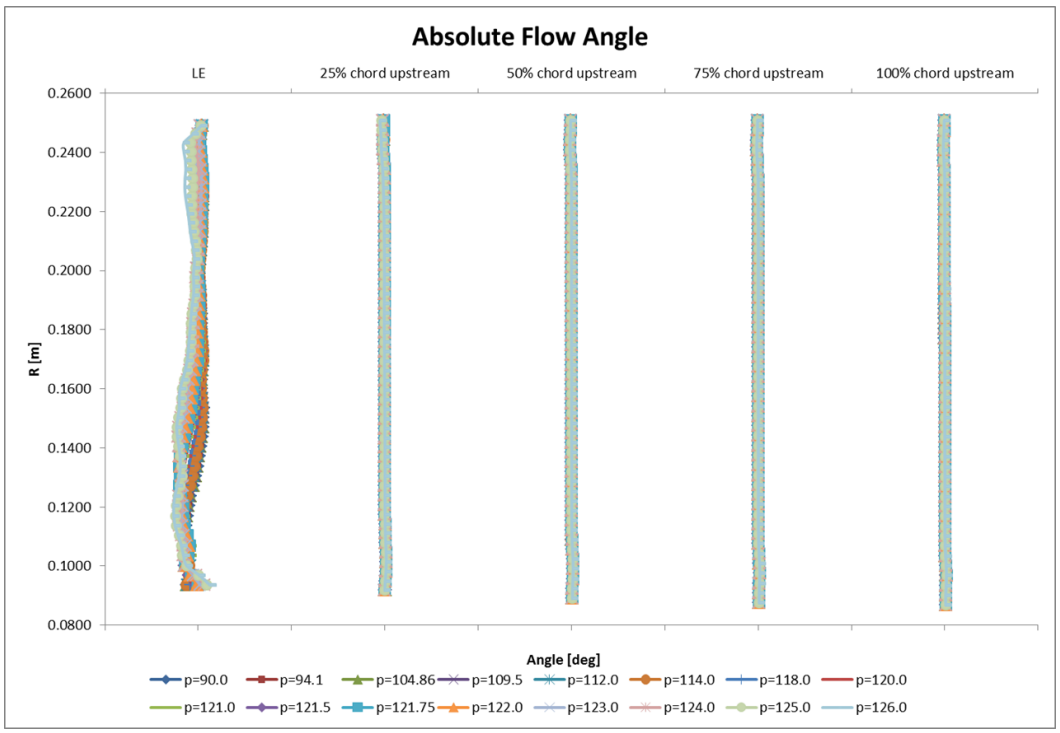

B. 7 Absolute flow angle spanwise distribution for the NASA Rotor 67 at 100% of design speed for the leading edge, and 25, 50, 75 and 100% of chord upstream of the leading edge.

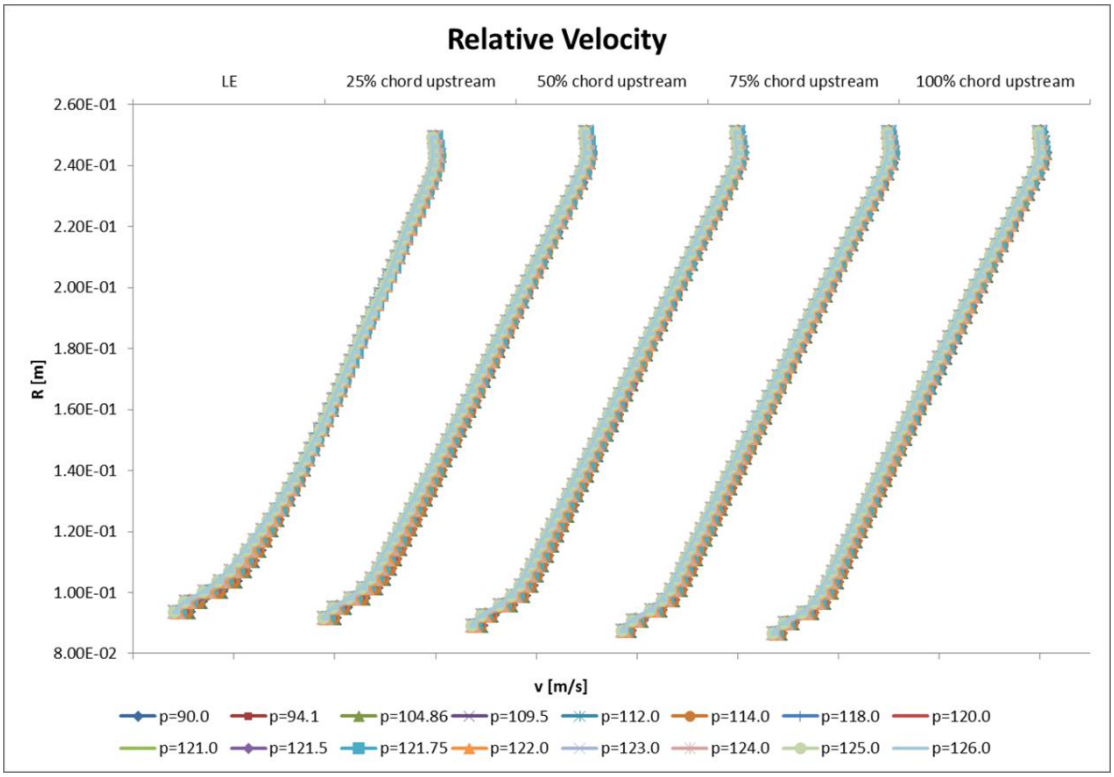

B. 8 Relative velocity spanwise distribution for the NASA Rotor 67 at 100% of design speed for the leading edge, and 25, 50, 75 and 100% of chord upstream of the leading edge.

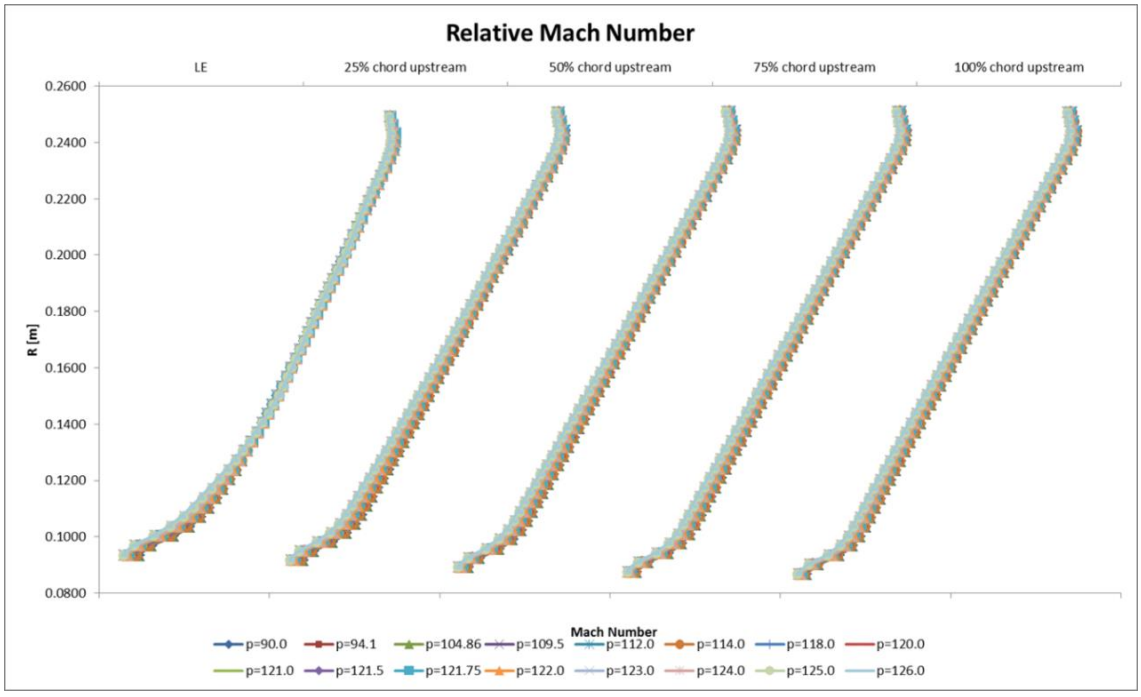

B. 9 Relative Mach number spanwise distribution for the NASA Rotor 67 at 100% of design speed for the leading edge, and 25, 50, 75 and 100% of chord upstream of the leading edge.

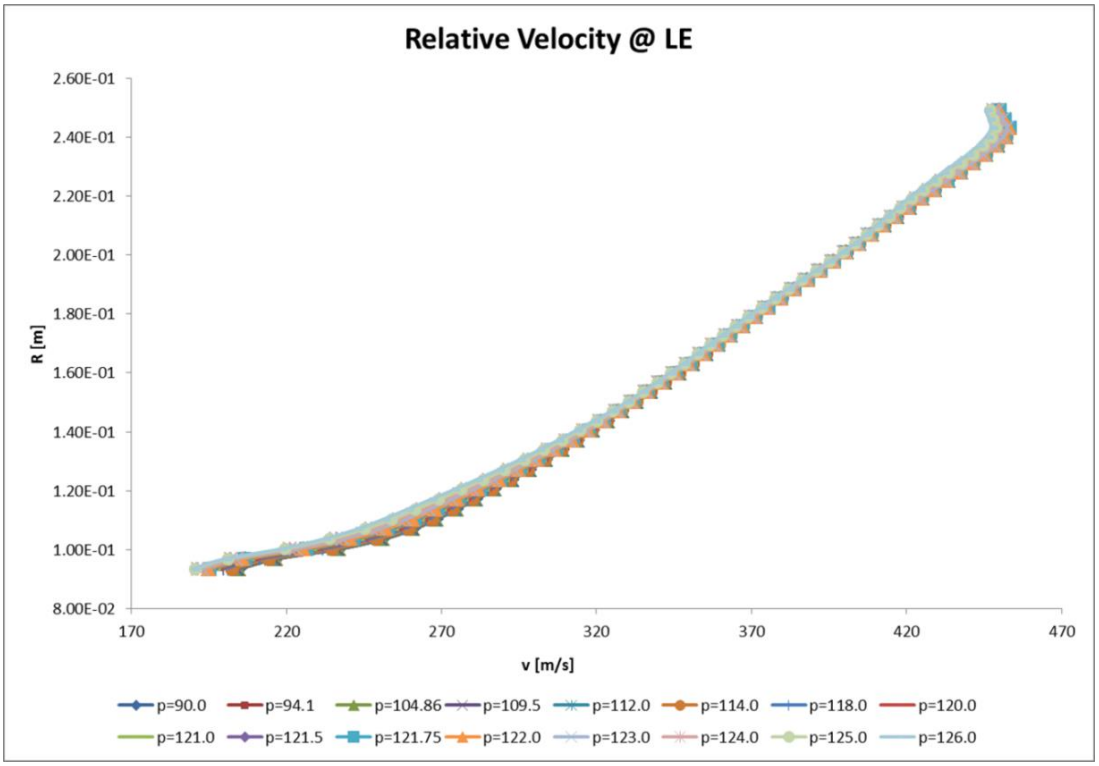

B. 10 Relative velocity spanwise distribution for the NASA Rotor 67 at 100% of design speed for the leading edge.

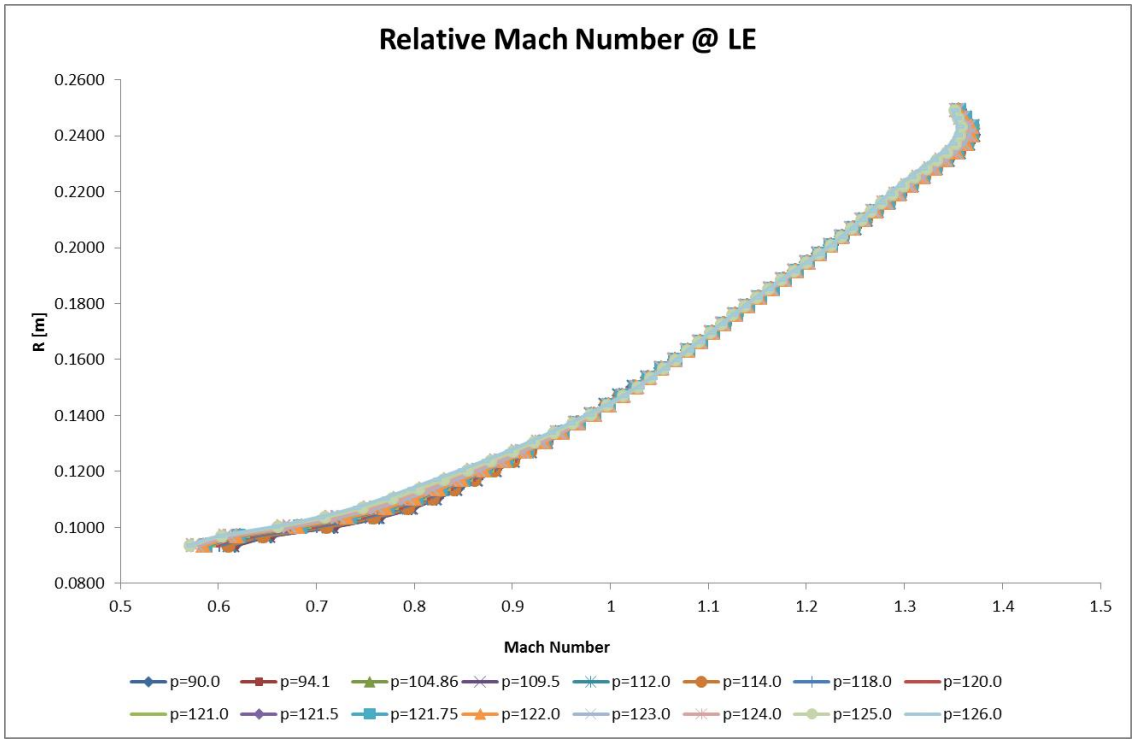

B. 11 Relative Mach number spanwise distribution for the NASA Rotor 67 at 100% of design speed for the leading edge.

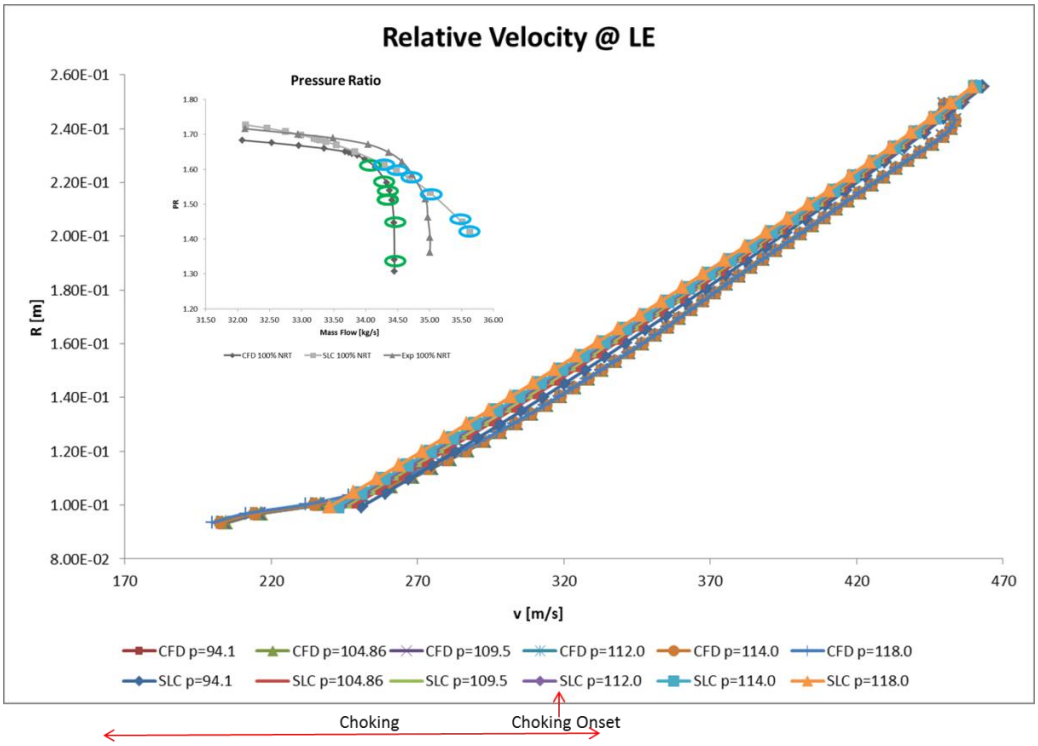

B. 12 Relative velocity spanwise distribution for the NASA Rotor 67 at 100% of design speed for the leading edge.

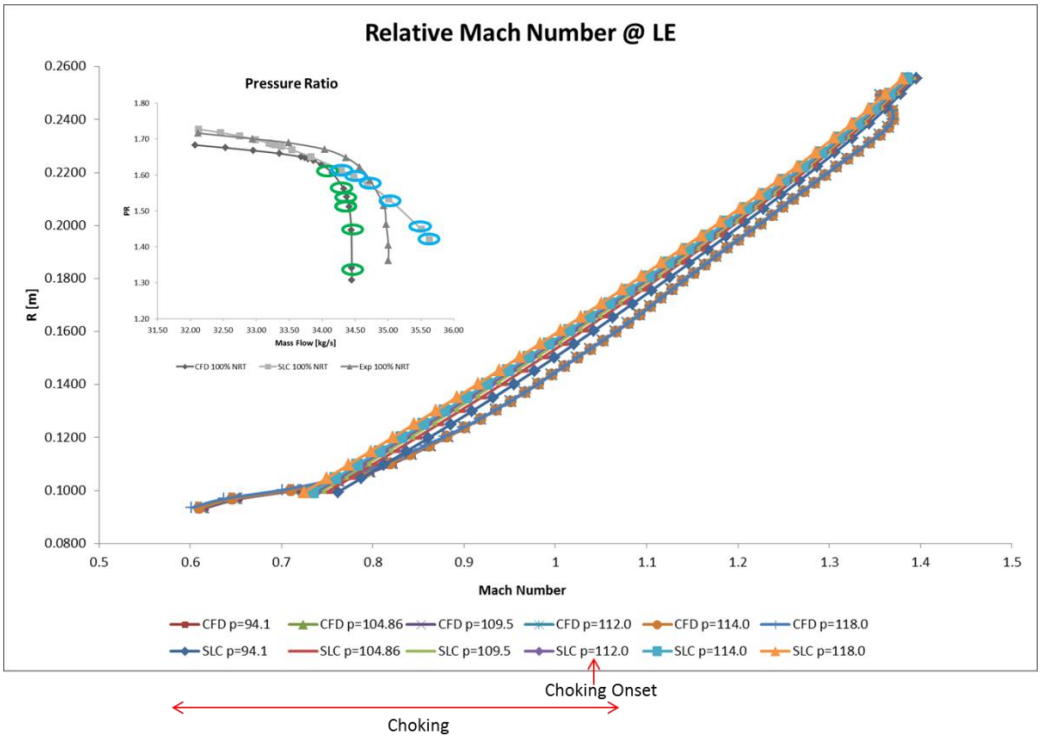

B. 13 Relative Mach number spanwise distribution for the NASA Rotor 67 at 100% of design speed for the leading edge.

Appendix C SOCRATES GUI Development

The all-time interest for developing robust and simple turbomachinery performance simulation tools since the first gas turbine generation has been expanding. In the last decades, more and more students and researchers from both, academia and industry, are getting involved in the air-breathing engine field. Unlike three-dimensional (3D) Reynolds-averaged Navier-Stokes numerical simulation codes, two-dimensional (2D) through-flow methods can provide a solution in minutes whilst offering acceptable results [14] [17] . In this context, there are very few open-source turbomachinery solvers that can be accessed [263], which have their own limitations. For instance, turbine codes have been made available, however, user needs to know the commercial package and have a license to run them [264]. Compressor and turbine algorithms have been generated as well, nevertheless, endwall blockage was not considered [265] [266]. A comprehensive axisymmetric streamline curvature design system was developed by Turner *et al*. [263], where input files are required to generate the compressor geometry and eventually, obtain the solution.

A two-dimensional streamline curvature axial-flow single-stage and multi-stage fan/compressor performance simulator, SOCRATES, was developed by Pachidis [14], Pachidis *et al*. [17] and Templalexis *et al*. [31], and further improved by Templalexis *et al*. [20] and Templalexis [118]. Software code was written in FORTRAN90. Templalexis *et al*. [20] explains the SOCRATES structure, where it can be found the code-word notation used for the variables and subroutines. In general, the 2-D SLC code works in 3 phases: input, iterative solution and outputs. In terms of the input files, the following data is processed: flow path geometry, blade leading and trailing edge row geometry, blade profile element data. Number of turbo-components, flow path points, blade row spanwise points, streamlines, speedline cases (called timesteps), and radial boundary points as established as general settings. Blockage factors and meridional mean-line velocities for each turbo-component are required as initialization values. Upon the boundary conditions, rotational speed, total temperature, total pressure, inlet mass flow or back static pressure are specified. Iterative solution scheme resolves the radial equilibrium equation to match the target mass flow or the outlet static pressure. The output files generated provide the flow field solution information for

every turbo-component and for every streamline. Additionally, for every speedline case, and for every turbocomponent, performance characteristics are obtained to build up the compressor map.

Considering that manually handling input files opens a window for errors and to avoid the user to familiarize with the FORTRAN syntaxis, a graphical-user-interface (GUI) was developed for SOCRATES. A schematic of the SOCRATES GUI process is shown in Figure C.1, where the main sections for inputs and outputs are laid-out. Figure C.2 shows the 3D representation for the NASA two-stage fan [246].

The following geometries have been modelled using the SOCRATES GUI to demonstrate the utilities, advantages, and the potential for academics to exploit the 2D SLC compressor performance simulation software: NASA rotor 67 [40], NASA rotor 66 [234], NASA two-stage fan [246], NASA QF-1 FAN [267] [268], NASA compressor 74A [269], and NASA two-stage fan with dampers [270].

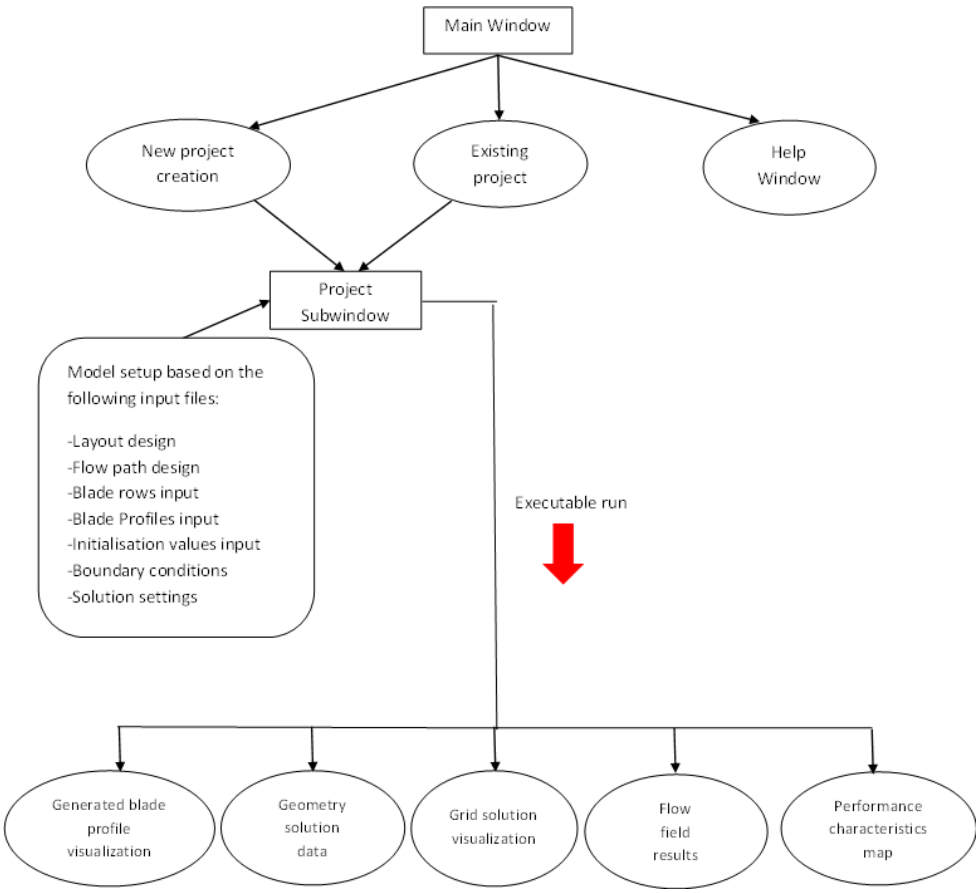

C. 1 Schematic to lay-out the SOCRATES GUI processes

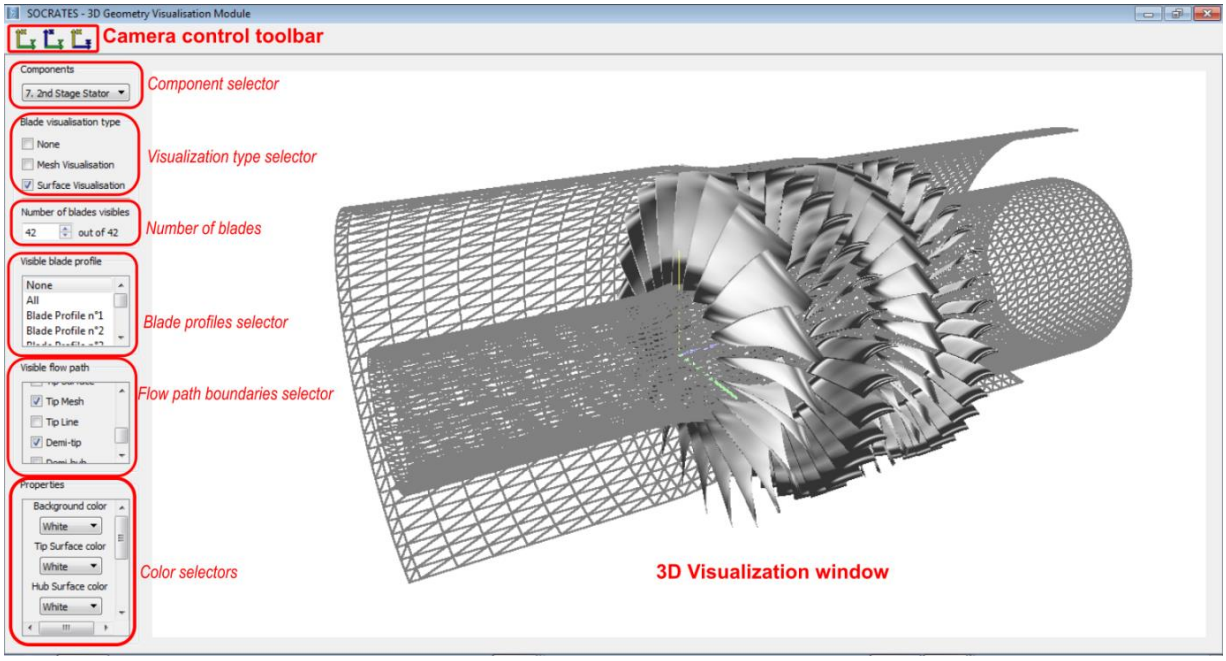

C. 2 3D Visualization for the NASA two-stage fan.